NGU REPORT 2018.010

Neotectonics in Nordland - Implications for petroleum exploration (NEONOR2)

GEOLOGY FOR SOCIETY

SINCE 1858

GEOLOGICAL SURVEY OF NORWAY

- NGU -

NORGES GEOLOGISKE UNDERSØKELSE
- NGU -

REPORT

GEOLOGY FOR SOCIETY

NORGES GEOLOGISKE UNDERSØKELSE
POSTBOKS 6315 TORGARDEN
7491 TRONDHEIM
TLF. 73 90 40 00

Report no.:	ISSN (print):	ISSN (online):	Grading:
2018.010	0800-3416	2387-3515	Open

Title:
Neotectonics in Nordland - Implications for petroleum exploration (NEONOR2)

Authors:
Olesen,O., Janutyte,I., Michálek, J., Keiding, M., Lindholm, C., Kierulf, H.P., Ottemöller, L., Gradmann, S., Maystrenko,Y.P., Rouyet, L., Lauknes,T.R., Dehls, J.F., Ask, M., Ask, D., Olsen, L., Ottesen, D., Rise, L.,Riis, F., A. Drottning, A. Tjåland, M.L. Strømme, Storheim, B.M.& S. Rodenay

Clients:
NGU, Forskningsrådet, Kartverket, NORSAR, UiB, LTU, Norut, NPD, AkerBP, DEA, Equinor, INEOS, Lundin, Neptune, Repsol, Shell & Total

County: Nordland, Troms

Municipality:

Map-sheet name (M=1:250.000):
Andøya, Bodø, Mo i Rana, Mosjøen, Narvik, Nordreisa, Saltdal, Sulitjelma, Svolvær, Vega

Total pages: 392
Map encl.: 1

Price (NOK):

Fieldwork carried out: 2013-2017

Date of report: 02.09.2018

Project no.: 354000

Person responsible: Marco Brönner

Summary

The individual papers and reports from the NEONOR2 project (Neotectonics in Nordland – implications for petroleum exploration) are compiled in the present report. The results are also summarized and compared to the results from previous research projects (e.g. NEONOR project 1997-2000). The NEONOR2 project was a collaboration project between NGU, Kartverket, NORSAR, Norut, NPD and the universities of Bergen and Luleå. The project was in addition sponsored by the Norwegian Research Council and eleven petroleum companies. NEONOR2 investigated neotectonic phenomena onshore and offshore through a multidisciplinary approach including geological, seismological and geodetic studies combined with rock mechanics, applied geophysics and numerical modeling.

In the framework of the NEONOR2 project, a 27 seismograph network monitored the seismicity during a 2.5 year period. More than 1200 earthquakes were registered and 123 focal mechanisms have been derived. The occurrence of earthquake swarms is correlating with high mountains located along the Nordland strandflat. The extension of the Nesna Shear Zone along the eastern margin of the Helgeland Basin and the Grønna Fault at the eastern margin of the Vestfjorden Basin are seismically active. There were dominant shallow, normal-faulting earthquakes onshore and mostly deeper, mixed type faulting earthquakes offshore, while mostly normal to strike-slip faulting was registered along the transitional coastal zone. In situ rock stress measurements onshore mainland Nordland show mostly compressional stress that is possibly related to the gravitational effects of the high topography. Geodetic data reveal extension and subsidence along the Helgeland coast. An updated compilation of all geodetic stations in Norway and Fennoscandia was analyzed for regional and local present-day strain patterns. Numerical modelling of the present-day strain and stress field shows that topography/bathymetry as well as deep structures (e.g. Moho depth and regional weakness zones) and sediment loading/unloading are controlling factors. The effect of the Pleistocene sediment redistribution on the subsurface temperature and stress has also been modelled. A flexural uplift caused by local erosion at the coast and deposition of the sediments along the continental margin seems most reasonable to explain the bulk of the observed stress and seismicity. Other mechanisms such as gravitational effects from local topography, the Mid-Atlantic Ridge (ridge push), glacial isostatic adjustments (GIA), crustal and mantle heterogeneities and groundwater flow are also contributing to the Nordland stress and seismicity. The most pronounced deposition-related negative thermal anomaly reveals a minimum of around -70°C at a depth of 17-20 km in the Lofoten Basin. The erosion-related positive anomaly shows a maximum of more than +27°C at depths of 17-22 km beneath the eastern part of the Vestfjorden Basin. The Nordland III area immediately to the south of 67°N shows earthquakes related to compressional faulting implying a large chance of sealing faults and little leakage of petroleum from potential reservoirs. The northern Nordland VI area offshore Lofoten appears, however, to be affected by extension with a larger potential for leaking reservoirs. The shallow part of the Ribban Basin adjacent to the Lofoten Archipelago may be in a compressional regime due to gravitational forces from the up to 1000 m high Lofoten mountains.

Keywords

Neotectonics	Seismology	Geodesy
Rock mechanics	Modelling	


The Research Council
of Norway


Kartverket


e·on


LULEÅ
UNIVERSITY
OF TECHNOLOGY


equinor


NORSAR


INEOS


norut


Lundin
Petroleum


OLJEDIREKTORATET


MAERSK
OIL


NORECO


UNIVERSITAS
BERGENSIS


REPSOL


AkerBP


DEA


GEOLOGICAL
SURVEY OF
NORWAY
- NGU -


VNG
Norge

CONTENTS

CHAPTER 1: NEONOR2 SUMMARY

Author: Odleiv Olesen[1]

Affiliations: [1]Geological Survey of Norway, P. O. Box 6315 Torgarden, 7491 Trondheim, Norway.

1. Introduction

The NEONOR2 project (Neotectonics in Nordland – Implications for petroleum exploration) was a partnership between the Geological Survey of Norway (NGU), the Norwegian Mapping Authority (Kartverket), NORSAR, the Norwegian Petroleum Directorate (NPD), Luleå Technical University (LTU) and the University of Bergen (UiB). The project was funded by the Norwegian Research Council, NGU, NPD, Kartverket, UiB, NORSAR, AkerBP (former Det norske), DEA (former RWE Dea), Equinor (former Statoil), INEOS (former DONG), Lundin, Neptune (former VNG), Repsol, Shell and Total (former Maersk). E.On and NORECO were originally participants in the project but their Norwegian activities were later acquired by DEA and AkerBP, respectively.

The Nordland offshore area is a promising province for petroleum exploration on the Norwegian continental shelf. However, one significant challenge relates to the severe Pleistocene uplift and erosion of the area. The effects are likely similar to those observed in the Hammerfest Basin in the Barents Sea (Nyland et al., 1992; Auriac et al. 2016; Zattin et al., 2016; Zieba et al., 2016). The removal of sedimentary overburden led to pressure decrease causing gas expansion and expulsion of oil from the traps. Uplift and tilting induced local extension, seal breaching and spillage. The cooling of the source rocks owing to vertical movement caused hydrocarbon generation to decrease. An improved understanding of the processes of uplift and erosion in time and space will therefore be important information in the petroleum exploration of the Nordland area. The main aim of the project has therefore been to investigate whether uplift and erosion-related processes similar in space and time to those known from the Barents Sea are applicable to the Helgeland, Vestfjorden and Ribban basins. To understand potential effects of motions in the past, we need to understand the present-day strain patterns, stress fields and temperature and unravel the different tectonic components that caused these features.

NEONOR2 is a development of the NEONOR1 Project (Neotectonics in Norway) which was carried out from 1997 to 2000 (Olesen et al., 2000, 2004). The Nordland area proved to be the tectonically most active area in Norway and it was concluded that neotectonic deformation processes constituted a geohazard and influenced the behaviour of fluids on the Norwegian continental shelf (Olesen et al., 2004). Chand et al. (2012) have later shown that unloading due to erosion and deglaciation in the SW Barents Sea resulted in opening of pre-existing faults and creation of new faults, facilitating fluid migration and eventual escape into the water from the subsurface. This is, e.g., expressed as pockmarks, gas hydrates, and even gas flares in the water column, indicating open fractures (Chand et al., 2012).

The results from each NEONOR2 work package have been partly presented as research papers in international, peer-reviewed journals and partly as reports. Some joint publications will also be prepared. A compilation of the papers and reports are included as chapters in the present report. The digital version of this report may be downloaded from http://www.ngu.no/side/ngu-rapporter.

The amount of sediments deposited along the continental margin in the Pleistocene Naust Formation has been well mapped during the last decade (Fig. 1; Rise et al., 2005; Dowdeswell et al., 2010) and has been used to constrain the amount and timing of onshore erosion. The high sedimentation rates during the last ice age, ~0.24-0.75 m/ky (Dowdeswell et al., 2010) and the substantial sediment erosion, which is also evident from deep Mesozoic weathering of basement rocks in the Lofoten-Vesterålen, Vestfjorden and Ranafjorden areas (Olesen et al. 2013b), indicated significant onshore exhumation and isostatic rebound. These crustal processes resulted most likely in flexuring and accompanying seismicity and fracture extension (Bungum et al., 2010; Olesen et al., 2013a,b).

The prime objectives of the NEONOR2 project were to:

- Improve understanding of regional-scale stress and strain regime in the Nordland area through a detailed monitoring of seismicity (Work package 1)
- Register geodetic movements (Work package 2)
- Map in situ stress state (Work package 3)
- Relate the new data sets to tectonics, exhumation and isostatic processes through modelling (Work package 4).

There were indications that the selected study area exhibits particularly irregular patterns of present-day uplift (Olesen et al., 2004; 2013b) and young exhumation, mainly Pleistocene according to Rise et al. (2005) and Dowdeswell et al. (2010). The effects of the respective stress patterns and recent changes may have influenced fluid pressure evolution and gas expansion within potential petroleum reservoirs and is therefore particularly interesting and relevant for oil exploration. Our secondary objectives are to:

- Obtain a new seismicity map of the Nordland region, relevant for geohazard evaluation
- Explore combined inversion methods to determine the regional stress field by integrating GPS, DInSAR, seismic data, in situ stress, and mapped faults
- Quantify the contribution of Pleistocene sediment redistribution on the present-day stress field using numerical modelling
- Estimate the Pleistocene palaeo-stresses and palaeo-temperatures using numerical modelling

The petroleum industry can apply the NEONOR2 results in their exploration programs for the study area and reduce risk by estimating the impact of recent uplift and neotectonics on subsurface conditions, such as temperature, stress, gas expansion and sealing of reservoirs.

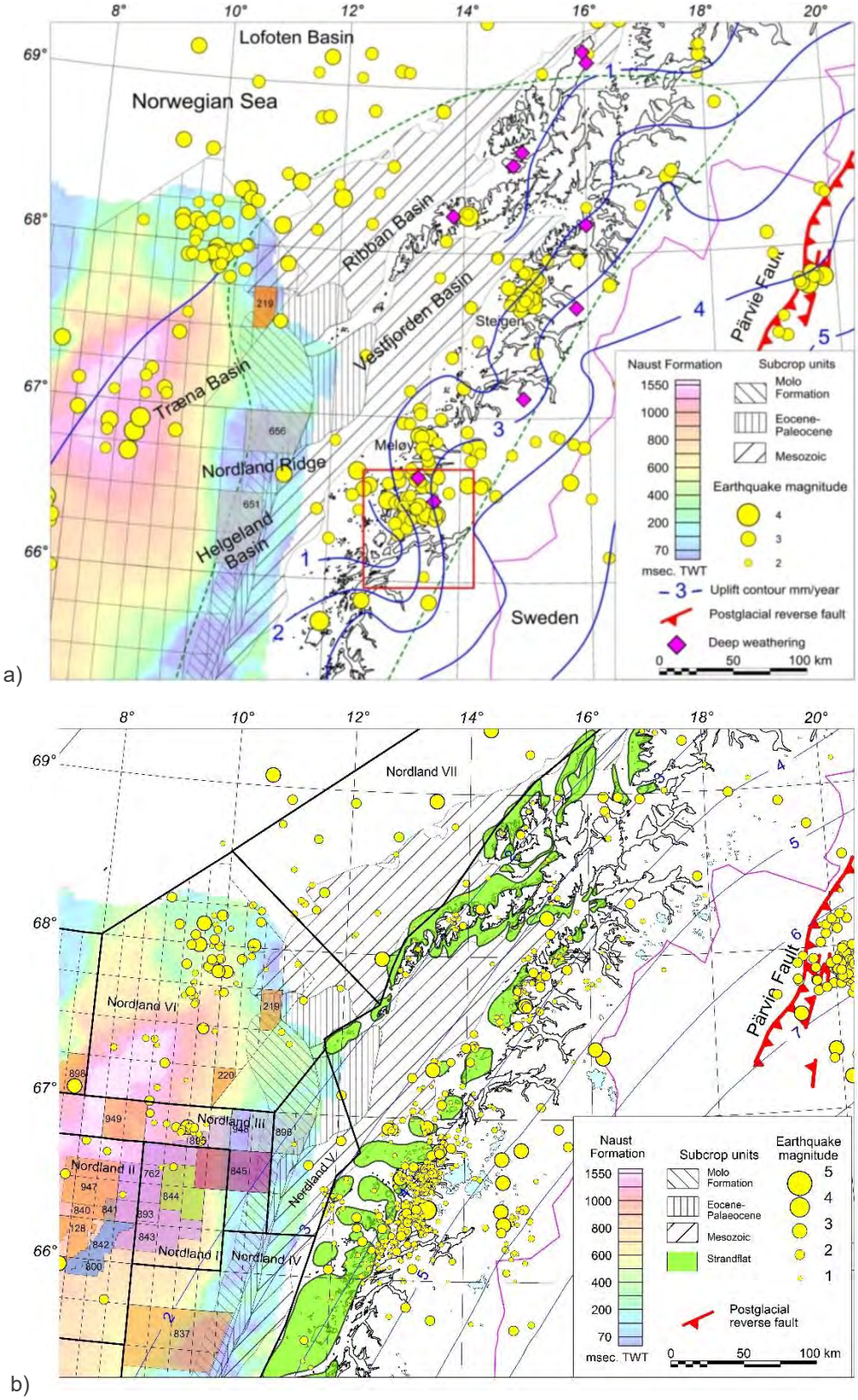

Figure 1. Indicators of neotectonic activity and related features in the Nordland area. Thickness of Naust Formation (in two-way travel time, where 1 ms is ~1 m) is adapted from Dowdeswell et al. (2010). Sub-cropping units (modified from Sigmond (2002) underlying the Naust Formation are Tertiary to Jurassic sedimentary rocks (hatched patterns). Exploration licenses within the offshore erosion area are depicted as coloured and numbered polygons. The Pärvie postglacial fault is adapted from Lagerbäck & Sundh (2008). a) Pre-NEONOR2 map. Earthquakes with magnitudes higher than 2.5 between 1980 and 2011 are shown in yellow (Bungum et al., 2010). The blue isolines represent the present-day uplift (Dehls et al., 2000). The interpreted catchment area of glacial erosion (green dashed line) and present shelf edge (violet line) are taken from Dowdeswell et al. (2010) b) NEONOR2 seismicity between 2013 and 2016 (Janutyte & Lindholm 2017; Michálek et al. 2008; Chapters 2 & 4 in this report) and present-day GIA-adjusted uplift (Vestøl et al., in prep.) The strandflat is adapted from Olesen et al. (2013b).

2. Project organisation

NGU had the key responsibility for the project. Odleiv Olesen carried out the overall management of the project with administrative support from Cyprien Habimana and Hild Sissel Thorsnes at NGU.

Conrad Lindholm of NORSAR led WP1. The Norwegian mobile seismic instrument pool is based and maintained at NORSAR. NORSAR shared the instrument deployment, data acquisition and processing with the University of Bergen (Janutyte et al., 2017; Janutyte & Lindholm, 2017; Michálek et al., 2018; Chapters 2-4 in the present report). The University of Bergen (Lars Ottemöller) was also responsible for the integration of new data with the Norwegian National Seismic Network (NNSN). NORSAR employed the postdoctoral fellow Ilma Janutyte for three years which were 50 % funded by NEONOR2. The post doctoral fellow Jan Michálek was employed for 25 months at the University of Bergen. Kristoffer Igland completed his Master theses at the University of Bergen utilizing NEONOR2 data, Anne Drottning and Norunn Tjåland continued working on the NEONOR2 data after finishing their master theses. NGU carried out a trenching and Ground Penetrating Radar (GPR) profile across the Nordmannvikdalen postglacial fault in Troms (Olsen et al., in press; Chapter 5) to clarify the palaeoseismology of northern Norway.

WP2 was a collaboration between Kartverket and NGU, led by Halfdan Pascal Kierulf (Kartverket). Kartverket was responsible for the GPS data collection and processing, as well as for interpretation of the uplift and subsidence patterns and lateral movements (Kierulf 2017; Chapter 6). Norut (Northern Research Institute) in Tromsø developed the software for processing of InSAR data and integration with GPS. The processing and interpretation of the DInSAR data was performed by Norut and NGU (Rouyet et al., 2018; Chapter 7).

Maria Ask at the Luleå University of Technology (LTU) was the leader of WP3 Rock mechanics (Ask & Ask, 2018; Chapter 8). Hydraulic stress measurements (HSMs) were conducted by Geosigma AB in September 2014 in the Leknes borehole. Poor ground conditions and insufficient space for setting up the equipment prevented HSMs at the Drag borehole, but it was possible to conduct logging in the borehole. Gert Andersen of Rambøll Dk conducted borehole logging. While the Drag Bh only was logged once with this full suite of logs, an additional logging run with the acoustic borehole televiewer was made after HSM testing to capture the orientation of tested fractures in the Leknes Bh.

Sofie Gradmann (NGU) led WP4 and performed the rock stress part of the numerical modelling (Gradmann et al., 2018; Chapter 9). Yuriy Maystrenko et al. (2017, 2018) carried out the 3D mapping of the lithosphere as well as the thermal modelling of the Lofoten area (Chapters 10 & 11). Maystrenko et al. (2018) studied also the potential triggering mechanisms of earthquakes in Norway (Chapter 13). Postdoctorate fellow Marie Keiding held a three-year position at NGU and analysed stress and strain data (Keiding et al., 2015, Chapter 12) in addition to updating and refining the 1:3 million NEONOR1 neotectonic map of Norway (Keiding et al. 2018a,b; Chapter 14; enclosed map). Leif Rise, Dag Ottesen (both NGU) and Fridtjof Riis (NPD) have previously been involved in mapping the offshore sediment formations and assisted in incorporating these data into the numerical models.

3. Methods

3.1 Seismological observations and analyses - Work package 1 (NORSAR-UiB-NGU)

The regional seismicity areas of the Nordland region between 66°N and 69°N (mainland and islands) have been monitored to obtain the best onshore and offshore coverage. This is to test and improve the presently known pattern of seismicity (in coastal areas and offshore basins), and to map the onshore-offshore extent of the tensional stress regime. To this purpose, 27 temporary seismic stations from the Norwegian seismometer pool were deployed, and the obtained data were fully integrated in the existing NNSN (http://www.geo.uib.no/seismo/nnsn), operated by UiB in cooperation with NORSAR. Most of the data could be retrieved in real time. We exchanged data with two contemporaneous collaborating seismological projects in northern Norway (ScanArray and SCANLIPS3, see below). Fig. 2 shows the densification of the existing network along the coastal stretch between Rana and Lofoten.

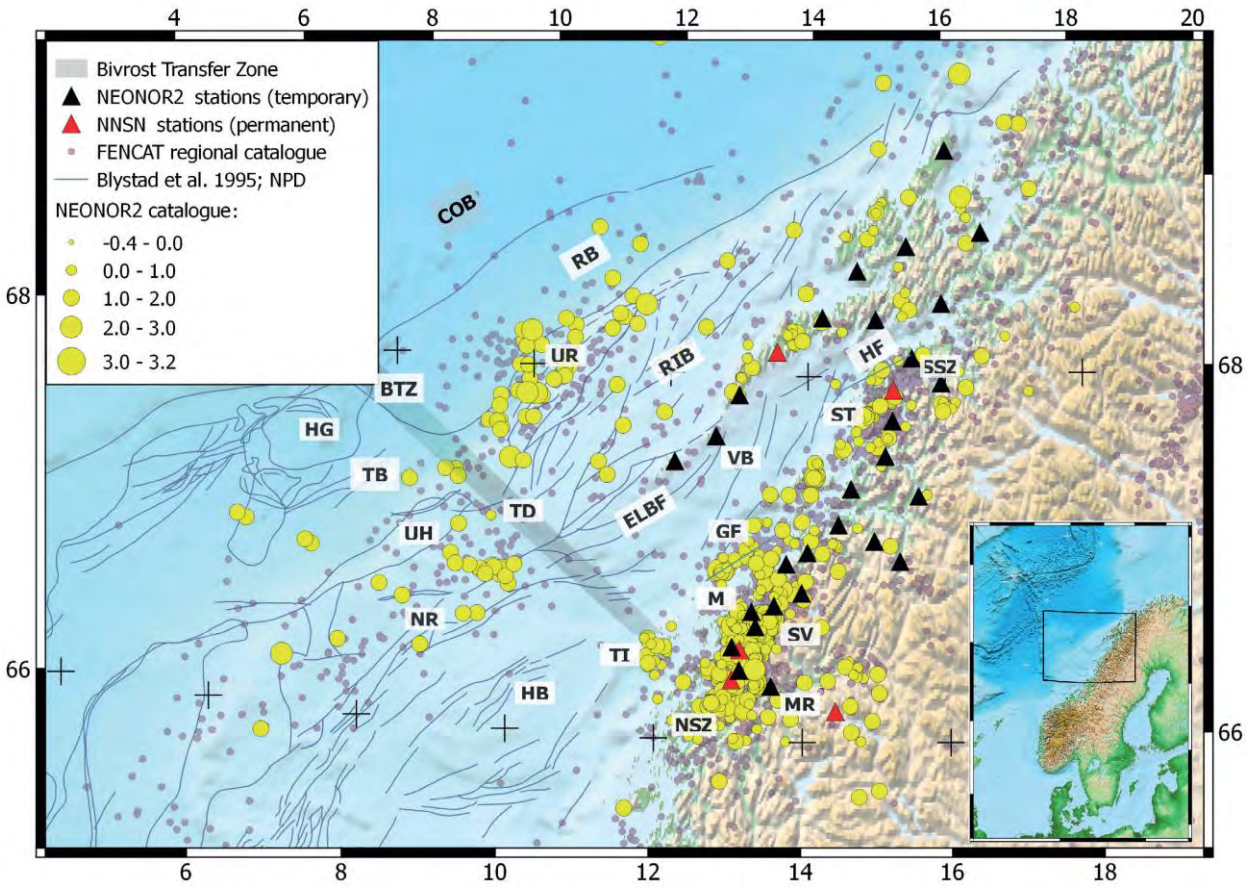

Figure 2. Map of the study area of Nordland: temporary (black triangles) and permanent (red triangles) seismic stations and earthquakes (yellow disks) recorded during the NEONOR2 project from August 2013 to May 2016 (Janutyte et al., 2017; Chapter 2). Tectonic structures and geographical locations: COB – Continent-Ocean Boundary; BTZ – Bivrost transfer zone, which is a broad transition zone rather than a particular structure (darker blue area); ELBF – East Lofoten Border Fault; GF – Grønna fault; HB – Helgeland Basin; HF – Hamarøya Fault; HG – Hel Graben; M – Meløy; MR – Mo i Rana; NR – Nordland Ridge; UH – Utgard High; NSZ – Nesna Shear Zone; RB – Rost Basin; RIB – Ribban Basin; SSZ – Sagfjord Shear Zone; ST – Steigen; SV – Svartisen; TB – Træna Basin; TI – Træna Island; TD – Trænadjupet; UR – Utrøst Ridge; VB – Vestfjorden Basin (Blystad et al., 1995; Olesen et al., 2002). Small purple dots show seismicity from the FENCAT (2017) catalogue which is primarily based on the NNSN and NORSAR locations.

The processing of the recorded data was based on well-established and simplified methods. Later also advanced methods such as the double-difference location technique (Waldhauser & Ellsworth, 2000) and travel time tomography were applied in order to improve the standard catalogue locations (Michálek et al., 2018; Chapter 4). The double-difference location algorithm is implemented in the hypoDD software which allows the combination of absolute travel-time differences obtained from the earthquake catalogue with differential travel times derived from waveform cross-correlation data. This allowed us to obtain relative locations with a precision of about 100 m using array data from more than 600 km distance. The research provided high-resolution seismicity maps of the study area, with a detection threshold near M=0. Also, a Bayesian location algorithm was tested in order to improve the relative location precision.

The high spatial resolution made it possible to correlate the results with some structural features. A dense seismic network facilitated inversion of source faulting parameters. Janutyte & Lindholm (2017) and Michálek et al. (2018) calculated the fault plane rupture solutions and the associated local stress field that is the cause for the local earthquake deformations. The determination of the principal stress vectors associated with regional stress directions represents a major grasp on the overall stress that has been an important boundary condition in the modelling of the regional deformation evolution (WP4).

We updated the database of the neotectonic claims in Norway (Olesen et al. 2013a). The postglacial age of the Nordmannvikdalen Fault in Troms has been questioned by Redfield & Hermanns (2016). We carried out a trenching and a Ground-Penetrating Radar (GPR) profile across the fault (Olsen et al. in press, Chapter 5 in the present report).

3.2 Geodetic observations and integration - Work package 2 (Kartverket-Norut-NGU)

The major objective of this work package was to improve the spatial resolution of the surface motions (i.e. at the mm scale) in the Nordland region and to link these to the seismological observations from WP1 and known geological structures.

Differential Interferometric Synthetic Aperture Radar (DInSAR) uses multiple radar images acquired over the same area at different times to determine the surface motion during the intervening period. While earlier methods used only two images, new methods utilize a time-series of 20 or more images, and obtain millimetric accuracy (Ferretti et al., 2000). For Fennoscandia, an archive exists of European Remote-Sensing radar images acquired between 1992 and 2000 containing 20-30 images. The original plan to utilize the new ESA Sentinel data was abandoned because of the delay of the Sentinel 1A and 1B satellite missions.

Kartverket (Norwegian Mapping Authority) runs a continuous network of approximately 160 permanent GPS stations distributed on the Norwegian mainland, Jan Mayen, Hopen, Bjørnøya and Svalbard. While the GPS network has been running for more than 20 years, the sites can only be considered stable since approximately 2000 (Kierulf et al., 2012). In addition to the Norwegian GPS network Kierulf (2017) selected a number of receivers from the IGS (International GPS Service) network to realize and maintain a stable reference frame. Data from both the European (EUREF) and Scandinavian (BIFROST) network was used to ensure control over large-scale phenomena such as plate tectonic and GIA signals. Crustal deformation is estimated based on a combination of data from local episodic epGNSS campaigns (three 5-day campaigns in 1999, 2008 and 2015) and continuously operating cGNSS stations in the area that were mainly established in 2008 and in 2009. To establish a local long-term stable reference frame, which is consistent both with the epGNSS network and the network of newer cGNSS, a three-step procedure for reference frame realization was used to get consistent results from all the stations in the area.

3.3 In situ stress measurements - Work package 3 (LTU)

In situ stress measurements offers stress data from intermediate depths (0-1 km), thus a link between geodetic and seismological data. The objective for testing was to determine the complete stress tensor, and its variation with depth. Stress determination in boreholes is usually conducted by combining different methods. We applied active and passive direct in situ stress measuring methods in two pre-existing boreholes (c. 800 m deep). Three types of active hydraulic fracturing methods, the hydraulic fracturing (HF), sleeve fracturing and hydraulic testing of pre-existing fractures (HTPF) methods (e.g. Haimson & Cornet, 2003) constrained the minimum principal stress (HF) and the three principal stresses (HTPF). Stress-induced borehole failures, i.e. breakouts and drilling induced fractures are passive methods that reveal the orientations of minimum and maximum principal stress orientations (e.g. Zoback et al., 2003). The different methods were integrated using the Integrated Stress Determination Method (e.g. Ask et al., 2009).

The original plan was to use the new and innovative LTU logging tool for deep boreholes funded by the Swedish Research Council. This rig was for technical reasons not available during the NEONOR2 project period. More conventional equipment had to be applied for the logging.

Furthermore, Trygve Gullestad Fintland in Equinor, Stavanger provided an additional 20 stress measurements from the Norwegian continental shelf. One of these measurements is located within the NEONOR2 area.

3.4 3D mechanical and thermal numerical modelling - Work package 4 (NGU)

A number of large-scale and local-scale sources of stress acts on a continental margin. In the Nordland region, the regional stress fields stem from the interaction of ridge push and GIA, local stress fields mainly result from lateral density variations (primarily topography and Moho) as well as the isostatic effects of sediment unloading and loading. Additional stress field contributions (e.g. tectonic) cannot be ruled out. Whereas the first three effects are fairly well constrained or merely add to the regional stress field, the present-day stress effects of the Pleistocene sediment redistribution are poorly known.

In this work package, we studied the interaction of these stress field components and their contribution to the present-day stress-field. The model of the present-day stress field was tested against sediment unloading/loading scenarios, which have been determined from mapping of the offshore sediment volumes. We also estimated the thermal effects of sediment re-distribution in the offshore Nordland area.

A 3D finite element analysis of a coupled system of differential equations (Stokes equation, incompressibility, rheological constraints and heat conduction) was performed on an adaptable mesh using the commercial software package COMSOL Multiphysics. Our models included surface topography, basement and Moho depths taken from literature and seismic profiles. The ‘background’ stress state originating only from internal body forces (e.g. variations

in topography) has shown significant deviatoric stresses, which are very often omitted in stress models. We applied the far-field stress fields (GIA, ridge-push, sediment redistribution) as effective force boundary conditions to the sides or base of the model. This approach allowed us to account for all stress sources at once but also to vary them separately in order to examine their relative contributions to the observed stress and strain concentration and orientation. A reference model was built that best fits the calculated stress fields to the observed ones derived in WP1 and WP2. Faults were included as pre-existing weakness zones, here represented by fault-like, internal mesh boundaries.

Knowledge of the offshore sediment distribution history enabled us to adapt the model to Pleistocene conditions and thereby estimate palaeo-stress fields and temperature in the Vestfjorden, Ribban and Helgeland basins. Changes in GIA and topographic stresses were also taken into account in the stress modelling.

Maystrenko et al. (2017; Chapter 10) built a 3D model of the lithosphere in the Nordland area. We could therefore calculate the thermal effects of the sediment removal and redistribution in the offshore basins (Maystrenko et al., 2018; Chapter 11).

We furthermore inverted the GPS dataset, in combination with earthquake moment tensors, to surface strain-rate and stress fields. A postdoctoral fellow (Marie Keiding) was employed in WP2 for a 3-years period. Her tasks were to compile and compare the different geophysical data sets as well as geological information (e.g. fault orientation) to derive a surface deformation field from GPS and DInSAR data, and to develop and apply the joint inversion of geodetic and seismological data (Keiding et al., 2015; Chapter 12).

4. Results

4.1 Seismological observations and analyses - Work package 1 (NORSAR-UiB-NGU)

1) Almost 1250 earthquakes (Fig. 2) were located in the Nordland area from the NEONOR2 deployment of 27 seismic stations (August 2013 to May 2016) and the permanent stations of the NNSN (Janutyte et al., 2017; Michálek et al., 2018; Chapters 2 & 4). The seismic activity was mostly sporadic during the monitoring period but in some areas, it was clearly episodic.

2) The most seismically active area is characterized by high-altitude mountains on the landward side of the strandflat (Figs. 2 & 3). This phenomenon may be related to the gravitational effects of the mountains combined with substantial coastal erosion in the Pleistocene. There were also wide-spread earthquake activity along the remaining part of the strandflat (Figs. 2 & 3).

3) An earthquake swarm with several hundred small seismic events was recorded between April 2015 and March 2016 in the Jektvik-Blokktinden-Tjongsfjorden area to the west of the Svartisen glacier (Janutyte et al. 2017; Michálek et al. 2018; Chapters 2 & 4). Michálek et al. (2018); Chapter 4) subdivided the swarm into three smaller clusters with a possible NW-SE trend (Fig. 4). The highest concentration of earthquakes occurs 3-7 km beneath the 1032 m high Blokktinden mountain (Cluster 2 in Figs. 4 & 5; Fig. 6). NW-SE and SW-NE profiles were constructed for all three clusters. It seems that the swarm is shallower on the eastern side while the activity at greater depths occurs towards the west implying that the swarm might be related to structures dipping towards the north-west.

4) A total of c. 20 earthquakes occurred along the Grønna fault (Fig. 3), about 30 km northwest of Meløy (Janutyte et al. 2017; Chapter 2). To the north, the Grønna fault passes into the boundary between the coastal mountains and the Vestfjorden sedimentary basin, and the new data show that the seismicity follows this structure (Fig. 3).

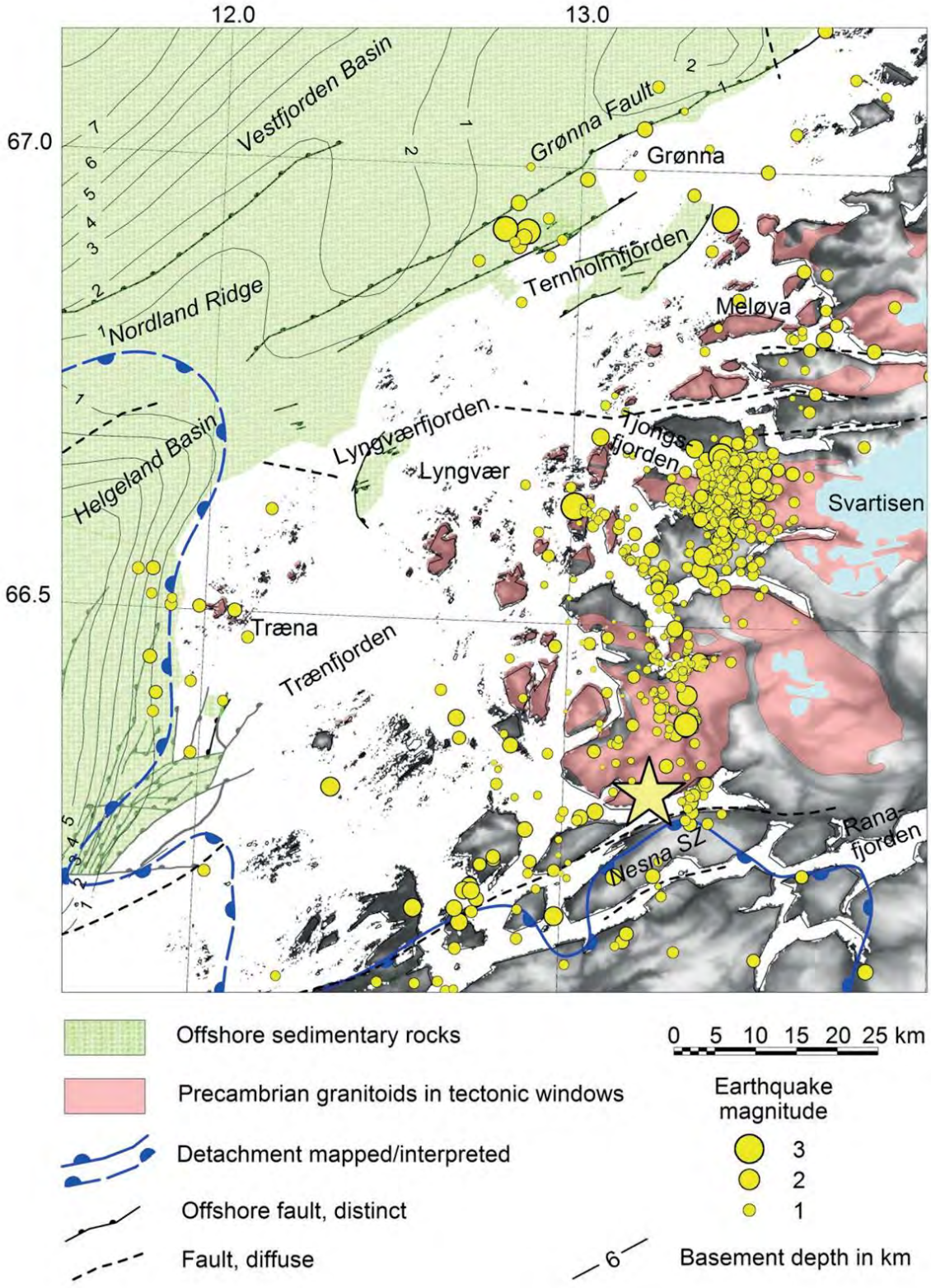

Figure 3. Seismicity in the northern Helgeland area (Janutyte et al., 2017; Chapter 2, this report). Data sources: Mesozoic sedimentary rocks – IKU (1995), Bugge et al. (2002), and Bøe et al. (2008); Precambrian granitoids – Gustavson & Gjelle (1991), and Gustavson & Blystad (1995); Detachments mainland – Eide et al. (2002); Detachments offshore – Olesen et al. (2002); Faults – IKU (1995), Bugge et al. (2002), Olesen et al. (2002), and Bøe et al. (2008); Basement depth – Olesen et al. (2002). The yellow star depicts the approximate location of the M 5.8 earthquake in 1819. Correlations between seismicity and tectonic-geological boundaries are observed along the Grønna Fault, the eastern flank of the Helgeland Basin and onshore to the north of the Nesna Shear Zone (NSZ). To the west of Svartisen, the earthquake swarm occurred from April 2015 to around March 2016 with several hundreds of weak and shallow seismic events. To the southwest of the earthquake swarm there could be distinguished a NW–SE-trending lineament that changes its orientation to NNW–SSE farther to the south.

5) A cluster of 15 earthquakes is located along the eastern border of the deep Helgeland Basin and the offshore extension of the Nesna Shear Zone (Fig. 3). These earthquakes coincide partly with the faults mapped by shallow seismic data (IKU, 1995).

6) The Naust–Kai depocentre could be associated with an area of increased seismic activity (Fig. 1). The seismicity is possibly controlled by deep crustal inhomogeneities (Janutyte et al., 2017).

7) No earthquakes were recorded on the Trøndelag Platform and in the larger Vestfjorden Basin area (Fig. 2; Janutyte et al., 2017; Michálek et al., 2018; Chapters 2 &4). These areas are most likely aseismic, although three years of dense monitoring in such areas of low deformation rates is not enough to make a conclusive statement.

8) A comprehensive database of 152 earthquake focal mechanism solutions for the study area (incl. 123 new focal mechanisms) show that seismicity onshore and offshore Nordland is different in type: with dominant shallow, normal-faulting earthquakes onshore and mostly deeper, mixed type faulting earthquakes offshore, while along the transitional coastal zone the faulting regime was mostly normal to strike-slip. (Figs. 7-8; Janutyte & Lindholm, 2017; Michálek et al., 2018; Chapters 3 & 4). Note that the focal mechanism quality assessment principles are different in Fig. 7 and 8.

9) The obtained distribution of nodal planes largely confirmed the onshore and offshore structural lineation found by e.g. Gabrielsen et al. (2002).

10) The results indicated that maximum horizontal compressional stress, s_H, directions in the offshore areas on a large scale originate from the plate-tectonic ridge push with NW–SE compression, whereas in the onshore regions s_H directions are better explained through local stress-generating sources such as topography and unloading/loading (glacial transport of sediments and/or growing/shrinking glaciers, e.g. the Svartisen glacier).

11) Two fault plane solutions below the Lofoten islands indicate normal faulting (Fig. 8). The extensional regime is most likely including the adjacent Nordland VII area.

12) The Nordmannvikdalen Fault (NF) in Troms represents one of two observed postglacial faults in Norway. The two faults constitute the northernmost part of the Lapland province of postglacial faults, occurring in large tracts of northern Sweden and northern Finland (Lagerbäck & Sundh, 2008; Palmu et al., 2015). The magnitude of the earthquake related to the Nordmannvikdalen faulting was in the range 5.3–6.5 when comparing with length and displacement of contemporary earthquakes (Wells & Coppersmith, 1994). The Nordmannvikdalen Fault appears, from new trenching (Olsen et al., in press; Chapter 5 in the present report), to have been formed in one single seismic event. The new GPR data show bedrock reflectors dipping approximately 38–52° towards the NE, below the NF scarp. The average angle of the terrain slope between the Nordmannvikdalen Fault scarp and the valley floor is 14°, and the altitude difference between the fault scarp and the Nordmannvikdalen valley floor is approximately 200 m (Olsen et al., in press; Chapter 5). We have found no reason to downgrade the fault to 'very unlikely to be neotectonics' as suggested by Redfield & Hermanns (2016).

13) Keiding et al. (2018a,b; Chapter 14) compiled pre-existing and new information on neotectonic deformation in Fennoscandia and made an update of the 1:3 million NEONOR1 neotectonic map of Norway (Dehls et al., 2000).

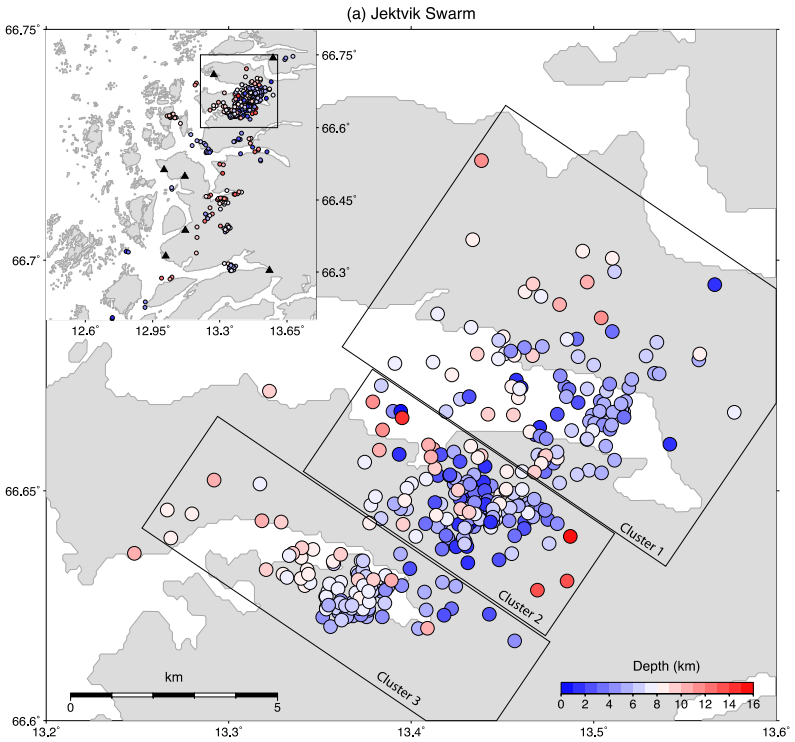

Figure 4. Detailed figure of the Jektvik earthquake swarm where colour indicates depth of hypocenter (Michálek et al., 2018, Chapter 4, this report). The Blokktinden mountain (Fig. 6) is located in the most dense cluster of earthquakes within Cluster 2.

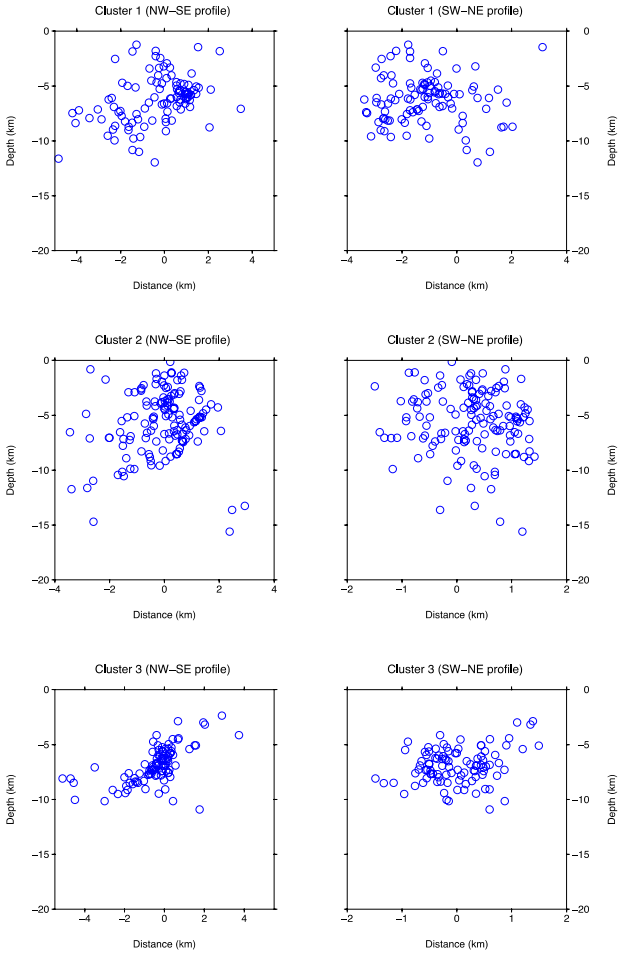

Figure 5. NW-SE and SW-NE depth profiles for earthquake clusters 1-3 (Michálek et al., 2018, Chapter 4, this report). The Blocktinden mountain is located in the most dense cluster of earthquakes within Cluster 2.

Figure 6. The highest concentration of earthquakes occurs 3-7 km beneath the 1032 m high Blokktinden mountain in the Jektvika-Tjongsfjorden area (Cluster 2 in Figs. 4 & 5). The view is to the south (http://exviking.net/lowland/large/pine-island.htm). A large rock avalanche has occurred along the western slope of the mountain and several locations with liquefied sand have been mapped in a 10 km wide area to the north.

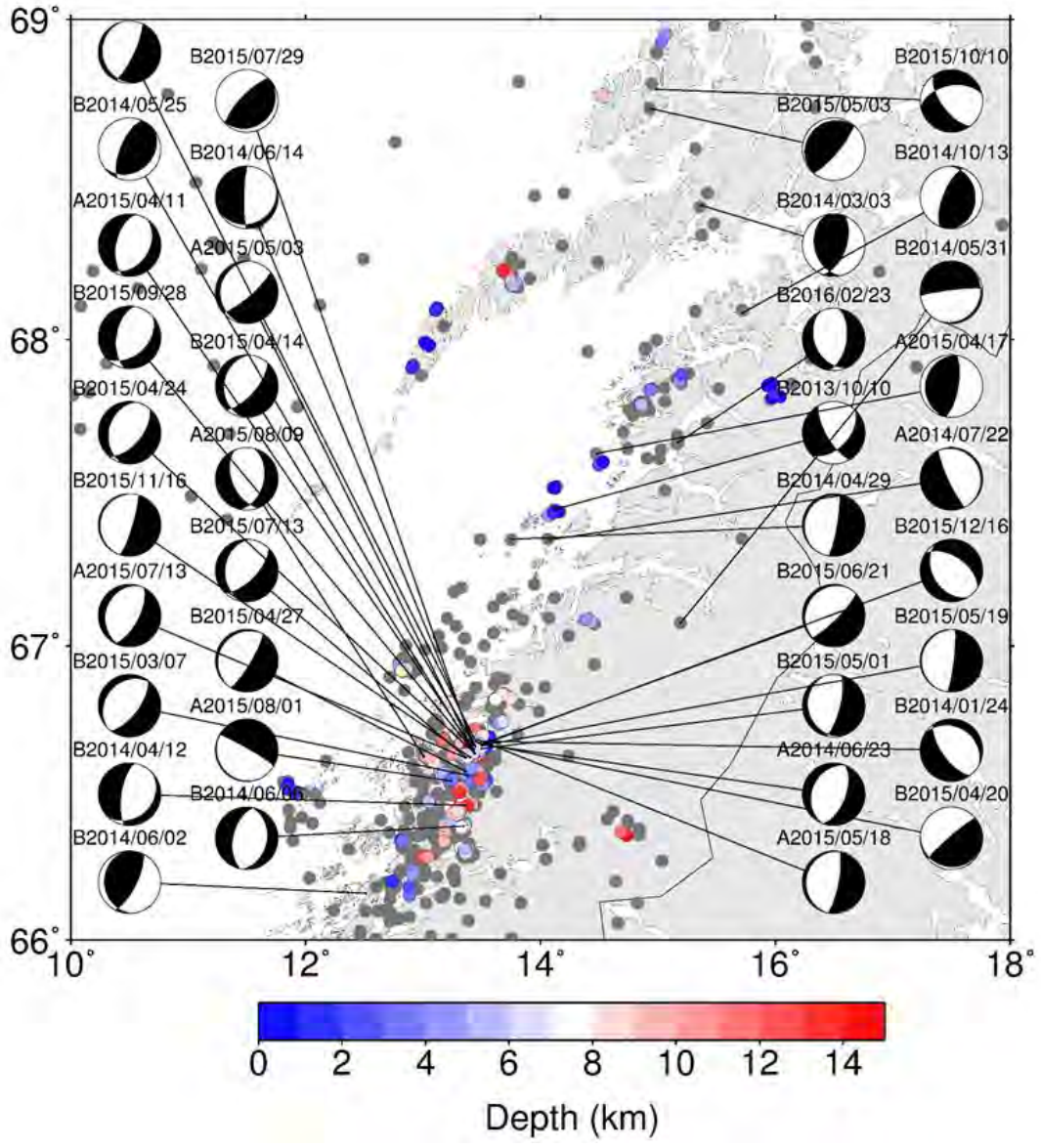

Figure 7. Fault plane solutions for A and B quality events (Michálek et al., 2017; Chapter 4). Most of the earthquakes are related to extensional faulting.

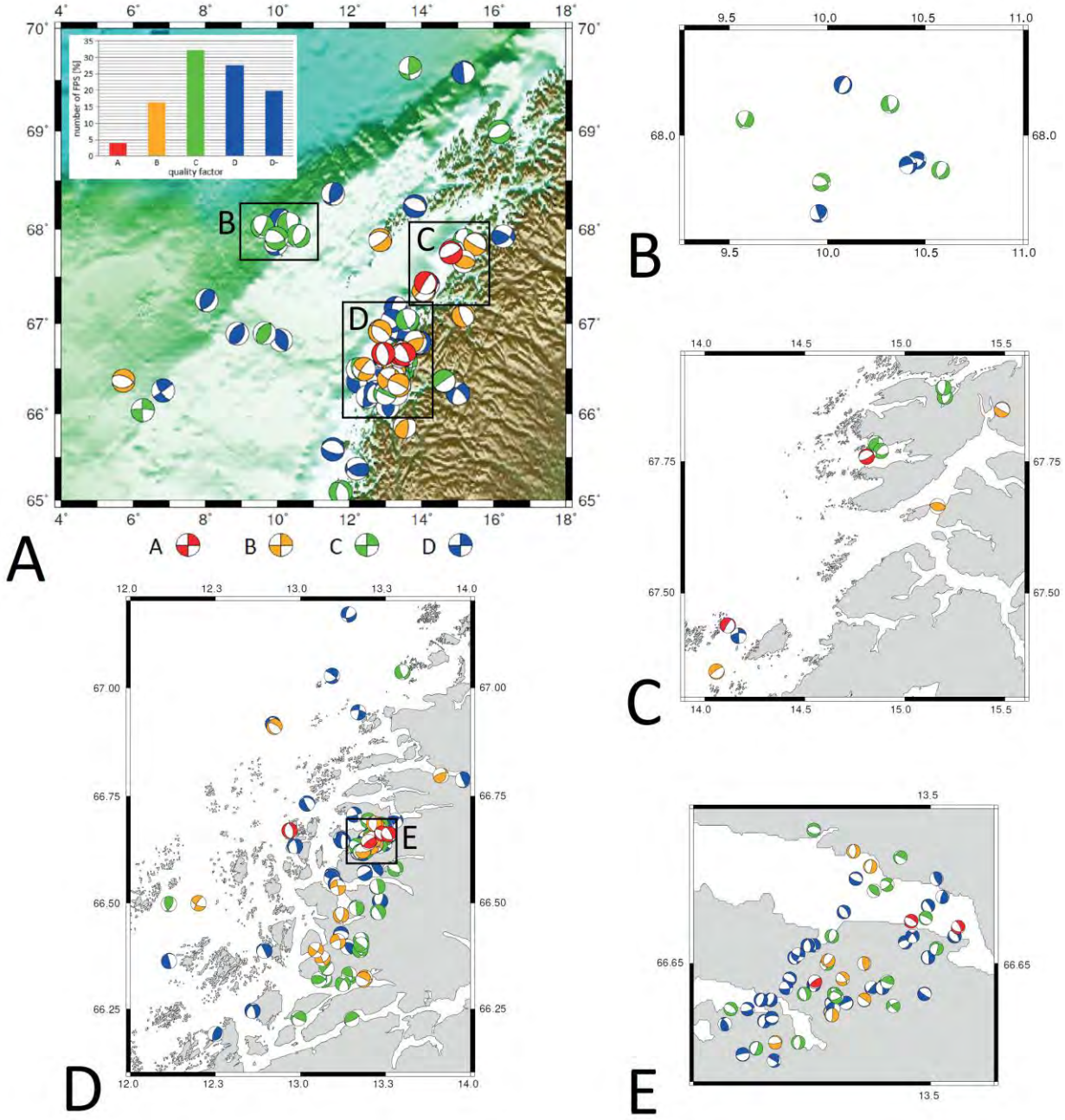

Figure 8. Final dataset of 152 focal mechanism solutions with indicated colour-coded quality factors (Janutyte & Lindholm, 2017; Chapter 4). (A) in the entire Nordland area, (B) along the continental shelf area, to the north of the Trænadjupet, (C) around the Steigen area, (D) the most seismically active coastal onshore area and (E) the earthquake swarm area to the west of Svartisen. Inset in (A): Distribution of quality factors of the focal mechanisms from best quality A through B and C to reasonable quality D. 'D-' marks focal mechanisms with 6 or less observations.

4.2 Geodetic observations and integration - Work package 2 (Kartverket-Norut-NGU)

1) The results from the GPS measurements support earlier findings that Ranafjord area of the Nordland is undergoing crustal spreading with horizontal displacement velocities of ca. 1.0 ± 0.2 mm/yr, predominantly in the east-west direction (Kierulf, 2017; Chapter 6, present report).

2) The results also show a gradient in the uplift along the coast of Nordland that is larger than predicted by existing glacial isostatic adjustment models (Fig. 10).

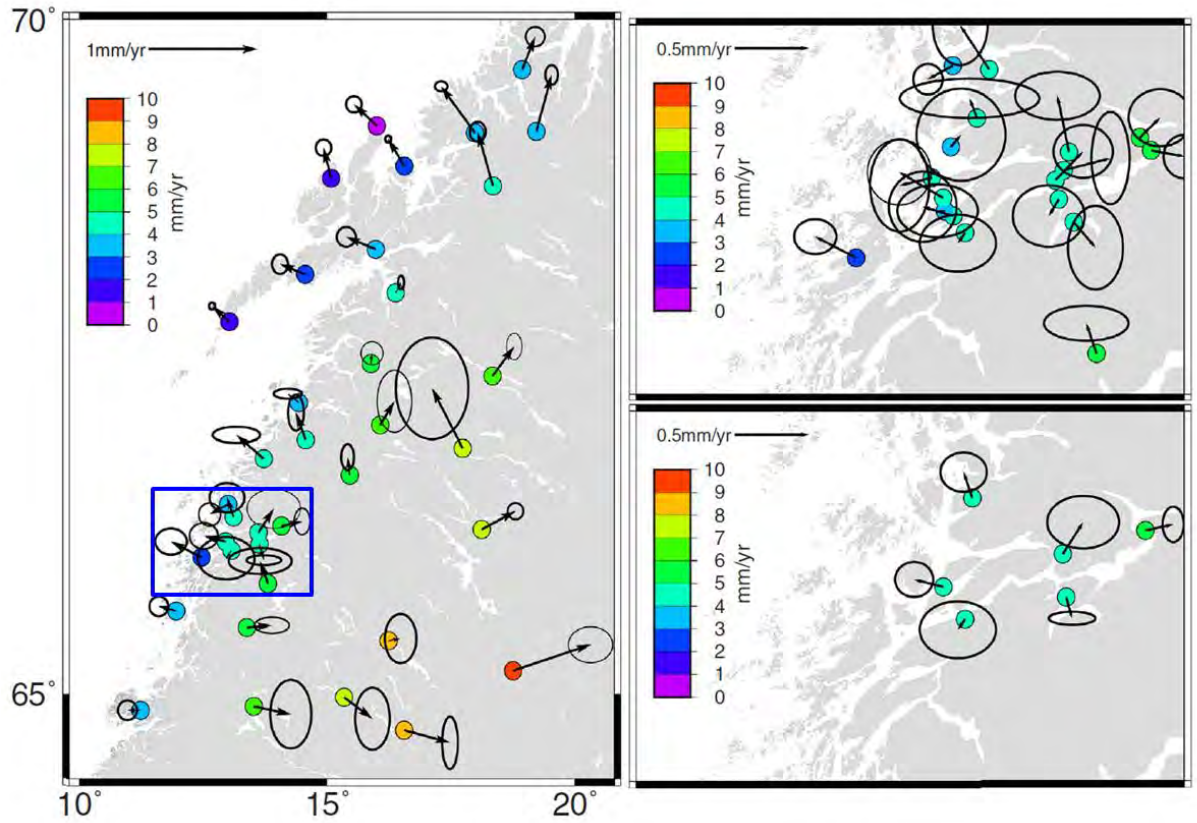

Figure 9. GNSS velocities in the Nordland area (Kierulf, 2017; Chapter 6). Arrows show the horizontal velocities after removal of the mean rigid rotation while colored circles show the vertical velocities. The horizontal uncertainties are shown with 1−σ 2D error ellipses. Upper right figure is the zoomed in area of the campaign network, while the lower right figure shows the averaged velocities for the campaign stations in the smaller Ranafjorden area (depicted by the blue frame in the left map).

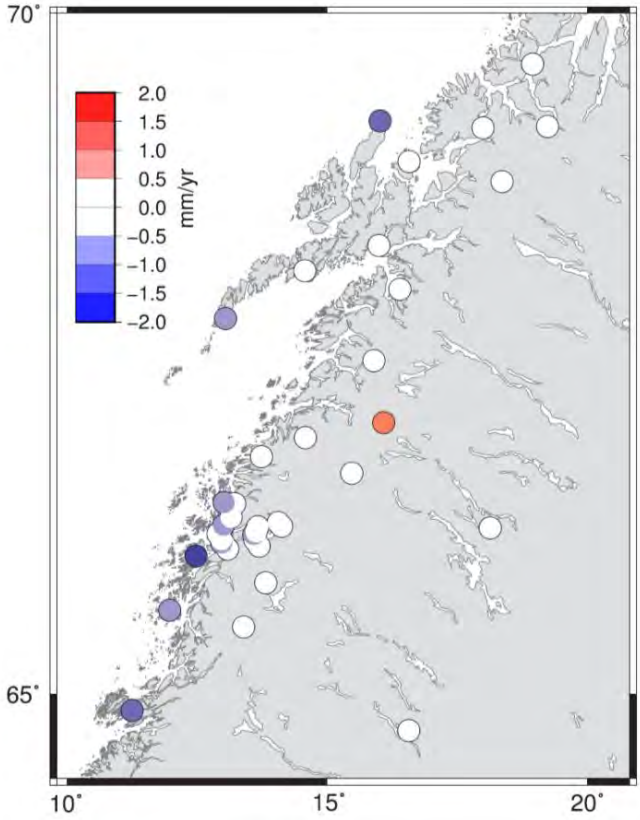

Figure 10. Residual GNSS uplift (Kierulf, 2017; Chapter 6). The colours show the differences between GNSS derived uplift and the best-fit GIA model from Kierulf et al. (2014). The uplift of the Helgeland coast and outer Lofoten is less than expected from the GIA model.

3) Rouyet et al. (2018; Chapter 7) carried out a satellite-based radar interferometry analysis (InSAR) for an area extending from Namsos to Bodø. The source of the data was the ERS-1 and ERS-2 satellites from the period 1993-2000. A small area around the Storglomvatn hydropower reservoir between profiles P3 and P4 in Fig. 11 and a large area on the Helgeland coast between profiles P4 and P9 in Fig. 11 show anomalous subsidence.

4) Fig. 12 shows a comparison between the GPS data (Fig. 9) and the InSAR (ERS1 and ERS2) data (Fig. 11) on the Helgeland coast. A constant bias is added to the InSAR data to have them in the same reference frame as the GPS. In most areas the GPS and InSAR show similar uplift, but in some areas especially at the outermost Islands, the differences are larger. This is probably due to an unwrapping error. The RMS of the overall agreement between GPS and InSAR is 1.0 mm/yr.

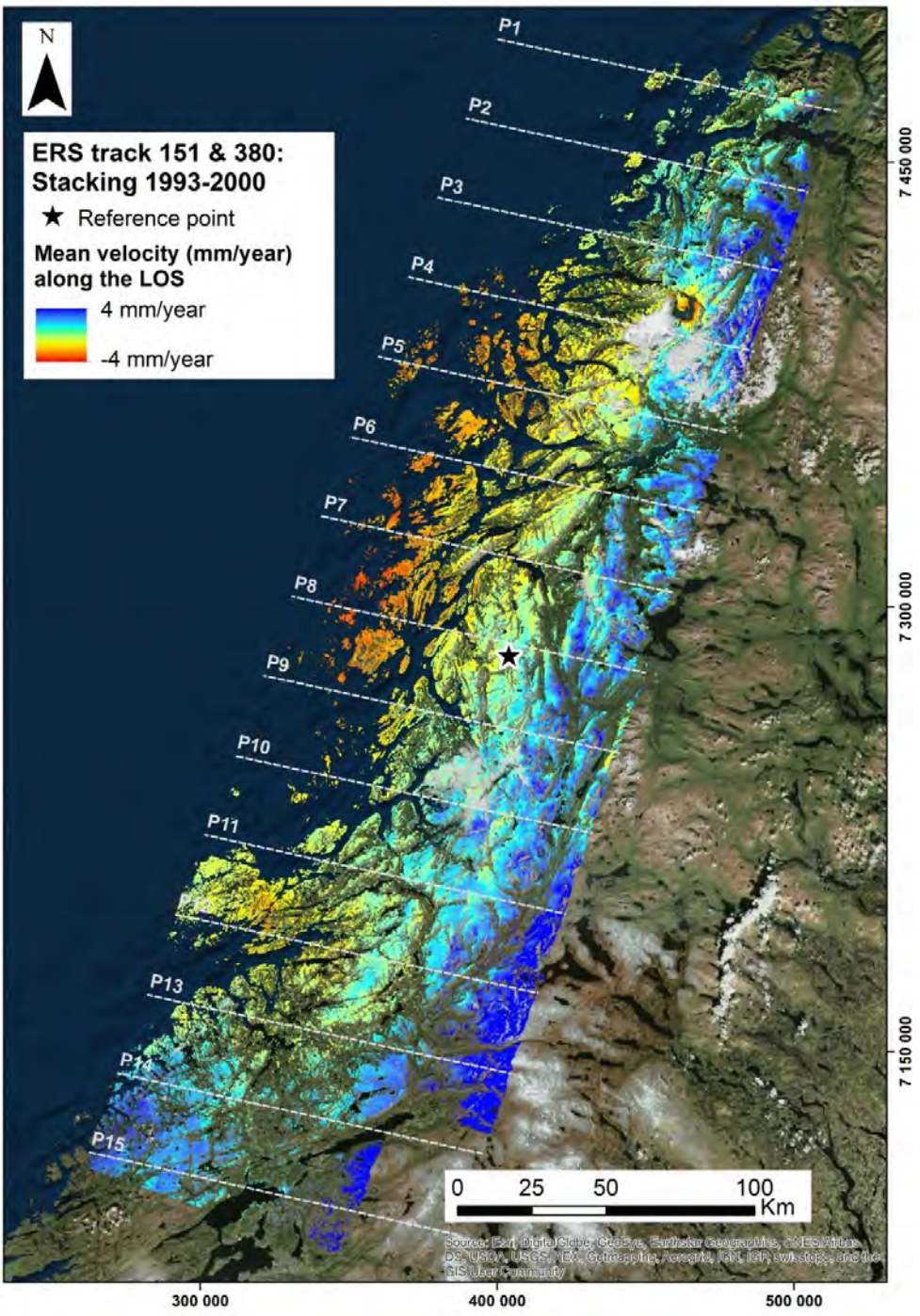

Figure 11. ERS track 151 and 380 deformation map from multi-annual stacking processing (average annual rate from 27 interferograms over eight years). Gray lines (P1-15) are the central lines of profiles visualized on each graph (Rouyet et al., 2018; Chapter 7).

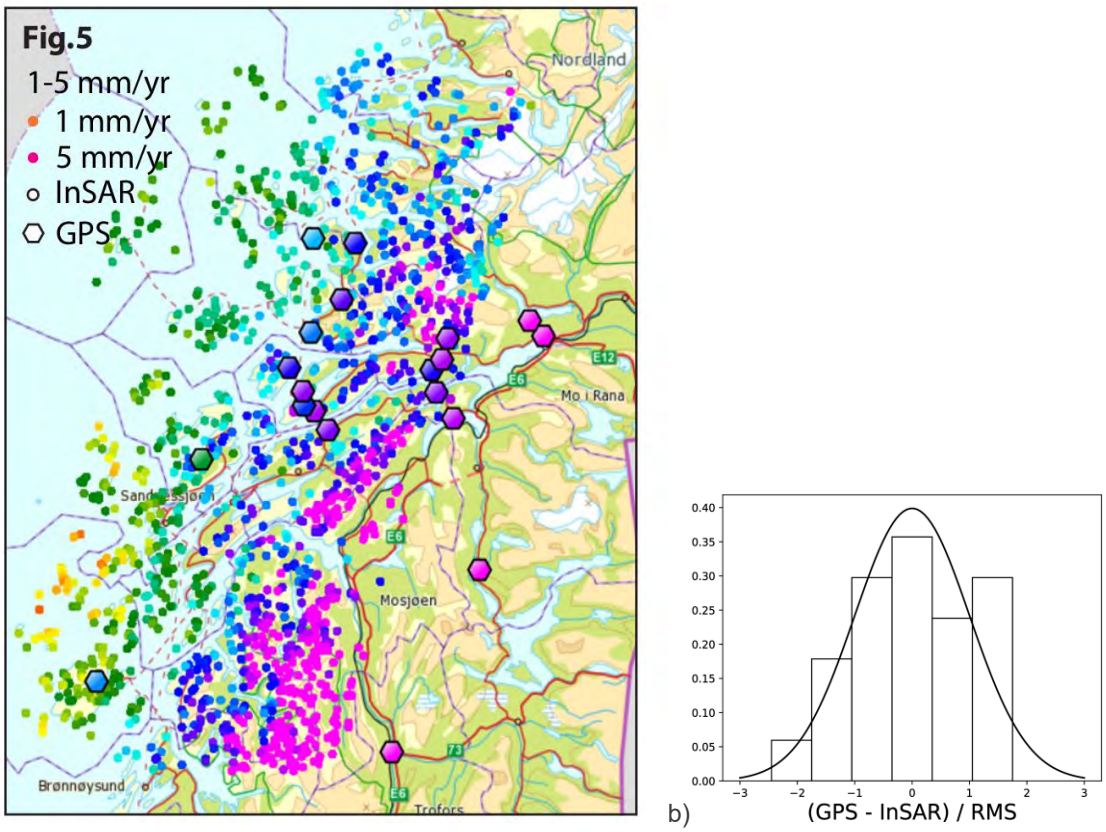

Figure 12. a) Uplift form GPS (Fig. 9) and InSAR (ERS1 and ERS2) (Fig. 11) on the Helgeland coast. b) Histogram of the difference between the GPS data and the InSAR) data. RMS=1.03 mm/yr. A constant bias is added to the InSAR data to have them in the same reference frame as the GPS.

4.3 In situ stress measurements - Work package 3 (LTU)

1) The results of the in-situ stress measurements (Ask & Ask, 2018; Chapter 8 in the present report) provide a good understanding on the state of stress in the Leknes Bh, and some limited information about the state of stress in the Drag Bh.
2) The differential stresses are significantly higher in the Leknes Bh than in the Drag Bh at the test depths of 337-354 m.
3) The differential horizontal stresses are unusual high in the Leknes Bh (Ask & Ask, 2018; Chapter 8). The mean orientation of maximum horizontal stress with respect to true North is 155±12°TN. This corresponds to grade “A” in World Stress Map (WSM; Heidbach et al. 2016) ranking quality system that is significantly higher than the pre-existing grades for in situ stress measurements on mainland of Nordland.
4) A limited number of stress-induced features were observed from 0.35-0.76 km depth in the Drag Bh. They suggest that the mean orientation of maximum horizontal stress with respect to true North is 3±15°TN (Ask & Ask, 2018; Chapter 8). With support from uniaxial compressive strength tests, the stress regime has been estimated to most likely be a reverse faulting regime at a depth of 354 m in Drag. These results are consistent with the orientation of maximum horizontal stress obtained from overcoring measurements in hydropower and road tunnels in the adjacent areas (Hanssen & Myrvang, 1986; Myrvang, 1993; Hanssen, 1993). The main difference is the swapping of the maximum and minimum horizontal stress axis. This is a commonly observed phenomenon in areas with high horizontal stresses.
5) Fig. 13 shows a subset of the WSM (Heidbach et al. 2016) for the Nordland area, with the new data included (Ask & Ask, 2018; Chapter 8). The Leknes data are the first quality A stress data in the region.

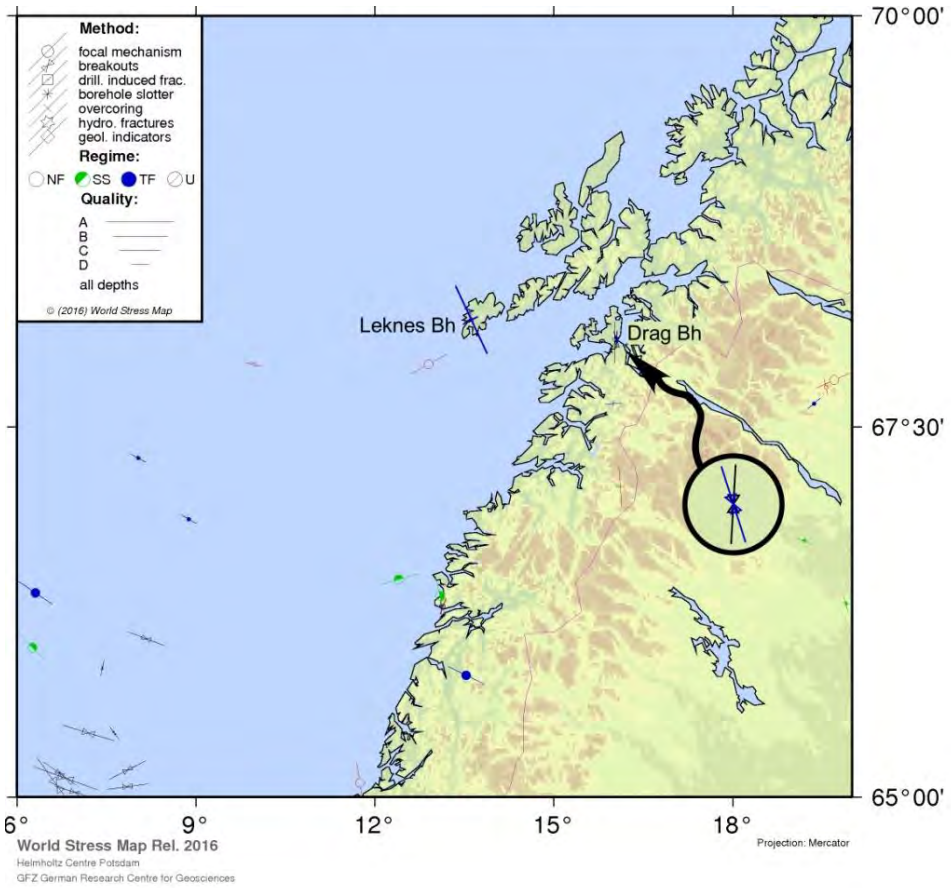

Figure 13. Subset of the world stress map (Heidbach et al. 2016) including the new data from the present study (Ask & Ask, 2018; Chapter 8). The black circle shows a blow-up of the D-quality data from the Drag Bh. The blue line is based on Type a borehole breakouts. The black line is based on all data.

4.4 3D mechanical and thermal numerical modelling - Work package 4 (NGU)

Keiding et al. (2015, Chapter 12 in the present report) investigated the regional influence of the glacial isostatic adjustment (GIA) on the deformation at the surface and at seismogenic depths in Fennoscandia (Figs. 14 &15, respectively). The surface strain rate field derived from geodetic data (Fig.14) is controlled by GIA which causes NW–SE extension of up to 4×10^{-9} yr $^{-1}$ in most of mainland Fennoscandia, surrounded by regions of radial shortening towards the centre of uplift. High uplift gradients (vertical strain rates) are observed in the Nordland region, possibly enhancing seismicity. The seismic deformation field (Fig. 15), derived from a new compilation of focal mechanisms, shows consistent NW–SE compression on the Norwegian continental margin and a tendency towards tension in mainland Fennoscandia. The seismic moment rate is at least two orders of magnitude smaller than the geodetic moment rate. Keiding et al. (2015) proposed that the low level of seismicity and the tendency towards tensional focal mechanisms in mainland Fennoscandia may be explained by the destructive interference of the regional stress from ridge push with the flexural stress due to GIA (Fig. 16). Other sources of stress such as high topography and flexuring due to sediment redistribution may also influence the state of stress in Fennoscandia, particularly in Nordland and southwestern Norway.

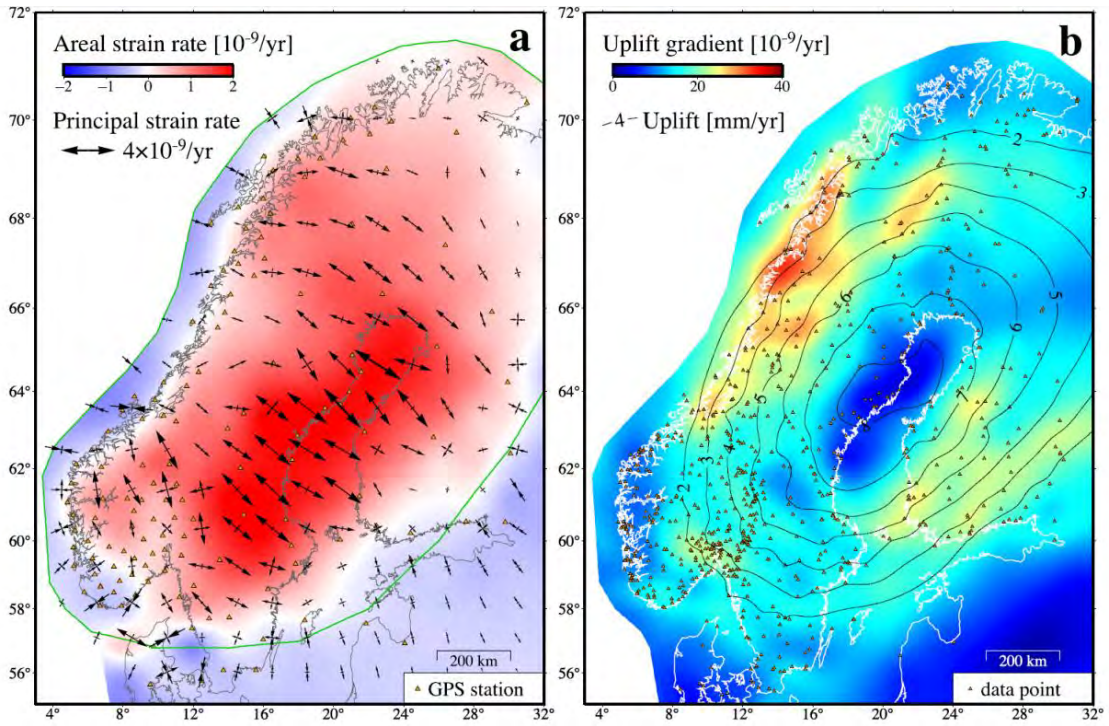

Figure 14. Surface deformation (Keiding et al., 2015; Chapter 12). a) Horizontal areal strain rates (contour colours) and principal strain rates (arrows), based on GPS velocities from Kierulf et al. (2014). Positive values of areal strain rates indicate expansion and negative values indicate contraction in the horizontal plane. The green line shows the region used for the estimate of the total geodetic moment rate. b) Uplift gradient based on GPS, levelling and tide-gauge data (Vestøl, 2006). The gradient field has been smoothed with a spatial low-pass filter before contouring.

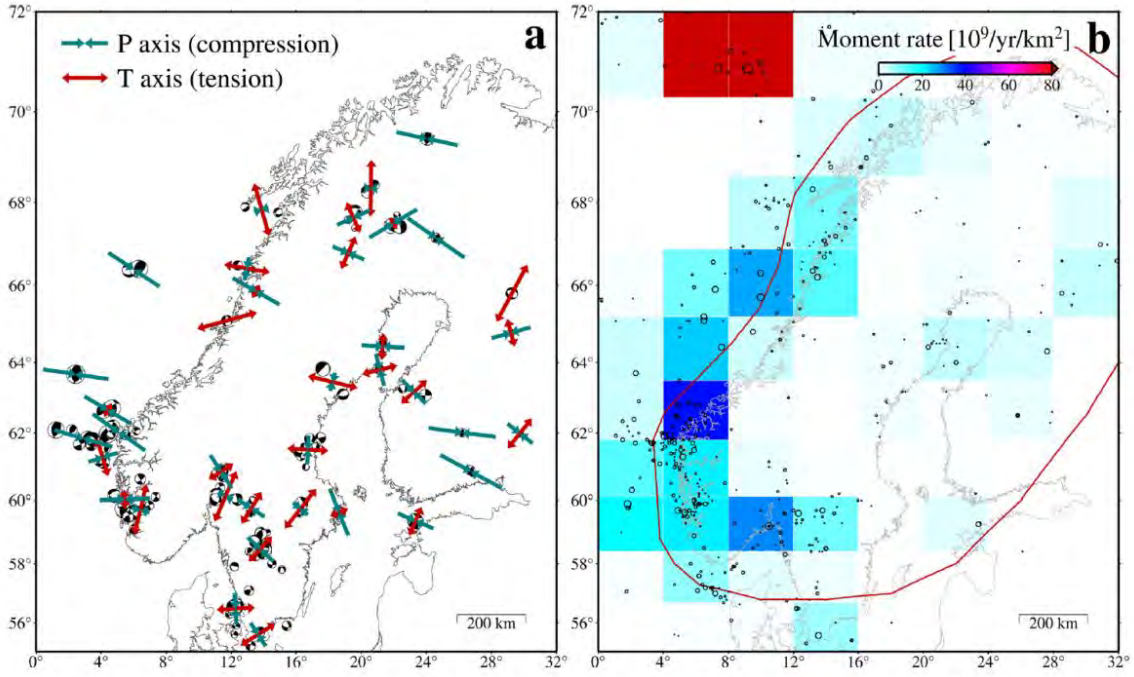

Figure 15. Deformation at seismogenic depth (Keiding et al., 2015; Chapter 12). (a) Focal mechanisms with horizontal P (compression) and T (tension) axes (without NEONOR2 data). Note that each pair of P and T axes only reflects the relative magnitudes of the two axes, not their absolute magnitudes relative to other events or event clusters. (b) Moment rates from summation of earthquake moments during 1900–2011 from the FENCAT catalogue. The red line shows the region used for the estimate of the total seismic moment rate.

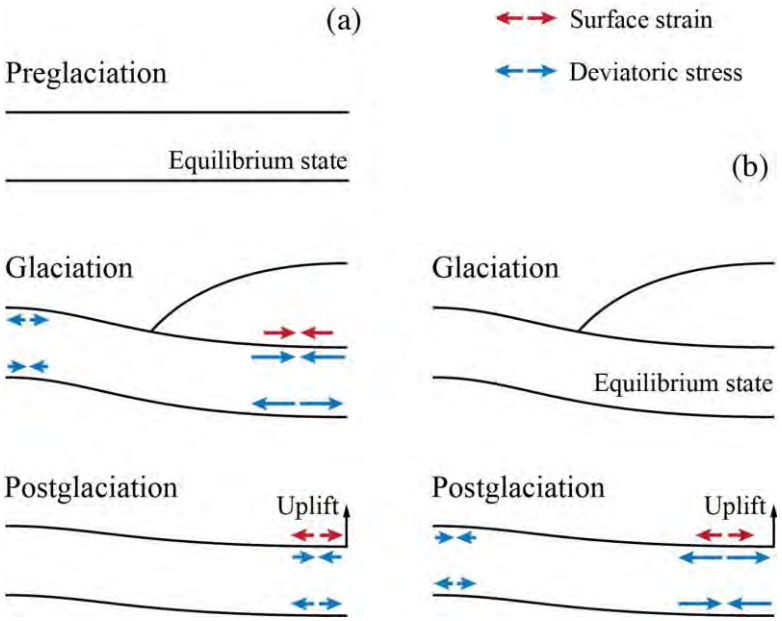

Figure 16. Two end-member cases for describing flexural stress induced by glacial isostatic adjustment (Keiding et al., 2015; Chapter 12). a) No relaxation of the stress due to the ice load has occurred before the onset of deglaciation. b) The stress due to the ice load has completely equilibrated before the onset of deglaciation. The figure is adapted from Fejerskov & Lindholm (2000, Fig. 5).

A lithosphere-scale 3-D structural model of the Lofoten-Vesterålen margin has been constructed to study the major structural features of the crystalline crust and the sedimentary cover (Maystrenko et al., 2017, Chapter 11 of the present report). All available published and/or released data have been used to set the initial 3-D model which has been validated by means of 3-D density forward modeling to obtain a gravity-consistent 3-D structural/density model. Results from the 3-D density modeling reveal that relatively thick sedimentary rocks are present in the distal Røst Basin below the lava flows. The presence of a low-density more than 20 km thick granitic body has been modeled within the middle-upper crystalline crust beneath the eastern part of the Vestfjorden Basin and the adjacent mainland. The results of the 3-D density modeling indicate also the presence of an atypical low-density lithospheric mantle beneath a large part of the Lofoten-Vesterålen margin which is required to fit the regional component of the modeled gravity with the observed one. The pronounced crustal feature within the model area is the Bivrost Lineament that appears to be the deeply seated lithosphere-scale boundary that delineates the Lofoten-Vesterålen segment from the Vøring margin showing contrasting densities and crustal thicknesses.

A 3-D temperature distribution within the Lofoten–Vesterålen segment of the Mid-Norwegian continental margin has been modelled to understand the thermal effects of late Cenozoic erosion of pre-existing sedimentary and crystalline rocks and subsequent deposition of glacial sediments during the Pleistocene (Maystrenko et al., 2018; Chapter 11 in the present report). The lithosphere-scale 3-D structural model of the Lofoten–Vesterålen area has been used as an approximation of the sedimentary infill, underlying crystalline crust and lithospheric mantle during the 3-D thermal modelling (Maystrenko et al., 2017; Chapter 10). The influence of late Cenozoic erosion and sedimentation has been included during the 3-D thermal calculations (Fig. 17). The results of the 3-D thermal modelling demonstrate that the mainland is generally colder than the basin areas within the upper part of the 3-D model. The thermal effects of the erosion and deposition also indicate that a positive thermal anomaly exists where sedimentary and crystalline rocks were eroded, and a negative thermal effect occurs in subareas affected by subsidence and sedimentation (Fig. 18). The erosion-related positive thermal anomaly reaches its maximum of more than +27°C at depths of 17–22 km beneath the eastern part of the Vestfjorden Basin. The most pronounced deposition-related negative anomaly shows a minimum of around −70°C at 17–20 km depth beneath the Lofoten Basin. The second negative anomaly is located within the northeastern part of the Vøring Basin and has minimum values of around −48°C at 12–14 km depth.

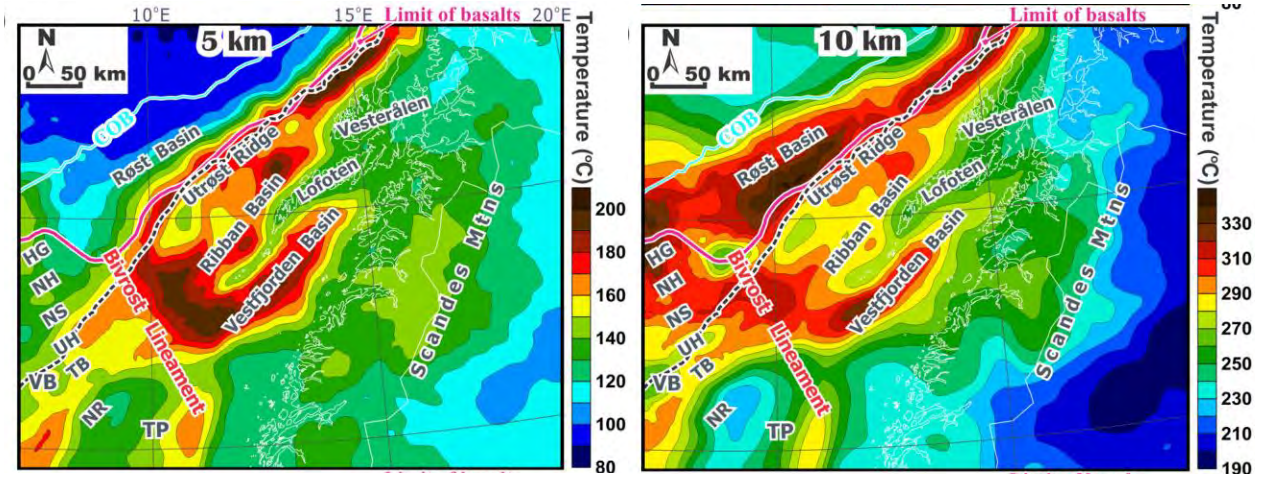

Figure 17. Maps with modelled temperatures (part of model in Maystrenko et al., 2018; Chapter 12 in the present report) at present day within the upper part of the 3-D thermal model, represented by the temperature horizontal slices for the depths (below sea level) of 5 km (left) and 10 km (right). The black dashed line corresponds to the present-day shelf edge. COB, continent-ocean boundary; HG, Hel Graben; NH, Nyk High; NR, Nordland Ridge; NS, Någrind Syncline; TB, Træna Basin; TP, Trøndelag Platform; UH, Utgard High; VB, Vøring Basin.

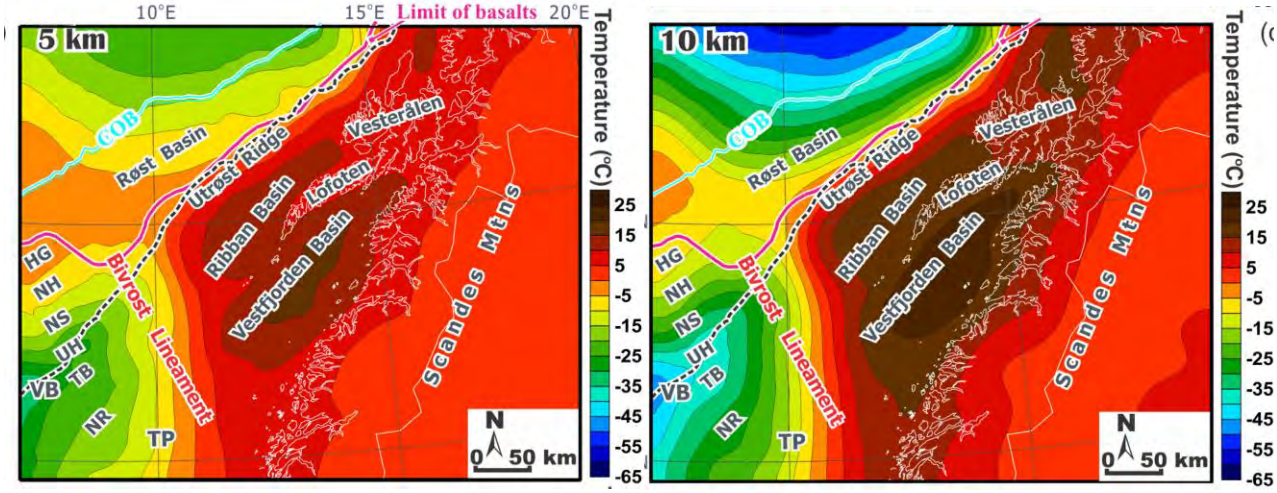

Figure 18. Thermal anomalies due to erosion and deposition during the Cenozoic, calculated as a difference between the modelled temperatures with the thermal effect of erosion/deposition and the modelled temperatures without this effect (part of model in Maystrenko et al., 2018, Chapter 12 in the present report). The map shows the thermal anomalies for the depths (below sea level) of 5 km (left) and 10 km (right). The black dashed line corresponds to the present-day shelf edge. COB, continent-ocean boundary; HG, Hel Graben; NH, Nyk High; NR, Nordland Ridge; NS, Någrind Syncline; TB, Træna Basin; TP, Trøndelag Platform; UH, Utgard High; VB, Vøring Basin.

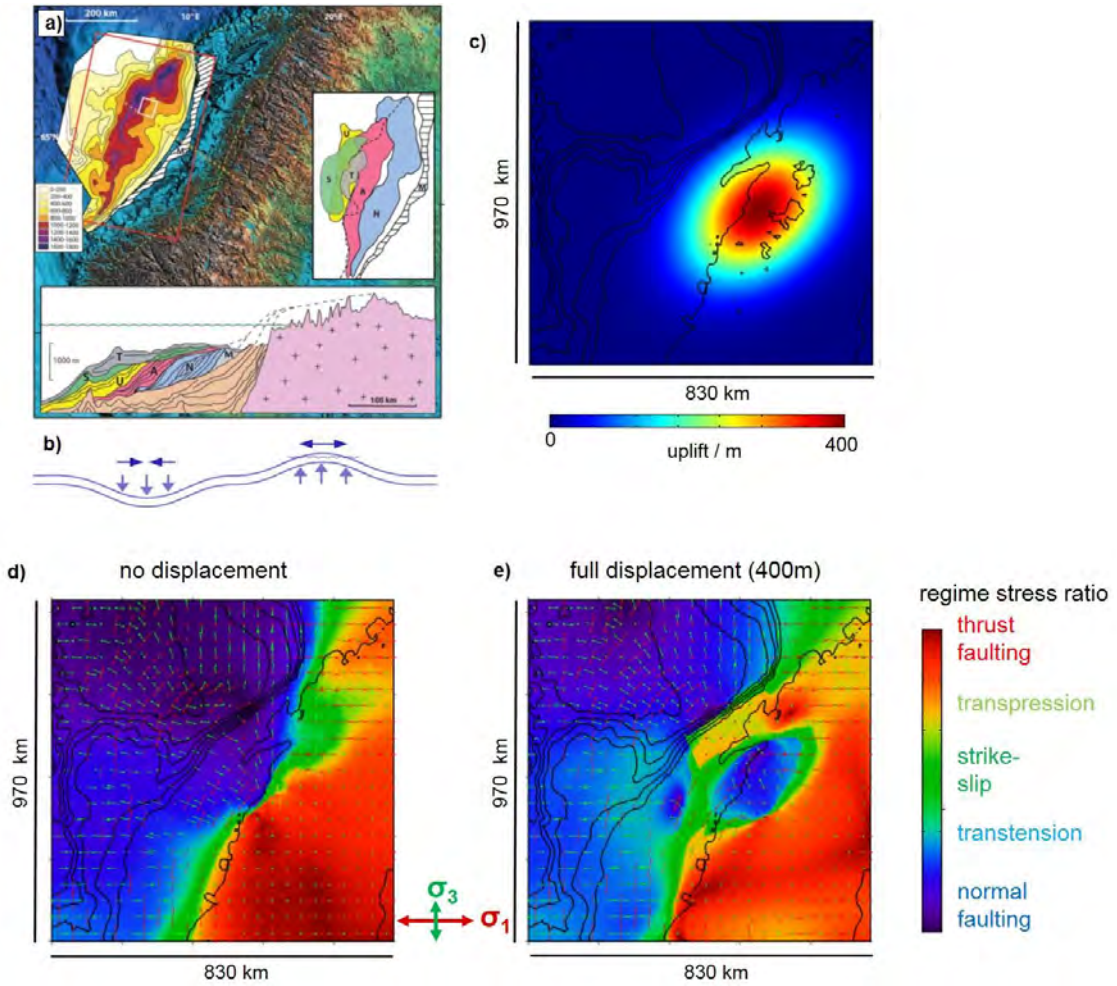

Figure 19. Model results of numerical experiments investigating the effects of erosional uplift at 2000 m burial depth (Gradmann et al., 2018, Chapter 9 in the present report). a) Observed Pleistocene deposition and erosion along the Nordland coast (Dowdeswell et al. 2010; b) Schematic flexuring response to the deposition in the west and erosion to the east. c) Test erosion model in the Vestfjorden area. d) Initial model with gravitational stress effects of crustal model (surface, top basement and Moho topography). e) Stress effect of 400 m isostatic uplift due to 500 m Pleistocene erosion (Gradmann et al., 2018, Chapter 9).

Gradmann et al. (2018, Chapter 9 in the present report) created finite element numerical models of crustal scale to study the 3D stress field, using existing geometric constraints from previous geophysical studies. The modelling of the present-day stress field evaluated the effect of ridge push, sediment loading/unloading, glacial isostasy and topography. The regional stress field is considered to stem from the interaction of ridge push and GIA (glacial isostatic adjustment); the local stress field mainly results from gravitational stresses, as well as the flexural effects of erosion and sediment deposition. The occurrence of earthquake swarms is to some degree correlating with high mountains located along the wide Nordland strandflat (Fig. 1b); thus reflecting the gravitational effect of the local topography.

Gradmann et al. (2018, Chapter 9) conclude that flexural uplift can lead to the extensional regime observed on the Nordland coast, assisted by the fault distribution. The modelled magnitude of the stress field modifications (see summary in Fig. 19 in the present Chapter and Fig. 15 in Chapter 9) presents a maximum scenario where stress release and dissipation are not considered. On the other hand, high erosion rates during the past glaciation may have kept (or brought back) the system close to extensional failure. When it comes to triggering of the earthquakes, an ongoing mechanism such as flexural uplift caused by present-day erosion seems most reasonable, especially where the uplift rate gradient is higher than predicted from the GIA model (Figs. 10 & 14).

The smallest effect is calculated for the process of glacial isostatic uplift. It barely modifies the background stress field. The Pleistocene sediment redistribution, which occurred mainly under glaciations can have modified the stress field significantly on a semi-regional scale (Gradmann et al. 2018; Chapter 9). We consider this process the main driver for the coastal extension, in particular in areas where erosion has been high.

a)

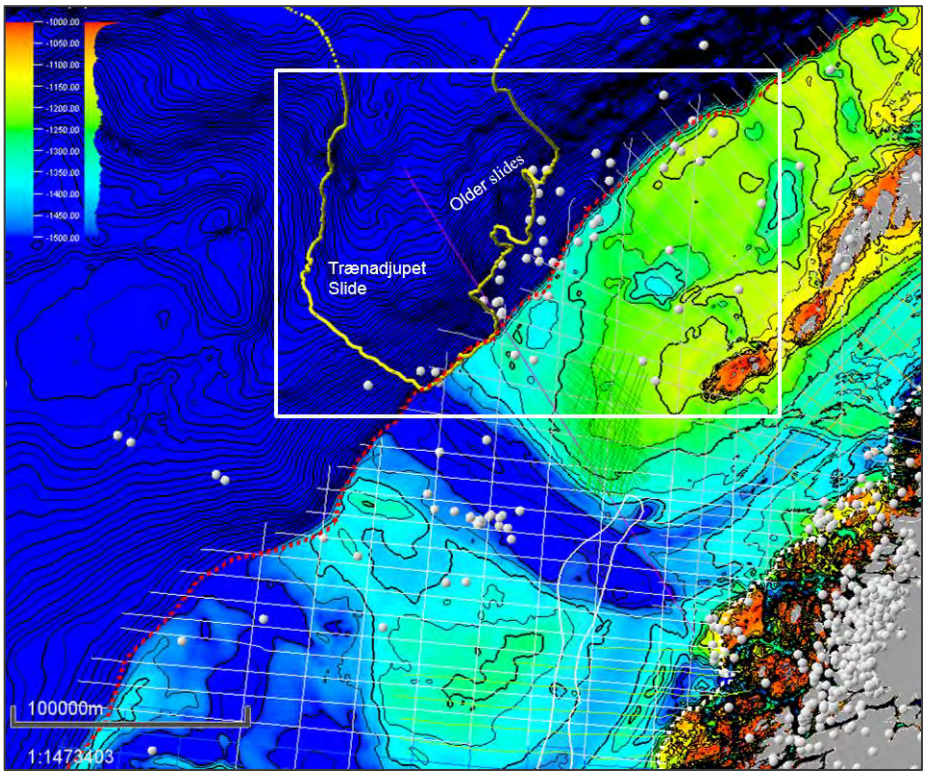

b)

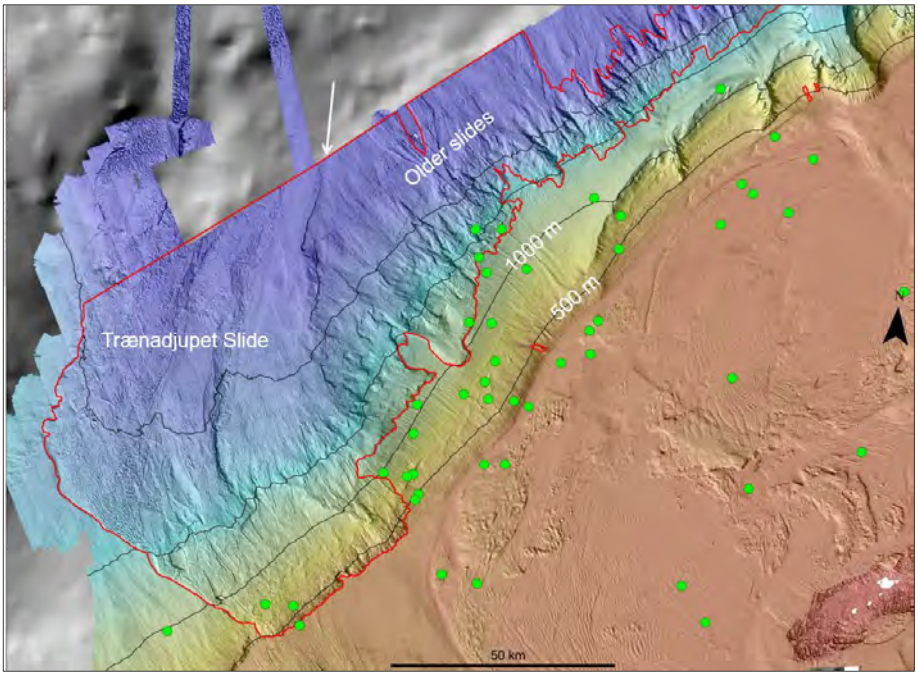

Figure 20. a) Bathymetry and NEONOR2 earthquakes (grey circles) in the Nordland area. The yellow line depicts the outline of the Trænadjupet Slide and older slides on the continental slope northeast of the Vøring Plateau. The Trænadjupet Slide occurred c. 4000 years ago and affected an area of c. 16 000 km^2 extending from the shelf break to more than 3000 m water depth in the Lofoten Basin (Laberg et al., 2002a,b). The slide mobilised an up to 180 m thick sediment package, comprising Late Weichselian glacigenic sediments and underlying contourites. The white frame depicts the location of the detailed map in Fig. b). b) Multibeam echo sounding data from the Trænadjupet slide area. The green circles represent the NEONOR2 earthquakes that are mostly occurring along the shelf break to the east of the slide scars and to the west of the Røst High (Fig. 21). The red line shows the outline of the Trænadjupet scar as well as older slide scars to the northeast.

Fig. 20 shows that more than 30 earthquakes occurred immediately to the east of the c. 4000-year-old Trænadjupet slide scar and older slides during the 2013-2016 period. Fig. 8b shows that eight fault plane solutions all indicate normal faulting and extension in this area. The extension can possibly be related to the unloading

caused by the c. 16 000 km^2 large and up to 180 m thick Trænadjupet slide. We can, however, not rule out an effect of pore pressure or gravitational effect of the steep bathymetry in this area. The occurrence of the earthquakes immediately outside the slide scar is puzzling.

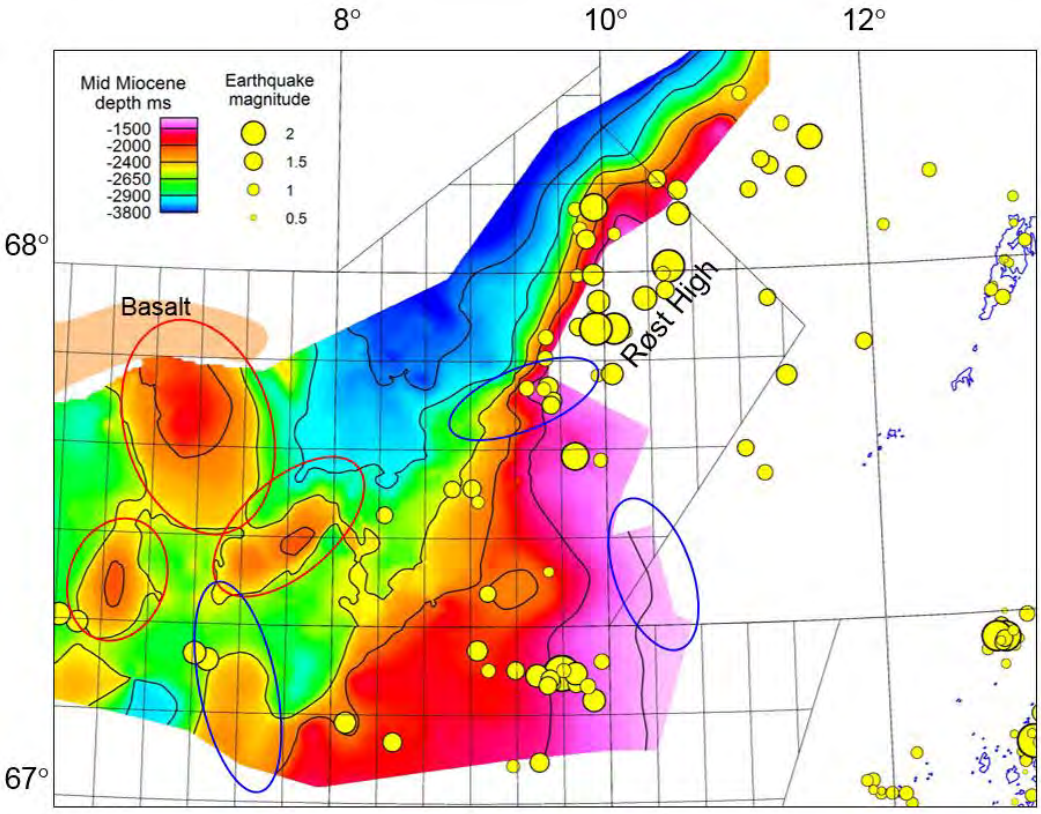

Figure 21. Mid Miocene two way time (ms) map with large compressional structures of Neogene age indicated by red and blue ellipses. The structures depicted by the black ellipses have also an older history (Eocene). The contour interval is 200 ms (NPD data).

Fig. 21 shows the location of Neogene compressional structures offshore the Lofoten Archipelago. The structures are located in the vicinity of the seismically active area. Some of the domes seem to be associated with present day seismicity at depth. The northermost earthquakes show extensional faulting while the sourternmost dome coincides with a compressionsl event (Fig. 8). New biostratigraphy and strontium isotope stratigraphy data (SIS) from two wells in the Skarv petroleum field at the steep western slope of the Nordland Ridge farther to the south (Eidvin, 2018) may have consequences for dating of Neogene tectonics in the whole study area. This segment of the Nordland Ridge is an anticlinal structure called the Sør High. The high is onlapped by sediments of Cretaceous to Neogene age, and has been uplifted in several tectonic events. A new biostratigraphic study of two wells from the Skarv Field (Eidvin, 2018) shows that the base of the glacigenic Pleistocene section is almost 200 m deeper than previously interpreted in the seismic data. The redated, glaciomarine, part is mainly fine-grained, with some crystalline pebbles. The section is characterized by a pattern indicating deposition as contourites. These sediments are tilted up towards the Sør High and consequently pre-date the last phase of anticline formation.

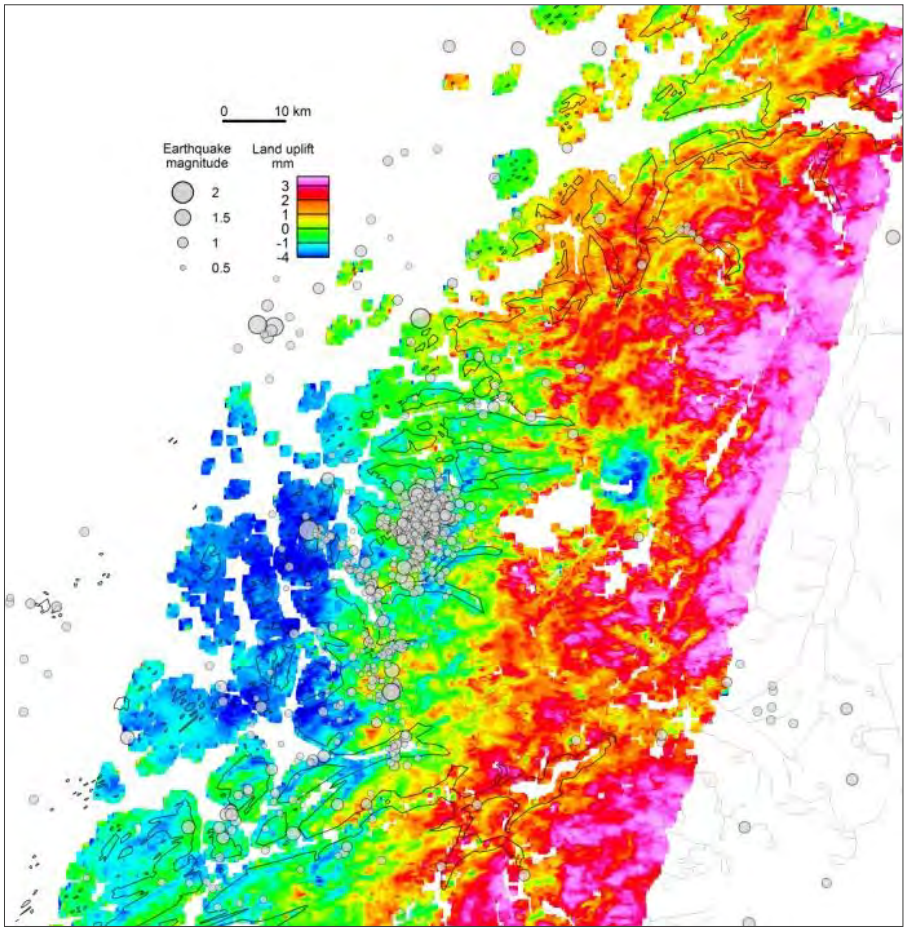

Figure 22. Interferogram (Rouyet et al. 2018; Chapter 7) showing the apparent subsidence at the coast of northern Helgeland between Sjona and Meløy (blue colours) - (unwrapped phase, integrated modulo 2pi in SAR geometry, 20.06.1999 –17.09.2000 track 380). The data are extrapolated to a distance of 700 m. The subsidence below the Storglomvatn hydropower reservoir in the central part of the map area can be seen as a blue circular area with c. 10 km diameter. The outline of the coastal subsidence area is somewhat different from the subsidence area in the data acquired between 01.06.1993 and 29.06.1995, (track 151 in Figs. 2 & 5 in Chapter 7). It is not possible to decide if this is an artifact of processing or a real subsidence difference in the two time intervals.

Figure 22 shows that the NEONOR2 seismicity occurs at the transition between an area of relative subsidence to the west and an uplift area to the east. The subsidence along the Helgeland coast area can also be seen on the residual GNSS (GPS) uplift data in Fig. 10. indicating that the relative subsidence is not a processing artifact or due to atmospheric disturbances.

Maystrenko et al. (2018; Chapter 13) have shown that the Nordland area is characterized by a temporal correlation between the number of earthquakes within the upper crystalline crust and intensity of rain and snow melt at the surface (Fig. 23). The zone of high seismic activity coincides spatially with a prominent, low-velocity and, most likely, thermally anomalous zone in the upper mantle (Fig. 24). Maystrenko et al. (2018; Chapter 13) conclude that the high seismicity is mainly controlled by the anomalous upper mantle, along with topography-induced gravitational potential energy and crustal density variations. A strong temporal correlation between seismicity and precipitation suggests that precipitation-related groundwater flow through fractured crystalline bedrock acts as a trigger on seismicity. The mechanism behind earthquake initiation is associated with a periodic pore-fluid pressure increase within the cracks and fractures of the upper-crustal crystalline bedrock resulting from groundwater recharge with gradual pore-fluid pressure diffusion to depth. The effects of glacial isostatic adjustment, Mid-Atlantic ridge push and Quaternary erosion or sedimentation superimpose on the seismicity above the anomalous mantle zones in Western Norway and the Nordland area, where conditions are especially favorable for strain and stress localization above a weak mantle.

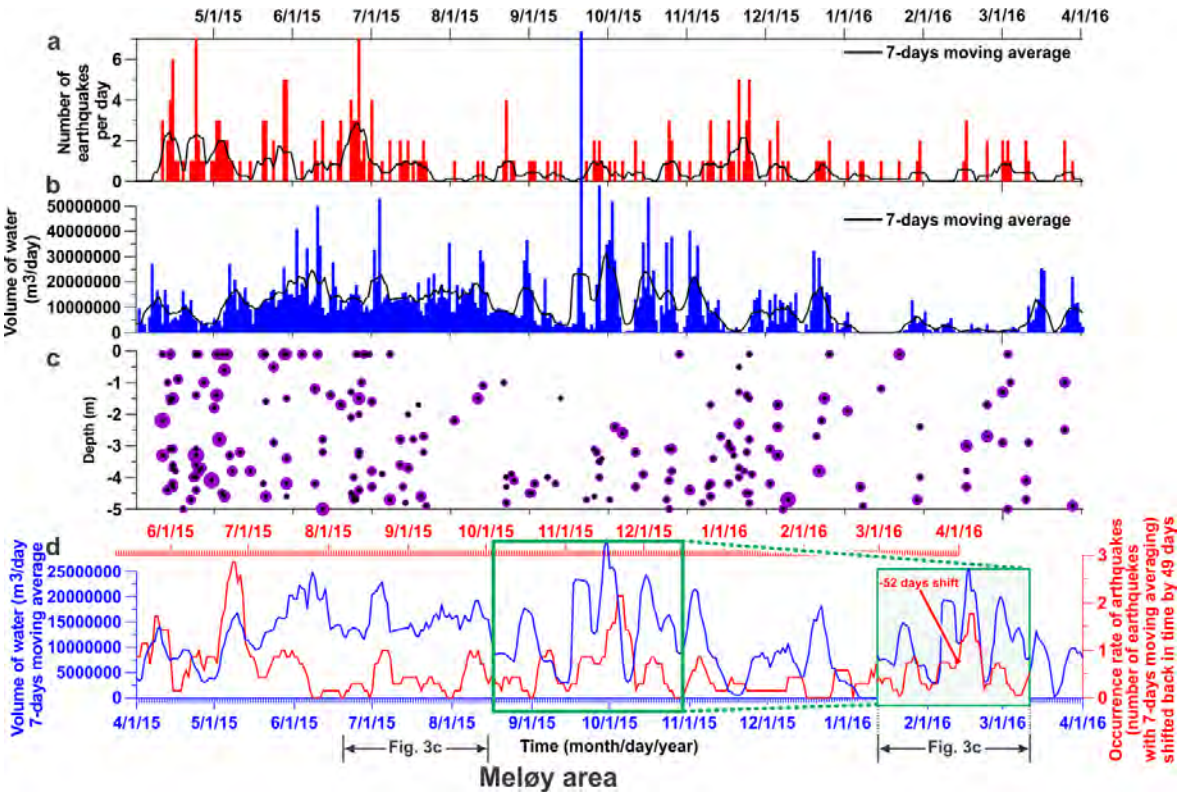

Figure 23. a) Number of shallow (not deeper than 5 km) earthquakes per day in the Meløy area (01.04.2015-01.04.2016) (Janutyte et al., 2017; Chapter 2). Earthquakes with undefined depth are also included. b) Total volume of precipitation-derived water at the Earth's surface in the Meløy area (Saloranta 2015, 2016; Senorge 2017). 7-day moving average is shown by the black line in a) and b). c) Location of earthquakes with depth (size of circles reflects magnitude of earthquakes). d) Correlation between the occurrence rate of earthquakes, represented by the 7-day moving averages, shifted by -49 (-52) days compared to a), and the averaged volume of water from b).

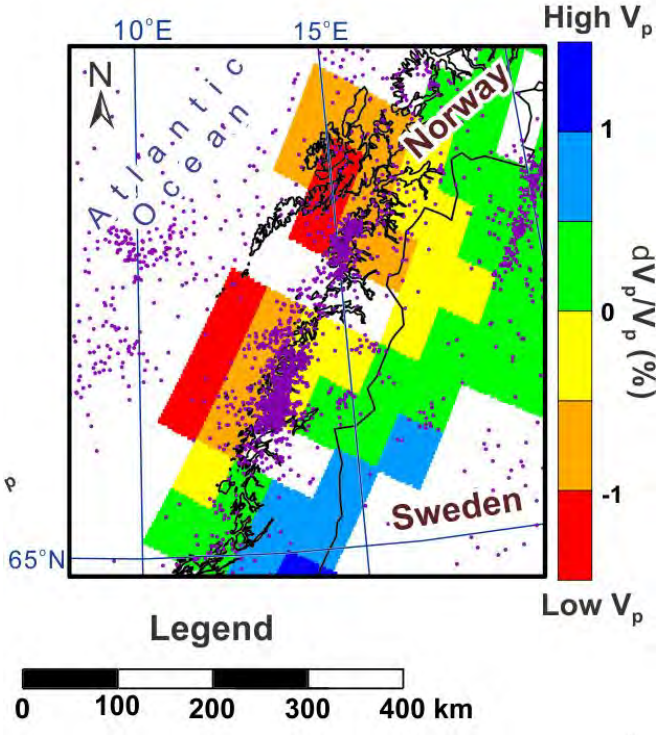

Figure 24. Upper-mantle P-wave velocity pattern at depths of 100-200 km with superimposed earthquakes within the Nordland area (Hejrani et al., 2017; Maystrenko et al., 2018; Chapter 13).

5. Discussion

The new data from the NEONOR2 project mostly comply with data that existed on beforehand. However, increased quality and quantity of the NEONOR2 data make the conclusions more reliable than before.

One of the apparent contradictions that existed in the previous data sets was the horizontal compression in the in-situ rock stress data (Hanssen & Myrvang, 1986; Hanssen 1993; Myrvang, 1993) and the extension that appeared from focal plane solutions (Hicks et al., 2000a, b). The new focal plane data reveal an extensional stress domain at a depth of 5-15 km for a large part of mainland Nordland (Janutyte & Lindholm, 2017; Michálek et al., 2018; Chapters 3 & 4 in the present report).

The borehole data from Leknes (Ask and Ask, 2018) indicate a compressional regime with σ_1 nearly horizontal in a NNW-SSE direction. We recognize that this may be either reflecting tectonic stress or gravitational stress related to the high mountains near Leknes and within a few km from the borehole both to the west and to the east. The results from this shallow borehole data diverge with the deeper earthquake data, both locally and regionally (e.g. Fig. 4 in Janutyte and Lindholm, 2017). When investigating earthquake focal mechanisms between 67.5° and 68.5°N from the shelf edge over Lofoten to Steigen a very clear picture emerges: Extensional faulting dominates. A strong dominance of extensional faulting is found from the shelf edge (17 km average depth), from two Lofoten earthquakes (17 and 26 km deep) and east into Steigen. While the earthquakes on the shelf edge and Lofoten are deep, the easternmost Steigen earthquakes are shallow with an average depth of 7 km. The findings from 19 earthquake focal mechanisms in this region clearly indicate a dominance of extensional regime, i.e. with σ_1 being vertical.

The original explanation for the high rock stress and surface spalling in Nordland was gravitational and related to the steep mountains in the area (Selmer-Olsen, 1963). Hanssen & Myrvang (1986) showed that the direction of the maximum horizontal stress was fairly constant and oriented N-S and that the surface spalling could even occur in flat areas. They concluded that the high stress was most likely related to non-gravitational tectonic forces. An E-W extensional regime could, however, also produce a relative consistent N-S oriented compressional and shallow stress when superimposed on an otherwise isotropic compressional stress. The observed shallow compressional stress can therefore be explained by a superposition of gravitational forces on the regional E-W oriented and extensional stress domain. This discrepancy can consequently be explained by a shift from shallow compression to a deeper extension. Hanssen (1998a,b) did in fact observe a transition from compressional stress through a strike-slip state at intermediate depth to a normal stress at a depth of 700 m and more in Nordland and western Norway.

The observed extensional regime from fault plane solutions below the Lofoten islands and the Utrøst Ridge (Fig. 8) is most likely including the Nordland VI and VII areas (Figs. 1b & 25). The chance of leakage from potential hydrocarbon fields is therefore quite high.

The new uplift data from InSAR and GPS measurements show that a large area along the Helgeland coast is subject to subsidence compared to previous data mostly based on repeated measurements of acorn barnacle and bladder wrack marks (Bakkelid, 1990, 1991, 1992; Dehls et al., 2002; Olesen et al., 2013b). We think that this discrepancy is mostly due to the limited number of observations in the old uplift map. Systematic errors in the measuring technique for the old data can not be totally ruled out. The subsidence area in the outer Ranafjord area registered by repeated measurements of acorn and bladder marks (Bakkelid, 1990, 1991, 1992; Olesen et al. 2013b) is not well reproduced in the new local GPS data set (Fig. 9).

The 28.6 km^2 large Storglomvatnet hydropower reservoir was filled during the period 1993-1997 (i.e. during the acquisition period 1993-1998 of the ERS data). The water level varies annually between 460 and 585 m above sea level and the reservoir capacity represents $3.5 \cdot 10^9$ m^3 which is the largest hydropower reservoir in Norway. The annual subsidence was c. 5 mm (Figs. 7 & 10, Chapter 7) and the total subsidence was c. 25 mm (Fig. 11, Chapter 7). There was no registered seismicity in the Storglomvatn area during the period 2013-2016.

Seismological and geodetic monitoring was carried out during the filling of the Blåsjø reservoir in SW Norway from 1986 to 1990 (Harsson & Bungum, 1992). This reservoir is regulated between 930 and 1055 m above sea level, has a storage capacity of $3.1 \cdot 10^9$ m^3 and is covering an area of 81 km^2 at maximum regulated height. An annual subsidence of 1.15 mm was observed and the total subsidence was reported to be several centimetres. However, no earthquakes were registered during the filling of the reservoir. A magnitude 3.7 earthquake occurred in the area in 2015.

6. Conclusions

New, large data sets of present-day crustal deformation were collected in the framework of NEONOR2. The highest seismicity occurs on the landward side of the wide strandflat characterized by high-altitude mountains, i.e. between 66°N and 67°N (Figs. 1b, 2 & 3). The area around the inselberg Blokktiden to the west of Svartisen had for instance a significant cluster of several hundred earthquakes between April and November 2015. The highest concentration of earthquakes occurs 3-7 km beneath the 1032 m high Blokktinden mountain (Fig. 3 and Cluster 2 in Figs. 4 & 5). The earthquake swarm is dipping to the northwest from a shallow depth on the eastern side of the mountain.

The ENE-WSW-trending Grønna fault at the boundary between the coastal mountains and the Vestfjorden sedimentary basin seems to be seismically active (Fig. 3). A cluster of earthquakes is also located along the eastern border of the deep Helgeland Basin and the offshore extension of the Nesna Shear Zone.

The diffuse seismicity pattern in Nordland is in agreement with a local flexural component. In summary, we conclude that flexural uplift can lead to the extensional regime observed on the Nordland coast, assisted by the fault distribution. When it comes to triggering of the earthquakes, an ongoing mechanism such as flexural uplift caused by local erosion seems most reasonable (Gradmann et al. 2018, Chapter 9 in the present report). Superposition of gravitational topography-related forces on the regional E-W oriented and extensional stress domain can also explain the observed shallow (< 800m) compressional stress regime in Nordland.

The offshore fault plane solutions in the Nordland III area south of 67°N latitude (Fig. 8) show generally a WNW-ESE oriented compression that is also complying with the World Stress Map data (Fig. 13) however, as shown in Janutyte and Lindholm (2017) the compressional direction is not well resolved in the dominating extensional regime. The compression can be related to the Pleistocene deposition of the Naust sedimentary wedge and is favorable for faults being sealed with only little leakage of petroleum from potential reservoirs. The focal plane solutions along the Nordland coast and the Lofoten Ridge-Utrøst Ridge area (Figs. 1, 7 & 8) exhibit an extensional regime compatible with erosion and flexuring. The western Ribban Basin and the Utrøst Ridge within the northern Nordland VI area offshore the Lofoten Archipelago appear to be affected by extension with a larger potential for leaking reservoirs. The shallow part of the Ribban Basin adjacent to the Lofoten Archipelago may, however, be in a compressional regime due to gravitational forces from the up to 1000 m high Lofoten mountains.

Figs. 20 & 21 reveal a spatial relationship between the NEONOR2 seismicity and the locations of the 4000 years old Trænadjupet slide and the observed Neogene domes along the continental slope to the west of the Røst High.

Using GNSS velocities and a new compilation of focal mechanism, Keiding et al. (2015, Chapter 12) find an extension of the Norwegian mainland, but a compression in outer coastal areas. However, they find that the seismic moment rates are varying more and have a magnitude at least two orders of magnitude smaller than the geodetic moment rates.

The effect of the Pleistocene sediment redistribution on the subsurface temperature has also been modelled. The erosion-related positive thermal anomaly reaches its maximum of more than +27 ºC at depths of 17-22 km beneath the eastern part of the Vestfjorden Basin (Figs. 1a & 24). The most pronounced deposition-related negative anomaly shows a minimum of around -70 ºC at 17-20 km depth beneath the Lofoten Basin. Most of the Nordland V, VI and VII areas as well as the eastern part of Nordland IV area (Fig. 24) is affected by the erosion-related positive thermal anomaly (i.e. the Ribban and Vestfjorden basins, the Nordland and Utrøst ridges and the western part of the Træna Basin).

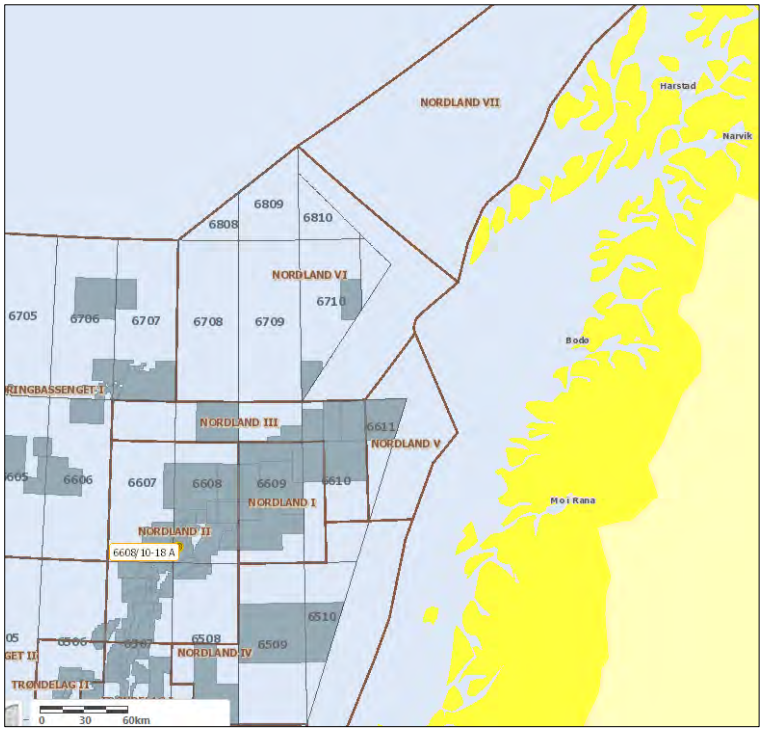

Figure 25. Part of the NPD Fact maps showing the locations of the Nordland I-VII areas http://gis.npd.no/factmaps/html_21/.

The NEONOR2 study focused on the onshore-offshore stress regime of the Nordland area, but the knowledge and insights gained here can most likely be transferred to other regions along post-glaciated passive continental margins, where it can serve as groundwork for future studies, e.g. along the Norwegian margin or other provinces in the circum Arctic region.

7. Recommendation for further work

It is recommended to combine processed differential SAR interferometry data (DInSAR) from the new Sentinel missions with new processing of local GPS measurements. The problem of going from relative velocity fields to absolute velocity fields can be solved by combining the DInSAR results with the results from the GPS network. GPS and DInSAR data are of very high temporal/low spatial or very high spatial/low temporal resolution, respectively. The two data sets complement each other, and we recommend constructing a high spatial-resolution 3D surface motion map which combines the two approaches (Samsonov & Tiampo, 2006).

We conclude that a more detailed modelling of the northern Nordland area would delimit the stress contributions from the sediment loading/unloading and the mainland topography and offshore bathymetry in more detail. The larger Nordland area is too extensive for a successful finite element modelling. A new and detailed modelling could also take advantage of future EPOS focal plane solutions, GPS data as well as the new InSAR data from the ESA Sentinel missions. The new data are partly acquired within the EPOS-N programme (European Plate Observing System – Norway sub-project) where several of the NEONOR2 partners are participating under the management of the University of Bergen. A marine seismic array will improve the location accuracy of the offshore earthquakes as well as the quality of the offshore fault plane solutions.

8. Acknowledgements

The project was funded by the Geological Survey of Norway (NGU), Norwegian Research Council, the Norwegian Mapping Authority (Kartverket), NORSAR, the Norwegian Petroleum Directorate (NPD), the University of Bergen (UiB), AkerBP (former Det norske), DEA (former RWE Dea), Equinor (former Statoil), INEOS (former DONG), Lundin, Neptune (former VNG), Repsol, Shell and Total (former Maersk). E.On and NORECO were originally participants in the project but their Norwegian activities were later acquired by DEA and AkerBP, respectively. Anne Liinamaa-Dehls translated Chapter 7 from Norwegian to English and proofread Chapters 1, 4, 8, 9 and 13.

She also compilated the individual chapters of the present report. Cyprien Habimana and Hild Sissel Thorsnes assisted in the administration of the NEONOR2 Project. Ingrid Anne Munz followed up the project at the Research Council of Norway. The sponsor representatives Arne Grønlie and Hans Konrad Johnsen from AkerBP, Klaus Dittmers from DEA, Anne-Lise Lysholm and Arnaud Santoire from E.On, Halvor Bunkholt, Peter Midbøe and Torbjørn Dahlgren from Equinor, Carlo Cavalli, Nigel Marsh and Sidiq Pramada from INEOS, Harald Brunstad and Håvard Buran from Lundin, Marcus Lang from Maersk, Reinert Seland from NORECO, Dag Bering from NPD, Gunnar Aschjem from Repsol, Rikkert Moeys from Shell and Alastair Welbon, Tim Allaway and Ben De Mol from VNG gave advice and support during the project period. We express our sincere thanks to these persons, institutions and companies.

9. References

Ask, D. & Ask, M.V.S. 2018: Results from the Neotectonics in Nordland - Implications for Petroleum Exploration (NEONOR2) project, Work package 3: In situ stress measurements. *Chapter 8, NGU Report 2018.010* (Present report).

Ask, D., Stephansson, O., Cornet, F.H., Ask, M.V.S. 2009: Rocha Medal: Rock stress, rock stress measurements, and the integrated stress determination method (ISDM). Rock Mechanics and Rock Engineering, 42: 559-584.

Auriac, A., Whitehouse, P.L., Bentley, M.J., Patton, H., Lloyd, J.M. & Hubbard, A. 2016: Glacial isostatic adjustment associated with the Barents Sea ice sheet: A modelling intercomparison. *Quaternary Science Reviews,* http://dx.doi.org/10.1016/j.quascirev.2016.02.011

Bakkelid, S. 1990: Innmåling av rur- og tangrandmerker i Nordland. *Statens kartverk Rapport 3/1990*, 90 pp.

Bakkelid, S. 1991: Innmåling av rur- og tangrandmerker i Troms og Nordland. *Statens kartverk Rapport 2/1991*, 91 pp.

Bakkelid, S. 1992: Mapping the rate of crustal uplift in Norway: parameters, methods and results. *Norsk Geologisk Tidsskrift 72*, 239–246.

Blystad, P., Brekke, H., Farseth, R.B., Larsen, B.T., Skogseid, J. & Torudbakken, B. 1995: Structural elements of the Norwegian continental shelf, Part II. The Norwegian Sea Region. *Norwegian Petroleum Directorate Bulletin 8,* 45 pp.

Bugge, T., Ringås, J.E., Leith, D.A., Mangerud, G., Weiss, H.W. & Leith, T.L. 2002: Upper Permian as a new play model on the mid-Norwegian continental shelf: Investigated by shallow stratigraphic drilling. *AAPG Bulletin 86,* 107–127.

Bungum, H. Olesen, O., Pascal, C., Gibbons, S., Lindholm, C. &. Vestøl, O. 2010: To what extent is the present seismicity of Norway driven by postglacial rebound? *Journal of the Geological Society, London 167,* 373-384.

Bøe, R., Smelror, M., Davidsen, B. & Walderhaug, O. 2008: Nearshore Mesozoic basins off Nordland, Norway: Structure, age and sedimentary environment. *Marine and Petroleum Geology 25*, 235–253.

Chand, S., Thorsnes, T., Rise, L., Brunstad, H., Stoddart, D., Bøe, R., Lågstad, P. & Svolsbru, T. 2012: Multiple episodes of fluid flow in the SW Barents Sea (Loppa High) evidenced by gas flares, pockmarks and gas hydrate accumulation. *Earth and Planetary Science Letters 331-332,* 305–314.

Dehls, J.F., Basilico, M. & Colesanti, C. 2002: Ground deformation monitoring in the Ranafjord area of Norway by means of the Permanent Scatterers technique, Geoscience and Remote Sensing Symposium, 2002. IGARSS '02. 2002 IEEE International, Volume 1: Toronto, 203-207.

Dehls, J.F., Olesen, O., Bungum, H., Hicks, E., Lindholm, C.D. & Riis, F. 2000: Neotectonic map, Norway and adjacent areas 1:3 mill. Geological Survey of Norway, Trondheim.

Dowdeswell, J.A., Ottesen, D. & Rise, L. 2010: Rates of sediment delivery from the Fennoscandian Ice Sheet through an ice age. *Geology* 38, 3–6.

Eide, E.A., Osmundsen, P.T., Meyer, G.B., Kendrick, M.A. & Corfu, F. 2002: The Nesna Shear Zone, north-central Norway: an $^{40}Ar/^{39}Ar$ record of Early Devonian – Early Carboniferous ductile extension and unroofing. *Norwegian Journal of Geology 82*, 317–339.
Eidvin, T. 2018: Biostratigraphy and strontium isotope stratigraphy (SIS) of the upper part of the Brygge Formation, Kai and Naust formations in well 6507/5-1 and cored section of the Naust Formation in well 6507/5-J-1 H from the the Skarv Field (Revfallet Fault Complex, Norwegian Sea shelf). Unpublished NPD report.

FENCAT, 2017. A joint Fennoscandian earthquake catalogue courtesy of University of Helsinki. Retrieved January 2017 from http://www.helsinki.fi/geo/seismo/english/bulletins/.

Fejerskov, M. & Lindholm, C.D. 2000: Crustal stress in and around Norway; an evaluation of stress-generating mechanisms. In Nøttvedt. A. (ed.): Dynamics of the Norwegian margin, Geological Society, London, Special Publications 167, 451-467.

Ferretti, A., Prati, C., & Rocca, F. 2000: Nonlinear subsidence rate estimation using permanent scatterers in differential SAR interferometry, Ieee Transactions on *Geoscience and Remote Sensing 38*, 2202-2212.Gabrielsen, R.H., Braathen, A., Dehls, J. & Roberts, D. 2002: Tectonic *lineaments of Norway. Norwegian Journal of Geology 82*, 153–174.

Gradmann, S., Olesen, O., Keiding M. & Maystrenko, Y.P. 2018: The regional 3D stress field of Nordland, northern Norway - insights from numerical modelling Chapter 9, NGU Report 2018.010 (Present report).

Gustavson, M. & Blystad, P. 1995: Geologisk kart over Norge, berggrunnskart BODØ, M 1:250 000. *Norges geologiske undersøkelse.*

Gustavson, M. & Gjelle, S.T. 1991: Berggrunnskart Mo i Rana, scale 1:250 000. *Norges geologiske undersøkelse.*

Haimson B.C. & Cornet, F.H. 2003: ISRM suggested methods for rock stress estimation; Part III:Hydraulic fracturing methods. J. Rock Mech. Min. Sc. 40, 1011-1020.

Haines, A.J. & Holt, W.E., 1993: A Procedure for Obtaining the Complete Horizontal Motions Within Zones of Distributed Deformation from the Inversion of Strain Rate Data. J. Geophys. Res. 98, 12,057-12,082

Hanssen, T. H. 1998a: Investigations of some rock stress measuring techniques and the stress field in Norway. Dr.Ing. Thesis, Norwegian University of Science and Technology, 188 pp.

Hanssen, T.H. 1998b: Rock stresses and tectonic activity. *In:* Proc. of the Rock Construction Conference, Section II Rock Mechanics, 27 November, 1998, Oslo. Alten, T., Hermann, S., Beitnes, A. & Berg, K. (Eds.) Norsk Jord- og Fjellteknisk Forbund, Oslo. pp. 29.1-29.24.

Hanssen, T. H. & Myrvang, A.M. 1986: Rock stresses and rock stress effects in the Kobbelv area, northern Norway. Proceedings Int. Symp. on Rock Stress and Rock Stress Measurements, Stockholm. Centek Publisheres, Luleå, Sweden.

Harsson, B.G. & Bungum, H. 1992: Multidisciplinary environmental monitoring of the Blåsjø reservoir area, Norway, A progress report. *Norwegian Mapping Authority Geodetic Publications 1992:1,* 36 pp.

Heidbach, O., Rajabi, M., Reiter, K., Ziegler, M. & WSM Team, 2016: *World Stress Map Database Release 2016*. GFZ Data Services. doi.org/10.5880/WSM.2016.001

Hejrani, B., Balling, N., Jacobsen, B. H. & England, R. 2017: Upper-mantle velocities below the Scandinavian Mountains from P- and S-wave traveltime tomography. *Geophys Journal International 208*, 177-192, doi:10.1093/gji/ggw370.

Hicks, E.C., Bungum, H. & Lindholm, C.D. 2000a: Stress inversion of earthquake focal mechanism solutions from onshore and offshore Norway. Norsk Geologisk Tidsskrift 80, 235-250.

Hicks, E., C., Bungum, H. & Lindholm, C.D. 2000b Seismic activity, inferred crustal stresses and seismotectonics in the Rana region, northern Norway. *Quaternary Science Reviews 19,* 1423-1436.

IKU, 1995. Shallow Drilling Helgeland 1992. IKU Sintef Group Information sheet no.: 15, Project 23.1684.00, Shallow Drilling, 2 pp.

Janutyte, I. & Lindholm, C. 2017: Earthquake source mechanisms in onshore and offshore Nordland, northern Norway. *Norwegian Journal of Geology 97*, 177–189. https://dx.doi.org/10.17850/njg97-3-03.

Janutyte, I., Lindholm, C. & Olesen, O. 2017: Relation between seismicity and tectonic structures offshore and onshore Nordland, northern Norway. *Norwegian Journal of Geology 97*, 161-175, doi:10.17850/njg97-03-02.

Keiding, M.,, Kreemer, C., Lindholm, C.D., Gradmann, S., Olesen, O. & Kierulf, H.P. 2015: A comparison of strain rates and seismicity for Fennoscandia: depth dependency of deformation from glacial isostatic adjustment. *Geophysical Journal International 202*, 1021–1028.

Keiding, M., Olesen, O. & Dehls, J. 2018a: Neotectonic map of Norway and adjacent areas, Scale 1:3 million, Geological Survey of Norway.

Keiding, M., Olesen, O. & Dehls, J. 2018b: Neotectonic map of Norway and adjacent areas, map description. *Chapter 14, NGU Report 2018.10* (Present report).

Kierulf, H.P. 2017: Analysis strategies for combining continuous and episodic GNSS for studies of neo-tectonics in Northern-Norway. Journal of Geodynamics 109, 32–40.

Kierulf, H.P., Ouassou, M., Simpson, M.J.R, & Vestøl, O. 2012: A continuous velocity field for Norway, Journal of Geodesy, 1–13, DOI 10.1007/s00190-012-0603-2.

Kierulf, H.P., Steffen, H., Simpson, M.J.R., Lidberg, M., Wu, P., H.W, 2014: A GPS velocity field for Fennoscandia and a consistent comparison to glacial isostatic adjustment models. *Journal of Geophysical Research: Solid Earth 119,* 6613–6629. http://dx.doi.org/10.1002/2013JB010889.

Laberg, J.S., Vorren, T.O., Mienert, J., Bryn, P. & Lien, R. 2002a: The Trænadjupet Slide: a large slope failure affecting the continental margin of Norway 4000 years ago. *Geo-Marine Letters* 22, 19-24.

Laberg, J.S, Vorren, T.O., Mienert, J., Evans, D., Lindberg, B., Ottesen, D., Kenyon, N.H. & Henriksen, S. 2002b: Late Quaternary paleoenvironmentand chronology in the Trænadjupet Slide area offshore Norway.*Marine Geology* 188, 35-60.

Lagerbäck, R. & Sundh, M. 2008: Early Holocene faulting and paleoseismicity in northern Sweden, Geological Survey of Sweden. *SGU Research Paper C 836,* 84 pp. SGU, Uppsala, Sweden.

Maystrenko, Y.P., Gernigon, L., Olesen, O., Ottesen, D., & Rise, L 2018: 3-D thermal effect of late Cenozoic erosion and deposition within the Lofoten–Vesterålen segment of the Mid-Norwegian continental margin. *Geophys. J. Int. 213*, 885–918. doi: 10.1093/gji/ggy013.

Maystrenko, Y.P., Olesen, O., Gernigon, L. & Gradmann, S., 2017. Deep structure of the Lofoten–Vesteåalen segment of the Mid-Norwegian continental margin and adjacent areas derived from 3-D density modeling, *J. Geophys. Res.,* 122, 1402–1433.

Maystrenko, Y.P., Brönner, M., Olesen, O., Saloranta, M. & Slagstad, T. 2018: Do elevated precipitation rates and anomalous upper mantle cause intraplate seismicity in Norway? *Chapter 13, NGU Report 2018.010* (Present report).

Myrvang, A. 1993: Rock stress and rock stress problems in Norway. *In* J.A. Hudson (ed.): *Comprehensive rock engineering. Vol. 3, Rock testing and site characterization.* Pergamon Press, pp. 461–471.

Michálek, J., Tjåland, N., Drottning, A., Strømme, M.L., Storheim, B.M, Rondenay, S. & Ottemöller, L. 2018: Report on seismic observations within the NEONOR2 project in the Nordland region, Norway. *Chapter 4, NGU Report 2018.10* (Present report).

Nyland, B., Jensen, L.N., Skagen, J., Skarpnes, O. and Vorren, T.O. 1992: Tertiary uplift and erosion in the Barents Sea: magnitude, timing and consequences. In Larsen, R. M., Brekke, H., Larsen, B. T. & Talleraas, E. (eds.): Structural and tectonic modeling and its applications to Petroleum Geology, 153-162. Elsevier, Amsterdam.

Olesen, O., Gjelle, S., Henkel, H., Karlsen, T.A., Olsen, L. & Skogseth, T. 1995: Neotectonics in the Ranafjorden area, northern Norway (Extended abstract). *Norges geologiske undersøkelse Bulletin 427,* 5-8.

Olesen, O., Lundin, E., Nordgulen, Ø., Osmundsen, P.T., Skilbrei, J.R., Smethurst, M.A., Solli, A., Bugge, T. & Fichler, C. 2002: Bridging the gap between the Nordland onshore and offshore geology. *Norwegian Journal of Geology 82*, 243–262.

Olesen, O., Blikra, L.H., Braathen, A., Dehls, J.F., Olsen, L., Rise, L., Roberts, D., Riis, F., Faleide, J.I. & Anda, E. 2004: Neotectonic deformation in Norway and its implications: a review. *Norwegian Journal of Geology 84*, 3-34.

Olesen, O., Bungum, H., Dehls, J., Lindholm, C., Pascal, C. & Roberts, D. 2013a: Neotectonics, seismicity and contemporary stress field in Norway – mechanisms and implications. *In* Olsen, L., Fredin, O. & Olesen, O. (eds.): *Quaternary Geology of Norway*, Geological Survey of Norway Special Publication 13, pp. 145–174.

Olesen, O. Kierulf, H.P., Brönner, M., Dalsegg, E. & Fredin, O. 2013b: Deep weathering, neotectonics and strandflat formation in Nordland, northern Norway. *Norwegian Journal of Geology 93,* 189-213.

Olsen, L., Olesen, O., Dehls, J.F. & Tassis, G. in press: Late-/postglacial age and tectonic origin of the Nordmannvikdalen Fault, northern Norway — to be or not to be. Submitted to Norwegian Journal of Geology.

Palmu, J.-P., Ojala, A.E.K., Ruskeeniemi, T., Sutinen, R. & Mattila, J. 2015: LiDAR DEM detection and classification of postglacial faults and seismically-induced landforms in Finland: a paleoseismic database. *Journal Geol. Soc. Sweden (GFF) 137:4*, 344-352, DOI:10.1080/11035897.2015.1068370

Redfield, T.F. & Hermanns, R.L. 2016: Gravitational slope deformation, not neotectonics: Revisiting the Nordmannvikdalen feature of northern Norway. Norwegian Journal of Geology 96, 1-29. http://dx.doi.org/10.17850/njg96-3-05.

Rise, L., Ottesen, D., Berg, K. & Lundin, E. 2005: Large-scale development of the mid-Norwegian margin during the last 3 million years. Marine and Petroleum Geology 22, 33–44.

Rouyet, L., Lauknes, T.R. & Larsen, Y. 2018; InSAR deformation analysis for Helgeland. *Chapter 7, NGU Report 2018.10* (Present report).

Saloranta, T.M. 2015: New version (v.1.1.1) of the seNorge snow Model and Snow Maps for Norway. Norwegian Water Resources and Energy Directorate Report 6-2014 30 ().

Saloranta, T. M. 2016: Operational snow mapping with simplified data assimilation using the seNorge snow model. *Journal of Hydrology* 538, 314-325, doi:10.1016/j.jhydrol.2016.03.061.

Selmer-Olsen, R. 1963: On rock stress (in Norwegian). Proc. of the Rock Engineering Conference, Oslo. Norwegian Tunneling Society, Oslo.

Senorge 2017: *Rain and snow melt maps*, <http://www.senorge.no/index.html?p=senorgeny&st=water&m=bmNVEGrey%3BMapLayer_qtt%3B&l=en&d=1501668000000&e=-1578728%7C6122545%7C2582816%7C8249375&fh=0%3B2468>.

Samsonov, S. & Tiampo, K 2006: Analytical optimization of InSAR and GPS dataset for derivation of three-dimensional surface motion, IEEE Geoscience and Remote Sensing Letters, 3, 107-111.

Sigmond, E.M.O. 2002: Geological map, land and sea areas of northern Europe, Scale 1:4 million. Geological Survey of Norway.

Vestøl, O. 2006: Determination of postglacial land uplift in Fennoscandia from leveling, tide-gauges and continuous GPS stations using least squares collocation. *Journal of Geodesy 80*, 248–258.

Vestøl, O., Ågren, J., Steffen, H. in prep: A new land uplift model for Fennoscandia and the Baltic Region.

Waldhauser, F. & Ellsworth, W.L. 2000: A double-difference earthquake location algorithm: method and application to the Northern Hayward Fault, California. *Bull. Seism. Soc. Am., 90(6),* 1353–1368.

Wells, D.L. & Coppersmith, K.J. 1994: Empirical relationships among magnitude, rupture length, rupture area, and surface displacement. *Bulletin of the Seismological Society of America 84*, 974–1002.

Zattin, M., Andreucci, B., de Toffoli, B., Grigo, D. & Tsikalas, F. 2016: Thermochronological constraints to late Cenozoic exhumation of the Barents Sea Shelf. *Marine and Petroleum Geology 73,* 97-104.

Zieba, K.J., Felix, M. & Knies, J. 2016: Pleistocene contribution to the net erosion and sedimentary conditions in the outer Bear Island Trough, western Barents Sea. *Arktos 2:23,* DOI 10.1007/s41063-016-0022-3

Zoback, M.D., Barton, C.A., Brudy, M., Castillo, D.A., Finkbeiner, T., Grollimund, B.R., Moos, D.B., Peska, P., Ward, C.D. & Wiprut, D.J. 2003: Determination of stress orientation and magnitude in deep wells. *Rock Mech. Min. Sc. 40,* 1049–1076.

CHAPTER 2: RELATION BETWEEN SEISMICITY AND TECTONIC STRUCTURES OFFSHORE AND ONSHORE NORDLAND, NORTHERN NORWAY

Authors: Ilma Janutyte[1], Conrad Lindholm[1] & Odleiv Olesen[2]

Affiliations: [1]NORSAR, 2027 Kjeller, Norway; [2]Geological Survey of Norway, P. O. Box 6315 Torgarden, 7491 Trondheim, Norway.

Journal: Norwegian Journal of Geology, Vol 97 Nr. 3

Publishing Date: 24. October 2017 (OA)

DOI: https://dx.doi.org/10.17850/njg97-3-02

Pages: 11

NORWEGIAN JOURNAL OF GEOLOGY Vol 97 Nr. 3
https://dx.doi.org/10.17850/njg97-3-02

Geological Society of Norway

Relation between seismicity and tectonic structures offshore and onshore Nordland, northern Norway

Ilma Janutyte[1], Conrad Lindholm[1] & Odleiv Olesen[2]

[1] *NORSAR, 2027 Kjeller, Norway.*
[2] *Geological Survey of Norway, P. O. Box 6315 Torgard, 7491 Trondheim, Norway.*

E-mail corresponding author (Ilma Janutyte): ilma@inbox.lt

A temporary network of 27 seismic stations was deployed from August 2013 to May 2016 along the coast of Nordland, northern Norway, where northwestern Europe's largest earthquake of magnitude 5.8 over the last two centuries has occurred. The NEONOR2 project aimed to improve our understanding of neotectonic movements, stress regime and the overall seismicity pattern in Nordland and the adjacent offshore areas. From the data retrieved from the temporary NEONOR2 deployment and the permanent stations of the Norwegian National Seismic Network, nearly 1250 earthquakes were located in the study area. During the monitoring period, the seismic activity in Nordland was mostly sporadic, but in some areas it was clearly episodic, especially to the west of the Svartisen glacier where an earthquake swarm with several hundred small seismic events was recorded from April 2015 until March 2016. The shallow swarm activity could possibly be partly related to the changes in the glacier mass and groundwater conditions. During the monitoring period, no earthquakes were recorded along the prominent Bivrost transfer zone, on the Trøndelag Platform and in the larger Vestfjorden Basin area, and it could therefore be concluded that these areas are aseismic; however, only three years of monitoring in such areas of low deformation rates is not enough to make strict conclusions. The observed lack of seismicity in the area generally confirmed earlier observations, though in this case with much more improved new data. The observations onshore provided clear indications of seismic activity along several previously unknown structures and well-defined lineaments trending NE–SW and NNW–SSE to the southwest of Svartisen, while a migration of the seismicity on some of these features was also recorded.

Keywords: seismicity in Nordland; earthquake swarm; magnitude of completeness; Bivrost transfer zone; offshore structures

Received 08. March 2017 / Accepted 28. August 2017 / Published online 24. October 2017

Introduction

The territory of Nordland with adjacent offshore regions is one of the seismically most active areas in Norway. Although the majority of the earthquakes are never felt, the Nordland region is capable of releasing larger earthquakes; and the largest known historical earthquake during the last two centuries in northwestern Europe with a magnitude of about M 5.8 occurred in 1819 in the Rana area (Muir-Wood, 1989; Bungum & Olesen, 2005). Another important feature of the seismicity in Nordland is that of earthquake swarms which generally occur along the coast (e.g., Atakan et al., 1994; Hicks et al., 2000a; Bungum et al., 2010). Moreover, it was reported that the territory of Nordland exhibits features of neotectonic movements (Dehls & Olesen, 2000), which together with the seismicity have been related to stress generation from the ridge push of the Atlantic Ocean, the post-glacial rebound, and the sediment redistribution and topography (e.g., Olesen et al., 2013a). In addition, the geological settings in Nordland are very complex: the Caledonian nappes are folded down to 5 km deep (Midtun, 1988; Olesen et al., 2002), intrusive igneous bodies, such as the Transscandinavian Igneous Belt (e.g., Gaal & Gorbatschev, 1987; Henkel & Eriksson,

Janutyte, I., Lindholm, C & Olesen, O. 2017: Relation between seismicity and tectonic structures offshore and onshore Nordland, northern Norway. *Norwegian Journal of Geology 97*, 161–175. https://dx.doi.org/10.17850/njg97-3-02.

1987; Larson & Berglund, 1992; Hogdahl et al., 2004), are located onshore, while the Moho depth varies from less than 20 km offshore to the west to more than 45 km onshore to the east with a convex Moho bulge under the Lofoten–Vesterålen region (Olesen et al., 2002; Maystrenko et al., 2017). As earthquakes generally occur along pre-existing zones of weakness and result from a buildup of stress and/or reduced effective shear strength along favourably oriented faults (e.g., Davis & Reynolds, 1996), all the factors mentioned above could influence the stress field and may have an effect on the tectonic structures, which are abundant in the Nordland area. In spite of many efforts (e.g., Muir-Wood, 2000; Fejerskov & Lindholm, 2000; Redfield & Osmundsen, 2015; Fjeldskaar et al., 2000), the relative contribution of the different stress components to the overall stress field in the area is not yet fully resolved. The NEONOR2 project (Neotectonics in Nordland - Implications for petroleum exploration; https://www.ngu.no/en/neonor2) in 2013–2017 aimed to improve the understanding of regional-scale stress and strain dynamics in the Nordland area through a detailed monitoring of seismicity, geodetic movements and the state of in situ stress. The first step in solving the fundamental questions is through understanding the overall distribution of seismicity in the region and its possible association with the main geological and tectonic features. This paper aims to investigate the relation between earthquakes and tectonic structures in the Nordland area, both onshore and offshore, based on the up-to-date seismological data obtained during the NEONOR2 project from August 2013 to May 2016. The results will subsequently be used in the 3-D numerical modelling to correlate these observations with the denudation and depositional history in order to estimate the Pleistocene palaeo-stresses and thermal fields in 3-D.

Tectonic structures

The bedrock geology of mainland Nordland is dominated by rocks of the Caledonian Upper and Uppermost Allochthons that were thrust onto lower nappe complexes and the subjacent Precambrian basement during the Scandian continent-continent collision in Silurian and Devonian time (Roberts & Gee, 1985). In the Devonian, the nappes were dismembered by a late gravity collapse phase of the Scandian orogeny (Rykkelid & Andresen, 1994; Braathen et al., 2002; Eide et al., 2002).

The offshore area of Nordland (Fig. 1) consists of the northern Trøndelag Platform, the Træna, Vestfjorden, Ribban and Røst basins, and the Nordland, Lofoten and Utrøst ridges (Blystad et al., 1995). A major tectonic structure/zone in the area is the Bivrost Lineament (Blystad et al., 1995) that was interpreted to represent a late-Caledonian detachment reactivated as a transfer zone (i.e., the Bivrost transfer zone, BTZ) during the subsequent rifting events (Olesen et al., 2002). The BTZ seems to divide the Precambrian rocks to the northeast from the Caledonian fold belt to the southwest. The Nesna Shear Zone (NSZ) on the mainland is the major extensional detachment that disrupted the Caledonian nappes (Braathen et al., 2002; Eide et al., 2002), while offshore to the west of Træna island, the NSZ sharply changes direction from N–S to E–W. The BTZ has most likely reactivated the NSZ or an échelon detachment parallel to the NSZ (Olesen et al., 2002). Slightly to the south of Svartisen, Gabrielsen et al. (2002) indicated two major fault trends: one group aligned NE–SW direction and the other group trending NW–SE. The NW–SE trend coincides well with the seismological observations by Hicks et al. (2000a), while Midtun (1988) reported minor offsets along the NE–SW-trending fracture zones.

Close to the Steigen area lies the Sagfjord Shear Zone (SSZ) that also formed during the gravity collapse of the Caledonide Orogen (Braathen et al., 2002). In the Lofoten and Vestfjorden areas there are two sets of lineaments trending ENE–WSW and NE–SW (Gabrielsen et al., 2002), while the Vestfjorden Basin (Blystad et al., 1995) is expressed as two half-grabens with opposing fault throw, i.e., polarity (Olesen et al., 2002). The southwestern half-graben is about 8 km deep and limited by the East Lofoten Border Fault to the northwest (Bergh et al., 2007), while the easternmost subbasin is 2–3 km deep and bordered by the Hamarøya fault to the southeast (Olesen et al., 2002). Along the Grønna fault, to the west of Bodø, there is a small, 1–2 km deep basin (Brekke et al., 1992; Olesen et al., 2002).

Offshore, the most important bathymetric features are the continental shelf edge and the Vestfjorden–Trænadjupet trough. The shelf edge is characterised by sharp changes in crustal structure and depth. For instance, the boundary between the Utrøst Ridge and the Røst Basin exposes significant changes in crustal thickness and is marked by south-to-westerly dipping faults (Mjelde et al., 1992).

Closer to the shelf edge, the Nordland Ridge represents a Mesozoic flexural structure dipping northwestward underneath the Træna Basin with few basement faults. Around the Træna Basin, the sedimentary Naust–Kai formation, which occurs in the southwestern area of offshore Nordland, reaches its maximum thickness of 1.5 km (Dowdeswell et al., 2010). The Træna island, which is closer to the coast, lies just on the assumed junction of the NSZ and the BTZ. To the south of Trænadjupet lies the Trænabanken; a shallow plateau of Quaternary age. Trænadjupet marks the offshore southwestern limit of the erosion path of the paleo-ice stream drainage during the last glaciation when the glacial deposits had been transported from the coastal and mainland areas towards the shelf edge (Ottesen et al., 2005).

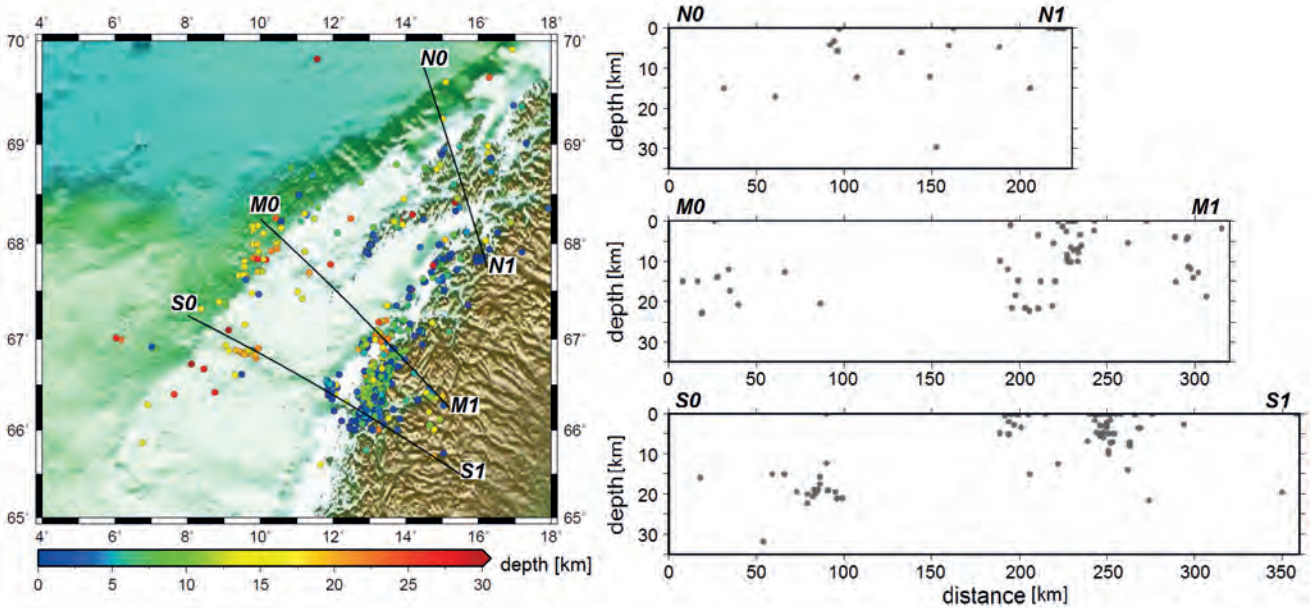

Figure 5. Depth distribution of earthquakes in Nordland and along indicated profiles: S0–S1 across the shelf edge, Trænadjupet and the area to the south of Svartisen; M0–M1 across the shelf edge, the Vestfjorden zone and the area to the north of Svartisen; and N0–N1 across the shelf edge, Lofoten and the Steigen area. The study revealed a general tendency for mainly deeper earthquakes (about 20 km deep) to occur offshore, whereas both shallow and deeper earthquakes are located along the coastline, e.g., 0–3 km deep around the Træna Island and 12–20 km deep along the northeastern part of the Grønna fault. Onshore, the depth of the earthquakes varies; around Svartisen and Steigen the earthquakes are mostly shallow (3–8 km deep) and under the Lofotens somewhat deeper (down to 15 km).

seismicity followed the coastline without penetrating farther into the onshore or offshore regions, with an exception just to the southwest of Svartisen. Also, some earthquakes followed the Lofoten archipelago, which is also an area where man-made explosions (mostly due to road construction) might have perturbed the dataset, so full credibility to this observation cannot be given. Farther offshore along the continental shelf some stronger earthquakes up to M 3.0 were detected, confirming earlier observations.

In Nordland, several areas of earthquake clustering have been distinguished (Figs. 1 & 4). At the northern end of the Nordland Ridge, an earthquake cluster with relatively high magnitude seemed to form an E–W-elongated distribution (however, this elongation might be a product of the location errors as the seismic network lies to the east and notheast) in an area dominated by structures trending NNE-SSW (Fig. 1). Another small and shallow cluster (Fig. 5) was observed around the Træna island closer to the shore. Whereas the Ribban and Røst basins appeared to have very low seismicity, the Utrøst Ridge, which lies in between the two basins, exhibited a quite pronounced earthquake activity.

The onshore area around Svartisen exhibited the highest concentration of microseismicity that showed clustering in time (i.e., swarm activity, Fig. 6) and in some cases the microseismicity possibly migrated along structures that have not been mapped as active faults earlier (Fig. 7B, C). The observed swarm activity showed similar features to the earlier known earthquake swarms in Meløy and Steigen.

An interesting observation in the new data was that there were somewhat larger earthquakes recorded following the Grønna fault, about 30 km northwest of Meløy (Fig. 1). To the north, the Grønna fault passes into the boundary between the coastal mountains and the Vestfjorden sedimentary basin, and the new data showed that the seismicity followed this structure.

Magnitude distribution

The local magnitude range of the recorded 1242 earthquakes was from M -0.4 to 3.2 with the majority of the dataset, i.e., 72%, up to M 1.0, 20% of the dataset between M 1.0 and 1.5, and nine earthquakes with M > 2.5 (Fig. 4). The strongest earthquake of M 3.2 recorded during the monitoring period occurred at the beginning of the swarm activity (end of April 2015) to the west of Svartisen, together with several M > 2.7 events close by. Due to the lower detection threshold, even very small earthquakes (down to M -0.4) were recorded onshore, while only stronger (M ≥ 1.2) earthquakes were recorded in the offshore areas (Fig. 4). The detection threshold magnitude for the offshore earthquakes to the north of Trænadjupet was M 1.2, while to the south of Trænadjupet the threshold was M 1.5. Along the continental shelf several earthquakes were recorded with magnitudes M ≥ 2.5.

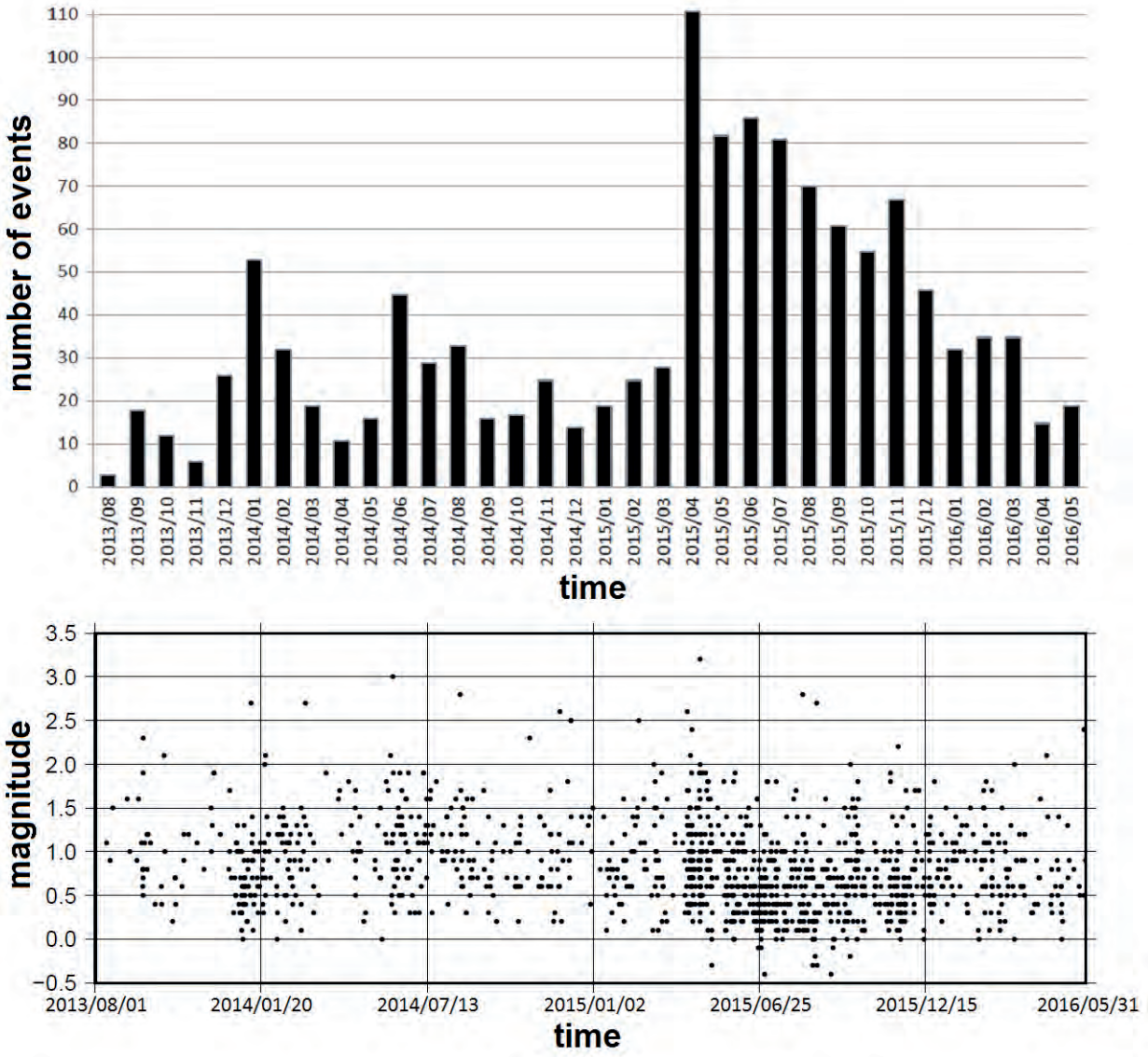

Figure 6. *(A) Number of earthquakes recorded per month by the local seismic network. (B) Magnitude vs. time distribution of the earthquakes. A significant increase in a number of recorded earthquakes in April 2015 was related to the earthquake swarm activity which occurred to the west of Svartisen. The earthquake swarm lasted almost a year with a diminishing intensity and mostly weak seismic events (up to M 1.0).*

Depth distribution

An estimation of hypocentre depth is one of the most crucial tasks. However, this is quite challenging, especially for the offshore earthquakes which occur farther away from the monitoring network. The depth uncertainties are, therefore, higher for the offshore events compared to the onshore events, i.e., 15 km and 6.5 km, respectively. The analysis of distribution of the hypocentre depth (Fig. 5) revealed a general tendency for shallower seismic events onshore and deeper offshore Nordland. The profile crossing the Trænadjupet bathymetric depression and area to the south of Svartisen (S0–S1 in Fig. 5) indicated that the majority of earthquakes onshore, including Træna island, occurred in the uppermost 8 km of the Earth's crust, whereas offshore closer to the shelf edge earthquakes occurred in the lower crust at about 25 km depth. The profiles farther to the north (M0–M1 and N0–N1 in Fig. 5) did not reveal such an obvious difference between the hypocentre depths onshore and offshore, however, it was noticed that the majority of offshore earthquakes mostly occurred deeper than 15 km. Within this depth range there were also observed earthquakes around the Grønna fault, while in the adjacent onshore area the earthquakes occurred in the uppermost 10 km of the crust. Farther inland, both shallow and deeper earthquakes were recorded. Earlier monitoring data indicated that around the Lofotens the earthquakes tended to be deeper (mostly more than 10 km), a feature which was also confirmed in our study (N0–N1 in Fig. 5).

Time distribution of the seismicity

We distinguished three periods of increased seismic activity in Nordland: from August 2013 to May 2014,

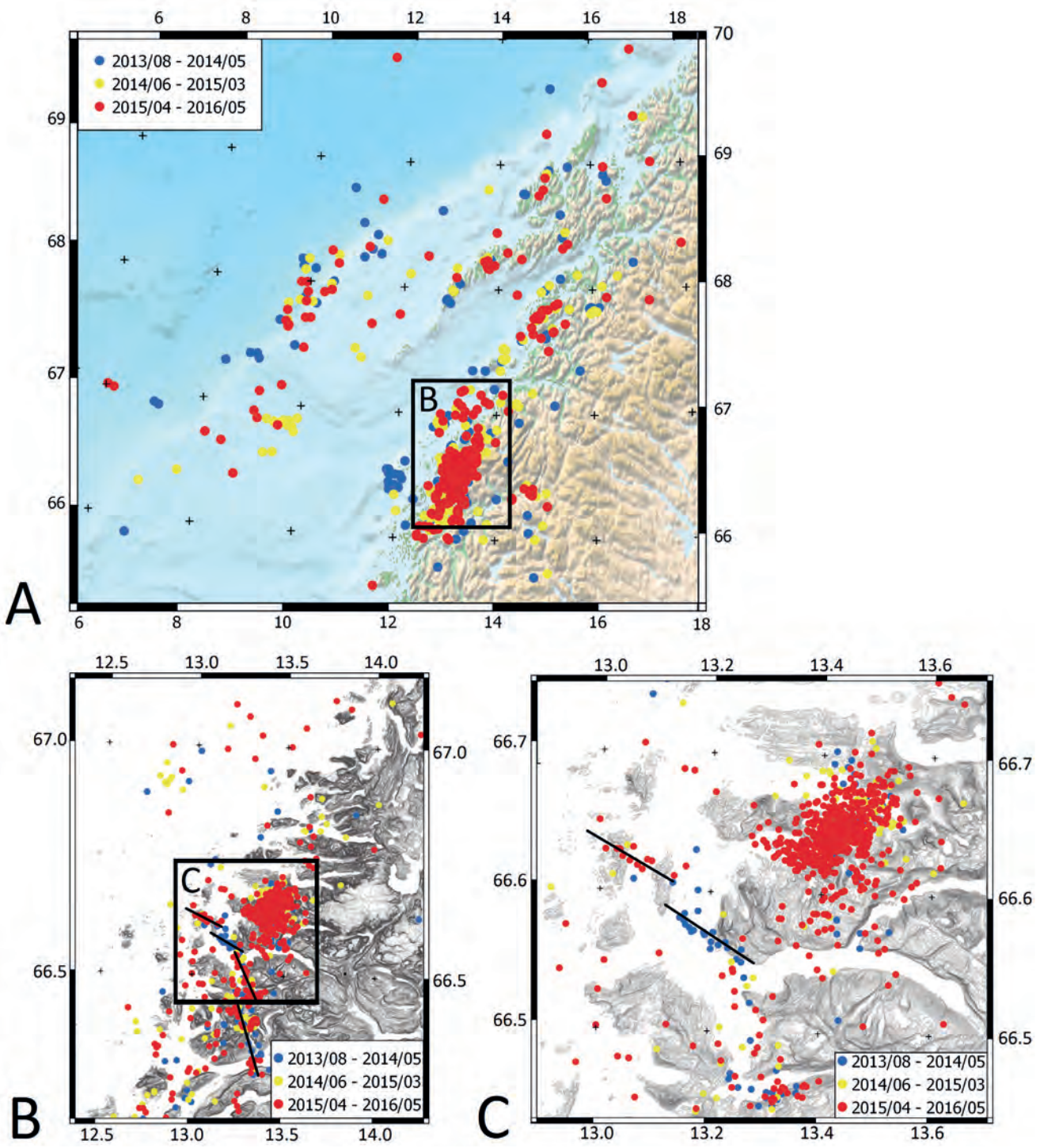

Figure 7. The spatio-temporal distribution of earthquakes in cluding swarm activity in specified areas of Nordland: (A) in the entire area of Nordland; (B) to the west and south of the Svartisen glacier; (C) the earthquake swarm area to the west of Svartisen. The black frames show enlargements in the indicated areas. The black lines indicate clear lineaments recognised in the seismicity distribution. The two lineaments in (C) occurred during short time periods and provided data showing that seismicity migrated from northwest to southeast.

from June 2014 to March 2015, and from April 2015 to May 2016 (Figs. 6 & 7). The seismic activity was persistent and significant during the entire NEONOR2 project period around Svartisen and along the continental shelf; however, along the shelf fewer earthquakes were recorded compared to the onshore areas. It is important to note that in some parts of Nordland the earthquake occurrence was clearly episodic, and we therefore distinguished several groups/clusters that were active over short time periods. In late 2013–early 2014 for about three months there was a burst of activity around the Træna island (Fig. 7A), while slightly later, in mid-2014, an enhanced activity was recorded for a couple of months around the Nordland Ridge, south of the Trænadjupet,

and in late-2015 there was a burst of seismicity around Steigen following a period of silence. However, the most significant activity was the earthquake swarm at the western foot of Svartisen with several hundreds of earthquakes that continued from April 2015 to around March 2016 (Fig. 7B, C).

Discussion

An overriding feature observed in the well-mapped offshore regions (e.g., Blystad et al.,1995) of Nordland was that the earthquakes were consistently located in the upper and lower crust close to the mapped faults or fault systems, while in the onshore coastal regions, where the crust is also strongly deformed, the earthquakes mostly followed the old structures.

Lineaments southwest of Svartisen

The seismicity to the southwest of Svartisen was not only persistent during the entire monitoring period, but also the earthquakes were clustering or migrating along linear trends, which may be interpreted as active tectonic lineaments or faults (Fig. 7B). In particular, two significant NW–SE-trending lines of earthquakes (Fig. 7C) were active only during short time periods, and there was also a tendency for the activity to migrate laterally along the lines from northwest to southeast. Farther to the south, there were indications of several potential lineaments trending mostly NW–SE (Fig. 7B), which is consistent with some of the fault trends recognised by Gabrielsen et al. (2002). This area was earlier studied by Hicks et al. (2000a) who also reported on the microseismicity following lines of mostly NW–SE trend and migrating with time. Thus, the observed seismicity has confirmed the migration and lineation trends that were first recognised by Hicks et al. (2000a). However, some lineaments were active during the entire monitoring period (Fig. 7B).

The Lurøy area, adjacent to Ranafjorden, where the most intense shaking from the historical earthquake of M 5.8 in 1819 was reported (Muir-Wood, 1989; Bungum & Olesen, 2005), still exhibits high levels of seismic activity (Figs. 7A & 8). Since the temporary NEONOR2 network was located north of Mo i Rana, the detection threshold was higher farther to the south; however, the network was capable of detecting the earthquakes in those areas. The fact that only a handful of earthquakes were recorded to the south of Mo i Rana is indicative that seismic activity to the south is indeed much lower than to the north of Ranafjorden.

West of Svartisen

The area just at the western foot of the Svartisen glacier exhibited a persistent and time-varying seismic activity (Figs. 7B, C & 8). One of the most interesting features in the new data was an observed earthquake swarm which occurred in this area from April 2015 to about March 2016. In the first half of the NEONOR2 project (i.e., before the swarm), only the northern part of the area was seismically active, but activity expanded farther to the south with the onset of the swarm activity (Fig. 7A). The earthquake swarm started in April 2015 with several stronger M > 2 events, while the strongest earthquake of M 3.2 occurred at the end of April (Fig. 6). During the peak activity, April to August 2015, there were recorded on average 80 earthquakes per month. Since then the swarm activity has continued and gradually decreased until the spring of 2016 with the earthquake epicentres scattered all over the area, but mostly in the southern part. The swarm events were generally weak, mostly up to M 1.0 (Fig. 6B) and shallow, 3 to 8 km deep (Fig. 5), which is very similar to the earlier observations of earthquake swarms in Nordland, close to Meløy (e.g., Bungum & Husebye, 1979) and Steigen (Atakan et al., 1994). Although some faint trends in the seismicity could be observed, from the earthquake distribution alone it was not possible to associate the earthquakes with the specific tectonic faults and lineaments mapped by Gabrielsen et al. (2002).

The earthquake swarm area is located to the west of the c. 1000 m high mountain plateau hosting the Svartisen glacier. Pascal & Cloetingh (2009) showed that the topography of southern Norway is to some degree controlling the orientation of in situ rock stress, which may also be the case for the Nordland region, although the altitude of the mountains is lower compared to southern Norway. On the other hand, the mountains in Nordland are situated close to the coast, thus the increased rock stress from the coastal topography may be sufficient to trigger/influence earthquakes along the zones of weakness. We also want to emphasise that the swarm area is located north of where the NSZ possibly changes its direction and merges offshore with the BTZ; thus, the area could host a complex network of faults.

The earthquakes recorded to the west of Svartisen are mostly shallow, and the cause of the earthquake occurrence in this area is not well understood. However, there is a hypothesis that the increased activity around the Svartisen glacier could be related to the glacier itself (i.e., yearly variations of ice growth or melting). Studies of the Svartisen glacier (Nesje & Dahl, 2000) showed several kilometres of glacier advancement of its western margin during the Little Ice Age in the 18th and 19th centuries, whereas the major retreats of its western border have been reported during the 20th century (Paul & Andreassen, 2009; Haug et al., 2009). The fact that the earthquake swarm started in April and peaked in early

summer could be related to changes in the groundwater from snowmelt, which is common at that time of the year. Local observations from drilling (Kurt Brandtzæg Jensen, pers. comm.) showed that the rock quality in large parts of the Svartisen massif is extremely poor with creeks penetrating the rock interior through large open cracks and fissures that would allow the meltwater to rapidly flow to the periphery of the Svartisen massif. The poor rock quality could be most likely related to fracturing, karstification and weathering (Olesen et al., 2013b). Therefore, we concluded that water penetration into the existing faults and yearly variations in the glacier mass might have influenced the earthquake activity in this area. In contrast to its periphery, no earthquakes were recorded under the Svartisen ice sheet itself. This phenomenon is still not well understood, even though similar situations have been observed in the vicinity of other ice sheets and glaciers (e.g., in Greenland, Voss et al., 2007).

Southeast of Svartisen

A scattered cluster of seismic events was recorded to the southeast of Svartisen. The area is populated with quarries and earthquakes occur here too; thus, it might be difficult to distinguish earthquakes from the man-made explosions, especially if no quarry reports are available. Reports from the Rana iron ore mine in Storforshei to the east of Svartisen show high horizontal stresses (Myrvang, 1993), and the rock quality is similarly poor as in the area to the west of Svartisen, a feature which may here also promote shallow earthquake activity related to meltwater flow. In addition, the seismic activity coincides with rapid changes in the depth to the Precambrian basement along the NSZ (Fig. 8).

Steigen area

The level of seismicity around Steigen, which hosted an earthquake swarm in 1992 (Atakan et al., 1994), was not particularly high during the NEONOR2 monitoring period, except for a small group of earthquakes in mid-2015 (Fig. 7A). The earthquake activity occurred inside the spoon-shaped Sagfjord Shear Zone (SSZ), and it might also have occurred close to this structure farther to the southeast (Fig. 1).

Lofoten

Deep structures, even below the Moho boundary, might influence the seismicity in the crust. As Maystrenko et al. (2017) noted, there are two low-velocity zones in Norway: one under the Lofotens and another beneath SW Norway (e.g., Kolstrup et al., 2015), and these zones coincide spatially with the areas of increased seismicity. Therefore, these authors suggested that the velocity anomalies could be one of the reasons for uplift, and could be partly associated with the earthquake activity in both areas. During the NEONOR2 project in the Lofoten area, mostly scattered and deeper (>15 km) earthquakes were recorded.

Coastline

In the coastal offshore areas the seismicity was higher on the eastern flank of the Vestfjorden Basin, i.e., to the west of Meløy, around the Grønna fault and its southern extension (Fig. 8), whereas the coastal regions south of the mouth of Ranafjord generally showed lower earthquake activity. During the NEONOR2 monitoring period, two earthquakes of M 2.5 and one earthquake of M 3.0 (Fig. 7A) were recorded to the west of Meløy, and as late as December 2016 also an earthquake of M 3.7. The strongest recorded earthquakes in this area of M ≥ 3.0 were mostly shallow (3–5 km deep), while a group of relatively deep earthquakes (15–20 km deep) was recorded underneath the shallow (1–2 km deep) half-graben which to the southeast is bordered by the Grønna fault. The wide range of earthquake hypocentres implies that there might be both deep and shallow seismically active tectonic structures in the vicinity of the Grønna fault.

The Vestfjorden Basin

The Vestfjorden area contains Mesozoic basement faults. Although the historical earthquake catalogues reported on a few earthquakes in the area, it cannot be ruled out that these earthquakes could have been mislocated due to the sparse permanent station network. Since there were no events recorded with the dense, temporary, NEONOR2 network, it could therefore be concluded that the Vestfjorden Basin is practically aseismic. However, the three-year monitoring period is too short to make definitive statements. On the other hand, it is very likely that the level of seismicity in the Vestfjorden area is much lower compared with the surroundings.

The Bivrost transfer zone

The offshore extension of the NSZ, which was possibly reactivated as a transfer zone (i.e., the BTZ) between the rifted segments in the Lofoten area to the northeast and the Helgeland and Træna basins to the southwest, was seismically quiet during the NEONOR2 project. Although the BTZ is a geological transition zone, as shown by Maystrenko et al. (2017), it did not appear to be an active earthquake source zone.

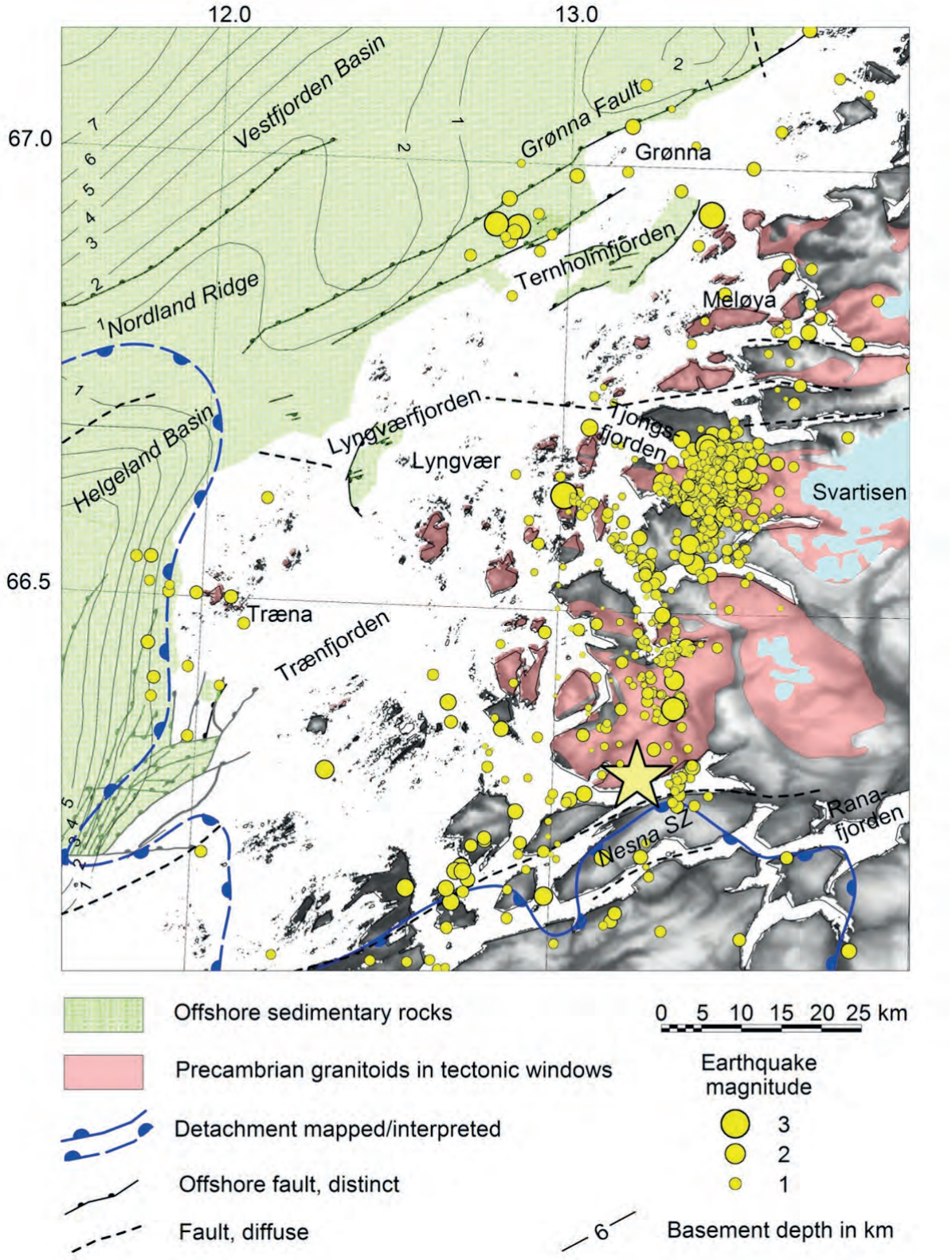

Figure 8. *Seismicity in the northern Helgeland area. Data sources: Mesozoic sedimentary rocks – IKU (1995), Bugge et al. (2002), and Bøe et al. (2008); Precambian granitoids – Gustavson & Gjelle (1991), and Gustavson & Blystad (1995); Detachments mainland – Eide et al. (2002); Detachments offshore – Olesen et al. (2002); Faults – IKU (1995), Bugge et al. (2002), Olesen et al. (2002), and Bøe et al. (2008); Basement depth – Olesen et al. (2002). The yellow star depicts the approximate location of the M 5.8 earthquake in 1819. Correlations between seismicity and tectonic-geological boundaries are observed along the Grønna Fault, the eastern flank of the Helgeland Basin and onshore to the north of the Nesna Shear Zone (NSZ). To the west of Svartisen, the earthquake swarm occurred from April 2015 to around March 2016 with several hundreds of weak and shallow seismic events. To the southwest of the earthquake swarm there could be distinguished a NW–SE-trending lineament that changes its orientation to NNW–SSE farther to the south.*

Continental shelf edge

On the continental shelf edge, earthquakes occurred sporadically during the entire project period (Fig. 7A). The earthquake distribution was consistent with the earlier observed pattern: relatively deep hypocentres (mostly in the lower crust), and the earthquakes followed the shelf edge with somewhat enhanced activity west of the Røst Basin and with clearly reduced activity south of the BTZ. The Ribban and Røst basins showed relatively sparse seismicity, and the large Trøndelag Platform and the Helgeland Basin also appeared to be practically aseismic (Fig. 1).

At the shelf edge the rapid changes in both the Moho depth and the density of the rocks have earlier been associated with earthquake occurrence (Fejerskov & Lindholm, 2000), while the deeper structures, mapped by Maystrenko et al. (2017), coincide quite well with the earthquake distribution observed at the northern end of the Nordland Ridge/Utrøst High (Fig. 1). This observation confirmed that the earthquake occurrence might be following the old zones of deformation and geological contacts.

Nordland Ridge and Træna island

The new data have confirmed the earlier observed seismicity pattern around the Nordland Ridge. In addition, an earthquake clustering was detected at the northern termination/bending of the Nordland Ridge, east of the Utgard High. This group of earthquakes occurred during a short period in the summer 2014 around the Nordland Ridge with deep hypocentres (about 20 km deep). Another time-space clustering of the earthquakes was observed closer to the coast, around Træna island, where the seismicity peaked in early 2014 but with only shallow hypocentres. These earthquakes coincide well with the mapped faults (IKU, 1995) along the eastern border of the deep Helgeland Basin and the offshore extension of the NSZ (Fig. 8).

Olesen et al. (2013a, b) pointed out that the seismicity in the Træna Basin could be influenced by the thickest unit of the Naust formation and related the earthquakes to loading of the crust, thus following the interpretation of Byrkjeland et al. (2000) for the eastern Lofoten Basin. A small cluster of earthquakes was located c. 30 km to the east of the maximum thickness of the Naust–Kai formation. Taking into account the focal depths, these earthquakes occurred deeper than in the area of the Naust formations.

Conclusions

The enhanced earthquake monitoring in Nordland during the NEONOR2 project improved our knowledge of the seismic conditions in the region. As a result, we obtained a more detailed seismicity map and interpreted the possible relationship between the earthquakes and the tectonic structures in the Nordland area. Our conclusions are the following:

1. During the NEONOR2 project, the magnitude of completeness in the Nordland area was lowered from magnitude M 1.8 to 1.0 onshore. Onshore, the smallest recorded earthquakes were of M -0.4, while offshore the detection threshold was M 1.2 to the north of Trænadjupet and M 1.5 to the south of Trænadjupet.

2. Seismic activity in Nordland was mostly persistent and sporadic (e.g., along the continental shelf edge and around Svartisen), but in some places it was episodic (e.g., around Steigen, the Nordland Ridge and west of Svartisen).

3. The most seismically active area in Nordland during the NEONOR2 project was to the west of Svartisen, where an earthquake swarm was recorded. The shallow swarm activity in this area could be partly associated with changes in the glacier mass and groundwater conditions.

4. During the monitoring period the offshore basins appeared practically aseismic or showed very little seismic activity. No earthquakes were recorded along the Bivrost transfer zone and in the Helgeland and Vestfjorden basins. Consequently, it could be concluded that the Bivrost transfer zone is tectonically quiet, and that the large offshore regions of the Trænabanken and Vestfjorden are very stable, which largely confirm earlier assumptions though with better data compared with the earlier observations. However, the three-year period of enhanced monitoring is too short a time to confirm a complete absence of seismicity in the offshore basins that are characterised by slow deformation rates. Relatively few earthquakes were recorded also north of the Røst Basin, along the continental shelf (west of Vesterålen).

5. The Naust–Kai depocentre could be associated with an area of increased seismic activity. However, the seismicity is possibly controlled by deep crustal inhomogeneities.

6. Seismicity along the coast was clearly less pronounced to the south of Mo i Rana compared to the coastline farther to the north.

7. There was a tendency for generally shallow (3 to 10 km deep) earthquakes to occur onshore and for deeper (15 to 25 km depth) earthquakes to be located offshore.

8. The seismicity was generally observed in the areas with faulted upper and/or lower crust. Offshore, the seismicity mostly appears to be following sharp changes in crustal depth, such as along the continental shelf edge and along the coastline.

9. To the south of Svartisen, the seismicity followed well-defined lineaments trending mostly NE–SW and NNW–SSE. Some of the lineaments were active only for a certain period of time, and there was also a lateral migration of seismicity along them (from northwest to southeast). However, other lineaments and structures remained active during the entire observation period.

10. Except for the Grønna fault and the eastern margin of the Helgeland Basin, it was not possible to associate the offshore earthquakes with specific faults. The pattern of the onshore earthquakes showed a good correlation with the structural trends mapped by Gabrielsen et al. (2002).

Acknowledgements. The present work was conducted with the support provided by the Norwegian Research Council to the Norwegian Geological Survey under grant number 228105/E30, and with additional funding from the Aker-BP, Dea, DONG Energy, E.ON, the Geological Survey of Norway (NGU), the Norwegian Mapping Authority (Kartverket), Lundin Norway, Maersk Oil, Noreco, NORSAR, Norske Shell, the Norwegian Petroleum Directorate, Repsol, Statoil and VNG. The primary event location and origin determination was conducted at the University of Bergen (UiB). Special thanks go to Yuriy Maystrenko for his comments and discussion, also to Björn Lund and an anonymous reviewer whose comments and suggestions significantly improved our manuscript.

References

Alsaker, A., Kvamme, L.B., Hansen, R.A., Dahle, A. & Bungum, H. 1991: The M_L scale in Norway. *Bulletin of the Seismological Society of America 81, 2, 379–398.*

Atakan, K., Lindholm, C.D. & Havskov, J. 1994: Earthquake swarm in Steigen, northern Norway: an unusual example of intraplate seismicity. Terra Nova 6, 180–194. https://doi.org/10.1111/j.1365-3121.1994.tb00652.x.

Bergh, S.G., Eig, K., Kløvjan, O., Henningsen, T., Olesen, O. & Hansen, J. 2007: The Lofoten–Vesterålen continental margin: a multiphase Mesozoic–Palaeogene rifted shelf as shown by offshore-onshore brittle fault-fracture analysis. *Norwegian Journal of Geology 87, 29–58.*

Blystad, P., Brekke, H., Færseth, R.B., Larsen, B.T., Skogseid, J. & Tørudbakken, B. 1995: Structural elements of the Norwegian continental shelf, Part II. The Norwegian Sea Region. Norwegian Petroleum Directorate Bulletin 8, pp. 45.

Bøe, R., Fossen, H. & Smelror, M. 2010: Mesozoic sediments and structures onshore Norway and in the coastal zone. NGU Bulletin 450, 15-32.

Braathen, A., Osmundsen, P.T., Nordgulen, Ø. & Roberts, D. 2002: Orogen-parallel, extensional denudation of the Caledonides in North Norway. Norwegian Journal of Geology 82, 225–241.

Brekke, H., Kalheim, J.E., Riis, F., Egeland, B., Blystad, P., Johnsen, S. & Ragnhildstveit, J. 1992: Formkart over inkonformitetsflaten under henholdsvis overjuralagrekken (nord for 69°N) og krittlagrekken (sør for 69°N) på norsk kontinentalsokkel, scale 1:2,000,000, *Norges Geologiske Undersøkelse.*

Bugge, T., Ringås, J.E., Leith, D.A., Mangerud, G., Weiss, H.M. & Leith, T.L. 2002: Upper Permian as a new play model on the Mid-Norwegian continental shelf; investigated by shallow stratigraphic drilling. American Association of Petroleum Geologists Bulletin 86, 107–127.

Bungum, H. & Husebye, E.S. 1979: The Meløy, northern Norway, earthquake sequence - a unique intraplate phenomenon. Norwegian Journal of Geology 59, 189–193.

Bungum, H. & Olesen, O. 2005: The 31st of August 1819 Lurøy earthquake revisited. Norwegian Journal of Geology 85, 245–252.

Bungum, H., Hokland, B.K., Husebye, E.S. & Ringdal, F. 1979: An exceptional intraplate earthquake sequence in Meløy, Northern Norway. Nature 280, 32–35. https://doi.org/10.1038/280032a0.

Bungum, H., Vaage, S. & Husebye, E.S. 1982: The Meløy earthquake sequence, Northern Norway; source parameters and their scaling relations. *Bulletin of the Seismological Society of America 72, 197–206.*

Bungum, H., Alsaker, A., Kvamme, L.B, & Hansen, R.A. 1991: Seismicity and seismotectonics of Norway and surrounding continental shelf areas. Journal of Geophysical Research 96, 2249–2265. https://doi.org/10.1029/90JB02010.

Bungum, H., Olesen, O., Pascal, C., Gibbons, S., Lindholm, C. & Vestøl, O. 2010: To what extent is the present seismicity of Norway driven by post-glacial rebound? *Journal of the Geological Society 167, 373–384.* https://doi.org/10.1144/0016-76492009-009.

Byrkjeland, U., Bungum, H. & Eldholm, O. 2000: Seismotectonics of the Norwegian continental margin. *Journal of Geophysical Research 105, 6221–6236.* https://doi.org/10.1029/1999JB900275.

Davis, G.H. & Reynolds, S.J. 1996: *Structural geology of rocks and regions, 2nd edition. Wiley, New Jersey 800 pp.*

Dehls, J. & Olesen, O. 1998: Neotectonics in Norway, Annual Technical Report 1997. NGU Report 98.016, 149 pp.

Dehls, J.F. & Olesen, O. 2000: NEONOR: Neotectonics in Norway: Annual Technical Report 1999. *NGU Report, 2000.001*, 207 pp.

Dowdeswell, J.A., Ottesen, D. & Rise, L. 2010: Rates of sediment delivery from the Fennoscandian Ice Sheet through an ice age. *Geology 38, 3–6.* https://doi.org/10.1130/G25523.1.

Eide, E.A., Osmundsen, P.T., Meyer, G.B., Kendrick, M.A. & Corfu, F. 2002: The Nesna Shear Zone, north-central Norway: an 40Ar/39Ar record of Early Devonian – Early Carboniferous ductile extension and unroofing. *Norwegian Journal of Geology 82*, 317–339.

Fejerskov, M. & Lindholm, C. 2000: Crustal stresses in and around Norway; an evaluation of stress generating mechanisms. *In Nottvedt, A. (ed.): Dynamics of the Norwegian Margin. Geological Society of London Special Publication 167, pp. 451–467.*

Fjeldskaar, W., Lindholm, C., Dehls, J.F. & Fjeldskaar, I. 2000: Postglacial uplift, neotectonics and seismicity in Fennoscandia. Quaternary Science Reviews 19, 1413–1422. https://doi.org/10.1016/S0277-3791(00)00070-6.

Gaal, G. & Gorbatschev, R. 1987: An outline of the Precambrian evolution of the Baltic Shield. *Precambrian Research 35, 15–52.* https://doi.org/10.1016/0301-9268(87)90044-1.

Gabrielsen, R.H. & Ramberg, I.B. 1979: Tectonic analysis of the Meløy earthquake area based on Landsat lineament mapping. *Norwegian Journal of Geology 59, 183–187.*

Gabrielsen, R.H., Braathen, A., Dehls, J. & Roberts, D. 2002: Tectonic lineaments of Norway. Norwegian Journal of Geology 82, 153–174.

Gustavson, M. & Gjelle, S.T. 1991: *Geologisk kart over Norge. Berggrunnskart Mo i Rana, scale 1:250,000, Norwegian Geoloical Survey.*

Gustavson, M. & Blystad, P. 1995: Geology map of Bodø, scale 1:250,000, Norwegian Geological Survey.

Haug, T., Rolstad, C., Elvehøy, H., Jackson, M. & Maalen-Johansen, I. 2009: Geodetic mass balance of the western Svartisen ice cap, Norway, in the periods 1968–1985 and 1985–2002. Annals of Glaciology 50, 191–197. https://doi.org/10.3189/172756409787769528.

Henkel, H. & Eriksson, L. 1987: Regional aeromagnetic and gravity studies in Scandinavia. *Precambrian Research 35, 169–180.* https://doi.org/10.1016/0301-9268(87)90052-0.

Hicks, E.C., Bungum, H. & Lindholm, C.D. 2000a: Seismic activity, inferred crustal stresses and seismotectonics in the Rana region, northern Norway. *Quaternary Science Reviews 19, 1423–1436.* https://doi.org/10.1016/S0277-3791(00)00071-8.

Hicks, E.C., Bungum, H. & Lindholm, C.D. 2000b: Stress inversion of earthquake focal mechanism solutions from onshore and offshore Norway. *Norwegian Journal of Geology 80, 235–250.* https://doi.org/10.1080/00291960051030545.

Hogdahl, K., Andersson, U.B. & Eklund, O. 2004: The Transscandinavian Igneous Belt (TIB) in Sweden: a review of its character and evolution. *Geological Survey of Finland, Special Paper 37, 1–125.*

IKU 1995: Shallow Drilling Helgeland 1992. IKU Sintef Group Information sheet no.: 15, Project 23.1684.00, Shallow Drilling, February 1995, 2 pp.

Kolstrup, M.L., Hung, S.H. & Maupin, V. 2015: Multiscale, finite-frequency P and S tomography of the upper mantle in the southwestern Fennoscandian Shield. Geophysical Journal International 202, 1, 190–218. https://doi.org/10.1093/gji/ggv130.

Larson, S.A. & Berglund, J. 1992: A chronological subdivision of the Transscandinavian Igneous Belt – three magmatic episodes? *Geological Society of Sweden 114, 459–460.* https://doi.org/10.1080/11035899209453912.

Lienert, B.R. & Havskov, J. 1995: A Computer Program for Locating Earthquakes both Locally and Globally. *Seismological research Letters 66, 26–36.* https://doi.org/10.1785/gssrl.66.5.26.

Maystrenko, Y.P., Olesen, O., Gernigon, L. & Gradmann, S. 2017: Deep structure of the Lofoten–Vesterålen segment of the Mid-Norwegian continental margin and adjacent areas derived from 3D density modeling. *Journal of Geophysical Research: Solid Earth 122, 2, 1402–1433.* https://doi.org/10.1002/2016JB013443.

Midtun, R.D. 1988: Regional geofysisk og geologisk tolkning av Høgtuva- og Sjona- grunnfjellsvinduene. *NGU Report 88.127*, 46 pp.

Mjelde, R., Sellevoll, M.A., Shimamura, H., Iwasaki, T. & Kanazawa, T. 1992: A crustal study off Lofoten, N. Norway, by use of 3-component ocean bottom seismographs. *Tectonophysics 212, 269–288.* https://doi.org/10.1016/0040-1951(92)90295-H.

Muir-Wood, R. 1989: Extraordinary deglaciation reverse faulting in northern Fennoscandia. *In Gregersen, S. & Basham, P.W. (eds.): Earthquakes at North Atlantic Passive Margins: Neotectonics and Postglacial Rebound, NATO ASI Series, Series C: Mathematical and Physical Sciences 266, pp. 141–173.*

Muir-Wood, R. 2000: Deglaciation Seismotectonics: a principal influence on intraplate seismogenesis at high latitudes. Quaternary Science Reviews 19, 1399–1411. https://doi.org/10.1016/S0277-3791(00)00069-X.

Myrvang, A. 1993: Rock stress and rock stress problems in Norway. *In* Hudson, J.A. (ed.): *Comprehensive rock engineering. Vol. 3, Rock testing and site characterization*. Pergamon Press, Oxford, pp. 461–471. https://doi.org/10.1016/B978-0-08-042066-0.50025-2.

Nesje, A. & Dahl, S.O. 2000: *Glaciers and environmental change (Key issues in environmental change). Routledge, Abingdon, 216 pp.*

Olesen, O., Lundin, E., Nordgulen, Ø., Osmundsen, P.T., Skilbrei, J.R., Smethurst, M.A., Solli, A., Bugge, T. & Fichler, C. 2002: Bridging the gap between the Nordland onshore and offshore geology. *Norwegian Journal of Geology 82, 243–262.*

Olesen, O., Bungum, H., Dehls, J., Lindholm, C., Pascal, C. & Roberts, D. 2013a: Neotectonics, seismicity and contemporary stress field in Norway – mechanisms and implications. In Olsen, L., Fredin, O. & Olesen, O. (eds.): *Quaternary Geology of Norway, Geological Survey of Norway Special Publication 13, pp. 145–174.*

Olesen, O., Kierulf, H.P., Bresen, M., Dalsegg, E., Fredin, O. & Solbakk, T. 2013b: Deep weathering, neotectonics and strandflat formation in Nordland, northern Norway. *Norwegian Journal of Geology 93*, 189–213.

Ottemoller, L., Voss, P.H. & Havskov, J. 2016: *SEISAN earthquake analysis software for Windows, Solaris, Linux and MacosX.*

Ottesen, D., Rise, D., Knies, J., Olsen, L. & Henriksen, S. 2005: The Vestfjorden–Trænadjupet palaeo-ice stream drainage system, mid-Norwegian continental shelf. Marine Geology 218, 175–189. https://doi.org/10.1016/j.margeo.2005.03.001.

Pascal, C. & Cloetingh, S.A.P.L. 2009: A quantitative analysis on the impact of gravitational potential stresses on passive margins with emphasis to the Mid-Norwegian Margin. *Earth and Planetary Science Letters 277*, 464–473. https://doi.org/10.1016/j.epsl.2008.11.014.

Paul, F. & Andreassen, L.M. 2009: A new glacier inventory for the Svartisen region, Norway, from Landsat ETM+ data: challenges and change assessment. *Journal of Glaciology 55, 607–618.* https://doi.org/10.3189/002214309789471003.

Redfield, T.F. & Osmundsen, P.T. 2015: Some remarks on the earthquakes of Fennoscandia: A conceptual seismological model drawn from the perspectives of hyperextension. *Norwegian Journal of Geology 94*, 233–262. https://doi.org/10.17850/njg94-4-01.

Roberts, D. & Gee, D.G. 1985: An introduction to the structure of the Scandinavian Caledonides. *In Gee, D. G., and Sturt, B.A. (eds.): The Caledonian Orogen – Scandinavia and related areas*, John Wiley and Sons, Chichester, pp. 55–68.

Rykkelid, E. & Andresen, A. 1994: Late Caledonian extension in the Lofoten area, northern Norway. *Tectonophysics 231, 157–169.* https://doi.org/10.1016/0040-1951(94)90127-9.

Voss, P., Poulsen, S.K., Simonsen, S.B. & Gregersen, S. 2007: Seismic hazard assessment of Greenland. *Geological Survey of Denmark and Greenland Bulletin 13, 57–60.*

CHAPTER 3: EARTHQUAKE SOURCE MECHANISMS IN ONSHORE AND OFFSHORE NORDLAND, NORTHERN NORWAY

Authors: Ilma Janutyte[1] & Conrad Lindholm[1]

Affiliations: [1]NORSAR, 2027 Kjeller, Norway

Journal: Norwegian Journal of Geology, Vol 97 Nr. 3

Publishing Date: 24. October 2017 (Online)

DOI: https://dx.doi.org/10.17850/njg97-3-03 (OA)

Pages: 13, plus 4-page supplement

NORWEGIAN JOURNAL OF GEOLOGY Vol 97 Nr. 3
https://dx.doi.org/10.17850/njg97-3-03

Geological Society of Norway

Earthquake source mechanisms in onshore and offshore Nordland, northern Norway

Ilma Janutyte[1] & Conrad Lindholm[1]

[1] *NORSAR, 2027 Kjeller, Norway.*

E-mail corresponding author (Ilma Janutyte): ilma@inbox.lt

In this paper we present a comprehensive database of 152 earthquake focal mechanism solutions for the Nordland area, northern Norway, and the adjacent offshore regions. 123 focal mechanisms are published for the first time. We developed an equation to objectively determine the quality of the focal mechanisms, while the equation was explicitly adjusted to the used dataset (not globally accepted). We used the equation to assign quality factors to the new focal mechanisms, while the quality of the earlier published focal mechanisms was kept as originally provided. About 20% of all focal mechanisms were set to the higher quality A and B, which was assigned to the onshore earthquakes only, whereas for offshore earthquakes the highest assigned quality was quality C, mostly due to larger azimuthal gaps. The results showed that seismicity onshore and offshore Nordland is different in type: with dominant shallow, normal-faulting earthquakes onshore and mostly deeper, mixed type faulting earthquakes offshore, while along the coast the faulting regime was mostly normal to strike-slip. The results indicated that maximum horizontal compressional stress, σ_H, directions in the offshore areas on a large scale originate from the plate-tectonic ridge push with NW–SE compression, whereas in the onshore regions σ_H directions are better explained through local stress-generating sources, such as topography. In our results we also recognised a possible relation between the Svartisen glacier massif and the enhanced seismicity in the surroundings, including an earthquake swarm activity to the west of the glacier. Moreover, in many onshore and offshore regions the nodal plane azimuths, obtained from the focal mechanisms, correlate well with the trends of geologically mapped onshore and offshore structures.

Keywords: focal mechanisms; Nordland; quality ranking system; stress axis; earthquake swarm

Electronic Supplement 1: Focal mechanisms

Received 9. April 2017 / Accepted 15. September 2017 / Published online 24. October 2017

Introduction

While the nature of earthquakes is not well understood in territories with complex geological and tectonic conditions, it is known that they generally occur along pre-existing zones of weakness and result from a buildup of stress and reduced effective shear strength along favourably oriented faults (e.g., Sibson, 1985). We also use these perspectives in our current attempt to interpret new focal mechanism results for the Nordland region of northern Norway.

The Nordland region, both onshore and offshore, exhibits one of the highest seismic activity rates in northern Norway. Although the earthquakes are mostly weak to moderate, the area has hosted the largest known historical earthquake of northern Europe in the last two centuries – the magnitude M 5.8 earthquake near Lurøy, at the mouth of Ranafjord in 1819 (Muir-Wood, 1989; Bungum & Olesen, 2005). In addition, several shallow earthquake swarms have previously been reported around Meløy and Steigen (e.g., Atakan et al., 1994; Hicks et al., 2000a; Bungum et al., 2010).

The NEONOR2 project (Neotectonics in Nordland – Implications for petroleum exploration; https://www.ngu.no/en/neonor2) aimed to improve our

Janutyte, I. & Lindholm, C. 2017: Earthquake source mechanisms in onshore and offshore Nordland, northern Norway. *Norwegian Journal of Geology 97*, 177–189. https://dx.doi.org/10.17850/njg97-3-03.

understanding of neotectonic crustal deformations, stress regime and the overall seismicity pattern in Nordland and the adjacent offshore areas. In the frame of the project, from August 2013 to May 2016, along the coast of Nordland – from Ranafjord in the south to Vesterålen in the north and also in the Lofoten archipelago – a temporary network of 27 seismic stations was deployed alongside the permanent Norwegian National Seismic Network (NNSN; Fig. 1). Using data from both the temporary and the permanent deployments 1242 earthquakes were located in the study area, including an earthquake swarm. In an earlier study (Janutyte et al., in press) we used the seismological monitoring results to obtain the seismicity distribution and identify the relation between the observed earthquakes and the major tectonic structures in the area, while our current study is focused on the focal mechanisms of the earthquakes, and aims to reveal the underlying stress-generating mechanisms.

Tectonic settings: stress sources and earthquake depths

The studies of Osmundsen et al. (2009) and Redfield & Osmundsen (2013) concluded that the uplift and landscape-forming tectonic activity in Norway are recent and even ongoing. The NEONOR1 project (Dehls & Olesen, 2000) conducted in Nordland in 1997–2000 could not convincingly verify that the observed surface features were truly of neotectonic origin. Consequently, the possibility could not be excluded, and it became the background for a second-phase investigation that was carried out in the framework of the NEONOR2 project during the years 2013–2017.

The geological conditions in the study area are very complex. Mainland Nordland is dominated by the Upper

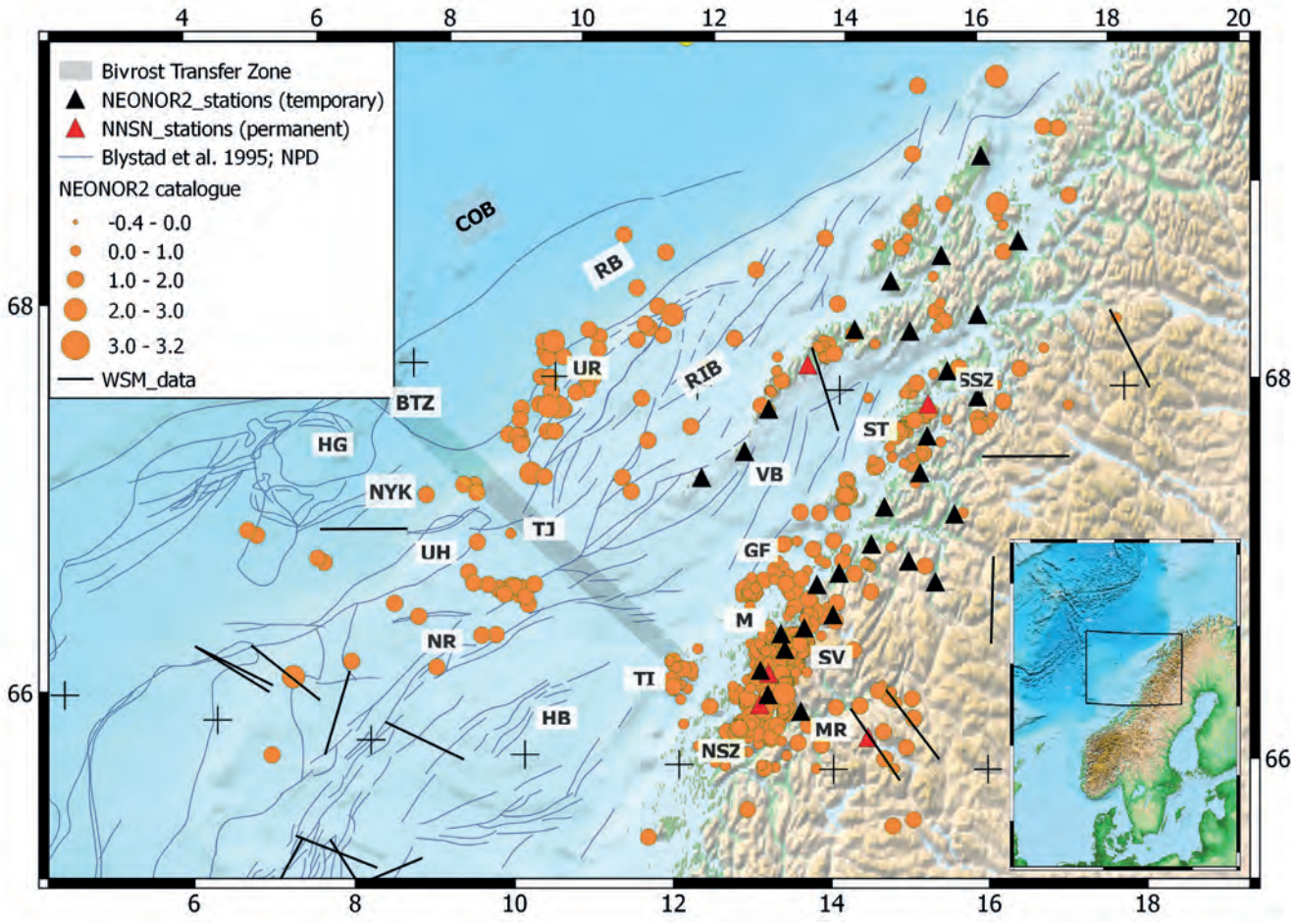

Figure 1. *Map of the study area of Nordland, northern Norway (see Inset), showing the seismic network together with the newly obtained earthquake distribution, and the main geological features. Black triangles – the temporary NEONOR2 seismic stations, red triangles – permanent seismic stations of the Norwegian National Seismic Network, orange disks – 1242 earthquakes recorded during the NEONOR2 project from August 2013 to May 2016, black rods – compressional stress directions from the World Stress Map project. Tectonic structures and sites: BTZ – Bivrost transfer zone, COB – Continent-Ocean Boundary, GF – Grønna fault, HB – Helgeland Basin, HG – Hel Graben, M – Meløy, MR – Mo i Rana, NR – Nordland Ridge, NSZ – Nesna Shear Zone, NYK – Nyk High, RB – Røst Basin, RIB – Ribban Basin, SSZ – Sagfjord Shear Zone, ST – Steigen, SV – Svartisen, TI – Træna Island, TJ – Trænadjupet, UH – Utrøst High, UR – Utrøst Ridge, VB – Vestfjorden Basin (Blystad et al., 1995; Olesen et al., 2002).*

and Uppermost Allochthons that were thrust onto the lower nappes and Precambrian basement during the Scandian continent-continent collision in Silurian and Devonian times (Roberts & Gee, 1985). In the Devonian period, the nappes were dismembered by a late gravitational collapse of the Caledonian orogen (Rykkelid & Andresen, 1994; Braathen et al., 2002; Eide et al., 2002). This complex and deformed upper crust hides faults and structures of which only a few have been mapped in detail, and the offshore-onshore connections of these structures have been only partly mapped. For the onshore areas, the seminal work of Gabrielsen et al. (2002) is the best existing database, while for the offshore areas the main structures are reasonably well mapped and described by Blystad et al. (1995) and later refined by others (e.g., Osmundsen et al., 2002).

In Fennoscandia, the stress indicators (i.e., earthquake focal mechanisms and shallow borehole measurements) at a regional scale consistently indicate a maximum horizontal principal stress, σ_H, of NW–SE trend that is perpendicular to the Mid-Atlantic Ridge, which indicates an influence of plate-tectonic motions and ridge push (Richardson et al., 1979; Pascal et al., 2005; Heidbach et al., 2008; Gregersen & Voss, 2009). The far-field stress modelling by Pascal & Gabrielsen (2001) around the northern North Sea and the mid-Norwegian margin showed that the relatively strong oceanic crust allows conservation of the applied boundary strain throughout the oceanic domain, and the boundary strain is almost totally transferred to the margin. This explains the NW–SE to WNW–ESE stress direction. Pascal et al. (2010) concluded that the present-day stress pattern in Fennoscandia is mostly governed by the ridge push and not by residual glacial loading stresses. However, many studies (e.g., Stroeven et al., 2016) have concluded that the influence of the regional Fennoscandian uplift is significant along Norwegian coastal areas, and there has also been reported an influence from a possible 'coastal bending' (e.g., Gudmundsson, 1999; Hicks et al., 2000a) due to a combination of onshore postglacial uplift, offshore sediment loading and a steep topographic relief (Olesen et al., 2013). Byrkjeland et al. (2000) and Fejerskov & Lindholm (2000) have suggested that regional and local stress factors, such as flexural stresses from sedimentary loading together with favourably oriented and sufficiently weak faults, are also required to explain the occurrence and distribution of earthquakes in the Nordland region. This was also supported by conclusions of Redfield & Osmundsen (2013) that the seismicity in northern Norway could be controlled more by the local vertical loads from the local topography than by the horizontal far-field forces. Thus, stress-generating forces of global, regional and local origin are all possible sources for the observed seismicity. However, it is far from well understood how each of the different components interact and contribute to the overall stress field and local deformations.

Offshore Nordland, the passive continental margin shows clear seismic activity along certain segments (Fig. 1), a feature that was also found by Hicks et al. (2000a). According to Jaeger et al. (2007), earthquakes along the continental shelf can also be caused by stress concentration related to density-contrasting materials, i.e., along the contact between the oceanic crust and the continental crust, as was also suggested by Fejerskov & Lindholm (2000). Moreover, it was earlier shown that offshore earthquakes are generally deeper (at least 15 km deep) and generally of reverse-fault character, which may be explained by large lateral structural variations (Bungum et al., 1991; Hicks et al., 2000b; Bungum et al., 2010).

Hicks et al. (2000a) and Byrkjeland et al. (2000) concluded that the maximum post-glacial uplift gradients around the Mo i Rana area follow the coast quite closely, which might be a main reason for the enhanced seismic activity in the region. They also found that the earthquakes were predominantly of normal to strike-slip faulting type, reflecting largely on a coast-perpendicular extensional regime (i.e., extensional stresses trending NW–SE). Olesen et al. (2013) concluded that some strike-slip earthquakes with coast-parallel compression could be associated with the locally enhanced uplift pattern and the related flexuring mechanism. Ttherefore, a coast-perpendicular extension could also be expected, as the crust may still be strongly flexed due to the recent erosion.

Two earlier reported earthquake swarms in the Nordland region around Meløy in 1978–1979 (Bungum et al., 1979) and Steigen in 1992 (Atakan et al., 1994) revealed mostly shallow earthquake hypocentres of 2 to 8 km depth. The Steigen swarm events were mostly of an oblique-normal faulting nature (Atakan et al., 1994), whereas the Meløy events resulted in mostly normal (Bungum et al., 1979; Bungum et al., 1982) and strike-slip (Vaage, 1980) faulting. From the NEONOR1 data collected in the Mo i Rana area during the 18 months of the monitoring, Hicks et al. (2000a) reported on several small swarm-like earthquake groups to the north of Ranafjord. These swarm-like events occurred mostly along NNW–SSE-trending lineaments, while some of the groups were seismically active only for a couple of months. The registered earthquakes were mostly along normal to strike-slip faults and their hypocentres in different groups varied from 4 to 12 km depth.

The most recent earthquake swarm activity was observed during the NEONOR2 project from April 2015 to about March 2016 to the west of Svartisen. During the swarm activity there were recorded several hundreds of small earthquakes and most of them were shallow, 3 to 8 km deep (Janutyte et al., in press), similar to the earlier reported earthquake swarms.

Dataset of focal mechanisms

From August 2013 to May 2016 the temporary NEONOR2 seismic network in the Nordland area recorded 1242 local earthquakes with magnitudes ranging from M -0.4 to 3.2 (Fig. 1). Due to the seismic network deployed on the mainland, the onshore earthquakes were recorded with a lower detection threshold and smaller azimuthal gaps compared to the earthquakes offshore. Also, usage of a robust 1–D velocity model in the region with such significant geological and tectonic variations (e.g., Maystrenko et al., 2017) led to an inherent uncertainty in the earthquake locations, and subsequently to the final focal mechanism results – a location precision that cannot be easily improved.

From all the located earthquakes we obtained 123 focal mechanisms (Fig. 2). In our analysis we also included focal mechanism solutions from earlier studies, such that our final dataset consists of 152 focal mechanisms (Electronic Supplement 1). To derive the new focal mechanisms we used three well-known algorithms: FOCMEC (Snoke et al., 1984), HASH (Hardebek & Shearer, 2002) and FPFIT (Reasenberg & Oppenheimer, 1985), which are all integrated into the SEISAN program package (Ottemoller et al., 2016). The data used for calculating the earthquake focal mechanisms were first-motions of P-phases with distinguishable polarities, and P/S amplitude ratios observed at the stations where the first arrivals were the direct phases (i.e., omitting reflected and refracted phases). The amplitude estimations for P- and S-waves were conducted on vertical and rotated, transverse, horizontal components (SH), respectively. We analysed the results obtained with the three methods and stability of the solutions across different algorithms in order to ensure maximum reliability of the results. In this paper, we present the focal mechanism solutions (Electronic Supplement 1) obtained with the FOCMEC program, which was found to be superior in terms of stability and robustness compared to the FPFIT and HASH programs, as in FPFIT the P/S amplitude ratios are not used, while FOCMEC also provides better control on managing errors in the final solution compared with the HASH program.

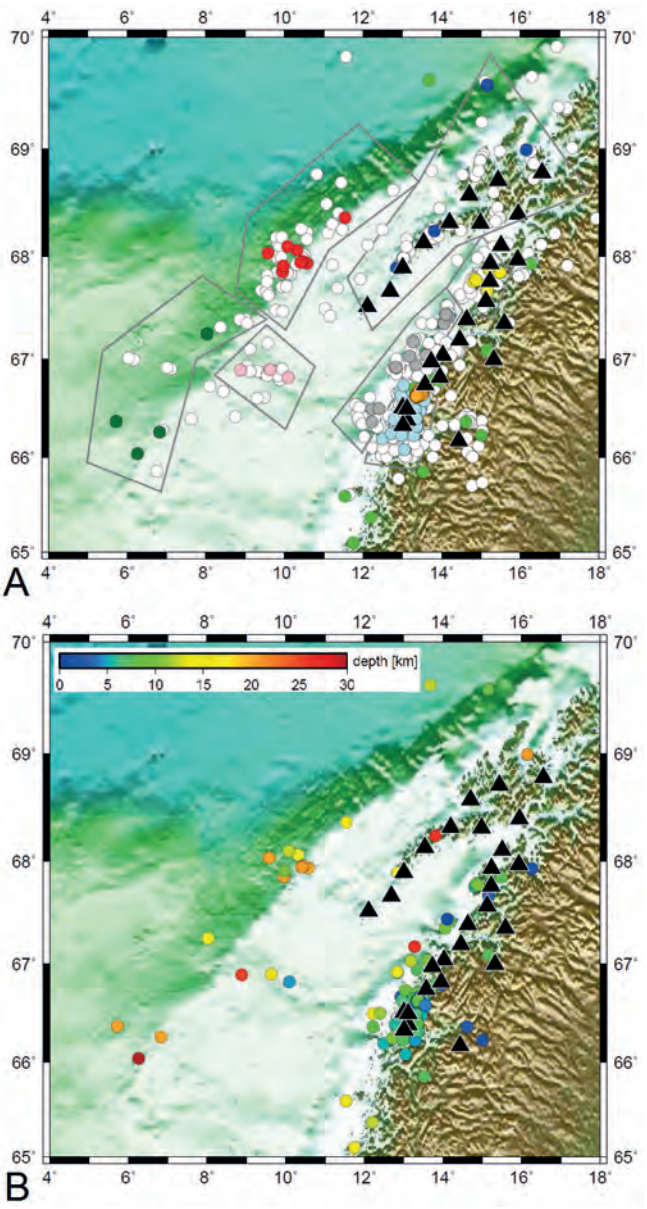

Figure 2. *(A) Distribution of seismicity obtained during the NEONOR2 project (white discs) and distinct groups of earthquakes with defined focal mechanisms (coloured discs): dark green – southern part of the shelf edge, red – northern part of the shelf edge, pink – Trænadjupet, grey – coastline, orange – west of Svartisen, light blue – SW of Svartisen, yellow – Steigen area, dark blue – Lofoten area, light green – not grouped single earthquakes. (B) Hypocentre depths of 152 earthquakes with defined focal mechanisms. The distribution of hypocentre depths shows a general tendency for shallower earthquakes onshore and somewhat deeper offshore and in the Lofotens. Black triangles show the seismic stations of the temporary NEONOR2 project and the permanent Norwegian National Seismological Network.*

Quality assessment of the focal mechanisms

Quality characterisation of earthquake focal mechanisms is generally conducted through a four-level alphabetical system where A stands for best quality and D for lowest quality (i.e., less trustworthy) results. The World Stress Map project (WSM, http://www.world-stress-map.org/) introduced a quality ranking based on Zoback & Zoback (1989), and the ranking has been improved over the years and most recently by Heidbach et al. (2010). While generally appreciating the seminal work that was conducted in developing the ranking system, we recognised that the WSM recommendations would prevent an effective quality determination (and comparison) when dealing with a dataset like ours. If we had followed the WSM recommendations, the majority of the obtained focal mechanisms, especially in the offshore

areas, would have been assigned to only the lowest quality D due to large azimuthal gaps. Therefore, we designed a quality scale that was adapted to the data on hand, and it turned out to be applicable and useful for a relative characterisation of the new 123 focal mechanisms.

Our developed equation for quality determination takes into account the uncertainties of event location (i.e., time residual and azimuthal gaps), number of observations (both first-motion polarity picks and P/S amplitude ratios) and consistency across the independently obtained focal mechanism solutions using three different algorithms (i.e., FOCMEC, FPFIT and HASH). Again, we want to emphasise that the developed quality scale is not globally applicable, but specifically adjusted for the NEONOR2 dataset analysed herein.

In our developed scale the quality factor, *qf*, is defined as follows:

$$qf = obs * 0.1 - comp * 0.4 - res * 0.2 - gap * 0.9 + 1.5 \quad (1)$$

where *obs* is the observation factor that includes both the amount of polarity readings, *pol*, and P/S amplitude ratios, *amp*, and the amount of errors of the polarities, *pol_err*, and the amplitude ratio errors, *amp_err*, in the best fitting solution obtained with the FOCMEC program:

$$obs = pol - pol\_err + 0.5*(amp - amp\_err); \quad (2)$$

comp is the compatibility factor among the focal mechanism solutions obtained using the three calculation methods; *res* is the factor of travel time residual (RMS) in the final event location; and *gap* is the factor defining the azimuthal gap in the final event location. The value of *comp* ranges from 0 (perfect fit) through 1 (good fit) to 2 (reasonable fit); value is set to 0 for RMS < 0.6 sec, to 1 for 0.6 ≤ RMS ≤ 0.9 sec, and to 2 for RMS ≥ 1.0 sec; and the *gap* value is set to 0 for gap < 90°, to 1 for 90° ≤ gap < 160°, and to 2 for gap ≥ 160°.

We designed Eq. 1 in such a way that most of the results are kept within approximate boundaries from 0 to 3, and the digital *qf* value is then transformed into a quality factor using the general mathematical rounding concept: *qf* ≥ 2.5 for quality A, 1.5 ≤ *qf* < 2.5 for quality B, 0.5 ≤ *qf* < 1.5 for quality C, and *qf* < 0.5 (also negative) for quality D (Fig. 3).

While analysing our dataset we concluded that 10 observations per event is a reasonable number to obtain good-quality results, therefore, we set the multiplication factor of 0.1 (Eq. 1) for weighting the number of observations. The multiplication factor for the azimuthal gap was set to 0.9 indicating its major significance, since better azimuthal coverage generally yields more reliable focal mechanism solutions. Moreover, as *comp* and *res* generally have less influence on the focal mechanism precision compared to the azimuthal gap, we assigned

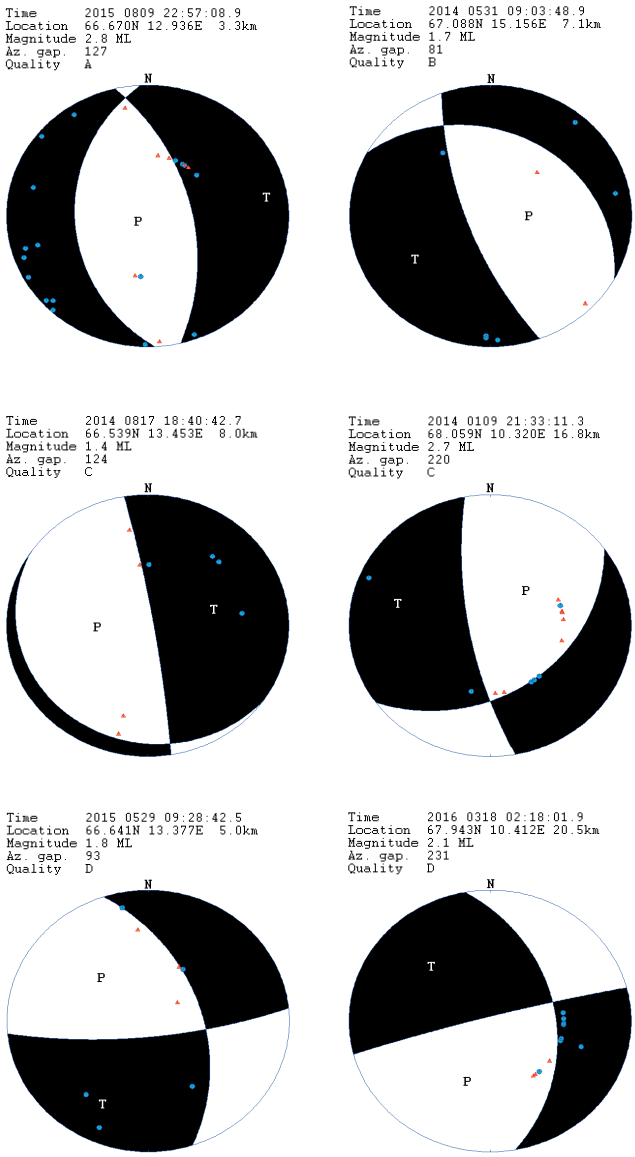

Figure 3. *Examples of focal mechanisms of qualities A, B, C and D of selected onshore and offshore earthquakes. A stands for best quality results, while D stands for lowest quality, i.e., least trustworthy, results. The earthquake information (origin time, location, magnitude and azimuthal gap) and the assigned quality factor are noted above the depicted focal mechanisms. The results were obtained with the FOCMEC program under the SEISAN program package. Quality A (upper left) and B (upper right) were assigned to the focal mechanisms of the onshore earthquakes only, while quality C (middle right) and D (bottom right) were assigned to the focal mechanisms of the offshore earthquakes mainly due to the generally larger azimuthal gaps. About 80% of the focal mechanisms of the onshore earthquakes were assigned with the lower quality C (middle left) and D (bottom left). On the focal sphere, the blue discs indicate first-motion compressional observations (polarity 'up'), while red triangles indicate dilatational first-motion observations (polarity 'down'). T shows the calculated tensional axis, i.e., minimum compressional stress trend, and P shows the pressure axis, i.e., maximum compressional stress trend. Theoretically, the compressional observations (blue discs) should fall within the tensional (black) quadrants, and the dilatational observations (red triangles) within the pressure (white) quadrants. If that was not the case in the calculated focal mechanism solution, those observations were considered as polarity errors. For instance, the quality A focal mechanism (upper left) solution has 3 polarity errors, the quality C focal mechanism (middle right) has one polarity error, and the quality D focal mechanism (bottom right) has one polarity error in their final results.*

their multiplication factors with lower weights 0.4 and 0.2, respectively. The last constant of 1.5 (Eq. 1) ensures the approximate boundaries between 0 and 3. In a theoretical case, when an earthquake has ten observations with *comp* = *res* = *gap* = 0, then *qf* = 2.5, which is the minimum requirement for quality A.

The focal mechanisms with few observations are less reliable, and therefore we set additional requirements for such focal mechanisms: if *obs* ≤ 6.5, then the highest possible quality could be C, and if *obs* ≤ 5.5 then the highest possible quality could be D only. The focal mechanisms of quality D with six or fewer observations are the least reliable (marked as 'D-' in Electronic Supplement 1; Inset of Fig. 4A).

Using the developed relation (Eq. 1) we assigned quality factors for 123 newly obtained focal mechanisms, while for 29 focal mechanisms from previous studies we retained the originally provided quality factors (Fig. 4A). 20% of the analysed dataset consists of the higher quality A and B solutions that were assigned to only the onshore earthquakes, whereas the focal mechanisms of the offshore earthquakes were assigned with the qualities C and D mostly due to the larger azimuthal gaps.

In our dataset, the average number of polarity readings for the onshore earthquakes was 7.8, and 12.4 for the offshore earthquakes, which was also related to the higher detection threshold offshore, i.e., generally stronger (M ≥ 1.2) recorded earthquakes. Onshore, the average number of calculated P/S amplitude ratios was 2.7, and 1.8 offshore, because many offshore earthquakes occurred far away from the network and therefore the direct waves were not the first arrivals. In the dataset, the largest number of observed polarities was 28 for an offshore earthquake of M 3.1. As the event occurred far away from the shore, the P/S amplitude ratios could not be used. Moreover, due to the large azimuthal gap (larger than 200 degrees) and differences in the solutions across the three calculation methods (the final FOCMEC solution showed no polarity errors), using the developed relation (Eq. 1) the quality of the focal mechanisms was set to C. Onshore we obtained two focal mechanisms – one of M 3.2 from the earthquake swarm and one of M 2.8 to the southwest of Svartisen – with 25 polarity readings and up to 8 amplitude readings, but with smaller azimuthal gaps compared with the offshore earthquake. Both focal mechanisms were assigned with quality A, even though their final solutions contained up to 4 polarity errors and several errors of amplitude ratios.

Analysis of the focal mechanisms

An earthquake focal mechanism provides the direction of slip and the orientation of the fault on which the earthquake occurred. While the absolute magnitudes of stresses cannot be resolved, the directions of the stresses (i.e., σ_1, σ_2, σ_3) can be obtained. These stresses are commonly rotated into the horizontal and vertical stresses (e.g., Lund & Townend, 2007) leading to the maximum horizontal stress axis, σ_H, the minimum horizontal stress axis, σ_h, and the vertical stress axis, σ_z. The relative shear-stress magnitude strongly influences whether the fault is susceptible to rupture, and the most decisive parameter is the ratio between the maximum and minimum stress magnitudes. In this study we used the simplified approach of focal mechanisms, and we were focused on σ_H, since we could not resolve the stress ratio, only the σ_H trend, which can be related to regional stress models that are tectonically driven on the global scale. In addition, when many high quality earthquake focal mechanisms are available from a small region, reflecting on a homogeneous stress field, σ_1 can be calculated from an inversion of the focal mechanisms. We attempted to conduct such an inversion for a group of earthquakes to the west of Svartisen, but the inversion failed due to non-homogeneity of the focal mechanism solutions (i.e., the convergence failed).

In our analysis we distinguished geographically several groups of earthquakes, while the grouping (Fig. 2A) was based on a hypothesis that earthquakes in the same area reflect on the same stresses and structures (i.e., underlaying tectonics), and it is therefore expected that the focal mechanisms in the group exhibit similarities in their source mechanisms. In this study, we analysed the focal mechanisms in terms of faulting type, distribution of azimuths of the nodal planes and calculated stress directions. During the analysis we took into account the solutions of all qualities based on an assumption that also low-quality focal mechanisms provide valuable information, albeit of a more uncertain nature. However, in the areas where also higher quality solutions (i.e., A and B) were available, we trusted more the results obtained from the latter solutions. The higher quality solutions in our dataset were assigned to 20% of the focal mechanisms of the earthquakes onshore or close to the shoreline, but unfortunately there were none offshore.

A focal mechanism derived using traditional (i.e., double-couple assumption) methods is non-unique in terms of source rupture: two fault (nodal) planes are equally plausible as an earthquake source from an observational perspective. Only by using additional and independent geological information can a real rupture plane be identified from the two nodal plane candidates. Therefore, it is not possible to directly link the defined focal mechanisms to any well-mapped or well-known faults, and both nodal planes must be considered as equally plausible candidates for the rupture plane. However, by

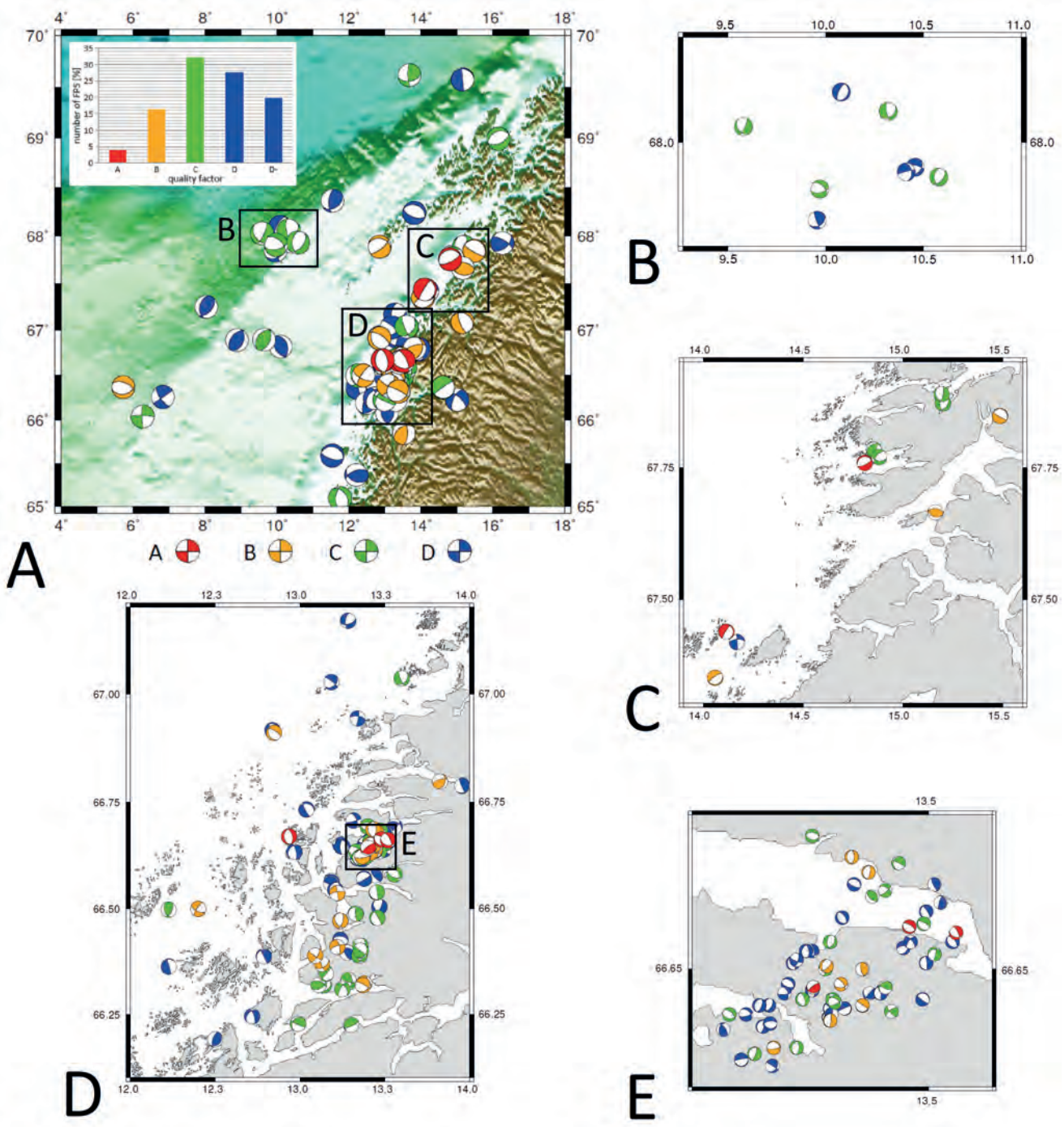

Figure 4. Final dataset of 152 focal mechanism solutions with indicated colour-coded quality factors: (A) in the entire Nordland area, (B) along the continental shelf area, to the north of the Trænadjupet, (C) around the Steigen area, (D) the most seismically active coastal onshore area, and (E) the earthquake swarm area to the west of Svartisen. Inset in (A): Distribution of quality factors of the focal mechanisms from best quality A through B and C to reasonable quality D. 'D-' marks focal mechanisms with 6 or less observations.

plotting the azimuths of both nodal planes it may be possible to reveal dominant trends that may reflect on seismically active structures. Our results indicated that the azimuths of nodal planes obtained from the earthquake focal mechanisms in different areas matched quite well with the azimuthal trends of the mapped faults along the shelf edge, coastline and around Svartisen (Figs. 1 & 5).

In addition, the type of faulting derived from the focal mechanisms may be used to relate earthquakes to particular tectonic structures. The majority of the obtained focal mechanisms are not pure, but rather mixtures of faulting types (i.e., oblique), and therefore the triangle plots suggested by Frohlich & Apperson (1992) proved to be very useful in our study to reveal the dominant types of faulting (Fig. 5). Our results indicated a dominant

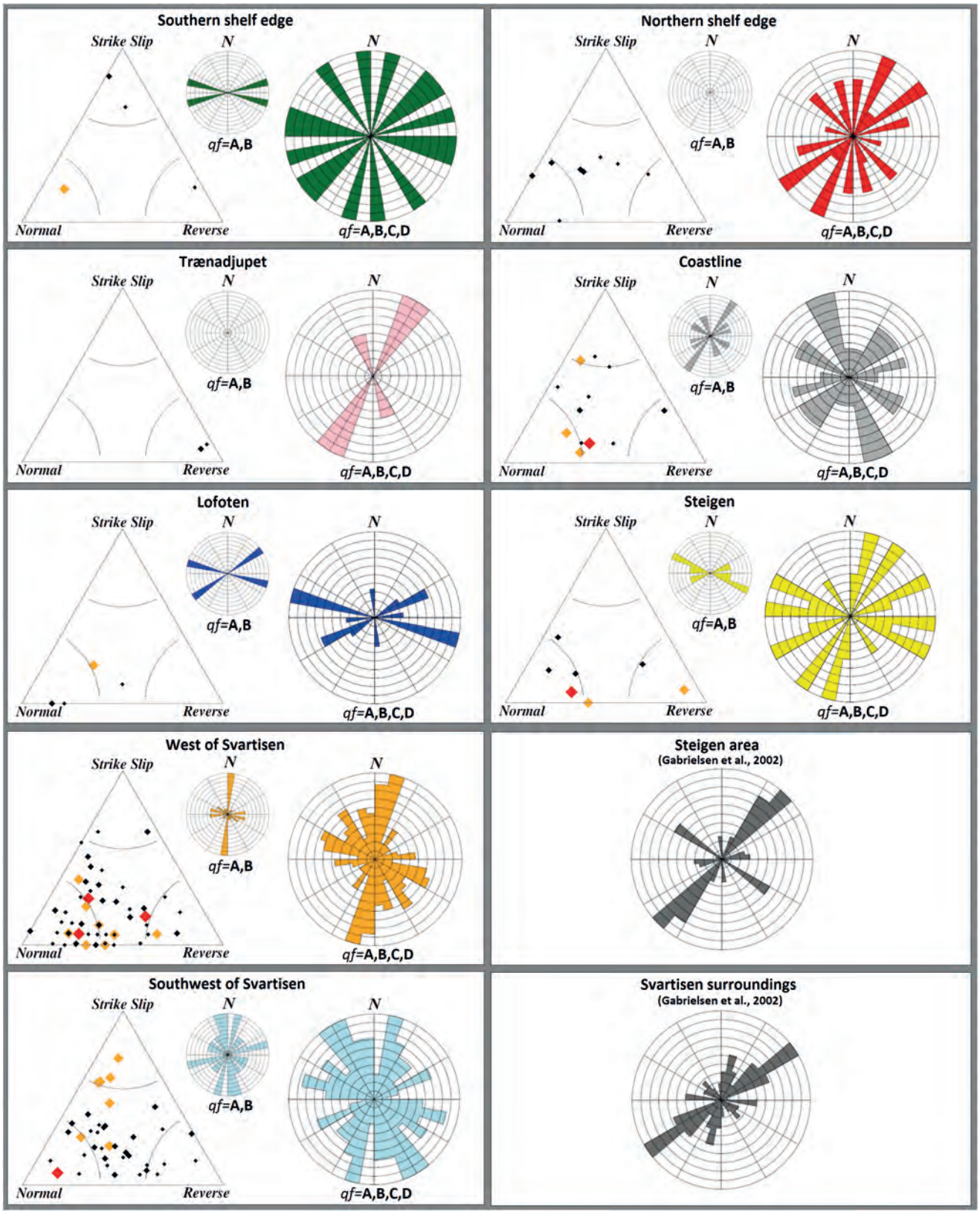

Figure 5. *Panels indicate the results obtained from analysis of the focal mechanisms in different regions of Nordland. Triangle plots show type of faulting obtained from focal mechanisms of different qualities: red – quality A, orange – quality B, black – quality C (bigger diamonds) and D (smaller diamonds). The rose diagrams indicate the azimuths of nodal plane directions obtained from the focal mechanisms of quality A and B only (smaller rose diagrams), and of all qualities A to D (bigger rose diagram). Empty rose diagrams, in the Trænadjupet and the northern shelf edge areas, mean that there is no data of quality A and B. For comparison, we also provide the trends of azimuths of the lineaments mapped on the surface by Gabrielsen et al. (2002) around Steigen and Svartisen, where the most intense onshore seismicity was recorded (lower right).*

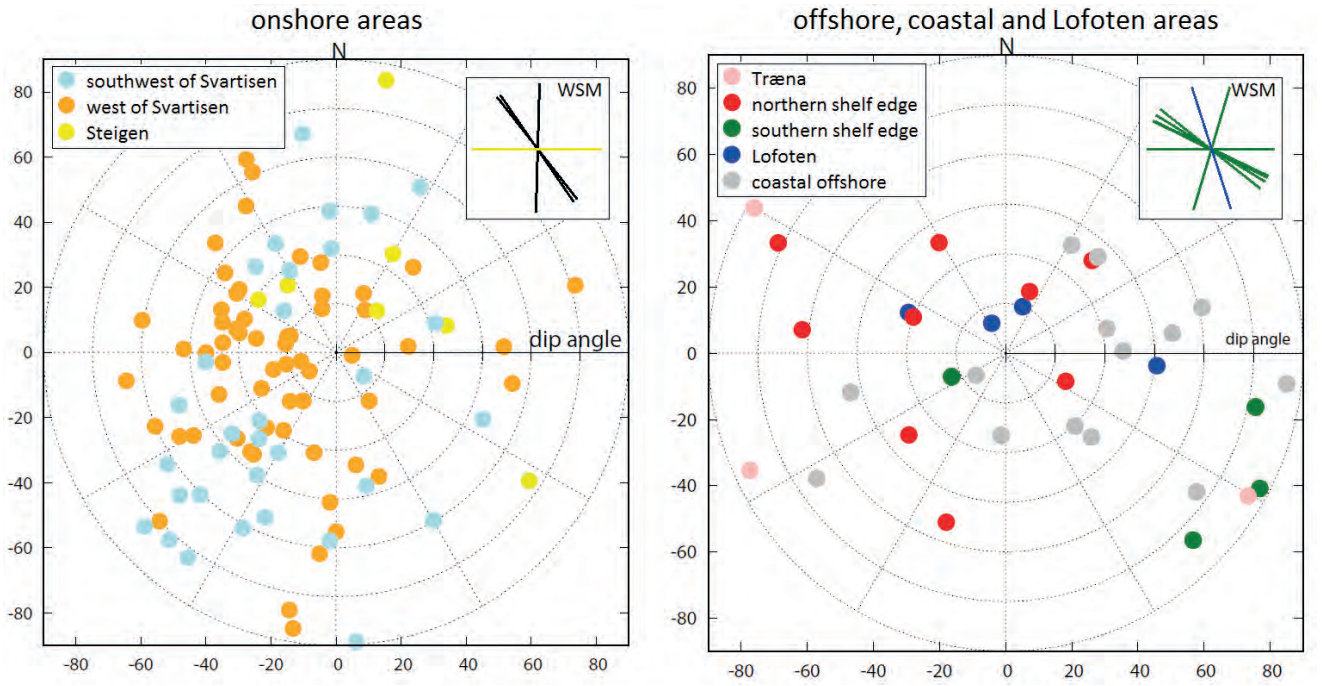

Figure 6. *Azimuth and dip of maximum compression axis, σ_1, obtained from the focal mechanisms in Nordland in the onshore and offshore areas. Insets show horizontal compression axis, σ_H, from the WSM project colour-coded according to different regions, while in black we indicate data from the onshore areas which are outside the specified regions, i.e., east and southeast of Svartisen. As the WSM data were usually obtained from boreholes, they are limited to the uppermost 2 km, whereas earthquakes, especially those offshore and in the Lofotens, are generally deeper.*

normal type in the majority of the distinguished groups onshore. Moreover, the horizontal compression axis, sH, trends obtained from normal or very oblique faulting types are dubious as s1 direction is subvertical. Therefore, to derive σ_H directions from focal mechanisms we used recommendations and software by Lund & Townend (2007), and thus obtained the azimuth and dip of the σ_1 vectors (Fig. 6).

Results and discussion

Below we discuss in more detail our observations and results obtained from the earthquake focal mechanisms in four specific areas.

West and southwest of Svartisen

The area to the west of the Svartisen glacier was the seismically most active during the NEONOR2 monitoring period. Here we also recorded an earthquake swarm with several hundreds of small earthquakes which occurred from April 2015 to March 2016. From all the swarm events we obtained 61 focal mechanisms, which mostly indicated normal faulting (Figs. 4E & 5). Also, dominant normal to strike-slip faulting was observed southwest of Svartisen from the analysis of 39 focal mechanisms (Figs. 4D & 5). The earthquakes in both areas were generally shallow (3 to 8 km deep; Fig. 2B) and many earthquakes in the southwestern part clustered along well-defined NW–SE-trending lines, indicating that the earthquakes probably migrated along the structures, which were interpreted as active faults (Janutyte et al., in press). The azimuths of nodal planes (Fig. 5) obtained from the focal mechanisms showed two clear trends: a NNE–SSW trend to the west of Svartisen, and a somewhat bimodal trend to the southwest of Svartisen with the nodal planes of NNW–SSE (along migration paths of the earthquakes) and NNE–SSW trends. These observations coincide quite well with the structural trends mapped by Gabrielsen et al. (2002) in the surroundings of Svartisen (Fig. 5).

The Svartisen massif (SV; Fig. 1) in Nordland is a *c.* 1000 m-high mountain hosting an ice sheet. Due to its steep relief, the massif is a likely candidate for local stress sources in the area. It was also found that the massif, including its peripheral regions, to a large extent consists of very poor quality rock with large cracks and faults allowing water (from precipitation and snowmelt) to easily penetrate from the glaciated regions to its periphery. Water lubricates the faults such that the friction is reduced and therefore smaller changes in stress conditions would be required to trigger earthquakes along the faults. This is a likely mechanism behind the earthquake swarm activity which was recorded at the western foot of the Svartisen massif from the spring of 2015. While modelling would be appropriate for long-term changes in the ice sheet, the observed intense local seismicity on the fringes of the massif indicate that short-term changes in the glacier might indeed influence the earthquake occurrence in the

area. However, the NEONOR2 monitoring did not cover a sufficiently long time window to confirm this.

Analysis showed that σ_H directions in different groups of earthquakes around Svartisen – 61 focal mechanisms to the west, 39 to the southwest, two to the north, one to the northwest and one to the southeast of the glacier – are almost tangential to the glacier, which would coincide with an assumption of local uplift due to the retreat (melting) of the glacier. However, it must be taken into account that the dominant type of faulting is normal, thus σ_1 directions are not very clear. Moreover, the lower quality C and D focal mechanisms obtained from single earthquakes, as it is in this case, might be uncertain; therefore, these results should be treated with caution. However, it is also important to note that the data on hand show a possible correlation between the earthquake swarm activity and the glacier.

As the earthquake swarm was recorded only once and did not repeat within the yearly cycle, it could therefore be concluded that other factors, not only the changes in the ice mass, could affect the earthquake occurrence in the area. Another possible stress source in the area is the Storglomvatn hydroelectric power station and lake, located to the north of Svartisen, with a capacity of 3.5 * 10^9 m^3 and a height of 128 metres. The power plant experiences large variations in water-filling cycles, and thus the changes in the water mass might significantly change the rock stresses and lubrication patterns around the area, although there is not enough data to allow us to hypothesise about the size of its effects on the local stress field. However, it is likely that significant changes in the lake level of Storglomvatn could reflect on the focal mechanisms of the shallow earthquakes.

Steigen and Lofoten area

The earthquakes in Steigen and Lofoten exhibited a dominant normal faulting type, with some high-quality focal mechanisms showing also reverse faulting around Steigen (Figs. 4C & 5). The hypocentre depth around Steigen was mostly shallow (down to 10 km depth) while it was somewhat deeper in the Lofoten area (down to 20 km depth; Fig. 2B). Even though the obtained focal mechanisms were not homogeneous in the Steigen area, the tendency for a NE–SW compression could be distinguished (Fig. 5). Moreover, the azimuths of nodal plane directions trending from NNE–SSW to ENE–WSW obtained from the focal mechanisms are consistent with the lineaments recorded by Gabrielsen & Ramberg (1979), and also with the direction of the nodal plane of the composite focal mechanism obtained by Atakan et al. (1994) from the Steigen earthquake sequences. The NNE–SSW trend (Gabrielsen & Ramberg, 1979) is parallel to the Vestfjord Basin and some post-Caledonian faults which were active in post-glacial times (Grønlie, 1922). This might indicate that faults and structures mapped on the surface are indeed active down to some depth.

In the Lofoten area, the azimuths of nodal planes showed a preference for the WNW–ESE trend, which is similar to the trends obtained by Gabrielsen & Ramberg (1979). The normal faulting in this area was also earlier observed by Hicks (1996) from a single-event focal mechanism that also indicated a coast-perpendicular extension. With a dominant normal faulting type the maximum compressional direction remained inconclusive (Figs. 4A, 5 & 6), while one borehole (WSM data) in the area indicated compressional stresses trending NNW–SSE (Figs. 1 & 6).

Coastal area

Along the coast the focal mechanisms indicated normal to strike-slip faulting (Fig. 5). The obtained σ_1 direction (Fig. 6) was bimodal, but with a slight preference for the NW–SE trend (i.e., coast-perpendicular compression). The azimuths of the nodal planes obtained from all focal mechanisms in the area indicated a dominant NNW–SSE trend, possibly due to the westerly extensions of the onshore faults, while several higher quality A and B focal mechanisms further to the north, closer to Steigen indicated NNE–SSW direction, which is parallel to the Vestfjord Basin and some post-Caledonian faults (e.g., Gabrielsen & Ramberg, 1979).

Around Meløy, Gabrielsen & Ramberg (1979) indicated the NNW–SSE-striking fault population as a likely candidate for earthquake occurrence, while NNE–SSW-trending active faults were reported by Bungum & Husebye (1979) from the Meløy earthquake swarm.

In an area about 30 km north of Meløy we obtained two focal mechanisms. Both focal mechanisms were of low quality D, and therefore might not be very reliable. However, from the locations we related the earthquakes to the NE–SW-trending Grønna structure (Fig. 1).

Offshore areas

In the offshore areas, the new focal mechanisms were of quality C and D, mainly reflecting the larger azimuthal gaps (Fig. 4A). On the other hand, the recorded earthquakes along the shelf edge were generally stronger ($M \geq 1.2$) and should therefore reflect the regional trends better. Also, due to larger source-to-receiver distances (more than 140 km), the P/S amplitude ratios could not be used, as they are applicable to direct P- and S-waves only. Consequently, we defined many focal mechanisms of the offshore earthquakes using only P-wave polarities. We separated the offshore region into three areas: the Trænadjupet, and the southern and the northern parts of the shelf edge (Fig. 2A). Around Trænadjupet the new and earlier data (Bungum et al., 1991) showed pure

reverse faulting as well as one earthquake slightly farther to the northwest of the Trænadjupet (Fig. 4A). These earthquakes clearly signify a σ_H of NW–SE trend, which is in compliance with the ridge push of plate tectonics. The E–W distribution of the epicentres at the northern tip of the Nordland Ridge does not match with any known fault azimuths. However, the NNE–SSW trends of the nodal planes (Fig. 5) coincide well with the mapped regional faults (Fig. 1), which could also indicate én echelon faulting.

To the south of Trænadjupet on the Vøring platform, two focal mechanisms denoted a strike-slip faulting while on the oceanic part of the shelf edge one earlier obtained focal mechanism indicated a normal faulting event (Fig. 4A). Here, we also obtained a NW–SE trend for σ_H, which is consistent with the WSM data (Figs. 1 & 6), and coincides with the ridge-push force. To the north of Trænadjupet along the shelf edge, the type of faulting was quite mixed while the nodal plane directions (Figs. 4B & 5) obtained from the focal mechanisms showed a clear NE–SW trend, which is in alignment with the strikes of regional faults. The NW–SE trend of σ_1 (Fig. 6) here also indicated an influence from the ridge push. This trend also coincides well with the WSM data (Figs. 1 & 6).

In summary, we found that onshore earthquake characteristics are very different from those of the offshore earthquakes. Onshore, the dominant faulting type is normal, whereas a rather mixed type is common for the offshore earthquakes. Offshore, the σ_1 direction indicated clear NW–SE compression, which is also consistent with the azimuths of the σ_H axis from the boreholes (Figs. 1 & 6), and is in accord with the ridge-push force of plate tectonics (e.g., Richardson et al., 1979). Onshore, σ_1 trends are more scattered and most likely reflect on the local stress sources (such as topography) and possibly short-term stress variations (e.g., around the Svartisen massif). The WSM borehole data onshore is very sparse and almost absent in some specific areas, and thus it is very difficult to correlate it with our results. However, when comparing σ_H trends obtained from boreholes and those from earthquakes one must bear in mind that the WSM data generally reflect the state of stress in the upper part of the crust (down to about 2 km), whereas earthquakes generally generated in the deeper crust.

Both the onshore and the offshore focal mechanisms indicated the azimuths on nodal planes (Fig. 5) of mostly NW–SW trend, which is generally consistent with the mapped regional faults in Nordland (Fig. 1).

Along the shelf edge, the dominant stress source is the ridge push of NW–SE trend while the obtained azimuths of the nodal planes of the earthquakes mostly trend NE–SW (Figs. 1 & 5), which in general is perpendicular to σ_H. According to the Andersonian model (e.g., Anderson, 1905), for a fault of this orientation to rupture in such a stress field, the fault must have an inclination that favours the shear stresses. Therefore, we assume that the offshore faults at a seismogenic depth (about 20 km deep) are somewhat inclined. However, some of the azimuths of the nodal planes obtained offshore indicate a NW–SE trend that is parallel to the regional stress field. Onshore, the Mid-Atlantic ridge push is dominated by the local stress sources (e.g., steep topography), as here we observe clear deviations from the regional stress pattern (Fig. 6). The extreme topography in the region with steep mountains and deep fjords should create substantial local vertical stresses that favour normal faulting, which we have in fact observed as the dominant type of faulting in the onshore areas of Nordland.

Conclusions

We compiled a dataset of 152 focal mechanisms for Nordland, northern Norway, that consists of 123 newly obtained focal mechanisms from the NEONOR2 project and 39 focal mechanisms from earlier studies. The dataset is now made available and presented here (Electronic Supplement 1) to help promote future investigations on this database.

We analysed the focal mechanisms in terms of faulting type, directions of azimuths of nodal planes and maximum compressional stress directions. The results shed more light on the stress conditions in this part of Norway. Our main conclusions are as follows:

- We developed a focal mechanism quality ranging system that was specifically adjusted to the new data. Using the developed relation (Eq. 1) we assigned the new 123 focal mechanisms with quality factors from best quality A to lowest quality D, while for the 39 focal mechanisms from earlier studies we maintained the quality factor as originally provided.

- Qualities A and B weres assigned to about 20% of all obtained focal mechanisms. The higher quality was assigned to the onshore earthquakes mainly because of their better station coverage compared to the earthquakes offshore where only lower quality, C and D, was assigned to the new focal mechanisms. In our study we analysed focal mechanism solutions of all qualities, as even low-quality results are valuable and carry information that contributes to recognising the general trends. However, we trusted more the results obtained from higher quality A and B focal mechanisms in the areas where such results were available.

- Onshore Nordland, the dominant faulting type is normal, while along the coast it is mostly normal to strike-slip, and in the offshore areas it is rather of a mixed character.

- In the offshore areas, strikes of the nodal planes obtained from the focal mechanisms mostly follow a NE–SW

trend, which is subparallel to the coastline and coincides with the mapped structural trends on the continental shelf, indicating that present-day earthquakes do indeed reactivate these old structures. In the onshore area of Nordland we resolved two dominant trends of azimuths of the nodal planes: the major trend is NNE–SSW, and the weaker trend WNW–ESE. Such a nodal plane distribution of the onshore earthquakes also coincides with trends of the structures mapped by Gabrielsen et al. (2002). Therefore, it can be concluded that the geologically mapped onshore structures might be seismically active and do reflect the present-day crustal deformation.

- The obtained maximum compression axis, σ_1, in the offshore areas indicated a clear NW–SE trend reflecting on the expected plate-tectonic ridge push. The maximum horizontal stress axis, σ_H, recorded in the onshore areas is more scattered and therefore related to the local stress sources, such as topography. Moreover, we interpreted the observed tendency of σ_H to follow the tangential direction to the Svartisen glacier as a manifestation of the influence of the changes in the ice-sheet and related processes (i.e., melting, accumulation, etc.), which, most likely, is one of the causes of the enhanced earthquake occurrence in the area. Offshore, the obtained compressional stress directions are consistent with the borehole breakouts from the World Stress Map (WSM) database, while onshore the obtained results partly correlate with the WSM data.

- As we observed seismicity along the shelf edge on NE–SW-trending faults, we concluded that the faults at seismogenic depth should be inclined, as this would satisfy rupturing conditions in the stress field from the NW-SE-oriented ridge-push force. Onshore, local stresses dominate mainly due to the steep topography that would invoke vertical stresses that favour normal faulting, which was observed in the onshore areas.

- From the three recorded seismic swarms in the Nordland area around Meløy in 1978–1979, Steigen in 1992 and to the west of Svartisen in 2015–2016, it could be concluded that shallow foci and extensional tectonics are the characteristic features of swarm activity in the coastal regions of Nordland.

Generally, the results showed that the seismicity onshore and offshore Nordland is different in character, with mostly deeper mixed faulting earthquakes offshore where stresses arising from the Mid-Atlantic ridge push dominate; and with mostly shallow, normal-faulting earthquakes onshore where local stresses rule over the regional stress pattern, while along the coast the faulting regime was mostly normal to strike-slip.

Acknowledgements. The present work was conducted with the support of the Norwegian Research Council to the Norwegian Geological Survey under grant number 228105/E30, and with additional funding from Aker BP, DEA, DONG Energy, E.ON, the Geological Survey of Norway (NGU), the Norwegian Mapping Authority (Kartverket), Lundin Norway, Maersk Oil, Noreco, NORSAR, Norske Shell, the Norwegian Petroleum Directorate, Repsol, Statoil and VNG. The primary earthquake locations used in our staudy were obtained at the Univerity of Bergen. We thank Björn Lund and John Townend for sharing with us their software on calculating horizontal stress orientations. We greatly appreciate the contributions of Odleiv Olesen and Yuriy Maystrenko through countless discussions. We also thank Roy H. Gabrielsen and an anonymous reviewers for their very useful comments and suggestions that greatly improved this manuscript.

References

Anderson, E.M. 1905: The dynamics of faulting. *Transactions of the Edinburgh Geological Society 8, 387–402.* https://doi.org/10.1144/transed.8.3.387.

Atakan, K., Lindholm, C.D. & Havskov, J. 1994: Earthquake swarm in Steigen, northern Norway: an unusual example of intraplate seismicity. *Terra Nova 6, 180–194.* https://doi.org/10.1111/j.1365-3121.1994.tb00652.x.

Blystad P., Brekke, H., Færseth, R., Larsen, B.T., Skogseid, J. & Tørudbakken, B. 1995: Structural elements of the Norwegian continental shelf. Part II: The Norwegian Sea Region. *Norwegian Petroleum Directorate Bulleting 8*, 45 pp.

Braathen, A., Osmundsen, P.T., Nordgulen, Ø. & Roberts, D. 2002: Orogen-parallel, extensional denudation of the Caledonides in North Norway. *Norsk Geologisk Tidsskrift 82*, 225–241.

Bungum, H. & Husebye, E.S. 1979: The Meløy, northern Norway, earthquake sequence – a unique intraplate phenomenon. *Norsk Geologisk Tidsskrift 59*, 189–193.

Bungum, H. & Olesen, O. 2005: The 31st of August 1819 Lurøy earthquake revisited. *Norwegian Journal of Geology 85*, 245–252.

Bungum, H., Hokland, B.K., Husebye, E.S. & Ringdal, F. 1979: An exceptional intraplate earthquake sequence in Meløy, Northern Norway. *Nature 280*, 32–35. https://doi.org/10.1038/280032a0.

Bungum, H., Vaage, S. & Husebye, E.S. 1982: The Meløy earthquake sequence, Northern Norway; source parameters and their scaling relations. *Bulletin of the Seismological Society of America 72*, 197–206.

Bungum, H., Alsaker, A., Kvamme, L.B. & Hansen, R.A. 1991: Seismicity and seismotectonics of Norway and surrounding continental shelf areas. *Journal of Geophysical Research 96, 2249–2265.* https://doi.org/10.1029/90JB02010.

Bungum, H., Olesen, O., Pascal, C., Gibbons, S., Lindholm, C. & Vestøl, O. 2010: To what extent is the present seismicity of Norway driven by post-glacial rebound? *Journal of the Geological Society 167, 373–384.* https://doi.org/10.1144/0016-76492009-009.

Byrkjeland, U., Bungum, H. & Eldholm, O. 2000: Seismotectonics of the Norwegian continental margin. *Journal of Geophysical Research 105, 6221–6236.* https://doi.org/10.1029/1999JB900275.

Dehls, J.F. & Olesen, O. 2000: NEONOR: Neotectonics in Norway: Annual Technical Report 1999. *Norges geologiske undersøkelse Report 2000.001*, 207 pp.

Eide, E.A., Osmundsen, P.T., Meyer, G.B., Kendrick, M.A. & Corfu, F. 2002: The Nesna Shear Zone, north-central Norway: an $^{40}Ar/^{39}Ar$ record of Early Devonian – Early Carboniferous ductile extension and unroofing. *Norwegian Journal of Geology 82*, 317–339.

Fejerskov, M. & Lindholm, C. 2000: Crustal stresses in and around Norway; an evaluation of stress generating mechanisms. *In Nottvedt, A. (ed.): Dynamics of the Norwegian Margin, Geological Society of London Special Publication 167*, pp. 451–467.

Frohlich, C. & Apperson, K.D. 1992: Earthquake focal mechanisms, moment tensors, and the consistency of seismic activity near plate boundaries. *Tectonics 11*, 279–296. https://doi.org/10.1029/91TC02888.

Gabrielsen, R.H. & Ramberg, L.B. 1979: Fracture paterns in Norway from Landsat imagery: results and potential use. *Proceedings, Norwegian Petroleum Society, Norwegian Sea Symposium, Tromso, NSS/123, 1–23.*

Gabrielsen, R.H., Braathen, A., Dehls, J. & Roberts, D. 2002: Tectonic lineaments of Norway. Norsk Geologisk Tidsskrift 82, 153–174.

Gregersen, S. & Voss, P. 2009: Stress change over short geological time: the case of Scandinavia over 9000 years since the Ice Age. *In* Reicherter, K., Michetti, A.M. & Silva, P.G. (eds.): *Palaeoseismology: Historical and Prehistorical Records of Earthquake Ground Effects for Seismic Hazard Assessment*, Geological Society of London Special Publications 316, 217–235. https://doi.org/10.1144/SP316.10.

Grønlie, O.T. 1922: Strandlinjer, moræner og skjælforekomster i den sydlige del av Troms fylke. *Norges geologiske undersøkelse 94, 1–39.*

Gudmundsson, A. 1999: Postglacial crustal doming, stresses and fracture formation with application to Norway. Tectonophysics 307, 407–419. https://doi.org/10.1016/S0040-1951(99)00107-9.

Hardebeck, J.L. & Shearer, P.M. 2002: A new method for determining first motion focal mechanisms. *Bulletin of the Seismological Society of America 92, 2264–2276.* https://doi.org/10.1785/0120010200.

Heidbach, O., Tingay, M., Barth, A., Reinecker, J., Kurfeß, D. & Müller, B. 2008: The World Stress Map database release 2008. DOU:10.1594/GFZ.WSM.Rel2008, 2008.

Heidbach, O., Tingay, M., Barth, A., Reinecker, J., Kurfeß, D. & Müller, B. 2010: Global crustal stress pattern based on the World Stress Map database release 2008. *Tectonophys 482, 3–15.* https://doi.org/10.1016/j.tecto.2009.07.023.

Hicks, E.C. 1996: *Crustal stresses in Norway and surrounding areas as derived from earthquake focal mechanism solutions and in situ stress measurements. PhD thesis, University of Oslo, Norway, 164 pp.*

Hicks, E.C., Bungum, H. & Lindholm, C.D. 2000a: Seismic activity, inferred crustal stresses and seismotectonics in the Rana region, northern Norway. Quaternary Science Reviews 19, 1423–1436. https://doi.org/10.1016/S0277-3791(00)00071-8.

Hicks, E.C., Bungum, H. & Lindholm, C.D. 2000b: Stress inversion of earthquake focal mechanism solutions from onshore and offshore Norway. *Norsk Geologisk Tidsskrift 80, 235–250.* https://doi.org/10.1080/00291960051030545.

Jaeger, J.C., Cook, N.G.W. & Zimmerman, R.W. 2007: *Fundamentals of Rock Mechanics. 4th edition*. Blackwell Publishing, Oxford, 475 pp.

Janutyte, I., Lindholm, C. & Olesen, O. (in press): Relation between seismicity and tectonic structures offshore and onshore Nordland, northern Norway. *Norwegian Journal of Geology 97.*

Lund, B. & Townend, J. 2007: Calculating horizontal stress orientations with full or partial knowledge of the tectonic stress tensor. *Geophysical Journal International 170*, 1328–1335. https://doi.org/10.1111/j.1365-246X.2007.03468.x.

Maystrenko Y., Olesen, O., Gernigon, L. & Gradmann, S. 2017: Deep structure of the Lofoten-Vesterålen segment of the Mid-Norwegian continental margin and adjacent areas derived from 3D density modeling. *Journal of Geophysical Research, Solid Earth 122, 1402–1433.* https://doi.org/10.1002/2016JB013443.

Muir Wood, R. 1989: Extraordinary deglaciation reverse faulting in northern Fennoscandia. *In Gregersen, S. & Basham, P.W. (eds.): Earthquakes at North Atlantic Passive Margins: Neotectonics and Postglacial Rebound, NATO ASI Series, Series C: Mathematical and Physical Sciences 266, pp. 141–173.*

Olesen, O., Lundin, E., Nordgulen, Ø., Osmundsen, P.T., Skilbrei, J.R., Smethurst, M.A., Solli, A., Bugge, T. & Fichler, C. 2002: Bridging the gap between the Nordland onshore and offshore geology. *Norwegian Journal of Geology 82, 243–262.*

Olesen, O., Bungum, H., Dehls, J., Lindholm, C., Pascal, C. & Roberts, D. 2013: Neotectonics, seismicity and contemporary stress field in Norway – mechanisms and implications. In Olsen, L., Fredin, O. & Olesen, O. (eds.): *Quaternary Geology of Norway, Norges geologiske undersøkelse Special Publication 13, pp. 145–174.*

Osmundsen, P.T., Sommaruga, A., Skilbrei, J.R. & Olesen, O. 2002: Deep structure of the Mid Norway Rifted Margin. *Norwegian Journal of Geology 82*, 205–224.

Osmundsen, P.T., Henderson, I., Lauknes, T.R., Larsen, Y., Redfield, T.F. & Dehls, J. 2009: Tectonic controls on topography and mass-wasting processes in northern Norway. *Geology 37*, 135–138. https://doi.org/10.1130/G25208A.1.

Ottemoller, L., Voss, P. & Havskov, J. 2016: *Seisan earthquake analysis software for Windows, Solaris, Linux and MacOS*, 534 pp.

Pascal, C. & Gabrielsen, R.H. 2001: Numerical modeling of Cenozoic stress patterns in the mid-Norwegian margin and the northern North Sea. *Tectonics 20*, 585–599. https://doi.org/10.1029/2001TC900007.

Pascal, C., Roberts, D. & Gabrielsen, R.H. 2005: Quantification of neotectonic stress orientations and magnitudes from field observations in Finnmark, northern Norway. *Journal of Structural Geology 27*, 859–870. https://doi.org/10.1016/j.jsg.2005.01.011.

Pascal, C., Roberts, D. & Gabrielsen, R.H. 2010: Tectonic significance of present-day stress relief phenomena in formerly glaciated regions. *Journal of the Geological Society of London 167*, 363–371. https://doi.org/10.1144/0016-76492009-136.

Reasenberg, P. & Oppenheimer, D. 1985: Fpfit, fpplot, and fppage: Fortran computer programs for calculating and displaying earthquake fault plane solutions. *U.S. Geological Survey, Technical report 85-739, 109 pp.*

Redfield, T.F. & Osmundsen, P.T. 2013: The long-term topographic response of a continent adjacent to a hyperextended margin: A case study from Scandinavia. *Geological Society of America Bulletin 125*, 184–200. https://doi.org/10.1130/B30691.1.

Richardson R.M., Solomon, S.C. & Sleep, N.H. 1979: Tectonic stress in plates. *Reviews of Geophysics 17*, 981–1019. https://doi.org/10.1029/RG017i005p00981.

Roberts, D. & Gee, D.G. 1985: An introduction to the structure of the Scandinavian Caledonides. *In Gee, D.G. & Sturt, B.A. (eds.): The Caledonian Orogen – Scandinavia and related areas*, John Wiley and Sons, Chichester, pp. 55–68.

Rykkelid, E. & Andresen, A. 1994: Late Caledonian extension in the Lofoten area, northern Norway. *Tectonophysics 231, 157–169.* https://doi.org/10.1016/0040-1951(94)90127-9.

Sibson, R.H. 1985: A note on fault reactivation. *Journal of Structural Geology 7*, 751–754. https://doi.org/10.1016/0191-8141(85)90150-6.

Snoke, J.A., Munsey, J.W., Teague, A.G. & Bollinger, G.A. 1984: A program for focal mechanism determination by combined use of polarity and SV-P amplitude ratio data. *Earthquake Notes 55, 15 pp.*

Stroeven A.P., Hättestrand, C., Kleman, J., Heyman, J., Fabel, D., Fredin, O., Goodfellow, B.W., Harbor, J.M., Jansen, J.D., Olsen, L., Caffee, M.W., Fink, D., Lundqvist, J., Rosqvist, G.C., Strömberg, B. & Jansson K.N. 2016: Deglaciation of Fennoscandia. *Quaternary Science Reviews 147*, 91–121. https://doi.org/10.1016/j.quascirev.2015.09.016.

Vaage, S. 1980: Seismic evidence of complex tectonics in the Meløy earthquake area. *Norsk Geologisk Tidsskrift 60*, 213–217.

Zoback, M.L. & Zoback, M. 1989: Tectonic stress field of the conterminous United States. *In* Pakiser, L.C. & Mooney, W.D. (eds.): *Geophysical Framework of the Continental United States*, Geological Society of America Memoir 172, pp. 523–539. https://doi.org/10.1130/MEM172-p523.

Electronic Supplement 1. All focal mechanisms analyzed in this study. Year, month, day, hour, minutes and seconds indicate the origin time of the earthquake, while latitude, longitude, depth and magnitude indicates its location and strength. Strike, dip and rake indicates parameters of the focal mechanism, while qf stands for quality factor. The reference indicates the source of the results: FOCMEC – obtained during this study using the FOCMEC program, while the numbers indicate the focal mechanisms obtained from earlier studies, for which the original quality estimates were maintained: 1* Bungum et al. (1991); 2* NORSAR Composite solution; 3* University of Bergen with unknown specifics; 4* Hicks et al. (2000a); 5* Hicks et al. (2000b); 6* Hicks (1996).

No.	Year	Month	Day	Hour	Min.	Sec.	Lat.	Long.	Depth	Mag.	qf	Reference	Strike	Dip	Rake
1	2012	7	2	22	36	17,5	66,08	13,053	5	2,4	D-	FOCMEC	169,1700	50,7300	77,0400
2	2013	4	19	9	28	40,4	66,498	12,225	15,9	3,3	C	FOCMEC	161,5800	46,0300	54,0400
3	2013	9	2	3	27	17,2	69,579	15,158	8	1,6	D-	FOCMEC	354,9300	90,0000	80,0000
4	2013	9	18	19	38	1,9	66,427	13,238	4,5	1,9	D	FOCMEC	115,6400	41,0300	-74,6600
5	2013	10	10	20	21	51,2	67,418	14,168	8	2,1	D	FOCMEC	355,6700	87,5000	29,9100
6	2013	12	26	15	33	34	68,241	13,813	25,8	1,4	D	FOCMEC	290,0000	30,0000	-90,0000
7	2014	1	9	21	33	11,3	68,059	10,32	16,8	2,7	C	FOCMEC	53,9500	35,5300	-30,6400
8	2014	1	11	18	28	21,9	66,566	13,187	4,5	0,9	D-	FOCMEC	286,4900	17,9600	55,7300
9	2014	1	22	14	25	52,6	66,579	13,445	8,7	0,9	D-	FOCMEC	306,5300	20,5900	75,6500
10	2014	1	24	19	36	33,2	66,681	13,447	4,6	2,1	B	FOCMEC	190,0000	20,0000	-90,0000
11	2014	3	7	21	36	52,7	66,944	13,34	7	2,7	D	FOCMEC	277,5300	65,9100	-6,8800
12	2014	4	21	22	24	58,5	66,364	12,226	8,2	1,8	D	FOCMEC	343,9200	85,0800	79,9600
13	2014	5	31	9	3	48,9	67,088	15,156	7,1	1,7	B	FOCMEC	159,6700	70,7100	-74,0800
14	2014	6	2	6	25	59,1	66,191	12,5	5	1,7	D	FOCMEC	198,1900	65,4100	78,9900
15	2014	6	4	16	42	10	68,366	11,544	15	2,1	D	FOCMEC	185,6700	63,0500	61,7000
16	2014	6	6	2	24	25,7	66,397	13,279	7	1,1	D	FOCMEC	278,4600	41,4100	40,8900
17	2014	6	7	3	34	54,4	66,893	9,637	14	3,1	C	FOCMEC	25,8200	50,1800	83,4800
18	2014	6	14	15	42	6,7	66,658	13,482	5,9	1,4	D	FOCMEC	219,3200	66,0700	-26,3400
19	2014	6	14	15	52	9	66,673	13,45	6	1,9	C	FOCMEC	132,1200	60,1300	84,2300
20	2014	6	15	20	58	9,3	67,759	14,808	5,3	1,2	A	FOCMEC	258,4700	20,5900	-75,6500
21	2014	6	23	11	4	45,8	66,663	13,481	5	2	A	FOCMEC	302,3300	65,1000	-84,4900
22	2014	7	9	6	47	4	66,818	10,096	4,9	2,1	D	FOCMEC	150,8200	50,1800	83,4800
23	2014	7	16	17	57	18,4	66,693	13,4	5	1,6	C	FOCMEC	104,9800	45,2200	-82,9500
24	2014	7	22	20	27	10	67,349	14,058	10	1,8	B	FOCMEC	73,0200	15,7900	-71,3200
25	2014	8	16	10	51	13,1	66,261	6,821	20	2,9	D	FOCMEC	145,7200	70,0800	1,8200
26	2014	8	17	6	53	10,3	67,438	14,115	1,4	1,6	A	FOCMEC	212,1800	80,1500	-79,8500
27	2014	8	17	18	40	42,7	66,539	13,453	8	1,4	C	FOCMEC	350,4400	85,0200	-84,9800
28	2014	8	23	4	35	49,8	66,637	13,442	5	1,2	B	FOCMEC	305,4400	85,0200	-84,9800
29	2014	10	18	18	2	26,6	66,798	13,826	7,4	1,3	B	FOCMEC	18,7400	34,7800	42,1900
30	2014	10	28	0	36	5,8	68,096	10,08	12	2,3	D-	FOCMEC	205,0000	65,0000	-90,0000
31	2014	11	20	8	38	12,5	67,848	15,486	7,5	1	B	FOCMEC	300,0000	10,0000	-90,0000
32	2014	11	28	19	48	26	67,85	9,957	20	2,6	D	FOCMEC	158,9700	81,8200	54,5900
33	2014	12	10	7	32	15,4	66,911	12,847	8	2,5	B	FOCMEC	157,6000	28,9000	-57,6200
34	2014	12	10	14	58	1,3	66,917	12,838	15	2,3	D	FOCMEC	152,2400	75,2300	-79,6500
35	2015	2	19	6	0	44,8	66,686	13,433	5	2,5	B	FOCMEC	2,8800	60,1300	-84,2300
36	2015	2	24	17	41	35,4	66,707	13,316	8	1,7	D	FOCMEC	339,6900	56,3600	-10,2700
37	2015	3	7	1	46	25,1	66,571	13,378	5	1,9	D-	FOCMEC	285,4100	14,1100	-44,5600
38	2015	4	11	3	13	30,5	66,649	13,442	8	2,6	C	FOCMEC	118,9600	15,7900	18,0200
39	2015	4	14	5	53	13,6	66,634	13,416	10	1,5	D	FOCMEC	10,0000	80,0000	90,0000
40	2015	4	14	6	7	9,5	66,639	13,417	8,4	2,1	C	FOCMEC	154,2100	65,4100	-78,9900
41	2015	4	16	5	12	31,9	66,638	13,419	8	2,4	C	FOCMEC	310,2400	44,8100	-35,5300
42	2015	4	20	10	7	50,4	66,677	13,435	11	1,5	D	FOCMEC	295,0000	25,0000	-90,0000
43	2015	4	23	18	28	2,4	66,664	13,493	8	1,9	C	FOCMEC	152,1000	17,9600	-55,7300

44	2015	4	24	9	40	37,8	66,643	13,401	5	3,2	A	FOCMEC	232,6000	75,5200	74,5000
45	2015	4	30	10	2	1,5	66,642	13,4	1,8	1,9	D	FOCMEC	200,2900	37,7000	-64,9600
46	2015	5	1	16	3	58	66,651	13,495	6	1,7	D	FOCMEC	355,0000	80,0000	-90,0000
47	2015	5	2	4	51	31,3	66,655	13,395	3	1,8	D	FOCMEC	200,2900	37,7000	-64,9600
48	2015	5	3	2	48	13,9	66,651	13,384	2,8	1,6	D	FOCMEC	178,4700	20,5900	-75,6500
49	2015	5	5	3	28	51,6	66,637	13,364	6,5	1,6	D-	FOCMEC	30,8400	56,3600	-71,8900
50	2015	5	5	21	29	26,6	66,658	13,415	4	1,1	C	FOCMEC	32,5700	42,2700	-67,3700
51	2015	5	11	22	3	7,2	66,644	13,38	5,3	1	D-	FOCMEC	310,5500	36,2200	-72,9100
52	2015	5	12	20	49	30,5	66,644	13,424	5,2	1,4	B	FOCMEC	323,9200	61,9800	-49,4800
53	2015	5	18	1	42	38,6	66,684	13,472	5	1,2	C	FOCMEC	197,3800	25,4600	-10,5900
54	2015	5	19	13	6	2,9	66,661	13,52	6	1,8	A	FOCMEC	335,1500	67,4800	-62,7700
55	2015	5	24	0	36	46,9	66,677	13,502	7,3	1,2	D	FOCMEC	153,6600	75,0600	84,8200
56	2015	5	29	9	28	42,5	66,641	13,377	5	1,8	D	FOCMEC	341,5900	48,3600	-18,8800
57	2015	5	29	9	34	45,2	66,639	13,392	4,2	1,2	C	FOCMEC	345,0000	65,0000	-90,0000
58	2015	6	24	21	9	22,1	66,643	13,401	4,6	0,9	C	FOCMEC	356,5400	73,7300	-53,3100
59	2015	6	26	8	48	44,4	66,632	13,415	3	1,3	B	FOCMEC	185,0000	10,0000	-90,0000
60	2015	6	30	8	30	30,6	67,037	13,6	10,4	1,1	C	FOCMEC	42,3300	35,5300	-30,6400
61	2015	7	4	5	20	43,9	67,872	15,2	4,7	1,8	C	FOCMEC	30,5700	37,7000	-64,9600
62	2015	7	13	2	58	33,1	66,634	13,331	6,7	2	C	FOCMEC	310,5400	51,6200	-70,7200
63	2015	7	15	2	7	51	66,652	13,387	3,7	0,9	D	FOCMEC	16,3100	69,7500	-14,9700
64	2015	7	20	13	29	52,6	66,643	13,461	4,8	1	C	FOCMEC	233,9600	24,8100	35,4200
65	2015	7	24	6	48	30,3	66,388	12,787	5,6	1,5	D	FOCMEC	244,2900	15,0000	0,0000
66	2015	7	28	9	41	52,8	66,65	13,239	7,7	0,9	D-	FOCMEC	158,2800	39,6700	-26,0300
67	2015	7	29	1	34	19,4	66,655	13,4	5,5	0,8	D-	FOCMEC	349,9000	68,5300	-57,5000
68	2015	7	29	15	17	26,8	66,642	13,459	5,7	0,8	D-	FOCMEC	87,4400	56,3600	71,8900
69	2015	7	29	21	42	3,1	66,646	13,25	7,2	0,7	D-	FOCMEC	181,7400	65,9100	-73,5300
70	2015	8	1	2	7	34,4	66,675	13,461	5,4	0,8	C	FOCMEC	301,3600	52,2400	-26,5700
71	2015	8	1	19	37	10,8	66,537	13,22	7,2	0,9	B	FOCMEC	259,6500	75,2300	-2,6600
72	2015	8	2	14	32	34,3	66,636	13,427	2,2	0,8	D-	FOCMEC	245,4400	85,0200	-84,9800
73	2015	8	9	22	57	8,9	66,67	12,936	3,3	2,8	A	FOCMEC	177,1000	35,3100	-81,3300
74	2015	8	9	23	1	17	66,634	12,967	6	0,9	D	FOCMEC	217,9300	27,9900	-43,2200
75	2015	8	11	1	6	48,2	66,788	13,956	2	1,1	D	FOCMEC	156,3100	85,0800	79,9600
76	2015	8	13	16	1	47,5	66,649	13,442	10,3	0,9	B	FOCMEC	168,1800	70,0800	84,6800
77	2015	8	17	10	34	53,1	66,559	13,183	4,4	0,8	D-	FOCMEC	109,1200	80,0400	84,9200
78	2015	8	19	10	52	10,2	66,623	13,368	5	0,9	B	FOCMEC	299,1400	17,9600	-55,7300
79	2015	8	24	12	55	13,2	67,933	10,578	19,7	2,5	C	FOCMEC	40,0600	48,3600	-62,7600
80	2015	9	2	18	36	59,9	66,733	13,038	8	1,7	D	FOCMEC	153,4700	75,9200	-69,3500
81	2015	9	22	16	28	31,9	66,327	13,288	4,5	1,5	C	FOCMEC	232,7600	37,7000	-20,2900
82	2015	9	23	0	40	50,3	66,332	13,286	3,7	1,1	C	FOCMEC	104,8500	69,3000	40,8900
83	2015	9	24	7	25	44,8	66,629	13,326	6,1	0,7	D-	FOCMEC	324,1300	63,0500	61,7000
84	2015	9	26	12	10	41,5	66,649	13,411	8	1,3	C	FOCMEC	274,5300	58,2300	-25,7000
85	2015	9	28	17	45	29,2	66,65	13,412	7,2	2	B	FOCMEC	46,1200	66,6000	-68,1200
86	2015	9	29	20	51	58,4	66,634	13,345	6,5	1,3	D-	FOCMEC	314,0900	38,2900	-36,2000
87	2015	9	30	12	26	39,1	66,654	13,502	7,8	1,6	C	FOCMEC	254,2400	28,9000	-29,0300
88	2015	10	6	16	5	5,3	67,784	14,854	10	1,3	C	FOCMEC	17,4100	66,6000	68,1200
89	2015	11	8	7	28	37,2	66,641	13,448	7,2	0,8	D	FOCMEC	220,6400	85,3000	69,9300
90	2015	11	11	19	46	59,5	66,227	15,012	1,8	1,5	D	FOCMEC	206,7400	60,5000	-28,3400
91	2015	11	16	1	5	44,6	66,63	13,359	6,2	1	D-	FOCMEC	218,0200	15,7900	-71,3200
92	2015	11	16	1	19	39,3	66,637	13,356	5,5	1,5	D	FOCMEC	200,0000	30,0000	-90,0000
93	2015	11	16	19	7	44,2	67,169	13,284	25,9	1	D-	FOCMEC	73,4500	54,0700	-37,4500

94	2015	11	17	16	14	6,7	68,994	16,157	20,9	2	C	FOCMEC	245,0000	35,0000	-90,0000
95	2015	11	22	9	33	45,5	66,617	13,367	6,1	1,4	D-	FOCMEC	122,0300	90,0000	55,0000
96	2015	11	26	0	32	41,9	66,623	13,387	6,1	1,7	C	FOCMEC	193,5800	30,3800	-80,0800
97	2015	11	30	2	59	6,3	66,671	13,507	9,6	0,7	D-	FOCMEC	342,2700	17,9600	55,7300
98	2015	12	9	4	32	19,6	66,635	13,466	4,7	1,8	C	FOCMEC	235,6900	69,7500	14,9700
99	2015	12	16	18	59	22,1	66,364	14,617	2,9	1,5	C	FOCMEC	99,8900	7,0700	-44,8900
100	2015	12	16	22	59	49,7	66,658	13,517	8	1,2	D	FOCMEC	323,4900	55,1500	-83,9000
101	2015	12	20	5	30	55,6	66,545	13,208	2	1,1	D	FOCMEC	27,3300	65,1000	-84,4900
102	2015	12	21	14	12	35,8	66,641	13,457	2,1	1,4	D	FOCMEC	180,0000	5,0000	-90,0000
103	2016	1	3	14	50	35	66,505	13,468	3,5	0,5	D-	FOCMEC	24,2200	72,7700	-58,4300
104	2016	1	6	7	27	35,1	66,656	13,476	6,9	1	D-	FOCMEC	260,1700	63,0500	-61,7000
105	2016	1	15	4	46	31,2	66,619	13,341	7,5	1	D-	FOCMEC	260,0000	80,0000	-90,0000
106	2016	1	16	21	3	44,7	66,621	13,352	5	1,4	C	FOCMEC	200,0000	15,0000	-90,0000
107	2016	1	17	8	44	32,7	67,929	16,271	1,5	1	D-	FOCMEC	48,0600	52,2400	26,5700
108	2016	1	17	12	30	15,7	66,666	13,425	2	0,9	D-	FOCMEC	325,0000	55,0000	-90,0000
109	2016	1	25	18	1	54,4	66,693	13,558	6,1	1	D-	FOCMEC	43,1200	73,7300	53,3100
110	2016	2	14	18	7	56,1	67,952	10,458	20	1,5	D	FOCMEC	283,2200	72,7700	-58,4300
111	2016	2	15	3	58	9	65,594	11,533	15	1,8	D-	FOCMEC	285,0000	25,0000	-90,0000
112	2016	2	15	10	39	33,6	66,472	13,238	13,3	1,5	B	FOCMEC	16,4800	63,0500	-61,7000
113	2016	2	15	13	32	3,2	66,636	13,415	2,3	1,1	D-	FOCMEC	179,8900	7,0700	-44,8900
114	2016	2	18	4	33	43,7	66,668	13,495	1,5	1,1	D-	FOCMEC	182,5200	17,9600	-55,7300
115	2016	2	23	11	27	58,3	67,665	15,163	2,6	1,7	B	FOCMEC	275,8200	50,1800	83,4800
116	2016	3	1	1	56	12,5	66,639	13,492	6	1,1	D	FOCMEC	125,8800	80,0400	-84,9200
117	2016	3	1	20	31	4,7	66,633	13,414	1,7	1,1	D-	FOCMEC	189,8900	7,0700	-44,8900
118	2016	3	2	15	1	25,1	65,37	12,204	12	1,8	D	FOCMEC	249,3600	58,6800	60,3500
119	2016	3	8	11	41	25,6	67,028	13,185	12	1,1	D	FOCMEC	307,5900	78,5600	-49,0200
120	2016	3	14	15	12	33,4	67,889	15,193	10	1,3	C	FOCMEC	10,5200	70,7100	-74,0800
121	2016	3	18	2	18	1,9	67,943	10,412	20,5	2,1	D	FOCMEC	255,2200	86,1700	-49,8900
122	2016	3	28	14	53	10	66,631	13,365	8	1,2	D	FOCMEC	105,4700	31,4700	-70,5700
123	2016	4	14	8	5	15,3	66,246	12,718	10,2	1,6	D	FOCMEC	221,1900	38,2900	-36,2000
124	1981	9	3	0	0		69,62	13,68	12	4,7	C	1*	178,3738	80,1618	45,1502
125	1987	4	4	0	0		67,25	8,03	15	3,6	D	1*	41,6270	49,7289	109,4222
126	1988	1	31	0	0		68,03	9,58	20	4,3	C	1*	24,7881	74,7929	-60,0224
127	1988	10	27	0	0		66,89	8,88	25	3,9	D	1*	216,3281	47,5095	98,9849
128	1990	5	16	0	0		66,04	6,26	30	3,4	C	5*	179,5658	83,6492	-7,8024
129	1991	12	16	0	0		67,91	9,97	10	2,4	C	5*	78,0817	56,4649	-126,2819
130	1992	1	1	0	0		67,77	14,88	10	1	C	2*	219,6940	59,8705	-130,5101
131	1992	8	14	0	0		67,89	12,85	17	3,7	B	5*	52,5210	71,2059	-111,7564
132	1993	9	13	0	0		66,37	5,72	20	3,9	B	6*	290,0052	55,9765	-71,5989
133	1997	1	1	0	0		66,31	13,25	5	1	C	2*	209,9367	67,0827	-45,9839
134	1997	11	21	0	0		66,41	13,22	7	2,3	B	4*	251,6294	75,1405	-26,3694
135	1997	11	25	0	0		66,5	12,4	11	2,7	B	4*	213,3706	75,1405	-153,6306
136	1997	11	28	0	0		66,32	13,14	11	1,7	C	4*	192,8647	71,2644	-111,3618
137	1997	12	26	0	0		66,32	13,11	11	1,8	C	4*	64,9284	50,2580	59,4850
138	1998	1	8	0	0		66,37	13,13	13	2,2	B	4*	158,2273	81,0934	-141,4519
139	1998	2	9	0	0		66,39	13,09	11	2,8	B	4*	125,5236	82,5023	-156,3183
140	1998	3	9	0	0		65,85	13,53	7	2,8	B	4*	1,2047	64,1812	56,3588
141	1999	4	9	0	0		66,39	13,35	8	2	C	5*	142,0902	58,1710	-127,7826
142	1999	8	23	0	0		65,1	11,75	15	3,1	C	5*	183,7086	57,0762	-66,2538
143	2005	6	24	4	25	40,5	66,479	13,456	5	3,2	C	3*	200,9300	18,3600	-39,8200

144	2006	12	31	12	50	40,5	66,413	13,356	7,1	1,7	C	3*	15,5200	37,1600	-22,2300
145	2007	1	15	13	22	34,8	66,226	13,301	4,8	1,9	C	3*	218,0000	16,0000	63,0000
146	2007	6	16	5	37	53,5	66,581	13,558	4	1,6	C	3*	338,7100	44,9100	-51,6100
147	2008	1	7	20	19	28,2	66,324	13,379	6	1,9	B	3*	17,0000	65,0000	-165,0000
148	2008	1	7	22	56	43,4	66,32	13,371	6	1,9	B	3*	297,7600	80,7300	-67,6900
149	2008	3	20	15	16	45,7	66,347	13,153	10,1	1,3	C	3*	136,9500	18,1100	6,1300
150	2008	11	2	0	42	0,1	66,228	12,989	7,3	2	C	3*	218,1400	29,0300	14,6700
151	2010	3	28	15	38	10,5	66,489	13,33	6,3	1,1	C	3*	279,1600	16,4800	13,6700
152	2010	8	2	11	54	32,7	66,402	13,358	7,5	1,8	C	3*	23,3600	22,7600	-14,5100

Chapter 4: Report on seismic observations within the NEONOR2 project in the Nordland region, Norway (Aug. 2013 - May 2016)

Authors: Jan Michálek[1], Norunn Tjåland[1], Anne Drottning[1], Marte Louise Strømme[1], Berit Marie Storheim[1], Stephane Rondenay[1] and Lars Ottemöller[1]

Affliation: [1]University of Bergen

1. Summary

The Nordland region (65-70N, 8-18E; Norway) belongs to one of the most seismically active parts in Norway. The NEONOR2 project (2013-2017) took aim to construct a geodynamic model of this area constrained by geophysical observations such as seismic monitoring, geodetic monitoring, InSAR images processing and in situ stress measurements.

This report describes the seismic monitoring of the Nordland region performed between August 2013 and June 2016 and results obtained during the project period by the University of Bergen. There were 27 temporary stations installed in the area (400 x 500 km) and about 1250 earthquakes with ML>0.0 were detected. Most of the registered seismic activity took place along the coast with several zones of clustered seismic activity. For those zones more detailed location methods were applied to retrieve focused locations and possibly better picture of the geological structures. Focal mechanisms were calculated for earthquakes with sufficient station coverage. A semi-automatic method for amplitude retrieval was developed and implemented into processing of focal mechanisms. Focal mechanisms of 85 earthquakes were analyzed and 40 fault plane solutions were evaluated as A and B quality. Those can be used for further interpretations. Based on teleseismic observation, receiver functions were computed that are sensitive to velocity contrasts beneath the station. These receiver functions were inverted to obtain the velocity structure. The results revealed relatively shallow depth of Mohorovicic discontinuity near the Lofoten archipelago (16 - 25 km) and getting deeper towards the mainland (around 40 km).

2. Introduction

Seismic monitoring of the Nordland region (65-70N, 8-18E; Norway) was performed between August 2013 and June 2016. The 27 temporary stations were distributed along the coastline mostly because of high topography in the region (Fig.1). Deployment and maintenance of stations were split between University of Bergen (UiB) and NORSAR (see Table 1 and Table 2)

Name	Participation
Lars Ottemöller	Project management at UiB, deployment/maintenance of stations, data processing, interpretation of results
Jan Michálek	Deployment/maintenance of stations, data processing, interpretation of results
Berit Marie Storheim	Data processing, station recovery
Marte Louise Strømme	Data processing, station deployment
Ole Meyer	Deployment of stations
Felix Halpaap	Deployment of stations
Andrea Demuth	Deployment of stations
Stephane Rondenay	Deployment of stations, Computation of receiver functions and interpretation
Norunn Tjåland	Detailed analyses – relative locations, earthquake source parameters
Anne Drottning	Detailed analysis – receiver functions, apparent S-velocities

Table 1: People from UiB involved in seismological monitoring and data processing.

3. Instrumentation

Two different sets of instruments were installed: Earth Data digitizer (EDR-210) with STS 2.5 or CMG-3ESPC sensors belonging to the Norwegian Broadband Pool and Nanometrics digitizers (Taurus) with Trillium 120PA sensors belonging to UiB (for details see Table 2). There were 27 temporary seismic stations deployed in the Nordland area. The deployment started in August 2013 and was finished in March 2014.

Stations were placed in inhabited areas where power supply was available. Overview of stations is in Table 2. Detailed description of sites including photos and contacts to people at sites is available at UiB (lars.ottemoller@uib.no).

3.1 Recording setup

All the stations were recording continuously 3 channels (ZNE) with 100 Hz sampling frequency. The data were always stored locally and at sites with enough GSM/ICE signal coverage the data were directly transmitted to the data server in Bergen via SeedLink protocol. Two stations were offline. The all 6 Taurus units could not communicate via SeedLink (one of them was offline in addition) and data from these stations were not included in real-time data repository but added to main data repository after each maintenance visit (at least once a year).

3.2 Changes in instrumentation

Instrumentation from station NBB12 was moved to a new location on 15.6.2014 and established as NBB40 station. Therefore, we count 27 stations and not 28 as in Table 2.

New station N2VG was installed on 27.4.2015 because of suddenly increased seismic activity SW of Svartisen (Jektvik, Tjong) in the end of April 2014.

3.3 Telemetry

Most of the deployed stations were connected to the Internet via GSM or ICE routers. From those stations (except for Taurus units) the data were available in real-time via SeedLink and collected on server in Bergen. Those data streams were added to the main repository immediately and were analyzed routinely within the NNSN network data processing. The quality of connection was varying (mostly with weather conditions) and sometimes the data were not transferred.

In the summer 2015 some of the ICE routers were replaced by a newer version of routers. This was required due to a change in the ICE network.

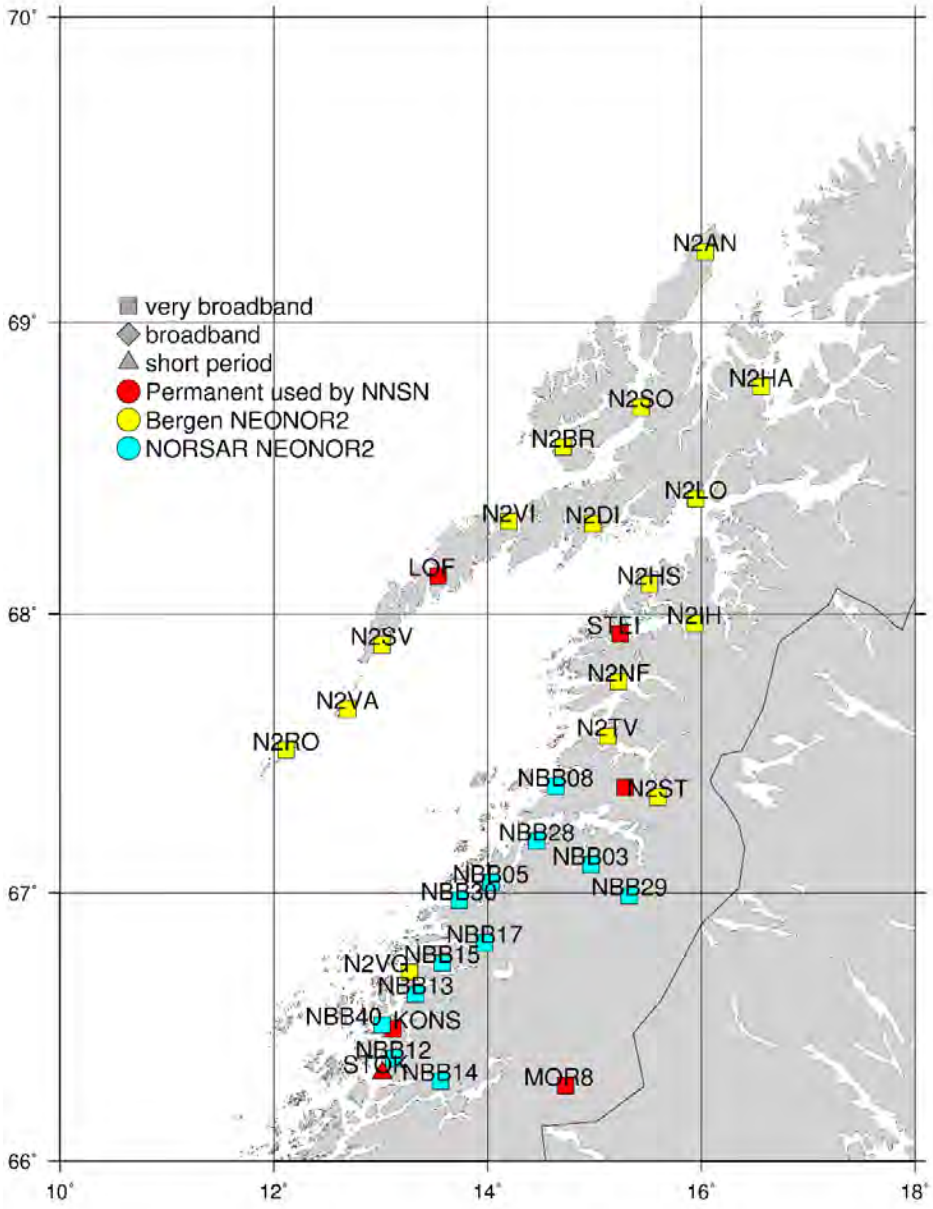

Figure 1. Map with seismic stations in Nordland. Yellow and turquoise stations were installed in NEONOR2 project

Table 2: List of temporary stations installed within NEONOR2 project

#	Station code	Location	Institution	Locality description	Lat	Long	Alt	Seismometer	Digitizer	Telemetry	Date of installation
1	N2AN	Skarsteinsdalen, Vesterålen	UIB	Quiet area, on floor of building in old military facility	69,2371	16,0353	61	Trillium 120PA	Taurus	ICE	19.08.2013
2	N2BR	Breivik, Vesterålen	UIB	Basement of private house	68,5788	14,7075	10	Trillium 120PA	Taurus	none	21.08.2013
3	N2DI	Digermulen	UIB	Basement of private house, thought to be on bedrock	68,3134	14,9863	9	STS2.5	EDR-210	none	22.11.2013
4	N2HA	Harstad, Vesterålen	UIB	In storage area of Hålogaland Kraft; expected to be noisy	68,7839	16,5611	14	Trillium 120PA	Taurus	ICE	20.11.2013
5	N2HS	Hamsund, Hamarøy	UIB	Birthplace of Knut Hamsun, Nordlandsmuseet, Hamsunstiftelsen	68,1033	15,5136	15	STS2.5	EDR-210	GSM	23.10.2013
6	N2IH	Innhavet, Hamarøy	UIB	Garage at private house	67,9662	15,9367	28	STS2.5	EDR-210	ICE	23.10.2013
7	N2LO	Lødingen, Vesterålen	UIB	In quiet storage area of Hålogaland Kraft	68,4004	15,9533	10	Trillium 120PA	Taurus	GSM	19.08.2013
8	N2NF	Nordfold, Steigen	UIB	Small house behind church, near shore	67,7610	15,2277	3	STS2.5	EDR-210	ICE	24.10.2013
9	N2RO	Røst Kommunehus	UIB	Basement of building (said to partly rest on rock). Røst "main" street rather close, but not much traffic, even in rush hours	67,5173	12,1158	4	STS2.5	EDR-210	ICE	01.11.2013
10	N2SO	Sortland, Vesterålen	UIB	In underground vault	68,7139	15,4380	1	Trillium 120PA	Taurus	ICE	23.08.2013
11	N2ST	Straumen, Sørfold	UIB	Garage/basement at elderly home	67,3487	15,5959	11	STS2.5	EDR-210	ICE	22.10.2013
12	N2SV	Sørvågen, Moskenes Kommune	UIB	Installed in garage	67,8914	13,0098	21	STS2.5	EDR-210	ICE	21.11.2013
13	N2TV	Tårnvik, Salten	UIB	Basement of private house (built on sand, moraine)	67,5675	15,1252	5	STS2.5	EDR-210	ICE	25.10.2013
14	N2VA	Værøy Kommunehus	UIB	Basement of building (said to partly rest on rock). Værøy "main" street rather close	67,6639	12,6935	5	STS2.5	EDR-210	ICE	29.10.2013

#	Station code	Location	Institution	Locality description	Lat	Long	Alt	Seismometer	Digitizer	Telemetry	Date of installation
15	N2VG	Vågaholmen	UIB	Ground floor, smooth concrete floor on rock (said). End of road, no traffic, one house and garage nearby (used rarely)	66,7090	13,2690	8	Trillium Compact 120	Taurus	GSM	27.04.2015
16	N2VI	Vinje, Gimsøy	UIB	Basement of private house, thought to be on bedrock	68,3212	14,1976	9	STS2.5	EDR-210	ICE	21.11.2013
17	NBB03	Karbøl	NORSAR	Rarely used barn	67,1031	14,9681	187	CMG-3ESPC	EDR-210	GSM	13.03.2014
18	NBB05	Inndyr	NORSAR	Rarely used workshop in the town	67,0368	14,0306	13	CMG-3ESPC	EDR-210	GSM	12.03.2014
19	NBB08	Skaug Oppverkstsenter	NORSAR	Basement of a school	67,3871	14,6364	12	CMG-3ESPC	EDR-210	ICE	11.03.2014
20	NBB12	Aldersund Church	NORSAR	Basement of church	66,3870	13,1199	20	STS2.5	EDR-210	ICE	01.10.2013
21	NBB13	Garage	NORSAR	Garage on rocksite	66,6275	13,3272	27	STS2.5	EDR-210	ICE	03.10.2013
22	NBB14	Nordeng Farm	NORSAR	Under stairs in disused storage of a barn	66,3030	13,5586	35	STS2.5	EDR-210		02.10.2013
23	NBB15	Halsa Church	NORSAR	Storage room of cemetary workshop	66,7435	13,5776	50	STS2.5	EDR-210	GSM	04.10.2013
24	NBB17	Glomfjord Bårehus	NORSAR	Separate storage room in a morgue of Glomfjord Kirke	66,8161	13,9581	153	STS2.5	EDR-210	ICE	04.10.2013
25	NBB28	Valnes	NORSAR	Used to be a ground water take-out place. Almost on the rock, uphill, remote site.	67,1909	14,4622	45	CMG-3ESPC	EDR-210	ICE	12.03.2014
26	NBB29	Røkland skole	NORSAR	A chamber in a bomb-room of a school.	66,9919	15,3292	35	CMG-3ESPC	EDR-210	GSM	13.03.2014
27	NBB30	Finnes	NORSAR	Basement of a private house. On concrete which is coupled with bedrock.	66,9732	13,7354	20	CMG-3ESPC	EDR-210	GSM	14.03.2014
28	NBB40	Tonnes	NORSAR		66,5130	13,0097	15	STS2.5	EDR-210	ICE	15.06.2014 Instrumentation initially at NBB12

3.4 Performance of stations

3.4.1 Data completeness

During the maintenance visits which were scheduled about twice a year the locally stored data were copied. These data were merged with “online” data and the final waveform dataset was created. Completeness of the continuous waveform data was checked by programs MSEEDINFO, MSI and CONGAP. Outputs from MSEEDINFO and MSI in individual years are shown below in Figures 2-7.

Installation of stations started in August 2013 already but only few stations were available in that year and therefore the completeness was not evaluated for 2013. Ideally all the locally stored data at stations should be 100% complete, however, this was not the case. We experienced hardware/firmware problems with Earth Data digitizers (EDR-210) which resulted in about 20% data loss, mainly during the first year. The problem was partially solved by contacting Earth Data and by upgrading firmware in problematic units. The problem was caused by failure of a hardware component which was not fulfilling specifications declared by the supplier. After the firmware upgrade the data completeness improved but not for at all stations. The problem is illustrated in Figure 8, where improvement of data completeness is shown after merging the offline and online repositories.

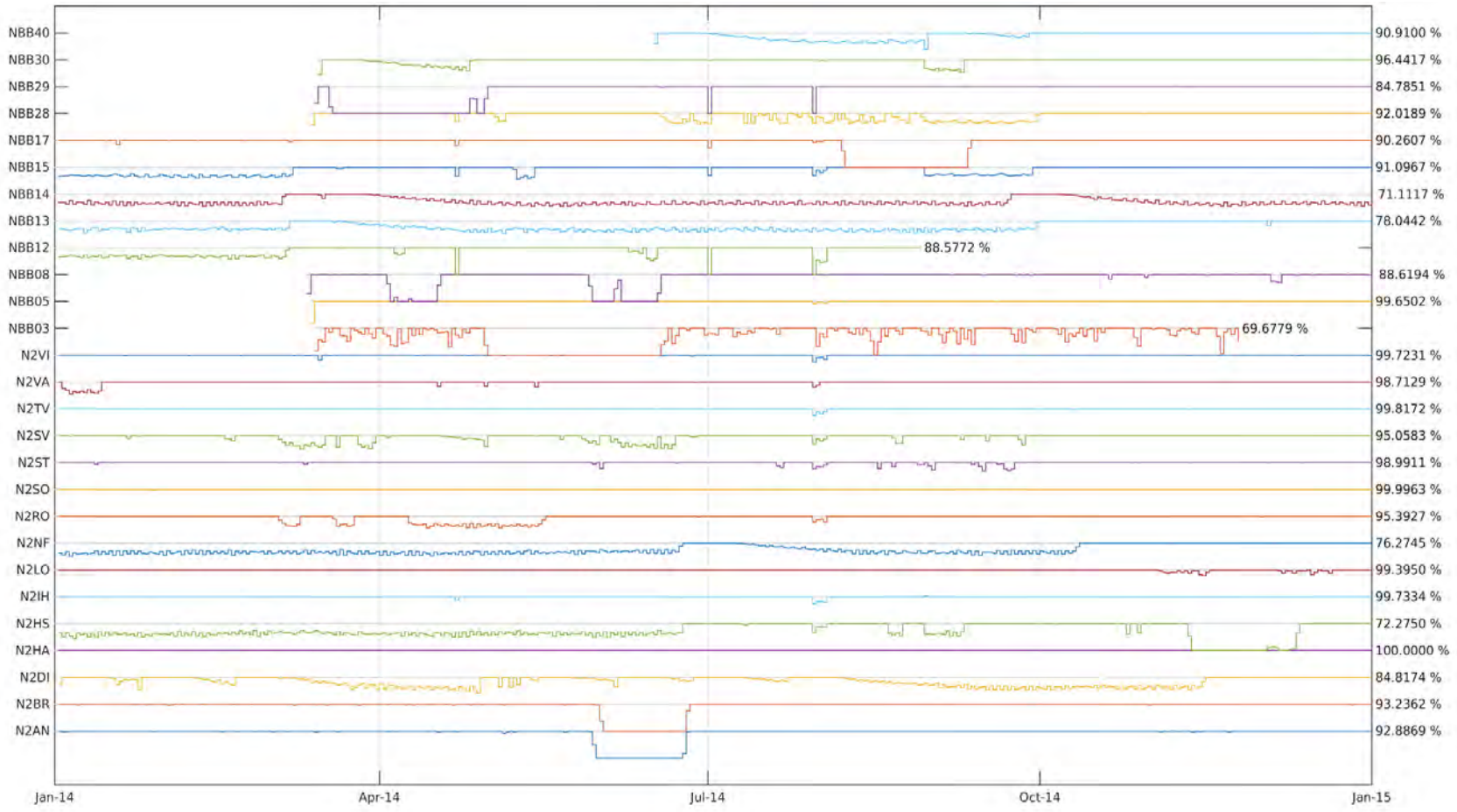

Figure 2. Data completeness Z-channels between Jan 1 - Dec 31, 2014. Percentage on the right side indicates the total completeness in evaluated period. Some stations were installed in spring 2014

Figure 3. Gaps detected in continuous waveform data in 2014

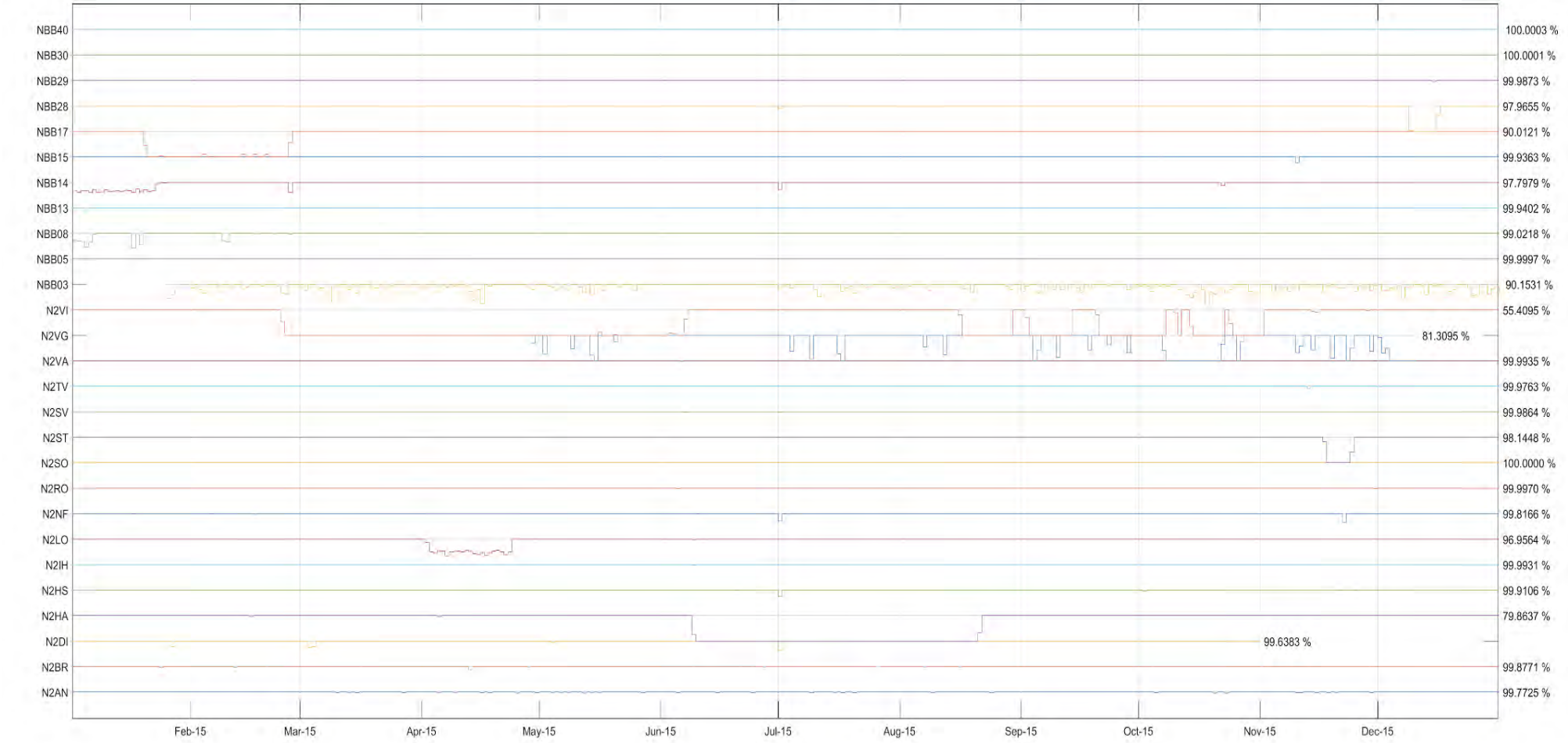

Figure 4. Data completeness Z-channels between Jan 1 - Dec 31, 2015. Percentage on the right side indicates the total completeness in evaluated period.

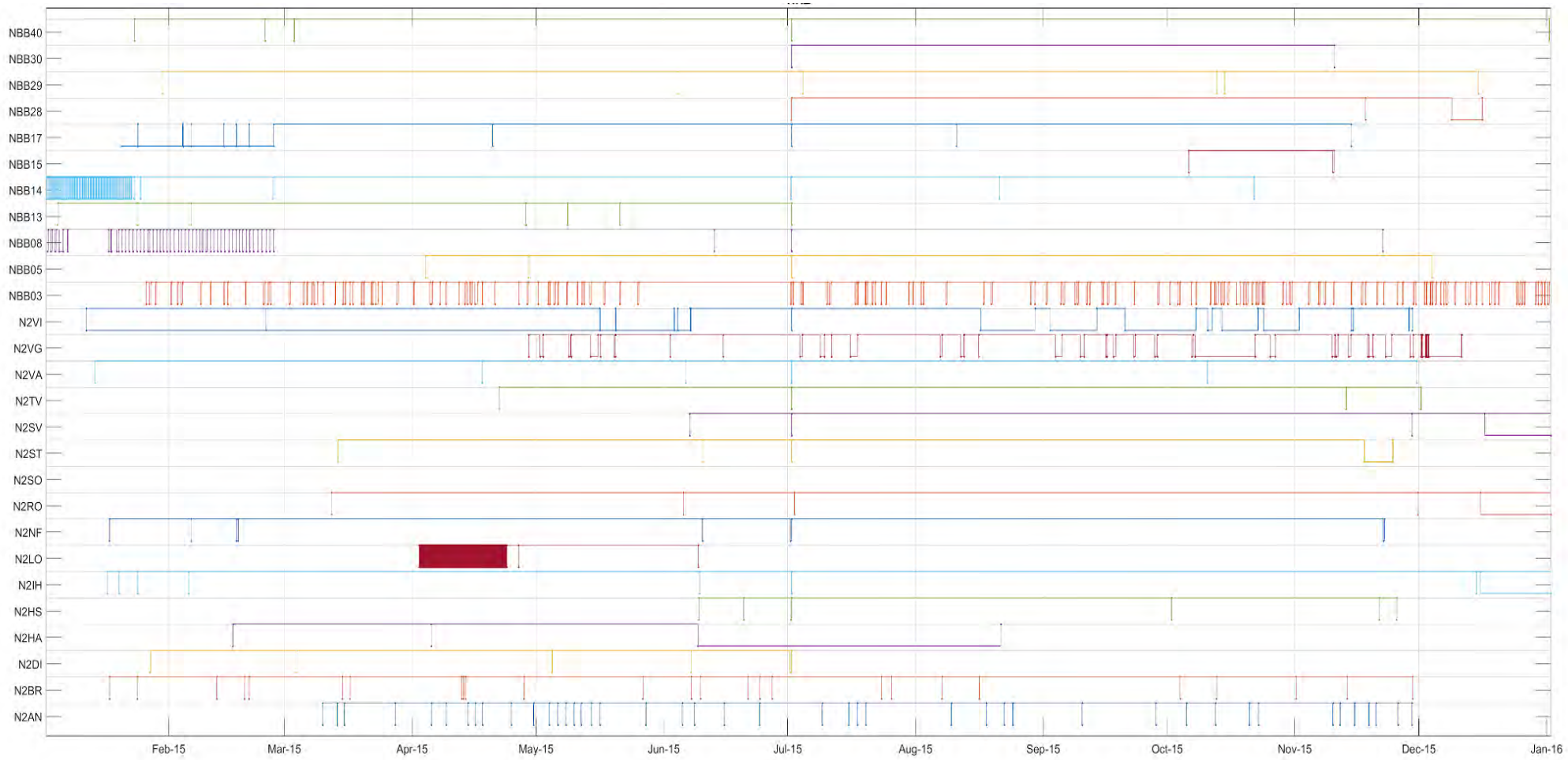

Figure 5. Gaps detected in continuous waveform data in 2015

Figure 6. Data completeness of Z-channels between Jan 1 - May, 2016. Percentage on the right side indicates the total completeness in evaluated period

Figure 7. Gaps detected in continuous waveform data in 2016. Stations not listed were without gaps in 2016.

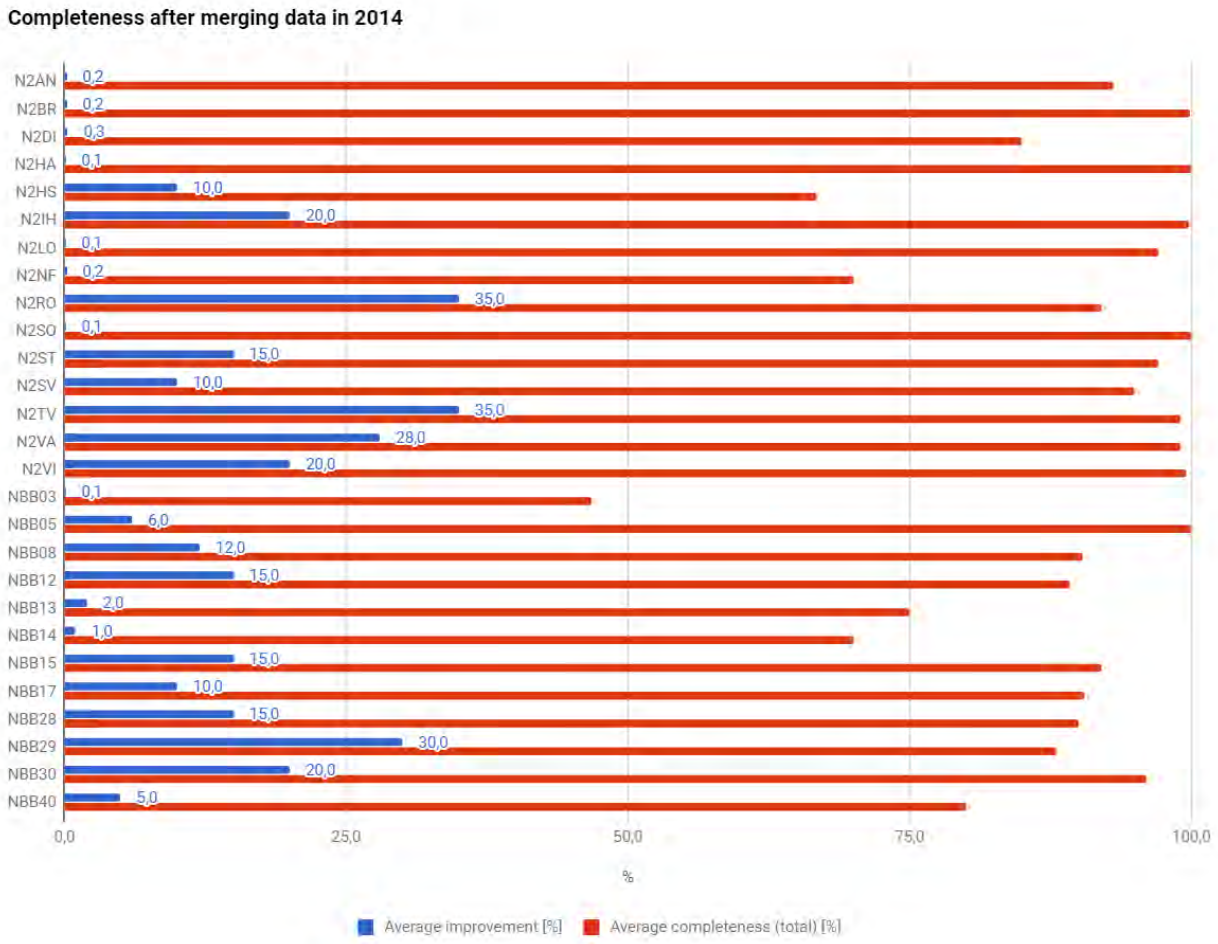

Figure 8. Example of improvement of data completeness from 2014 after merging offline (local storage) and online (received via SeedLink) data repositories. Incompleteness of data was caused by hardware problems.

3.4.2 Power spectral density of noise

Performance of the stations in terms of noise was evaluated by calculating the power spectral density (PSD) of one month of data starting from May 1, 2014. The mean values of PSD on vertical component from all NEONOR2 stations are in Figure 9, together with high and low levels of New Low Noise Model (NLMN; Peterson, 1993). Detailed figures of PSD analysis (all channels, all stations) can be found in Attachment 1. Permanent station LOF was evaluated as well for comparison.

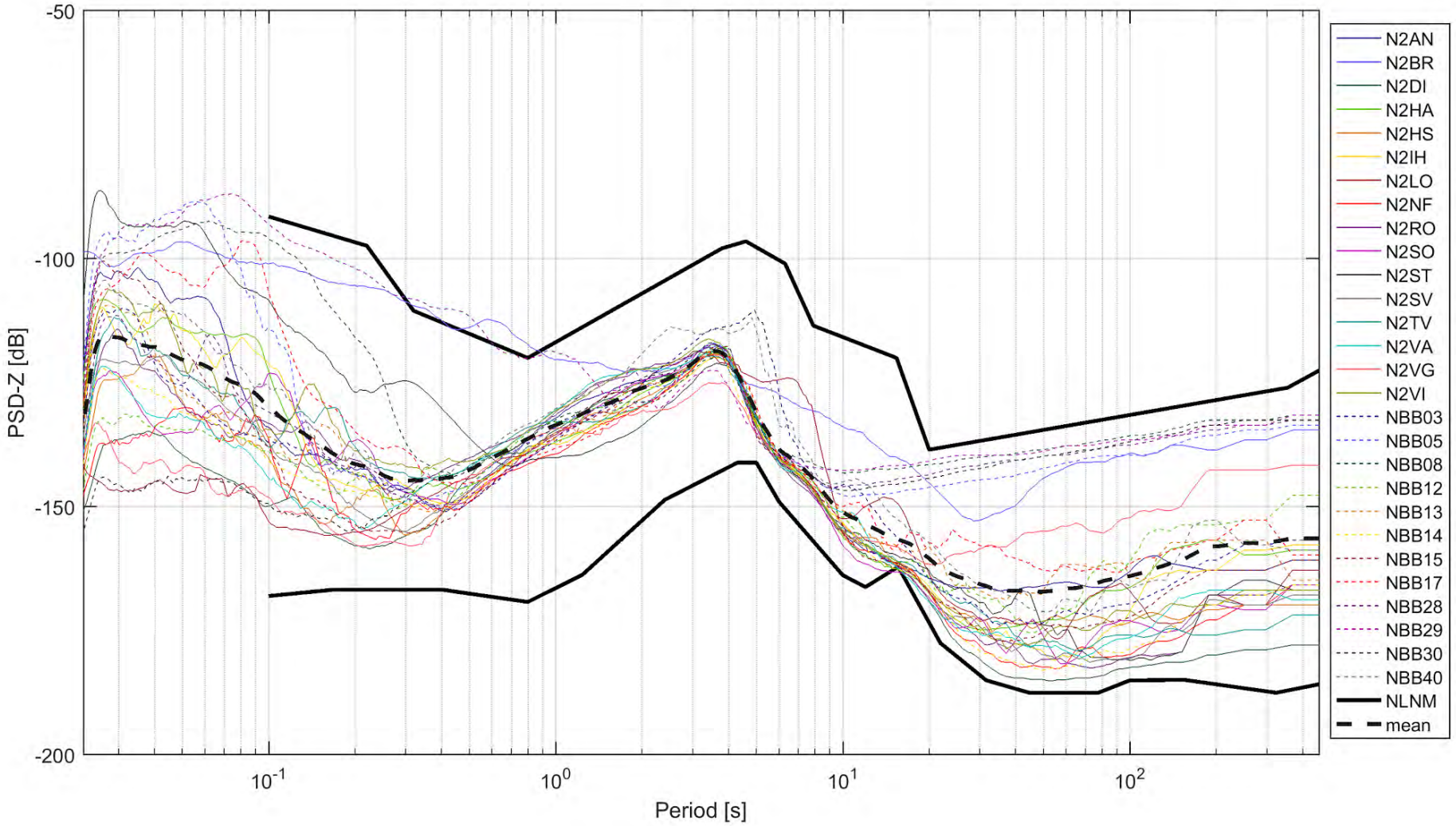

Figure 9. Mean values of PSD on vertical component (Z) from NEONOR2 stations

3.5 Waveform data availability

The merged and unified waveform data are available at UiB (Lars.Ottemoller@uib.no) and were also uploaded to the GFZ seismological data repository (Potsdam) as part of the ScanArray initiative. This means the data can now be used by ScanArray partners and in the future (2021-) will be openly available.

The temporary network is registered with code 2D.

3.6 Overview of seismicity

The data from online stations were included in the routine processing of events from the Norwegian National Seismic Network (NNSN). I.e. phase detection, polarity of first arrival, localization and magnitude were retrieved on daily basis as well as classification of events (local/regional/distant, explosion/probable explosion/earthquake). Focal mechanisms were routinely calculated only for larger earthquakes (M>2.5) inside the network where the coverage was sufficient. Only first arrival polarities were used for such focal mechanisms.

3.7 Earthquake catalogue

The earthquake catalogue contains 1278 events in total (ML>-0.4) with 450 events of M_L>1.0 and about 30 of ML>2.0. The largest earthquake recorded was of ML=3.2. Distribution of earthquake magnitudes is in Figure 10.

Magnitude-frequency distribution (Gutenberg-Richter relation) in Figure 11 is showing magnitude of completeness around 1.0. For the 1278 recorded events there are 13116 P phases and 15523 S phases (Figure 16). Events were detected at 110 stations in total of which 27 were NEONOR2.

Earthquakes were located with the HYPOCENTER program (Lienert and Havskov, 1995) that is implemented in SEISAN. The velocity model used for location (Havskov and Bungum, 1987) is shown in Table 3, with Vp/Vs = 1.74.

Table 3: Velocity model used for locating all local and regional events

P-wave velocity (km/s)	Depth to layer interface (km)
6.2	0.0
6.6	12.0
7.1	23.0
8.05	31.0
8.25	50.0
8.5	80.0

List of earthquakes is attached in Atachment2 in the simplified Nordic format (output of NORHEAD routine). The same dataset (together with historical and relative locations) is also available in KML format for Google Earth – Attachment3.

Earthquakes are located mostly along the coastline and also also along the continental margin – 130 – 170 km W of coastline (Figure 13). The most active was the Jektvik area (W of Svartisen) where about 650 events are located. Interesting finding is that there is relatively aseismic zone starting in Vestfjorden in the north continuing to SW in a band of width of about 70 km. Location errors are shown in Figure 14. Horizontal location errors of the onshore events (inside the network) are mostly up to 4 km but for the off shore events it increases to 8 km or more. Similar trend is for the vertical location error but the error values are even bigger. Travel-time residuals of both P- and S-waves are showing normal distribution (Figure 15) with slight shift towards positive values for S-waves. This is even better visible in Figure 17 where station residuals for S-waves are having higher residuals in the eastern part of the network.

Number of detected phase-arrivals is increasing with magnitude (as documented in Figure 16). It is quite obvious that number of detected phases was increased during the project period when the temporary stations were installed.

There were 664 events classified as explosions or probable explosions. These events are included in Attachment 3 and most of them are located in the Rana Gruber mining area. From Figure 12, we see that the explosions are made mainly around 5 specific day times (00:00, 04:00, 12:00, 16:00 and 20:00).

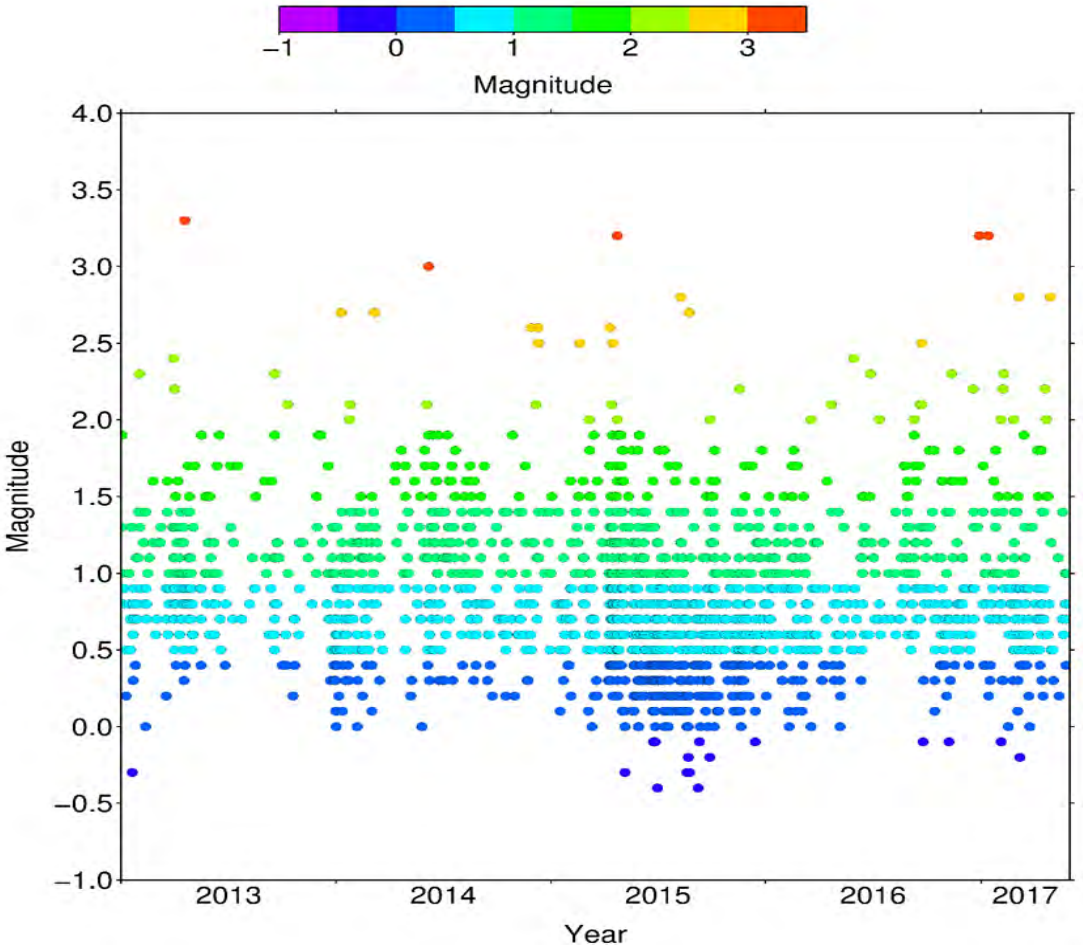

Figure 10. Distribution of earthquake magnitudes in time

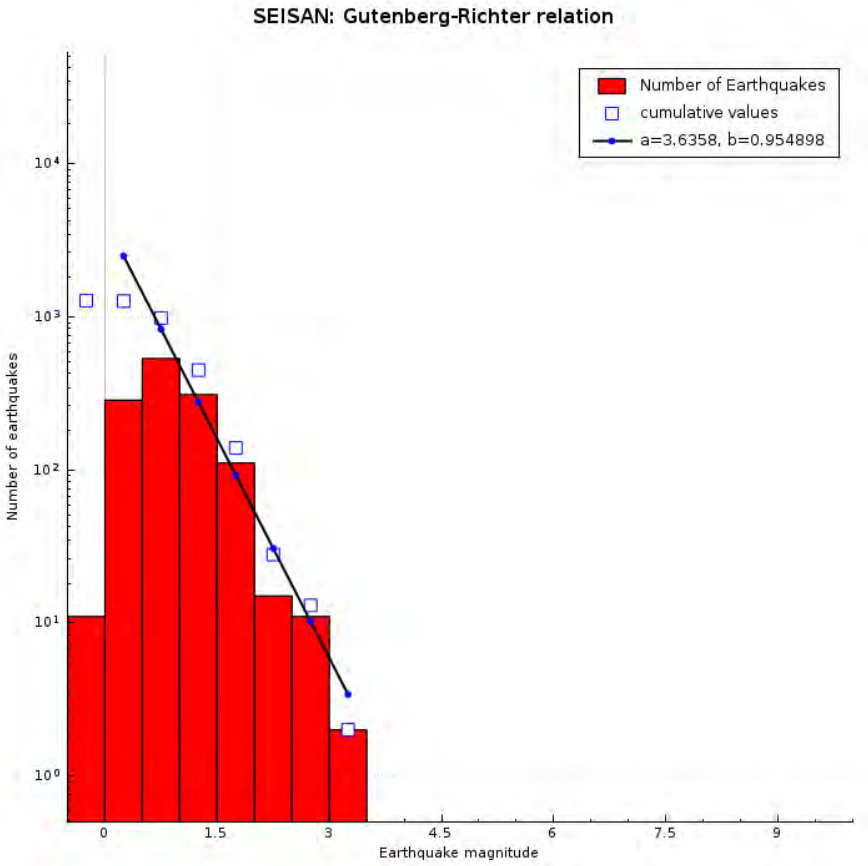

Figure 11. Magnitude-frequency distribution

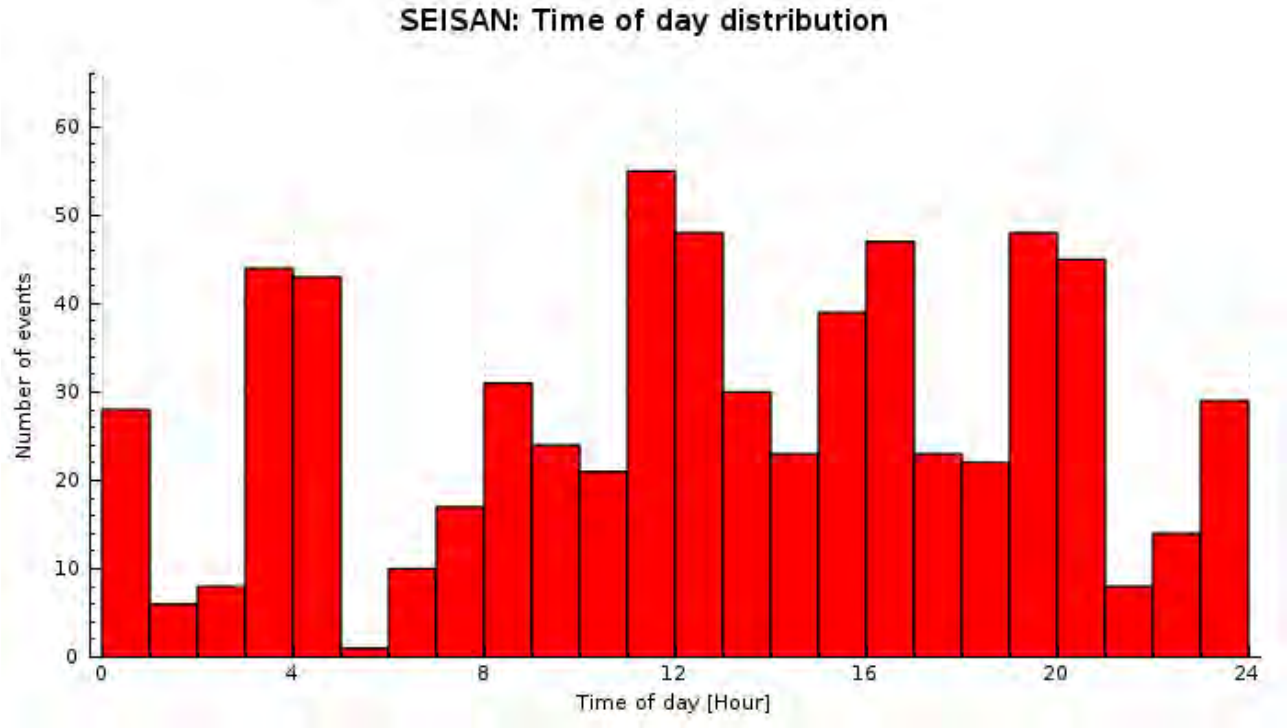

Figure 12. Distribution of 664 detected explosions in day-time (one hour bins)

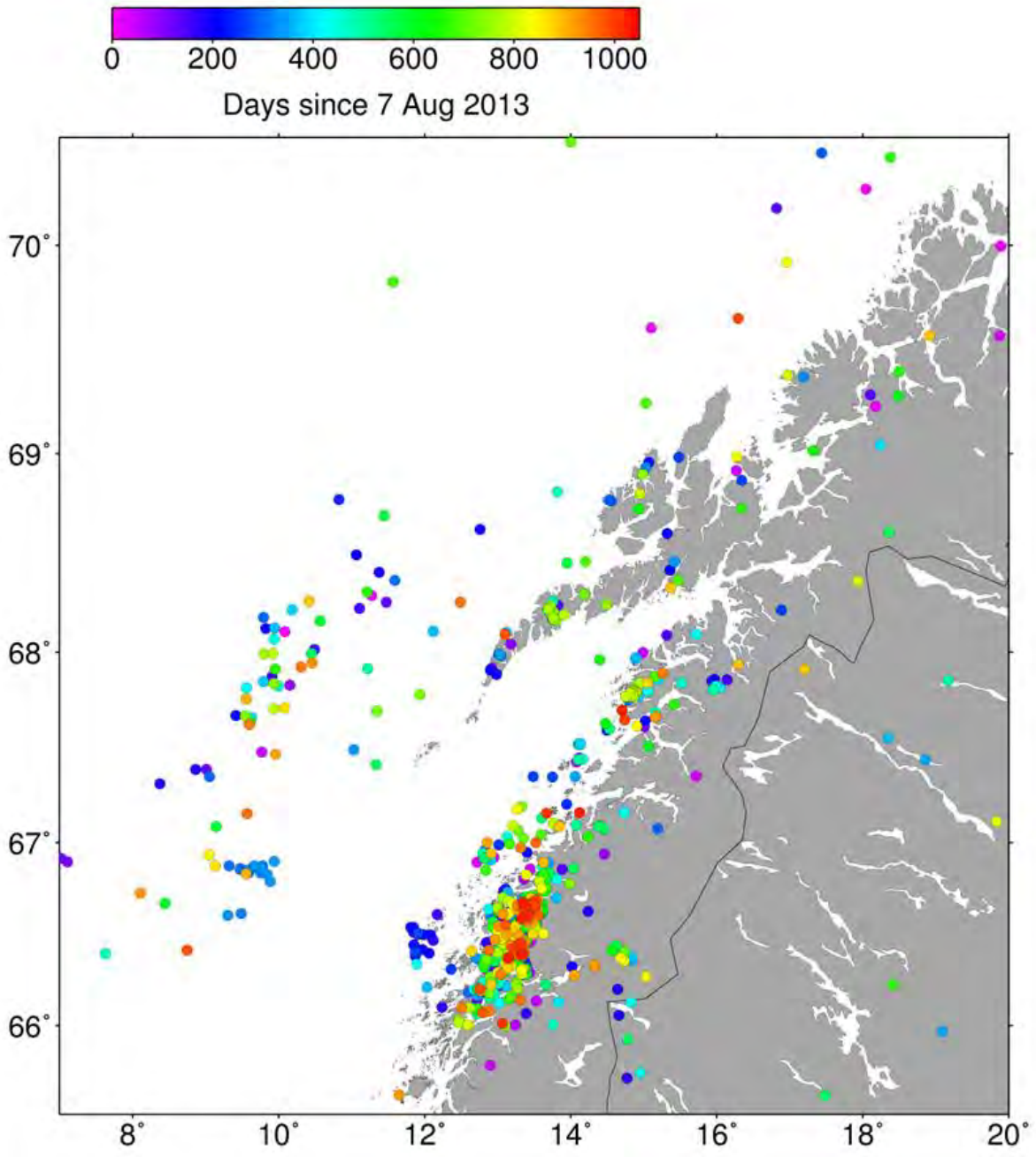

Figure 13. Distribution of earthquakes in map color coded by time since 7 Aug, 2013

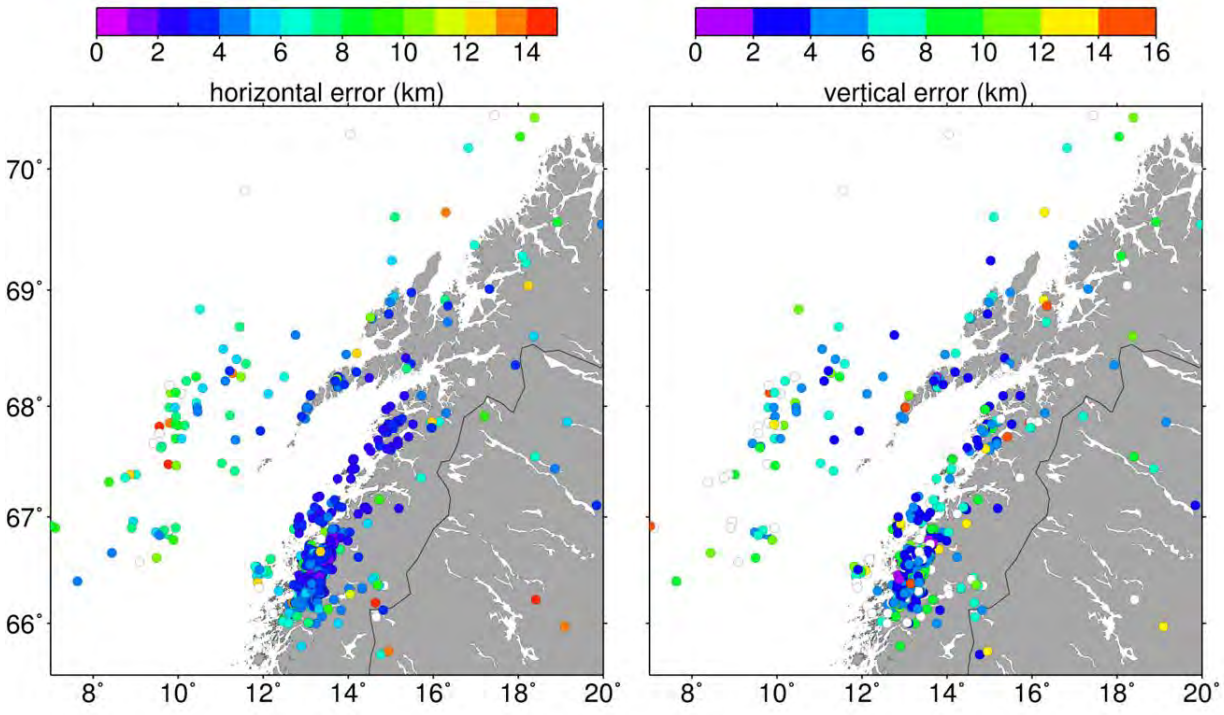

Figure 14. Horizontal and vertical location errors of individual events

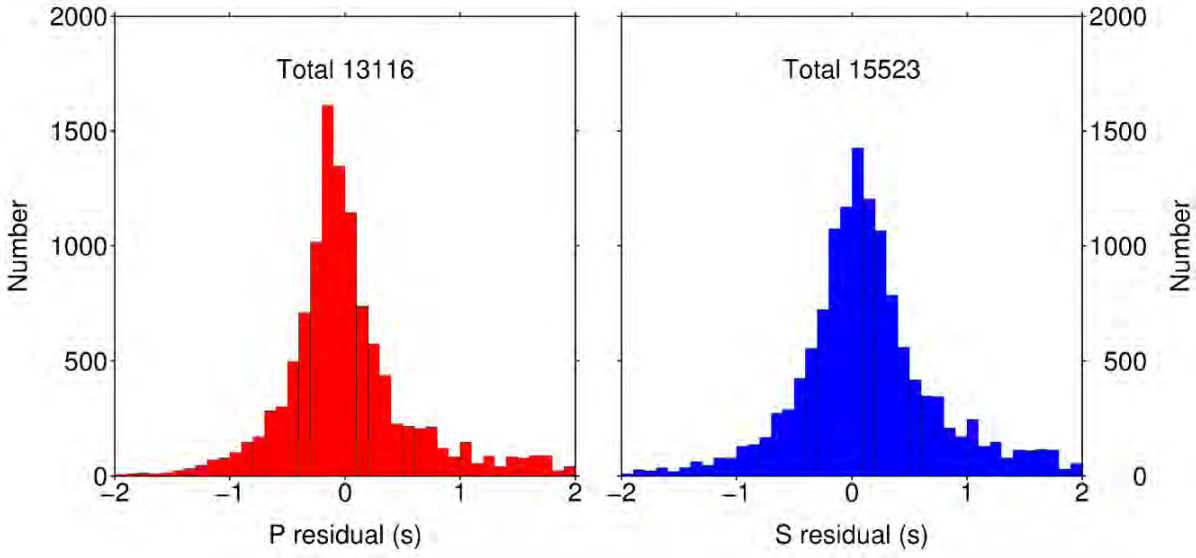

Figure 15. Travel-time residuals for all recorded events

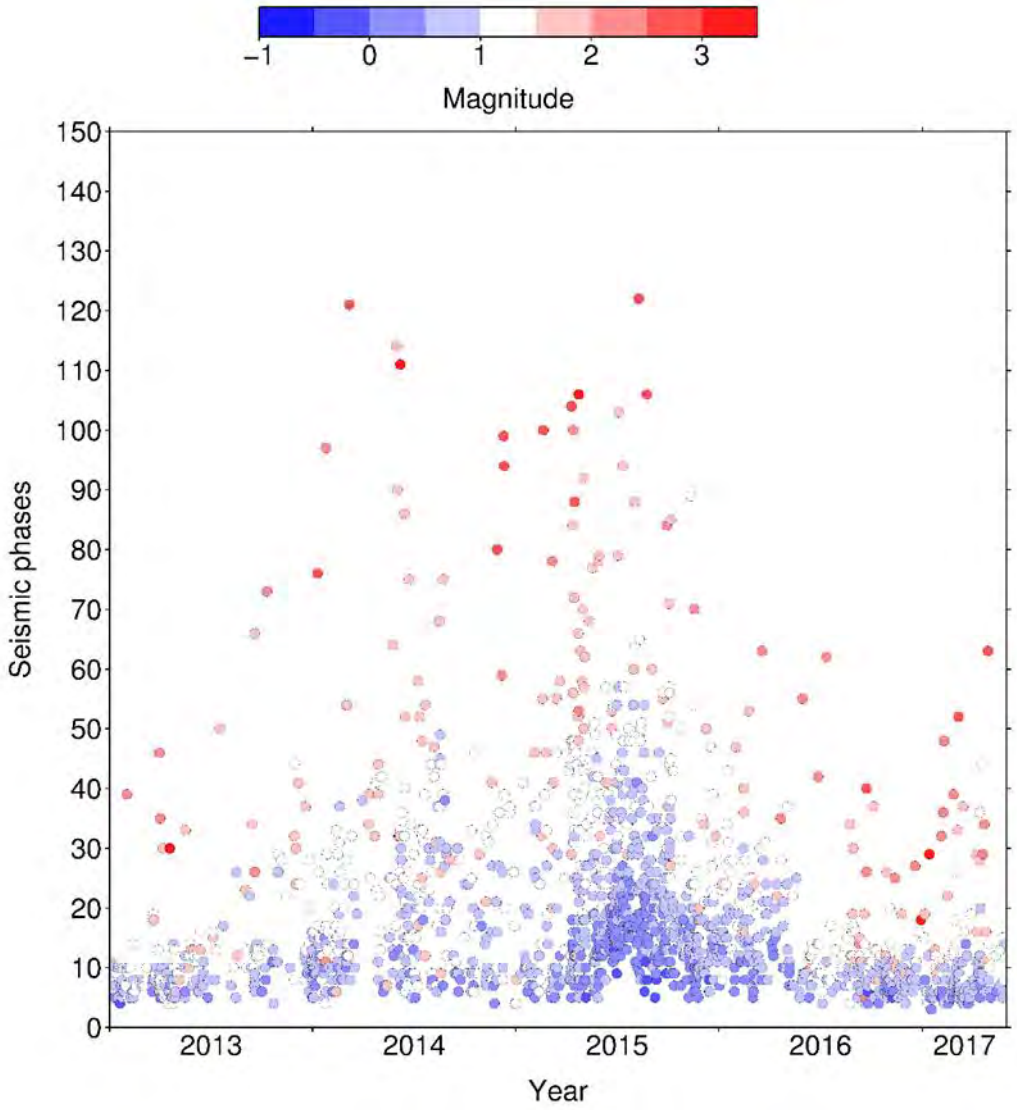

Figure 16. Number of seismic phases for each event plotted in time. Color code corresponds to magnitude.

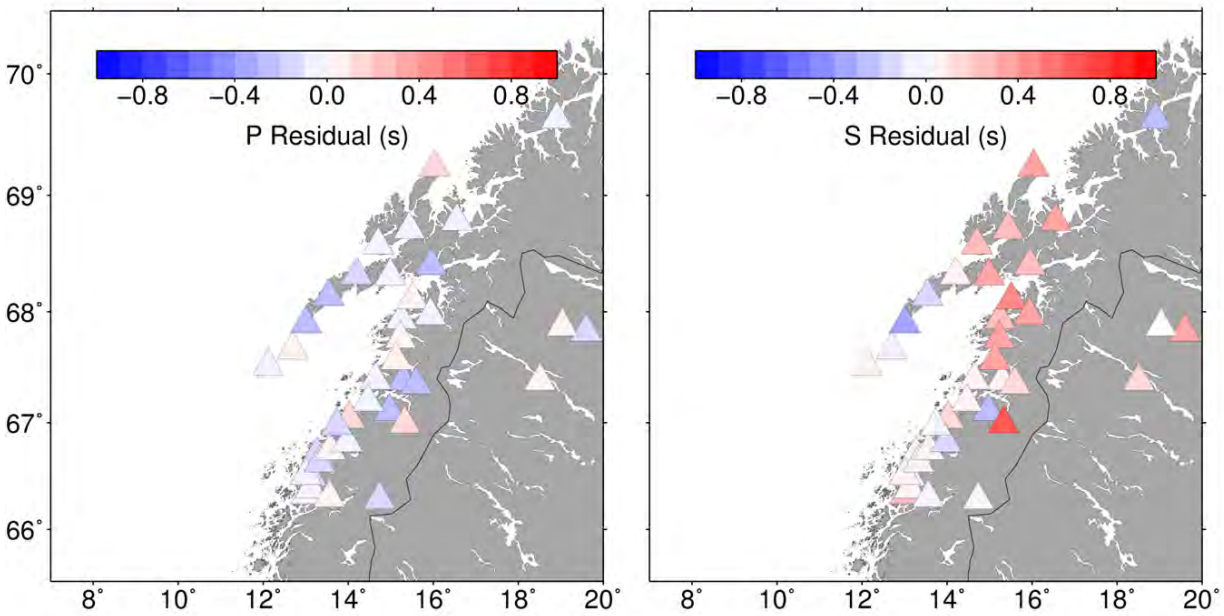

Figure 17. Station residuals for P- and S-waves

4. Detailed analyses

There were several more detailed analyses performed in addition to routine data processing. Those analyses are described within the four following sections: Focal mechanisms (Jan Michálek), Relative earthquake locations (Norunn Tjåland), Earthquake source parameters (Norunn Tjåland) and Joint-inversion of receiver functions and apparent S-velocities for the crustal structure (Anne Drottning).

4.1 Focal mechanisms (Jan Michálek)

Most of the earthquakes were located along the coast and for those the focal sphere coverage was mostly fine but earthquakes offshore close to the shelf margin the situation was much worse. As the focal mechanisms are used for analysis of the stress field and further as boundary conditions in numerical modelling it is crucial to provide stable and robust fault plane solutions (FPS). The simplest way to retrieve FPS is to use first motion polarities. If there are not enough polarities for stable FPS, amplitudes or amplitude ratios are used as additional information but their usefulness is still debated. Šílený (1989), Zahradník et al. (1989) and Rögnvaldsson & Slunga (1993) investigated the theoretical radiation patterns and compared them to observed amplitudes and polarities of mining tremors and small earthquakes but corrections for attenuation, free surface effect and geometrical spreading, which are usually not well known, must be taken into account. Amplitude ratios on the other hand (Kisslinger, 1980; Rau et al., 1996; Hardebeck & Shearer, 2003) are free from some of the corrections and should be easier to make use of once the amplitudes are determined correctly.

More advanced methods such as full waveform moment tensor inversion is difficult to use for M<3.0 earthquakes even though various approaches were developed (brief overview in e.g. Fojtíková & Zahradník, 2014). Those methods require good focal sphere coverage and high signal-to-noise ratio waveforms.

We are focused on a common and simple approach for FPS retrieval such as FOCMEC (Snoke, 2003) and we are trying to utilize it in a more effective way in terms of input data, namely amplitudes and their ratios.

4.1.1 Methods

There are various programs for FPS determination using different methods and four of them are implemented in the SEISAN software package (Havskov & Ottemöller, 1999). FPFIT (Reasenberg & Oppenheimer, 1985) and PINV (Suetsugu, 1998) programs are using first motion polarities only but HASH (Hardebeck & Shearer, 2002) and FOCMEC (Snoke, 2003) allow to use amplitude ratios in addition. Despite the methods are different they are using the same input data. It means that quality of the first polarity onsets and amplitude values are influencing results of all the methods.

4.1.2 Polarity readings

Picking of the P-wave polarity onset seems to be an easy task but several principles should be followed. The data cannot be filtered or a zero-phase filter must be applied and the right phases must be identified. At the epicentral distances between 100 and 150 km the refracted phase appears in addition to the direct wave and their interference can distort the onset. The onset itself can be also very emergent or weak either due to proximity to the nodal plane or due to low signal-to-noise ratio. We developed a tool in SEISAN which allows quick review of the polarity readings at all available stations using the same time window. The tool gives an overview on quality of the readings as well as comparison between stations and the polarity can be edited.

4.1.3 Amplitude readings

The correct estimate of amplitude is not difficult but should be done carefully. The filter should be applied to the signal with the right frequency limits according to the size of the earthquake and hence its corner frequency. The earthquakes we are processing are within 1.8-3.2 in ML magnitude range and their corner frequency can go down to 2 Hz (depending on stress drop).

To retrieve automatic amplitude readings of the P- and S-wave we decided to use the direct waves only (Pg, Sg), i.e. using stations up to 100 km of epicentral distance only to ensure having the same wave type at all stations. The amplitude reading of P-phase was made on vertical component and amplitude of S-phase on transverse (rotated) component. An automated procedure for amplitude readings was developed in SEISAN which allows to automatically evaluate the amplitudes in both time and spectral domain. In time domain the amplitude is determined as a half value of the maximum peak-to-peak amplitude. In spectral domain a Gaussian function is fitted to the spectrum to smooth out the original spectrum. Peak of this best-fitted curve is used as the spectral amplitude. The amplitude is evaluated from narrowly band-passed filtered signal (one octave filter). The narrow band also accommodates better the Gaussian shape of spectra. The time window we used was 2.4 sec width starting 0.4 sec before the phase onset but we also tested various window lengths. The window length is not influencing the amplitude as long as the main phase is whole inside the window. The length of the P-wave window is limited to beginning of the S-onset in case of close station to the hypocentre. The 10% cosine taper was applied to smooth the signal at window edges. Different filter ranges were used (2-4 Hz, 3-6 Hz, 4-8 Hz and 5-10 Hz) to test variability of the automatic readings (example in Figure 19).

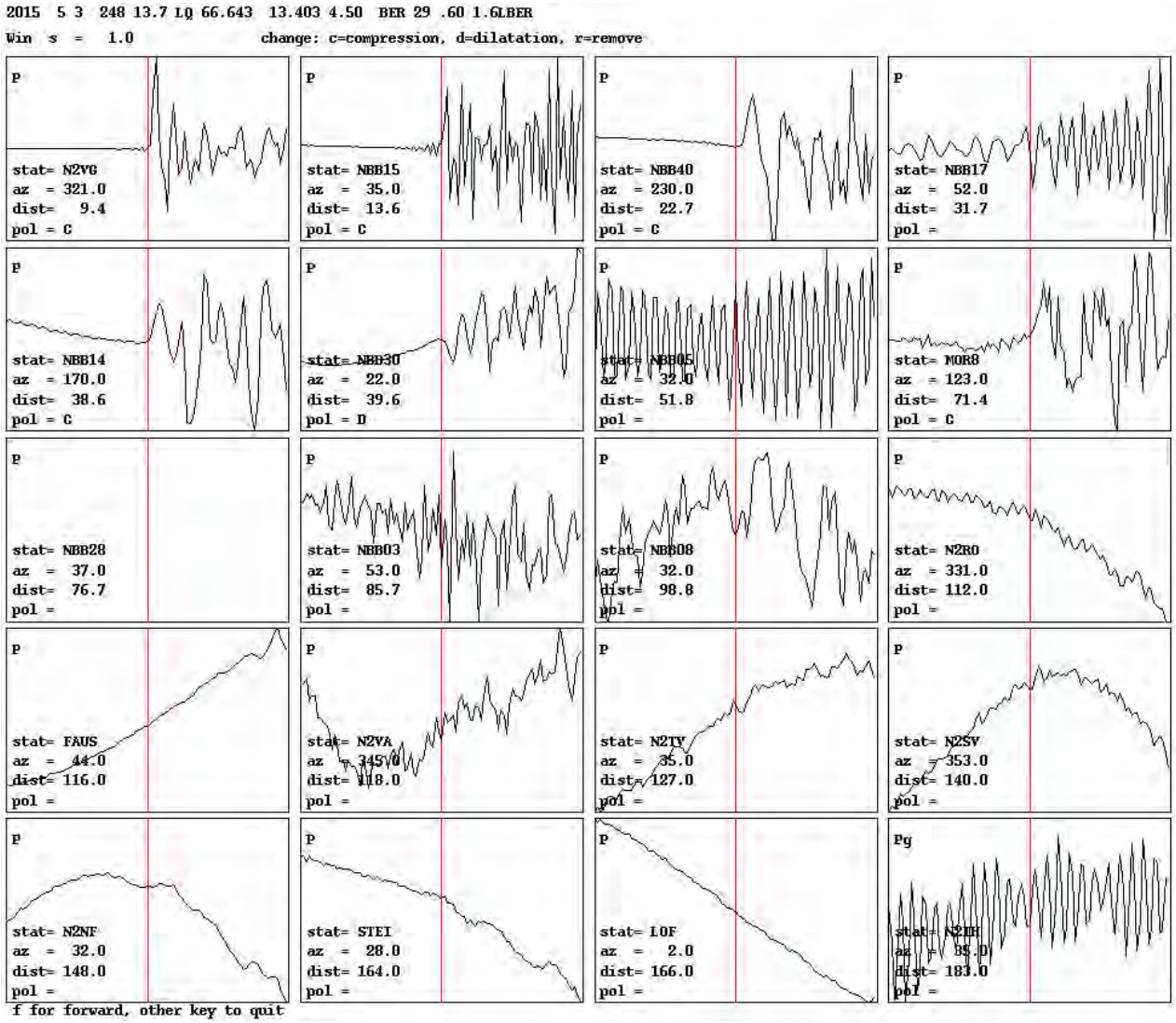

Figure 18. Tool developed in SEISAN allowing fast check and reading of the first arrival polarity

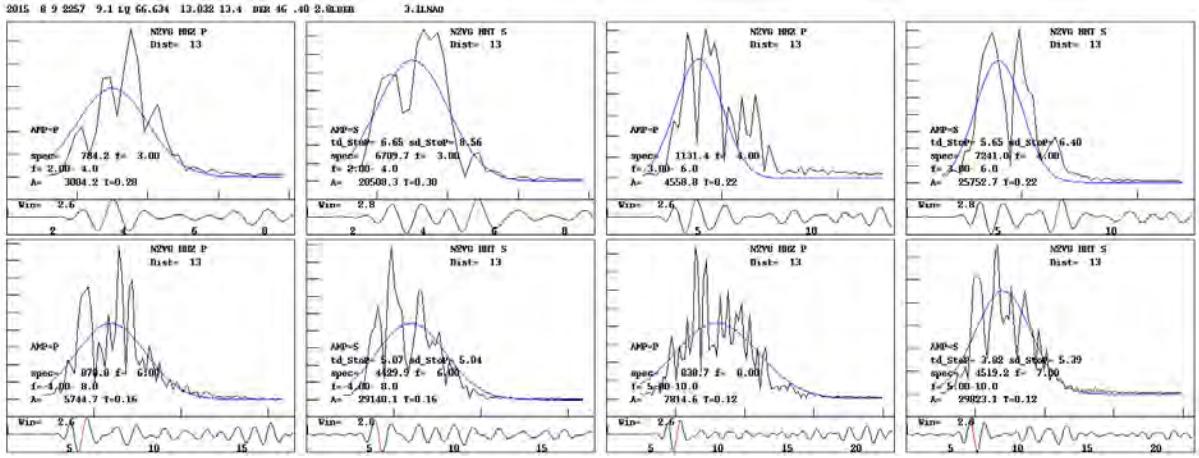

Figure 19. Signal and its spectrum for different frequency bands at station N2VG (13 km epicentral distance). The labels on x-axis correspond to frequency. Time window of the signal is always 2.4 sec.

4.1.4 Amplitude ratios

We analyzed the amplitude readings with respect to usage of data type (raw data, velocity and displacement), frequency band and time window. As we are using amplitude ratios and not amplitudes directly it is not necessary to correct the signal for instrument response but we tested this by comparing amplitudes of raw data, displacement and velocity. Figure 20a shows variability of ratios for individual data types (raw, displacement, velocity) across different frequency bands for one selected earthquake. It is possible to see that the data type selection influences the ratios much less than the frequency band (compare to Figure 20b). From Figure 20c one could see a systematic decrease of amplitude ratios as the frequency band was moved towards higher frequencies but this is not valid for all the stations and some are indicating no (NBB15) or opposite trend (NBB30, NBB40). This could be caused by frequency-dependent attenuation which can be different for P- and S-waves but was assumed same in this study. Another important finding from Figure 20c is that the ratios in each frequency band are very similar for both - data type (raw, displacement, velocity) and domain (time and spectral). The independency of amplitude ratios on domain is also shown in Figure 21.

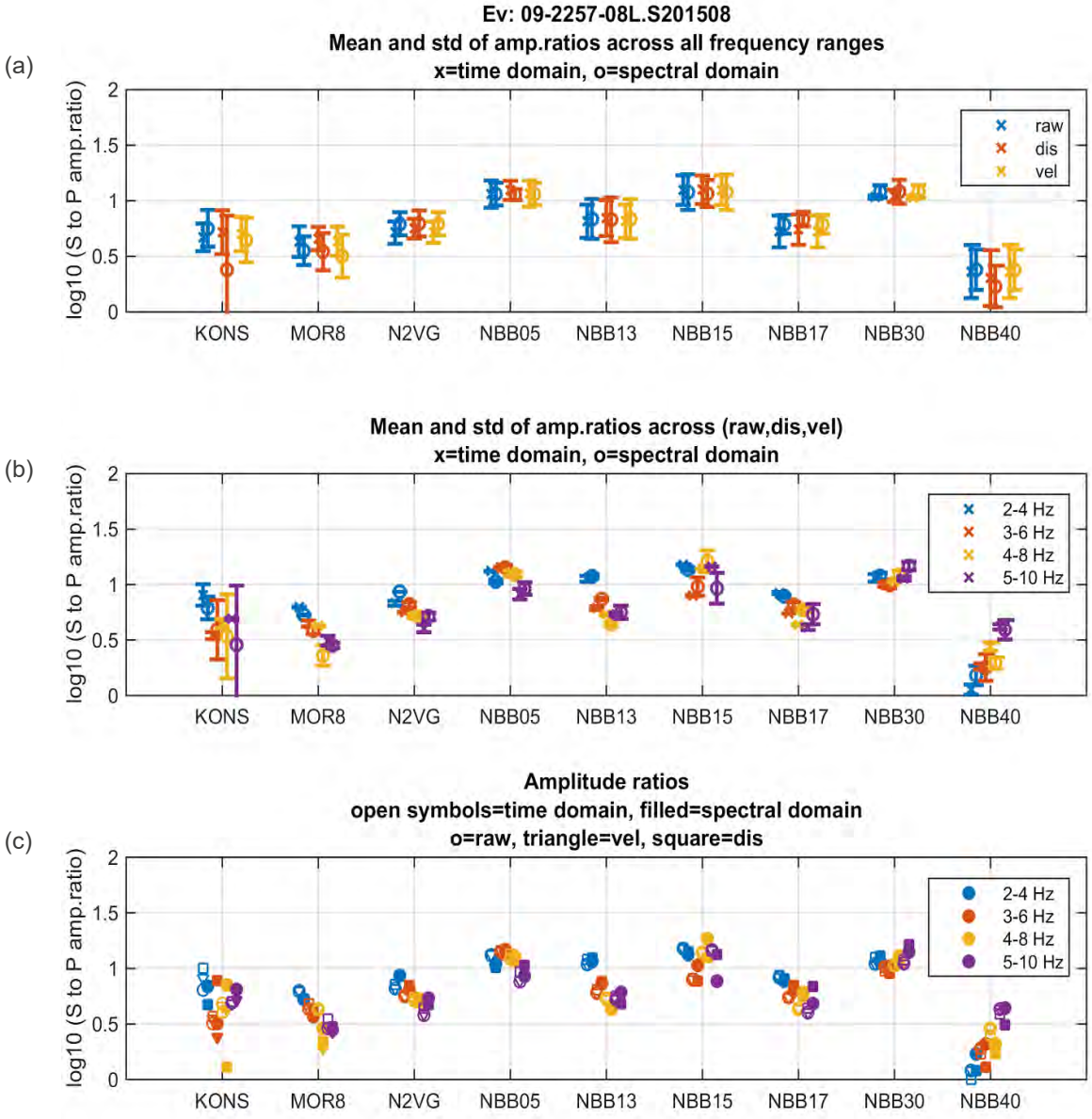

Figure 20. Comparison of amplitude ratios: a) mean and std across all frequency ranges, b) mean and std across data type (raw, displacement and velocity) and c) all the individual values used in plots a) and b).

We also tested influence of the time window 1, 2 and 3 sec on amplitudes (Figure 21) but it seems that only 1 sec window in time-domain can lead to underestimating of the amplitude at more distant stations as the phase is not represented fully in the short window.

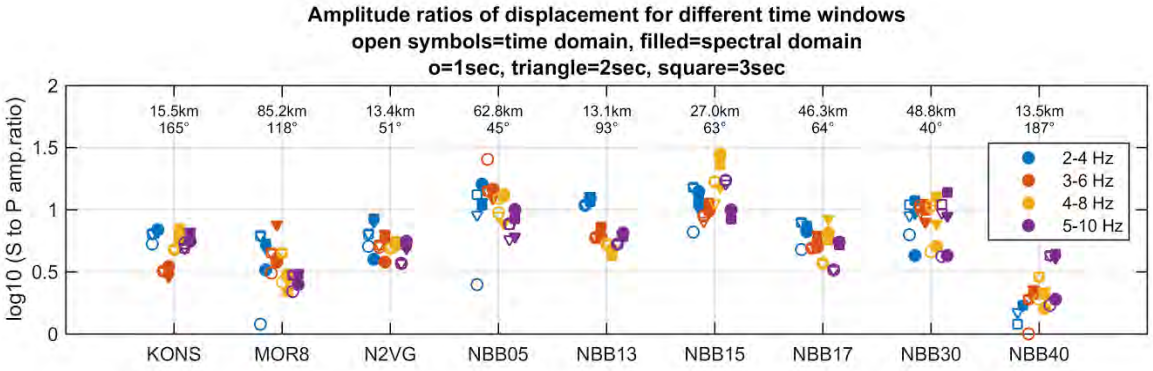

Figure 21. Influence of time window (TW) on automatic amplitudes (same event as in Fig.3). Circles are used for 1 sec TW, triangles for 2 sec TW and squares for 3 sec TW. Open symbols are related to time domain and filled ones to spectral domain.

Amplitude ratios obtained from time- and spectral- domain should be very similar. This is demonstrated in Figure 22 where amplitude ratios for one event are plotted (for various frequency bands and various input waveform types). Ideally the amplitude ratios should be aligned along the 1:1 line (dashed line in Figure 22).

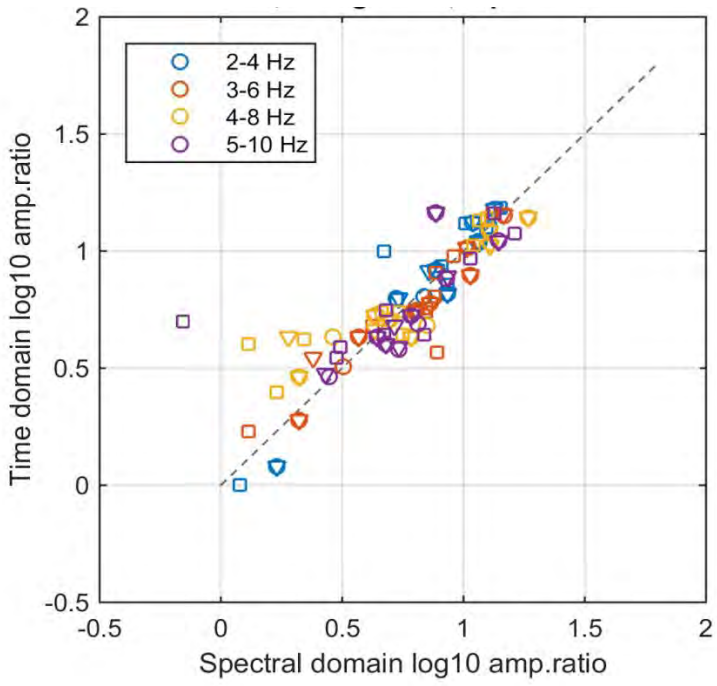

Figure 22. Comparison of amplitude ratios at individual stations obtained from time- and spectral- domain for event on 2015-08-09 22:57:08. Time window of 2 sec was used. Circles are amplitude ratios determined from raw data, triangles from velocities and squares from displacements.

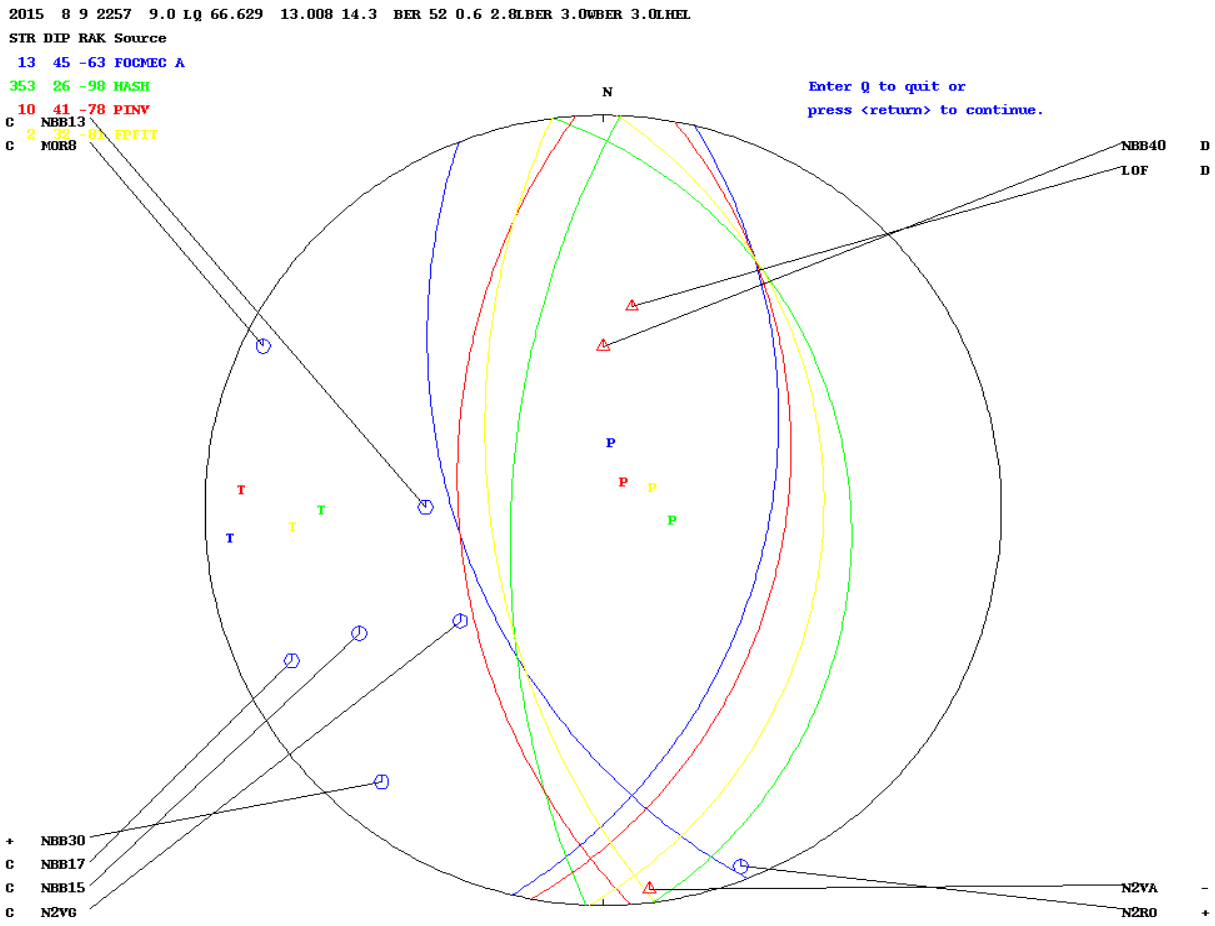

Figure 23. Example – focal sphere coverage by stations for event ML2.8 (2015-08-09 22:57; N66.629 E13.008). Fault plane solutions from FOCMEC, HASH, PINV and FPFIT methods are shown in different colors.

4.1.5 FPS analysis

For the analysis of the amplitude ratios we used FOCMEC (implemented in SEISAN). The first approach was try to find FPS using the polarities only using as many polarity readings as possible. The not very clear polarities on vertical component we verified also by comparing to polarity on radial component which has to have the same polarity. By this approach we were able to get about 14 polarities in the best case but to find at least some FPS we had to allow for polarity errors (1-3). If we added SH/P amplitude ratios we were not able to find any FPS without allowing for about half amplitude ratio errors which is too many as we believe that our amplitude readings are robust and correct. Another reason for not fitting the amplitude ratios could be a significant non-DC mechanism which is not expected in this area with respect to the tectonic setting.

Then we revised the approach and tried to use the clear polarity onsets only (Jechumtalova Z., 2016; pers. communication). For revision of polarities we also used the knowledge of how individual stations were performing during the whole project and stations which were often noisy were excluded. This reduced number of polarities significantly (e.g. from 14 to 8) in some cases, in some not (e.g. from 6 to 5). Reducing number of polarities increased number of possible FPS of course but for most events there were only several groups (2-3) of similar FPSs varying either in strike or dip. Including of amplitude ratios started to be more efficient and less of amplitude ratios had to be excluded (0-30%). This approach decreased the number of FPS down to 2-20 but all very similar now, usually with varying dip or strike within small range of 10 degrees.

FPS of the event is dependent on depth. Therefore, absolute relocation and analysis of depth stability was checked for each event. It was found that very distant stations (200 km or more) can negatively influence the depth as 1D velocity was used but the velocity at such distances can be different from close-by stations. Hence weighting of the stations with distance was used in relocations and stations farther than 100 km were damped and stations at farther than 150 km were excluded from localization procedure (XNEAR 100 150; option in SEISAN).

4.1.6 FPS results

Altogether 85 events were analyzed for FPS. Only 40 of them are of A or B quality which could be assumed as stable and could be therefore used for other studies/conclusions. Figure 24 is showing distribution of quality and their relation to number of obtained solutions and number of polarity readings. Some A and B quality earthquakes have many solutions but in such cases all the solutions were very similar. It is clear that quality decreases with decreasing input quantities (polarity and amplitude ratios) but the most important, which is not visible in this figure, was the focal sphere coverage by the stations. In general earthquakes in the middle of the network have better focal sphere coverage than earthquakes along the edge or outside of the network.

Figure 25 is showing focal mechanisms of A and B quality FPS. Events in the Tjong region (W of Svartisen) are showing mostly normal faulting with extension axis in NW-SE direction. In this region the events had good focal sphere coverage and therefore also FPS of smaller events could be analyzed. List of analyzed focal mechanisms is in Appendix 1.

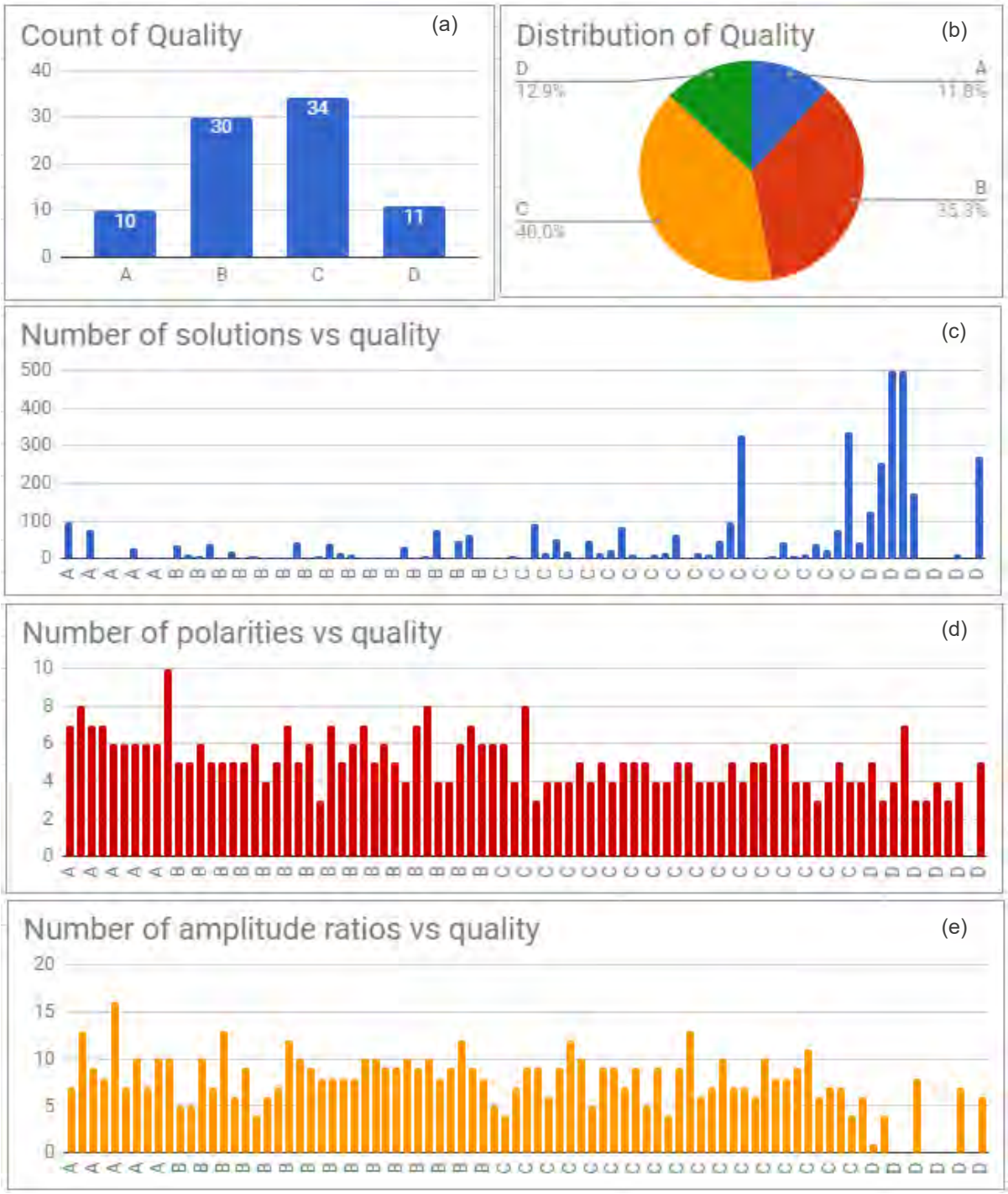

Figure 24. Distribution of FPS quality and (c) its relation to number of solutions, (d) number of polarity readings and (e) number of amplitude ratios.

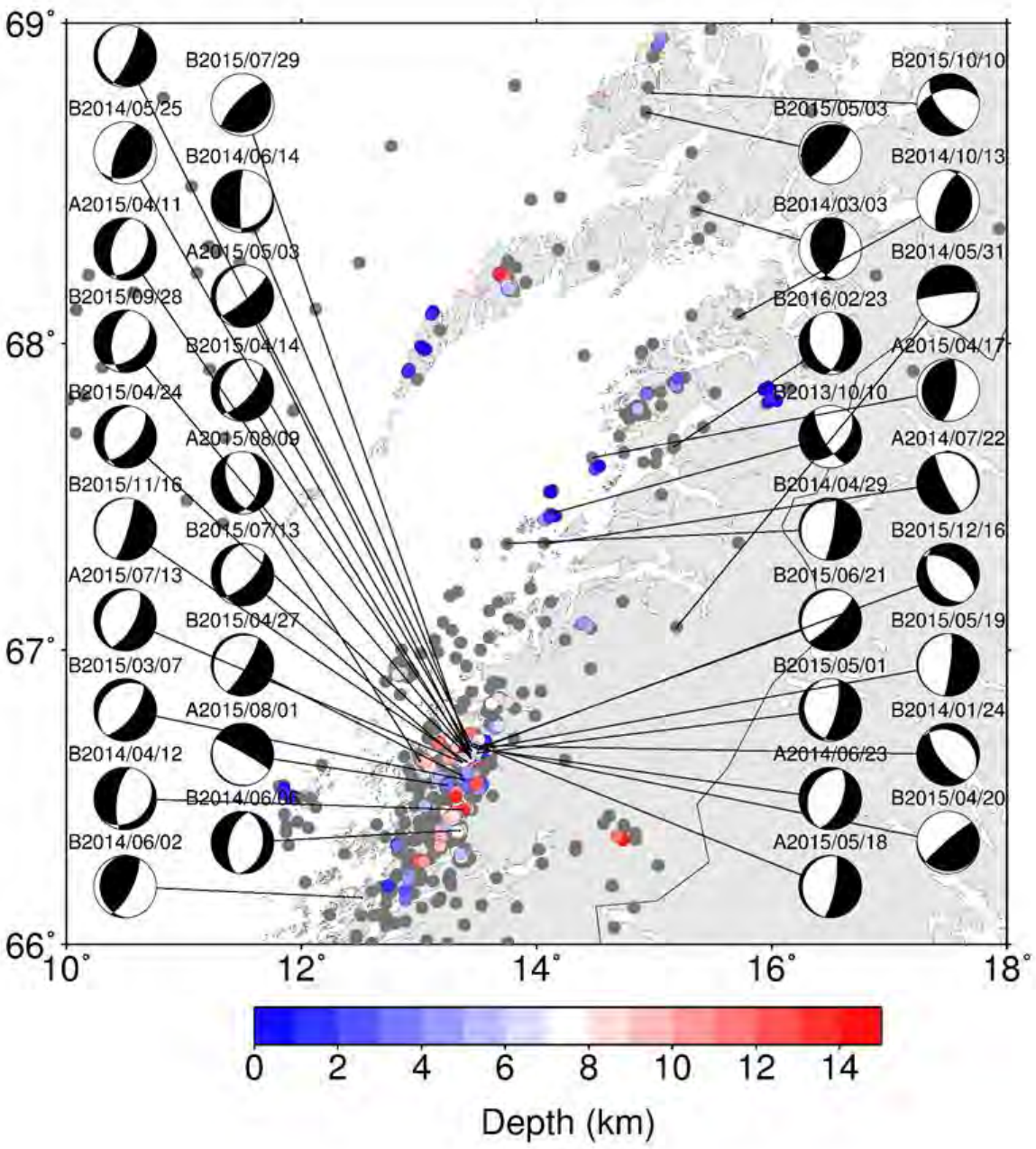

Figure 25. Fault plane solutions for A and B quality events.

4.2 Relative earthquake locations (Norunn Tjåland)

All the earthquakes were processed by the double-difference relocation method, developed by Waldhauser and Ellsworth (2000), in order to improve the standard catalogue locations. The double-difference location algorithm is implemented in the hypoDD software which allows the combination of absolute travel-time differences obtained from the earthquake catalogue with differential travel times derived from waveform cross-correlation data.

4.2.1 Double-difference method

The classical absolute location methods aim to minimize the residual between the observed and calculated travel times from the hypocenter to the seismic station for single events. The accuracy of these methods is controlled by errors in arrival times and by inaccuracies in the velocity model (Stein and Wysession, 2003). The double-difference approach minimizes the difference between the observed and calculated travel time differences (or double-differences) for pairs of earthquakes recorded at common stations.

It is based on the assumption that the ray paths of two events, *i* and *j*, will be similar if the hypocentral distance

between the two events is small compared to the distance between the event and a common station, *k*. Then, the travel time difference between two events observed at a common station will be due to the spatial offset between the two events and any effect from velocity heterogeneities will cancel out, except from in a small region between the two events where the ray path is different (Waldhauser and Ellsworth, 2000).

In the double-difference method, earthquake pairs are created and located relative to each other. The double-difference, or the residual between observed and calculated travel time difference for earthquake pairs, is given by equation 3.1.

$$dr_k^{ij} = \left(t_k^i - t_k^j\right)^{obs} - \left(t_k^i - t_k^j\right)^{cal}$$

The double-difference equation is linearised and the resulting problem is then one in which the residual for events *i* and *j*, recorded at station *k*, is linearly related to perturbations, Δm^i and Δm^j , of their hypocentral parameters, through the partial derivatives of the travel times for each event with respect to the unknown, represented by **m** in equation:

$$\frac{\partial t_k^i}{\partial m}\Delta m^i - \frac{\partial t_k^j}{\partial m}\Delta m^j = dr_k^{ij}$$

$$\boldsymbol{WGm} = \boldsymbol{Wd}$$

All double-difference equations can be combined into a system where the partial derivative matrix **G**, is of size M × 4N , where M is the number of double-difference observations and N is the number of events; **d** is the data vector of double-difference residuals for all event pairs; **m** is a vector of length 4N containing the changes in the hypocentral parameters ($\Delta x, \Delta y, \Delta z, \tau$) that are being solved for, and **W** is a diagonal matrix to weight each equation (Waldhauser and Ellsworth, 2000).

The system can be solved in a weighted least-square sense which will give the least square solution **m**. Depending on the size of the data set, the system can be solved using the method of singular value decomposition (SVD) or the conjugate gradient algorithm (LSQR).

$$\widehat{\boldsymbol{m}} = (\boldsymbol{G^T W^{-1} G})^{-1} \boldsymbol{G^T W^{-1} d}$$

The initial solution is taken from the staring locations and the a priori weights. It continuous with sets of iterations where the residuals and locations improves. In addition, the data is reweighted by multiplying the a priori weights with misfit weights that reject or downweight observations with large residuals, and with distance weights that downweight data for event pairs with large inter-event distances. The iterations stop when the RMS residual reaches a certain threshold value that depend on the noise level of the data, when the adjustment in the hypocentral parameters is below a chosen threshold, or when the number of iterations have reached its maximum (Waldhauser and Ellsworth, 2000).

Waveform cross-correlation

Cross-correlation can be used to measure waveform similarity, and high correlation may indicate similar focal mechanism and closely spaced hypocenters (Schaff et al., 2004). CORR is a program in the earthquake analysis software, SEISAN, which creates the input file for hypoDD. This file stores differential travel times for pairs of earthquakes and weights ranging from 0-1 according to the squared coherency. These are the a priori weights assigned for the cross-correlation data. The similarity between two signals *x* and *y* can be measured by the cross-correlation function r_{xy} given in equation 3.5 (Ottemöller et al., 2014). Highly accurate arrival times for both P and S-phases can be determined for similar waveforms through cross-correlation.

$$r_{xy}(i) = \frac{\sum_{j=1}^{n} x_j y_{(j+i-1)}}{\sqrt{\sum_{j=1}^{n} x_j^2}\sqrt{\sum_{j=1}^{n} y_{j+i-1}^2}}$$

Waveform similarity is measured between all events by the cross-correlation function utilized in CORR. A phase window of 1-sec for P-phase, and 2-sec for S-phase on vertical component records is selected, in addition to a passband of 3-8 Hz. For event pairs to be correlated a minimum number of three stations are required, a maximum distance of 10 km between event pairs, and a maximum distance of 250 km between event and station. 3231 P-wave and 2756 S-wave differential times are obtained from the waveform cross-correlation with a correlation value greater than 0.80, indicating that there are earthquakes with highly similar waveforms.

HypoDD relocation

The earthquakes are relocated in hypoDD using both cross-correlation data and catalogue data. The first step of the relocation process is the preprocessing of the catalogue data in the ph2dt program. This program creates the input file (dt.ct) that stores absolute travel times from earthquake catalogues for earthquake pairs observed at common stations. Travel time differences for event pairs with a separation distance of less than 10 km and at stations not more than 200 km away, are obtained during the preprocessing of the data. Event pairs can be linked to neighbouring events such that a continuous chain of event pairs that are located in close proximity to each other are formed. Each event can be linked to a maximum of 20 neighbouring events that occur within the search radius and meets the criteria of at least eight phase pair links. Phase pairs that have at least eight observations would typically be considered as a strong link, because there is at least one observation for the eight degrees of freedom (Waldhauser, 2001). There are 9736 linked event pairs and the average number of links per pair is 12, while the average offset between linked events is 3.2 km. The number of catalogue P and S differential times is 46,917 and 63,049, respectively.

These differential times, together with the differential times obtained from the cross-correlation, are used as input to the hypoDD program to determine double-difference relocations. After differential time match there is 946 events from a total of 115,953 differential times. From this, 927 are clustered events, while 19 are isolated events. In order to control the stability of the inversion, events are grouped into clusters. To form a continuous cluster, a minimum of eight catalogue links for each event pair are required which creates 33 separate clusters of varying size, the largest one containing 742 events and the smallest ones not more than two.

All relocations in hypoDD are based on a one-dimensional velocity model given in Table 4 and shown in Figure 26. The model is the standard velocity model for Norway, developed by Havskov and Bungum (1987), with additional layers to obtain a more gradual velocity increase with depth. It consists of twelve layers and considers a constant v_p/v_s ratio of 1.73. The model was developed for western Norway.

Velocity model used in hypoDD

Depth of layer (km)	Layer velocities (km/s)
0.0 - 2.0	6.20
2.0 - 4.0	6.27
4.0 - 6.0	6.34
6.0 - 12.0	6.40
12.0 - 23.0	6.60
23.0 - 31.0	7.10
31.0 - 50.0	8.05
50.0 - 80.0	8.25
80.0 -	8.50

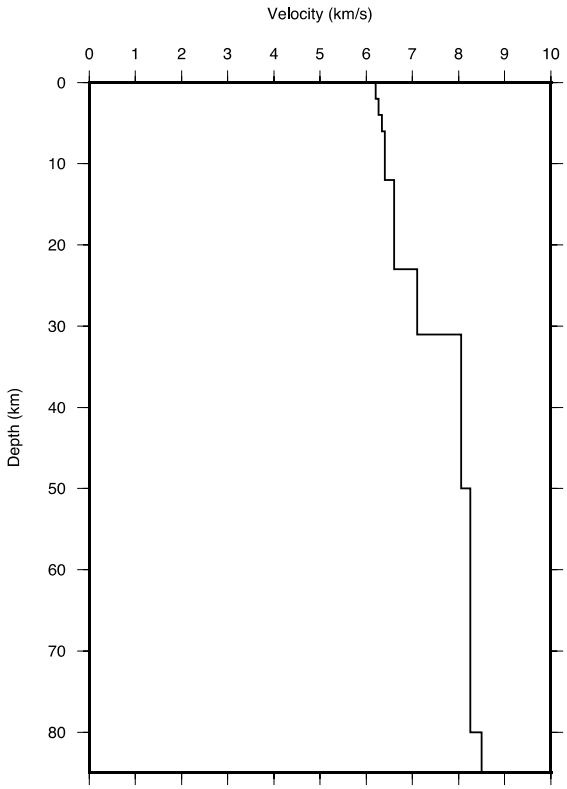

Figure 26. One-dimensional P-wave velocity model, the standard velocity model for Norway by Havskov and Bungum (1987) with additional layers.

4.2.2 Results of double-difference relocation with hypoDD

In the Nordland area, defined by 12.4−13.8°E and 66.2−66.8°N, a total of 742 clustered events are located. Through an iterative procedure with weighting and re-weighting of data, there are 483 remaining events that are relocated. The hypoDD output show a continuously decrease in the hypocentral parameter values from first to final iteration. The mean absolute change in east-west direction (DX) decrease from 476 m to 22 m. In north-south direction (DY), 424 m converge down to 19 m. Depth (DZ) changes from 3116 m to 66 m, while origin time (DT) go from 74 ms to 3 ms. The double-difference relocations, shown in Figure 27, exhibit improved clustering and an overall more focused seismicity image achieved for the Nordland area. Vertical sections of the seismicity reveals that the distribution of hypocenters at depth is clearly improved, and that the effects from layer boundaries in the velocity model is limited (Figure 27 b,c).

The robustness of the relocations is systematically tested by varying the input parameter values. By doing this it is possible to identify the most critical parameters for forming of event pairs, linking to neighboring events and clustering. The hypoDD output indicates that the choice of input parameter values gives reliable and robust relocations. However, more testing could be done to assess the accuracy of the double-difference locations.

List of relocated earthquakes is in Attachment 4 and also included in Attachment 3 for visualization in Google Earth.

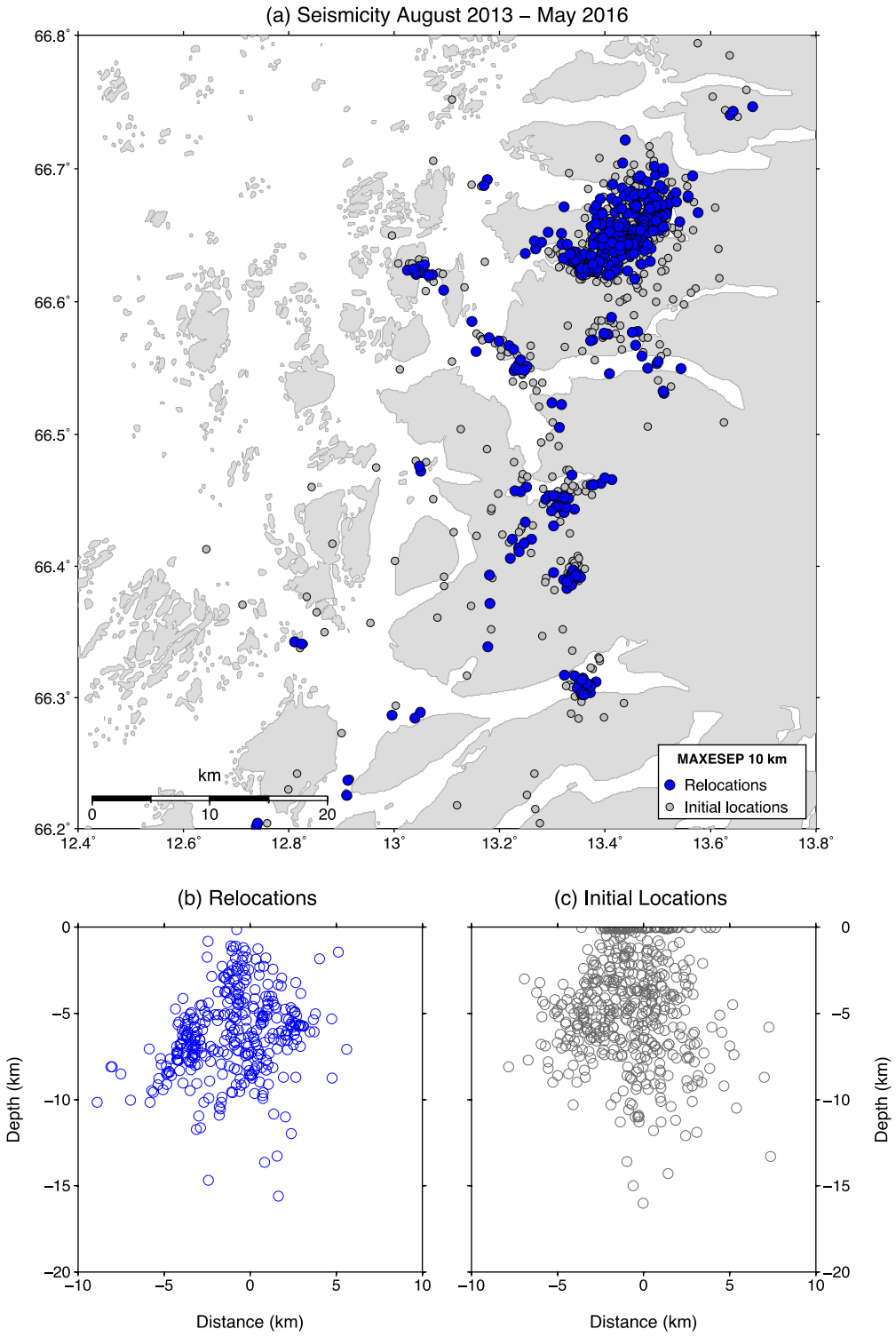

Figure 27. Double-difference relocations using a maximum hypocentral separation of 10 km between event pairs. Blue circles are relocations and grey circles are initial locations.

The majority of the relocated earthquakes occur in the largest cluster that extends SW-NE, where the seismicity can possibly be associated with an earthquake swarm. This swarm is surrounded by more diffuse activity. Further south, five smaller clusters of similar size are identified. They have no clear trend, except from a possible NW-SE trending feature towards southwest. The depth distribution of the seismicity varies from surface down to about 15 km depth. Figure 28 presents the relocated earthquakes with color that indicates hypocenter depth and shows that there is some spatial variation of depth in the area.

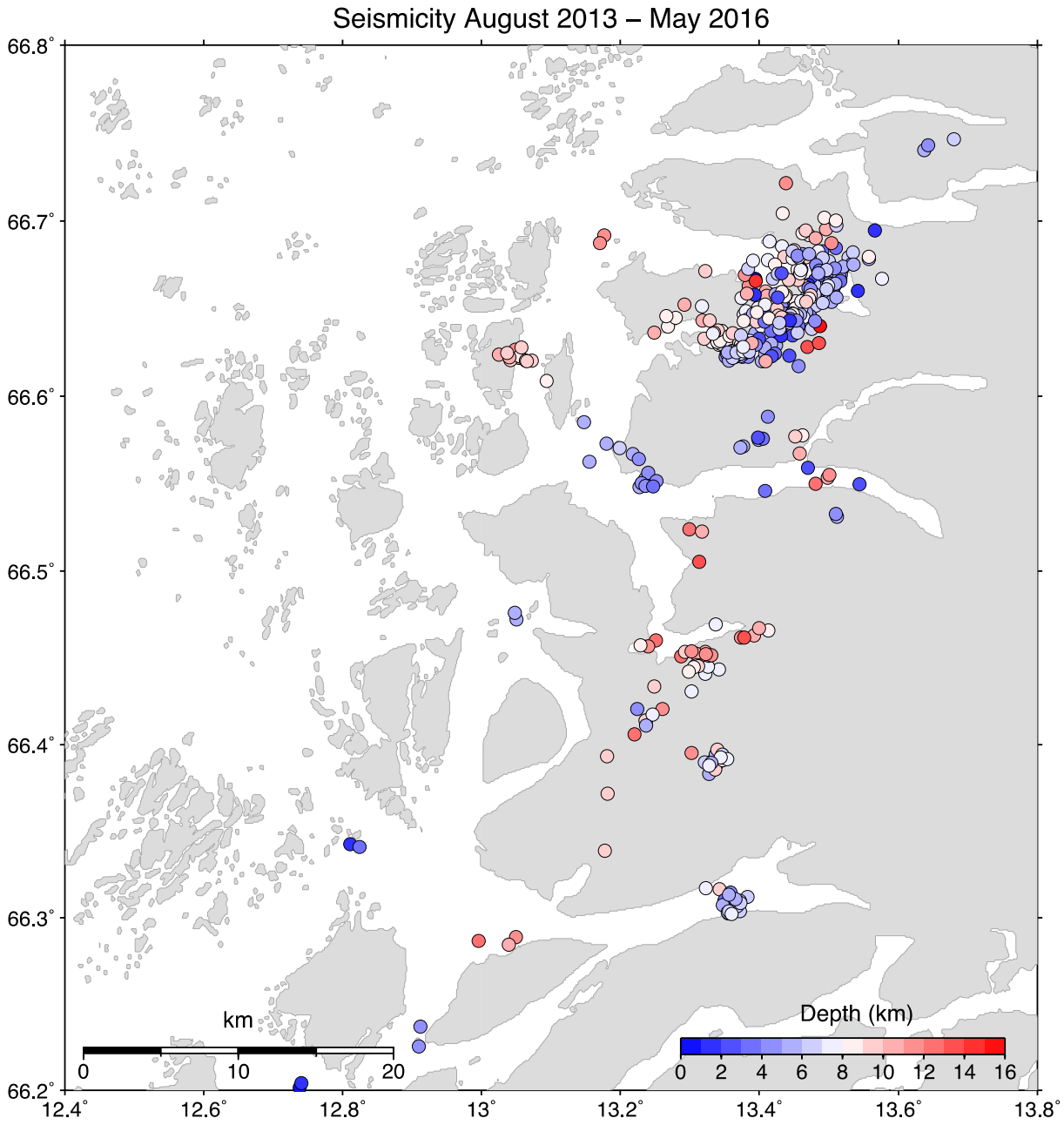

Figure 28. Double-difference relocations using a maximum hypocentral separation of 10 km between event pairs. Colour indicates hypocenter depth.

Depth profiles

The double-difference relocations can be studied closer by making profiles that might reveal structures at depth. Depth profiles are made along and across the apparent seismicity trend for each cluster. The relocated events can be separated into eight clusters that vary in size, orientation, depth and degree of clustering. The earthquake swarm in Jektvik represents the largest cluster of events and can be subdivided into three smaller clusters with a possible NW-SE trend. Figure 29 provides more details of the swarm. Although the seismicity appears rather diffuse, it seems that it is shallower on eastern side. The activity in this area can be separated into three smaller clusters where it seems to be a trend of more shallow earthquakes occurring in eastern direction, while activity at greater depths occur towards west. Width and length of profiles are indicated by the size of rectangles. NW-SE profile and SW-NE profile are made for all three clusters and the result is given in Figure 30. In general, difficult to observe clear patterns, but within Cluster 3 it is possible to observe what might be a structure dipping towards north-west, which is also indicated by the coloured hypocenters in Figure 28.

Southwest of Jektvik swarm, the relocated events in Cluster 4 and Cluster 5 indicate the presence of NW-SE linear features (Figure 31). The earthquakes in Cluster 4 occur at about 8-12 km depth, which is greater than the activity occurring at around 5 km depth in Cluster 5. The depth profiles of these clusters show no patterns of clear

structures. This is also the case for Cluster 6, which is suggested to have a NE-SW trend (Figure 32).

The two remaining clusters, Cluster 7 and Cluster 8, appear as clusters with no linear trend. They are similar in both size and depth distribution. The east-west and north- south trending profiles across the cluster reveals a deeper vertical pattern over a smaller horizontal distance as seen in Figure 33.

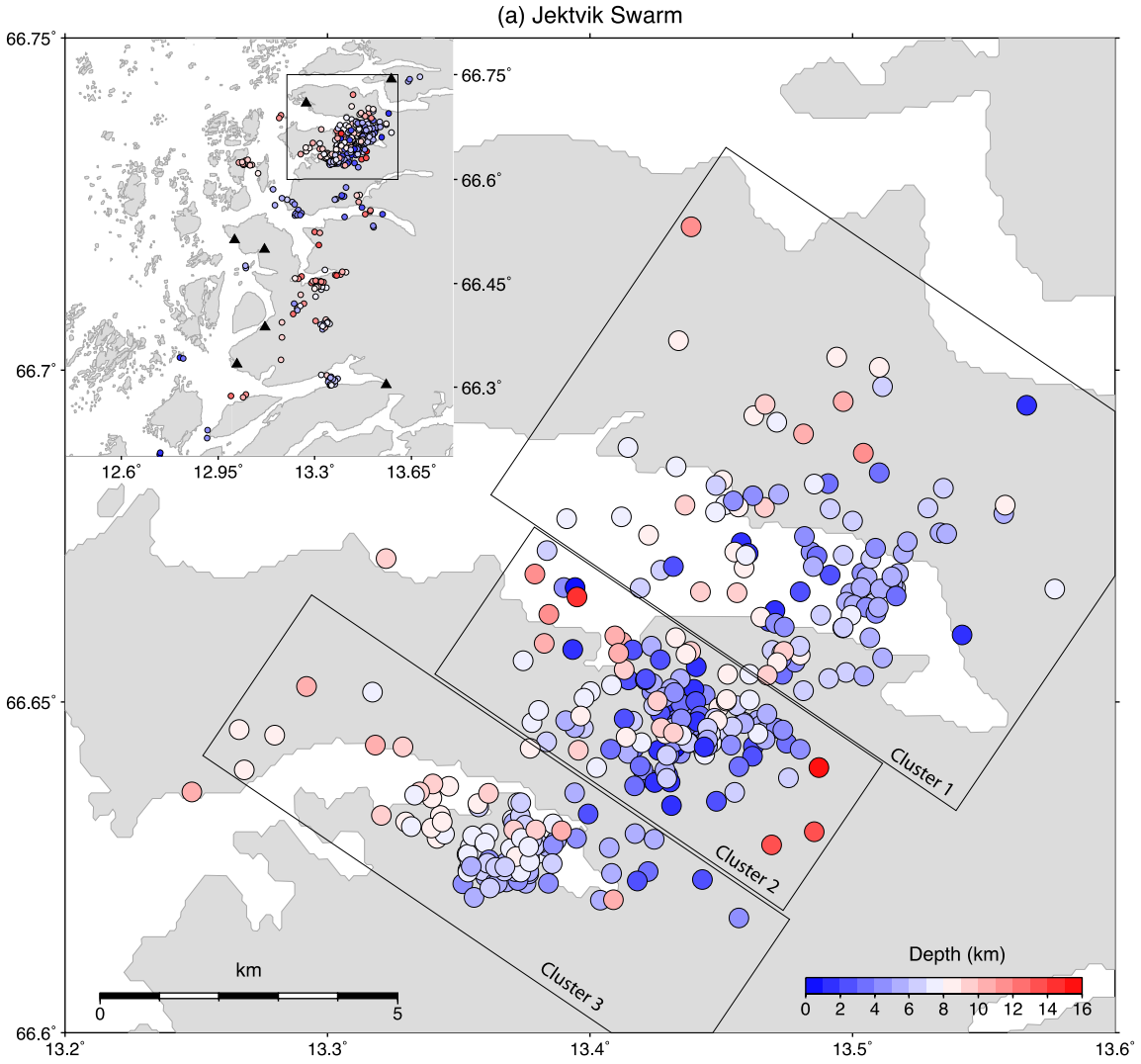

Figure 29. Detailed figure of Jektvik Swarm where colour indicates depth of hypocenter

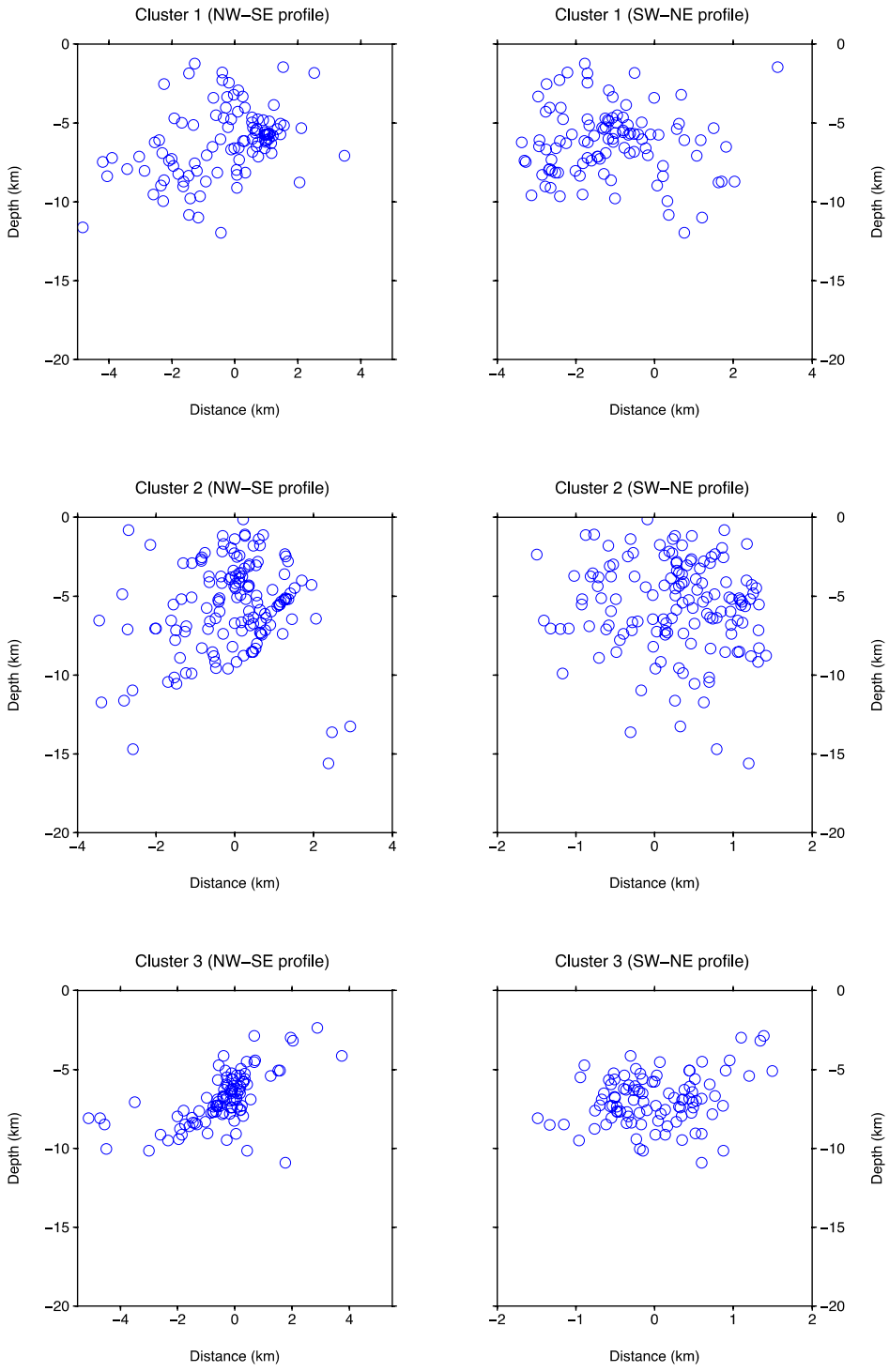

Figure 30. NW-SE and SW-NE profiles for clusters 1-3.

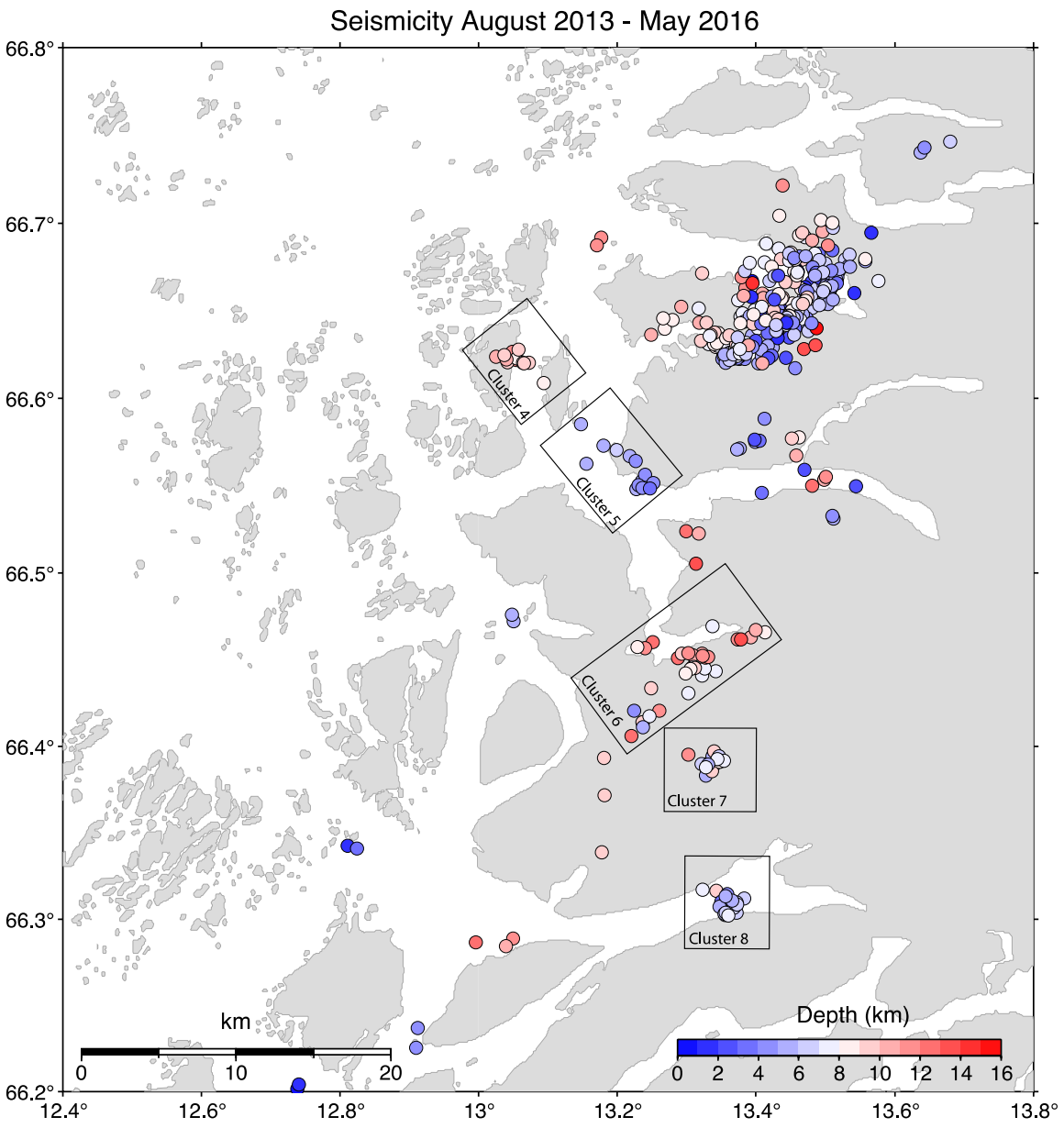

Figure 31. Double-difference relocations using a maximum hypocentral separation of 10 km between event pairs. Colour indicates hypocenter depth. Width and length of cross-sections are indicated by size of rectangles.

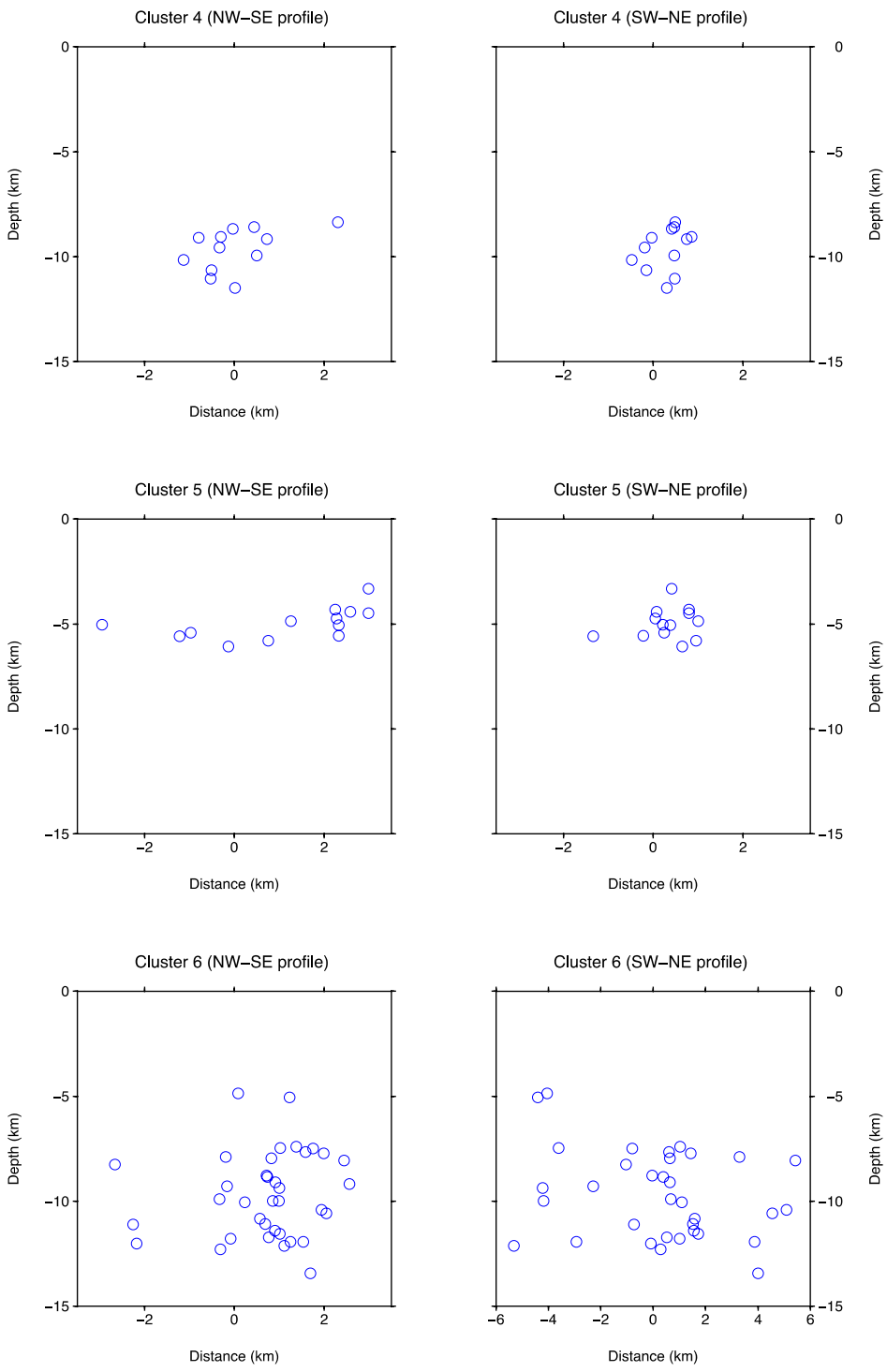

Figure 32. NW-SE and SW-NE profiles for clusters 4-6.

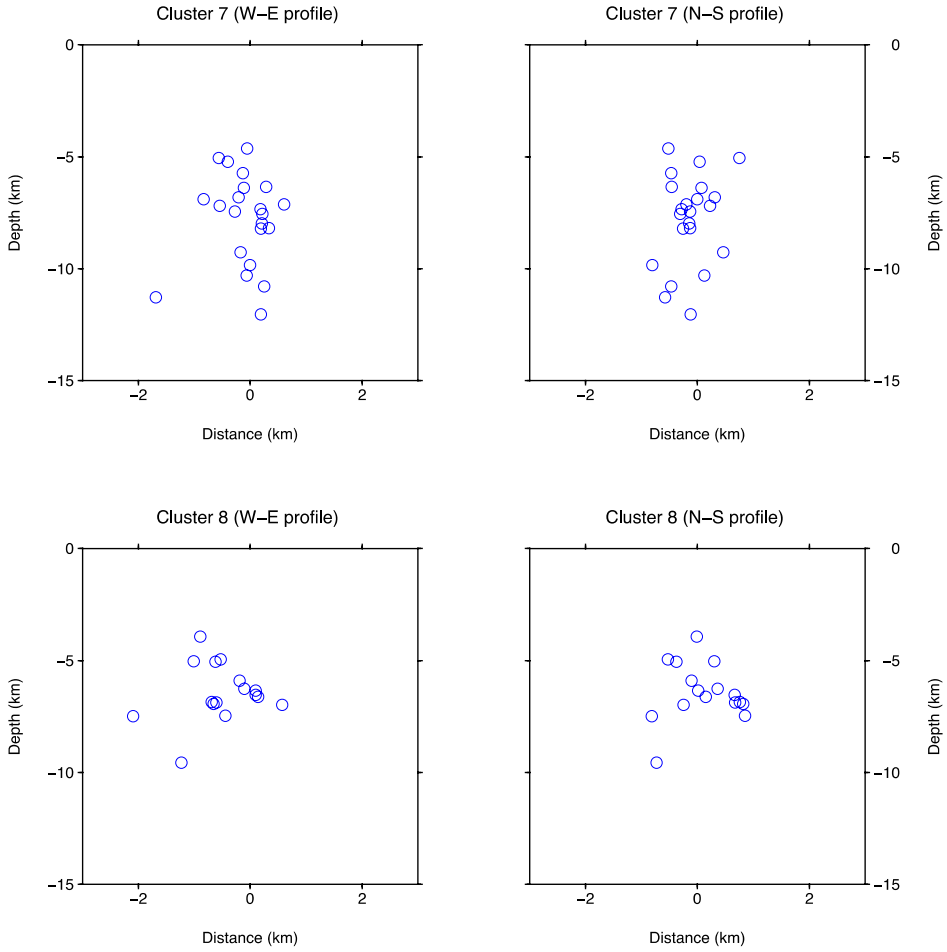

Figure 33. W-E and N-S profiles for clusters 7 and 8.

4.2.3 Discussion

The double-difference algorithm of Waldhauser and Ellsworth (2000) was used to relocate earthquakes in the Nordland area in northern Norway. By using the double-difference relocation and waveform correlation methods, the location uncertainty caused by errors in arrival times and in the velocity model is minimized. Although, in this case, the use of cross-correlated events has no significant effect on the final relocations. The relocations presented in this study indicate an overall improvement of the original locations. As the clustering of hypocenters improves, the seismicity pattern becomes more focused. Several clusters were identified and could possibly be associated with tectonic structures.

Analysis of the most seismically active area suggests that the earthquake swarm west of Svartisen glacier consists of three separate clusters. The hypocenter depths are generally shallow with a tendency of deeper events towards north-west (Figure 29). The distribution of earthquakes with depth along NW-SE profiles also indicate structures dipping towards north-west. In opposite direction, along NE-SW trending profiles, no clear linear trends could be identified (Figure 30). Even though some spatial organisation of earthquakes was observed, the double-difference relocations alone cannot be directly correlated with fault lines. However, the indicated trends are consistent with fault plane solutions that imply NW-SE and NE-SW orientations. Smaller clusters of earthquakes occur south-west of the swarm where some might indicate NW-SE trending structures. Some of these clusters were also active during the NEONOR1 project (Hicks et al., 2000). The available fault plane solutions from the area suggest predominantly normal faulting and with some reverse faulting in north and south direction.

The underlying cause of the seismicity in Nordland is unclear. However, it has been suggested that the seismicity is influenced by glacial isostatic adjustments. In addition, there are regional stresses from ridge push, as well as more local sources from topography and sediment flexure that can cause the activation of old weakness zones in the area (Hicks et al., 2000). The presence of the Svartisen glacier not far from the earthquake swarm is another

factor that could possibly have an impact on the seismicity.

4.3 Earthquake source parameters (Norunn Tjåland)

4.3.1 Method and data processing

Empirical Green's function method

Source characteristics of earthquakes in the Nordland area in Norway can be determined using the empirical Green's function method introduced by Mueller (1985). Small earth- quakes can be used as empirical Green's functions (EGFs) to remove path, site and instrument effects from the seismogram of a larger earthquake of interest, provided that the earthquakes are collocated, recorded on the same station, and that the EGF approximates a delta function in the frequency band of interest. If these criteria are met, the deconvolution of an EGF from the larger earthquake results in the source time function of the larger event.

By spectral division in the frequency domain, the effects from path, site and instrument can be removed by dividing the spectra of the larger event, R(ω), by the spectra of the smaller event, Z(ω), defined as an empirical Green's function (Ammon, 1991).

$$H(\omega) = \frac{R(\omega)Z^*(\omega)}{\phi(\omega)} G(\omega)$$

$$\phi(\omega) = max\{Z(\omega)Z^*(\omega), c \cdot \max\{Z(\omega)Z^*(\omega)\}\}$$

Deconvolution instability is avoided by adding a water-level of 10^{-6}, that will replace zeroes or small values in the denominator, the spectra of the EGF, with a value corresponding to the water-level parameter c. This parameter will be a fraction of the maximum amplitude of Z(ω) (Clayton and Wiggins, 1976).

In order to control the bandwidth and to remove noise, the source time function is multiplied by the transform of a Gaussian filter.

$$G(\omega) = \xi \exp\left(\frac{-\omega^2}{4a^2}\right)$$

The width of the Gaussian is controlled by the alpha parameter a which is set to 100 for least possible filtering. ω is the frequency in radians and the constant ξ normalize the Gaussian filter according to the amplitude (Ammon, 1991).

Cluster analysis

Waveform similarity is a good starting point for empirical Green's function analysis, as it indicates close location and similar mechanism for the smaller EGF event and the larger earthquake of interest. Earthquakes recorded on at least three stations with a minimum correlation of 0.95 is used in order to cancel the effects from path, site and station. The cluster analysis is done in the XCLUST program in SEISAN (Ottemöller et al., 2014), which finds five clusters of correlated events. The number of events within each cluster varies from 7-43 events (Figure 34).

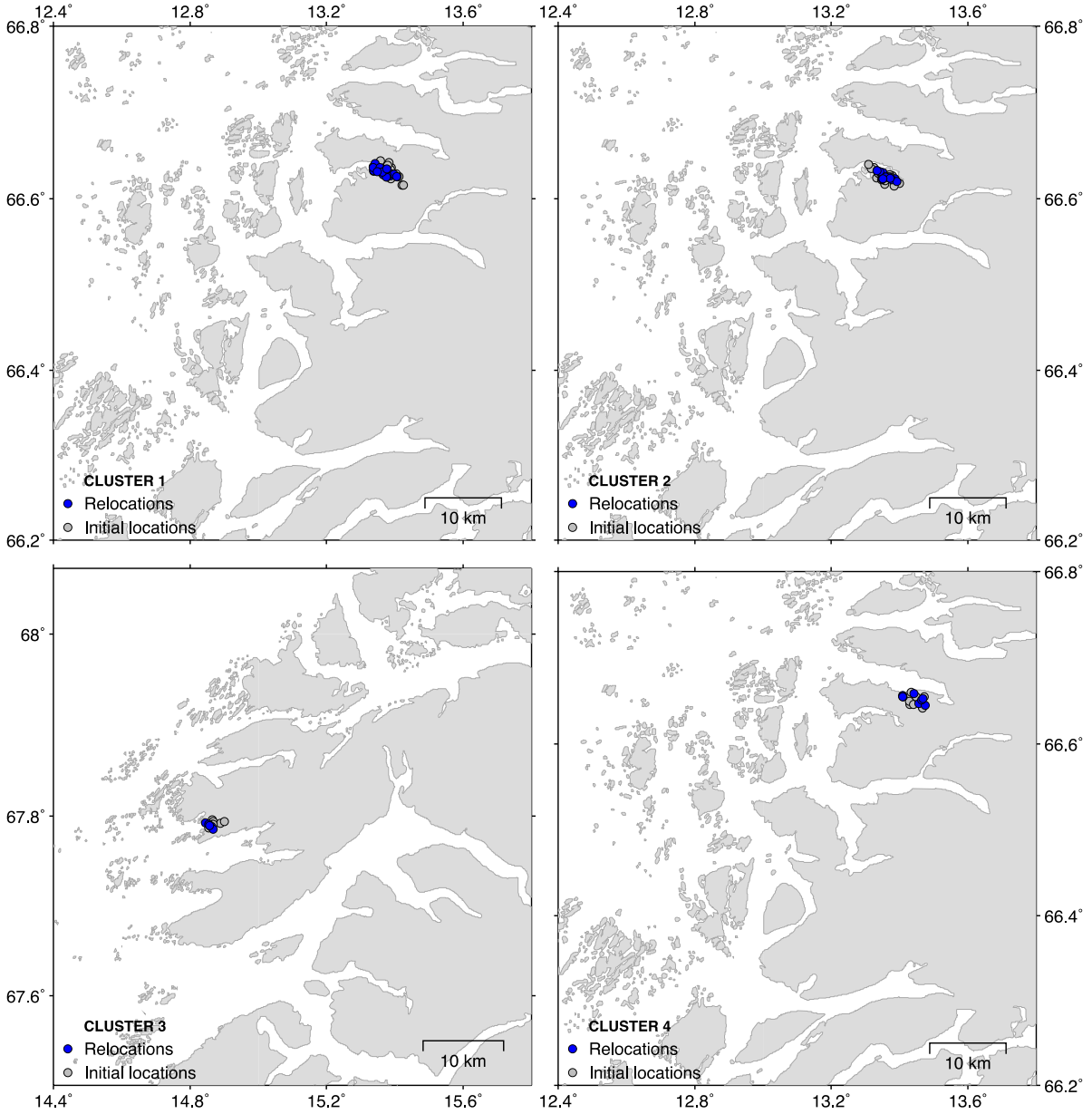

Figure 34. The double-difference relocation of clusters used in the empirical Green's function analysis.

4.3.2 Results

Empirical Green's function analysis

The water-level deconvolution is done in DECON which is a program in the SEISAN software (Ottemöller et al., 2014). S-waves on the vertical component for up to six stations are used to determine source time functions. This allows comparison of source time functions for varying azimuth. The source time functions of 11 master events (M_L 1.0 to 1.8) are isolated through deconvolution using smaller magnitude events (M_L 0.1 to 0.9) as empirical Green's functions. The result of the deconvolution of two correlated events recorded on the seismic station NBB40 is shown in Figure 35. In the upper right corner the seismogram of the master event (M_L 1.8) and the empirical Green's function (M_L 0.3) are displayed. To the left is the spectral traces for each event. The result from the spectral division is shown below, while the deconvolved source time function and the reconvolved seismogram is in the lower right corner.

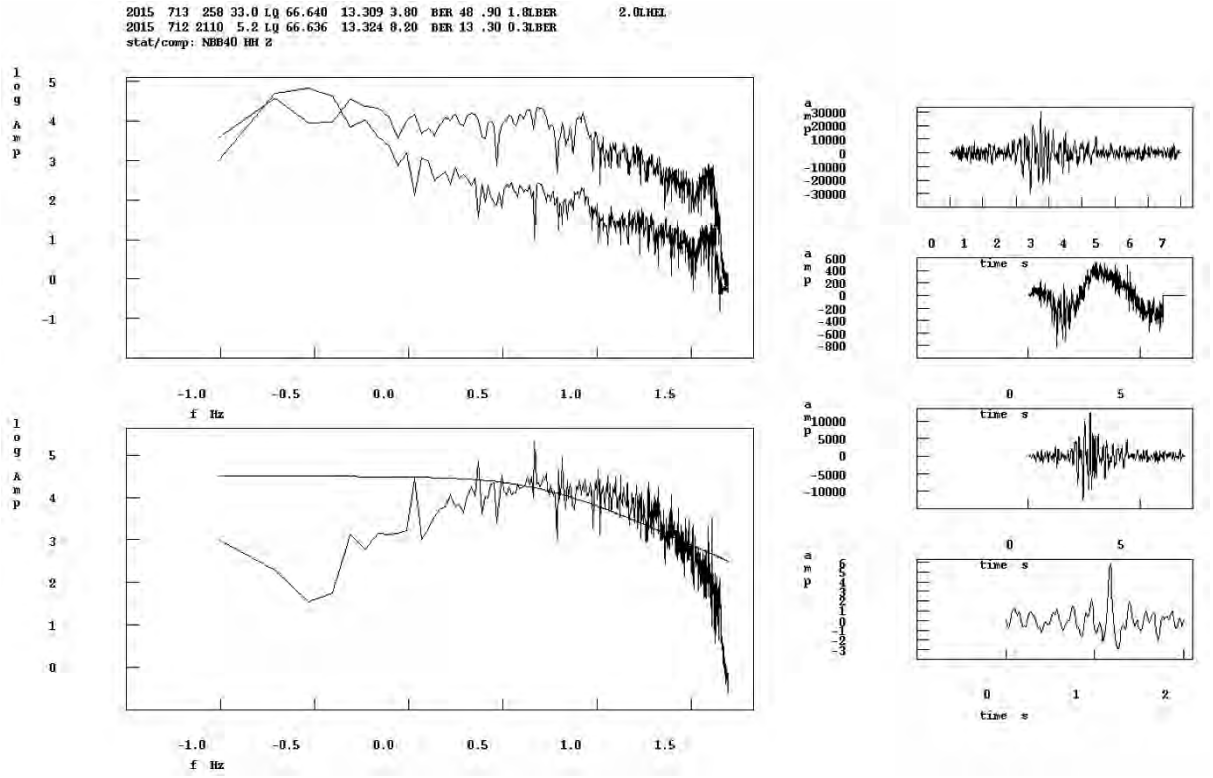

Figure 35. Deconvolution of seismogram of a smaller event, referred to as an EGF, from a larger master event, will remove instrument, travel path and site effects and give the source time function of the larger event. The computed spectrum line is adjusted according to the observed spectral shape.

The magnitude 1.8 event, occurring on 13 July 2015, is located inside Cluster 2. Nine source time functions are obtained for this master event, using correlated earthquakes of magnitude 0.1 to 0.9 as empirical Green's functions (Figure 36). It has an estimated duration of 0.09 seconds, which is the average for 29 source time functions at six different stations. The shape of the source pulse is generally clear and consistent which makes the duration estimates more reliable. However, with much noise it can be challenging to make a good estimate of source pulse duration.

A comparison of the source time functions obtained for a magnitude 1.1 event occurring on 14 July 2015 at station NBB13 and N2VG is given in Figure 37. The source time functions that has been derived for the larger 1.7 magnitude event on 26 November 2015 is shown is Figure 38 and has an average duration of 0.10 seconds.

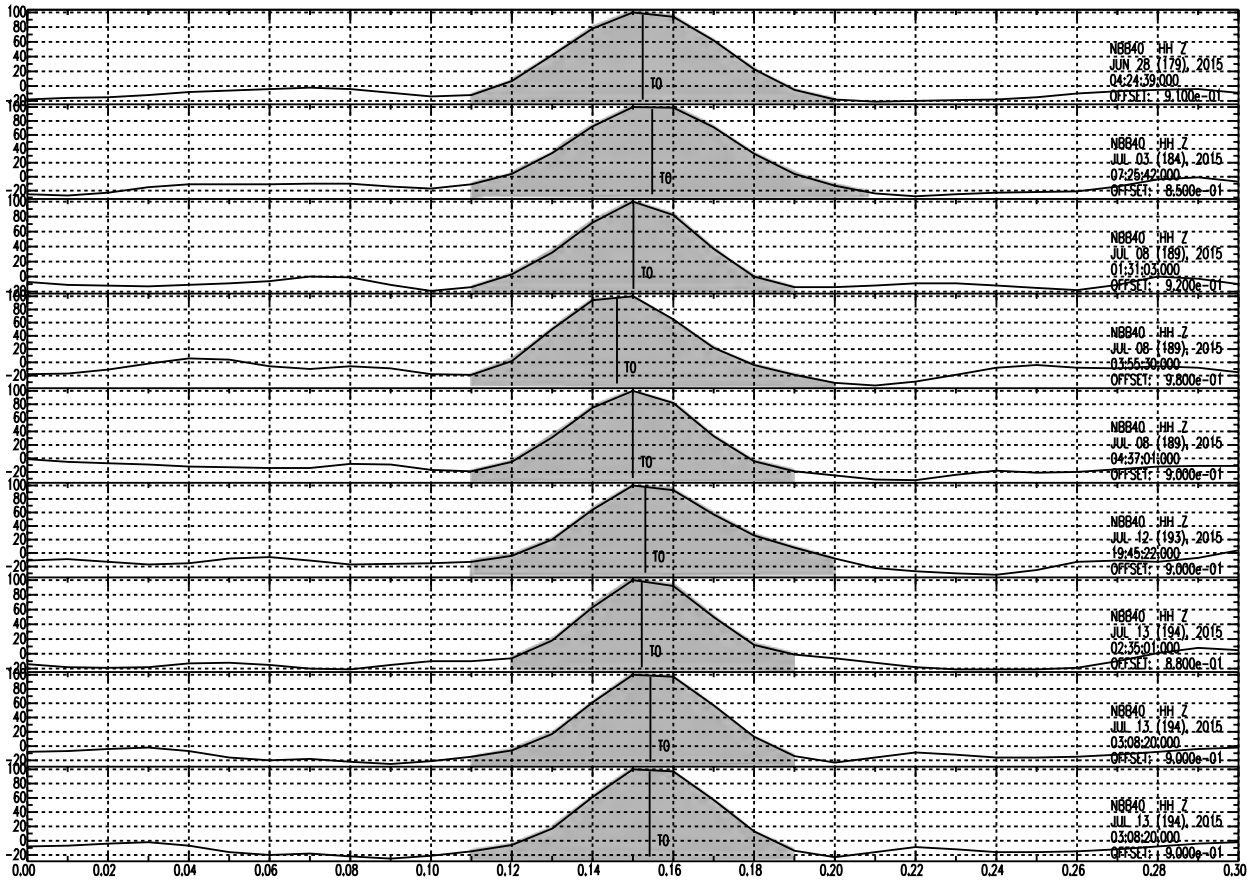

Figure 36. Nine source time functions deconvolved from event 7 occurring 13 July 2015 and recorded at vertical component on station NBB40. Duration is measured within the grey area and an average duration of 0.09 is estimated. For demonstration purposes, the waveforms are aligned at their peaks and normalized according to maximum amplitude.

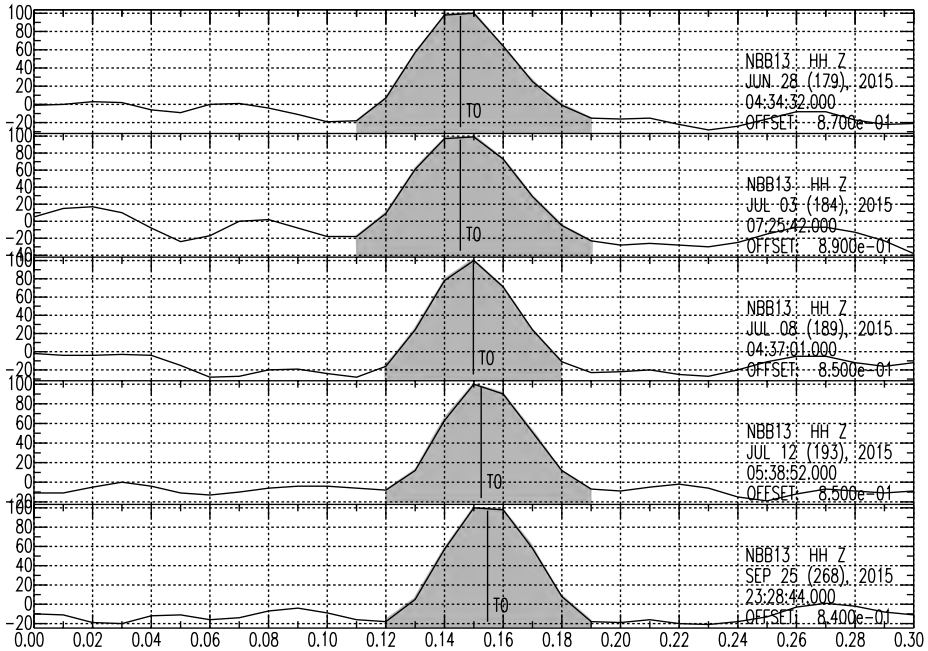

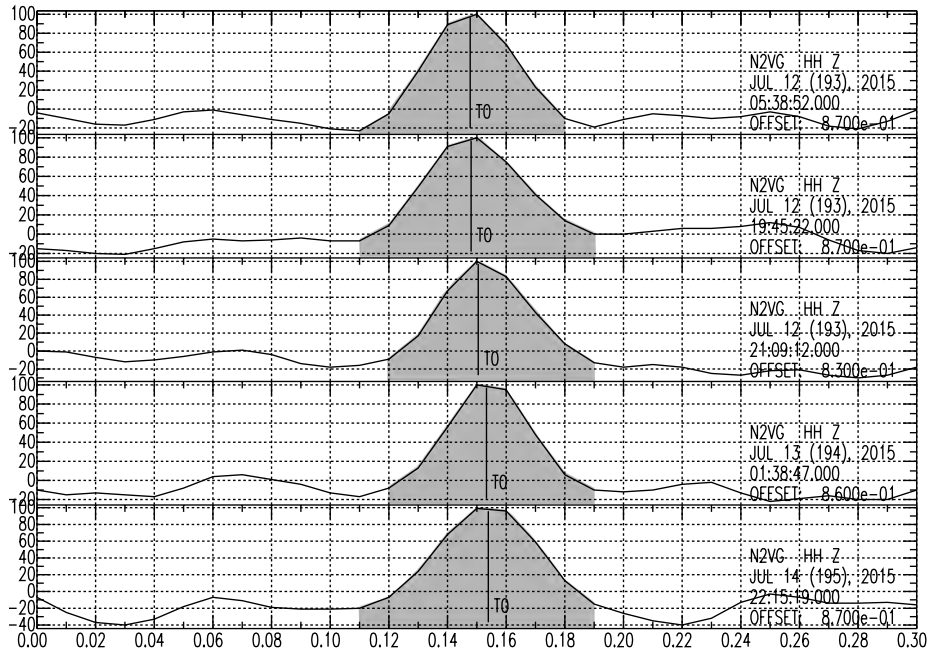

Figure 37. The source time function of event 9 on 14 July 2015, which shows the consistency of source time duration for stations NBB13 and N2VG. The onset can easily be measured from first to second zero crossing. The event was deconvolved with five smaller mangnitude events located within the same cluster. The average source duration for five stations is 0.07 seconds.

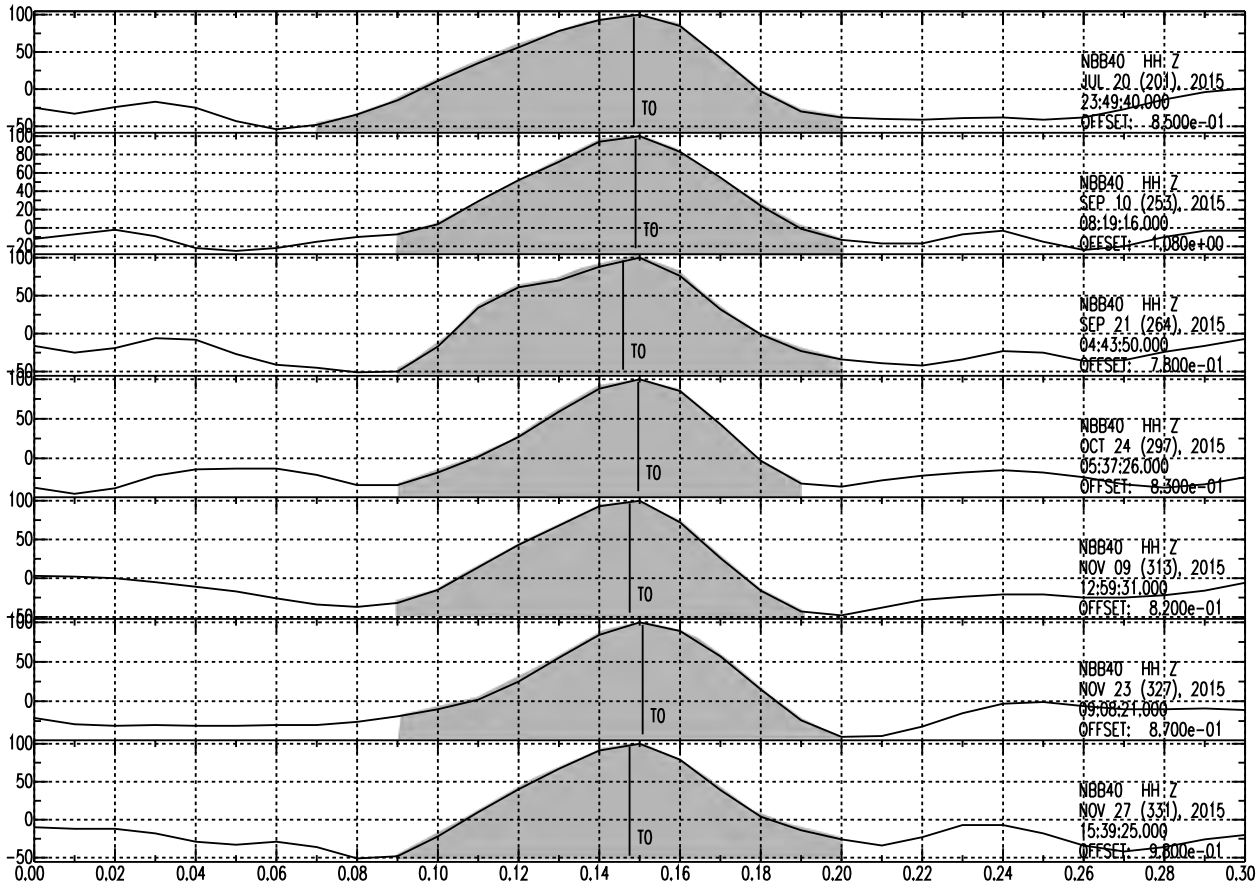

Figure 38. Seven deconvolved source time functions of event 1 on 26 November 2015. The result is compared to three stations and gives an average duration of 0.10 seconds.

4.3.3 Source parameters

A spectral analysis is carried out in SEISAN to determine seismic moment (M_0), corner frequency (f_c), source radius (r), stress drop (σ), and moment magnitude (M_W). An automatic spectral fit is selected using the autofit option, which tries to fit the Brune spectrum to the observed spectrum. The calculations of the the spectral parameters are based on the Brune (1970) model (Ottemöller et al., 2014). The resulting source parameters obtained from the spectral analysis are included in Table 5. Stress drop ranges from 0.1 to 0.7 bar for seismic moment of 1.2×10^{11} to 2.1×10^{12} Nm. These are average values based on several spectra and will be compared to the source parameters estimated from the source time functions obtained in the empirical Green's function analysis.

Once the source duration, τ, is measured, it can be converted into an estimate of the source radius following Boatwright (1980) that assumes a circular fault model

$$r = \frac{\tau_{1/2}\, v}{1 - \left(\frac{v}{c}\right) \sin\theta}$$

where source radius, r, is related to the rise time, $\tau_{1/2}$ (assumed to be half the total duration). v is the rupture velocity assumed to be 0.8β (2.72 km/sec), c is the S-wave velocity and θ is the take off angle with respect to the fault normal, where an average θ of 45° is assumed.

Then, using the formula of Eshelby (1957) the static stress drop is calculated as

$$\Delta\sigma = \frac{7}{16} \frac{M_0}{r^3}$$

This results in stress drop values from 0.05 to 0.4 bar for seismic moment of 1.2×10^{11} to 2.1×10^{12} Nm, which are consistent with the values from the spectral analysis (Table 5).

As an alternative to Boatwright (1980) source model, the source time duration can be converted into corner frequency using $f_c = \frac{2}{\pi\tau}$ (Lay and Wallace, 1995). Source radius can then be estimated as

$$r = 0.37v/f_c$$

where v is the S-wave velocity and f_C is the corner frequency. The value 0.37 is the κ_S factor for S-waves (Brune, 1970). The estimated source parameter values using these formulas are presented in Table 6 and shows that for the same seismic moment values, the calculated stress drop seem to be slightly higher compared to those obtained in the previous case and compared to the spectral values. However, the stress drops are still quite low, ranging from 0.2 to 1.6 bar from smallest to largest magnitude.

Table 5: Source parameters obtained from the spectral analysis, which can be compared to the estimates made by converting source duration into source dimension following Boatwright (1980) model.

Event	Date (ddmmyyyy)	Time (hhmm)	Lat (°N)	Lon (°E)	Depth (km)	M_L	τ (s)	r (km)	σ (bars)	M_0 (Nm)	f_{c-spec} (Hz)	r_{spec} (km)	σ_{spec} (bar)	M_w
1	26112015	0032	66.6278	13.3657	8.105	1.7	0.10	0.31	0.3	1.8E12	4.03	0.33	0.2	2.0
2	16112015	0119	66.6291	13.3735	7.084	1.3	0.08	0.25	0.2	5.8E11	6.13	0.23	0.4	1.6
3	20122015	1723	66.6333	13.3737	6.755	1.3	0.08	0.25	0.1	4.8E11	6.74	0.20	0.3	1.5
4	28032016	1453	66.6337	13.3736	5.850	1.2	0.07	0.22	0.2	4.5E11	4.89	0.22	0.2	1.6
5	03112015	1648	66.6361	13.4214	7.473	1.0	0.06	0.18	0.1	1.3E11	6.97	0.17	0.1	1.3
6	25102015	0132	66.6267	13.3769	6.476	1.0	0.07	0.22	0.05	1.2E11	9.07	0.13	0.2	1.2
7	13072015	0258	66.6232	13.3515	7.198	1.8	0.09	0.28	0.4	2.1E12	4.88	0.30	0.7	2.0
8	08072015	0356	66.6253	13.3694	5.923	1.1	0.06	0.18	0.2	2.7E11	7.70	0.17	0.2	1.3
9	14072015	2149	66.6248	13.3587	6.757	1.1	0.07	0.22	0.1	3.4E11	8.22	0.25	0.5	1.5
10	03102015	1828	67.7851	14.8671	8.344	1.4	0.08	0.25	0.1	4.2E11	5.28	0.21	0.4	1.7
11	20072015	1329	66.6470	13.4568	7.901	1.0	0.07	0.22	0.1	2.5E11	7.75	0.18	0.3	1.5

Table 6: Source parameter estimates based on the conversion of source time duration into corner frequency following Lay and Wallace (1995).

Event	Date (ddmmyyyy)	Time (hhmm)	Lat (°N)	Lon (°E)	Depth (km)	M_L	τ (s)	f_c (Hz)	r (km)	σ (bars)	M_0 (Nm)	f_{c-spec} (Hz)	r_{spec} (km)	σ_{spec} (bar)	M_w
1	26112015	0032	66.6278	13.3657	8.105	1.7	0.10	6.37	0.20	1.0	1.8E12	4.03	0.33	0.2	2.0
2	16112015	0119	66.6291	13.3735	7.084	1.3	0.08	7.95	0.16	0.6	5.8E11	6.13	0.23	0.4	1.6
3	20122015	1723	66.6333	13.3737	6.755	1.3	0.08	7.95	0.16	0.5	4.8E11	6.74	0.20	0.3	1.5
4	28032016	1453	66.6337	13.3736	5.850	1.2	0.07	9.09	0.14	0.7	4.5E11	4.89	0.22	0.2	1.6
5	03112015	1648	66.6361	13.4214	7.473	1.0	0.06	10.6	0.12	0.3	1.3E11	6.97	0.17	0.1	1.3
6	25102015	0132	66.6267	13.3769	6.476	1.0	0.07	9.09	0.13	0.2	1.2E11	9.07	0.13	0.2	1.2
7	13072015	0258	66.6232	13.3515	7.198	1.8	0.09	7.07	0.18	1.6	2.1E12	4.88	0.30	0.7	2.0
8	08072015	0356	66.6253	13.3694	5.923	1.1	0.06	10.6	0.12	0.7	2.7E11	7.70	0.17	0.2	1.3
9	14072015	2149	66.6248	13.3587	6.757	1.1	0.07	9.09	0.14	0.5	3.4E11	8.22	0.25	0.5	1.5
10	03102015	1828	67.7851	14.8671	8.344	1.4	0.08	7.95	0.16	0.4	4.2E11	5.28	0.21	0.4	1.7
11	20072015	1329	66.6470	13.4568	7.901	1.0	0.07	9.09	0.14	0.4	2.5E11	7.75	0.18	0.3	1.5

4.3.4 Discussion

In this work source parameters of earthquakes in the Nordland area have been determined using the empirical Green's function method. Smaller events are treated as EGFs of a larger event of interest. Given that the master

event and the EGFs are collocated events of different size and recorded at a common station, it is assumed that the effects from path, site and station are removed from the seismogram of the larger event, and that it is the source time function of the master event that is obtained.

Applying the empirical Green's function method, earthquakes with seismic moment of 1.2×10^{11} to 2.1×10^{12} Nm appear to have low stress drop of 0.05 to 0.4 bar following the formula of Boatwright (1980), where source duration is used to estimate source radius. When source duration is first converted into corner frequency using the relation of Lay and Wallace (1995), stress drop are ranging from 0.2 to 1.6 bar. The latter gives slightly smaller source radius, which results in larger stress drop as it is inversely proportional to the cube of source radius according to the model of Eshelby (1957). In addition, source radius and stress drop are estimated from spectral methods. Source radius in the range from 0.13 to 0.33 km and stress drop from 0.1 to 0.7 bar were found. These values are comparable to those found in the first attempt where source radius is estimated using the source duration directly and indicate that the empirical Green's function approach is viable.

However, it is worth noting the fairly large uncertainties in stress drop estimates which can be determined within a factor of 2-3 (Stein and Wysession, 2003). There is also some uncertainty related to the seismic moment estimates and the source durations, which at times were difficult to determine because of noise. Considering the tectonic environment, it is interesting with such low stress drop values in this area. Unfortunately, no events above magnitude 1.8 had high enough correlation to be included in the EGF analysis and this limited range of magnitudes makes it difficult to consider scaling relationships of the earthquakes in Nordland. However, future work could make an attempt of including larger earthquakes in the analysis and derive stress drop values from source spectra in order to address source scaling and earthquake self-similarity of smaller magnitude earthquakes.

4.4 Joint-inversion of receiver functions and apparent S-velocities for the crustal structure (Anne Drottning)

The goal of this work was to estimate crustal structure and S-velocities for the seismic stations within the Nordland area by inversion of receiver functions and polarization data.

4.4.1 Data

The stations used in the inversion are shown in Figure 39. Most of the stations were deployed between 2013 and 2016 as a part of the NEONOR project. The data for each station were downloaded through the GLImER database on the form of already processed receiver functions.

The stations vary from being temporary or permanent, and so the data recorded at each station is of various quality as well. To account for this and avoid recorded signals which disturbed the stacked receiver function, some events were removed.

The criteria to remove the events were:

i. If the transverse component of the recorded event indicated anisotropy or dipping layers.
ii. If the radial receiver function consisted of mainly noise.
iii. If the incident peak was not clear.

If the number of events remaining for the station is less than 5, the station is ignored in the inversion as this will not give a stacked receiver function of high enough quality.

One of the stations which were most improved through this quality check was N2BR, located in the North-Eastern part of Lofoten. A comparison of the two data types before and after the quality check is shown in Figure 40. From the stacked radial receiver function, a periodic noise was removed through the quality check. When looking at the radial receiver function up to 10 seconds there is a clear difference as well. Here the incident peak is stronger after the quality check, and the largest peak after this is also changed.

For the apparent S-velocity, the updated data is stable for longer periods than before. This all shows the importance of the quality check.

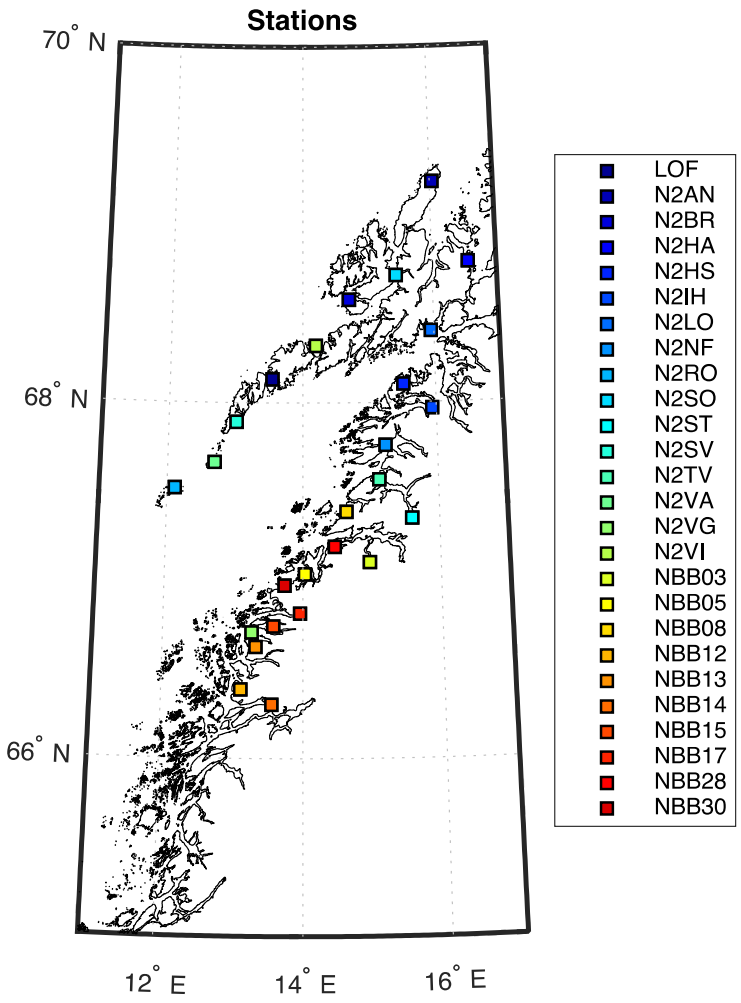

Figure 39. Map showing the location for the stations used in the inversion

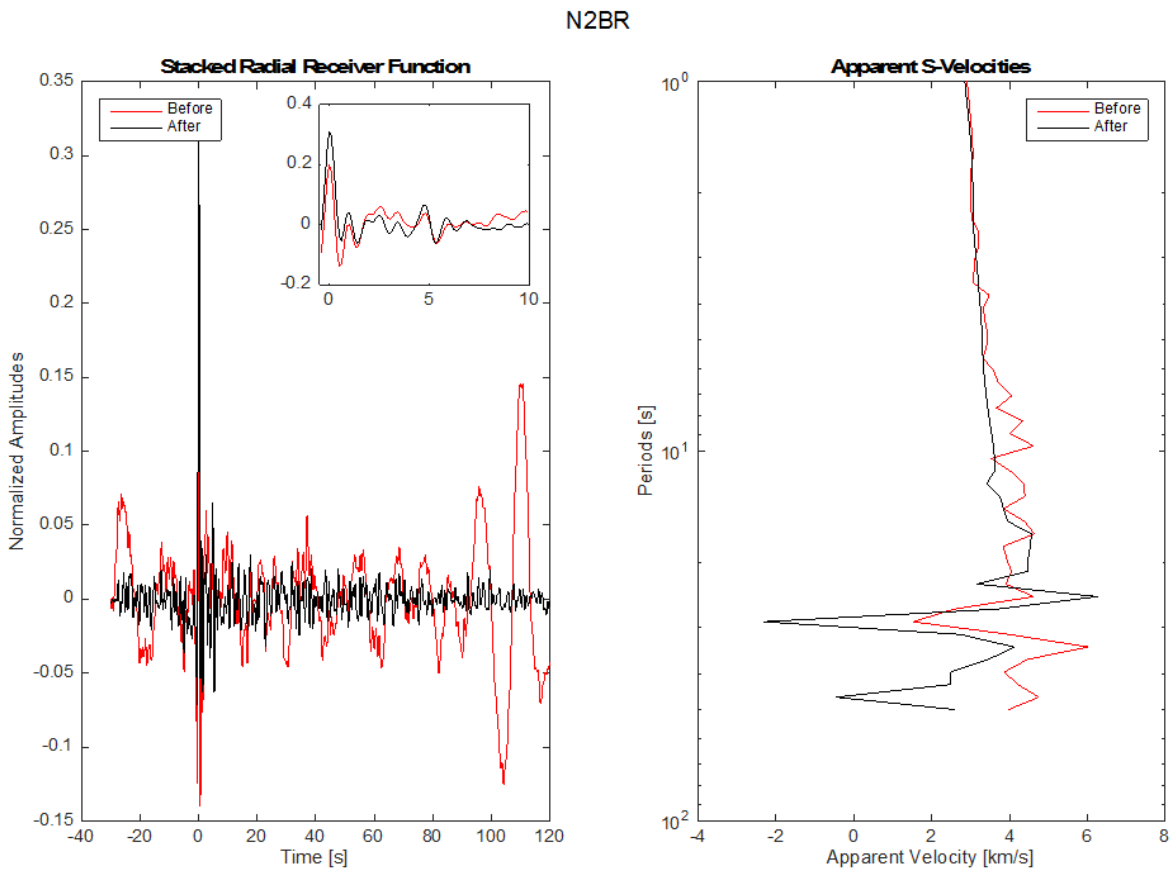

Figure 40. The data for N2BR before and after the quality check was performed. Before is marked in red, after in black. Also included is a zoomed in comparison of the stacked radial receiver function from -0.5 s to 10 s.

An important aspect of this quality check is how it affects the inversion results. This is shown in Figure 41. This figure shows how the velocity structures differ. The velocities are well resolved in both cases, while the Moho depths are resolved differently. Besides this, most of the same layer depths are estimated.

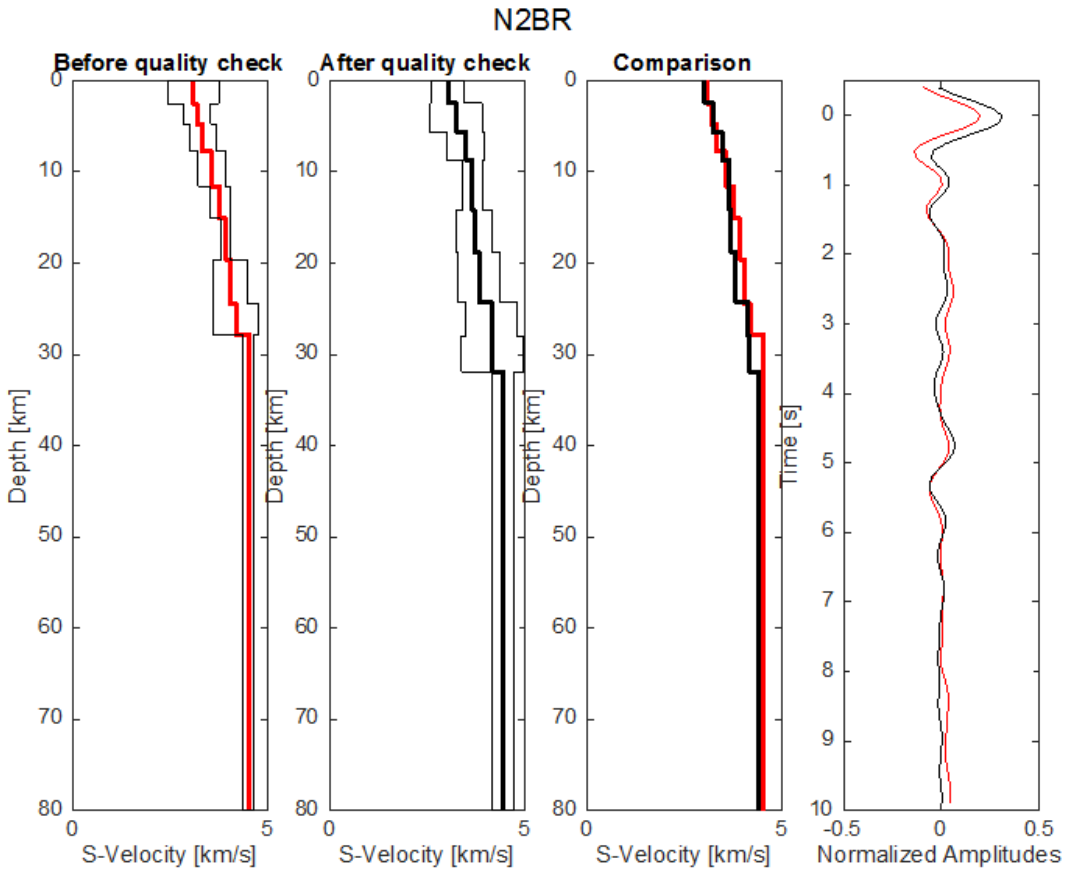

Figure 41. Inversion results for N2BR before and after the quality check. Velocity structures in black shows the results before, and red shows after. Also included are the error bars. To the furthest right, the stacked radial receiver function is shown.

4.4.2 Methods

The joint-inversion finds the iterative, linearized, weighted least squares solution described by, amongst others, Tarantola and Valette (1982). The two data types used in the inversion are the stacked receiver function and the apparent S-velocity. The apparent S-velocity is estimated following the method described by Svenningsen and Jacobsen (2007).

By inverting the data, the S-velocities and delay times are estimated. The delay times and velocities are used to estimate the corresponding layer depths following Equation Nr.2 of Zhu and Kanamori (2000). Different configurations of the inversion affect the results. Through previous synthetic testing (not included here) the following configurations were deemed best fitting:

a. Equal weights of the data types, meaning that both data types are fitted as well as possible
b. Fixed parametrization of eight layers over the half-space.

For the inversion, multiple starting models were used where one S-velocity structure were estimated based on each. 33 starting models were used, as displayed in Figure 4. The starting models can be categorized into four basic structures; based on the observations, global models, constant velocity and constant velocities in two layers.

The starting model based on the observations uses the delay times picked from the stacked receiver function, and crustal velocities from the apparent S-velocities. The global models used are CRUST1.0[1] and iasp91[2], with additional layers included for some. The fixed velocity starting models range from 4 km/s to 5 km/s with a step of 0.1, while for the fixed velocities two layers are used with different crustal and mantle velocities. For both these, the Moho depth is set to be random and ranging between 20 and 60 km.

[1] Downloaded for free at https://igppweb.ucsd.edu/~gabi/crust1.html
[2] Downloaded for free at http://ds.iris.edu/spud/earthmodel/9991809

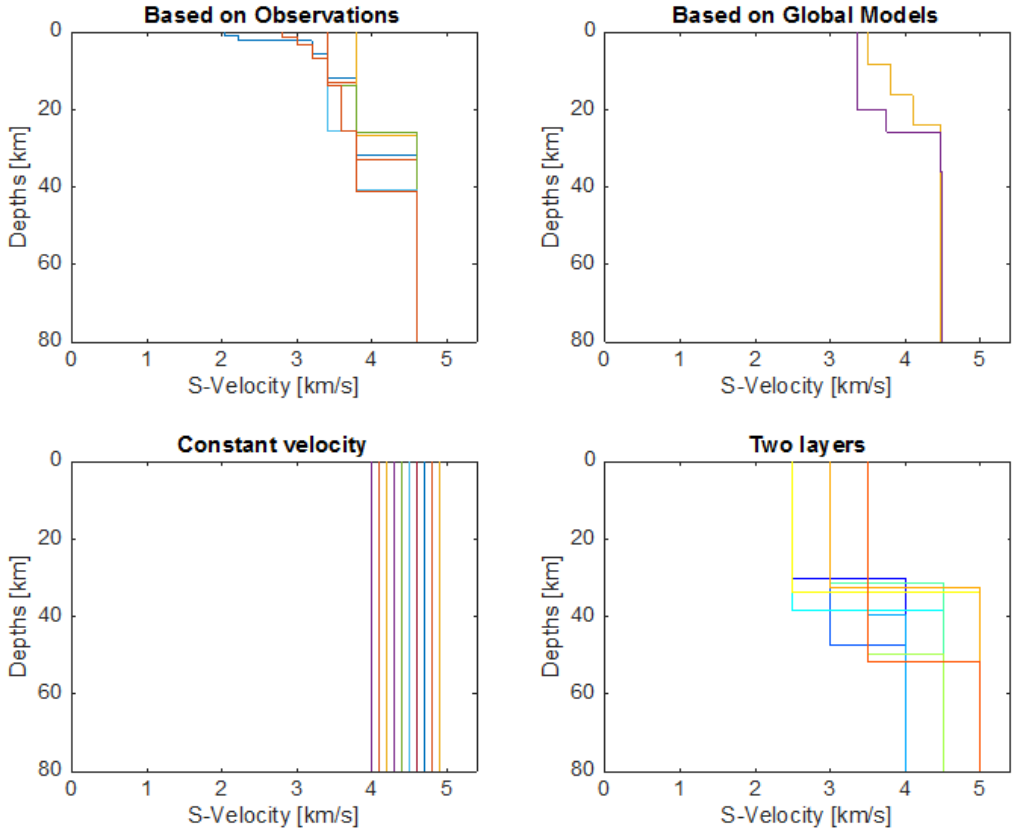

Figure 42. The starting models used in the inversion method. The starting models are sorted depending on what they are rooted in.

4.4.3 Results

For each station, 33 velocity structures are estimated. Before taking a weighted mean of these, they are quality checked following four criteria.

1. The mantle velocity must be larger or equal to 4 km/s.
2. The resolved structure can not contain any layers below 80 km (as the inversion is made for resolving structures down to maximum 80 km)
3. The error must be lower than the mean of all the errors.
4. The S-velocity of the shallowest layer must be 2 km/s or larger.

All the resulting velocity structures with error bars are shown in Figure 43. The resulting velocity structure is taken as the weighted mean of the results, with the error bars based on the standard deviation.

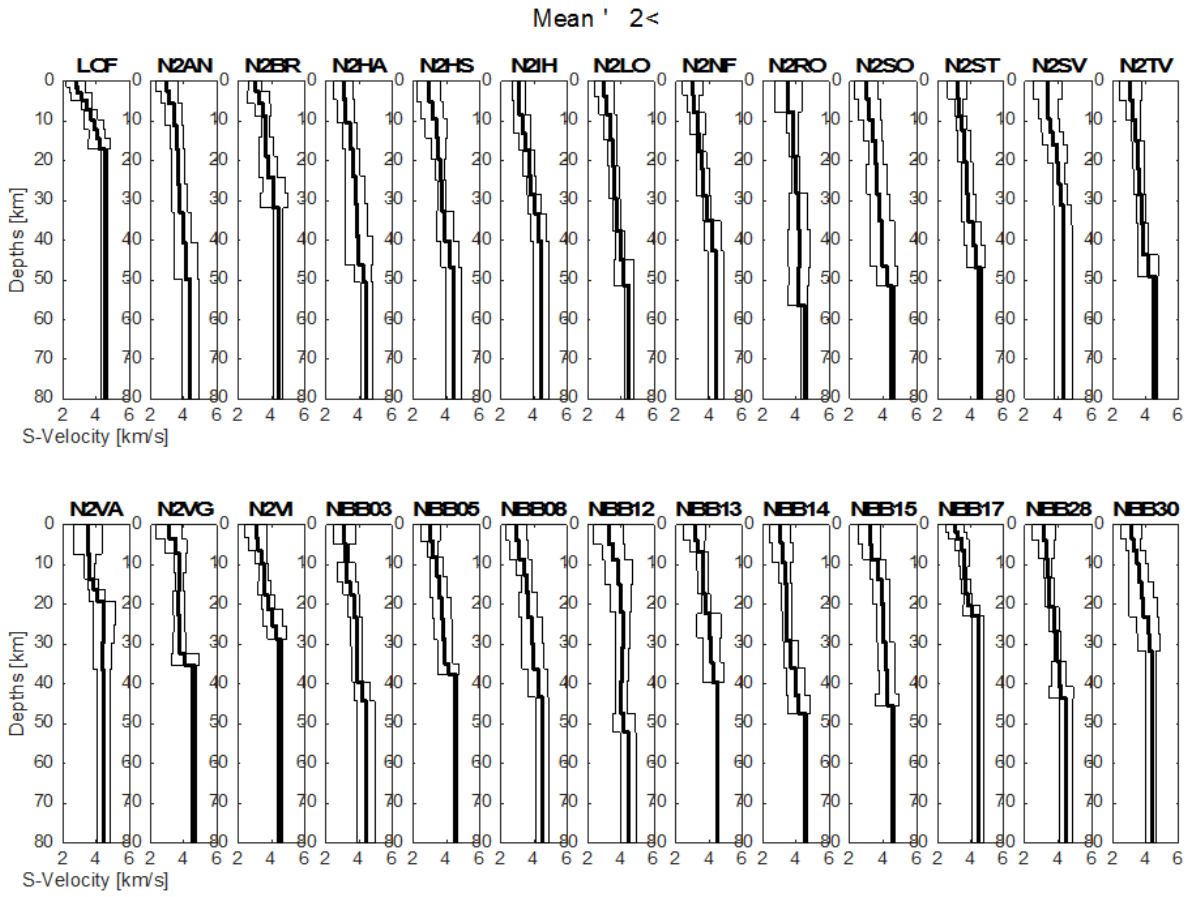

Figure 43. Velocity structures with error bars for all the stations

From each of these structures, the Moho depth was picked manually as the strongest jump in velocity where the lower velocity was in the order of mantle velocity. The picked Moho depths in the area are displayed as a Moho map in Figure 44. Shallowest Moho depths are in the southern part of Lofoten. From this point and towards the North-East the Moho rapidly deepens. It also deepens towards the coast. Along the Northern Norwegian coast, the Moho depths also experiences local changes.

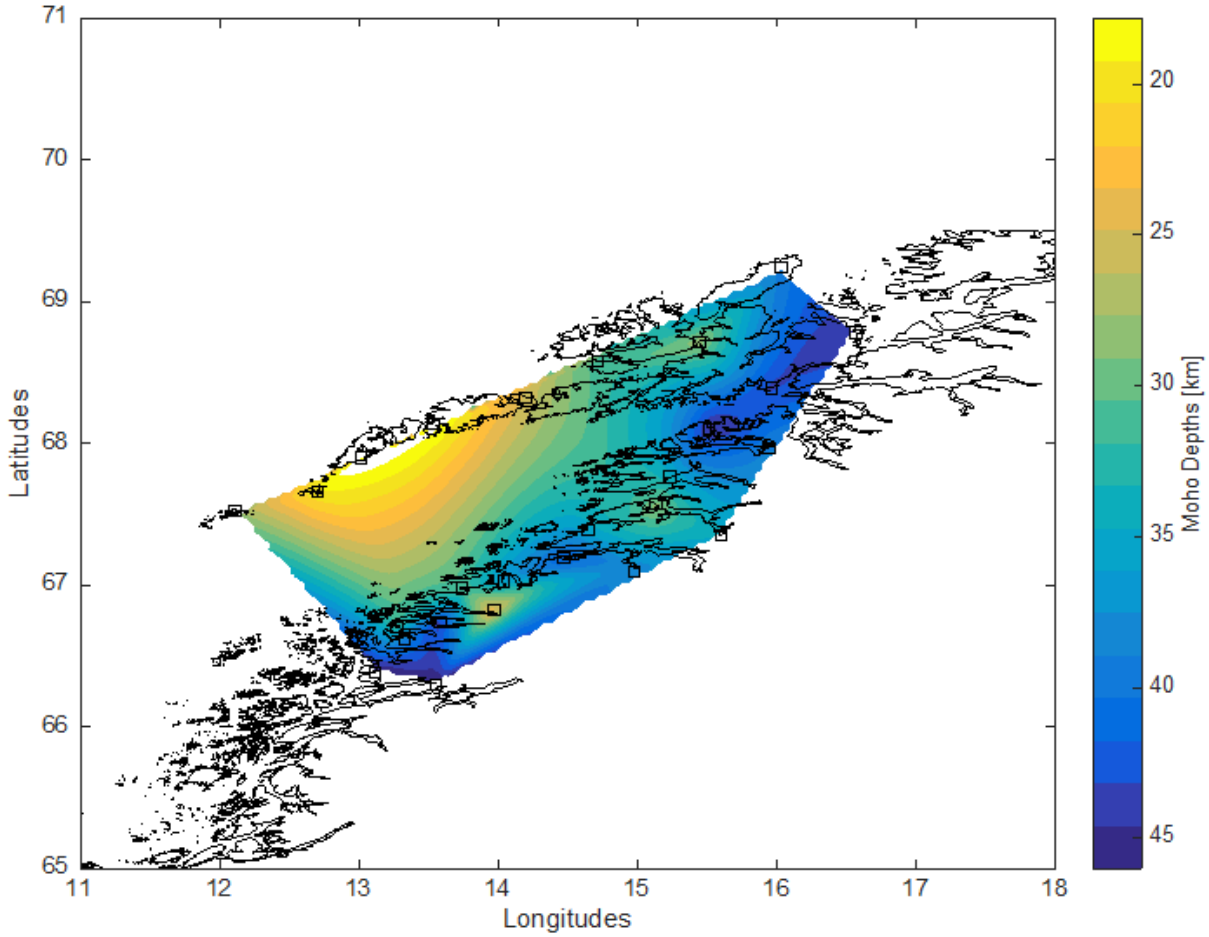

Figure 44. Moho map of the Nordland area based on the velocity structures estimated from the inversion method.

To examine the Moho developments, two profiles were used, as shown in Figure 45. Profile A focuses on the development of the crustal and mantle S-velocities along Lofoten from the Southern part towards the North-East. Profile B shows the development along the coast.

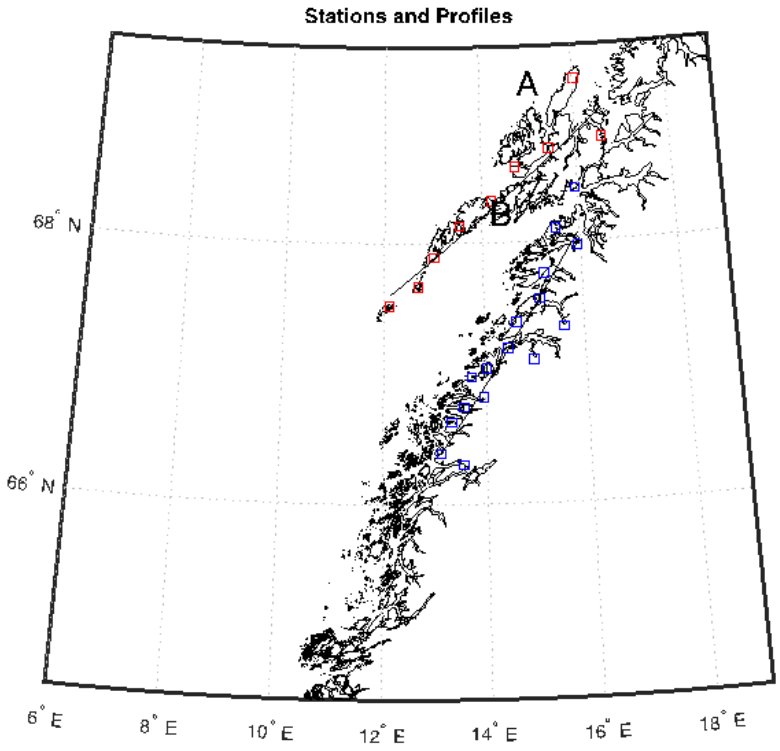

Figure 45. The profiles and their corresponding stations used for further examinations. The stations included in Profile A are displayed in red and the stations used in Profile B are displayed in blue.

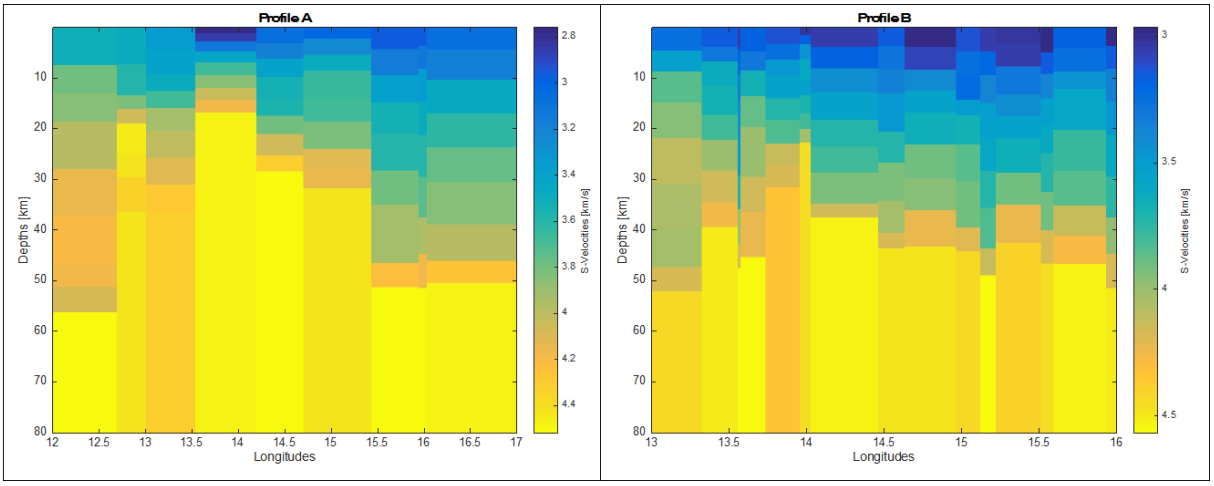

Figure 46. Crustal and mantle S-velocities down to 80 km along each of the profiles. The structures are sorted according to increasing longitude.

The S-velocities through the crust down to 80 km along the profiles are shown in Figure 46. Profile A in Figure 46 shows high S-velocities in the South-Western part of the profile, with a rapid deepening of the high S-velocities towards North-East. This can indicate a rapid deepening of the Moho depth towards the North-East with a localized Moho minimum beneath the Southern part of Lofoten.

Profile B shows a less varying depth of the high velocities, with more localized variations towards the North-East. This indicates a more stable crust affected by the local geology.

5. Technical issues with stations

This is part is describing technical issues we observed during the project. Collection of stations was finished 21.5.2016 (UiB) except for station N2VG which was collected later in June 2016. The technical problems influenced completeness of data (check Figures 4-7).

5.1 Digitizers

5.1.1 Nanometrics

There were 6 stations running on Nanometrics system (Taurus units). Most of them were running without any problems delivering almost complete data. There were some issues though:

N2HA - there was an error on internal 8GB CF memory on 9.6.2015 and the STORE (ringbuffer system) had to be moved from internal to external 32 GB CF 22.8.2015 (performed remotely by Suzan Kowalski from Nanometrics). Since then running fine.

N2LO - incomplete data between 1.-22.4. 2015 (about 50%) but it is not clear why

N2VG - station was deployed in late April 2015. There was an issue with broken battery charger in October 2015 (similar problem occurred N2HA before). The unreliable charger was replaced but Taurus haven't started again and had to be replaced by new unit in January 2016.

5.1.2 EarthData

The EDR-210 digitizers had problem with recording incomplete data on local storage. Data from online stations were sometimes more complete then from local storage. This problem was mostly solved by installing new firmware. Two upgrades of the firmware were done overcome data recording issues. The latest firmware version was V3.31. The gaps were usually from few minutes to several hours. Some problems remained.

N2DI - during merging offline and online data was found that some files are corrupted. The issue was found during converting into SeisComp archive using the mseed2mseed (GIPP tools). The issue was discussed with Christopher Lendl (GFZ, GIPP tools developer). It seems that random part of memory was dumped into the mseed file instead of the seismic signal.

N2VI - data gap between 23.2.-6.6.2015 in offline data (local storage).

N2IH - data until 10.1.2016 (also 1.5h from 26.1.), restarted by itself 19.5.2016 9:22. No indication of low battery voltage (status from aux3 files). Digitizers (at all stations) were power-supplied via battery which should cover short term power outages (up to 15 hours).

NBB03 - many days with incomplete data as before the firmware upgrade. The firmware upgrade from January 2015 didn't help.

NBB28 - 6 days of data missing after day 341 (in 2015)

NBB29 - data until 04.03.2016, missing days 65-69, 71-88, 90-end. Voltage was always between 12.2V and 13.8V (status from aux3 files). EDR failure.

We also observed problem when connecting remotely to the digitizer. When the external disk was switched to always available, the unit stopped recording. It also did not work while "usba" was mounted (changed via web interface).

5.2 Power supply

N2VA - digitizer was down due to low voltage, charger in err 5 mode, data until 28.3.2016. There were some construction works (new electric cables and new distribution box) on the wall just above the sensor (started around 15.3.2016). The box with digitizer was moved to slightly new position. Not clear why the battery charger went into error mode.

N2VI - data missing from days 057-112 (26.2.-21.4.2016) – probably due to power outage. The voltage dropped down to 11V at 25.2.2016 01:26 within one minute (from initial 14V) and was slowly decreasing down to 9.6V when EDR turned off (25.2.2016 17:24). The battery was able to cover ca 16 hours.

5.3 Telemetry

In November 2015 the ICE routers were replaced by its new version. After replacement, there were still connectivity issues related to firmware at the new ICE routers. Router went offline once it lost connection and was not able to reconnect. Firmware upgrade was performed by Øyvind Natvik remotely in the second half of January 2016 at all routers but some of them still had problems (N2IH, N2VI).

6. Attachments

- Attachment 1: PSD_allStations-NEONOR2.pdf
- Attachment 2: NEONOR2-EQlocations_1278ev_noExplos.out
- Attachment 3: NEONOR2-seismicity-FinalReport_2018-01-04.kmz
- Attachment 4: NEONOR2-relocations-hypoDD.reloc

7. References

Ammon, C. J. (1991), 'The Isolation of Receiver Effects from Teleseismic P Waveforms', Bulletin of the Seismological Society of America 81(6), 2504–2510.

Boatwright, J. (1980), 'A spectral theory for circular seismic sources; simple estimates of source dimension, dynamic stress drop, and radiated seismic energy', Bulletin of the Seismological Society of America 70, 1–27.

Brune, J. N. (1970), 'Tectonic Stress and the Spectra of Seismic Shear Waves from Earth- quakes', Journal of Geophysical Research 75(26), 4997–5009.

Bungum, H., Olesen, O., Pascal, C., Gibbons, S., Lindholm, C. and Vestøl, O. (2010), 'To what extent is the present seismicity of Norway driven by post-glacial rebound?', Journal of Geological Society 167, 373–384.

Clayton, R. W. and Wiggins, R. A. (1976), 'Source shape estimation and deconvolution of teleseismic bodywaves', Geophys. J. R. Astron Soc. 47, 151–177.

Eshelby, J. D. (1957), 'The determination of the elastic field of an ellipsiodal inclusion and related problems', Proceedings of the Royal Society of London A: Mathematical, Physical and Engineering Sciences 241(1226), 376–396.

Fejerskov, M. and Lindholm, C. D. (2000), Crustal stress in and around Norway: an evaluation of stress-generating mechanisms, in A. e. a. Nødttvedt, ed., 'Dynamics of the Norwegian Margin', Vol. Special Publications 167, Geological Society of London, pp. 451–467.

Fojtíková, L., & Zahradník, J. (2014). A New Strategy for Weak Events in Sparse Networks: The First-Motion Polarity Solutions Constrained by Single-Station Waveform Inversion. Seismological Research Letters, 85(6), 1265–1274. doi:10.1785/0220140072

Hardebeck, J. L. and Shearer, P. M. (2002). A new method for determining first motion focal mechanisms. Bull. Seismol. Soc. Am., 92:2264–2276.

Hardebeck, J. L., & Shearer, P. M. (2003). Using S/P Amplitude Ratios to Constrain the Focal Mechanisms of Small Earthquakes. Bulletin of the Seismological Society of America, 93(6), 2434–2444. doi:10.1785/0120020236

Havskov J., and Bungum, H. (1987): Source parameters for earthquakes in the northern North Sea. Norsk Geologisk Tidskrift,Vol.67, pp 51-58.

Havskov, J. and Bungum, H. (1987), 'Source parameters for earthquakes in the northern North Sea', Norsk Geologisk Tidsskrift 67, 51–58.

Havskov, J., & Ottemöller, L. (1999). SeisAn earthquake analysis software. Seismological Research Letters, 70(5), 532–534. doi:10.1785/gssrl.70.5.532

Hicks, E. C., Bungum, H. and Lindholm, C. D. (2000), 'Seismic activity, inferred crustal stresses and seismotectonics in the Rana region, Northern Norway', Quaternary Science Reviews 19, 1423–1436.

Jechumtálová, Z., & Šílený, J. (2005). Amplitude ratios for complete moment tensor retrieval. Geophysical Research Letters, 32(22), 1–4. doi:10.1029/2005GL023967

Kisslinger, C. (1980). Evaluation of S to P amplitude ratios for determining focal mechanisms from regional network observations. Bull. Seism. Soc. Am. 70, 999-1014.

Lay, T. and Wallace, T. C. (1995), Modern Global Seismology, Vol. 58, Academic Press.

Mueller, C. S. (1985), 'Source pulse enhancement by deconvolution of an empirical Green's function', Geophysical Research Letters 12(1), 33–36.

Ottemöller, L., Voss, P. and Havskov, J. (2014), Seisan earthquake analysis software for Windows, Solaris, Linux and macOSX.

Peterson, J., 1993. Observations and modelling of background seismic noise. Open-file report 93-322, U. S. Geological Survey, Albuquerque, New Mexico.

Rau, R.-J., Wu, F. T., & Shin, T.-C. (1996). Regional Network Focal Mechanism Determination Using 3D Velocity Model and SH/P Amplitude Ratio. Bulletin of the Seismological Society of America, 86(5), 1270–1283. Retrieved from http://www.bssaonline.org/content/86/5/1270.short

Reasenberg, P. and Oppenheimer, D. (1985). Fpfit, fpplot, and fppage: Fortran computer programs for calculating and displaying earthquake fault plane solutions. Technical report, U.S. Geol. Survey.

Rögnvaldsson, S. T., & Slunga, R. (1993). ROUTINE FAULT PLANE SOLUTIONS FOR LOCAL NETWORKS: A TEST WITH SYNTHETIC DATA. Bulletin of the Seismological Society of America, 83(4), 1232–1247.

Schaff, D. P., Bokelmann, G. H. R., Ellsworth, W. L., Zanzerkia, E., Waldhauser, F. and Beroza, G. C. (2004), 'Optimizing Correlation Techniques for Improved Earthquake Location', Bulletin of the Seismological Society of America 94(2), 705–721.

Šílený, J. (1989). The mechanism of small mining tremors from amplitude inversion. Pure Appl. Geophys. 129, 309-324.

Slunga, R. (1981). Earthquake source mechanism determination by use of body-wave amplitudes—an application to Swedish earthquakes. Bulletin of the Seismological Society of America, 71(I), 25–35. Retrieved from http://bssa.geoscienceworld.org/content/71/1/25.short

Snoke, J. A. (2003). FOCMEC: FOcal MEChanism determinations, in International Handbook of Earthquake and Engineering Seismology, Chapter 85.12,W. H. K. Lee, H. Kanamori, P. C. Jennings, and C. Kisslinger (Editors), Academic Press, San Diego, California.

Stein, S. and Wysession, M. (2003), An Introduction to Seismology, Earthquakes, and Earth Structure, Blackwell Publishing.

Suetsugu, D. (1998). Practice on source mechanism, iisee lecture note. Technical report, Tsukuba, Japan.

Svenningsen, L. and Jacobsen, B. H. (2007). Absolute S-velocity estimation from receiver functions. Geophysical Journal International, 170(3):1089-1094

Tarantola, A and Valette, B. (1982). Generalized non-linear inverse problems solved using the least-squares criterion. Reviews of Geophysics, 20(2):219-232

Vavryčuk, V. (2011). Tensile earthquakes: Theory, modeling, and inversion, J. Geophys. Res. 116, no. B12320, doi: 10.1029/ 2011JB008770.

Waldhauser, F. (2001), 'hypoDD - A Program to Compute Double-Differences Hypocenter Locations', U.S Geol. Survey, Menlo Park, CA .

Waldhauser, F. and Ellsworth, W. L. (2000), 'A double-difference earthquake location algorithm: Method and application to the northern hayward fault, California', Bulletin of the Seismological Society of America 90(6), 1353–1368.

Zahradník, J., J. Janský, V. Vavryčuk, and J. Zedník (1989). Focal mechanisms of selected events of the West Bohemia earthquake swarm 1985/86 constrained by P-wave amplitudes. Rev. de Geofysica, 45, 217-230.

Zhu, L. P. and Kanamori, H. (2000). Moho depth variation in Southern California from teleseismic receiver functions. Journal of Geophysical Research-Solid Earth, 150(B2):2969-2980.

8. Annexes

8.1 Appendix 1 – List of fault plane solutions

Procedure and analysis of focal mechanisms is described in chapter Focal mechanisms (Jan Michálek).

Table is sorted in time and includes all earthquakes for which the fault plane solutions (FPS) were analyzed. Only earthquakes with A and B quality should be considered for further analysis. Qualities C and D are just for indication that the trial was made. Some C and D FPS angles are empty as there were too many not similar solutions. There are many solutions also for some A or B quality earthquakes but in such case all the solutions were very similar.

Description of columns:

Location … approximate location with respect to known places from map
Polarities … number of polarities used in FPS search
AmpRatios … number of amplitude ratios (SH/P) used in FPS search
AmpRatErr … number of allowed amplitude ratio errors in FPS search
Solutions … number of obtained FPS solutions (not indicated how similar they are)

Fault plane solutions of events recorded within NEONOR2 project

Date	Time	ML	Lat	Lon	Depth	Location	Strike	Dip	Rake	Quality	# Polarities	# AmpRatios	# AmpRatErr	# Solutions
2013-10-10	20:21:51	2.1	67.450	14.117	8.0	9km W of Landegode	43	51	-26	B	5	5	2	37
2014-01-09	21:33:12	2.7	68.014	10.490	12.0	100km W of Å	0	0	-98	D	5	1	0	125
2014-01-24	19:36:33	2.1	66.680	13.494	4.5	Tjong	144	66	-80	B	5	5	1	13
2014-03-03	05:09:44	1.5	68.424	15.368	29.9	18km NE of Digermulen	167	37	63	B	6	10	1	9
2014-03-07	21:36:52	2.7	66.948	13.405	3.5	Svenningen; 10km N of Meløy	187	20	-83	C	6	4	3	2
2014-04-12	10:42:20	1.7	66.462	13.366	5.9	12km SEE of Konsvik	47	26	-55	B	5	7	2	40
2014-04-29	06:04:32	1.7	67.353	13.759	3.7	28km W of Bodø	218	9	-62	B	5	13	4	5
2014-05-01	06:48:22	1.0	66.396	13.198	8.3	4km E of NBB12				D	3	4	0	254
2014-05-25	01:57:10	1.5	66.668	13.436	2.0	Tjongsfjord	203	67	77	B	5	6	2	20
2014-05-31	09:03:48	1.8	67.076	15.192	6.6	Skjerstafjorden	263	84	-83	B	5	9	0	3
2014-06-02	06:25:58	1.7	66.161	12.516	0.1	Dønna	175	21	60	B	6	4	0	7
2014-06-04	16:42:10	2.1	68.342	11.478	13.1	90km W of Leknes				D	4	0	0	500
2014-06-06	02:24:25	1.1	66.393	13.344	7.0	15km NE of STOK	192	54	-89	B	4	6	0	2

2014-06-06	21:42:23	1.1	66.665	13.461	2.0		205	64	86	C	4	7	2	9
2014-06-07	03:34:54	3.0	66.874	9.649	15.0	Bivrøst				D	7	0	0	500
2014-06-10	00:15:02	0.9	66.634	13.057	11.0	10km W of Jektvik				D	3	8	2	173
2014-06-14	15:52:09	1.9	66.662	13.447	6.9	Tjong	64	16	-28	B	5	7	0	5
2014-06-23	11:04:45	1.9	66.669	13.493	4.8	Tjong	202	30	-89	A	7	7	2	96
2014-07-09	06:47:03	1.9	66.861	9.775	12.6	Bivrøst				D	3			
2014-07-22	20:27:10	1.9	67.351	14.078	14.3	W of Bodo	336	8	-89	A	8	13	4	2
2014-10-13	22:20:24	1.1	68.085	15.723	19.1	16km NNW of Innhavet	355	24	65	B	7	12	2	4
2014-10-18	18:02:26	1.7	66.805	13.825	4.3	Glomfjorden				C	8	9	4	1
2014-12-03	05:38:17	1.2	67.876	19.095	20.7	60km NNE of SALU				D	4	0		
2014-12-10	07:32:15	2.6	66.915	12.835	5.6	37km NWW from Halsa	87	86	-85	B	7	9	2	63
2014-12-10	14:58:01	2.5	66.929	12.791	9.8		59	72	-84	B	6	8	3	5
2015-02-19	06:00:44	2.5	66.681	13.451	5.0	Tjong	25	78	-81	A	7	9	4	78
2015-02-24	17:41:35	1.6	66.687	13.411	7.1	Tjong				D	3			
2015-03-07	01:46:24	2.0	66.566	13.378	5.0	Melfjorden	223	24	-84	B	5	10	5	45

2015-04-11	03:13:30	2.6	66.654	13.430	4.8	Blok (Tjong)	34	37	-72	A	7	8	4	2
2015-04-14	06:07:09	2.1	66.643	13.432	5.0	Blok (Tjong)	41	67	-74	B	6	9	3	1
2015-04-16	05:12:31	2.4	66.643	13.427	5.0	Blok (Tjong)	338	48	-30	C	3	9	2	93
2015-04-17	05:18:11	1.0	67.633	14.485	9.3	30 km W of N2TV	10	72	90	A	6	16	8	1
2015-04-20	10:07:50	1.5	66.674	13.473	7.4	Tjong	229	84	82	B	3	8	1	9
2015-04-24	09:40:38	3.2	66.639	13.441	2.2	Blok (Tjong)	40	59	-75	B	7	8	3	39
2015-04-27	04:44:32	1.9	66.578	13.367	4.0	6km SSE of Jektvik	212	10	-89	B	5	8	2	14
2015-05-01	16:03:58	1.7	66.655	13.501	6.4	Tjongsfjorden	14	74	-81	B	6	8	2	10
2015-05-03	02:48:13	1.6	66.647	13.430	1.7	Blok (Tjong)	49	78	-79	A	6	7	2	4
2015-05-03	06:51:01	1.7	68.726	14.929	21.3	20km W of Sortland	40	78	88	B	7	10	2	1
2015-05-05	21:29:26	1.1	66.648	13.434	2.2	Blok (Tjong)	177	5	-67	C	4	6	2	14
2015-05-08	21:07:28	1.0	66.641	13.405	2.3	Blok (Tjong)	123	56	-82	C	4	9	3	52
2015-05-18	01:42:38	1.2	66.686	13.466	5.6	Tjong	192	12	-89	A	6	10	2	27
2015-05-19	13:06:02	1.8	66.666	13.502	5.5	Tjong	188	6	-89	B	5	10	2	1
2015-05-24	00:36:46	1.1	66.683	13.509	6.3	Tjong	210	16	-89	C	4	12	4	19

2015-05-25	18:05:01	0.9	67.961	14.403	3.6	35km W of STEI	31	80	86	C	5	10	5	1
2015-05-28	06:38:36	0.6	66.652	13.453	4.3	Blok (Tjong)	197	12	-79	C	4	5	0	46
2015-05-28	12:26:41	1.0	66.649	13.399	1.8	Blok (Tjong)	222	76	86	C	5	9	2	15
2015-05-29	09:28:42	1.8	66.641	13.423	2.0	Blok (Tjong)	308	28	-85	C	4	9	3	25
2015-06-07	16:31:32	1.2	66.649	13.458	5.6	Blok (Tjong)	184	14	-89	C	5	7	1	83
2015-06-12	00:10:52	1.4	66.642	13.437	1.8	Blok (Tjong)	357	82	-83	C	5	9	5	11
2015-06-12	03:27:44	0.7	66.643	13.477	3.3	Blok (Tjong)	24	74	-83	C	5	5	1	5
2015-06-18	04:02:12	0.8	66.853	12.851	5.0	23km NW from Vågaholmen	121	5	-67	C	4	9	3	12
2015-06-19	03:01:27	0.3	66.669	13.413	2.0	Tjongsfjorden	220	84	88	C	4	4	1	17
2015-06-20	05:32:50		66.995	13.165	15.0	20km NNW of Meløy	192	7	34	D	4	7	0	11
2015-06-21	04:28:01	0.6	66.671	13.505	3.9	Tjong	45	80	-87	B	6	9	4	5
2015-06-26	08:48:44	1.3	66.631	13.440	1.3	Blok (Tjong)	180	5	-89	C	5	9	2	65
2015-06-30	08:30:30	1.0	67.044	13.604	11.0	Reksøyan	154	74	-87	C	5	13	5	3
2015-07-01	00:36:40	0.6	66.663	13.522	6.5	Tjongsfjorden	233	10	0	C	4	6	1	17
2015-07-13	02:58:33	1.9	66.624	13.360	8.7	Blok (Tjong)	28	66	-85	A	6	7	2	2

2015-07-13	03:27:58	1.0	66.625	13.367	6.0	Blok (Tjong)	44	65	-71	B	5	9	3	2
2015-07-24	06:48:30	1.4	66.360	12.913	11.6	5km NW of STOK	32	63	-73	C	4	7	3	10
2015-07-29	01:34:18	0.7	66.670	13.420	3.7	Tjongsfjorden	224	74	88	B	4	10	4	30
2015-08-01	19:37:10	1.0	66.546	13.238	6.7	Melfjorden	143	5	-67	A	6	10	3	4
2015-08-01	02:07:34	0.9	66.665	13.479	9.5	Tjongsfjorden	226	78	82	C	4	10	2	49
2015-08-02	01:41:00	0.6	66.676	13.424	6.7	Tjongsfjorden	338	48	-30	C	5	7	2	96
2015-08-09	22:57:08	2.8	66.629	13.008	14.3	Gjerdøya	13	45	-63	A	10	10	2	1
2015-08-09	23:01:17	0.9	66.627	13.047	9.3	10km W of Jektvik	97	60	-11	C	4	7	3	328
2015-08-11	01:06:47	1.2	66.787	14.000	0.0	Svartistunnelen				D				
2015-08-19	10:52:09	0.8	66.635	13.362	7.2	Blok (Tjong)	7	52	-28	C	5	6	1	3
2015-09-02	18:37:00	1.6	66.702	13.143	17.2	6km W of Vågaholmen	168	20	52	C	5	10	2	5
2015-09-22	16:28:31	1.5	66.627	13.047	9.3	9km W of NBB14	241	77	29	C	6	8	2	6
2015-09-23	00:40:49	1.1	66.308	13.349	8.0	Sjona	31	30	-50	C	6	8	2	44
2015-09-24	07:25:44	0.9	66.630	13.347	8.3	1km NEE of NBB13				D	5	6	4	272
2015-09-26	12:10:41	1.4	66.642	13.452	6.4	Blok (Tjong)	19	84	-87	C	4	9	2	8

2015-09-28	17:45:28	2.0	66.646	13.431	8.8	Blok (Tjong)	48	42	-58	B	7	9	2	2
2015-10-01	10:23:58	1.6	68.190	13.905	18.2	13km NEE of Leknes	170	10	0	C	4	11	2	10
2015-10-10	01:50:43	1.0	68.785	14.984	19.3	20km NW of Sortland	144	64	-46	B	8	10	5	6
2015-11-10	01:03:43	1.0	66.479	13.052	7.1	3.5km SW of KONS	104	78	-79	C	3	6	1	39
2015-11-16	01:19:38	1.3	66.627	13.398	6.0	Blok (Tjong)	198	8	-89	B	4	8	2	75
2015-11-17	16:14:05	2.2	68.967	16.254	21.4	20km NNW from Harstad	35	53	77	B	6	5	3	5
2015-12-09	04:32:19	1.7	66.639	13.449	5.9	Blok (Tjong)	114	78	88	C	4	7	2	22
2015-12-16	22:59:49	1.2	66.675	13.544	8.2	Tjong	149	40	-70	B	4	9	3	2
2016-01-15	04:46:31	1.0	66.622	13.372	5.9	3.5km E of Jektvik	243	78	-87	C	5	7	2	77
2016-02-23	11:27:58	1.7	67.669	15.175	0.1	12km N of Tårnvika	9	57	-70	B	6	12	7	46
2016-03-08	22:16:26	1.0	66.446	13.143	7.9	6km S of KONS	40	29	-72	C	4	4	0	337
2016-05-03	09:58:20	1.4	66.660	13.523	6.7	Tjong	176	85	80	C	4	6	1	44

CHAPTER 5: LATE-/POSTGLACIAL AGE AND TECTONIC ORIGIN OF THE NORDMANNVIKDALEN, NORTHERN NORWAY

Authors: Lars Olsen[1], Odleiv Olesen[1], John Dehls[1] & Georgios Tassis[1]

Affiliation: [1]Geological Survey of Norway, P.O. Box 6315 Torgarden, N-7491 Trondheim

Summary

The NF – Nordmannvikdalen Fault (NF) represents one of the two observed postglacial faults in Norway. The two faults constitute the northernmost part of the Lapland province of postglacial faults, occurring in large tracts of northern Sweden and northern Finland. The 1.3 km long, NW–SE trending NF is thought to be a normal fault with scarp height increasing from less than 0.50 m in the NW to c. 1.50 m in the SE. A tectonic origin of the Nordmannvikdalen Fault, which seems to be aseismic today, has recently been questioned and alternative causes as either gravitational collapse or overburden creep have been suggested. We carried out three 3-5 m deep trenches and two ground penetrating radar (GPR) profiles in September 2017 to study the fault at depth. The trenching reveals deformation structures within the lodgement till. The faulting led to cracking of the ground, forming a vertical wedge-shaped crevice, with a width similar to previously recorded large ice wedges and ice wedge casts (fossil ice wedges) in polygonal pattern ground in Arctic areas. The width increases with increasing scarp height, i.e. the vertical displacement. The crevice was filled with sediment, snow and water freezing to ice, with subsequent infilling, during melting seasons, of more debris from the side walls of the host material and cryoturbated and soliflucted soil. The Nordmannvikdalen Fault appears, from the trenching, to have been formed in one single seismic event. The new GPR data show bedrock reflectors dipping approximately 38–52º towards the NE, below the NF scarp. The average angle of the terrain slope between the Nordmannvikdalen Fault scarp and the valley floor is 14º, and the altitude difference between the fault scarp and the Nordmannvikdalen valley floor is approximately 200 m. We find no reason to downgrade the fault to 'very unlikely to be neotectonics'.

1. Introduction

Two postglacial faults have been suggested on mainland Norway. The NE–SW-oriented, reverse Stuoragurra Fault (Olesen, 1988; Muir Wood, 1989; Olesen et al., 1992; Dehls et al., 2000) in western Finnmark and the NW–SE-oriented, normal Nordmannvikdalen Fault (Bakken, 1983; Sollid & Tolgensbakk, 1988; Tolgensbakk & Sollid, 1988; Dehls et al., 2000), constitute the Norwegian part of the postglacial Lapland Fault Province (Fig. 1). The Nordmannvikdalen Fault is located c. 70 km to the north of a 130 km long gap between the Stuoragurra and Pärve faults, and may represent an accommodation or conjugate fault to the extensive system of NE–SW trending reverse faults (Olesen et al., 2004). The Nordmannvikdalen Fault is located within the Reisa Nappe Complex in the Upper Allochthon of the Caledonian Orogen, and represents the only northern Fennoscandian postglacial fault outside the Precambrian Shield. The fault is sub-parallel to regional gravity and magnetic anomalies, which are interpreted to represent structures in the underlying Proterozoic basement, situated at a depth of ca. 3 km in this area (Olesen et al., 1990; Dehls et al., 2000).

There has been speculation of ongoing tectonic activity in the Lyngen area. Holmsen (1916) estimated postglacial uplift from levelling of shorelines in northern Troms. The uplift shows negative anomalies diverging from the regional trend of the order of 5 m in the Lyngen area. This effect was attributed to the mafic and ultramafic massifs within the Lyngen Gabbro (Ophiolite). The interpretation is, however, hampered by poor age control on the formation of the shorelines (Olesen et al. 2004). Redfield & Hermanns (2016) presented evidence for active faults in the N–S trending Lyngen Fjord and along the NW–SE trending Kåfjorddalen, Skibotndalen and Signaldalen as well as along the NE–SW trending Kågsundet and Maursundet. They based their findings mostly on InSAR data.

The Stuoragurra Fault is located within the regional Mierujavri–Sværholt Fault Zone separating the Proterozoic Kautokeino Greenstone Belt in the NW from the Archaen Jergul Gneiss Complex in the SE. The Stuoragurra Fault consists of numerous sections that often overlap, forming an en échelon pattern. Reverse faults with en échelon structures are described from California, Australia, Basin and Range Province (USA), New Zealand, page 322-355 in Yeats et al. (1997). Postglacial faults in northern Finland show similar type of en echelon structures. Numerous trenching have not revealed any strike-slip components of these faults. The total length of the Stuoragurra Fault is 80 km with a c. 20 km wide gap without any apparent faulting in the central part of the fault. The maximum scarp height is 7 m. The dip is 50–60º implying a maximum reverse displacement of approximately 10 m. The till above

the Stuoragurra Fault is folded forming a blind thrust.

The interpretation of the character and age of the Nordmannvikdalen Fault (Figs. 2 and 3) has been based on airphoto-interpretation, trenching and ground penetrating radar (Bakken, 1983; Tolgensbakk & Sollid, 1988; Sollid & Tolgensbakk, 1988; Dehls et al., 2000; Redfield & Hermanns, 2016). Previous studies, with the exception Redfield & Hermanns (2016), have related the NF to tectonic faulting. Redfield & Hermanns (2016) reinterpreted the existing data and carried out a shallow trenching (location shown in Fig. 3) and concluded that the NF was a gravity-induced fault or an overburden creep phenomenon. They could not find any offset of the Quaternary overburden at the fault scarp. Their observation excludes the NF being a DSGSD – Deep-seated Gravitational Slope Deformation structure. Dehls et al. (2000) excluded a gravitational origin for three reasons: 1) The scarp is not arcuate in shape. The curvature seen in map view is due to the topography. 2) No accommodation structures along the sides of the fault structure are observed. 3) No toe of a reverse fault can be seen along the valley floor.

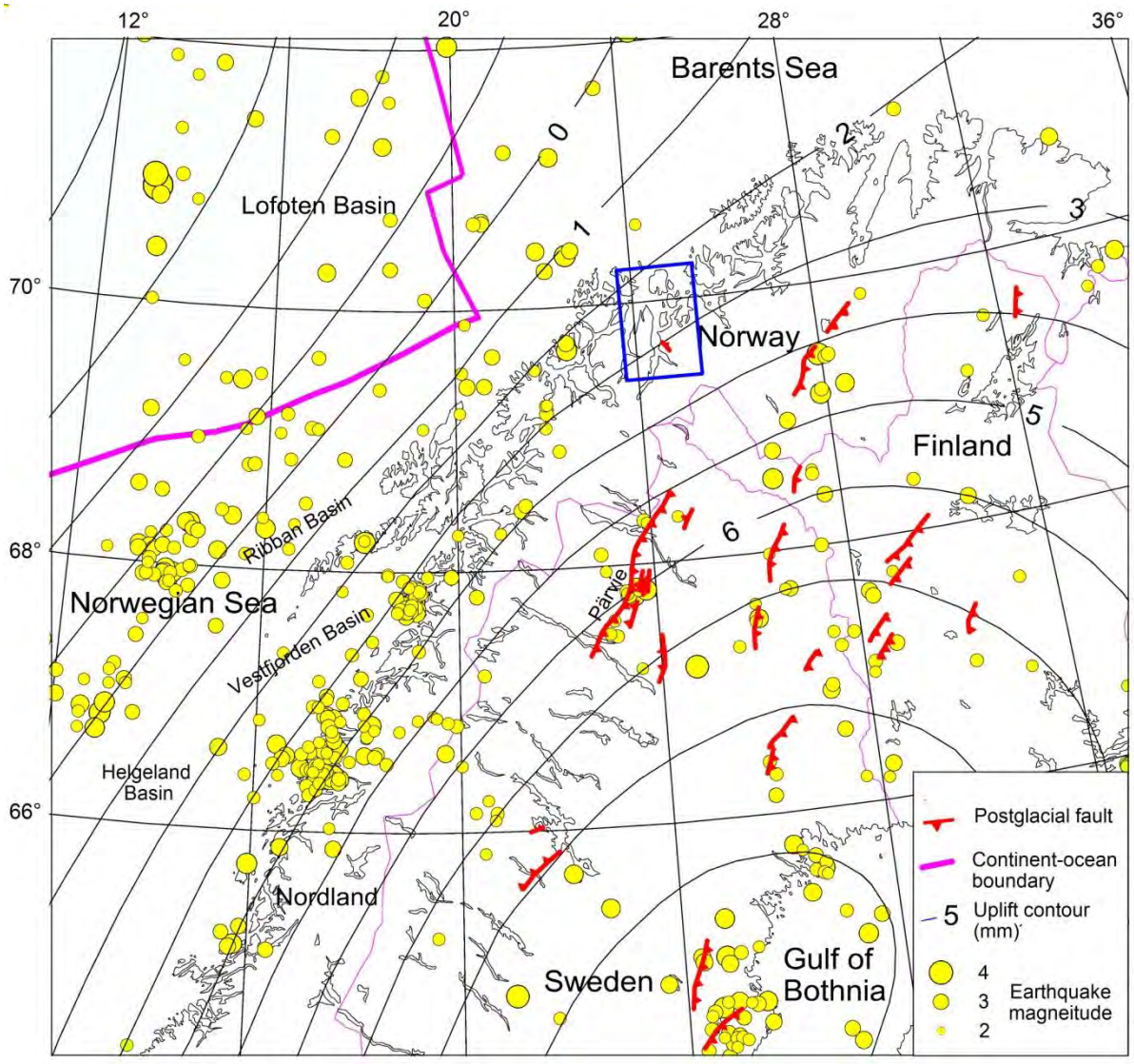

Figure 1. Postglacial faults (Olesen et al. 2013; Palmu et al. 2015; Mikko et al. 2015) land uplift (Vestøl et al., in prep.) and seismicity (1990–2012) in northern Fennoscandia from the web pages of the Institute of Seismology at the University of Helsinki; http://www.seismo.helsinki.fi/english/bulletins/index.html. A lower threshold at magnitude 2.0 has been applied to reduce contamination by explosives. The Lyngen–Kåfjord area as shown in Fig. 2 is depicted by the blue frame.

The fault locally splits into two or three semi-parallel branches (Bakken, 1983; Dehls et al., 2000; Redfield &

Hermanns, 2016). En échelon structures occur especially in the northwestern part of the fault (Fig. 4). The fault-bounded depressions along the fault scarp and along the semi-parallel, assumed fault-related lineaments (Fig. 4) most probably occur in the overburden, similarly to normal faults in New Zealand (Beanland et al., 1990; Yeats et al., 1997). There is a high number of rock avalanches in the vicinity of the Nordmannvikdalen Fault indicating a relationship between palaeoseismicity and slope failures (Braathen et al., 2004; Osmundsen et al., 2009). The northwestern end of the scarp terminates against a bouldery moraine from late-glacial ice lobes (Dehls et al., 2000). Due to the large size of the blocks, any ruptures of less than a few metres vertical displacement of the ground surface would be hidden by the big moraine blocks. It is therefore impossible to determine the relative ages of the fault and the moraine, which in addition was subsequently partially transformed to a rock glacier. It is possible that the moraine conceals the original side of the slump (vertical displacement). However, there is no evidence pointing towards this. The eastern end of the scarp terminates against the scree deposit (talus) below the Kistefjellet mountain (Figs. 3 and 4A). Here, there is clearly no evidence for faulting. Since the fault scarp has its maximum height (c. 1.5 m) at this location a continuation underneath the scree deposit is likely.

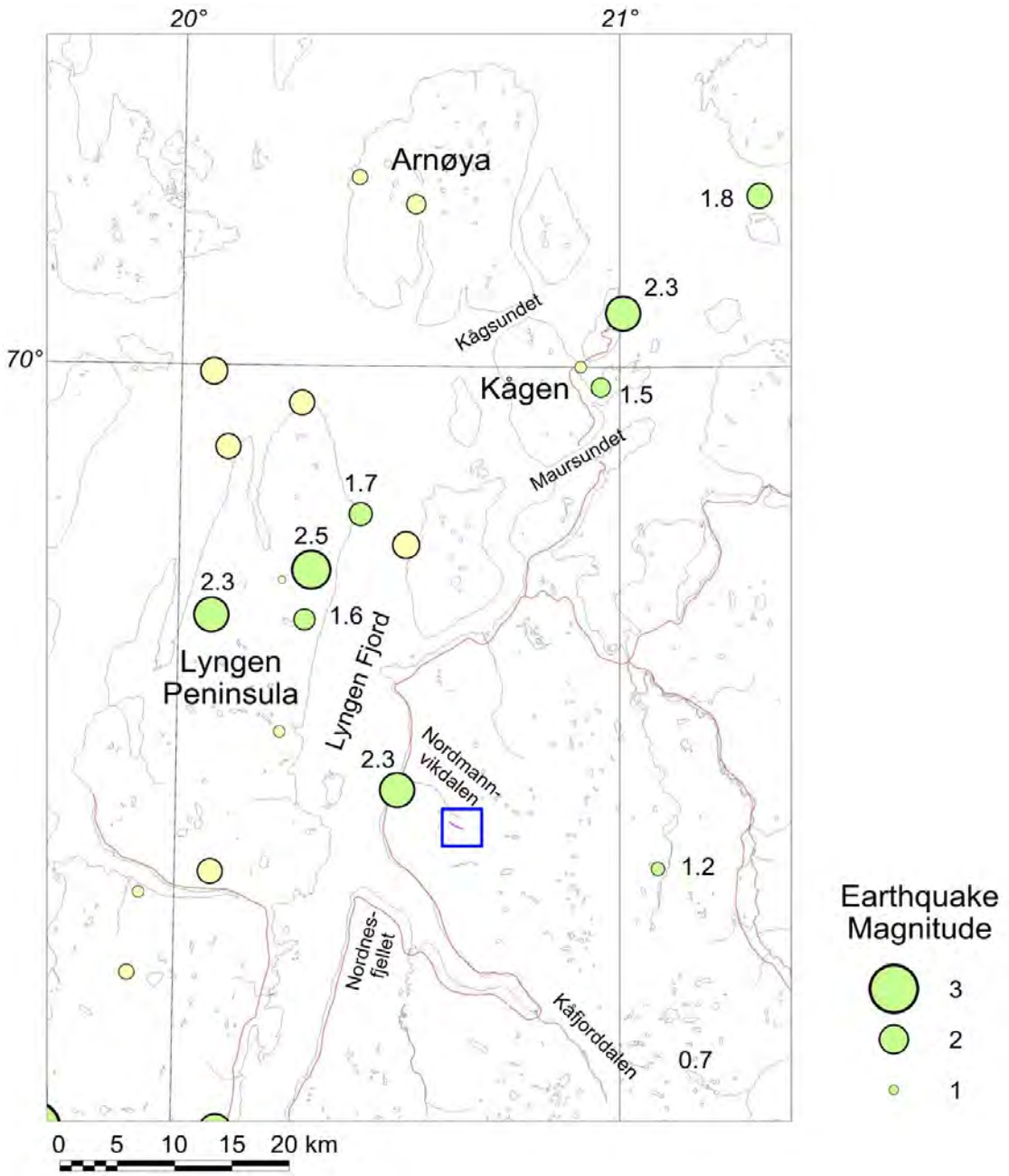

Figure 2. Map of the northern Troms area showing the Nordmannvikdalen Fault in red within the blue frame and earthquakes (pale green and yellow circles). The reported seismic events in the outer Lyngen Fjord (Redfield & Hermanns, 2016) are based on recordings at the NORSAR seismic array in Karasjok located c. 200 km to the east. The University of Bergen includes additional recordings from their seismic stations in Tromsø and Kautokeino located 60 and 140 km to the west and southeast, respectively. These improved epicentres shown in the present map locate around the Lyngen peninsula and the island of Arnøya. The latter 1999 earthquakes are most likely related to blasting during the molo construction at Årviksand harbour in the winter of 1999 (Olesen et al., 2013). Explosion filtering of the earthquakes remove much of the seismicity in the area (shown in yellow). The filter removes smaller than magnitude 2.0 events occurring between 08:00 in the morning and 18:00 in the afternoon (Conrad Lindholm, pers. comm. 2017). The location of the map is shown by the blue frame in Fig. 1.

There has been speculation of ongoing active tectonic activity in the Lyngen area. Holmsen (1916) estimated postglacial uplift from levelling of shorelines in northern Troms. The uplift shows negative anomalies diverging from the regional trend in the order of 5 m in the Lyngen area. This effect was attributed to the mafic and ultramafic massifs within the Lyngen Gabbro (Ophibolite). The interpretation is, however, hampered by poor age control on the formation of the shorelines (Olesen et al. 2004). Redfield & Hermanns (2016) presented evidence for active faults in the N–S trending Lyngen Fjord and along the NW–SE trending Kåfjorddalen, Skibotndalen and Signaldalen as well as along the NE–SW trending Kågsundet and Maursundet. They based their findings on seismicity and InSAR data.

In September 2017, we excavated the overburden in three c. 10–15 m long and 3–5 m deep trenches across the scarp of the Nordmannvikdalen Fault, in order to collect more information in support of or against a neotectonics origin for the fault. In addition, new ground penetrating radar data were collected.

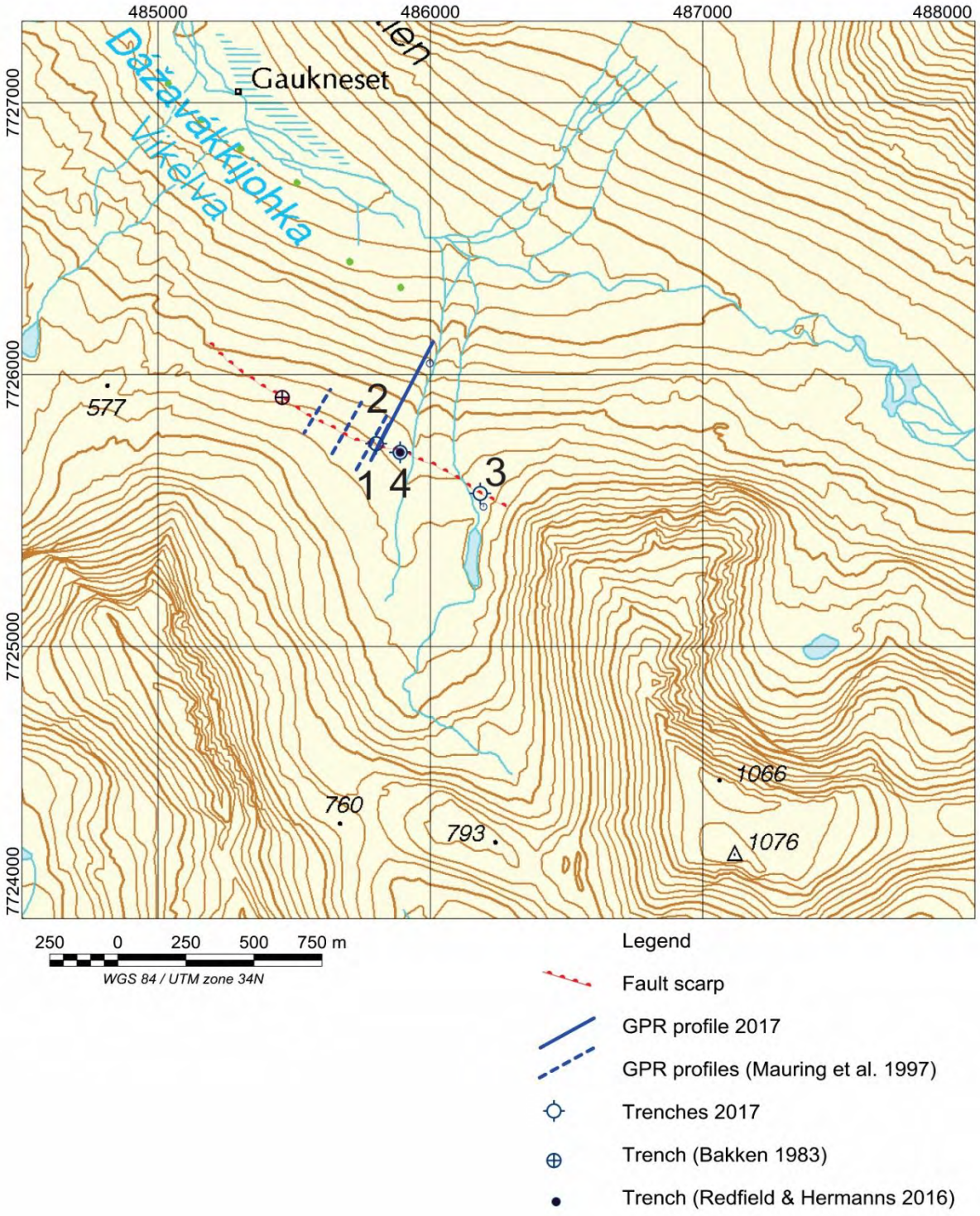

Figure 3. Topographic map of the Nordmannvikdalen area showing postglacial fault scarp. Trenches and bedrock outcrops in addition to the location of the new 50 MHz profile and the previous 50 MHz ground penetrating radar profiles by Mauring et al. (1997) and Dehls et al. (2000). The location of the map is depicted by the blue frame in Fig. 2. Parts of the mountains Nordmannviktinden and Kistefjellet are located in the SW (lower left) and in the SE (lower right), respectively.

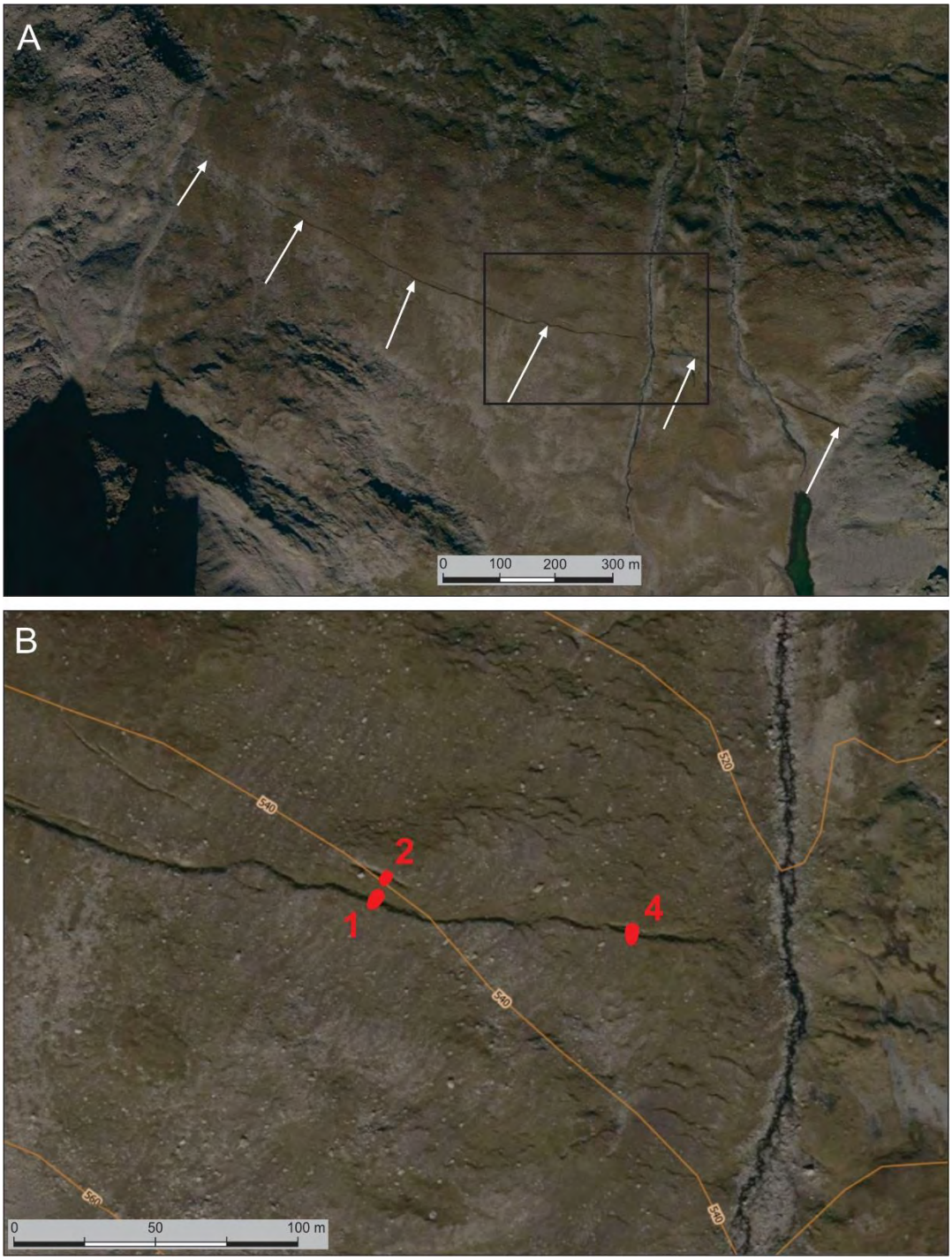

Figure 4. (A), upper panel – The Nordmannvikdalen Fault which can be observed from the boulder scree deposit in the east (right) to the lateglacial moraine and younger rock glacier deposit in the west (left). (B), lower panel – The middle part of the Nordmannvikdalen Fault and location of trenches 1, 2 and 4. The latter is also the location where Redfield & Hermanns (2016) did their trenching in cryoturbated soil across the fault scarp. Photographs are from www.Norgeskart.no.

2. Methods

2.1 Ground Penetrating Radar

The Ground Penetrating Radar (GPR) technique is probably the most commonly used geophysical method due to quick, easy, inexpensive and nonintrusive collection of data and its ability to thus provide very detailed and continuous images of the subsurface. Mapping of underground layers and/or linear features is based on the

propagation and reflection of high frequency EM – electromagnetic waves and later processing and interpretation of the resulting radargrams (Jol, 2009). Data were acquired using the Malå RTA system (Snake), since it was easier to transport to the survey area and is more suitable for high inclination terrain. The Snake system utilizes an in-line antenna setting enclosed in a flexible cord that allows it to be maneuvered easily and efficiently through dense vegetation and uneven terrain without affecting ground contact. In this sense, two profiles were collected using the 100 MHz antenna and one with 50 MHz. All profiles intersected the superficial manifestation of the fault perpendicularly and data were collected starting uphill and walking down towards the base of the valley. The topographic difference in elevation for the longest profile is almost 50 m over 500 m of horizontal distance (50 MHz antenna), therefore a standard migration is essential in order to precisely determine the true geometry of the detected structures and more importantly, of the fault itself. Furthermore, it is suspected that some of the dipping reflectors seen in the older GPR profiles performed in the same region might be halved hyperbolas induced by boulders present in the subsurface. With the choice of a realistic propagation velocity, migration will again help collapse any possible hyperbolas whose right-hand legs might interfere with interpreting actual dipping lineaments. In this study, the 100 MHz antenna profiles did not return good results, so we will only present the relatively low frequency 50 MHz radargram since it presents the highest depth penetration and unveils the most meaningful reflections. Data were processed, modelled and interpreted using RadExplorer v. 1.42 (DECO Geophysical, 2005).

2.2 Trenching

Information from Quaternary geological maps of the area (Bakken 1983, Tolgensbakk & Sollid 1988), added with field observations and vertical air-photographs from internet (www.norgeibilder.no) helped us to choose locations for trenching across the NF escarpment.

For 3-5 metres deep trenching we used a 3-tons machine excavator which was transported by helicopter in three separate parts and mounted together in the trenching area. Traditional observations and records of the Quaternary stratigraphy and structures (sediment types, layering, deformation structures, textures, etc.) in each excavated section were then performed, without any use of more sophisticated instruments than compass, metre measure, knife and spade.

3. Results from GPR measurements and trenching

The ground surface in the fault area is characterized by till, with superimposed solifluction features, up to a few metres long and wide. Some of the solifluction tongues reach, with their top surfaces, up to 50–60 cm above the surrounding terrain, and cryoturbation may occasionally reach more than 1 m below ground surface. The bedrock in this area is dominated by hornblende biotite schists of the Upper Allochthon's Kåfjord Nappe (Zwaan et al. 2006). The fault is interpreted as a normal fault (Dehls et al., 2000). The quality of the new migrated Ground Penetrating Radar (GPR) data is substantially higher than the vintage data interpreted by Dehls et al. (2000) and Redfield & Hermanns (2016). The new GPR profile normal to the fault line shows a possible fault structure that reaches the bedrock surface immediately below the fault scarp. The fault plane has a dip of c. 45˚. The total thickness of the loose deposits, mainly glacially derived, on bedrock, is apparently c. 8–9 m just below the fault scarp seen at the surface. The NF seems to have reactivated one of several faults in the bedrock. The faults make up a 10–15 m wide set of lens-shaped structures (Figs. 5 and 6). Different faults within this zone seem to have been active as accommodation structures causing ditches semi-parallel to the main scarp. The activated part of the fault complex makes a bend at a depth of c. 10 m below the bedrock surface. The dip of the fault changes from c. 45º to c. 38º (Fig. 6). Other postglacial faults in northern Fennoscandia also occur within 10–20 m wide fault zones, such as the Stuoragurra Fault in Finnmark (Olesen et al., 1992, 2013) and the Isovaara–Riikonkumpu fault complex in Finnish Lapland (Ojala et al., 2017).

If the total overburden on bedrock was 100% frozen during the fault event, then the fault plane (with 45˚ dip) would probably reach the ground surface a few metres in "uphill" position, and not where it is really located. This is because 100% frozen overburden would behave almost as hard rock during movement, which means that it would act more as a continuation of bedrock than as unconsolidated sediment, all the way through the overburden and to the ground surface. As the fault scarp in the ground surface is located just at or only c. 1–2 m "uphill" from the vertical projection of the fault line on the bedrock surface, as interpreted from the GPR data (see above), it is likely that a lower, significant part of the overburden was *not* frozen during the fault process. However, the upper at least 2–3 m of the overburden were most likely frozen during the fault process, as described below.

Results from the excavations show that a 2–3 m, or more, deep wedge of cryoturbated and soliflucted soil, more than

0.7 m wide on top, fills a vertical crevice (fissure?) below the fault scarp and below a vertical semi-parallel crevice 10 m "downhill" from the fault scarp (Figs. 7, 8 and 9). The ground surface between the fault scarp, which is up to 1.5 m high, and the semi-parallel sediment-filled crevice appears as a graben structure since the "downhill" escarpment of the natural shallow trough overlying the soil sediment wedge is c. 0.2–0.4 m higher than the "uphill" escarpment (Figs. 10 and 11). The graben structure seems thus to be bounded by a conjugate fault set. The vertical crevices were most likely formed when the upper 2–3 m (or more) of the sediment overburden were frozen, an environment similar as it is during initiation of ice wedge formation during formation of polygon ground patterns in arctic areas. These sediment-filled crevices in the Nordmannvikdalen Fault area are similar to large ice wedge casts, which have developed after melting of large ice wedges that may range from 1 cm to 3 m width and penetrating up to 10 m downwards into frozen ground (Péwé, 1974). Ice wedge formation and survival through melting seasons is only known from dry Arctic areas where the annual mean temperature is below –6 ºC.

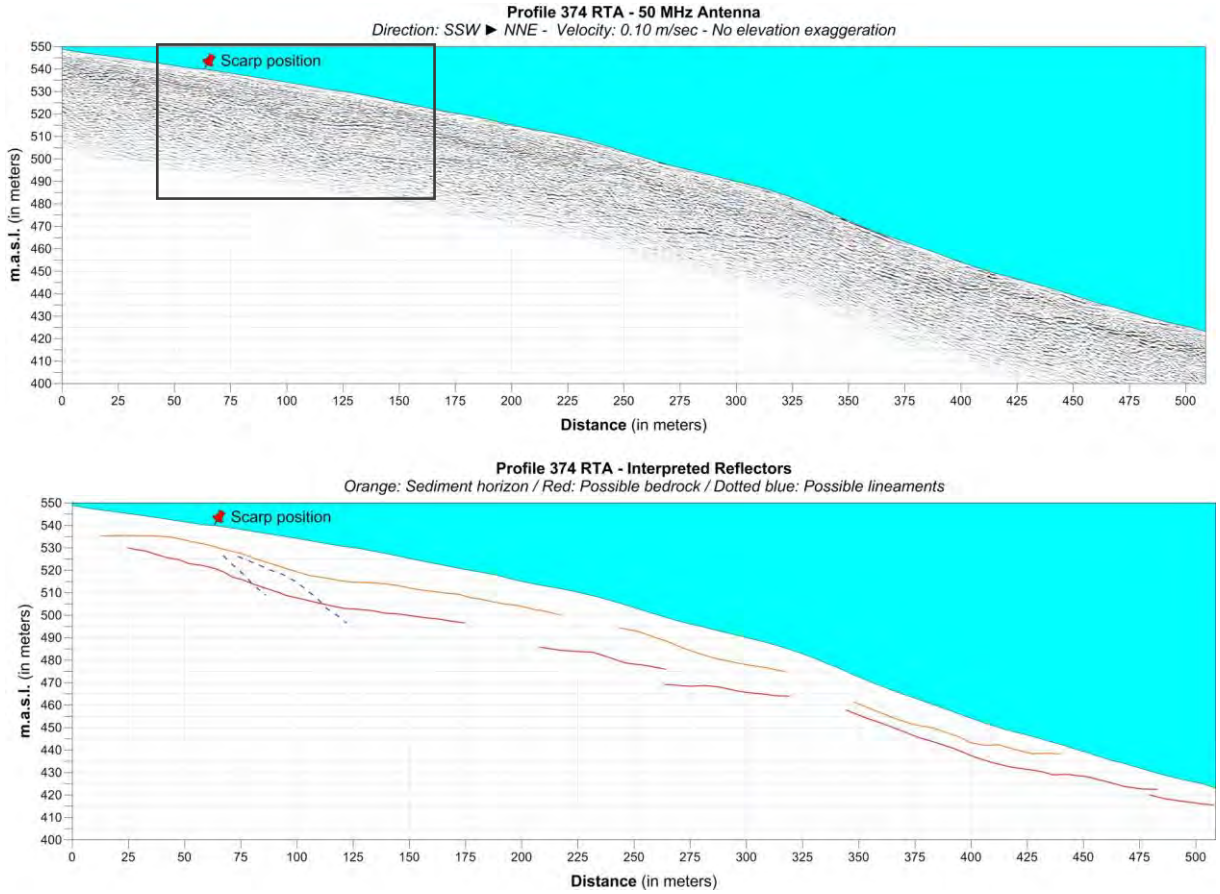

Figure 5. Ground Penetrating Radar (GPR) profile perpendicular to the Nordmannvikdalen fault. (A, upper panel) The figure shows clean GPR data without interpretations indicated. (B, lower panel) The orange reflector most likely represents the bedrock surface below the lodgement till and the red reflector is probably from within the bedrock zone. Two prominent much steeper reflectors (dashed lines) occur within a c. 10 m wide zone. The southern (left) reflector can be extrapolated to just a few metres downhill from the surface location of the fault scarp. The rectangular box in the upper panel depicts the location of the zoom-in part of the profile shown in Fig. 6.

The host surficial material along the NF area is mainly till of basal lodgement type, with characteristics such as striated stones and boulders, lodgement and shearing planes, and matrix supported and well consolidated character, as observed during the excavations. However, the till here also includes lenses and zones with sand and gravel, and small zones with almost clast supported character, which altogether gives a variable appearance in vertical sections.

Subsequent to the fault event, with formation of the accompanying crevices and graben structure (Fig.14) the geological process probably proceeded as follows: The open crevices were filled with water (snow?) and some sediments from adjacent loose material --> freezing -> ice wedge formation -> melting down to some dm to m depth -> soil formation (biogenic input, water circulation, chemical alterations) -> freezing of topsoil, cryoturbation and

solifluction -> repeated melting down to some dm to m depth, infilling of soil from the upper part of the overburden, accompanied with further soil formation -> repeated freezing -> repeated melting and infilling of soil, and so on. Subsequent to the initial crevice formation, the process was more or less the same as during ice wedge formation in arctic areas, with an ice wedge cast (fossil ice wedge) as end product where enough melting in time and depth has occurred.

Finally, melting down to more than 2–3 m depth resulted in cavities and/or tunnels appearing below the sediment wedges (Figs. 8, 9 and 10), due to melting of ice and overlying blocking of the crevice from coarse grained material in the lower part of the sediment wedges. Some of these cavities and/or tunnels are still open, whereas many of these are presumed to have been filled with sediments, leaving the ground surface with natural shallow troughs following on top of the respective crevices. This interpretation is also compatible with the results from the c. 5 m deep trenching by Bakken (1983).

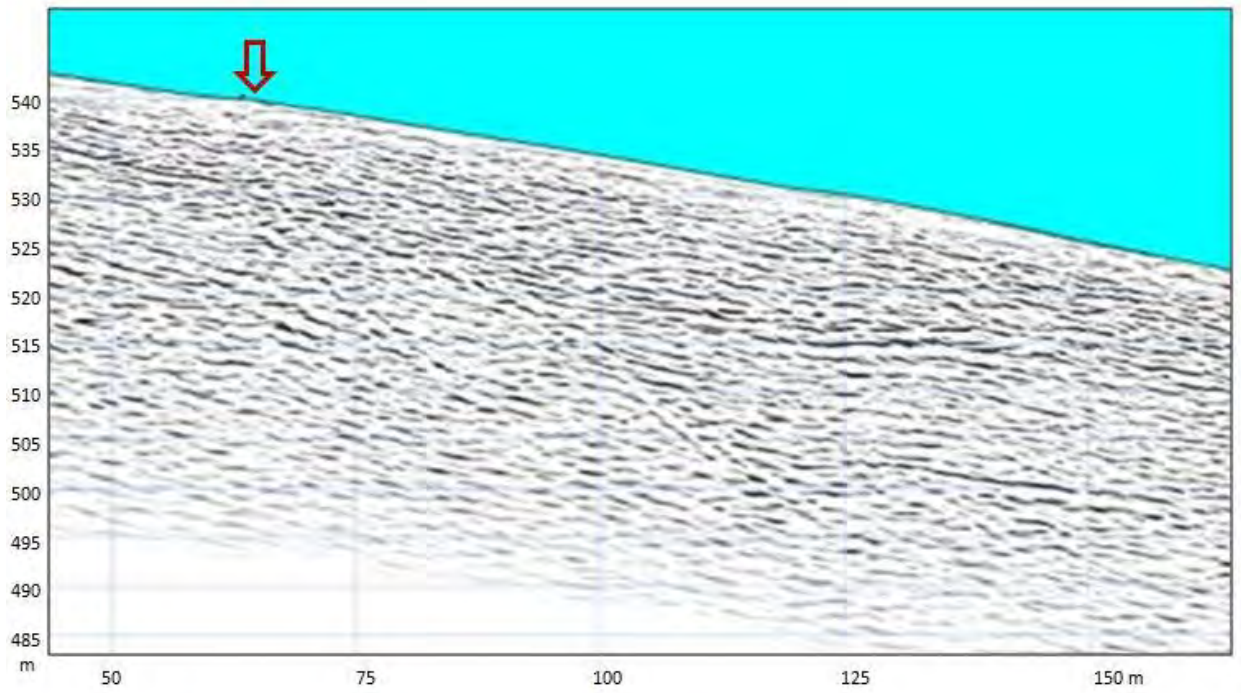

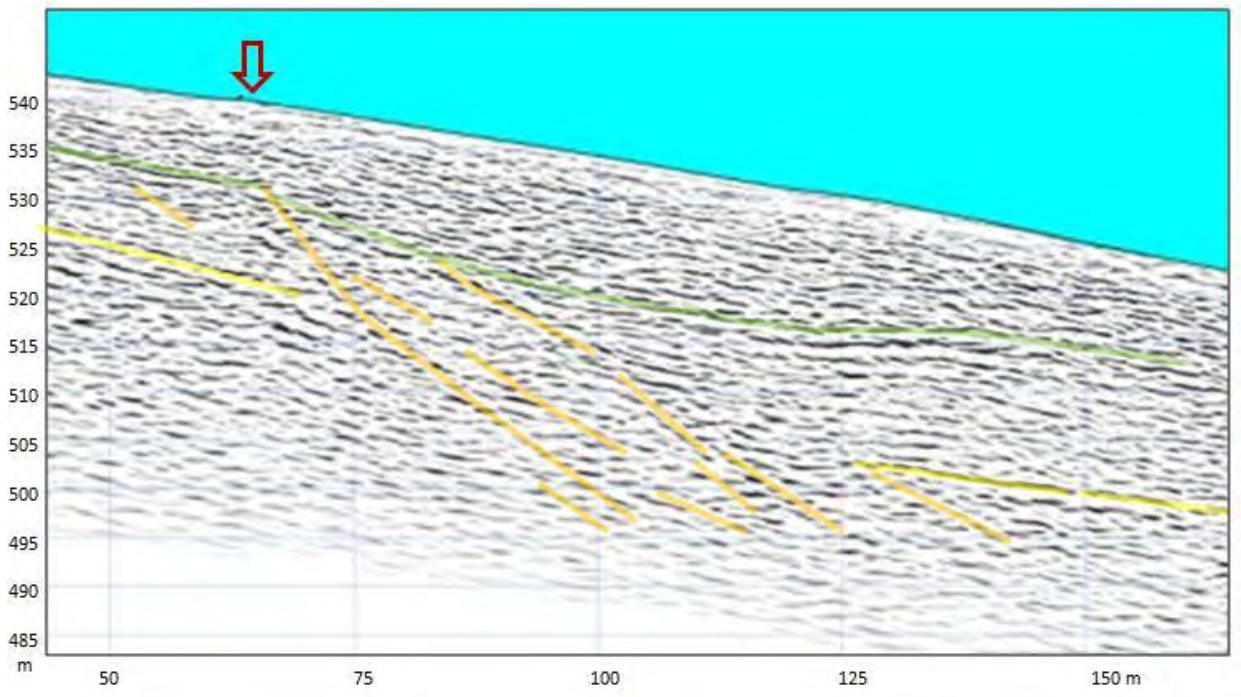

Figure 6. (A,B) Detail of the GPR profile across the Nordmannvikdalen Fault in Fig. 4. The green reflector indicated in the lower panel (B) most likely represents the bedrock surface below the lodgement till. Two to three prominent reflectors (orange lines) occur within a c. 10 m wide zone. The southern (left) reflector can be extrapolated vertically to just a few metres downhill from the surface location of the fault scarp.

When were the sediment wedges formed? – Most of these may have been formed in the early part of the Holocene, but not before significant soil formation had taken place, i.e. after several hundred years. Infilling of sediments, cryoturbation, and solifluction in the scarp slope in several phases, in combination with soil formation, comprise the further geological processes. These may have continued for several hundred years, and have continued to some extent through the entire Holocene. The strongest cryoturbation most likely took place in the cold phases (with ice growth in the high ground glacier areas) during Holocene, as for example c. 10200, 8200, and 2500 years B.P., and during the Little Ice Age (1620–1920 A.D.)

Redfield & Hermanns (2016) interpreted a tectonically active N–S trending fault in the outer Lyngen Fjord from recordings at the NORSAR seismic array in Karasjok, which is located 200 km to the east. The University of Bergen includes additional recordings from their seismic stations in Tromsø and Kautokeino, located 60 and 140 km to the west and southeast, respectively. These improved epicentres (Fig. 2) lend no support for the Lyngen Fjord active fault. Explosion filtering of the earthquakes removes much of the apparent seismicity in the area (shown in yellow in Fig. 2). The filter removes events less than magnitude 2.0 that occurred between 08:00 in the morning and 18:00 in the afternoon (Conrad Lindholm, pers. comm. 2017). Approximately 40 % of the real earthquakes will also be removed in this process.

InSAR anomalies of several mm across the NW–SE trending valleys of Kåfjorddalen, Skibotndalen and Signaldalen (Osmundsen et al., 2009; Redfield & Hermanns, 2016) have been used as arguments for active faults along these valleys. These findings are, however, inconsistent with the present-day seismicity in the area as shown in Fig. 2. Interseismic fault creep have been observed along active plate boundaries e.g. along the strike–slip faults belonging to the San Andreas fault system in California (Sylvester, 1995). However, aseismic faults are relatively rare in intraplate regions. The lack of evidence for active tectonics in the northern Troms area was also pointed out by Olesen et al. (2013).

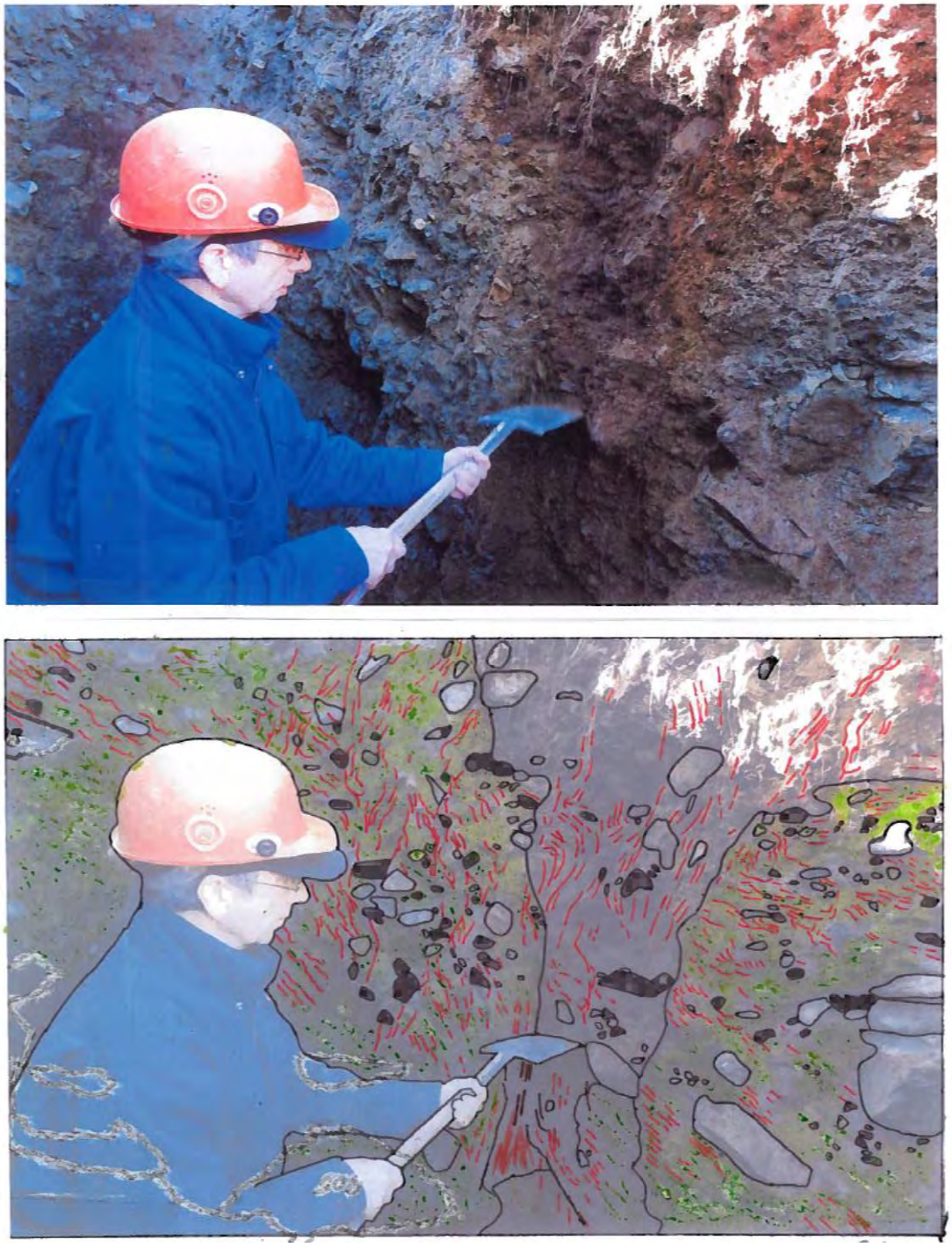

Figure 7. Section across and normally to the fault scarp, trench 1. A deep soil wedge penetrates the hosting compact lodgement till there. Fragmented line segments indicate shear and/or sliding planes. The till does not include distinct sediment horizons which can be followed from one side to the other of the sediment wedge.

Figure 8. Cavity under coarse clast material at depth in sediment wedge filling the fault crevice recorded in trench 1.

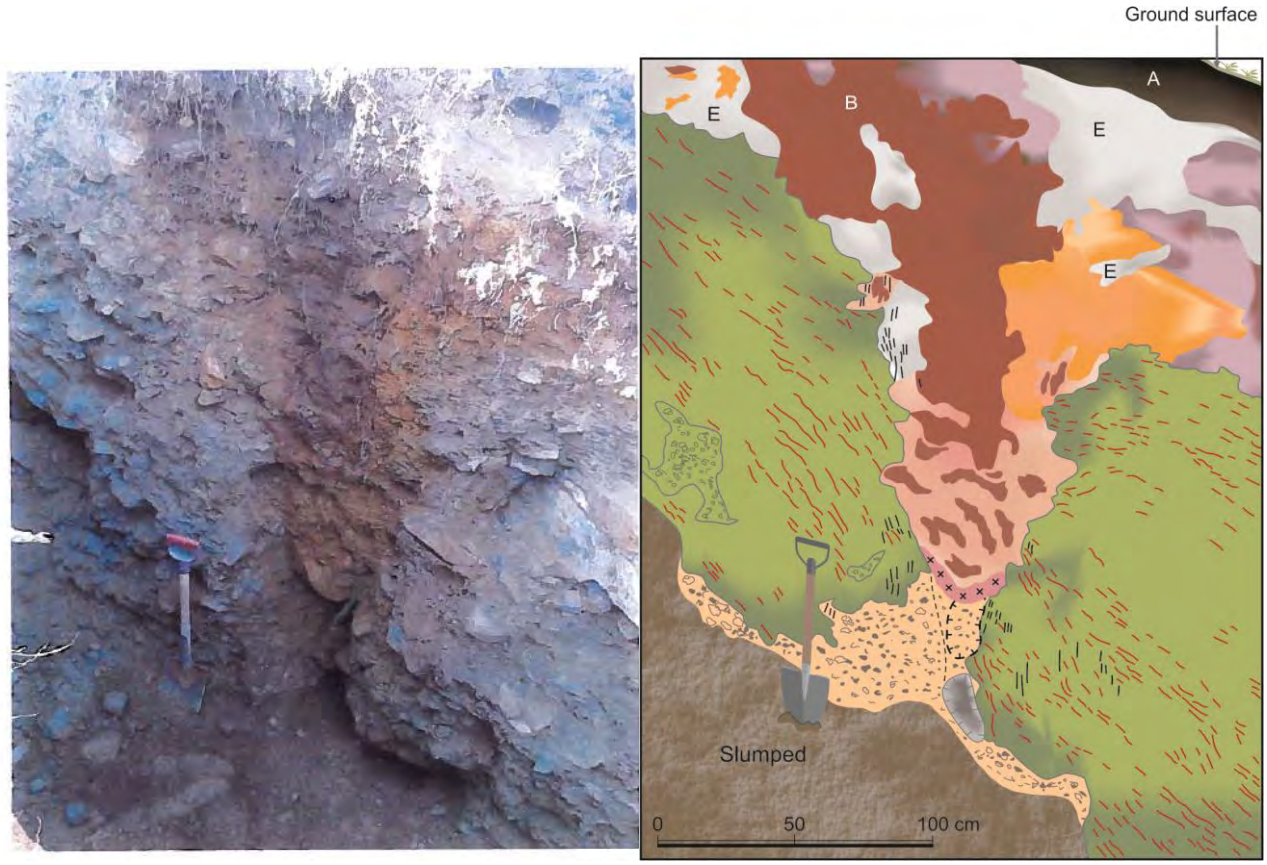

Figure 9. Section across and normal to the fault scarp, trench 1, Nordmannvikdalen – with a sediment wedge of strongly cryoturbated and disturbed soil, ending in a cavity in the lower part (below the wedge apex). Red line segments in the outline to the right indicate a combination of depositional, sliding and shearing structures in the till, whereas blue line segments indicate sliding, mainly from vertical displacement during fault event, but possibly also later during slumping and infilling of sediments in the fault crevice and underlying cavities.

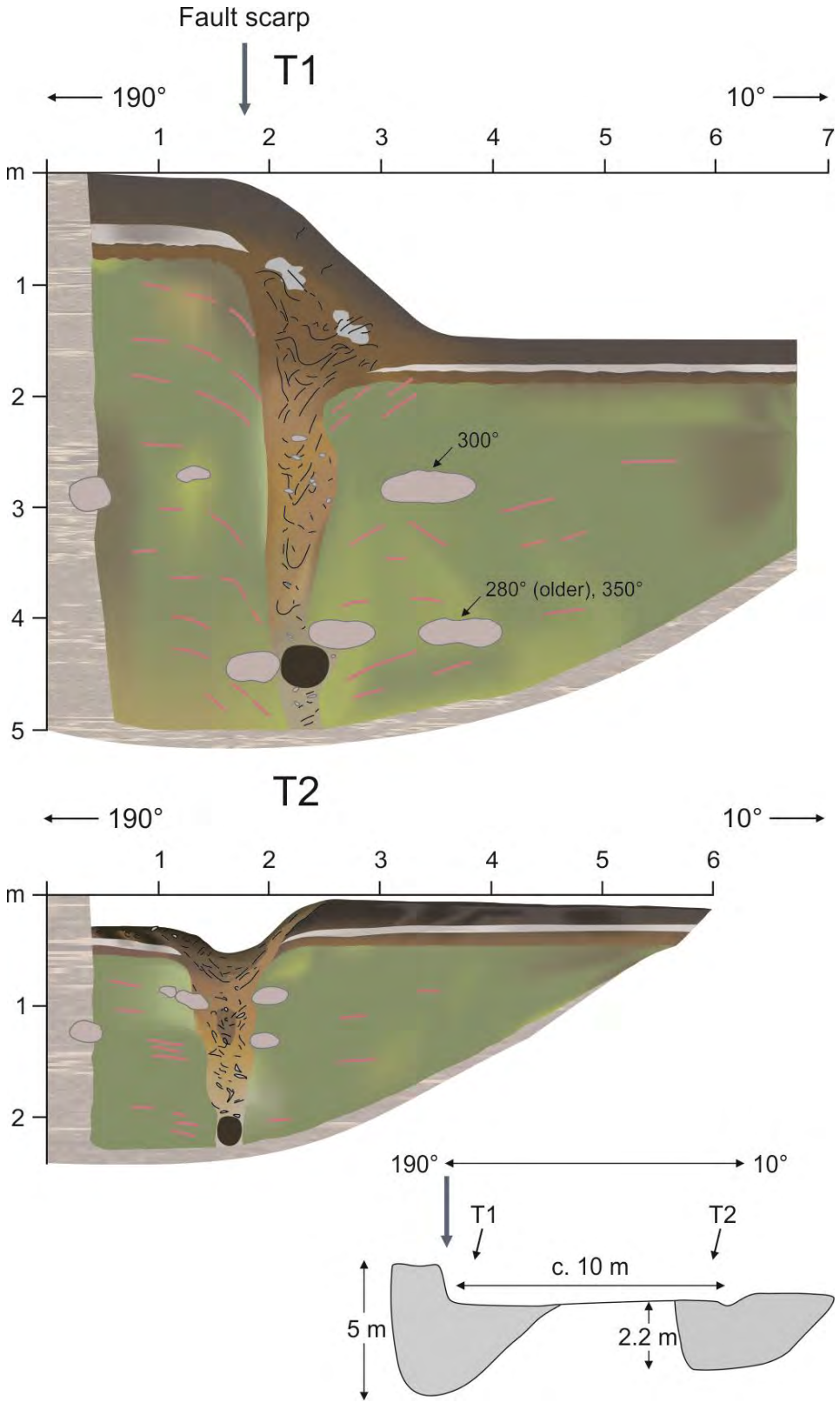

Figure 10. Outline of the first two trenches (T1 and T2) in Nordmannvikdalen. The orientations of the sections are normal to the fault. Notice the cavity at depth in the lower part of both sediment wedges. The combined sections indicated below illustrate a cross-section of the graben like structure appearing in Fig. 11.

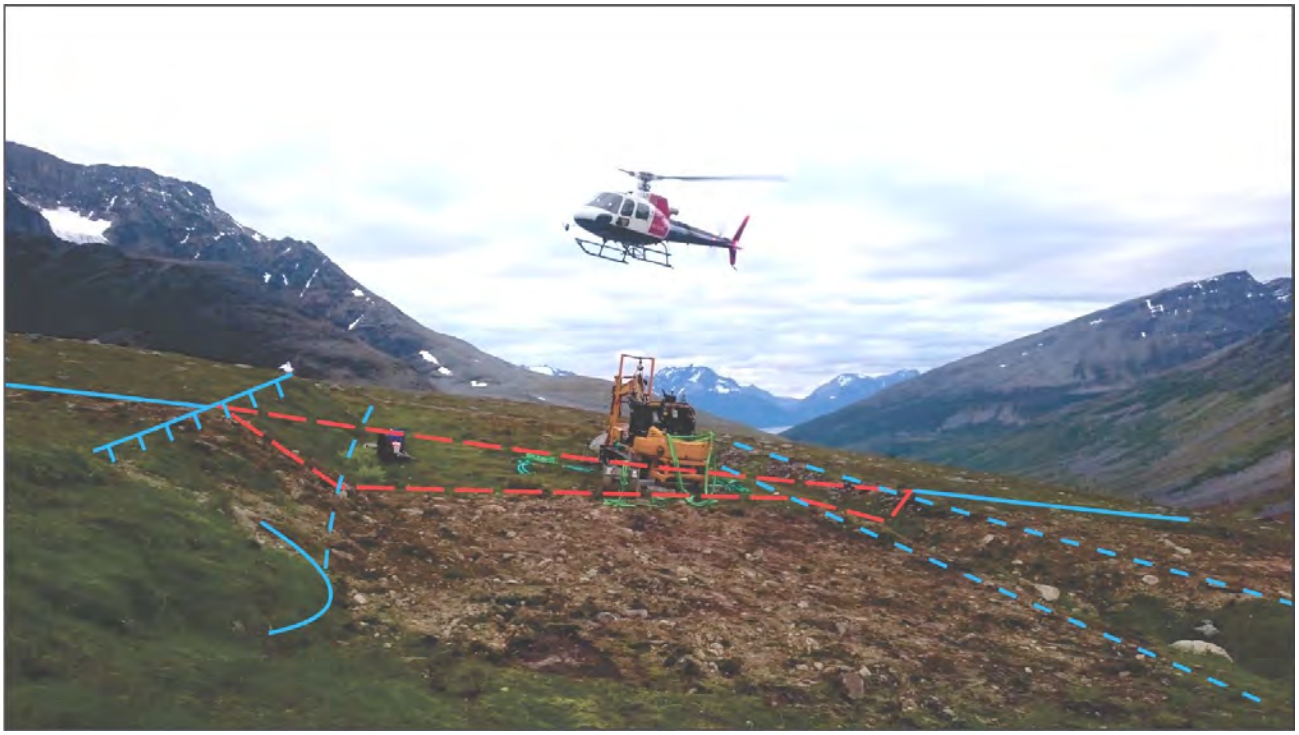

Figure 11. A graben like structure appears in a downhill surface profile normal to the fault scarp (hatched blue line to the left) and the semi-parallel trough (between stippled blue lines to the right). Notice also the solifluction tongues which are masking the fault scarp in a narrow zone to the left.

Figure 12. Nordmannvikdalen trench 3, southern (left) and western (right) walls. For location, see Fig. 3, close to the end of the fault scarp in southeast.

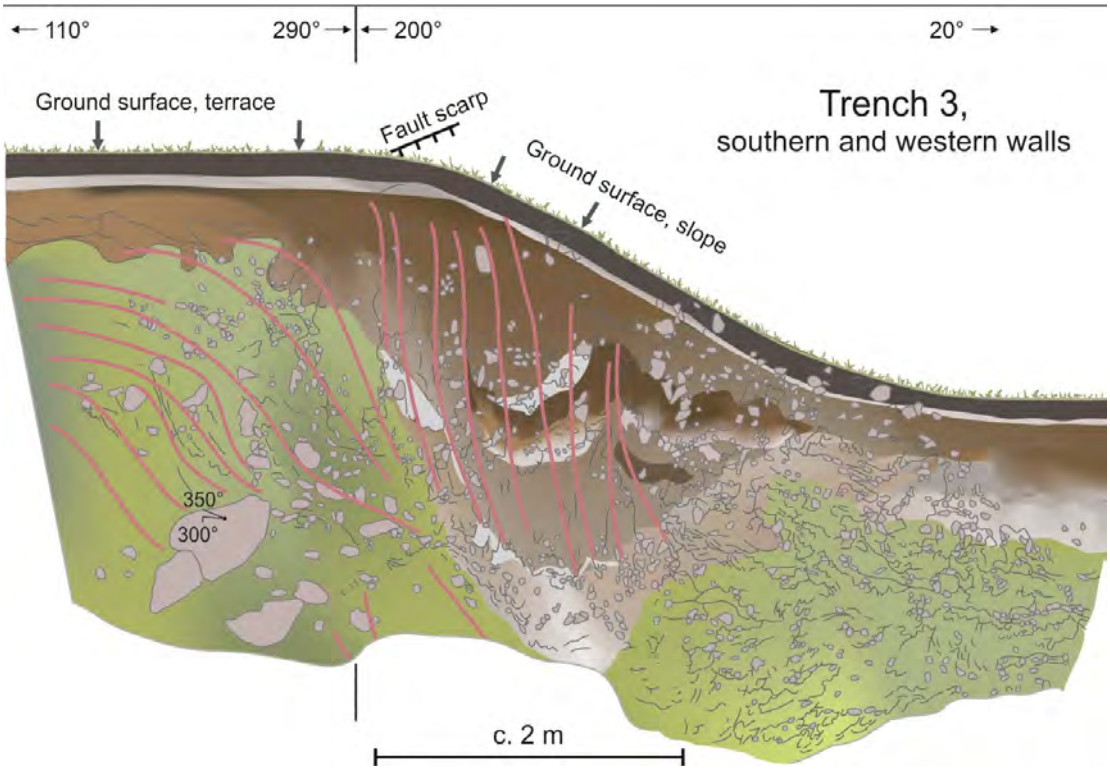

Figure 13. Outline of combined sections in trench 3, southern (left) and western (middle and right) walls. The wall sections are here slightly rotated around a vertical axis (vertical black line segments), so that a 3D-view of the walls may be imagined from this 2D-view. Reddish lines representing a combination of depositional, shearing, sliding and deformational planes are indicated. Also shown, with brownish colours, is the collapsed and further cryoturbated soil, and, with greenish colour the lodgement till. Glacial striation towards 300° (older) and 350° on a big boulder to the left is also indicated.

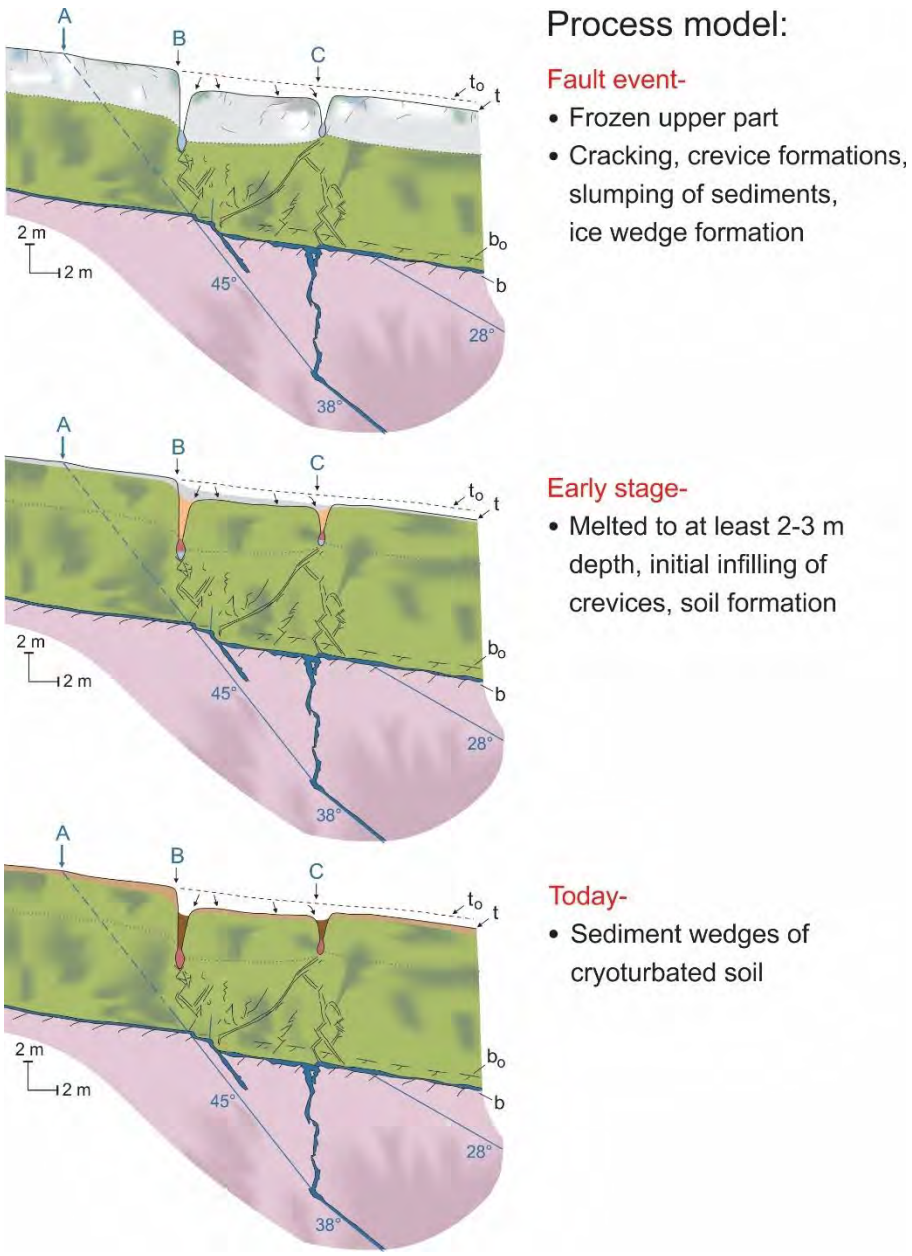

Figure 14. Outline of a profile through the overburden based on data from trenches 1 and 2 in Nordmannvikdalen, and interpretation of the ground penetrating radar profile shown in Figs. 5 and 6. The orientation of the outlined profile is normal to the fault. Letter A – This indicates the assumed location of surface traces of the fault if the sediment overburden was (mainly) finegrained and) totally frozen (deep permafrost) during faulting event. B – position of the Nordmannvikdalen fault scarp, just a few metre upslope from the vertical projection of the fault plane outgoing in the bedrock surface inferred from the georadar data (see Fig. 6). C – position of the semi-parallel trough (see Fig. 10). The letters t_0 and t indicate sediment surface position and b_0 and b bedrock (pink) surface position before and after fault event, respectively. Steepness (in degrees) of bedrock reflectors which may represent fault planes also indicated.

4. Discussion

Redfield & Hermanns (2016) used the empirical relationship determined from a global dataset of earthquake magnitudes and the corresponding fault dimensions by Wells & Coppersmith (1994) to reject the NF as a tectonic fault. Wells & Coppersmith (1994) calculated a regression line from the observation data of observed fault length and offset compiled from historic earthquakes. The original observation data show, however, more than one order of variation along this line. The fact that the fault displacement to fault length ratio is an order of magnitude higher than the average for earthquake-related faulting is consequently not a valid criterion for discarding the NF as a tectonic fault. The anomalously high scarps compared to fault length have already been pointed out by e.g. Muir

Wood (1989). Fenton (1994) took this variation into consideration when they concluded that most postglacial faults have a displacement–length ratio between 0.00001 and 0.001. The NF ratio (1.5/1300 = 0.00115) falls just above the highest part of this range. The Pasmajärvi Fault in northern Finland has a height/length ratio of 0.0008–0.0016 (Kujansuu, 1964). The N–S trending and NE–SW sections of the Ismunden Fault in Central Sweden have height/length ratios of 6/3500=0.0046 and 8/22000=0.00036 (Berglund & Dahlström, 2015), respectively. These examples show that the height/length ratio of the Nordmannvikdalen Fault is high but not anomalous compared to other postglacial faults in northern Fennoscandia.

The NF is the only structure within the Kåfjord 1:50.000 map sheet that offsets the Quaternary overburden (Bakken 1983; Sollid & Tolgensbakk, 1988). Redfield & Hermanns (2016) argue, however, that the NF is located between two DSGSDs at the mountains of Kistefjellet and Nordmannviktinden. Tolgensbakk & Sollid (1988) classified these phenomena as glacial-formed escarpments. Neither Bakken (1983), nor Redfield & Hermanns (2016) reported any evidence of displacement of the Quaternary overburden or bedrock surface along the suggested DSGSDs and there is consequently not much support for the interpretation of deep-seated gravitational slope deformation at these mountains.

We apply the criteria by Fenton (1994) and Muir Wood (1993) for the identification of postglacial faulting:

1) Offset of an originally continuous surface or sedimentary sequence of postglacial or late-glacial age. The surface of the lodgement till is offset along an at least 1.3 km long linear to curvilinear escarpment, which is accompanied in some parts with an adjacent, parallel shallow trough. Dehls et al. (2000) fit a plane with a dip of 28º through this line revealing that the structure is not a shallow structure in the Quaternary overburden as suggested by Redfield & Hermanns (2016).

2) Reasonably consistent direction and amount of slip along the length of the fault. The height of the fault decreases gradually from c. 1.5 m in the SE to c. 0.2 m in the NW (Dehls et al., 2000; Redfield & Hermanns, 2016)

3) The ratio of displacement to overall length of the feature should be less than 1/1,000. For most faults this ratio is between 1/1,000 and 1/10,000. The Nordmannvikdalen Fault has a ratio of approximately 1/1,000 (1.5 m/1,300 m). The fault is most likely longer than 1.3 km since the height of the fault scarp is c. 1.5 where the fault encounters the boulder fields at the foot of Kistefjellet and less than 0.5 m north of Nordmannviktinden. It is not possible to trace the continuation of the fault scarp at these locations. It is, however, not likely that the fault reached the surface for a longer distance than 2 km.

4) Exclusion of gravity-induced sliding as the driving mechanism of faults in areas of moderate to high relief. The fault is sub-parallel to the Nordmannvikdalen valley. The terrain has an average slope of c. 14º between the escarpment and the valley floor. The slope is gentle when comparing with the mountainous areas in the vicinity of Nordmannvikdalen. It is not likely that the fault scarp is controlled by low-friction graphite schists since the fault is not parallel to the layering or foliation of the bedrock (Dehls et al., 2000). Ojala et al. (2017) reported graphite schist from drill holes through the postglacial Isovaara–Riikonkumpu fault in northern Finland. We have found evidence for neither released high-pressure fluids, nor gases that could have reduced the friction of the structure before faulting. This phenomenon is reported from the reverse Stuoragurra Fault in Finnmark by Dehls et al. (2000). The elevation difference between the fault scarp and valley bottom is c. 200 m. Gravity-induced sliding is less likely to occur when the elevation difference is less than 300 m (Varnes et al. 1989). Other DSGSDs in Norway are usually located 400–1100 m above the floor of the fjord or the valley (like the Berill (1100 m), Nordnesfjellet (900 m), Kvasshaugen (400 m) and Åkneset (1100 m)). The slope of these deformation structures has usually an angle of c. 30º, i.e. more than twice as steep as the terrain below the Nordmannvika Fault. The apparent slope angle of 34–38º in Fig. 10 of Redfield & Hermanns (2016) is caused by the 2.5 exaggeration factor of the vertical axis.

5) No signs of glacial modification (such as striation or ice-plucking) of fault scarps, especially those controlled by banding, bedding or schistosity. There is no sign of glacial modification of the fault scarp, which implies that a warm based erosive glacier has never covered the fault scarp. Warm based ice characterized deglaciation of all Norwegian fjord valleys, including Nordmannvikdalen. The NF is therefore of postglacial age and was subaerially, not subglacially formed. The Nordmannvikdalen valley was deglaciated shortly before the Younger Dryas chronozone (12.9-11.5 kyr BP) (Dahl & Sveian, 2004), which consequently represents a maximum age of the fault. The scarp is locally modified by Holocene solifluction.

6) Exclusion of mechanisms such as glaciotectonics (ice push features), collapse due to ice melting and differential compaction or deposition over a preexisting erosional scarp being the cause of an apparent offset in overburden. The Quaternary overburden consists of massive lodgement till with no sign of differential compaction or deposition over the scarp, except in the adjacent vertical wedge zones where the postglacial infill sediments are clearly less compacted.

Topographical map data shows that the downhill surface gradient is less than 20 degrees in the area where the NF is located, which is much less than suggested by Redfield & Hermanns (2016) and is itself in odd with their hypothesized DSGSD origin of the NF. The results from our GPR measurements, observations in the field and trenching showed in addition that:

- Bedrock structures with reflectors sloping with relatively steep angles, up to 45 °, are traceable up to the bedrock–overburden interface at c. 10 m depth close to the NF location. One of these, at 45 ° dip angle, reaches the bedrock surface just a few metres downhill from the NF scarp, and is likely to represent the NF fault plane interception in the GPR profile.
- The extended trenching, both vertically and horizontally, of the previous trench that Redfield & Hermanns (2016) used as basis for their observations, showed that their record did not reach deeper than within the cryoturbated soil zone, which did not give any information of possible other deformation or displacement associated with faulting.
- Similarly as found by Bakken (1983) in the western part of the fault scarp the new trenching in the middle of the scarp showed that vertical sediment wedges occurred in lodgement till just under the NF scarp, and also under a trough lineament semi-parallel to and c. 10 m separated from the NF scarp. The zone between these features appears as a shallow graben structure with conjugate normal fault boundaries. Cavities occur also under the apex of the sediment wedges.
- Trenching close to the eastern end of the fault scarp showed a wider collapsed zone (> 2 m wide) just under and downhill from the fault scarp. The topsoil in and just under the scarp slope is both cryoturbated and further collapsed to a depth of at least 2.5–3 m. These features, together with the sediment wedges and cavities below, as mentioned above, indicate initially frozen ground (permafrost) and subsequent melting, sediment infilling and collapse of sediments in open semi-linear cracks longer than any semi-linear frost cracks reported from pattern ground fields in Arctic areas, and also water circulation at depth, in combination with periods of cryoturbation in the top soil along the NF and semi-parallel structures. The evidence of permafrost conditions during the fault event indicates that the age of the fault is most likely Younger Dryas, which is the last and only known interval since deglaciation of this area when permafrost conditions reached several metres depth.
- Solifluction features are abundant in the NF area and the fault scarp has locally clearly been modified by periglacial processes, but not formed by them. And since even Redfield & Hermanns (2016) actually ruled out their own hypothesis of DSGSD origin of the NF scarp, we can just support their discussion, the slope angle is simply much too low, and a different mechanism is needed to lead to the formation of the at least 1.3 km long NF scarp, and that is a tectonic mechanism.

Lagerbäck and Sundh (2008) argue that the Weichselian deglaciation was unique since no faulting has been observed subsequent to the previous glaciations in northern Sweden. Landforms generated during these glaciations can still be observed in northern Sweden since the inland ice was frozen to the ground during most of the glacial periods, except in some areas where such features may be strongly deformed or eliminated, as e.g. in zones with series of long flutes or drumlins (Nordkalott Project, 1986), which indicate ice streaming and therefore warm-based ice with at least partially erosive glacier conditions in later parts of the last glaciation. Pore pressure building up under a thick ice and a thick permafrost zone could have contributed to the anomalously large horizontal stress and low vertical stress in the bedrock at the time of deglaciation as suggested by Muir Wood (1989) and Lagerbäck and Sundh (2008). The indications of at least partial permafrost conditions during the postglacial faulting in Nordmannvikdalen support this conclusion.

5. Conclusions

The Nordmannvikdalen Fault fulfils all six criteria defined by Fenton (1994). We therefore maintain that the structure should be classified as (A) 'Almost certainly neotectonics' as proposed by Dehls et al. (2000) and Olesen et al. (2004, 2013). The elevation difference of 200 m and the 14º average angle of the slope are too small to induce gravitational sliding. The trenching of the fault scarp clearly shows that the scarp is formed during faulting and cannot be related to overburden creep processes. The length of the fault scarp of at least 1.3 km disqualifies it as a feature related to cracking of ground surface during abrupt extreme temperature fall in Arctic areas, since all reported or known and mapped such linear features in patterned Arctic ground are less than a few tens of metres in length (Ballantyne & Harris, 1994). However, when cracking of the frozen ground during the fault event had happened, then the further development with ice wedge and subsequent ice-wedge cast formation proceeded similarly as known from Arctic areas. We find consequently no support for the suggestion by Redfield & Hermanns (2016) to downgrade the fault to (E) 'very unlikely to be neotectonics', and we find neither any evidence for the numerous active faults in the northern Troms area as suggested by these authors (op.cit.). The final conclusion is that we still favour a tectonic origin of the Nordmannvikdalen Fault. The magnitude of the earthquake related to the

Nordmannvikdalen faulting was in the range 5.3–6.5 when comparing with length and displacement of contemporary earthquakes (Wells & Coppersmith, 1994). The wide range of the estimate is related to the anomalous height/length ratio of the fault.

Acknowledgements

This study has been supported in the framework of the NEONOR2 project by the Norwegian Research Council, the Geological Survey of Norway, the Norwegian Petroleum Directorate, the Norwegian Mapping Authority, AkerBP, DEA Norge, E.ON Norge, Ineos, Lundin Norway, Maersk Oil Norway, Norske Shell, Norwegian Energy Company (Noreco), Repsol Exploration Norge, Statoil and VNG Norge. Tom Gunnar Isaksen og Roy Steinar Karlsen from Manndalen Maskin carried out the trenching of the Nordmannvikdalen Fault. Helitrans transported the excavator from Nordmannvika to the trenching site in Nordmannvikdalen. The land owners Anette Susanne Lyngmo Seppäla and Veli-Matti Rikhart Seppäla and the municipality of Kåfjord granted permission and provided support for the trenching. Changes based on comments from the two reviewers Winfried Dallmann and Raimo Sutinen have significantly improved the manuscript. Irene Lundqvist drafted Figs. 7, 9–11 and 13–14. We express our sincere thanks to all these persons, companies and institutions.

6. References

Bakken, A.J.H. 1983: Nordmannvikdalen kvartaergeologi og geomorfologi. MSc thesis, University of Oslo, 126 pp.

Ballantyne, C.K. & Harris, C. 1994: The Periglaciation of Great Britain. Cambridge University Press 1994, 330 pp.

Beanland, S., Blick, G.H. & Darby, D.J. 1990: Normal faulting in a back arc basin: Geological and geodetic characteristics of the 1987 Edgecumbe earthquake. Journal of Geophysical Research 95, 4693–4707.

Berglund, M. & Dahlström, N. 2015: Postglacial fault scarps in Jämtland, central Sweden. Geologiska Föreningens i Stockholm Förhandlingar (GFF) 137, 339–343. http://dx.doi.org/10.1080/11035897.2015.1036361.

Braathen, A., Blikra, L.H., Berg, S.S. & Karlsen, F. 2004: Rock-slope failures of Norway; type, geometry, deformation mechanisms and stability. Norwegian Journal of Geology 84, 67–88.

Dahl, R. & Sveian, H. (red.) 2004: Ka dokker mein førr stein! Geologi, landskap og ressurser i Troms. Norges geologiske undersøkelse, 154 pp.

DECO Geophysical 2005: RadExplorer 1.4. The software for GPR data processing and interpretation. User Manual. www.radexpro.ru

Dehls, J.F., Olesen, O., Olsen, L. & Blikra, L.H. 2000: Neotectonic faulting in northern Norway; the Stuoragurra and Nordmannvikdalen postglacial faults. Quaternary Science Reviews 19, 1447–1460. http://dx.doi.org/10.1016/S0277-3791(00)00073-1.

Fenton, C.H. 1994: Postglacial faulting in eastern Canada. Geological Survey of Canada Open file Report 2774, 98 pp. http://dx.doi.org/10.4095/193973.

Holmsen, G. 1916: Om strandlinjers fald omkring gabbro-omraader (Summary in English). Norsk Geologisk Tidsskrift 4, 7–20.

Jol, H. M. (Ed.) 2009: Ground Penetrating Radar Theory and Applications. Elsevier Science, 544 pp.

Kujansuu, R. 1964: Nuorista sirroksista Lapissa. Summary: Recent faults in Lapland. Geologi 16, 30–36.

Lagerbäck, R. & Sundh, M. 2008: Early Holocene faulting and paleoseismicity in northern Sweden, Geological Survey of Sweden. SGU Research Paper C 836, 84 pp. SGU, Uppsala, Sweden.

Mauring, E., Olesen, O., Rønning, J.S. & Tønnesen, J.F. 1997: Groundpenetrating radar profiles across post-glacial faults at Kåfjord, Troms, and Fidnajohka, Finnmark. Norges geologiske undersøkelse Report 97.174, 11 pp.

Mikko, H., Smith, C. A, Lund, B., Ask, M., & Munier, R. 2015: LiDAR-derived inventory of

25 post-glacial fault scarps in Sweden. J. Geol. Soc. Sweden (GFF) 137:4, 334–338, doi:10.1080/11035897.2015.1036360, 2015.

Muir Wood, R. 1989: Extraordinary deglaciation reverse faulting in northern Fennoscandia.

In Gregersen, S. & Basham, P.W. (eds.): Earthquakes at North-Atlantic Passive Margins: Neotectonics and Postglacial Rebound, Kluwer Academic Publishers, Dordrecht, The Netherlands, pp. 141–173. http://dx.doi.org/10.1007/978-94-009-2311-9-10.

Muir Wood, R. 1993: A review of the seismotectonics of Sweden. Swedish Nuclear Fuel and Waste Management Company (SKB) Technical Report 93–13, 225 pp.

Nordkalott Project 1986: Map of Quaternary geology, sheet 2: Glacial geomorphology and paleohydrography, Northern Fennoscandia, 1:1 mill. Geological Surveys of Finland, Norway and Sweden, 1986. ISBN 91-7158-378-5.

Ojala, A.E.K., Mattila, J., Ruskeeniemi, T., Palmu, J.-K., Lindberg, A., Hänninen, P. & Sutinen, R. 2017: Postglacial seismic activity along the Isovaara–Riikonkumpu fault complex. Global and Planetary Change 157, 59–72.

Olesen, O. 1988: The Stuoragurra Fault, evidence of neotectonics in the Precambrian of Finnmark, northern Norway. Norsk Geologisk Tidsskrift 68, 107–118.

Olesen, O., Roberts, D., Henkel, H., Lile, O.B. & Torsvik, T.H. 1990: Aeromagnetic and

gravimetric interpretation of regional structural features in the Caledonides of West Finnmark and North Troms, northern Norway. Norges geologiske undersøkelse Bulletin 419, 1-24.

Olesen, O., Henkel, H., Lile, O.B., Mauring, E. & Rønning, J.S. 1992: Geophysical investigations of the Stuoragurra postglacial fault, Finnmark, northern Norway. Journal of Applied Geophysics 29, 95–118.

Olesen, O., Blikra, L.H., Braathen, A., Dehls, J.F., Olsen, L., Rise, L., Roberts, D., Riis, F., Faleide, J.I. & Anda, E. 2004: Neotectonic deformation in Norway and its implications: a review. Norwegian Journal of Geology 84, 3–34.

Olesen, O., Bungum, H., Dehls, J., Lindholm, C., Pascal, C. & Roberts, D. 2013: Neotectonics, seismicity and contemporary stress field in Norway – mechanisms and implications. In Olsen, L., Fredin, O. & Olesen, O. (eds.): Quaternary Geology of Norway, Geological Survey of Norway Special Publication 13, pp. 145–174.

Osmundsen, P.T., Henderson, I., Lauknes, T.R., Larsen, Y., Redfield, T.F. & Dehls, J. 2009: Active normal fault control on landscape and rock-slope failure in northern Norway. Geology 37, 135–138.

Palmu, J.-P., Ojala, A.E.K., Ruskeeniemi, T., Sutinen, R. & Mattila, J. 2015: LiDAR DEM

detection and classification of postglacial faults and seismically-induced landforms in Finland: a paleoseismic database. J. Geol. Soc. Sweden (GFF) 137:4, 344-352, DOI:10.1080/11035897.2015.1068370

Péwé, T.L. 1974: Geomorphic processes in polar deserts. In Smiley, T.L. & Zumberge, J.H. (eds.): Polar Deserts and Modern Man, Tucson, University of Arizona Press, pp. 33–52.

Redfield, T.F. & Hermanns, R.L. 2016: Gravitational slope deformation, not neotectonics: Revisiting the Nordmannvikdalen feature of northern Norway. Norwegian Journal of Geology 96, 1-29. http://dx.doi.org/10.17850/njg96-3-05.

Sollid, J. L. & Tolgensbakk, J. 1988: Kvartærgeologisk og geomorfologisk kartlegging på Svalbard og fastlands-Norge. Abstract, Nordic Geological Winter-Meeting, Copenhagen, 380–381.

Sylvester, A.G. 1995: Nearfield vertical displacement in the creeping segment of the San Andreas fault, central California, 1975 to 1994. Tectonophysics 247, 25–47.

Tolgensbakk, J. & Sollid, J.L. 1988: Kåfjord, kvartærgeologi og geomorfologi 1634 II, scale 1:50,000, Geografisk institutt, University of Oslo.

Varnes, D. J., Radbruch-Hall, D. H. & Savage, W. Z. 1989: Topographic and structural conditions in areas of gravitational spreading of ridges in the Western United States. USGS Professional Paper 1496, 28 pp.

Vestøl, O., Ågren, J., Steffen, H. in prep: A new land uplift model for Fennoscandia and the Baltic Region.

Wells, D.L. & Coppersmith, K.J. 1994: Empirical relationships among magnitude, rupture length, rupture area, and surface displacement. Bulletin of the Seismological Society of America 84, 974–1002.

Yeats, R.S., Sieh, K. & Allen, C.R. 1997: The geology of earthquakes. Oxford University Press, New York, 568 pp.

Zwaan, K.B., Dangla, P. & Quenardel, J.M. 2006: Bergrunnskart Kåfjord 1634 II, scale 1:50,000, Norges geologiske undersøkelse.

CHAPTER 6: ANALYSIS STRATEGIES FOR COMBINING CONTINUOUS AND EPISODIC GNSS FOR STUDIES OF NEO-TECTONICS IN NORTHERN-NORWAY

Authors: Halfdan Pascal Kierulf[1]

Affiliations: [1]Geodetic Institute, Norwegian Mapping Authority, Hønefoss, Norway, [2]Department of Geosciences, University of Oslo, Oslo, Norway

Journal: Journal of Geodynamics, 109

Publishing Date: 14 July 2017 (Online)

DOI: http://dx.doi.org/10.1016/j.jog.2017.07.002 (OA)

Pages: 9

Journal of Geodynamics 109 (2017) 32–40

Contents lists available at ScienceDirect

Journal of Geodynamics

journal homepage: www.elsevier.com/locate/jog

Analysis strategies for combining continuous and episodic GNSS for studies of neo-tectonics in Northern-Norway

Halfdan Pascal Kierulf[a,b,*]

[a] Geodetic Institute, Norwegian Mapping Authority, Hønefoss, Norway
[b] Department of Geosciences, University of Oslo, Oslo, Norway

ARTICLE INFO

Keywords:
GNSS campaign
Episodic GNSS
Regional reference frame realization
Neo-tectonics
Glacial isostatic adjustment

ABSTRACT

Crustal deformation in the seismically active Nordland area in Northern Norway is estimated based on a combination of data from local episodic epGNSS campaigns (three 5-day campaigns in 1999, 2008 and 2015) and continuously operating cGNSS stations in the area that were mainly established in 2008 and in 2009. To establish a local long-term stable reference frame, which is consistent both with the epGNSS network and the network of newer cGNSS, a three-step procedure for reference frame realization is used to get consistent results from all the stations in the area. Analysis of the main error sources shows that uncertainties for the episodic epGNSS stations are around 0.2 mm/yr in the horizontal components and 0.5 mm/yr in the vertical component. The results support earlier findings that Ranafjord area of the Nordland is undergoing crustal spreading with horizontal displacement velocities of ca. 1.0 ± 0.2 mm/yr, predominantly in the east-west direction. The results also show a gradient in the uplift along the coast of Nordland that is larger than predicted by existing glacial isostatic adjustment models.

1. Introduction

For more than two decades Global Navigation Satellite System (GNSS) observations have successfully been used for geodynamical studies. Phenomena like plate tectonics (e.g. Gordon and Stein, 1992), glacial isostatic adjustment (GIA) (e.g. Steffen and Wu, 2011), earthquakes (e.g. Blewitt et al., 2009) and the solid earth response to variations in hydrological loadings (e.g. Van Dam et al., 2001) have been studied.

The International GNSS Service (IGS) provides GNSS data from approximately 500 permanent and continuously operating GNSS stations (cGNSS) globally. Organizations like IAG Reference Frame Sub-Commission for Europe (EUREF) and the US National Geodetic Survey (NGS) collect and release data from regional cGNSS networks. National mapping agencies and other institutions collect cGNSS data on a national level. In addition, GNSS data from campaigns, named episodic GNSS stations (epGNSS), are collected. The epGNSS can be used for national or regional datum realization (e.g. the EUREF-89 campaign used for the realization of ETRF89, Torres et al., 2009), stability measurements (e.g. Kierulf et al., 2002) or geodynamic studies (e.g. Hudnut et al., 1994). The stations are normally occupied between a few hours and a few months in each campaign. If the goal is to detect crustal deformation or other movements, the campaign has to be repeated.

Results from cGNSS are more precise and more reliable than results from epGNSS. On the other hand, epGNSS observations often provide improved spatial coverage (often from a dense network over a geographical limited area) and longer observation history. Hence, epGNSS could give valuable information and provide constraints on geophysical phenomena. In remote areas with lack of infrastructure, epGNSS have been the only practical possible solution. Alothman et al. (2016) demonstrate how epGNSS data combined with cGNSS improved the estimate of plate rotation of the Arabic plate. By combining epGNSS and cGNSS, Saria et al. (2014) studied the kinematics of the East African rift, Leonard et al. (2007) investigated the tectonic processes in the northern Canadian Cordillera and Pesci et al. (2009) improved strain rate estimates in the Central Apennine of Italia. Kierulf et al. (2009) used epGNSS to find the spatial pattern of the elastic response on glacial melting in Northwestern Svalbard.

The Norwegian mainland is located on the stable Eurasian plate, but intra plate deformations have been detected (e.g. Olesen et al., 2013). The largest and most studied phenomena is GIA. In Scandinavia GIA-models explain most of the signal (Steffen and Wu, 2011). However, for the west coast of Northern Norway the discrepancies between observations and the GIA-models have been larger (Kierulf et al., 2014). In the Nordland area neo-tectonic processes have been detected and increased seismic activity is registered with frequent earthquakes of magnitude between one and three (Fig. 1). The largest known historical earthquake was in 1819 with magnitude 5.9 (Bungum and Olesen,

* Correspondence to: Geodetic Institute, Norwegian Mapping Authority, Hønefoss, Norway.

http://dx.doi.org/10.1016/j.jog.2017.07.002
Received 23 November 2016; Received in revised form 23 June 2017; Accepted 8 July 2017
Available online 14 July 2017

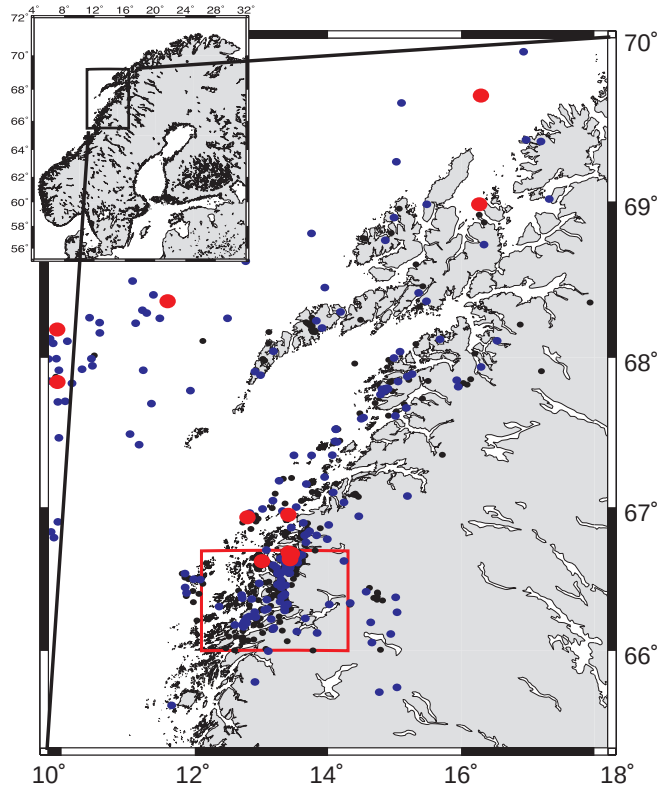

Fig. 1. Earthquakes in Nordland between August 2013 and May 2016 (from the NEONOR2 project, Janutyte et al., 2017). Black dots have magnitude less than one, blue dots have magnitude between one and two and red dots have magnitude larger than two. The red square is the Ranafjord area discussed in the text. (For interpretation of the references to color in this figure legend, the reader is referred to the web version of the article.)

2008). Fault-plane solutions indicate north-south compression and east-west extensional faulting (Hicks et al., 2000). Olesen et al. (2013) found surface deformations in the Ranafjord area (red square in Fig. 1).

The first goal of this paper is to develop a GNSS analysis strategy to obtain a consistent, robust and accurate crustal velocity field in the Nordland area (study area) based on the Norwegian cGNSS network and epGNSS. The challenge is to establish a local long-term stable reference frame consistent with both the epGNSS network (campaigns in 1999, 2008 and 2015) and the network of newer cGNSS (established after the 2008 campaign, but sufficiently long to be used for geodynamical studies).

The second goal is to identify the different contributions to the error budget for epGNSS data and to give realistic uncertainty estimates for the velocities of the stations. The velocity field will be compared with geophysical processes effecting the earth crust in Nordland and the discrepancies discussed.

2. GNSS analysis

In this investigation the GNSS data were processed with the software "GPS At MIT"/Global Kalman filter (GAMIT/GLOBK). The analysis strategy described in Herring et al. (2015), have been used, with a 10 degree cut-off elevation, igs08.atx antenna phase center model, the Vienna Mapping Functions (VMF1) (Boehm et al., 2006) tropospheric mapping function and the FES2004 ocean loading model (Scherneck, 1991). Atmospheric loading is not included and higher order ionosphere disturbances are not modelled. Atmospheric loading (Dach et al., 2011) and ionospheric corrections (Petrie et al., 2011) are spatially correlated. Hence, the three-step reference frame realization strategy described in Section 3 reduces the effect of these corrections.

To keep the processing time acceptable (less than three months in total on eight xeon cpu cores), the GNSS data was divided into several sub-networks that were analyzed individually (see Fig. 2). For each day the loosely constrained sub-network solutions were combined to one daily solution.

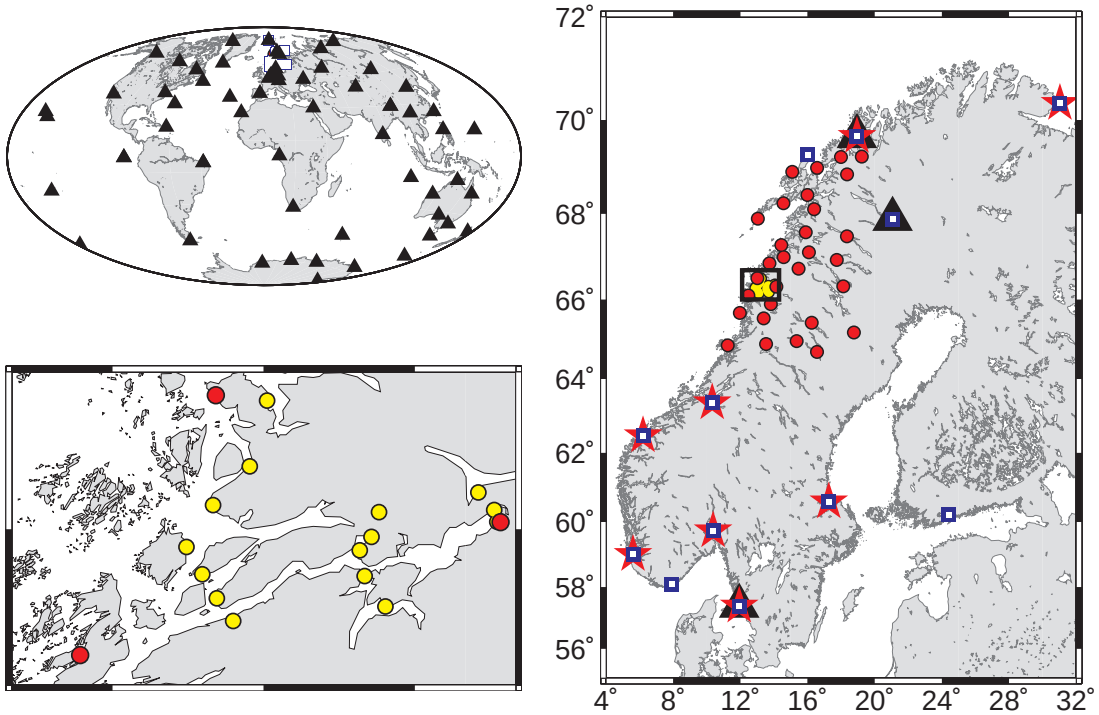

Fig. 2. The GNSS station networks used in this study. The networks are: the epGNSS-network (yellow circles), the regional cGNSS-network mainly established in 2008 and 2009 (red circles), Norwegian and Swedish networks of long-term operating cGNSS established in 1999 or earlier (blue squares) and two global networks from IGS list of CORS (black triangles). Red stars mark cGNSS used in the simulation of epGNSS in Section 5. The lower left panel is the Ranafjord area, enlarged from the black rectangle in the right panel. (For interpretation of the references to color in this figure legend, the reader is referred to the web version of the article.)

3. Reference frame realization

A loosely-constrained GNSS network solution is normally transformed to the reference frame using a network of stations either globally or from the region of interest. Using a regional network solution will remove most of the so-called common mode signal (see e.g. Wdowinski et al., 1997) and give more accurate velocity estimates (e.g. Williams et al., 2004; Kierulf et al., 2013), but the results are de-coupled from the global reference frame (see e.g. Legrand et al., 2010, for an analysis of limitations of regional reference frames). To ensure consistency with the global solution, but exploit the advantages of regional network solution a two-step procedure can be used for reference frame realization. First realize a global solution and then a regional solution based on the output of the global solution.

In the global realization (first step), the daily loosely-constrained solutions are transformed to a global reference frame using a global network of cGNSS as reference stations. In this study approximately 60 long-term operating continuous global distributed IGS stations realized in International Terrestrial Reference Frame (ITRF2014) (Altamimi et al., 2016, black triangles of Fig. 2) were used. From the daily results of this global solution, positions and velocities are estimated and combined to the global reference frame solution.

To realize a regional solution, the procedure can be repeated, but this time using the regional stations in the transformation to the global solution from the first step (see the hatched path in Fig. 3).

In this study, most stations are either epGNSS observed in 1999, 2008 or 2015, or cGNSS, but established after the 2008 campaign. No continuous stations in the study area were operated in parallel with all three campaigns, so no local cGNSS are available to link the epGNSS and cGNSS networks through the entire observation period. Changes in the regional or global network (e.g. removing old stations or establishment of new stations) or unaccounted geophysical phenomena (e.g. earthquake or hydrological loadings), might introduce a small time-dependent error signal in the reference frame realization. This signal might affect GNSS stations with different observation histories differently, meaning the velocity solution for the epGNSS and cGNSS are not fully consistent.

To reduce this risk an intermediate regional reference frame realization was introduced. In an extra second step only regional cGNSS surrounding the study area and operated during the complete time span, i.e. 1999 to present (blue squares in Fig. 2), were used in the transformation to the global solution from first step. From the daily results of this intermediate solution, positions and velocities were estimated, and combined to the intermediate reference frame solution.

In the final regional solution, the reference frame was realized using both the epGNSS and the regional cGNSS (red and yellow circles in Fig. 2) in the transformation to the intermediate solution from the second step. This three-step procedure is sketched in Fig. 3.

The idea behind this procedure is that the intermediate solution is as consistent as possible both with the newer cGNSS as well as with the epGNSS for the complete observation period, while the final step removes most of the common mode signal in the study area.

4. Velocities and uncertainties cGNSS

It is widely recognized that GNSS time-series have a more complex noise structure than only white noise (Johnson and Agnew, 1995; Zhang et al., 1997; Mao et al., 1999; Williams et al., 2004). This fact has limited consequences for the velocity estimates, but has significant impact on the estimated velocity uncertainties. The cGNSS time-series analysis strategy used in this study includes both white noise and power law noise, where the spectral index also was estimated.

The velocities, spectral indices and uncertainties were estimated using the software Cheetah. Cheetah is a successor of the time-series

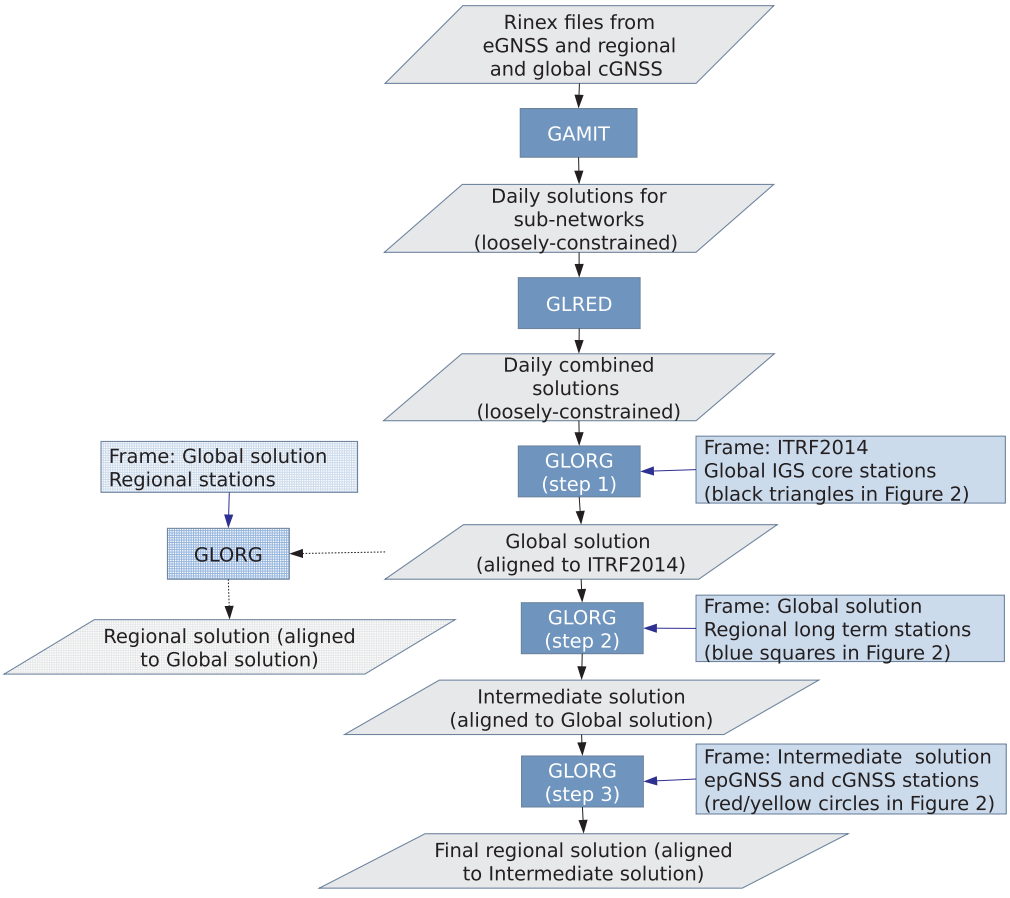

Fig. 3. Float diagram for GNSS reference frame realization. GLRED and GLORG are GAMIT/GLOBK-modules to combine daily loosely-constrained solutions and for reference frame realizations, respectively. The light blue rectangles display the reference frame and GNSS networks used in the alignment. The gray parallelograms display the input/output products. The hatched path is the second step of the usual two-step procedure that is improved in this study. (For interpretation of the references to color in this figure legend, the reader is referred to the web version of the article.)

analysis software CATS (Williams, 2008) and uses the differencing method that was described in Bos et al. (2008). Outliers were removed in a preliminary analysis using an in house least square program based on a 3σ-criteria. Annual and semi-annual signals where solved for in the time-series analysis. Heaviside functions were also included to compensate for coordinate changes for all known antenna and radome changes as well as where jumps in the time-series were obvious after a visual inspection.

Velocities and uncertainties for the final regional solution are included in Table 3. Velocities and uncertainties were also estimated from the global solution and the intermediate solution. The mean reduction of the uncertainties for the final regional solution relative to the global solution are 32%, 30% and 51%, in north, east and height component, respectively (12%, 13% and 21% relative to the intermediate solution). All noise parameters were reduced. In the global solution the mean power law indices were 0.74, 0.71 and 0.76, in north, east and height component, respectively. For the regional solution the mean power law indices were 0.63, 0.65 and 0.59. The mean improvement was 15%. The power law sigmas were also reduced on average by 18%, while the mean white noise sigma was reduced by only 3%. I.e. results in the final regional solution contains less correlated noise, the regional time-series are “whiter”. The removed common mode signal consists of a large fraction correlated noise. Its origin could be mis-modelled large-scale effects like satellite orbits, Earth Orientation Parameters (EOP), antenna phase center or geophysical phenomena with large spatial footprints. Williams et al. (2004) and Dmitrieva et al. (2015) have earlier showed a decrease in correlated noise in time-series when the common mode signals are removed.

5. Results epGNSS

Quantifying the velocity uncertainties for epGNSS is not straightforward. Four main issues, including how they affect the results, are addressed below.

5.1. Problem (i) obtaining good noise characteristics

The epGNSS time-series contain too sparse data to estimate accurate noise parameters. There are several approaches to compensate for this. One possibility is to make a “qualified-guess” of the noise parameters. Assuming that the cGNSS time-series have similar noise characteristics as the epGNSS, the noise parameters from these can be used. Another widely used approach is to scale the formal uncertainties of the velocities, so called variance component estimation. E.g. Alothman et al. (2016) estimated a scale factor based on maximizing the log-likelihood function of the estimated plate motion model. A third alternative is to study variations in velocity estimates for simulated epGNSS time-series extracted from cGNSS. This study makes use of this last approach.

Time-series for epGNSS were simulated by extracting “campaigns” from eight Norwegian and Swedish regional time-series from stations operated continuously from 1999 until today (red star in Fig. 2). Different combinations of campaigns are simulated (see Table 1). One such combination of campaigns is named an *epGNSS-scheme*. The jumps estimated with heaviside functions were used to correct the time-series before the simulated epGNSS time-series were extracted. For each epGNSS-scheme and for each station the velocities in north, east and height were estimated. This was repeated 1000 times, where the start day for each campaign was randomly chosen in each repetition. The standard deviation of the velocity for each epGNSS-scheme is:

$$\sigma = \sqrt{\frac{\sum_{j=1}^{m}\sum_{i=1}^{n}(r_{i,j} - R_j)^2}{\mathrm{nm}}}, \quad (1)$$

where $n = 1000$ (the number of simulations) and $m = 8$ (the number of stations). The estimated velocity for station j in the ith simulation is $r_{i,j}$ and the velocity estimated from the complete time-series for station j from 1999 until today is R_j. The results are included in Table 1.

Not surprisingly, the standard deviation reduces when the number of campaigns and/or length of campaigns is increased. However, the most important factor is the time span from the first to the last campaign. Doubling the time compensates for the difference between 30 days versus 1-day campaigns, or yearly campaigns versus only two campaigns.

The epGNSS-scheme with three 5-days campaigns with 16 years between first and last campaign, correspond to the epGNSS measurements in this study. The standard deviations in this case are 0.06 mm/yr, 0.06 mm/yr and 0.23 mm/yr in north, east and height, respectively. Note that the middle campaign has a very little effect on these standard deviations. However, such an extra campaign is mandatory to detect problems in the individual campaigns (see Section 5.3).

5.2. Problem (ii) to quantify offsets due to equipment change

Geodetic time-series are hampered by jumps (see e.g. Williams, 2003). If the jumps can be identified in the cGNSS time-series (see e.g. Gazeaux et al., 2013), it can be resolved and accurate velocities estimated. In epGNSS time-series, the possibility to detect and resolve jumps is limited.

Antenna changes are the most frequent reason for artificial jumps. Coordinate changes due antenna changes are estimated as part of cGNSS time-series analysis. The standard deviations, σ_C, of the coordinate changes due to antenna changes are 1.9 mm, 2.2 mm and 6.4 mm in north, east and height, respectively ($\sigma_C = \sqrt{\sum_{i=1}^{n} C_i^2/n}$, where the C_is are the estimated coordinate changes).

If the antenna is changed, it is common practice to replace the cGNSS cable and receiver at the same time. This is similar to the situation for epGNSS, where both the antenna, receiver and additional equipment are changed from campaign to campaign. It is therefore realistic to use the estimated coordinate changes due to antenna changes as proxy for the coordinate changes from one campaign to the next (disregarding possible blunders in the setup, see the discussion in Section 5.3).

To test the effect of equipment changes on the uncertainties of the epGNSS time-series, the test with the simulated epGNSS-schemes (Table 1) was repeated, but this time with a randomized offset for each campaign. The offsets are assumed to be normal distributed with standard deviation σ_O. A coordinate change is the difference of two consecutive offsets. Since two offsets are independent, the variance: $\sigma_C^2 = \sigma_{O-O}^2 = 2{\cdot}\sigma_O^2$, and hence, the standard deviation of the offset: $\sigma_O = \sigma_C/\sqrt{2}$. The results are included in Table 2.

As in the case without equipment changes, the time difference between the first and last campaign is more important than the number of occupations and the number of observation days in each campaign.

In the three left columns the effect of three independent one day campaigns instead on one single campaign, was tested. This greatly improves the precision. Actually, these results show that three independent one-day campaigns in the campaign years give better results than one 30-day campaign. The offset of two equipment changes (and blunders) are expected to be independent, hence, the effect on the uncertainties of such changes reduces with the square root of the number of independent setups. The effect of geophysical phenomenaes lasting several days, like atmospheric loading, will also be reduced by using three independent observations instead of several consecutive days.

The standard deviations in the epGNSS-scheme closest to the observed epGNSS used in this study are 0.14 mm/yr, 0.15 mm/yr and 0.47 mm/yr in north, east and height, respectively. The epGNSS-scheme in Table 2 is not exactly the same as in the epGNSS-scheme for the observations. The simulation was therefore repeated, but this time using the same years as the campaigns (1999, 2008 and 2015) and restricting the time of the campaigns to the same months as the real campaigns. The standard deviations were then almost identical

Table 1
Standard deviation of the velocity variations for simulated epGNSS-schemes. Length is the time span in years from first to last campaign. Nb is the number of campaigns evenly distributed from the first to the last campaign. 1 day, 5 days and 30 days are the number of consecutive days in each campaign and three times mean three independent 1-day campaigns each campaign year. The mid epoch of all simulations was in 2007. The numbers are in mm/yr. Numbers in bold are the epGNSS-scheme closest to the observed epGNSS used in this study.

Length	Nb	N	E	U	N	E	U	N	E	U	N	E	U
		1 day			5 day			30 days			1 day three times		
2	2	0.72	0.67	1.92	0.46	0.43	1.14	0.30	0.31	0.81	0.46	0.45	1.33
2	3	0.67	0.61	1.82	0.44	0.40	1.10	0.30	0.30	0.79	0.45	0.45	1.33
4	2	0.37	0.33	0.99	0.25	0.20	0.59	0.17	0.15	0.38	0.24	0.21	0.68
4	3	0.35	0.31	0.97	0.25	0.20	0.58	0.18	0.14	0.38	0.24	0.22	0.68
4	5	0.30	0.27	0.83	0.22	0.19	0.53	0.17	0.14	0.38	0.21	0.19	0.63
8	2	0.19	0.18	0.48	0.12	0.11	0.32	0.10	0.10	0.27	0.13	0.13	0.33
8	3	0.18	0.17	0.48	0.12	0.11	0.32	0.10	0.08	0.27	0.13	0.12	0.34
8	5	0.15	0.14	0.43	0.11	0.09	0.28	0.09	0.08	0.22	0.12	0.11	0.30
8	9	0.13	0.12	0.36	0.09	0.09	0.27	0.08	0.08	0.25	0.10	0.09	0.26
12	2	0.14	0.12	0.35	0.10	0.08	0.23	0.07	0.06	0.19	0.09	0.09	0.23
12	3	0.13	0.11	0.34	0.09	0.07	0.23	0.07	0.05	0.19	0.09	0.09	0.24
12	5	0.10	0.10	0.31	0.07	0.07	0.23	0.05	0.06	0.20	0.07	0.08	0.22
12	7	0.09	0.09	0.27	0.06	0.06	0.18	0.05	0.05	0.16	0.07	0.07	0.19
12	13	0.07	0.07	0.21	0.05	0.05	0.17	0.04	0.06	0.17	0.05	0.06	0.15
16	2	0.09	0.09	0.33	0.05	0.06	0.25	0.04	0.04	0.21	0.06	0.06	0.19
16	3	0.09	0.09	0.32	**0.06**	**0.06**	**0.23**	0.05	0.05	0.20	0.07	0.06	0.20
16	5	0.07	0.08	0.26	0.05	0.06	0.20	0.04	0.05	0.18	0.06	0.05	0.17
16	9	0.06	0.06	0.21	0.04	0.05	0.16	0.03	0.04	0.16	0.05	0.05	0.14
16	17	0.05	0.05	0.18	0.03	0.04	0.15	0.03	0.04	0.17	0.04	0.04	0.12

(0.13 mm/yr, 0.15 mm/yr and 0.46 mm/yr in north, east and height, respectively).

5.3. Problem (iii) to detect blunders in the station setup

A major concern with epGNSS is the risk of blunders in the station setup. It is impossible to detect such blunders based on only two campaigns. However, with more than two campaigns, one can calculate velocities based on different combinations of campaigns. If these velocities differ then blunders can be identified. With three campaigns, as is the case in this study, the velocity based on the first and second campaign (1999 and 2008) and the velocity based on the second and third campaign (2008 and 2015), can be estimated. The difference in these two velocities, will be named *velocity change* in the rest of this Section. A large velocity change indicates something wrong with the station setup.

In Fig. 4 the effect of a 10 mm offset in the 2015 campaign (left) and the 2008 campaign (middle) are illustrated. In the left figure, the velocity change is 1.4 mm/yr, while the effect on the estimated velocity (velocity bias) is 0.6 mm/yr. In the middle figure, the velocity change is 2.5 mm/yr, while the velocity bias is almost negligible ($\sim$0.05 mm/yr). I.e. an erroneous observation in the middle campaign is easy to detect and has very little influence on the velocity estimate. An erroneous measurements in the last campaign is harder to detect, but has larger consequences. The ratio between velocity bias and velocity change is 0.43 in the first case and close to zero in the second case. An erroneous observation in the middle campaign with approximately half the magnitude of the last erroneous observation (right figure), gives a velocity bias of 0.6 mm/yr and almost no velocity change. Such errors are almost impossible to detect.

The velocity changes in the epGNSS time-series varies from -1.00 mm/yr to 0.32 mm/yr, from -0.66 mm/yr to 0.66 mm/yr and -2.39 mm/yr to 2.08 mm/yr in north, east and height, respectively. The standard deviation of the observed velocity changes are 0.48 mm/yr, 0.46 mm/yr and 1.22 mm/yr.

In the simulation with the epGNSS-scheme closest to the situation in this study (three 5-days campaigns and 16 years between the first and

Table 2
Standard deviation of the velocity variations for simulated epGNSS-schemes including offset from equipment changes. Table information is the same as for Table 1.

Length	Nb	N	E	U	N	E	U	N	E	U	N	E	U
		1 day			5 days			30 days			1 day three times		
2	2	1.18	1.30	3.81	1.07	1.19	3.37	0.99	1.16	3.28	0.75	0.83	2.38
2	3	1.12	1.28	3.70	1.03	1.14	3.32	1.01	1.18	3.26	0.74	0.78	2.43
4	2	0.61	0.62	1.92	0.55	0.60	1.74	0.51	0.57	1.65	0.39	0.40	1.17
4	3	0.60	0.65	1.88	0.53	0.58	1.71	0.50	0.57	1.61	0.38	0.41	1.19
4	5	0.54	0.57	1.67	0.50	0.52	1.56	0.47	0.53	1.49	0.33	0.36	1.08
8	2	0.30	0.33	0.92	0.27	0.30	0.85	0.26	0.30	0.83	0.20	0.21	0.58
8	3	0.30	0.32	0.93	0.28	0.30	0.87	0.25	0.30	0.82	0.20	0.21	0.59
8	5	0.27	0.30	0.85	0.25	0.27	0.78	0.24	0.26	0.76	0.17	0.19	0.53
8	9	0.23	0.24	0.71	0.20	0.22	0.64	0.20	0.22	0.66	0.14	0.16	0.45
12	2	0.21	0.22	0.64	0.19	0.20	0.58	0.17	0.19	0.57	0.13	0.15	0.40
12	3	0.21	0.21	0.62	0.18	0.20	0.59	0.17	0.20	0.58	0.13	0.14	0.41
12	5	0.18	0.19	0.60	0.16	0.19	0.54	0.15	0.17	0.52	0.11	0.13	0.37
12	7	0.17	0.17	0.51	0.15	0.16	0.47	0.14	0.16	0.47	0.10	0.12	0.33
12	13	0.12	0.14	0.42	0.11	0.13	0.38	0.11	0.13	0.38	0.08	0.09	0.26
16	2	0.15	0.17	0.52	0.13	0.16	0.48	0.12	0.14	0.44	0.10	0.11	0.32
16	3	0.15	0.17	0.50	**0.14**	**0.15**	**0.47**	0.13	0.16	0.45	0.11	0.11	0.33
16	5	0.14	0.15	0.45	0.12	0.14	0.41	0.12	0.14	0.41	0.09	0.09	0.29
16	9	0.11	0.12	0.38	0.10	0.12	0.34	0.10	0.11	0.34	0.07	0.08	0.24
16	17	0.09	0.09	0.29	0.08	0.09	0.28	0.08	0.09	0.29	0.06	0.06	0.19

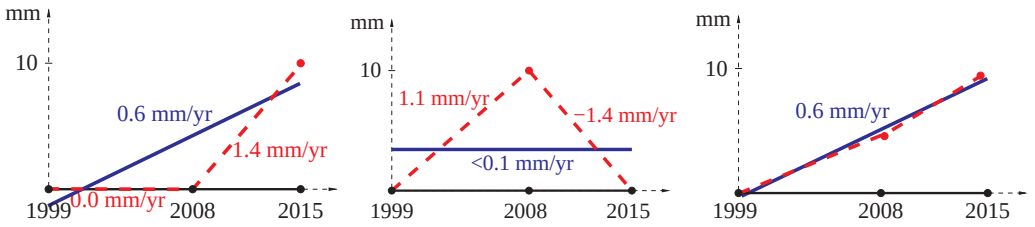

Fig. 4. Effect of error in the setup. Black dots are the "true" position and black lines the corresponding regression lines. Red dots are the erroneous "measured" points with 10 mm offset in all figures except the 2008 value in the right figure. This offset are slightly below 5 mm. Blue lines are the regression lines including the erroneous "measured" points. Red lines are the regression lines including the 1999- and 2008-campaigns and the regression lines including the 2008- to the 2015-campaigns. Red and blue numbers are the velocities corresponding to the red and blue lines respectively. All campaigns have the same associated uncertainty. (For interpretation of the references to color in this figure legend, the reader is referred to the web version of the article.)

Table 3
GNSS velocities. The stations NE03 to NE20 are the epGNSS in the Ranafjord area. Their uncertainties are estimated using the estimation procedure described in Section 5.5. The rest are Norwegian and Swedish cGNSS in the area. Their uncertainties are estimated using a white – plus power law – noise model.

Station	Latitude	Longitude	North (mm/yr)	East (mm/yr)	Up (mm/yr)
NE03	66.33067	14.11476	15.49 ± 0.10	14.41 ± 0.10	6.01 ± 0.24
NE05	66.35871	14.05195	15.66 ± 0.13	14.29 ± 0.15	5.45 ± 1.26
NE08	66.17626	13.68298	15.43 ± 0.19	14.24 ± 0.13	4.78 ± 0.69
NE09	66.22514	13.60074	15.49 ± 0.14	13.99 ± 0.17	4.61 ± 0.45
NE10	66.26629	13.58106	15.80 ± 0.12	14.24 ± 0.14	4.29 ± 0.26
NE11	66.28775	13.62783	15.67 ± 0.21	14.38 ± 0.09	4.75 ± 0.64
NE12	66.32731	13.65756	15.96 ± 0.11	13.98 ± 0.20	4.68 ± 0.43
NE13	66.15297	13.07892	15.61 ± 0.13	13.89 ± 0.18	4.60 ± 0.90
NE14	66.18936	13.01379	15.75 ± 0.16	13.72 ± 0.16	4.73 ± 0.48
NE15	66.20011	12.96610	15.70 ± 0.12	13.87 ± 0.19	4.06 ± 0.32
NE16	66.22797	12.95611	15.87 ± 0.15	13.61 ± 0.15	4.65 ± 0.28
NE17	66.27164	12.89340	15.66 ± 0.21	13.66 ± 0.14	4.30 ± 0.45
NE18	66.33851	12.99900	15.77 ± 0.21	13.96 ± 0.21	3.83 ± 0.82
NE19	66.50467	13.21360	15.95 ± 0.18	13.71 ± 0.13	4.24 ± 0.43
NE20	66.40019	13.14452	15.80 ± 0.09	13.87 ± 0.33	4.49 ± 0.76
TRO1	69.66272	18.93965	15.05 ± 0.06	14.84 ± 0.06	3.17 ± 0.15
FINC	69.23124	17.98716	15.33 ± 0.03	14.27 ± 0.04	3.59 ± 0.17
BALC	69.24025	19.22654	15.20 ± 0.06	15.01 ± 0.04	3.87 ± 0.22
BARC	68.86045	18.35093	15.34 ± 0.06	14.60 ± 0.05	4.19 ± 0.27
ANDO	69.27837	16.00870	15.42 ± 0.05	13.86 ± 0.05	1.06 ± 0.13
BJAC	69.00035	16.56523	15.39 ± 0.02	14.11 ± 0.02	2.72 ± 0.08
MYRC	68.91472	15.08700	15.65 ± 0.05	13.84 ± 0.05	1.77 ± 0.12
LODC	68.41238	15.98592	15.35 ± 0.06	13.96 ± 0.06	3.79 ± 0.15
SVOC	68.23207	14.56207	15.55 ± 0.06	13.68 ± 0.05	3.00 ± 0.30
LOFS	67.88779	13.03655	15.82 ± 0.02	13.44 ± 0.02	2.00 ± 0.09
KJOC	68.09944	16.38738	15.26 ± 0.04	14.45 ± 0.02	4.19 ± 0.12
KOBC	67.58001	15.89014	15.35 ± 0.07	14.39 ± 0.07	5.16 ± 0.25
SSJ1	67.48838	18.34132	15.12 ± 0.08	15.19 ± 0.05	6.62 ± 0.29
BODX	67.28751	14.43397	15.56 ± 0.03	13.97 ± 0.09	3.79 ± 0.11
SULC	67.11971	16.07785	15.43 ± 0.19	14.64 ± 0.11	7.06 ± 0.40
MOLC	67.00742	14.57330	15.70 ± 0.11	14.07 ± 0.05	4.61 ± 0.39
KVI0	66.94249	17.73906	15.49 ± 0.31	14.67 ± 0.23	7.20 ± 0.38
ORNC	66.86352	13.72638	15.78 ± 0.05	13.72 ± 0.15	4.54 ± 0.30
LONC	66.73731	15.46363	15.49 ± 0.08	14.41 ± 0.04	5.89 ± 0.17
LURC	66.51306	13.01008	15.59 ± 0.07	13.69 ± 0.07	3.63 ± 0.15
ARJ0	66.31802	18.12487	15.05 ± 0.05	15.48 ± 0.05	7.84 ± 0.07
DONC	66.09812	12.47165	15.90 ± 0.08	13.52 ± 0.10	2.76 ± 0.31
BLEC	65.88896	13.81041	15.77 ± 0.08	14.11 ± 0.20	5.47 ± 0.49
VEGS	65.67317	11.96374	15.88 ± 0.06	13.59 ± 0.06	3.77 ± 0.22
TROC	65.53863	13.38528	15.65 ± 0.05	14.38 ± 0.11	5.68 ± 0.34
SLU0	65.43155	16.24543	15.22 ± 0.15	14.99 ± 0.10	8.15 ± 0.24
MLA0	65.18814	18.75862	15.01 ± 0.11	16.23 ± 0.14	9.59 ± 0.14
SAX0	64.97177	15.34746	15.15 ± 0.19	15.00 ± 0.11	7.76 ± 0.38
VIL0	64.69785	16.55993	15.04 ± 0.16	15.51 ± 0.05	8.38 ± 0.08
ROYC	64.89697	13.52551	15.55 ± 0.21	14.65 ± 0.13	6.36 ± 0.40
VIKC	64.86371	11.24216	15.93 ± 0.06	13.61 ± 0.06	3.70 ± 0.24

last campaign in Table 2), the velocity changes can be estimated in addition. The standard deviation of the simulated velocity changes were 0.49 mm/yr, 0.54 mm/yr and 1.57 mm/yr. I.e. the standard deviations of the observed velocity changes are at the same level as the standard deviations of the simulated velocity changes. Consequently, there are no indication of blunders in the station setup.

Each campaign was conducted following the same procedures; the routine for the equipment setup was the same, the antennas were fixed to the ground markers with forced centering, and high quality geodetic equipment was used in all campaign setups. The properties of the epGNSS are therefore as similar as possible as the cGNSS and the possibility for setup blunders minimal. The agreement of standard deviations for the measured and simulated velocity changes gives weight to this conclusion.

The lack of standardized procedures for station setup and, in particular, the procedure and device for precise mounting of the antenna, are likely the major error source for velocity estimates based on epGNSS.

5.4. Problem (iv) estimating non-linear station movements

Non-linear station movements, e.g. periodic signals, changes in hydrological loadings or earthquakes, are almost impossible to detect in epGNSS time-series. However, for signals with a spatial footprint larger than 50 km, one can assume that epGNSS are exposed to the same geophysical phenomena as the cGNSS in the same area. The annual signal from the cGNSS time-series in the area are 0.6 mm, 0.7 mm and 1.2 mm in north, east and height, respectively. The corresponding values for the semi-annual harmonics are 0.2 mm, 0.2 mm and 0.6 mm. All campaigns were conducted during the summer months, which reduces the influence of the annual harmonic signal. The epGNSS observations span 15 years, the effect of annual signals are therefore negligible. However, previous studies have shown that local loading changes, from water reservoirs and glaciers, could introduce non-linear movements (Van Dam et al., 2001).

The largest glacier in the Nordland area is Svartisen, it is 369 km^2. Rolstad et al. (2009) found a negative mass balance of western Svartisen of 2.6 m water equivalent from 1985 to 2002. On Engabreen, a glacier arm of Svartisen, the total negative mass balance is approximately 6 m water equivalent from 1999 to 2015 (Andreassen et al., 2015). The campaign network is located more than 20 km from Svartisen and the maximal induced uplift is therefore neglectible (below 0.1 mm/yr using the approach for computing elastic loading from Farrell, 1972).

Storglomvatnet is a 29 km^2 water reservoir located 35 km from the closest epGNSS. The water level of the reservoir was increased by approximately 120 m during the 1990s. The resulting subsidence of this increased hydrological loading has been observed with Interferometric Synthetic Aperture Radar (InSAR). Close to the reservoir the subsidence was observed to be approximately 6 mm/yr between 1995 and 2000, but with smaller values of subsidence with increasing distance to the reservoir (Rouyet et al., 2016). The water level in the reservoir is allowed to vary approximately ± 60 m, with an associated elastic height variation of ± 0.8 mm at a distance of 35 km. The mean yearly variation in water level is approximately ± 10 m (Bøsnes et al., 2014). The campaigns are performed in the summer period with similar reservoir filling. For the long-term velocity determination (1999–2015) the effect is therefore negligible. The closest cGNSS (ORNC), was established only 20 km from Storglomvatnet and might experience yearly variations exceeding 1 mm. Due to an observation time of more than seven years, the introduced variations in the estimated velocity of this station are below the estimated uncertainty. The effect on the horizontal

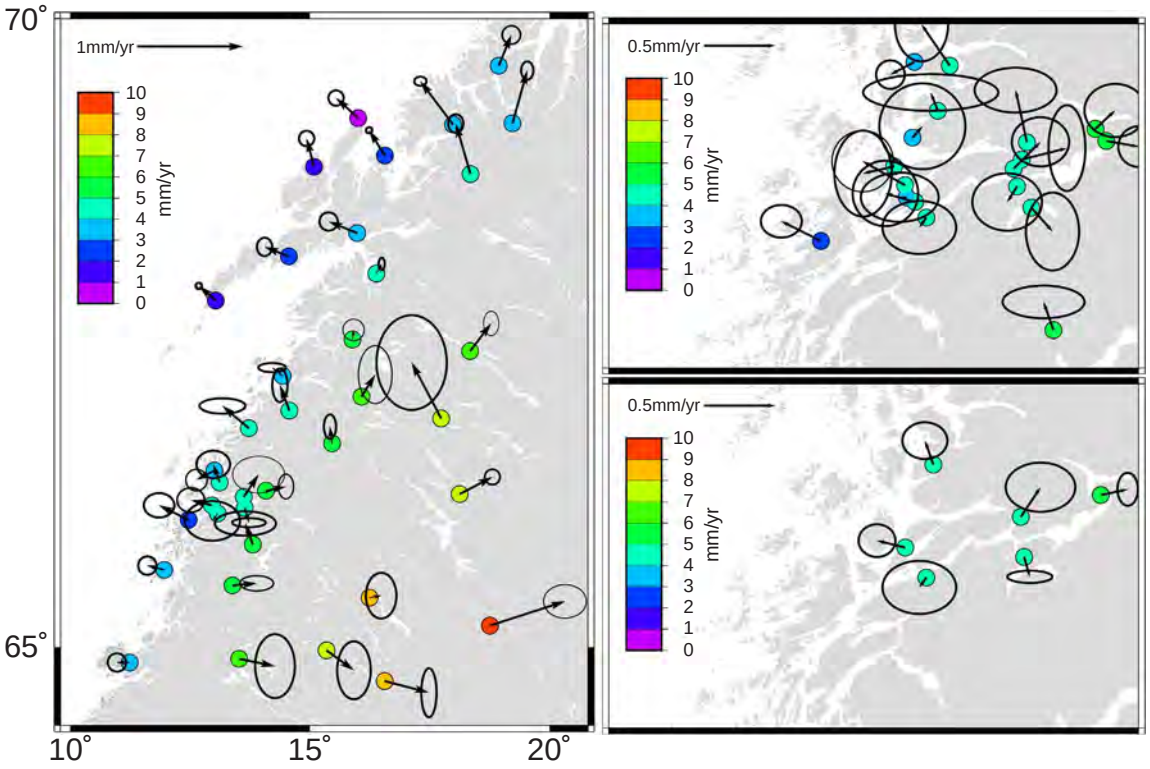

Fig. 5. GNSS velocities. Arrows show the horizontal velocities after removal of the mean rigid rotation while colored circles show the vertical velocities. The horizontal uncertainties are shown with $1-\sigma$ 2D error ellipses. The left figure is the Nordland area. Upper right figure is the same zoomed into the area of the campaign network, while the lower right figure shows the averaged velocities for the campaign stations in smaller local areas. (For interpretation of the references to color in this figure legend, the reader is referred to the web version of the article.)

component is even less.

The Nordland area is known to be seismically active and the possibility of small non-linear motions related to the seismicity can not be excluded. Unfortunately, the epGNSS with only three campaigns spanning 16 years are not able to detect such motions.

5.5. Velocities and uncertainties of epGNSS

The standard deviations given in Table 2 reflect the variations due to the reduced data amount (problem (i)), the different equipment used (problem (ii)) and to a large extent the effect of non-linear movements (problem (iv)). The problem with blunders in the station setup (problem (iii)) are discussed above and are likely small, but cannot be excluded.

The values in Table 2 are based on variations relative to the station velocities during the complete time-series from 1999 until present (the R_j in Eq. (1)). These velocities have also uncertainties. To obtain the final uncertainties for our epGNSS velocities, the mean uncertainties from the 15 years long time-series closest to our study area (TRO1, ANDO, ARJ0 and VIL0) are added in quadrature (square root of the sum of squares) to the numbers from the simulations in Table 2. The numbers from Table 2 are scaled by the ratio of the formal uncertainties of the velocities of the epGNSS and the mean formal uncertainties of the velocities from the simulated epGNSS time-series.

The velocities from the epGNSS are calculated with weighted least square adjustment. The velocities as well as their uncertainties are included in Table 3 and plotted in Fig. 5 together with the results from the cGNSS.

The epGNSS results indicate spatially consistent picture with outward spreading from the center of the epGNSS network and with relatively consistent velocities for neighboring stations in smaller area. The overall variations of the velocities for the individual stations relative to the average for these smaller areas are 0.08 mm/yr, 0.12 mm/yr and 0.42 mm/yr in north, east and height, respectively. The averaged velocities underpin the picture of spatial coherence of the deformations and are plotted in lower right panel of Fig. 5.

6. Discussion and conclusions

This study has, through a rigorous strategy for regional reference frame realization, shown how to combine epGNSS and cGNSS networks in a homogeneous long-term stable reference frame. The regional reference frame was realized in a three-step procedure to improve the spatial consistency of the network and the stability over the time span of our observations. The final uncertainties for the cGNSS velocities were reduced by approximately 30% in the horizontal components and 50% in the vertical component relative to the global results. In the regional epGNSS time-series the RMS of the residuals were reduced by 9% in north, 23% in east and 14% in height relative to the global time-series.

Realistic uncertainties for the epGNSS velocities have been estimated by identifying and quantifying the individual contributors to the error budget. As shown previously, the most important factor for accurate velocity estimation with epGNSS is the time span from the first to the last campaign. Longer campaigns give only a small improvement. However, several short campaigns in the campaign year are superior to one long campaign. Campaigns in between have less influence on the estimated velocities than the first and last campaign. However, such in between campaigns are mandatory to detect blunders in the station setup and to increase our confidence in the velocity estimates.

The geodetic results in this study show an east west gradient of the uplift and an outwards spreading in the Ranafjord area of almost 1 mm/yr. The velocity uncertainties are around 0.2 mm/yr in the horizontal components and 0.5 mm/yr in the vertical for the epGNSS. The velocity uncertainties for the best cGNSS are approximately one fourth of these estimates.

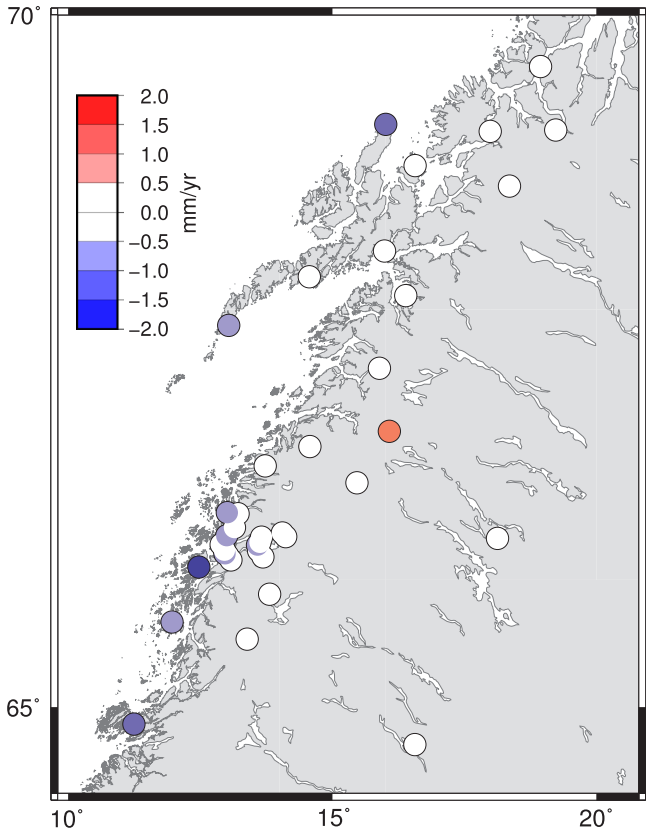

Fig. 6. Residual GNSS uplift. The colours show the differences between GNSS derived uplift and the best-fit GIA model from Kierulf et al. (2014). (For interpretation of the references to color in this figure legend, the reader is referred to the web version of the article.)

Most of the measured uplift signal can be attributed to GIA. In Kierulf et al. (2014) more than 2000 GIA-models with varying ice history and varying rheological properties, were compared with a GNSS derived velocity field and a best-fit model was identified. In Fig. 6 the differences between the new observations and the uplift from the best-fit GIA-model are plotted. The differences are below ± 0.5 mm/yr for almost all stations except the outer coastal stations, here the uplift is over predicted and the observed gradient larger than expected from the GIA-model. Discrepancies between GIA-models and observations might be explained by: (1) Erroneous rheological properties in the GIA model, e.g. omission of lateral inhomogenities in the earth model. (2) Error in the ice loading history. (3) Other neo-tectonic processes. (4) Error in GNSS measurements.

The observed extension in the Ranafjord area is consistent with the fault-plane solutions from Hicks et al. (2000) in the east-west direction, but the results do not agree with the north-south compression also shown in this study. Using GNSS velocities and a new compilation of focal mechanism, Keiding et al. (2015) find an extension of the Norwegian mainland, but a compression in outer coastal areas. However, they find that the seismic moment rates are varying more and have a magnitude at least two order of magnitude smaller than the geodetic moment rates. Olesen et al. (2013) suggests that sediment redistribution along the coast is causing flexuring and faulting in the lithosphere that coincides with the increased seismicity and might contribute to an increased uplift gradient. However, the sedimentation area (Olesen et al., 2013) is too far west to contribute directly to the subsidence for most of the coastal stations.

The Strandflat (Reusch, 1894) is the geomorphological word of a landscape covering most of the Norwegian west coast. The timing and mechanism of its formation has been under debate for a long time (e.g. Reusch, 1894; Nansen, 1922). Olesen et al. (2013) pointed at deep weathering processes as an important contribution. The study was based on analysis of GNSS, seismic, electrical resistivity and magnetism data. The new velocities estimated in this paper agree with the Ranafjord velocities used in Olesen et al. (2013), but demonstrate also that our existing geophysical knowledge in the Nordland area is insufficient to fully explain the geodetic observations. The velocity field developed in this study can be a foundation for further geophysical and GIA studies in the area.

Acknowledgements

Holger Steffen analyzed the Northern Swedish GNSS network with GAMIT. Lars Bockmann, Knut Gjerde and Oskar Johnsrud from the Norwegian Mapping Authority performed the three GNSS campaigns in the Ranafjorden area in 1999, 2008 and 2015. Thanks to Michael Dähnn and Matthew Simpson as well as Rui Fernandes and one other anonymous reviewer for comments and suggestions improving the document. This work was supported through the NEONOR2 project (nr: 228105) by Norwegian Research Council, Geological Survey of Norway, Norwegian Petroleum Directorate, Aker BP, DONG E & P Norge, E.ON E & P Norge, Lundin Norway, Maersk Oil Norway, Norske Shell, Norwegian Energy Company (Noreco), Repsol Exploration Norge, DEA Norge, Statoil and VNG Norge.

References

Alothman, A., Fernandes, R.M., Bos, M., Schillak, S., Elsaka, B., 2016. Angular velocity of Arabian plate from multi-year analysis of GNSS data. Arab. J. Geosci. 9 (8), 1–10. http://dx.doi.org/10.1007/s12517-016-2569-5.

Altamimi, Z., Rebischung, P., Mtivier, L., Collilieux, X., 2016. ITRF2014: a new release of the international terrestrial reference frame modeling nonlinear station motions. J. Geophys. Res.: Solid Earth 121 (8), 6109–6131. http://dx.doi.org/10.1002/2016JB013098.

Andreassen, L., Huss, M., Melvold, K., Elvehøy, H., Winsvold, S., 2015. Ice thickness measurements and volume estimates for glaciers in Norway. J. Glaciol. 61 (228), 763–775. http://dx.doi.org/10.3189/2015JoG14J161.

Blewitt, G., Hammond, W.C., Kreemer, C., Plag, H.-P., Stein, S., Okal, E., 2009. GPS for real-time earthquake source determination and tsunami warning systems. J. Geodesy 83 (3–4), 335–343. http://dx.doi.org/10.1007/s00190-008-0262-5.

Boehm, J., Werl, B., Schuh, H., 2006. Troposphere mapping functions for GPS and very long baseline interferometry from European Centre for Medium-Range Weather Forecasts operational analysis data. J. Geophys. Res. 111, B02406. http://dx.doi.org/10.1029/2005JB003629.

Bos, M., Fernandes, R., Williams, S., Bastos, L., 2008. Fast error analysis of continuous GPS observations. J. Geodesy 82, 157–166. http://dx.doi.org/10.1007/s00190-007-0165-x.

Bungum, H., Olesen, O., 2008. The 31st of August 1819 Lurøy earthquake revisited. Nor. J. Geol. 85, 245–252 ISSN:029-196X.

Bøsnes, E., Elvehøy, H., Vatne, V., Kvambekk, Å., 2014. Storglomfjord-utbyggingen, hydrologiske underskelser 2014. Norges vassdrags-og energidirektorat Tech. rep.

Dach, R., Böhm, J., Lutz, S., Steigenberger, P., Beutler, G., 2011. Evaluation of the impact of atmospheric pressure loading modeling on GNSS data analysis. J. Geodesy 85 (2), 75–91. http://dx.doi.org/10.1007/s00190-010-0417-z.

Dmitrieva, K., Segall, P., DeMets, C., 2015. Network-based estimation of time-dependent noise in GPS position time series. J. Geodesy 89 (6), 591–606.

Farrell, W.E., 1972. Deformation of the Earth by surface loads. Rev. Geophys. 10 (3), 761–797. http://dx.doi.org/10.1029/RG010i003p00761.

Gazeaux, J., Williams, S., King, M., Bos, M., Dach, R., Deo, M., Moore, A.W., Ostini, L., Petrie, E., Roggero, M., Teferle, F.N., Olivares, G., Webb, F.H., 2013. Detecting offsets in GPS time series: first results from the detection of offsets in GPS experiment. J. Geophys. Res.: Solid Earth 118 (5), 2397–2407. http://dx.doi.org/10.1002/jgrb.50152.

Gordon, R.G., Stein, S., 1992. Global tectonics and space geodesy. Science 256 (5055), 333–342. http://dx.doi.org/10.1126/science.256.5055.333.

Herring, T., King, R., Floyd, M., McClusky, S., 2015. Introduction to GAMIT/GLOBK Release 10.6. Mass. Instit. of Technol, Cambridge Tech. rep.

Hicks, E.C., Bungum, H., Lindholm, C.D., 2000. Seismic activity, inferred crustal stresses and seismotectonics in the Rana region, Northern Norway. Quat. Sci. Rev. 19 (14-15), 1423–1436. http://dx.doi.org/10.1016/S0277-3791(00)00071-8.

Hudnut, K.W., Bock, Y., Cline, M., Fang, P., Feng, Y., Freymueller, J., Ge, X., Gross, W.K., Jackson, D., Kim, M., King, N.E., Langbein, J., Larsen, S.C., Lisowski, M., Shen, Z.-K., Svarc, J., Zhang, J., 1994. Co-seismic displacements of the 1992 landers earthquake sequence. Bull. Seismol. Soc. Am. 84 (3), 625–645.

Janutyte, I., Lindholm, C., Olesen, O., 2017. Relation between seismicity and tectonic structures offshore and onshore Nordland, northern Norway. Norsk Geologisk Tidsskrift Submitted for publication.

Johnson, H.O., Agnew, D.C., 1995. Monument motion and measurements of crustal velocities. Geophys. Res. Lett. 22 (21), 2905–2908. http://dx.doi.org/10.1029/

95GL02661.
Keiding, M., Kreemer, C., Lindholm, C.D., Gradmann, S., Olesen, O., Kierulf, H.P., 2015. A comparison of strain rates and seismicity for Fennoscandia: depth dependency of deformation from glacial isostatic adjustment. Geophys. J. Int. 202, 1021–1028. http://dx.doi.org/10.1093/gji/ggv207.
Kierulf, H.P., Bockmann, L., Kristiansen, O., Plag, H.-P., 2002. Foot-print of the space-geodetic observatory, Ny-Ålesund, Svalbard. In: Vandenberg, N., Beaver, K. (Eds.), Proceedings of the Second IVS General Assembly, Tsukuba, Japan, 4–6 February 2002. NASA Goddard Space Flight Center, Greenbelt, MD, pp. 86–90.
Kierulf, H.P., Ouassou, M., Simpson, M., Vestøl, O., 2013. A continuous velocity field for Norway. J. Geodesy 87 (4), 337–349. http://dx.doi.org/10.1007/s00190-012-0603-2.
Kierulf, H.P., Plag, H.-P., Kohler, J., 2009. Measuring surface deformation induced by present-day ice melting in Svalbard. Geophys. J. Int. 179 (1), 1–13. http://dx.doi.org/10.1111/j.1365-246X.2009.04322.x.
Kierulf, H.P., Steffen, H., Simpson, M.J.R., Lidberg, M., Wu, P., H.W, 2014. A GPS velocity field for Fennoscandia and a consistent comparison to glacial isostatic adjustment models. J. Geophys. Res.: Solid Earth 119, 6613–6629. http://dx.doi.org/10.1002/2013JB010889.
Legrand, J., Bergeot, N., Bruyninx, C., Wöppelmann, G., Bouin, M.-N., Altamimi, Z., 2010. Impact of regional reference frame definition on geodynamic interpretations. J. Geodyn. 49 (3–4), 116–122 WEGENER 2008 – Proceedings of the 14th General Assembly of Wegener.
Leonard, L.J., Hyndman, R.D., Mazzotti, S., Nykolaishen, L., Schmidt, M., Hippchen, S., 2007. Current deformation in the northern Canadian Cordillera inferred from GPS measurements. J. Geophys. Res.: Solid Earth 112 (B11401). http://dx.doi.org/10.1029/2007JB005061.
Mao, A., Harrison, C.G.A., Dixon, T.H., 1999. Noise in GPS coordinate time series. J. Geophys. Res. 104 (B2), 2797–2816. http://dx.doi.org/10.1029/1998JB900033.
Nansen, F., 1922. The strandflat and isostasy. Skrifter Videnskapsselskapet i Kristiania. Matematisk-Naturvitenskaplig klasse 2, 1–313.
Olesen, O., Kierulf, H.P., Brönner, M., Dalsegg, E., Fredin, O., Solbakk, T., 2013. Deep weathering, neotectonics and strandflat formation in Nordland, northern Norway. Nor. J. Geol. 93 (3–4), 189–213 ISSN:029-196X.
Pesci, A., Teza, G., Casula, G., 2009. Improving strain rate estimation from velocity data of non-permanent GPS stations: the central Apennine study case (Italy). GPS Solut. 13 (4), 249–261. http://dx.doi.org/10.1007/s10291-009-0118-3.
Petrie, E.J., Hernández-Pajares, M., Spalla, P., Moore, P., King, M.A., 2011. A review of higher order ionospheric refraction effects on dual frequency GPS. Surv. Geophys. 32 (3), 197–253. http://dx.doi.org/10.1007/s10712-010-9105-z.
Reusch, H.H., 1894. Strandflaten, et nyt trek i Norges Geografi. Norges geologiske undersøkelse 14, 1–14.
Rolstad, C., Haug, T., Denby, B., 2009. Spatially integrated geodetic glacier mass balance and its uncertainty based on geostatistical analysis: application to the western Svartisen ice cap. Nor. J. Glaciol. 55, 666–680. http://dx.doi.org/10.3189/002214309789470950.
Rouyet, L., Lauknes, T.R., Larsen, Y., 2016. InSAR deformasjonsanalyse Helgeland. Tech. Rep. 21, NORUT, ISSN:1890-5526.
Saria, E., Calais, E., Stamps, D.S., Delvaux, D., Hartnady, C.J.H., 2014. Present-day kinematics of the East African Rift. J. Geophys. Res.: Solid Earth 119 (4), 3584–3600. http://dx.doi.org/10.1002/2013JB010901.
Scherneck, H.-G., 1991. A parametrized solid earth tide model and ocean tide loading effects for global geodetic baseline measurements. Geophys. J. Int. 106 (3), 677–694. http://dx.doi.org/10.1111/j.1365-246X.1991.tb06339.x.
Steffen, H., Wu, P., 2011. Glacial isostatic adjustment in Fennoscandia – a review of data and modeling. J. Geodyn. 52 (3–4). http://dx.doi.org/10.1016/j.jog.2011.03.002. 160-2004.
Torres, J.A., Altamimi, Z., Boucher, C., Brockmann, E., Bruyninx, C., Caporali, A., Gurtner, W., Habrich, H., Hornik, H., Ihde, J., Kenyeres, A., Mäkinen, J., Marel, H., Seeger, H., Simek, J., Stangl, G., Weber, G., 2009. Status of the European Reference Frame (EUREF). In: Sideris, M.G. (Ed.), Observing our Changing Earth. International Association of Geodesy Symposia, vol. 133. Springer, Berlin, Heidelberg, pp. 47–56. http://dx.doi.org/10.1007/978-3-540-85426-5_6.
Van Dam, T., Wahr, J., Milly, P.C.D., Shmakin, A.B., Blewitt, G., Lavallée, D., Larson, K.M., 2001. Crustal displacements due to continental water loading. Geophys. Res. Lett. 28 (4), 651–654. http://dx.doi.org/10.1029/2000GL012120.
Wdowinski, S., Bock, Y., Zhang, J., Fang, P., Genrich, J., 1997. Southern California permanent GPS geodetic array: spatial filtering of daily positions for estimating coseismic and postseismic displacements induced by the 1992 landers earthquake. J. Geophys. Res. 102 (B8). http://dx.doi.org/10.1029/97JB01380. 18,057–18,070.
Williams, S.D.P., 2003. Offsets in global positioning system time series. J. Geophys. Res.: Solid Earth 108 (B6). http://dx.doi.org/10.1029/2002JB002156.
Williams, S.D.P., 2008. CATS: GPS coordinate time series analysis software. GPS Solut. 12 (2), 147–153. http://dx.doi.org/10.1007/s10291-10007-10086-10294.
Williams, S.D.P., Bock, Y., Fang, P., Jamason, P., Nikolaidis, R.M., Prawirodirdjo, L., Miller, M., Johnson, D.J., 2004. Error analysis of continuous GPS position time series. J. Geophys. Res. 109, 1–19. http://dx.doi.org/10.1029/2003JB002741.
Zhang, J., Bock, Y., Johnson, H., Fang, P., Williams, S., Genrich, J., Wdowinski, S., Behr, J., 1997. Southern California permanent GPS geodetic array: error analysis of daily position estimates and site velocities. J. Geophys. Res. 102 (B8). http://dx.doi.org/10.1029/97JB01380. 18,035–18,055.

CHAPTER 7: INSAR DEFORMATION ANALYSIS FOR HELGELAND

Authors: Line Rouyet, Tom Rune Lauknes, Yngvar Larsen, Norut

Affiliation: Norut, Sykehusvegen 23, 9019 Tromsø

This chapter presents the satellite-based InSAR results over Helgeland coast using ERS-1 and ERS-2 data for the period 1993-1999. Two independent satellite paths in the southbound geometry (descending orbit) have been analyzed. By analyzing the selected interferograms, maps are generated that display average annual velocity. A time series analysis using the SBAS technique been carried out for the area around Storglomvatn, for those points that meet quality requirements.

1. Content

This is a summary report for a satellite-based radar interferometry analysis (InSAR) conducted over an area extending from Namsos to Bodø. The source of the data is the ERS-1 and ERS-2 satellites from the period 1993-2000.

Section 2 provides information about the study area. The theoretical background for processing and main classification of satellite data are presented in Section 3. Sections 4 and 5 contain the deformation results provided by InSAR processing. Section 4 focuses on regional trends (land elevation) while Section 5 analyzes the local deformation around Storglomvatn reservoir and selected individual sites. The discussion and conclusion are presented in Section 6.

2. Study Area

A large area of the Helgeland coast is the focus of this study. Figure 1 displays the area that was selected for InSAR analysis (Section 4) as well as the various satellite tracks. The area of interest stretches from Sandnessjøen to Bodø. The range of each satellite track is approximately 100 km, and the total size of the study area is approximately 100x400 km.

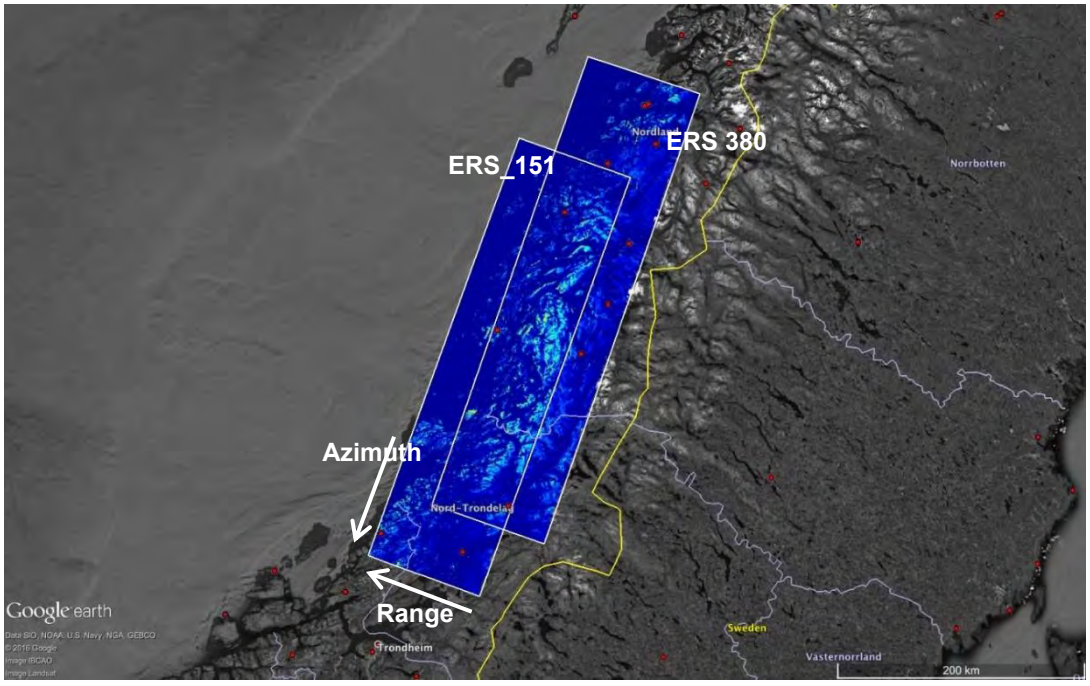

Figure 1. An overview of the two satellite tracks used in the analysis. The colors illustrate the average coherence (quality measure). The red dots represent GPS stations.

3. Satellite data and methods

The results presented in Sections 4 to 5 are based on the following satellite data sets:

-30 images from ERS-1 and-2 in descending geometry from track 151 between 1993 and 1999;

-29 images from ERS-1 and-2 in descending geometry from track 380 between 1993 and 2000;

-42 images from Sentinel-1a and-1b in ascending geometry from track 73 between 2015 and 2016.

The main characteristics of the satellite data sets are described in Table 1. The processing of data has been carried out using GSAR (Norut software, Larsen, et al., 2005).

Artikkel I. Table 1. Main characteristics of satellite data.

Data set	Frequency bands	Repeat times [days]	Multilooking factor and resolution [m]	Time period	Total scenes available/ selected	LOS Orientation /Angle of refraction [°]
ERS track 151	C (λ: 5.55 cm)	35	6x36 142x143	06.1993 – 09.1999	30 / 20	288 / 23
ERS track 380				05.1993 – 10.2000	29 / 17	288 / 23
Sentinel-1 track 73	C (λ: 5.55 cm)	12 (6 fra 09-2016)	Full resolution 20x5	03.2015 – 11.2016	42 / 42	257/334

The main aim of the project is to identify long-term trends related to continental uplift on a regional scale (Section 4). Results have been attained through stacked multi-annual satellite images (Sandwell & Price, 1998; Emardson et al., 2003). This technique reduces the noise from atmospheric effects (turbulence) by calculating the weighted average from the interferograms. The stacking technique provides no information on temporal variations (time series), but is an effective and well-known method for studying large scale deformation over a long period of time. We are not interested in seasonal patterns, so we select only interferograms that combine images with the temporal baseline (difference in time) greater than 200 days. In addition, we have set a restrictive threshold of 200 m, the accepted spatial distance between the two satellite paths (spatial baseline). This minimizes phase errors due to uncertainties in the elevation model. All the results presented are shown in the average annual rate (mm/year) along the radar's target direction "line-of-Sight" (LOS).

Processing parameters are presented in Table 2.

Table 2. InSAR stacking processing parameters using ERS data

Multi-year stacking						
Dataset	Master geometry for co-registering	Max baseline [m]	Min. / Max. temporal baseline [days]	Total generated interferograms	Selected interferograms	Coherent threshold use
ERS track 151	1998-08-28	200	200 / max. interval	61	27	0.1 i 25% av interferograms
ERS track 380	1995-07-16			76	25	0.1 i 30% av interferograms

Figure 2. shows two separate high-quality interferograms. A trend in east-west direction is already evident.

Figure 3. (track 151) and Figure 4. (track 380) show the temporal distribution vs. the spatial distance between the satellite orbit for different scenes (baseline plot), as well as the interferograms generated used in stacking and SBAS processing. The black lines are the interferograms that were selected; the red shows interferograms that were removed due to their low quality.

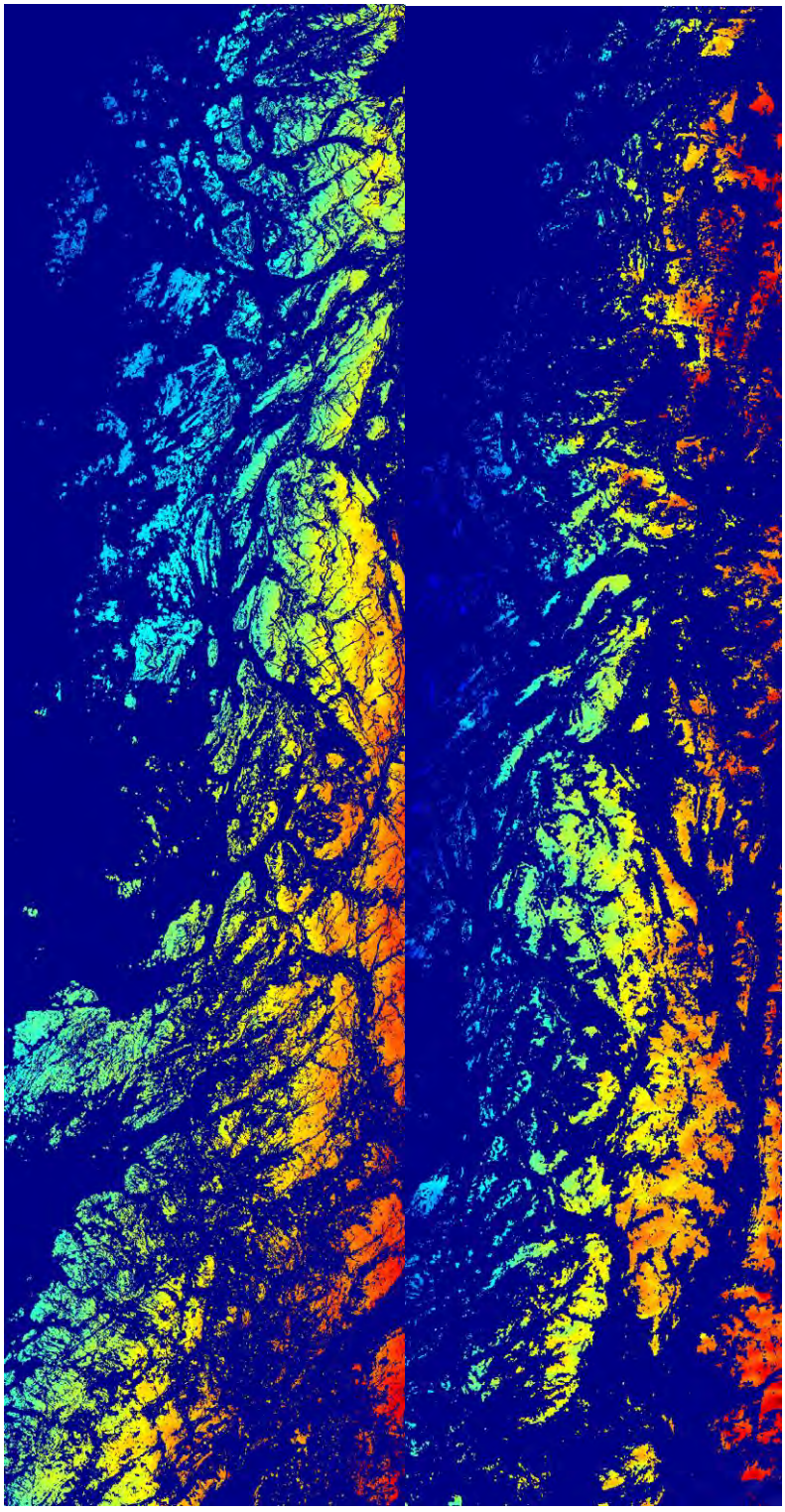

Figure 2. Examples of interferograms that illustrate unwrapped phase (integrated modulo 2pi) in SAR geometry (left: Track 151 01.06.1993 – 29.06.1995/To right: 20.06.1999 – 17.09.2000 track 380).

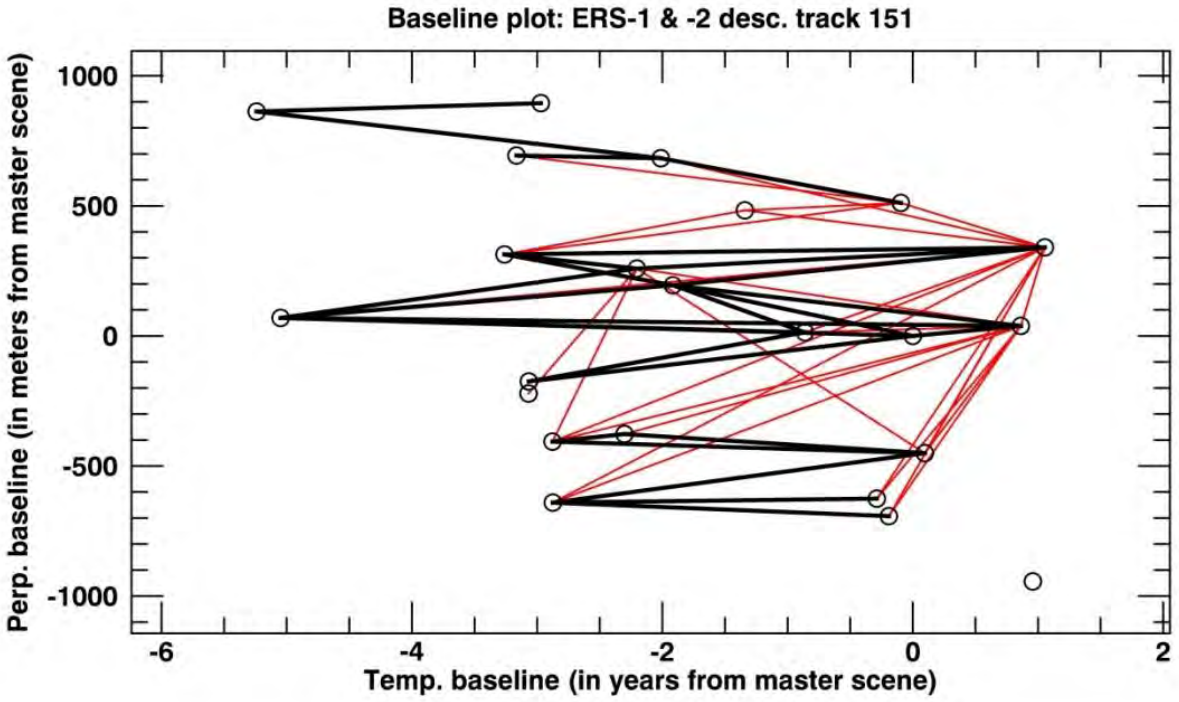

Figure 3. Baseline plot ERS-1 &-2 descending track 151 (circles: scenes; lines: interferograms; in red: rejected interferograms; in black: selected interferograms).

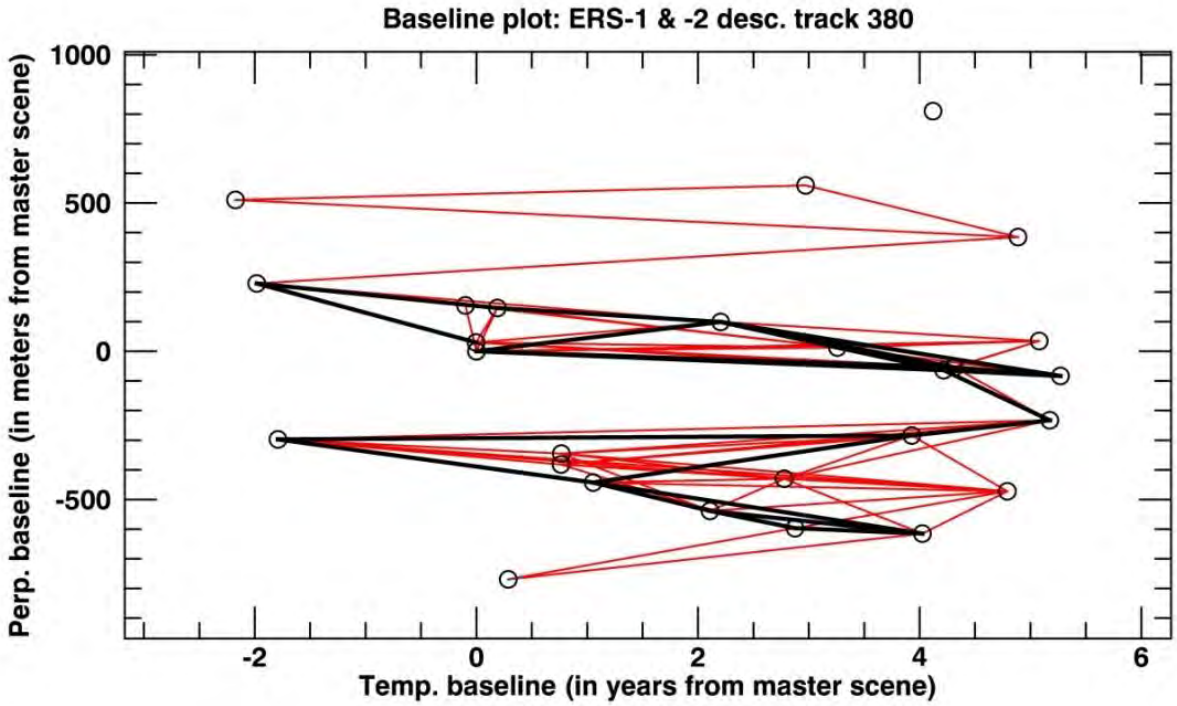

Figure 4. Baseline plot ERS-1 &-2 Descending track 380 (circles: scenes; lines: Interferograms; in red: rejected interferograms; in black: selected interferograms).

Two additional methods of processsing have been applied to allow for a more local analysis of the deformations:

- The SBAS technique (Small BAseline subst, Berardino et al., 2002) was used to process the ERS track 380, in order to capture the time series around Storglomvatn Reservoir. For multi-annual stacking processing, several interferograms have been used (including brief temporal baseline) and results have been corrected for variations in atmosphere.
- PSI methodology (persistent scatters Interferometry, Ferretti, et al., 2000) was used to process Sentinel-1 track 73 to achieve a better spatial resolution for infrastructure.

4. InSAR results: regional uplift

Using the multi-annual stacking methodology on the area covered by ERS-1/2 track 151 and track 380, we can measure a distinct east-west deformation trend. This is shown in Figure 5. (track 151) and Figure 6. (track 380). The deformation around Storglomvatn Reservoir (in the northwest corner of Figure 6.) is also visible on a regional scale.

From these results it is possible to create profiles (Figs. 7-9). Velocities here are converted to vertical. Values are plotted along the radar range direction. We have generated a profile every 30 km from the beginning of track 380 to the end of track 151. Lines shown on Figs. 5 and 6 are the central line in the azimuth direction (the graphs include data from +/-14.7 km from this line).

A map that visualizes both tracks together (Figure 11.) and the other profiles are in annex (Figure 13 to Figure 27.).

It should be noted that:

1. Velocity values are calibrated toward a point (Black star on Figs. 5 and 6). Values correspond to relative movements in relation to the selected point, not to the absolute deformation of the surface.

2. We have not filtered for either atmospheric or orbit error in order to avoid eliminating the real deformation signal. However, the turbulent part of atmospheric disturbance is subdued by averaging many interferograms. A residual due to a stratified (layered) atmosphere can be expected.

3. In areas with poor coverage and low pixel density due to the sea or vegetation, some unwrapping error can be expected. An example of such a site is in the southeast corner.

Results show that:

1. Results from both tracks are generally consistent. On the map we see that the deformation and spatial pattern between tracks 151 and 380 are comparable. On the profiles it is even clearer. The breaks that are visible on some profiles are explained by points 2-3 above.

2. In addition to the general trend, the deformation for the Storglomvatn reservoir is visible, both on the map (Fig. 6) and the profile (Fig. 7).

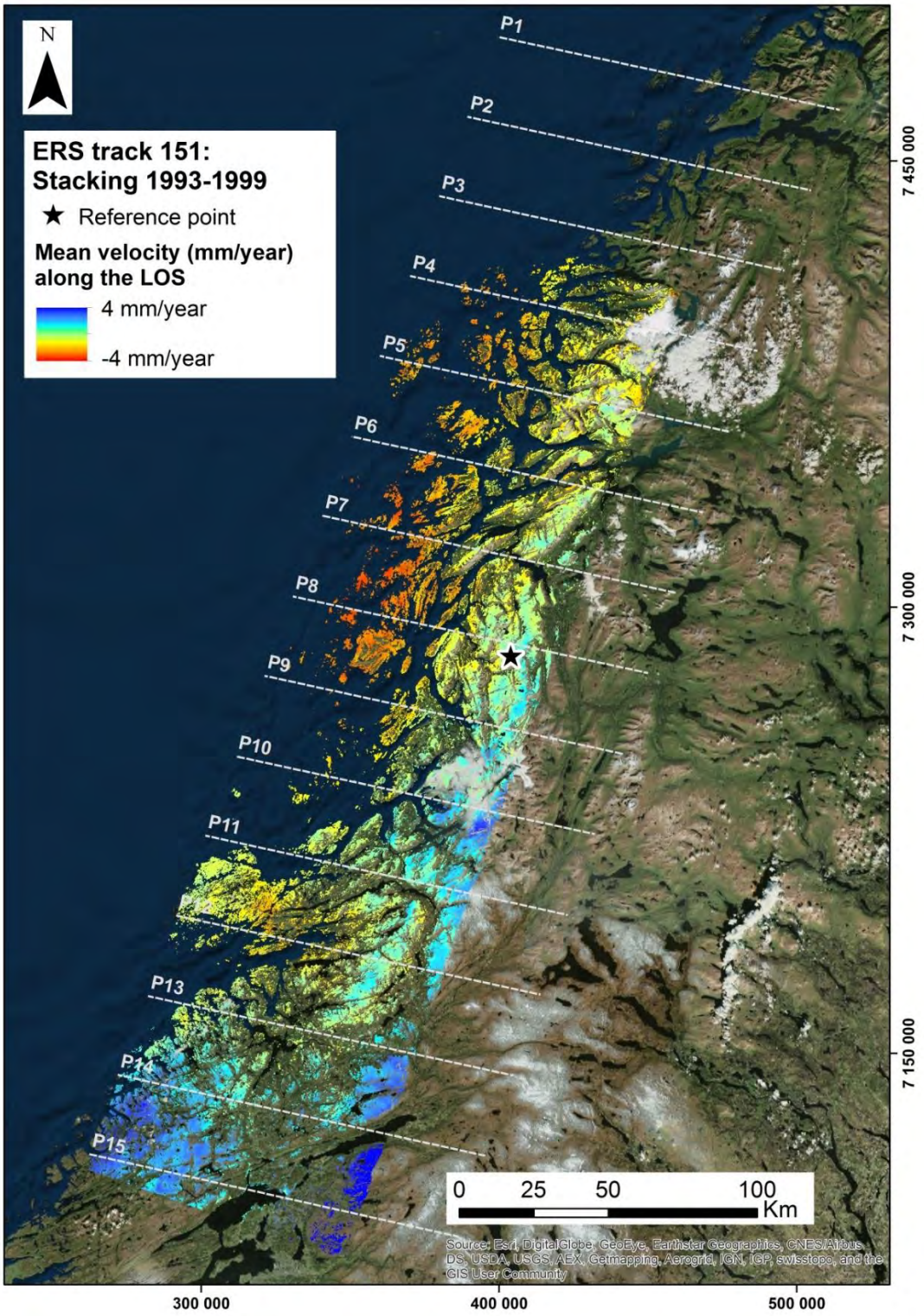

Figure 5. ERS track 151 deformation map using multi-annual stacking processing (average annual rate from 27 interferograms over seven years). The gray lines (P1-15) are the centre lines of profiles visualized on each graph.

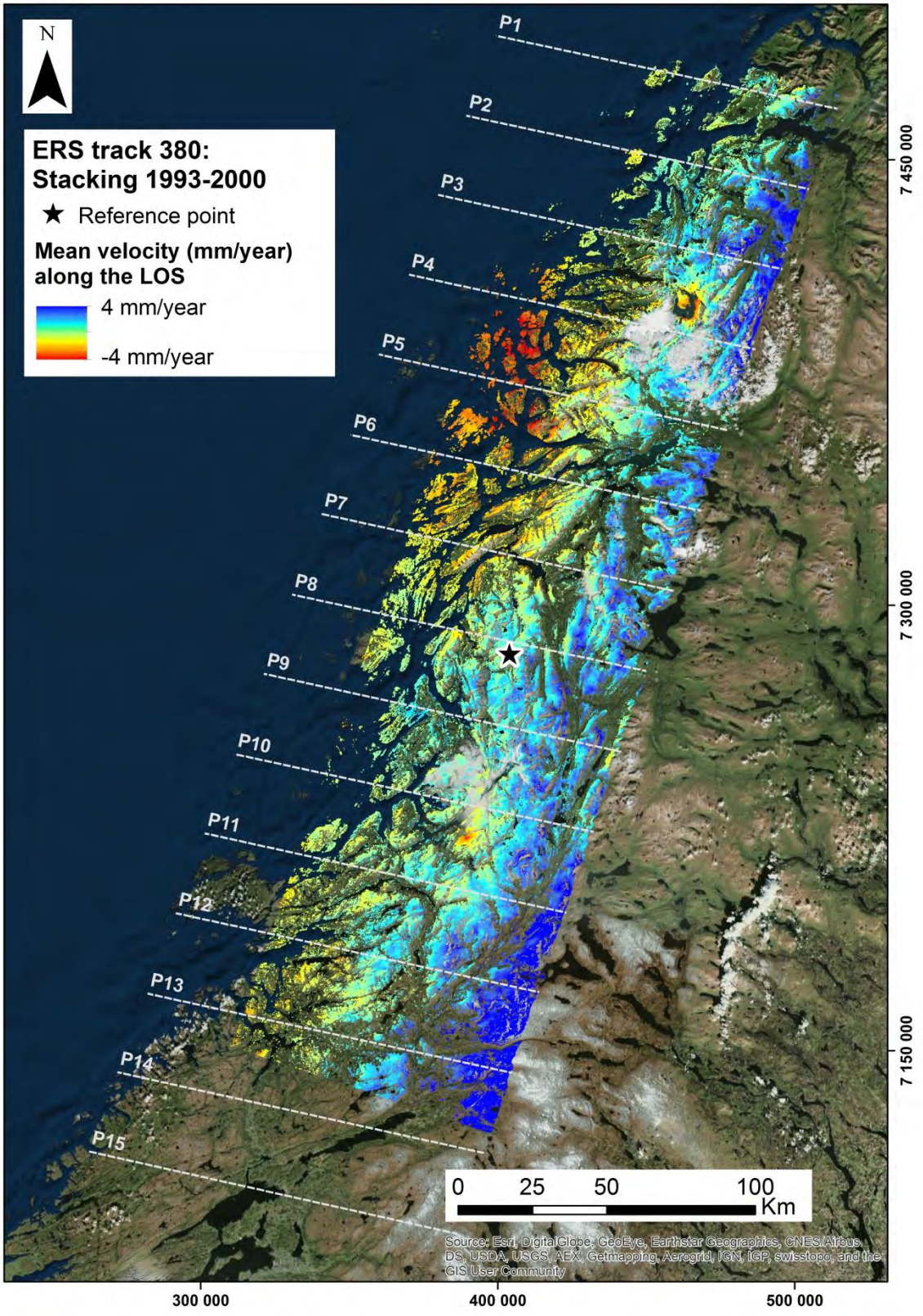

Figure 6. ERS track 380 deformation map using multi-annual stacking processing (average annual rate from 25 interferograms over eight years). The gray lines (P1-15) are the centre lines of profiles visualized on each graph.

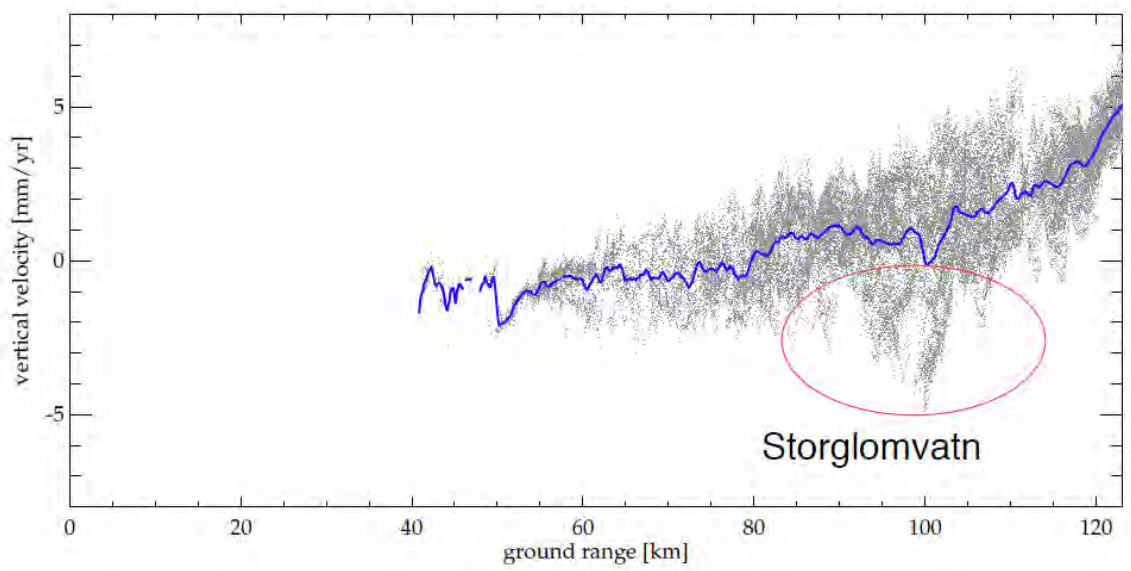

Figure 7. The vertical deformation trend along profile P3. Light dots: Track 380. Profiles in range direction +/-14.7 km from the central line from Figure 5 and Figure 6. Blue Line: Smoothed average of Track 380.

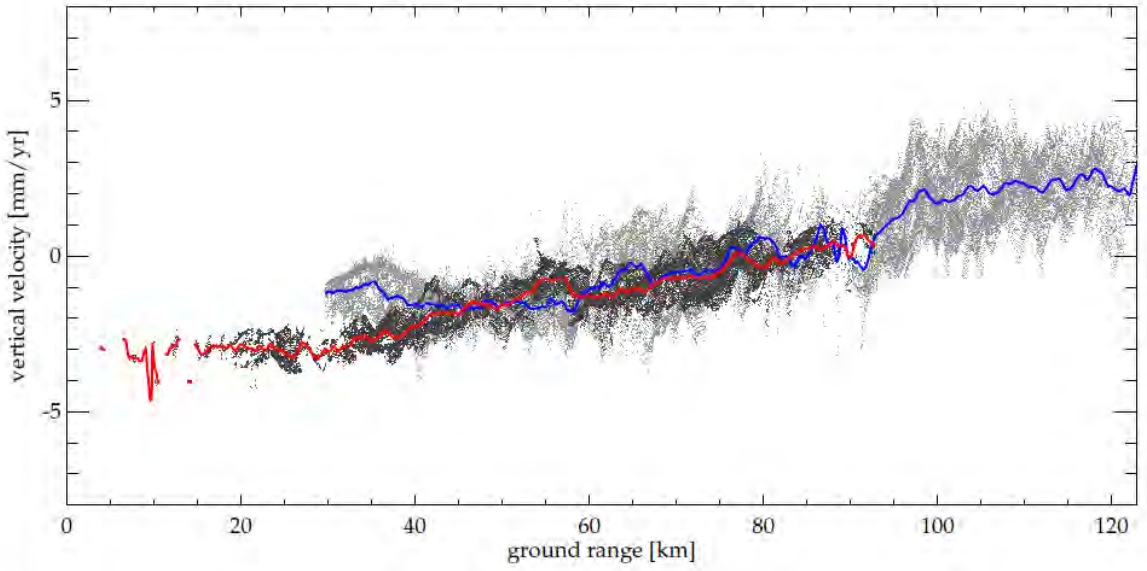

Figure 8. The vertical deformation trend along profile P7. Light dots: Track 380. Dark dots: Track 151. Profiles in range direction +/-14.7 km from the central line from Figs. 5 and 6. Blue Line: Smoothed average of track 380. Red Line: Smoothed average of track 151.

Artikkel II.

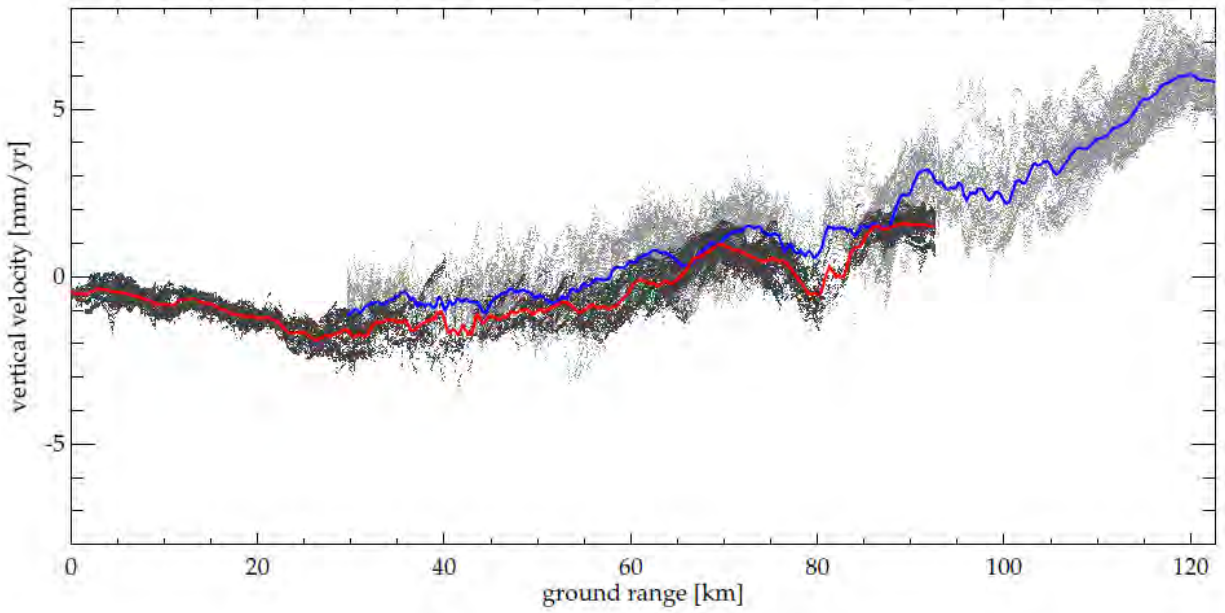

Figure 9. The vertical deformation trend along profile P12. Light dots: Track 380. Dark dots: Track 151. Profiles in range direction +/-14.7 km from the central line from Figure 5. and Figure 6.. Blue Line: Smoothed average of track 380. Red Line: Smoothed average of track 151.

5. InSAR results: local deformation

In the area surrounding Storglomvatn reservoir (covered by ERS track 380) we have used the SBAS methodology to generate the time series. A map of the average yearly speed (mm/year) along radar aiming direction (LOS) appears on Figure 10.. An example of the time series is presented in Figure 11.. It shows the subsidence from 1996 related to the filling of the reservoir. The deformation seems to stabilize in 1999.

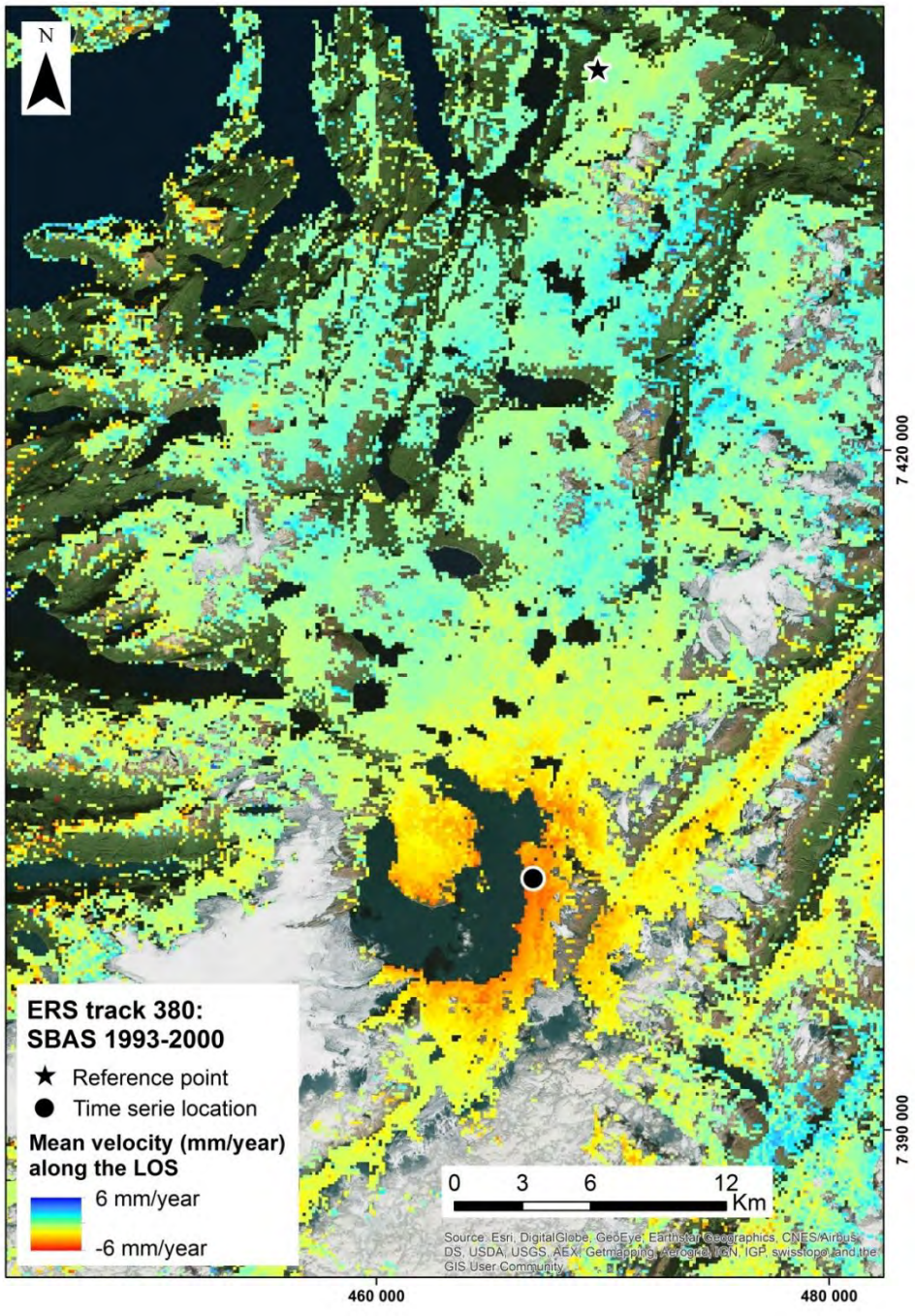

Figure 10. ERS track 380 deformations map from SBAS processing (58 Interferograms over 8 years).

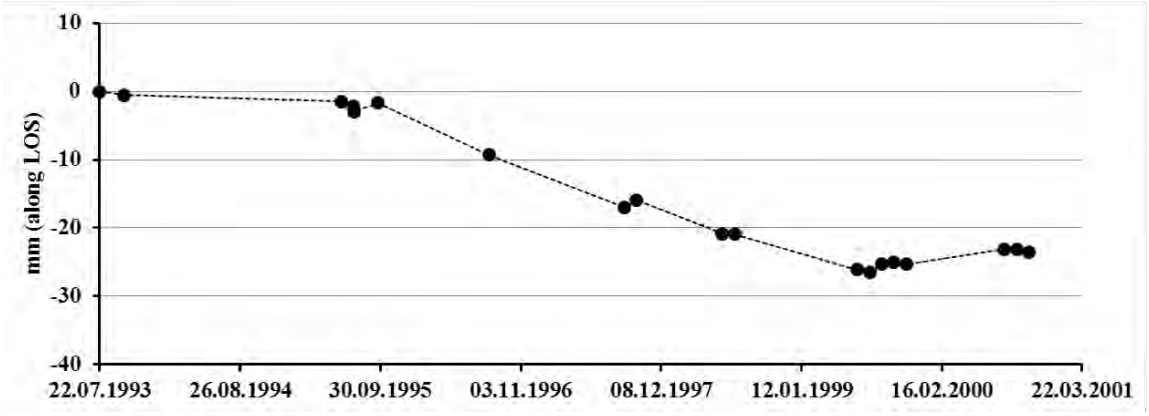

Artikkel III.

Figure 11. Examples of time series analysis (position: Circle on Fig. 10)

6. Summary

This report deals with InSAR processing of ERS-1 and ERS-2 data sets over the Helgeland coast, for the period 1993 – 2000. Velocity fields for two different satellite tracks, relative to a selected common reference point, have been estimated by using the interferogram stacking methodology. The two different satellite tracks provide comparable results, not only for studying spatial patterns, but also for studying profiles along the radar range direction. InSAR processing is done with minimal filtration, so the differences between the data sets can be explained by the non-compensated atmosphere effects,

Moreover, a SBAS time series analysis has been performed for the Storglomvatn area. After the reservoir had been filled up, the area displayed non-linear deformation.

7. References

Berardino, P., Fornaro, G., Lanari, R. & Sansosti, E. 2002. A new algorithm for surface deformation monitoring based on small baseline differential SAR interferograms. IEEE Transactions on Geoscience and Remote Sensing, 40(11), 2375–2383. doi:10.1109/TGRS.2002.803792.

Emardson, T.R., Simons, M., Webb, F.H. 2003. Neutral atmospheric delay in interferometric synthetic aperture radar applications: Statistical description and mitigation. Journal of Geophysical Research, 108(B5), 2231. doi:10.1029/2002JB001781.

Ferretti, A., Prati, C. & Rocca, F. (2000). Nonlinear subsidence rate estimation using permanent scatterers in differential SAR interferometry. IEEE Transactions on Geoscience and Remote Sensing, 38(5), 2202–2212. doi:10.1109/36.868878.

Larsen, Y., Engen, G., Lauknes, T. R., Malnes, E., & Høgda, K.-H. 2005. A generic differential SAR processing system, with applications to land subsidence and SWE retrieval. Proc. ESA Fringe 2005, ESA ESRIN, Frascati, Italy, November 28–December 2.

Sandwell, D.T. & Price, E.J. 1998. Phase gradient approach to stacking interferograms. Journal of Geophysical Research. 103(B12), 30,183–30,20.

8. Attachments

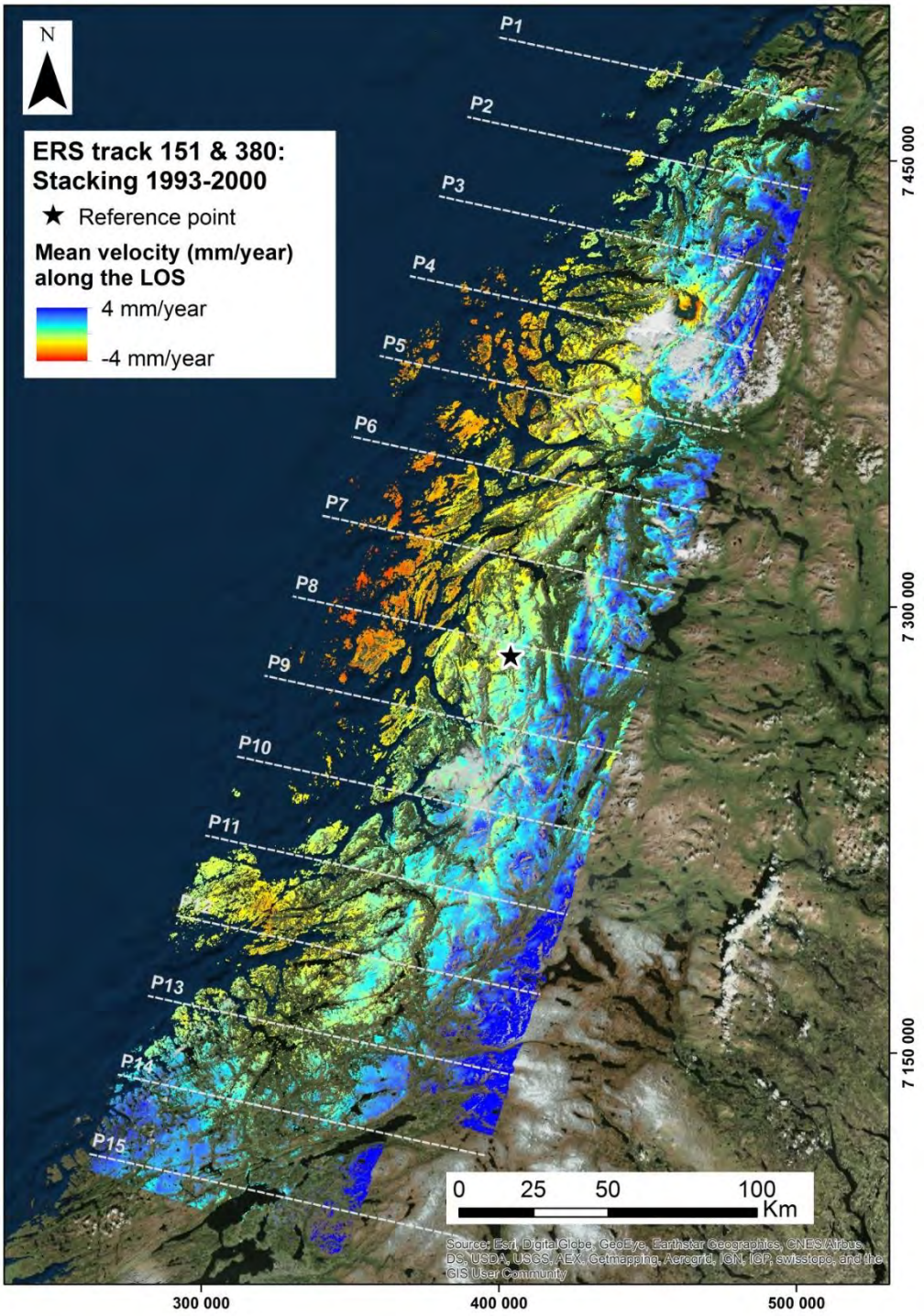

Figure 12. Overlay of ERS track 151 and 380 deformation map from multi-annual stacking processing (average annual rate from 27 interferograms over eight years). Gray lines (P1-15) are the central lines of profiles visualized on each graph.

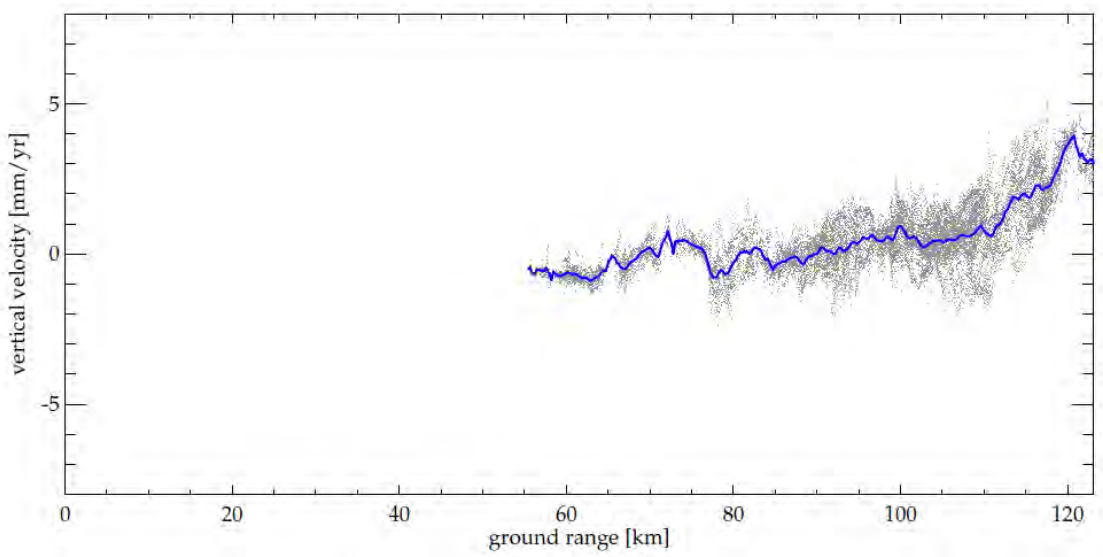

Figure 13. Vertical deformation trend along profile P1. Light dots: Track 380. Profiles in range direction +/-14.7 km from the central line from Figure 11.. Blue Line: smoothed average line track 380.

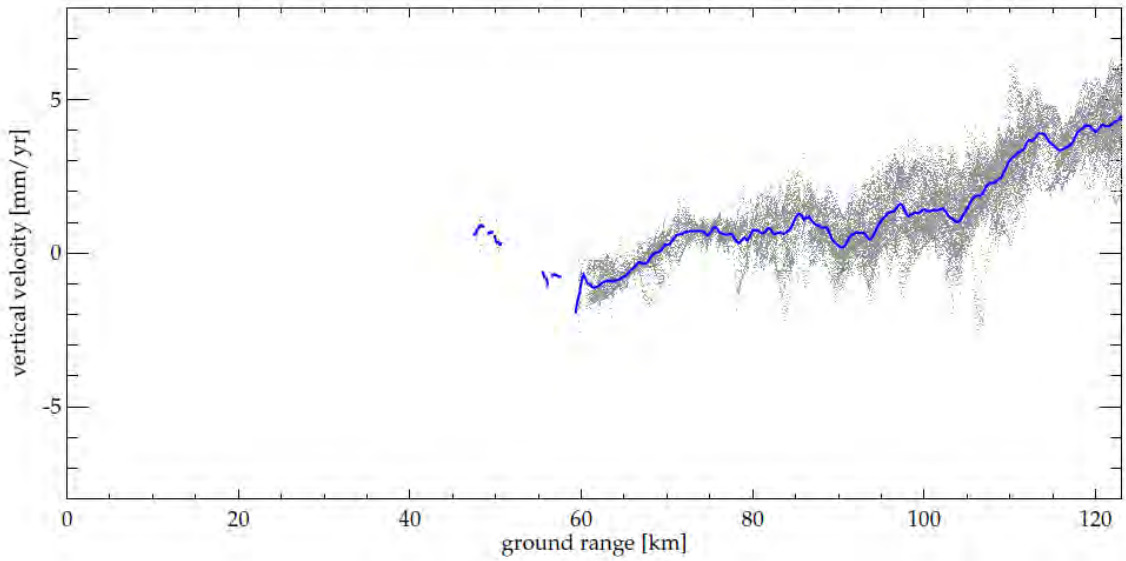

Figure 14. Vertical deformation trend along profile P2. Light dots: Track 380. Profiles in range direction +/-14.7 km from the central line from Figure 11.. Blue Line: smoothed average line track 380.

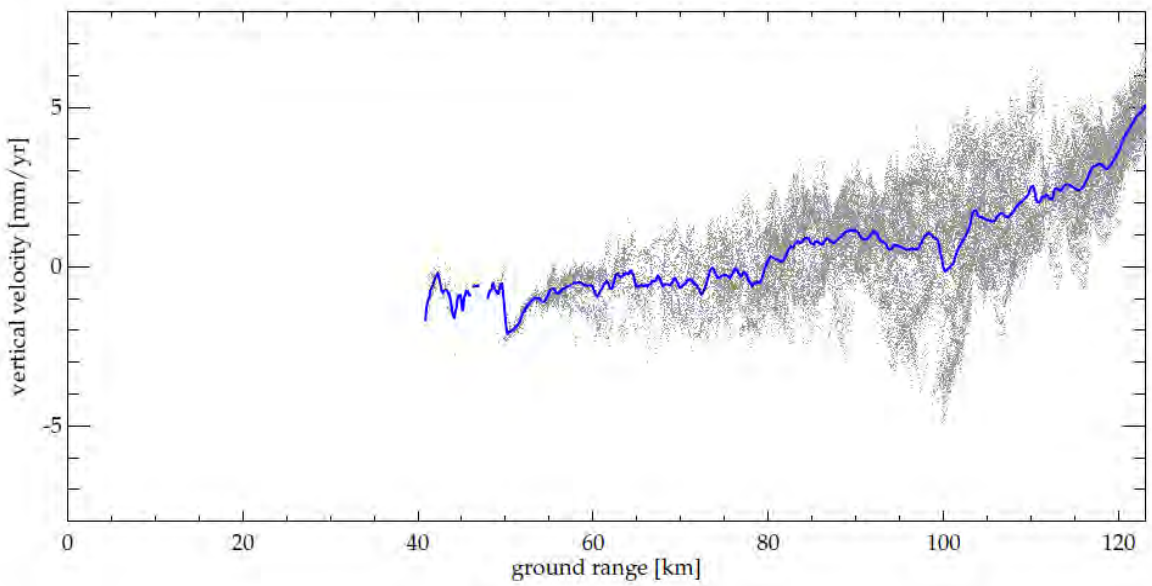

Figure 15. Vertical deformation trend along profile P3. Light dots: Track 380. Profiles in range direction +/-14.7 km from the central line from Figure 11.. Blue Line: Smoothed average line track 380.

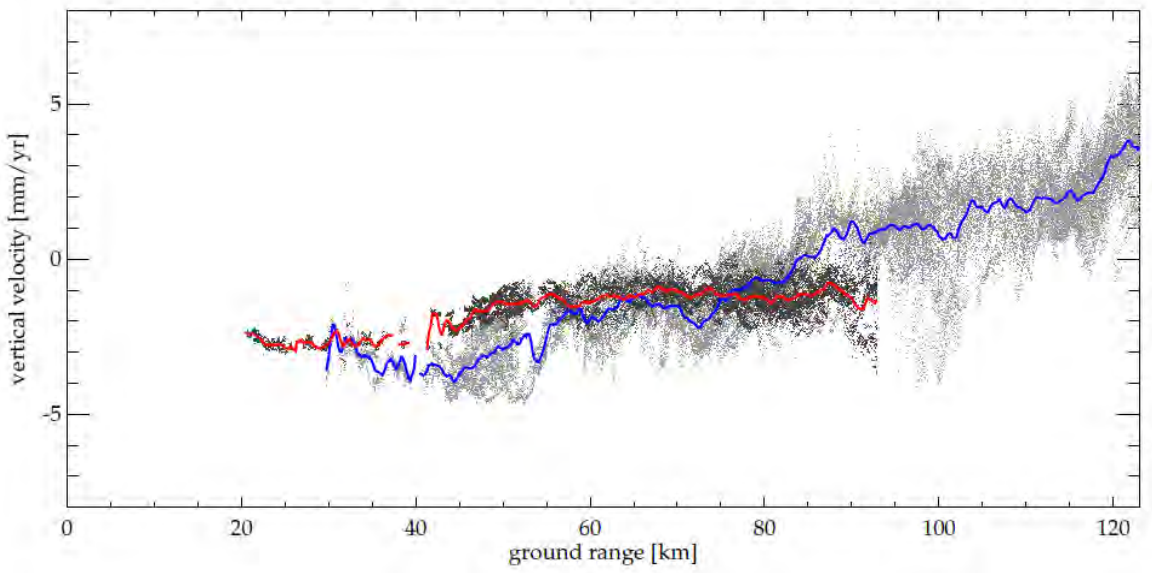

Figure 16. Vertical deformation trend along profile P4. Light dots: Track 380. Dark dots: track 151. Profiles in range direction +/-14.7 km from the central line from Figure 11.. Blue line: Smoothed average line track 380. Red Line: smoothed average line track 151.

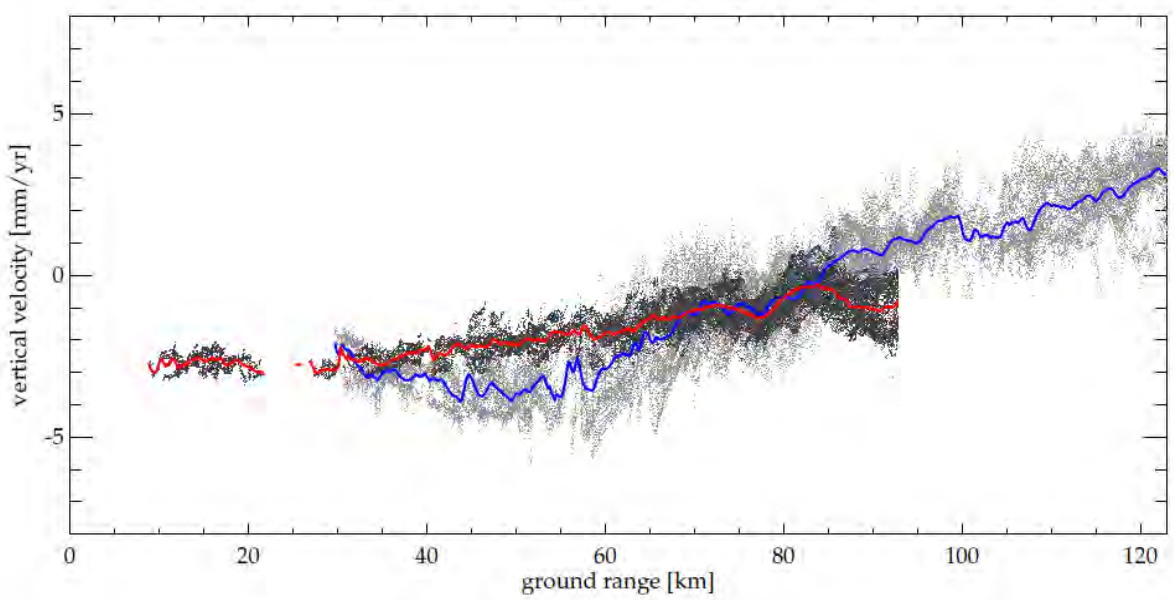

Figure 17. Vertical deformation trend along profile P5. Light dots: Track 380. Dark dots: track 151. Profiles in range direction +/-14.7 km from the central line from Figure 11.. Blue line: Smoothed average line track 380. Red Line: Smoothed average line track 151.

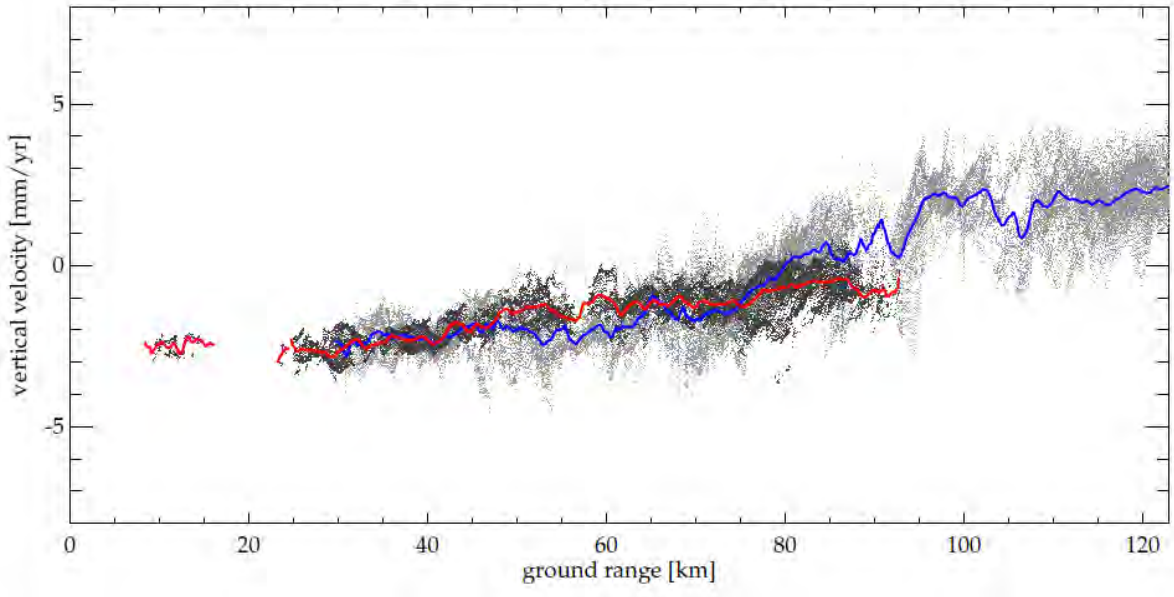

Figure 18. Vertical deformation trend along profile P6. Light dots: Track 380. Dark dots: track 151. Profiles in range direction +/-14.7 km from the central line from Figure 11.. Blue line: Smoothed average line track 380. Red Line: Smoothed average line track 151.

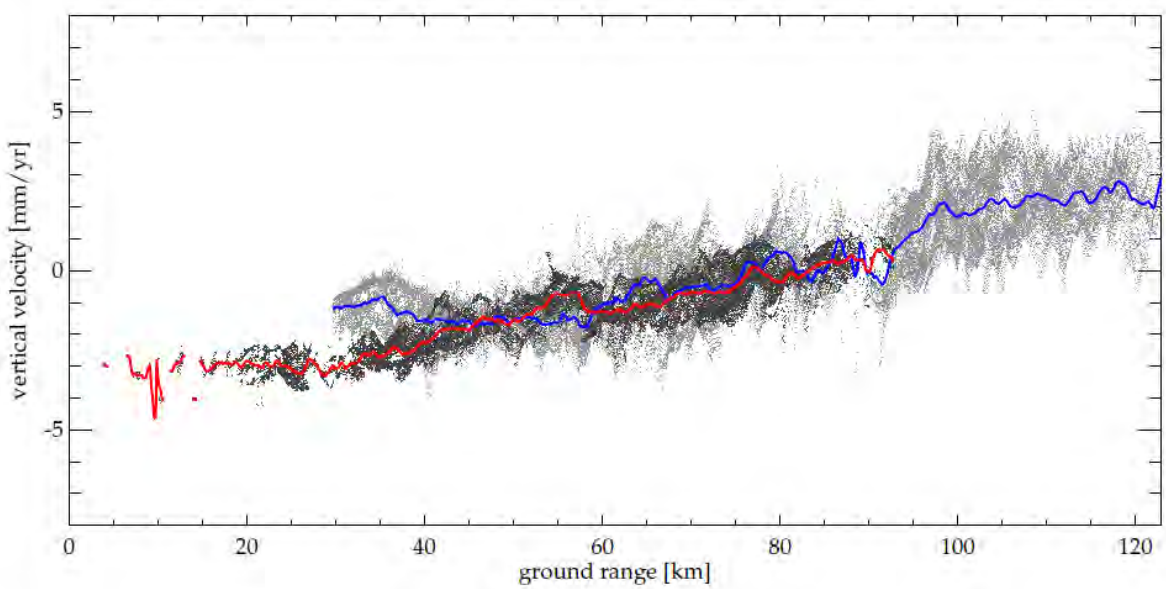

Figure 19. Vertical deformation trend along profile P7. Light dots: Track 380. Dark dots: track 151. Profiles in range direction +/-14.7 km from the central line from Figure 11.. Blue line: Smoothed average line track 380. Red Line: Smoothed average line track 151.

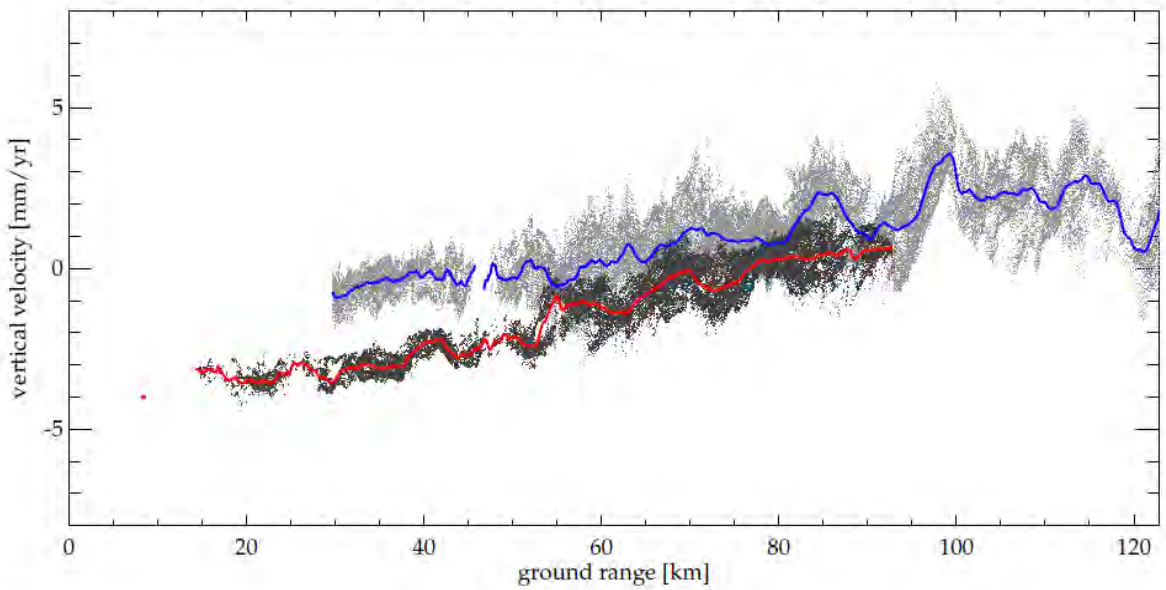

Figure 20. Vertical deformation trend along profile P8. Light dots: Track 380. Dark dots: track 151. Profiles in range direction +/-14.7 km from the central line from Figure 11.. Blue line: Smoothed average line track 380. Red Line: Smoothed average line track 151.

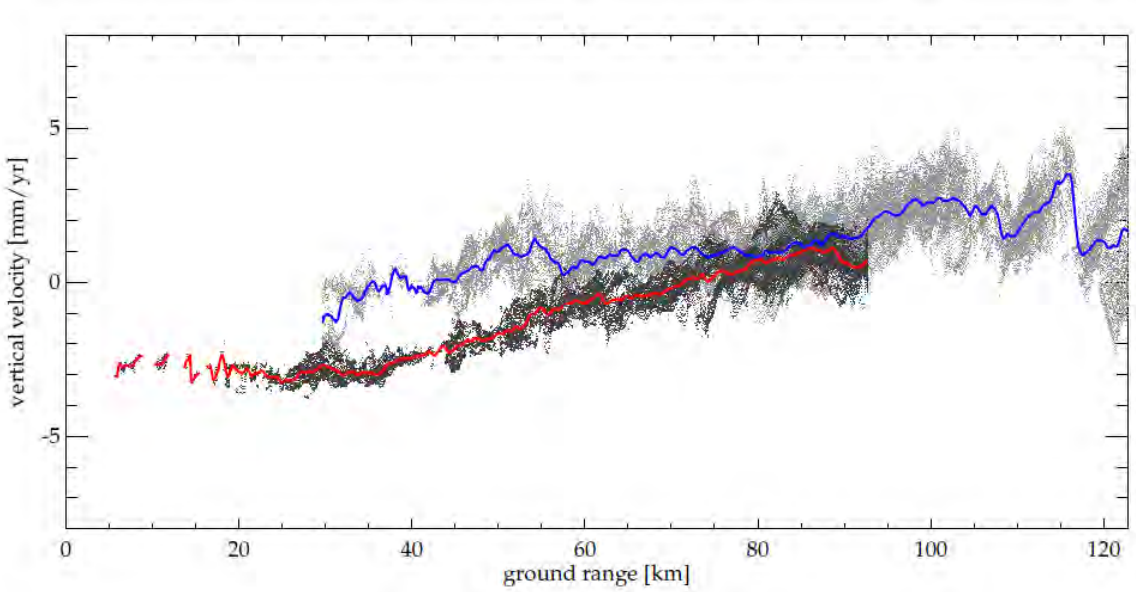

Figure 21. Vertical deformation trend along profile P9. Light dots: Track 380. Dark dots: track 151. Profiles in range direction +/-14.7 km from the central line from Figure 11.. Blue line: Smoothed average line track 380. Red Line: Smoothed average line track 151.

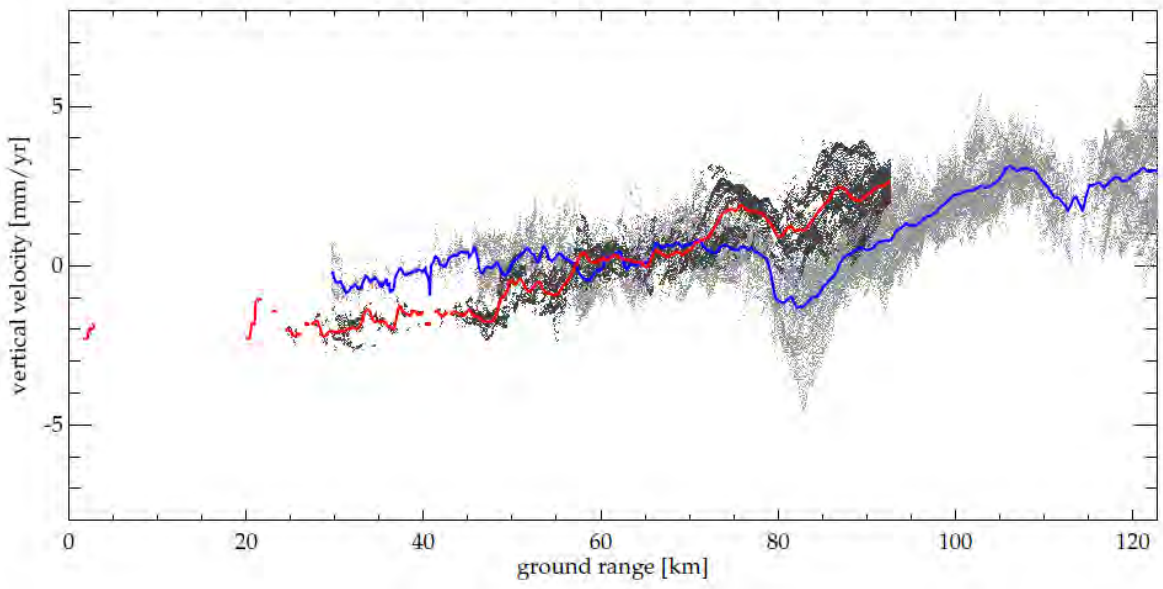

Figure 22. Vertical deformation trend along profile P10. Light dots: Track 380. Dark dots: track 151. Profiles in range direction +/-14.7 km from the central line from Figure 11.. Blue line: Smoothed average line track 380. Red Line: Smoothed average line track 151.

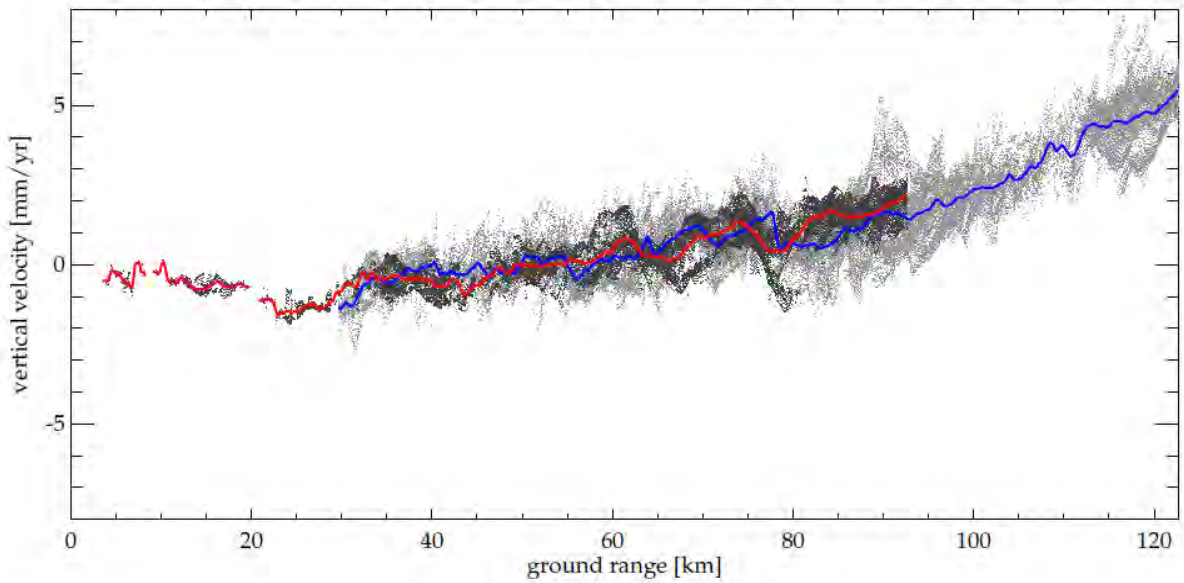

Figure 23. Vertical deformation trend along profile P11. Light dots: Track 380. Dark dots: track 151. Profiles in range direction +/-14.7 km from the central line from Figure 11.. Blue line: Smoothed average line track 380. Red Line: Smoothed average line track 151.

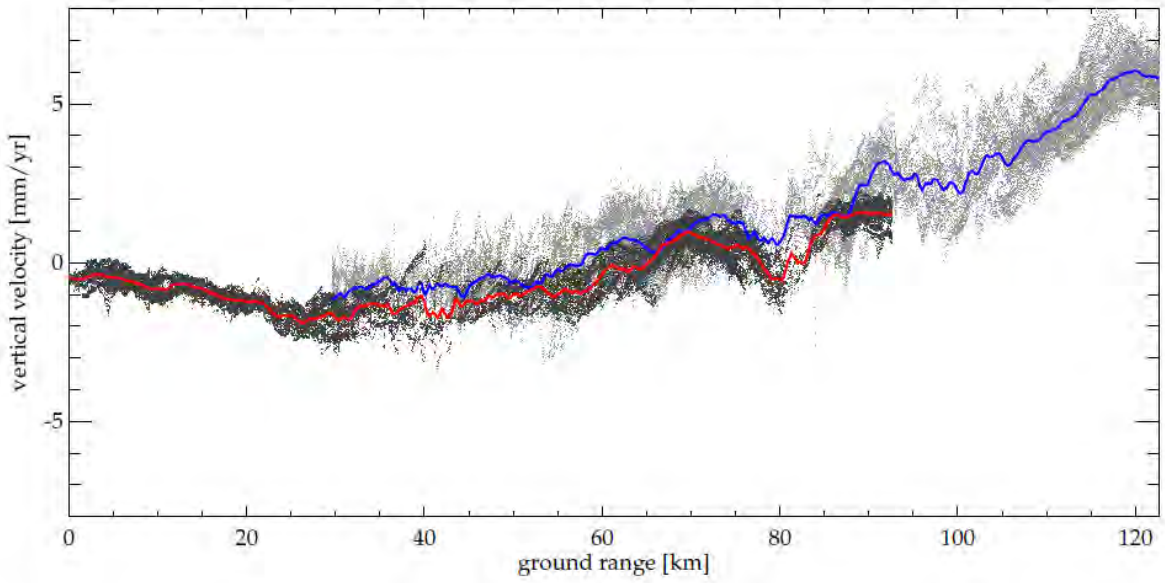

Figure 24. Vertical deformation trend along profile P12. Light dots: Track 380. Dark dots: track 151. Profiles in range direction +/-14.7 km from the central line from Figure 11.. Blue line: Smoothed average line track 380. Red Line: Smoothed average line track 151.

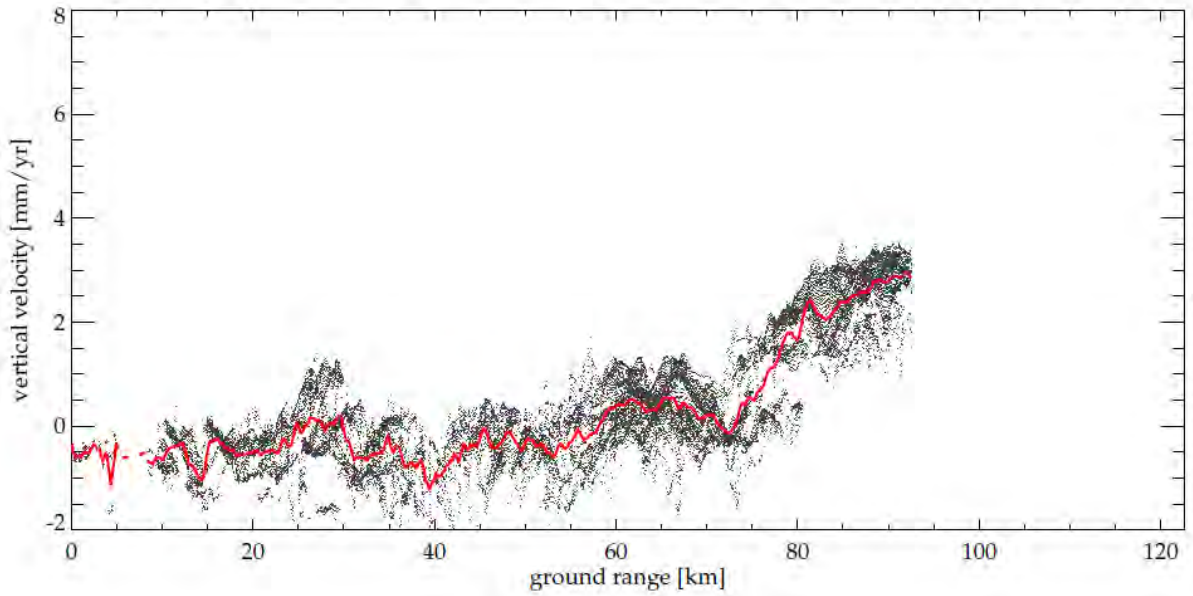

Figure 25. Vertical deformation trend along profile P13. Dark dots: track 151. Profiles in range direction +/-14.7 km from the central line from Figure 11.. Red Line: Smoothed average line track 151.

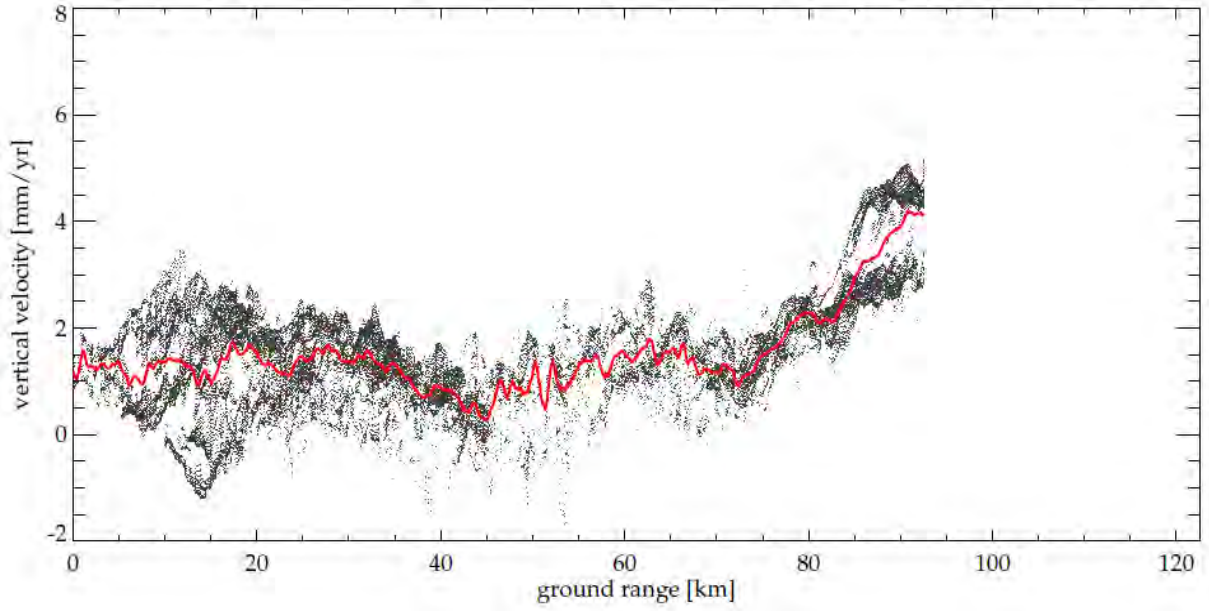

Figure 26. Vertical deformation trend along profile P14. Dark dots: track 151. Profiles in range direction +/-14.7 km from the central line from Figure 11... Red Line: Smoothed average line track 151.

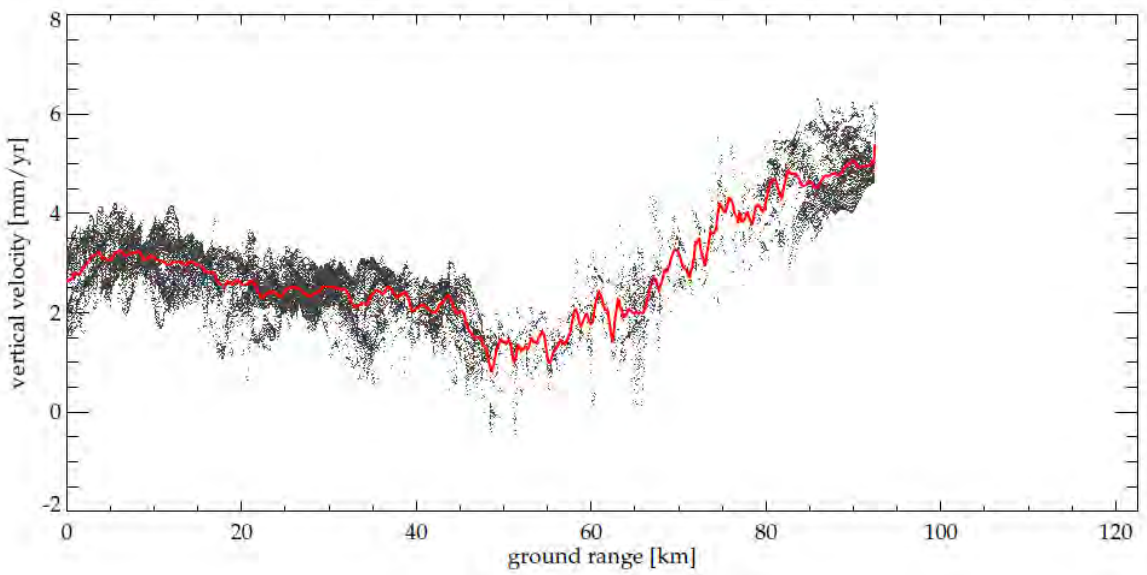

Figure 27. Vertical deformation trend along profile P15. Dark dots: track 151. Profiles in range direction +/-14.7 km from the central line from Figure 11.. Red Line: Smoothed average line track 151.

CHAPTER 8: RESULTS FROM THE NEOTECTONICS IN NORDLAND - IMPLICATIONS FOR PETROLEUM EXPLORATION (NEONOR2) PROJECT, WORK PACKAGE 3: IN SITU STRESS MEASUREMENTS

Authors: Maria Ask[1], Daniel Ask[1,2]

Affiliations:[1]Division of Geosciences and Environmental Engineering, Luleå University of Technology, SE-971 87 Luleå, Sweden; [2]FracSinus Rock Stress Measurements AB, Gevärsvägen 20, SE-975 93 Luleå, Sweden

1. Abstract (Introduction)

Nordland in northern Norway is characterized by enhanced seismicity and uplift that makes it the most tectonically active area in Norway. This study is part of a project entitled Neotectonics in Nordland - Implications for Petroleum Exploration, which aims at enhancing the understanding of regional-scale stress and strain dynamics in Nordland, and to impact risk and hazard assessment and petroleum exploration.

The objective of this study is to determine the state of stress in boreholes. We have applied two borehole stress measurement methods: hydraulic stress measurements, and mapping of stress-induced features in the borehole wall. The hydraulic measurements are conducted in two steps, using wire-line activated straddle packers to measure stress magnitudes, and an acoustic borehole televiewer to measure the stress orientation. Three types of measurements have been conducted, hydraulic fracturing, sleeve fracturing and hydraulic tests on pre-existing fractures. Two types of stress-induced features have been investigated, borehole breakouts and drilling-induced fractures, and these features are detected with acoustic borehole televiewer.

The Geological Survey of Norway has drilled two 0.8 km deep near-vertical boreholes on opposite sides of the Vestfjord in Nordland, just North of 68° N. Borehole Leknes Bh is located on Lofoten archipelago at about 13°E, and borehole Drag Bh is located on the Norwegian mainland, at about 16°E. Unfortunately, the Drag Bh could not be accessed for hydraulic stress measurements, so these were only conducted in the Leknes Bh.

The results of this study provide a good understanding on the state of stress in the Leknes Bh. First, the results show that one principal stress is vertical, and only slightly lower than the horizontal minimum stress. The maximum horizontal stress is significantly greater in comparison. From 0.1 to 0.8 km depth, vertical-, minimum- and maximum horizontal stresses increase linearly from 2.6-20.8 MPa, 4.8-21.4 MPa, and 23.7-37.7 MPa, respectively. The differential horizontal stresses are unusually high. The mean orientation of maximum horizontal stress with respect to true North is 155±12°TN. This corresponds to “A” in WSM ranking quality.

A limited number of stress-induced features were observed from 0.35-0.76 km depth in the Drag Bh: Eight borehole breakouts and three drilling induced fractures had a combined length of 15.4 m. This suggests that the mean orientation of maximum horizontal stress with respect to true North is 3±15°TN. Six stress indicators were detected near and five stress indicators were detected away from pre-existing fractures. The two groups provided similar variances. Results from uniaxial compressive strength tests supports the existence of a reverse-faulting stress regime at 354 m depth in the Drag Bh. Results suggests that the rock mass in the Drag Bh and Leknes Bh are suitable for constraining stress polygons. The results suggest that the horizontal differential stresses are significantly higher in Leknes Bh than in Drag Bh at the test depths (337-354 m).

The unusual high differential stress and maximum horizontal stress suggest that it is likely caused by tectonic stress sources, whereas the vertical and minimum horizontal stresses may reveal the input from the weight of the overburden (gravitational stresses).

2. Objectives

The NEONOR2 project is organized within four work packages (WPs). The input of each WP is clearly highlighted in the project objectives, as stated in the proposal text: *“the prime objective of our project is to promote understanding of regional-scale stress and strain dynamics in the Nordland area through a detailed monitoring of seismicity (Work package 1), and to link this to geodetic movements (Work package 2) and in*

situ stress state (Work package 3), and in turn also to tectonics, exhumation and isostatic processes through modelling (Work package 4).”

The detailed objectives for WP 3 are:

- To conduct direct measurements of effective in-situ stress in two boreholes, 0.8 km deep (Leknes, Drag)
- To determine the complete stress tensor, and its variation with depth in the boreholes

2.1 Deliverables and milestones

Two main deliverables were identified, both which had sub-deliverables. Table 1 summarizes the completion date for the deliverables. Work within WP 3 was progressing according to, or ahead of plan until Deliverable 3.2.2, which is has unfortunately been delayed. Table 2 lists the publications and planned publications of WP3. An initial technical report with all test results has been completed (*Ask et al. 2018*) and work is ongoing to submit the results to peer-reviewed journal.

Table 1: Deliverables and milestones for Work package 3

Deliverable	Description	Milestone
3.1.1	Complete analyses of borehole breakouts and drilling-induced fractures using existing borehole televiewer data from two boreholes in Leknes and Drag	31.12.2013
3.1.2	Submit results for publication	01.03.2014
3.2.1	Conduct measurements of in-situ stress in the Leknes and Drag boreholes using hydraulic fracturing equipment and the NGU borehole televiewer tool	31.09.2014
3.2.2	Submit results for publication	TBS*

Del., deliverable; *, TBS, to be submitted

Table 2: Contributions of Work package 3

Reference	Status
Ask, M.V.S., D. Ask, H. Elvebakk, O. Olesen, 2015. Stress Analysis in Boreholes Drag Bh and Leknes Bh, Nordland, North Norway. Rock Mech Rock Eng, 48:1475–1484. DOI 10.1007/s00603-014-0683-9.	Published
Ask, D., Ask, M., Fredriksson, P., Mattson, K-J., 2018. Initial report of hydraulic stress measurements in the Leknes Bh, Lofoten, Norway. Technical report, NGU	Ready to publish*
Ask, M., D. Ask, Olesen, O., 2018. Hydraulic stress measurements in the Leknes Bh, Nordland, North Norway	To be submitted*
Ask, M., Wenning, Q., D. Ask, Olesen, O., 2018. Assessing stress orientation and stress regime in Boreholes Drag Bh and Leknes Bh, Nordland, North Norway	To be submitted*

* The technical report will be published after the results have been submitted to peer-reviewed journal for publication

3. Study area

The Nordland area, which extend 64.9 to 69.3°N is characterized by enhanced tectonic activity compared to other parts of onshore Norway, (Figure 1). There is a rapid change in crustal and lithosphere thickness from ocean to continental setting. A recent study based on 3D density modelling (*Maystrenko et al. 2017*) suggests that Moho depths increase from 11 km in the oceanic crust to 48 km under the mainland. Figure 1 shows that the continent-ocean boundary (COB) is located offshore Lofoten.

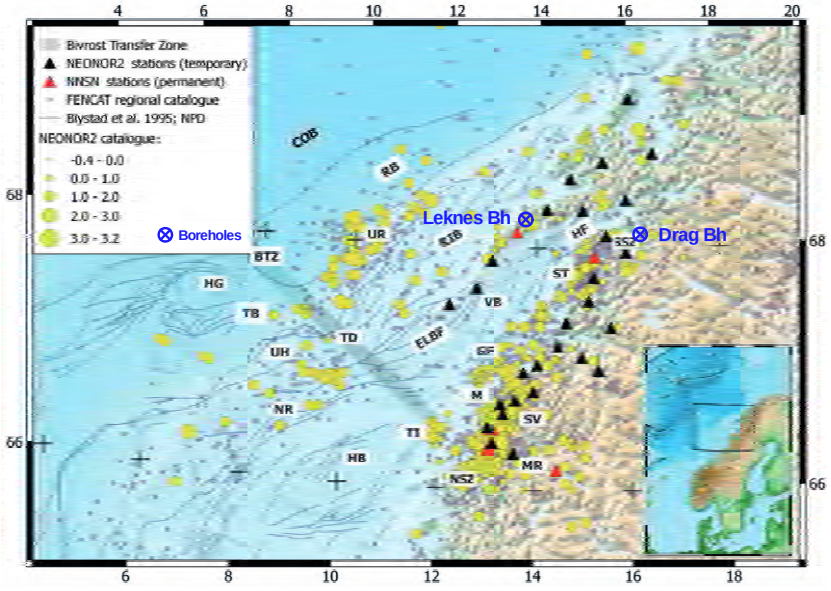

Figure 1. Stress measurements have been conducted in two 0.8 km deep near-vertical and 56 mm-diameter boreholes (Table 3). The boreholes are located on opposite sides of the Vestfjord bight, just north of 68°N, that separates the Lofoten archipelago from the Norwegian mainland, in Drag (Drag Bh) and Leknes (Leknes Bh; Figure 1). The boreholes were drilled within the CONTInental Crust and Heat Generation In 3D (KON-TIKI) project (Olesen et al. 2007). Subsequently, the boreholes were logged (Elvebakk & Rønning 2011). The lithostratigraphy of both boreholes are shown in Figure 2.

Table 3: Borehole data

Borehole	Coordinates	Elevation (masl[1])	Borehole length (mbl[2])	Deviation (°)
Drag Bh	68.036 N, 16.022E	24	780	<5
Leknes Bh	68.167 N, 13.642E	27	800*	<5

[1]masl, meter above sea level; [2]mbl, meter borehole length

The Drag Bh penetrated Tysfjord granite of Transcandinavian Igneous Belt (TIB) affinity (*Olesen et al. 2007*). The TIB is about 1400 km long and up to 200 km wide, and extends from SW Sweden to NW Norway (*Åhäll & Larsson 2000*). It is composed of magmatic plutonic rock and associated volcanic rocks and subordinate mafic and hybrid rocks of c. 1810-1770 Ma age. TIB may have been formed in an active continental margin setting, with eastward subduction beneath Baltica and back-arc extension (e.g. *Wilson 1980*). Around 420 Ma, the Caledonian orogeny influenced TIB rocks in NW Norway (*Skår 2002*). Very high values of heat generation have been measured in the Drag Bh, which are attributed to the nature of the TIB.

Leknes Bh has a more varying geology than observed in the Drag Bh, as it penetrated Archean gneisses and/or the Lofoten anorthosite-magnerite-charnockite-granite (AMCG) complex (*Olesen et al. 2007*). The upper part of the borehole is composed of granitic orthogneiss (0-540 mbl). The interval from 540 to 590 mbl is composed of alternating layers of diabase and gneiss. Below From 592-800 mbl, light grey granite was recovered.

4. Methods

We have applied two methods to measure rock stress, namely hydraulic stress measurements (HSM), and mapping of stress-induced features in the borehole wall. The hydraulic measurements comprise of hydraulic fracturing (HF), sleeve fracturing (SF) and hydraulic tests on pre-existing fractures (HTPF). Testing methodology and interpretation of raw data were undertaken in accordance with recommendations of the International Society for Rock Mechanics (ISRM; *Haimson & Cornet 2003*). HF, SF and HTPF tests are conducted with the same test equipment. Measurements are made in three steps. First, suitable test sections are selected. Second, the borehole is pressurized to initiate a new fracture, or open a pre-existing fracture (Figure 2A). Third, the orientation of the tested fracture is measured. Here, we have identified suitable test sections (step 1) and mapped the orientation of tested fractures (step 3) using an acoustic borehole televiewer (BHTV; Figures 2B-C).

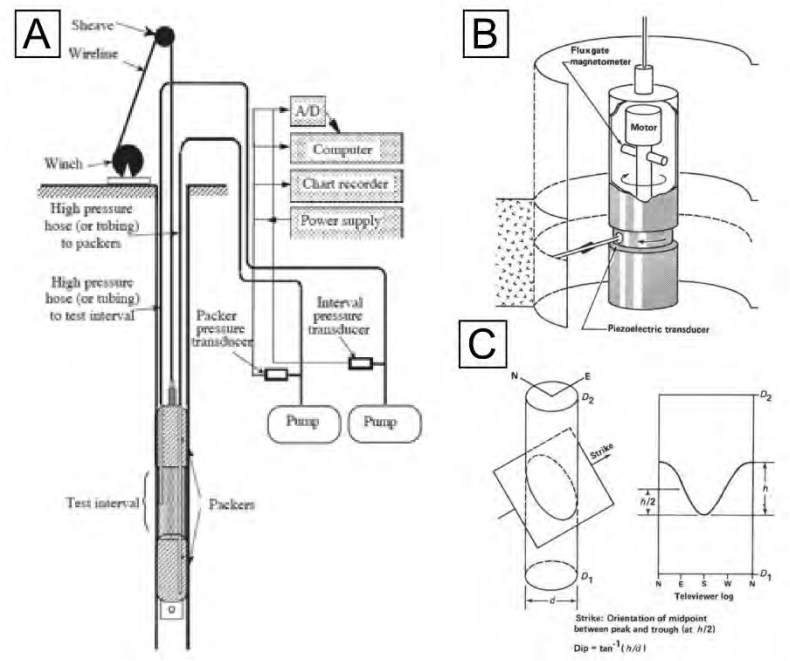

Figure 2. Schematic views of typical equipment for (A) pressure-generating equipment for hydraulic stress measurements (from Haimson & Cornet 2003), (B) Borehole televiewer tool in operation, and (C) how planar fractures in the borehole is interpreted in 2D (B-C are from Hickman et al. 1984, Zemanek et al. 1970).

Mapping of stress-induced features involves identifying of borehole breakouts (BB; *Bell & Gough 1979*) and drilling-induced fractures (DIF; *Brudy & Zoback 1993, 1999*). The orientation of these features is mapped with a BHTV. Testing methodology and interpretation of raw data were carried out in accordance with recommendations of the World Stress Map (WSM; *Tingay et al. 2016*). We also tried constraining the stress magnitudes, following methods developed by Mark Zoback's research group over the last 30 years (e.g. *Zoback et al. 2003; Zoback 2007*).

5. Theory

The theory of both HSM and mapping of stress-induced features in the borehole wall are based on *Kirsch* (*1898*) and *Jaeger & Cook* (*1969*). They described how stress is distributed around a cylindrical hole in a plate consisting of an ideal elastic and isotropic material subjected to a homogeneous stress field with one principal stress acting parallel to the hole. The borehole and surrounding anisotropic stress field results in stress concentrations around the borehole, including radial (σ_{rr}), circumferential ($\sigma_{\theta\theta}$), shear stresses ($\sigma_{r\theta}$), and axial stresses (σ_{zz}). At the borehole wall, these stresses are (e.g. *Zoback et al. 2003*):

$$\sigma_{rr} = \Delta P \tag{1}$$

$$\sigma_{\theta\theta} = (\sigma_H + \sigma_h - 2 \cdot \Delta P) - 2 \cdot (\sigma_H - \sigma_h) \cdot \cos 2\theta - \Delta P - \sigma^{\Delta T}$$

$$\sigma_{r\theta} = 0$$

where σ_H and σ_h are the maximum and minimum horizontal stresses, θ is the angle measured from the direction of σ_H. ΔP is the pressure difference between the fluid pressure in the borehole (P_w) and the formation pressure (pore pressure, (P_0), $\Delta P = P_w - P_0$), and $\sigma^{\Delta T}$ is the coolong stress. Figure 3 shows how $\sigma_{\theta\theta}$ varies along the borehole with respect to the orientation of one principal stress acting perpendicular to the vertical borehole, the maximum horizontal stress (σ_H).

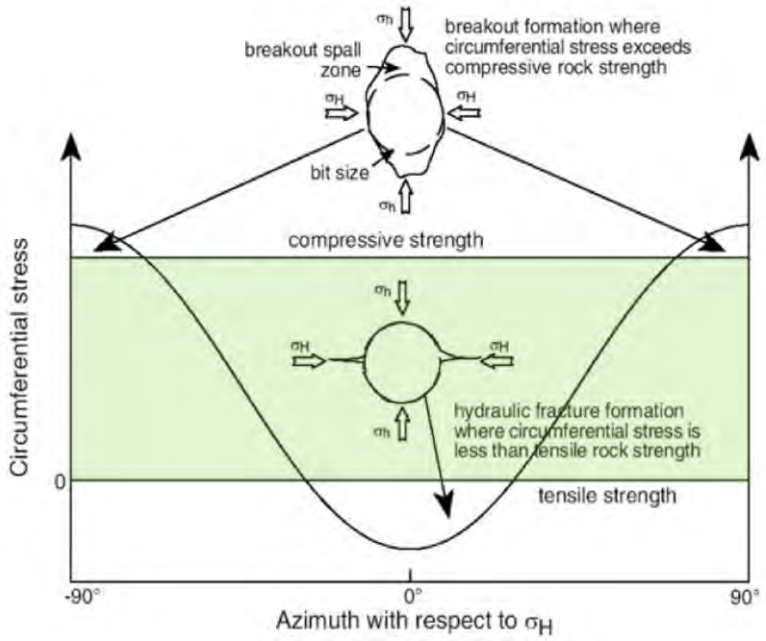

Figure 3. At the borehole wall, the circumferential stress ($\boldsymbol{\sigma_{\theta\theta}}$) varies with the azimuth of the principal stresses. It is minimum in the direction of the maximum horizontal stress ($\boldsymbol{\sigma_H}$) and maximum in the direction of the minimum horizontal stress ($\boldsymbol{\sigma_h}$) for a borehole drilled in the direction of vertical stress ($\boldsymbol{\sigma_v}$). Hydraulic fractures and drilling induced fractures (DIF) occurs if $\boldsymbol{\sigma_{\theta\theta}}$ exceeds the tensile strength of the wellbore wall, at $\boldsymbol{\sigma_H}$=0°N, and borehole breakouts (BB) form if $\boldsymbol{\sigma_{\theta\theta}}$ exceeds the compressive strength of the borehole wall, at $\boldsymbol{\sigma_H}$=90°N. No borehole failures occur if the rock strength exceeds $\boldsymbol{\sigma_{\theta\theta}}$, i.e. the green shaded area. Modified after Tingay et al. (2016), Hillis & Reynolds (2000)

Maximum stress concentrations ($\sigma_{\theta\theta}^{max}$) occur at θ=90° and 270° with respect to σ_H (2a). If $\sigma_{\theta\theta}^{max}$ is greater than the cohesive strength (C_0), BBs will form parallel with the direction of σ_h (Figure 2). Minimum stress concentrations ($\sigma_{\theta\theta}^{min}$) occur at θ=0° and 180° with respect to σ_H (2b). If $\sigma_{\theta\theta}^{min}$ overcomes the tensile strength (T), DIFs, SFs or HFs will form parallel with the direction of σ_H.

$$\sigma_{\theta\theta}^{max} = \sigma_{\theta\theta}(\theta = 90°) = 3 \cdot \sigma_H - \sigma_h - \Delta P \quad (2a)$$

$$\sigma_{\theta\theta}^{min} = \sigma_{\theta\theta}(\theta = 0°) = 3 \cdot \sigma_h - \sigma_H - \Delta P \quad (2b)$$

5.1 Hydraulic- and sleeve fracturing

For a vertical borehole aligned with a principal stress direction, the classical HF test (*Hubbert & Willis 1957*) yields magnitude and orientation of σ_h (and orientation of σ_H), and a crude estimate of σ_H magnitude based on the breakdown pressure, rock tensile strength, and a hypothesis of the pore pressure effect. The magnitude of σ_h is directly obtained from the shut-in pressure (P_s) (3a). For low permeable saturated rocks, it is assumed that P_0 is unaffected before the tensile fractures are formed, because the fracturing fluid does not percolate in the formation. The Terzaghi's effective stress concept ($\sigma_H{}' = \sigma_H - P_0$) can be applied. As a result, the crude determination of σ_H is based on T in the direction of $\sigma_{\theta\theta}^{min}$ ($\sigma_{\theta\theta}^{min} = -T$), and equation (2b) can be re-written (3b; *Haimson & Cornet 2003*):

$$\sigma_h = P_s \quad (3a)$$

$$\sigma_H = T + 3 \cdot \sigma_h - P_b - P_0 \quad (3b)$$

Figure 4 is a pressure-time diagram that displays how the parameters are derived (*Haimson & Cornet 2003*). In general, the value of T is difficult to determine with precision in the lab and in the field. *Bredehoeft et al*. (*1976*) suggested that T is the difference between P_b and the re-opening pressure (P_r) (4a), and to expand (3b) into (4b):

$$T = P_b - P_r \quad (4a)$$

$$\sigma_H = 3 \cdot \sigma_h - P_r - P_0 \quad (4b)$$

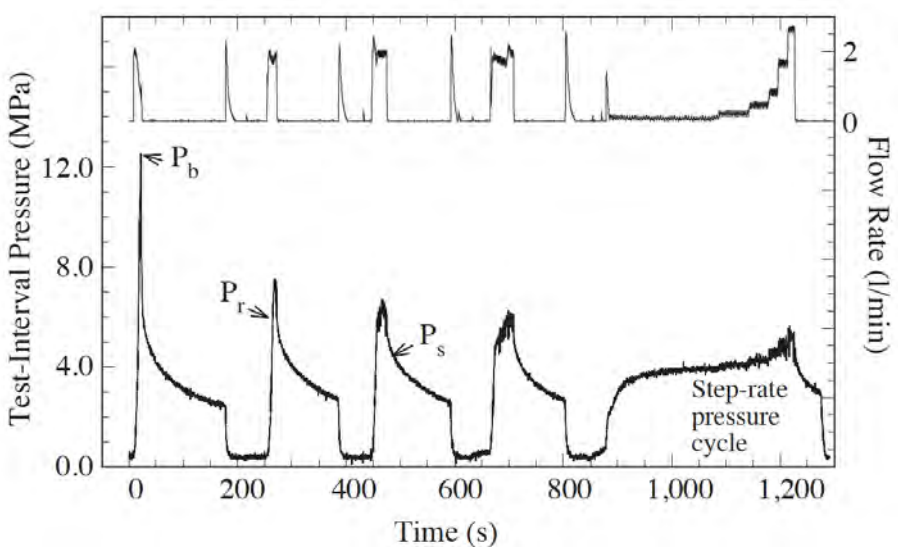

Figure 4. Test results from a HF test showing pressure- and flow rate versus time, and how the breakdown- ($\boldsymbol{P_b}$), re-opening- ($\boldsymbol{P_r}$) and shut-in ($\boldsymbol{P_s}$) pressures are determined (from Haimson & Cornet 2003).

There are several problems with the HF theory. Some papers have shown that P_r depends on the pressurization rate (*Ratigan 1992; Cornet 1993; Rutqvist et al. 2000*). Furthermore, it is difficult to objectively interpret P_r because the volume pumped into the system widely exceeds the volume entering the fracture plane (*Ito et al. 1999*). In addition, a numerical study by *Rutqvist et al.* (*2000*) showed that the induced fracture disturbs the assumption of a linear-elastic, homogeneous and isotropic material and suggests that P_r is always close to the magnitude σ_h, independent upon the magnitude of σ_H. In conclusion, the (4b) method is still the best option when no other data are available, even though it may only provide a crude estimate of the σ_H-magnitude.

The SF tests serve to improve the HF test sequence. Unlike HF tests, SF tests nearly always guarantee that an axial fracture will be induced SF tests also provide means to derive P_b and T without introducing water, thereby reducing percolation effects (*Stephansson 1983; Thiercelin & Desroches 1993; Thiercelin et. al 1994*). Once the SF cycles have been completed, the downhole equipment is hoisted so that the test section is placed over the axially induced fracture. At this position, a conventional HF test is run. The combined SF/HF approach may solve both horizontal stress magnitudes as well as their orientation.

5.2 Hydraulic testing of pre-existing fractures

In thrust regimes, the fracture plane may rotate during propagation, giving an estimate of the vertical stress component. This is the main reason for undertaking the HTPF tests. These tests determine if rotation is indeed a problem. They also provide the vertical stress gradients and improve the crude estimate of maximum horizontal stress from HF tests or combined SF and HF tests.

The HTPF methodology is a crucial complementary test to the SF and HF tests. The methodology allows determination of the vertical stress component, which cannot be addressed using SF or HF. It also provides an independent verification of the tensor components obtained by SF and HF. This is indeed critical as SF and HF measurements in thrust conditions ($\sigma_H > \sigma_h > \sigma_v$), where induced fractures have a tendency to rotate to the horizontal plane and may lead to serious misinterpretations if not identified.

The inversion procedure is based on a least squares measure of misfit and the Tarantola-Valette gradient algorithm (*Tarantola & Valette 1982; Cornet & Valette 1984*). It assumes a linear variation of the stress field throughout the volume sampled by the tests considered for the inversion.

The choice of parameterization for stress calculation depends on the number of measurement points and the range of orientations of the tested fractures (*Haimson & Cornet 2003*). The full stress tensor can be

characterized by six parameters, implying that a minimum of six different tests must be conducted. The measurements must be made on fractures with unique dip and azimuth to solve the stress tensor (σ_n^m):

$$\sigma_n^m = \boldsymbol{\sigma}(\boldsymbol{X}_m) \cdot \boldsymbol{n}_m \cdot \boldsymbol{n}_m \quad (5)$$

where $\boldsymbol{X_m}$ is the location of the m^{th} measurement point, σ_n^m is the measured normal stress on the fracture plane with normal $\boldsymbol{n}_m$.

In some cases, the number of required tests can be reduced if certain assumptions are made. For example, if the vertical stress is assumed to be a principal stress, the number of unknowns is four. If the vertical principal stress is assumed to be equal the weight of the overburden, the number of unknowns is three. In other cases, the number of tests must be increased. This may be necessary if the distance between measured points is long enough to require inclusion of stress gradients. *Haimson & Cornet* (*2003*) parameterize the stress field by assuming a linear variation along the borehole axis in which HTPF tests are made:

$$\boldsymbol{\sigma}(\boldsymbol{X}_m) = \boldsymbol{\sigma}(\boldsymbol{X}_0) + (\boldsymbol{X}_m - \boldsymbol{X}_0) \cdot \boldsymbol{\alpha} \quad (6)$$

where the stress at point $\boldsymbol{X_m}$ can be expressed as a linear function of the stress at point $\boldsymbol{X_0}$ and $\boldsymbol{\alpha}$ is the stress gradient along the borehole axis. Generally, (6) consists of 12 parameters, and requires at least 14 tests to solve the stress tensor. With similar assumptions as for (5), the number of unknowns can be reduced to 10.

The analyses also require the definition of misfit functions, which defines the difference between observed and computed values in the stress model. Misfit functions should address errors of both normal stress and orientation determinations.

5.3 Stress induced features

Borehole breakouts (BB) are stress-induced enlargements of the borehole cross section (*Bell & Gough 1979*). They appear when the stress concentration around the borehole exceeds the rock strength (Figure 2). BBs form on diametrically opposite sides of the borehole, are parallel to the minimum horizontal stress (σ_h) and in the direction of $\sigma_{\theta\theta}^{max}$ (2a). Drilling-induced fractures (DIF) show the σ_H orientation (*Brudy & Zoback 1999*), which is the direction of $\sigma_{\theta\theta}^{min}$ (2b). Depending on the orientation of the borehole in space and the state of stress, there are two types of DIFs: DIFs are sub-parallel to the borehole axis, and those that have en-echelon pattern inclined toward the borehole axis. The former type shows that borehole axis is aligned with a principal stress direction, whereas the latter shows that the borehole axis is inclined from a principal stress direction.

Tingay et al.（*2016*）presents the World Stress Map (WSM) guidelines for data interpretation. The WSM has developed a ranking system, which considers the number of observations, the consistency of results, and the reliability of the data as a tectonic indicator. A weighted mean azimuth orientation and standard deviation for the stress-induced features in each hole is obtained from *Mardia* (*1972*), and is described in detail in *Tingay et al.*（*2016*）. The lengths of the individual stress indicators are taken into account to enhance the dominant azimuth orientation. 47 plots the World Stress Map ranking scheme for BBs and DIFs, analysed in image logs (*Tingay et al. 2016*). Because the same quality criteria are valid for both BB and DIFs, we conclude that it is appropriate to jointly consider BB and DIF data in this study.

WSM quality criteria for stress indicators in this study (WSM 2008)

A	B	C	D	E
Hydraulic fracture (HF)				
≥5 HF orientations in a single well with sd ≤ 12°. Depth ≥ 300 m, distributed over a depth range ≥ 300 m	≥4 HF orientations in a single well with sd ≤ 20°. Depth ≥ 100 m, distributed over a depth range ≥ 200 m	≥3 HF orientations in a single well with sd ≤ 25°. Depth ≥ 30 m, distributed over a depth range ≥ 100 m	Single HF orientation	Wells in which only stress magnitudes are measured, without information on orientations
Borehole breakout (BB) from image logs				
≥ 10 distinct BB zones and combined length ≥ 100 m in a single well with sd ≤ 12°	≥ 6 distinct BB zones and combined length ≥ 40 m in a single well with sd ≤ 20°	≥ 4 distinct BB zones and combined length ≥ 20 m in a single well with sd ≤ 25°	< 4 distinct BB zones or < 20 m combined length with sd ≤ 40°	Wells without reliable BB or with SD > 40°
Drilling induced fractures (DIF)				
≥10 distinct DIF zones and combined length ≥ 100 m in a single well with sd ≤ 12°	≥6 distinct DIF zones and combined length ≥ 40 m in a single well with sd ≤ 20°	≥4 distinct DIF zones and combined length ≥ 20 m in a single well with sd ≤ 25°	< 4 distinct DIF zones or < 20 m combined length with sd ≤ 40°	Wells without reliable DIF or with SD > 40

When formed, BBs and DIFs reveal the continuous variation in stress orientation over depth, which is unique among all other existing methods of stress determination. On the other hand, it is not as straightforward to constrain stress magnitudes from these features. One reason is that the specific failure mechanisms of BBs are poorly known. *Plumb* (*1989*) concluded that the specific failure mechanisms depend of rock strength, depths, and state of stress and the geometry of the breakout is governed by lithology. Several groups have attempted to constrain the stress field (orientation and magnitude). Significant contributions have been made by Mark Zoback's research group and are summarized in *Zoback et al. (2003)* and *Zoback* (*2007*). Early studies include (1) estimate of the stress regime from the breakout depth distribution (*Barton et al. 1988; Moos & Zoback 1990*) and (2) estimate of the principal stress magnitudes from breakout shape (*Zoback et al. 1985; Barton et al. 1988; Zheng et al. 1988; Peska & Zoback 1995*). The results have been applied in estimate the stress magnitudes in a number of deep boreholes in crystalline rock, including the Cajun Pass (e.g. *Vernick & Zoback 1992*) and the Fenton geothermal well (*Barton et al. 1988*), the KTB borehole in Germany (e.g. *Brudy et al. 1997*), and the Siljan boreholes (Gravberg-1 and Stenberg-1) in Sweden (*Zajac & Stock, 1997; Lund & Zoback 1999*). These methods also have been successfully adopted for sedimentary reservoirs (cf. *Zoback 2007*) and sedimentary rock, for example in scientific boreholes of the Integrated Ocean Drilling Program (e.g. *Chang et al. 2010; Saffer et al. 2013*). In many cases, the analyses have access to in situ leak off- and extended leak off tests, and pore pressure measurements from the borehole under analyses. Other analyses used the borehole shape as well as laboratory strength data (uniaxial compressive strength, internal friction angle/coefficient).

The stress polygon was first developed by *Zoback et al.* (*1987*) to graphically reveal the possible stress states for a given depth and pore pressure, in the $\sigma_h - \sigma_H$-plane (i.e., S_{hmin} and S_{Hmax}, respectively in Figure 4). Stress polygons are developed in four steps. The first step is to plot σ_v (i.e., S_v in Figure 4), which is assumed to be equal to the weight of the overburden:

$$\sigma_v = \sum_{i=1}^{n} \rho_i \cdot g \cdot D_i \qquad (7)$$

where ρ_i is the mean mass density of the rock layer i, g is the local gravitational acceleration (9.82 m/s^2), D_i is the thickness of layer i, and n is the number of layers overlaying the test zone. The second step is to define the lower boundary of the $\sigma_h - \sigma_H$ relationship. Because $\sigma_h \leq \sigma_H$, the stress state where $\sigma_h > \sigma_H$ is impossible. We plot the stress state $\sigma_h = \sigma_H$, which includes possible stress states above and including $\sigma_h = \sigma_H$, and impossible stress states below $\sigma_h = \sigma_H$ (Figure 5).

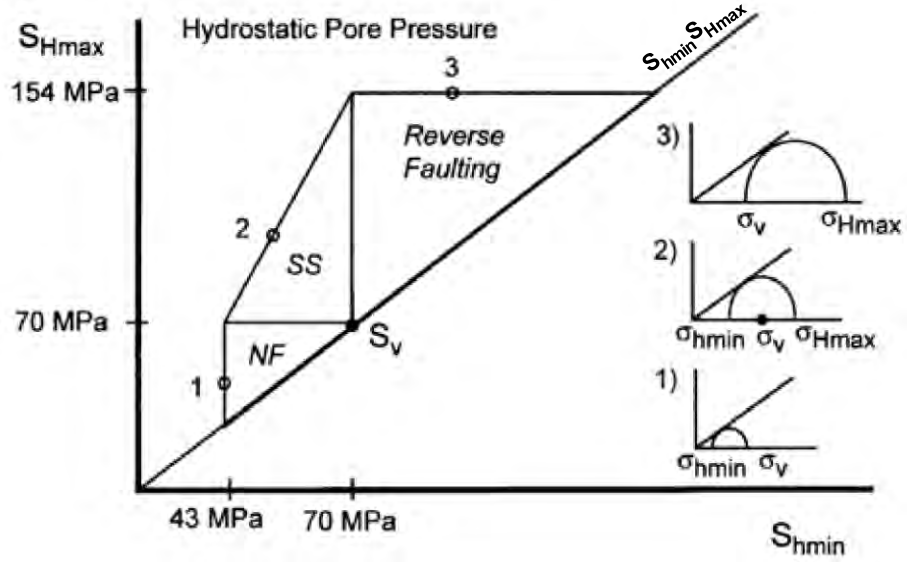

Figure 5. The stress polygons that define possible magnitudes of horizontal principal stresses for a specific vertical stress (S_v), μ and P_p are shown in $\sigma_h - \sigma_H$ diagram. The stress polygons are based on Andersonian faulting theory and Coulomb failure criterion in (8b). Mohr circles (1-3) shows the Andersonian faulting regimes that define the circumference of the polygon (modified from Zoback et al. 2003 and references therein)

The third step is to map the possible stress states for the Andersonian stress regimes (*Anderson 1951*) with normal faulting ($\sigma_v > \sigma_H > \sigma_h$), strike-slip faulting ($\sigma_H > \sigma_v > \sigma_h$) and reverse faulting ($\sigma_H > \sigma_h > \sigma_v$). Figure 5shows the Mohr's circles for the three stress states, and the horizontal line at S_v marks the limit between normal- and strike slip faulting regimes (NF and SS, respectively), and the vertical line at S_v marks the limit between the SS and reverse faulting (RF) regimes.

The fourth step is to constrain the limit for the different stress regimes. It is assumed that the internal friction of the rock mass marks the outer boundaries of the faulting regimes. *Barton et al.* (*1988*) regarded the frictional strength of pre-existing faults limits the ratio of shear- to normal stress acting on the faults (*Jaeger & Cook* 1979):

$$\frac{\sigma_1}{\sigma_3} = \frac{S_1 - P_p}{S_3 - P_p} = \left(\sqrt{(\mu^2 + 1)} + \mu\right)^2 \quad (8a)$$

where σ_1 is the major principal stress, σ_3 is the minor principal stress, P_p is the pore fluid pressure, μ is the coefficient of internal friction, and S_1 and S_3 are principal stresses in the three Andersonian stress regimes. (8a) can be re-written:

$$\frac{\sigma_v - P_p}{\sigma_h - P_p}(\text{normal faulting}) = \left(\sqrt{(\mu^2 + 1)} + \mu\right)^2 \quad (8b)$$

$$\frac{\sigma_H - P_p}{\sigma_h - P_p}(\text{strike} - \text{slip faulting}) = \left(\sqrt{(\mu^2 + 1)} + \mu\right)^2 \quad (8c)$$

$$\frac{\sigma_H - P_p}{\sigma_v - P_p}(\text{reverse faulting}) = \left(\sqrt{(\mu^2 + 1)} + \mu\right)^2 \quad (8d)$$

Normally, the coefficient of internal friction (μ) and the cohesive strength (C_0) are constrained from a combination of uniaxial- and triaxial compression laboratory tests on drill cores. However, a rough estimate

can be obtained from uniaxial compression tests only if a clear shear fracture is developed (Figure 5A) according:

$$\phi = 2 \cdot \varphi - 90 \quad (9)$$

$$\mu = \tan \phi$$

where φ is the orientation of the fracture from the plane perpendicular to the axial stress (σ_1) and ϕ is the internal friction angle (e.g. *ASTM 2010; Fossen 2016*). Further, the cohesive strength is obtained from the Mohr-Coulomb fracture criterion:

$$\sigma_s = C_0 + \sigma_n \cdot \tan \phi = C_0 + \sigma_n \cdot \mu \quad (10a)$$

where the shear stress (σ_s) and the normal stress (σ_n) acting at the fracture are obtained from the uniaxial compressive strength (σ_c) and φ (*ASTM 2010*):

$$\sigma_s = \sigma_c \cdot \sin \varphi \cdot \cos \varphi \quad (10b)$$

$$\sigma_n = \sigma_c \cdot \cos^2 \varphi$$

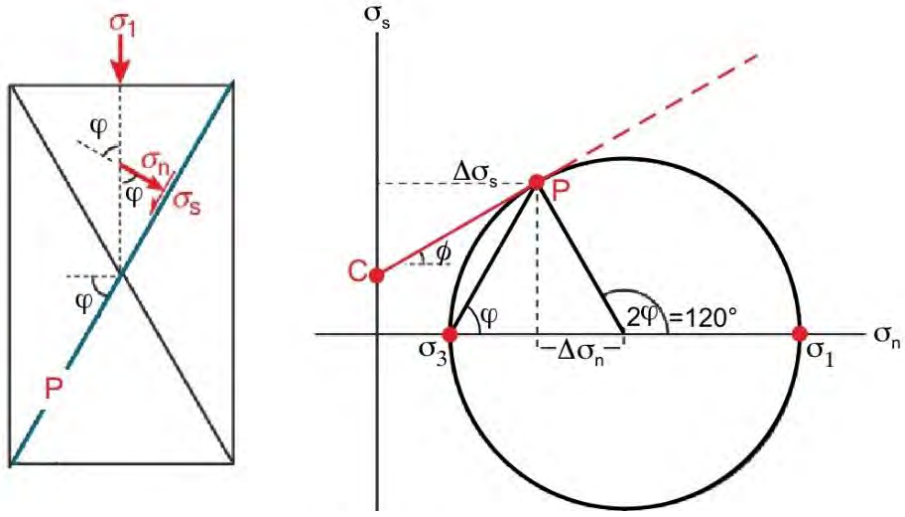

Figure 6. The relationships between core sample dimensions on Mohr Circle and the Coulomb failure criterion (modified after Fossen 2016 and ASTM 2010). The uniaxial compressive strength (σ_c) corresponds to σ_1 at failure, with σ_3=0. See text for further explanations.

Uniaxial compressive strength tests provide data on the uniaxial compressive strength (σ_c), elastic properties: Young's modulus (E) and Poissons ratio (ν), as well as frictional relationships (cf. Figure 6). The latest *ASTM* (*2010*) standard provide details how σ_c, E and ν are determined:

$$\sigma_c = \frac{F}{A} \quad (11a)$$

$$E = \frac{\Delta\sigma}{\Delta\varepsilon_a} \quad (11b)$$

$$\nu = -\frac{\Delta\varepsilon_l}{\Delta\varepsilon_a} \quad (11c)$$

$$\rho = \frac{M_t}{\pi \cdot r^2 \cdot L} \quad (11d)$$

where : F is the axial force at failure A is the cross sectional area of the sample, $\Delta\sigma$ is the axial stress interval, $\Delta\varepsilon_a$ is the axial strain interval, $\Delta\varepsilon_l$ is the lateral strain interval, M_t is the weight of the sample, r is the sample radius, and L is the sample length. Elastic properties for two stress intervals have been

determined: (1) For the secant properties (E_s, ν_s), (11b-c) are derived from connecting the origin to 50% of σ_c; and (2) For the tangent properties (E_t, ν_t), the values are derived from tangent to the stress strain curve at 50% of the maximum strength.

Equations (8b-8d) result in the vertical line through (1) for NF, the inclined line through (2) for SS, and the horizontal line through (3) for RF in Figure 5.

The final step is to consider possible stress states that can be constrained from the rock strength within BB and DIF zones. The red lines in Figure 7 shows possible stress states for BB zone, derived from (13), and the blue line shows possible stress state for DIFs from (14). Several studies have focused on the estimation of possible magnitudes of σ_H and σ_h at the initiation of BBs from their width and rock strength. *Zoback et al.* (*1985*) presented a relationship between the half width of the breakout (ϕ_b) and the angle of breakout initiation with respect to σ_H (θ_b), which also is shown graphically in Figure 7:

$$90 = \phi_b + \theta_b \tag{12}$$

As shown above, BBs are initiated at $\sigma_{\theta\theta}^{max}$. *Zoback et al.* (*1985*) applied the Navier-Coulomb criterion and assumed that breakouts form if the cohesive strength (C_0) is exceeded, and that the $\sigma_H - \sigma_h$ relationships also depend on θ_b. Thus, this estimate provides lower boundary of the $\sigma_H - \sigma_h$ magnitudes. Subsequent work (see above) also has incorporated the influence from pore pressure (P_p), excess mud weight (ΔP), and cooling stress ($\sigma^{\Delta T}$), as presented by *Zoback et al.* (*2003*):

$$\sigma_H = \frac{\left(C_0 + 2 \cdot P_p + \Delta P + \sigma^{\Delta T}\right) - \sigma_h \cdot (1 + 2 \cdot \cos(2 \cdot \theta_b))}{1 - 2 \cdot \cos(2 \cdot \theta_b)} \tag{13}$$

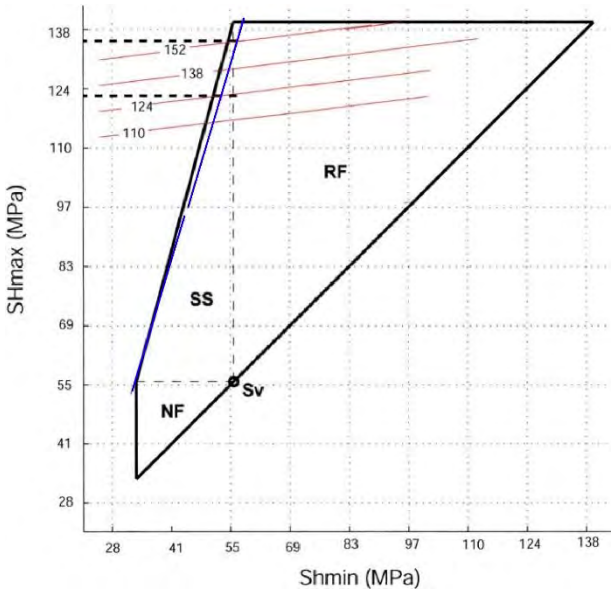

Figure 7. Example of stress polygon. Possible stress states have been constrained from borehole breakouts (red lines) and drilling induced fractures (blue) described in the text (modified after Zoback et al. 2003).

As, DIFs, HFs and SFs all are initiated at $\sigma_{\theta\theta}^{min}$, which also form the base for HF theory. *Brudy* & *Zoback* (*1999*) applied hydraulic fracturing theory for mode I fracturing formation at the borehole wall. Since then, the influence of $\sigma^{\Delta T}$ has been included (*Zoback et al. 2003*):

$$\sigma_{\theta\theta}^{min} = 3 \cdot \sigma_h - \sigma_H - 2 \cdot P_p - \Delta P - \sigma^{\Delta T} \leq T \tag{14a}$$

By assuming that $\sigma^{\Delta T}$ and T are negligible ($\sigma^{\Delta T} = T \approx 0$), and that the mud weight is similar to the pore pressure (i.e. $\Delta P \approx 0$), (14a) can be rewritten:

$$\sigma_H = 3 \cdot \sigma_h - 2 \cdot P_p \tag{14b}$$

Interestingly, *Zoback et al.* (*2003*) showed that the conditions for DIF formation are very similar to the SS faulting regime in frictional equilibrium. Using μ=0.6, they rewrote Equation (8c):

$$\sigma_H = 3.1 \cdot \sigma_h - 2.1 \cdot P_p = 3 \cdot \sigma_h - 2 \cdot P_p + 0.1 \cdot \left(\sigma_h - P_p\right) \approx 3 \cdot \sigma_h - 2 \cdot P_p \quad (15)$$

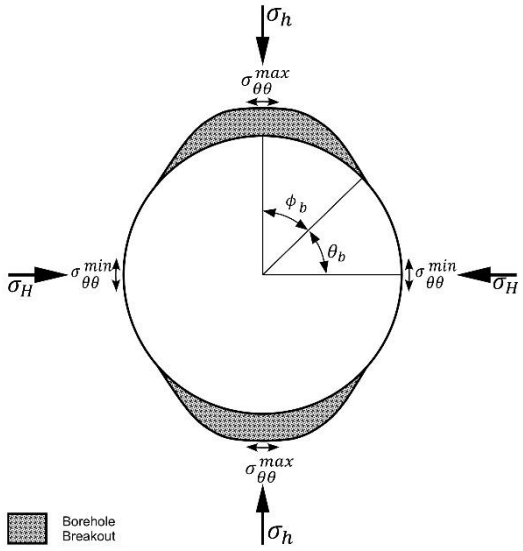

Figure 8. Borehole breakout development, see further discussion in the text (modified after Barton 1988).

6. Stress data

Elvebakk & Rønning (*2011*) logged the Drag Bh and Leknes Bh (Figure 8) with temperature, water conductivity, formation resistivity, P- and S-wave sonic velocity, natural gamma radiation (NGR), deviation, and BHTV tools. While the Drag Bh was logged to total depth, the Leknes Bh was only partially logged, due to winch problems. Figure 9 shows example of borehole televiewer data of BBs and DIFs.

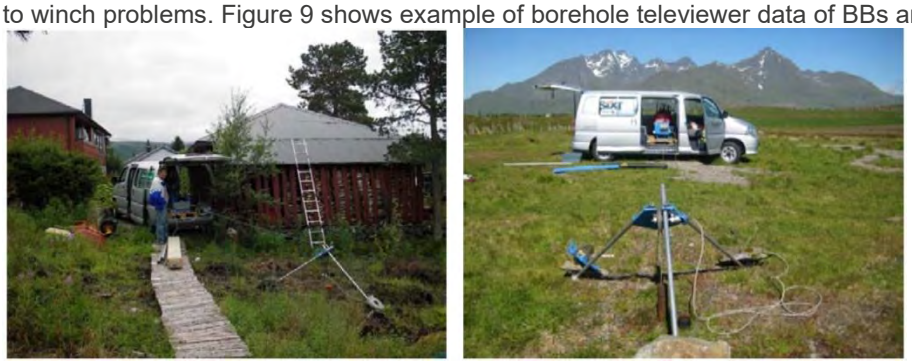

Figure 9. Logging conducted in the Drag Bh (left) and Leknes Bh (right) boreholes (from Elvebakk et al 2011).

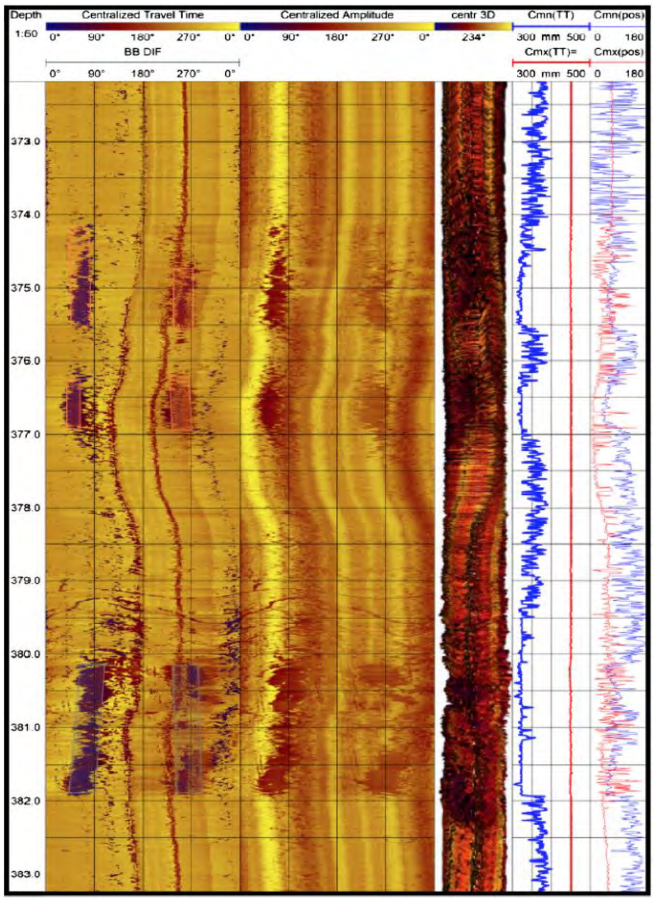

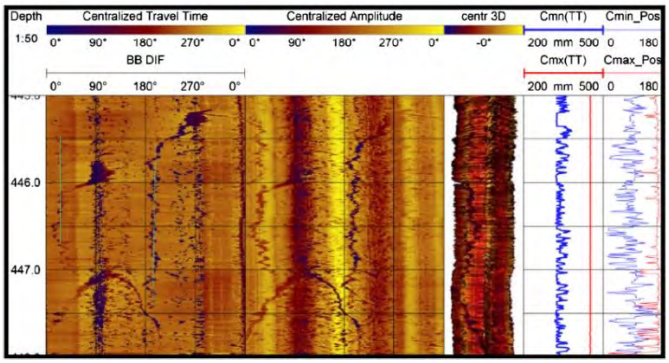

Figure 10. Borehole televiewer images of borehole breakouts (A) and drilling induced fractures (B) detected in the Drag Bh. Keys: Orange squares show borehole breakouts, Grey squares indicate borehole elongation near pre-existing structure, Turquoise lines indicates drilling-induced fractures (from Ask et al. 2015).

HSMs were conducted by Geosigma AB in September 2014 in the Leknes Bh (Figure 11). Poor ground conditions and insufficient space for setting up the equipment prevented HSMs at the Drag Bh, but it was possible to conduct logging in the borehole. Gert Andersen of Rambøll Dk conducted borehole logging (*Andersen 2018*). Table 5 lists the logging tools that were run in both boreholes. While the Drag Bh only was logged once with this full suite of logs, an additional BHTV logging was run after HSM testing to capture the orientation of tested fractures in the Leknes Bh.

Hydraulic stress measurements (HSMs) are conducted in three steps. First, the borehole length is pre-logged with the BHTV. Potential test sections are selected from the BHTV log and by inspection of the drill

core. Second, the packer system is lowered to the selected test interval, which and the packers and the test section between the packers subsequently is pressurized (Figure 2A). A new fracture is generated within the test section during HF tests, whereas the packers generate a new fracture during SF tests. During HTPF tests, a pre-existing fracture is carefully opened. The normal stress of the tested fracture is determined in this test. Third, the orientation of the tested fracture is logged with the BHTV. The orientation of HF, SF and HTPF fractures are mapped using the log composite software WellCAD (http://www.alt.lu/software.htm). WellCAD is also used to map BBs and DIFs.

The first BHTV log before and after HSM testing are the PRE-LOG and POST-LOG, respectively. The logging before HSM testing revealed that the borehole diameters were 60 mm, and not 56 mm as stated in *Olesen et al.* (*2007*) and *Elvebakk & Rønning* (*2011*). The result was that Geosigma brought HSM packers with a better-suited diameter to field. Rambøll Dk had no centralizer for the for the borehole dimensions, LTU manufactured a non-magnetic centralizer in advance of testing (Figure 11). After testing, the centralizer was given to NGU. The original delivery (*Andersen 2014*) included erroneously oriented BHTV data. This was discovered during the analyses of results in 2017, and resulted in a revised logging report (*Andersen 2018*).

A *B*

Figure 11. Images from the hydraulic stress measurements (HSM) campaign conducted in Leknes Bh in September 2014. A, Pre-logging by Rambøll, i.e. step 1 of HSM stress tests described in text (Andersen 2018); B, Hydraulic stress tests by Geosigma AB, B, i.e., step 2 of HSM stress tests (Ask et al. 2018).

Figure 11. Two non-magnetic centralizers were manufactured at LTU before testing, here mounted on the Geovista BHTV (cf. 4).

Rambøll Dk logging tools and their specifications (from Andersen 2018)

Tool	Recorded logs	Dimension	Source type
BHTV. GeoVista Acoustic televiewer (Ultrasonic borehole imager)	Full waveform acoustic amplitude and traveltime, 360° orientated acoustic image, 360° very high resolution caliper, Borehole azimuth and dip and natural gamma	210 x 4.2 cm	
NGRS. GeoVista Natural Gamma	Natural gamma	70 x 3.8 cm	
CAL3. GeoVista 3-arm caliper	3-arm caliper	1.18 x 3.8 cm	
TCME GeoVista Fluid temp/cond	Fluid temperature and conductivity	70 x 3.8 cm	
TRIS. GeoVista UnCompensated Density	Density uncompensated. Source detector spacing 11 cm.	165 x 3.8 cm	10 mCu Cs137
DLL3. GeoVista Focused Formation resistivity	Deep and short formation resistivity	222 x 3.8 cm	
GeoVista Winch	1500 m cable		

As mentioned above, two types of data are recorded during HSM tests (Figure 2): Magnitude measurements are obtained using wire-line activated straddle packers and the orientation measurements are made with a BHTV. To allow precise depth correlation for both systems, natural gamma logging is recoded during magnitude and orientation data collection. Figures 12-14 shows examples of HSM data.

A

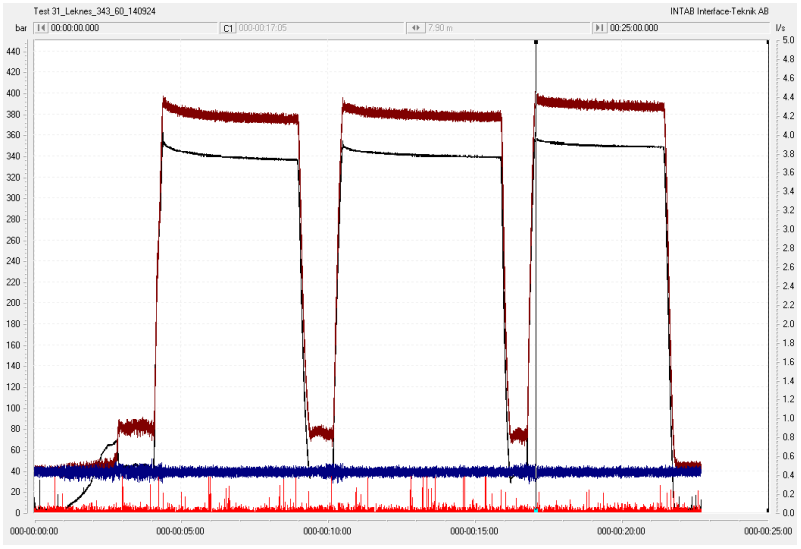

B

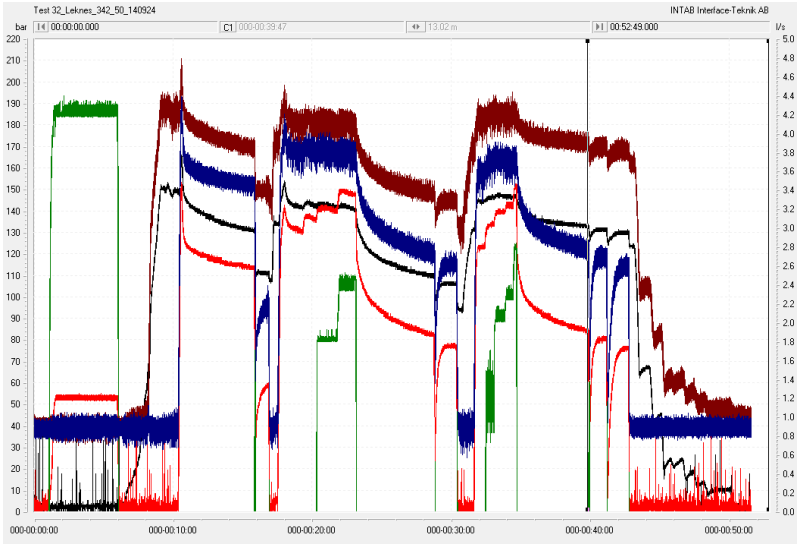

C

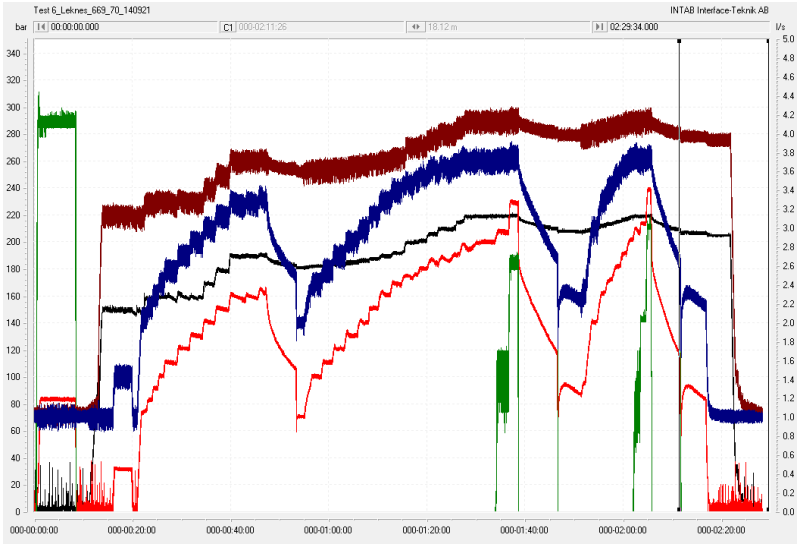

Figure 12. Example of pressure-flow-time diagram from hydraulic stress measurements. A, Sleeve fracturing test SF10 (test number 31) at 343.60 mbl; B, Hydraulic fracturing test HF15 (test number 32) at 342.50 mbl; and C, Hydraulic testing of pre-existing fracture test HTPF19 (test number 6) at 669.70 mbl. Brown and black lines denote packer pressure measured downhole and at surface, respectively, blue and red lines denote test section pressure measured downhole at surface, respectively. Green line denotes flow rate.

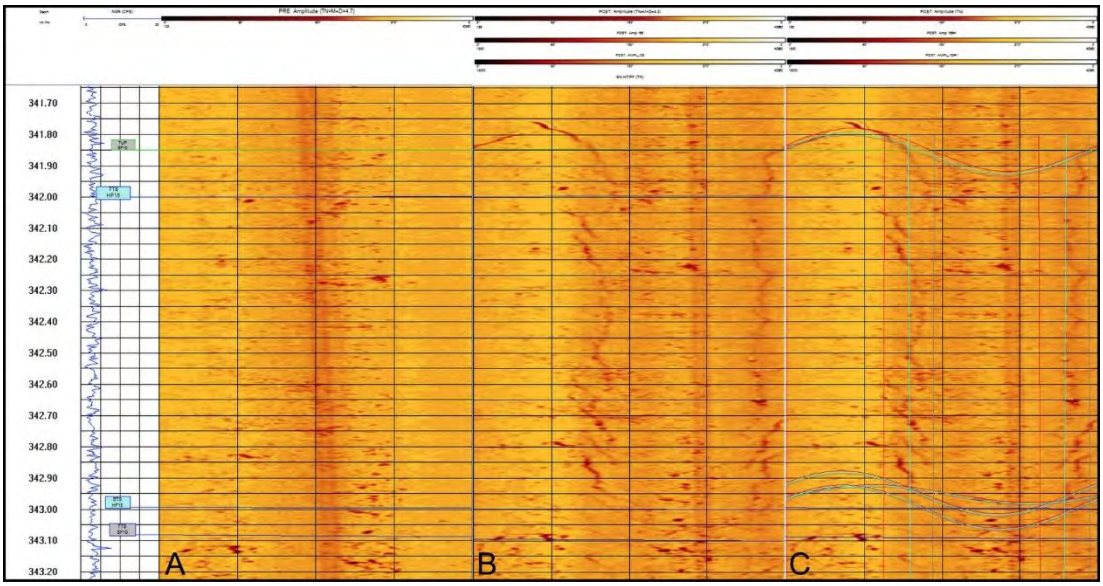

Figure 13. Borehole televiewer images of sleeve fracturing test number SF10 that subsequently was activated in hydraulic fracturing test number HF15. A, Pre-log amplitude image of test interval; B, Post-log amplitude image of test interval without interpretation; and C, Post-log amplitude image of test interval with interpretation. The grey labels show top of packer (TUP) and top of test section (TTS) for SF10. The turquoise label labels show TTS and base of test section (BTS) for HF15. The axial interpretations in (C) shows the lower (red) to upper (grey) ranges, as well the best-average interpretation (turquois) of the induced fracture. The sinusoids interpretations also highlight induced fractures that could have been activated during testing.

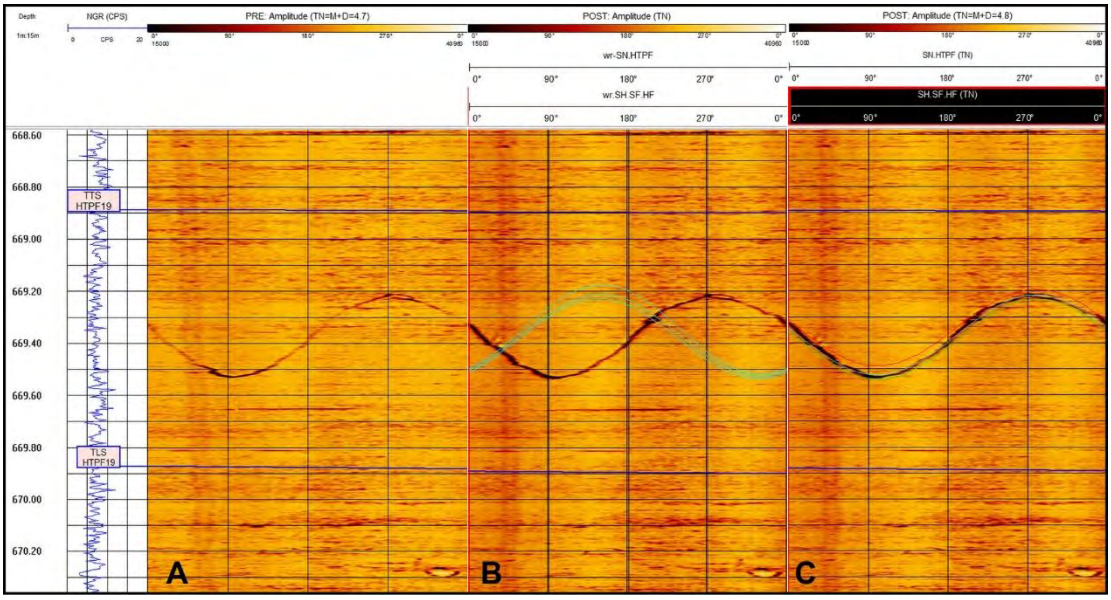

Figure 14. Borehole televiewer images of hydraulic testing of pre-existing fractures test HTPF19. A, Pre-log amplitude image of test interval; B, Post-log amplitude image of test interval without interpretation; and C, Post-log amplitude image of test interval with interpretation. The pink labels show top and base of packers (TTS and BTS, respectively) for HTPF15. The sinusoids interpretations in (C) show the lower (red) to upper (grey) ranges, as well the best-average interpretation (turquois) of the induced fracture. The green sinusoids in (B) shows the interpretation made on the erroneous-oriented log of the original delivery (Andersen 2014).

The BHTV log also was used to investigate potential occurrences of BBs and DIFs, as observed in the pre-existing BHTV data by *Ask et al.* (*2015*). Figure 16 shows same BBs of Figure 9A, while Figure 17 shows the same DIF as of Figure 9B, plus a newly identified potential DIF at the base of the Drag Bh, which was not observed in the pre-existing data.

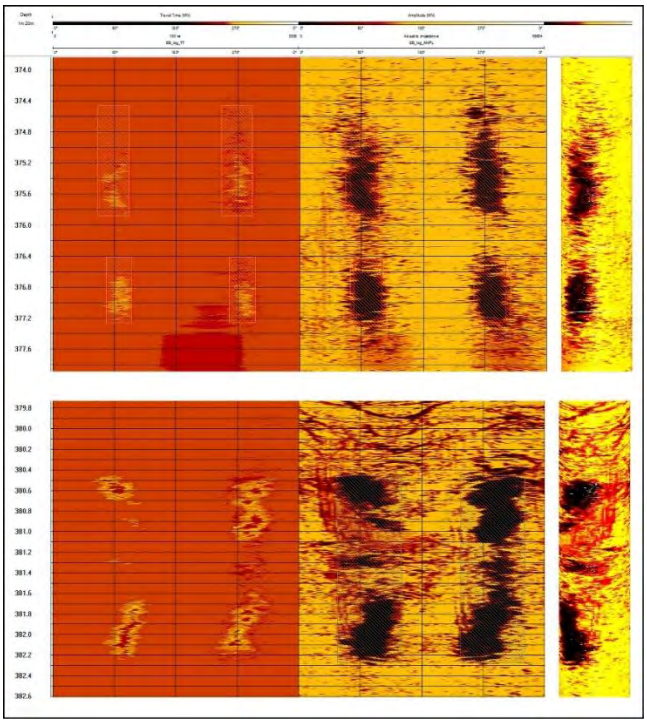

Figure 15. Borehole televiewer images of two pairs of minor borehole breakouts detected in Drag Bh. Andersen (2018) collected the data.

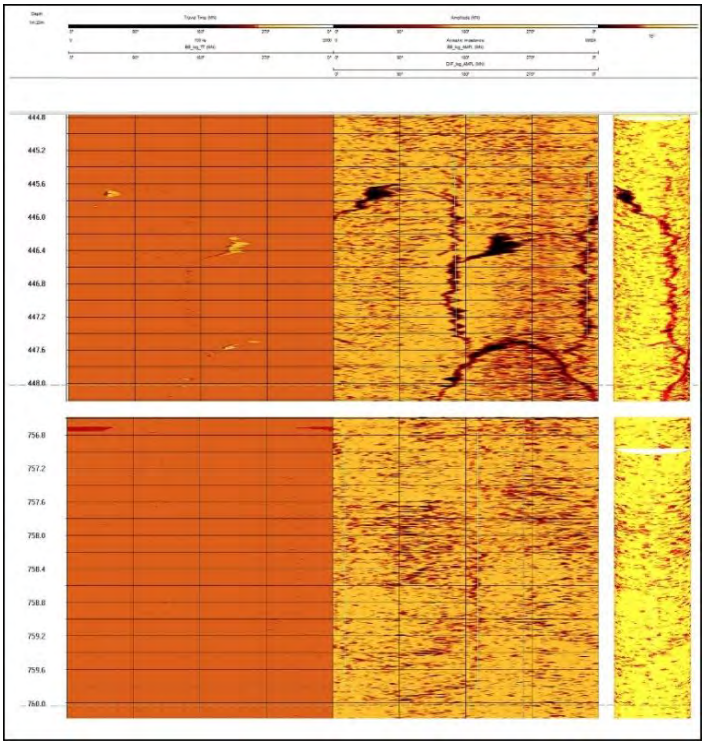

Figure 16. Borehole televiewer images of a suspected drilling induced fracture near a pre-existing fracture (top), and, apparently, in intact rock (bot). Andersen (2018) collected the data.

To constrain the stress magnitudes, a suite of uniaxial compressive strength tests has been conducted. Drill core samples were collected to from the NGU core repository in Løkken, with support from Rolf Lynum. Samples were collected from two levels in the Drag Bh, which contain BBs and DIFs. Core samples were also collected from two levels in the Leknes Bh. They were collected from similar depths as in the Drag Bh, at depths where HF tests have been conducted. This way, the stress magnitudes from DIFs would be constrained using HF test results. Thus, a means to calibrate the stress magnitudes from DIFs in the Leknes Bh using HSM data. A suite of parameters was collected from uniaxial compressive strength testing (cf. (11a-d) and Figure 5): bulk density (ρ), uniaxial compressive strength (σ_c), orientation of fracture (φ),

internal friction angle (ϕ), internal friction coefficient (μ), as well as elastic properties of the samples (E, ν). Figure 18 shows the cores after testing.

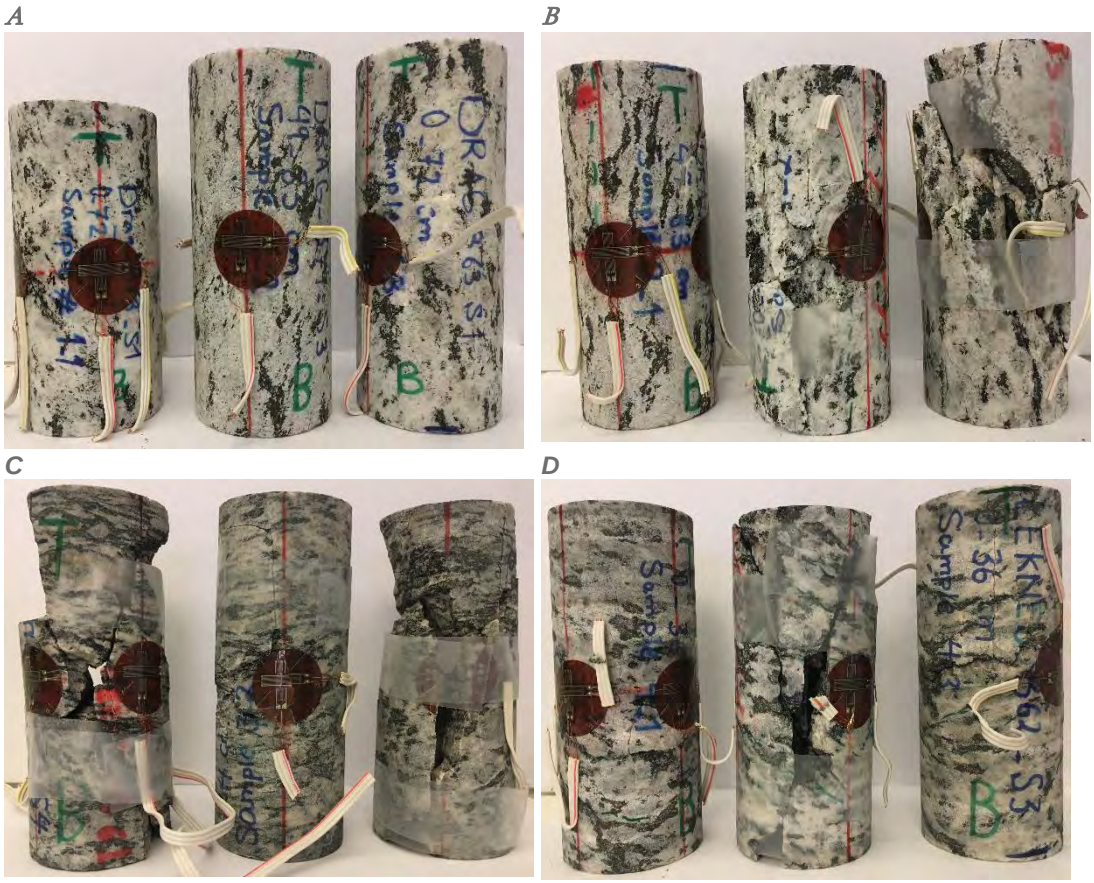

Figure 17. Core samples subjected to rock mechanic testing. From left to right: A, Samples 1-1, 1-2, and 1-3; B, Samples 2-1, 2-2, and 2-3; C, Samples 3-1, 3-2, and 3-3; and D, Samples 4-1, 4-2, and 4-3. See further sample details in Table 8.

Figures 18 and 19 shows the full logging suite collected in the Drag Bh and Leknes Bh during step 1 of the HSM campaign. It should be noted that the density log is uncompensated, but that the data has been inter-calibrated against discrete density measurements from cores in the LKAB iron mine in Kiruna. This result in unrealistic high values, but the trend is correct.

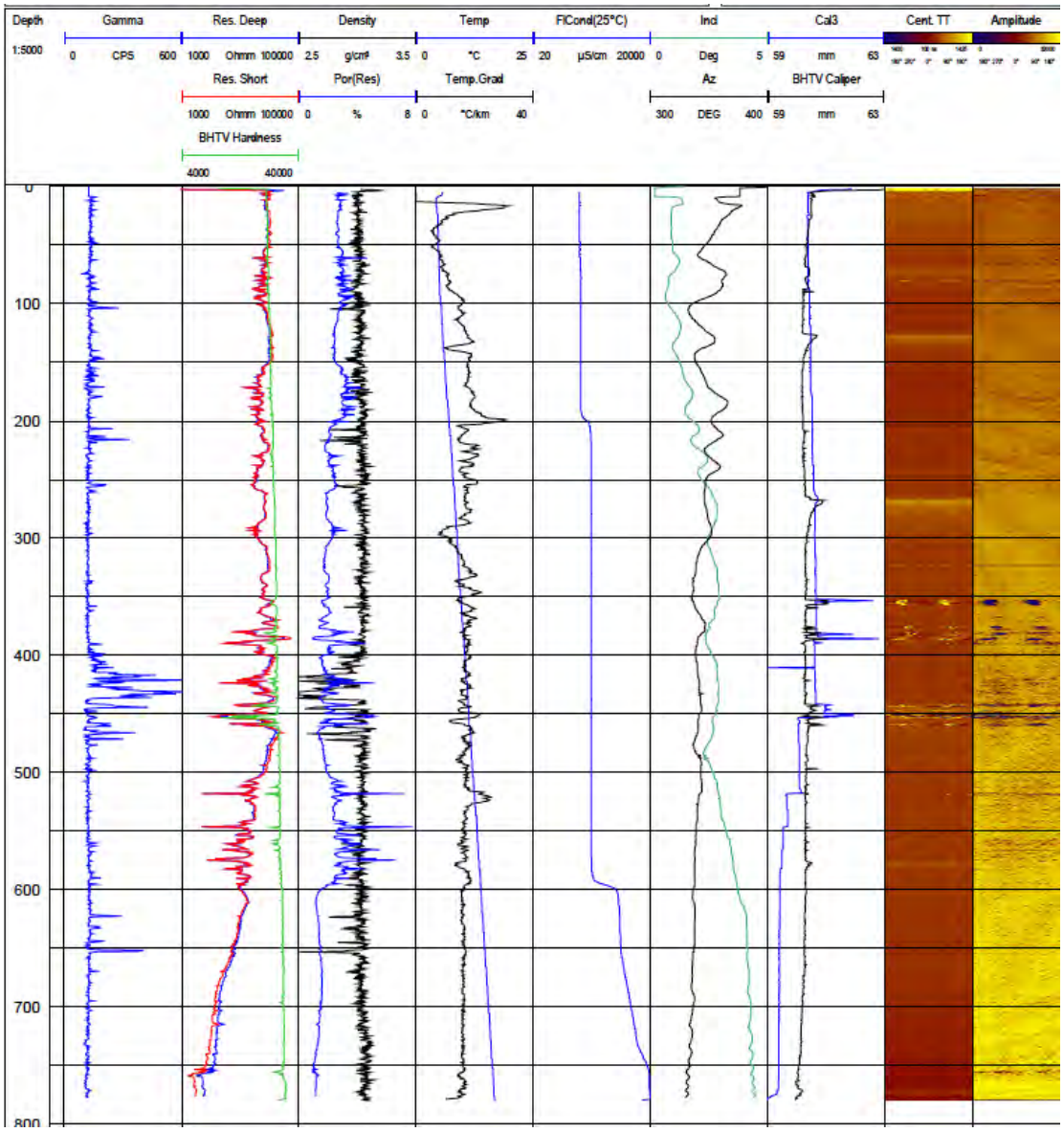

Figure 18. Logging data collected in Drag Bh. Further details are given in Table 5 (from Andersen 2018).

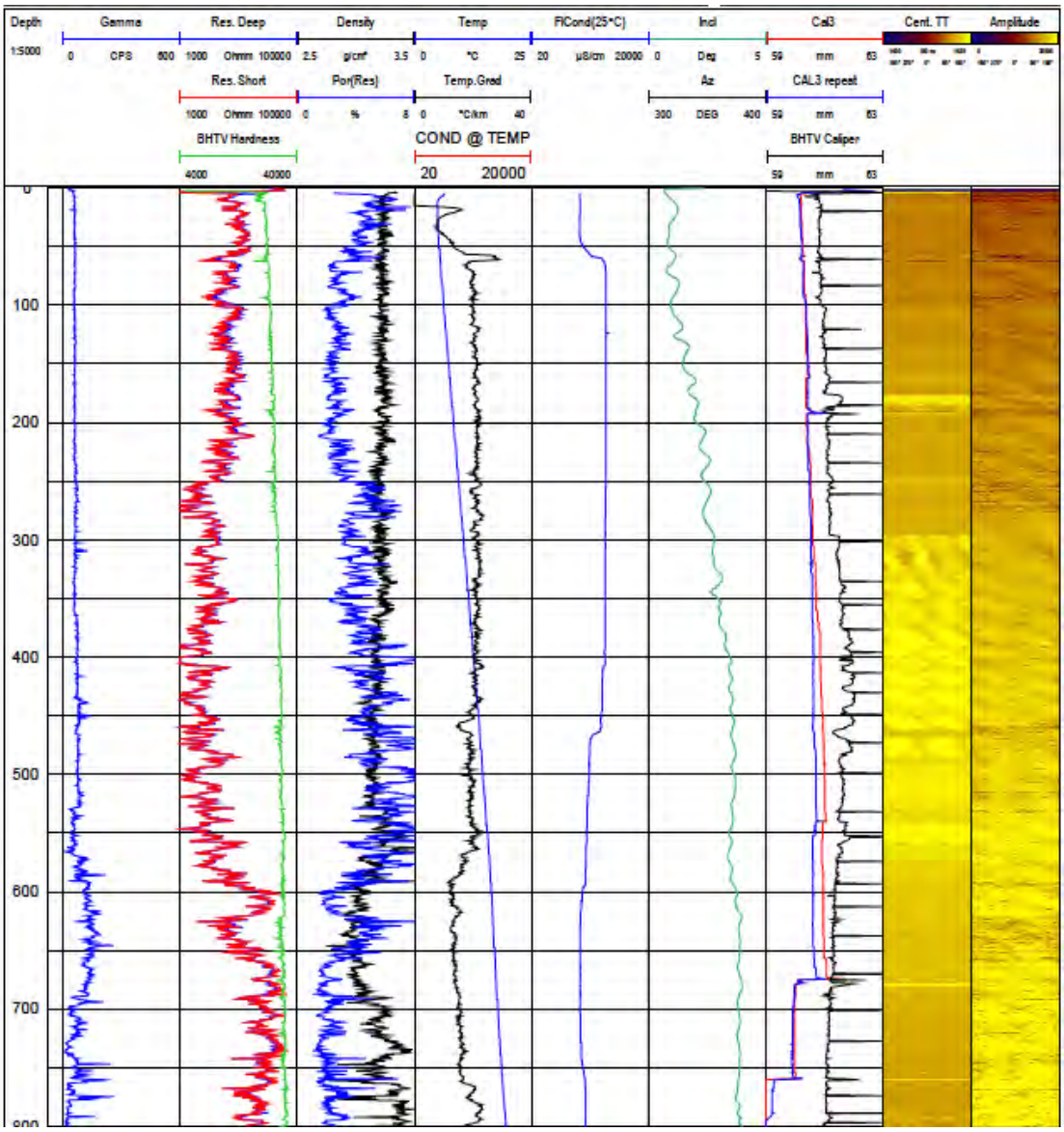

Figure 19. Logging data collected in Leknes Bh. Further details are given in Table 5 (from Andersen 2018).

7. Results

7.1 Stress-induced borehole failure

Results from the BHTV analyses based on old NGU data have been published (*Ask et al. 2015*). The results of were in most practical aspects inconclusive, mainly due to poor data quality. The data analysis has revealed erroneously high-borehole diameter, and several artefacts such as eccentric logging tool, rugose borehole wall, spiral hole, tool sticking and missing data. Four intervals with passive in situ stress indicators (borehole breakout and drilling-induced fractures) were found in travel time and amplitude images of the Drag Bh, suggesting approximately N–S orientation of maximum horizontal stress. However, these intervals are not found in cross-plots. Either result yields the lowest World Stress Map ranking quality (E quality; Table 4).

The new BHTV data is of significantly better quality than the NGU data, thanks to the use of centralizers of the tool. However, original borehole conditions that formed during drilling (i.e. spiral hole) are remaining, and influence the data quality. The potential stress indicators mapped in *Ask et al.* (*2015*) are in general duplicated, but with improved constrain on orientation and distribution, as shown in Figures 10, 16 and 17. Mapped BBs are wider in the amplitude log than in the travel time log. This is because amplitude is more

sensitive than travel time to detect defects in the rock, and can detect if some material is already partly destroyed before it is visible on the travel time image (*Deltombe & Schepers 2000*). Because the amplitude log can detect existing BBs as well as potential breakout areas, we have based the interpretations of BBs on the travel time images. On the other hand, DIFs rarely are visible in the travel time log. Therefore, DIF interpretations are derived from the amplitude log. The results show that BB and DIFs only are found in the Drag Bh, and Table 6 presents the results from BB and DIF mapping. It represents a more detailed BB and DIF analyses compared with *Ask et al.* (*2015*), as allowed by the improved data quality. The stress indicators have been groped in two types, where "Type a" indicates that the BB or DIF formed away from pre-existing fractures, and "Type b" indicates that they formed near pre-existing fractures. This can signal that the stress field is modified by the fracture (cf. Figure 23).

Table 4: Stress-induced features observed in the Drag Bh

Pair	SI[11]	Type[2]	Depth (mbl)	Azimuth (°MN	Opening[3] (°)	Length (m)	σ_H (°TN)	Average length (m)	θ_b (°TN)
1	BB	a	354.44	68.61	34.42	4.14	163	4.14	86
			354.44	248.61	34.42	4.14			
2	BB	a	375.42	91.21	37.15	0.82	7	0.82	110
			375.41	272.69	37.15	0.82			
3	BB	a	376.87	99.38	37.15	0.67	14	0.67	118
			376.87	279.38	37.15	0.67			
4	BB	b	380.70	95.48	56.47	0.47	18	0.54	124
			380.79	291.27	56.47	0.61			
5	BB	b	381.43	105.33	28.98	0.57	25	0.57	120
			381.43	294.61	28.98	0.57			
6	BB	b	381.98	104.77	62.41	0.47	15	0.465	130
			381.95	274.92	39.38	0.46			
7	BB	b	385.91	67.62	49.78	1.42	162	1.42	93
			385.91	247.62	49.78	1.42			
8	BB	b	459.34	82.11	52.01	0.68	177	0.68	108
			459.34	262.11	52.01	0.68			
9	DIF	b	446.32	164.95	0.00	2.18	170	2.18	-
			446.32	344.95	0.00	2.18			
10	DIF	a	510.36	2.63	0.00	0.74	7	0.74	-
			510.36	182.63	0.00	0.74			
11	DIF	a	758.33	13.39	0.00	3.12	18	3.12	-
			758.33	193.39	0.00	3.12			

[1]SI, Stress Indicator, either borehole breakout (BB) or drilling Induced fracture (DIF), [1]Type, a, SI detected away from pre-existing fracture; b, SI detected near/at pre-existing fracture(s), [3]Opening corresponds to the full width of the breakout, i.e. $2 \cdot \phi_b$.

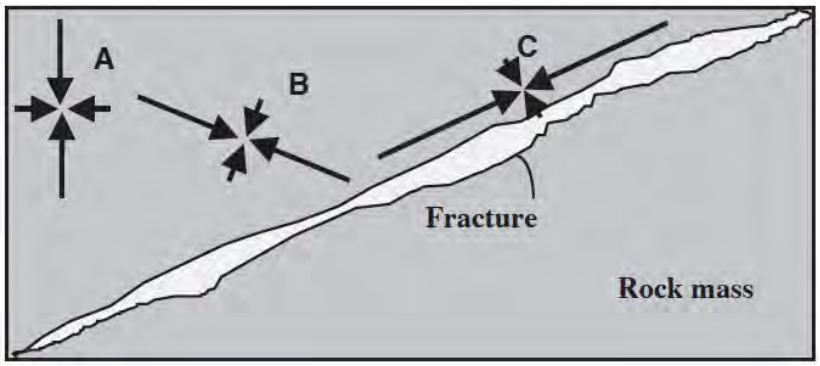

Figure 23. Schematic view of how the stress field is influenced by an open fracture (or filled fracture having contrasting strength than the surrounding rock mass (from Hudson et al. 2003).

In general, because fractures may disturb the stress field, "Type a" BB and DIFs are considered to reflect the contemporary in-situ stress field more accurately than those of "Type b". At the same time, the observed

DIFs (Types a and b) could reveal pre-existing axial fractures; at this stage, we have not verified this with respect to core. The range of individual BB and DIF orientations are similar for “Type a” and “Type b” stress indicators (Table 5), with exception for BB pair 1 which has a different orientation (σ_H=163°TN) compared to more N-S oriented σ_H for remaining “Type a” stress indicators (their σ_H ranges from 7-18°TN). The change in orientation from BB Pair 1 corresponds to over 30° shift in stress orientation, and could reflect a discontinuous stress field. However, it may also reflect the natural variation of stress in Drag Bh, as the result of variation in orientation of foliation (as observed in the HSM data, e.g. Figure 13). We also observe significant variation in orientation of foliation in the drill cores on which uniaxial compression strength tests were conducted (see below), especially for the samples from the Drag Bh. This influences the internal friction angle and could generate downhole variation in σ_H. In total, σ_H range from 162-18°TN for all observations (Table 6). This suggests that pre-existing fractures formed in a similar stress field as the contemporary, and/or that the fractures are tight with similar properties as the surrounding rock. However, because the available data is sparse, it is difficult to do more detailed interpretations.

Table 7 summarizes mean values, obtained from circular statistics (*Mardia 1972*) for the observed BB and DIFs. According to the WSM quality ranging scheme (Table 4), the obtained values result in WSM quality D at best. It is noted that only BB “Type a” suggests NNW-SSE σ_H orientation, whereas all data considered has N-S σ_H orientation.

Table 5: Average stress orientation and data quality in Drag Bh

Stress indicator[1]	Type	Number of zones	Average $\sigma_H \pm sd$ (°TN)	Combined length (m)
BB	a	3	163±24	5.6
BB, DIF	a	5	1±16	9.5
BB, DIF	b	6	6±14	5.9
BB, DIF	a, b	11	3±15	15.4

Table 8 lists all parameters derived from uniaxial compressive strength tests (cf. (11a-d), i.e. density, uniaxial compressive strength, secant- and tangential Young’s modulus (E_s and E_t, respectively), and secant- and tangential Poisson’s ratio (ν_s and ν_t, respectively). In addition, the orientation of the fracture at failure has been measured. From (9-10), values used to constrain the internal friction angle and -coefficient, and the cohesive strength are derived. Figure 17 shows that the samples generally were subjected to multiple failures. For example, across and along foliation failure planes were generated at failure. In addition, the orientation of foliation could vary significantly, especially for the samples from the Drag Bh. The general observation is that foliation is steeper in the samples from Drag, than for those from Leknes.

Table 6: Results from uniaxial compression testing

SL[1]	SID[2]	Depth (mbl)	No[3]	$\rho \pm sd$ [4] (t/m3)	$\sigma_c \pm sd$[5] (MPa)	$E_s \pm sd$[6] (GPa)	$E_t \pm sd$[7] (GPa)	$\nu_s \pm sd$ [8] (-)	$\nu_t \pm sd$ [9] (-)
				Drag Bh					
1	B63-1, 0-72 cm	353.48-354.20	3	2.68±0.01	2.68±0.01	19±1	42±3	0.16±0.03	0.41±0.14
2	B79-3, 49-83 cm	446.64-446.81	3	2.67±0.01	2.67±0.01	45±1	71±5	0.23±0.03	0.34±0.07
				Leknes Bh					
3	B61-4, 0-90 cm	336.84-337.74	3	2.74±0.01	2.74±0.01	29±2	48±14	0.16±0.02	0.40±0.04
4	B62-3, 0-36 cm	341.69-342.04	3	2.72±0.04	2.72±0.04	27±4	53±11	0.17±0.03	0.32±0.08

[1]SL, Sample Level, [2]SID, Sample ID (core box-section, interval), [3]No, number of samples tested), [4] ρ, density, sd, standard deviation, [5]σ_c, uniaxial compressive strength, [6]E_s, Secant Young's modulus, [7]E_t, Tangent Young's modulus, [8]ν_s, Secant Poisson's ratio., [9]ν_t, Tangent Poisson's ratio.

Table 7: Fracture orientation and internal friction properties of samples

Sample Level	Sample ID core box-section, interval	Depth (mbl)	No of samples	φ (°HOR)	ϕ (°)	μ (-)
		Drag Bh				
1	B63-1, 0-72 cm	353.48-354.20	3	≥ 60	≥ 30	≥ 0.6
2	B79-3, 49-83 cm	446.64-446.81	3	≥ 65	≥ 40	≥ 1.7
		Leknes Bh				
3	B61-4, 0-90 cm	336.84-337.74	3	≥ 60	≥ 30	≥ 0.6
4	B62-3, 0-36 cm	341.69-342.04	3	≥ 60	≥ 30	≥ 0.6

Sample numbers 1-1 to 1-3 were collected from the shallow BB at 354 mbl (Pair 1 of Table 6). Sample numbers 2-1 to 2-3 were collected a few meters below the BB at 459 mbl (Pair 8 of Table 6), and from the DIF at 446 mbl (Pair 9 of Table 6). The samples in Leknes were collected from the site of HF and SF tests. Sample numbers 3-1 to 3-3 were collected from a HF test at 337.5 mbl, whereas Samples 4-1 to 4-3 were collected a HF test at 342.5 mbl, just above a SF test at 343.6 mbl.

We observe that failure occurred across the foliation, and have measured an orientation of the fracture of 60° from horizontal in Samples 1, and 65° in Samples 2. However, also sub-vertical samples, along the foliation have been measured. As a result, internal friction angles of 30° and 40° are included in the stress polygon that has been constructed for BB Pair 1 (Figure 24, Tables 6-8). It is clear that failure envelope due to frictional failure (cf. (8a-c)) grows with increasing ϕ. At the same time, C_0 decreases with increasing ϕ. Figure 24 suggests that the stress regime most likely is RF, with possible values of σ_h and σ_H ranging from 9.3-17.1 MPa and 18.4-21.1 MPa, respectively. The σ_h-σ_H relationship for BB magnitudes (cf. (13)), also indicates that a strike-slip faulting regime could occur if σ_h is lower than σ_v (=9.3 MPa) and greater than frictional failure in a strike slip regime (σ_h≈8.3 MPa). The corresponding range σ_H magnitudes would be just over 18 MPa (Figure 24A). These results are based on an internal friction angle (ϕ) of 30°, which result in a cohesive strength (C_0) of 37 MPa for Samples 1-1 to 1-3. BHTV data the breakout initiation angle (θ_b) of 86°TN has been measured (Table 6). The frictional boundary for ϕ=40° is included in gray.

In the samples from the Leknes Bh, the tendency is that fractures form across foliation. The dominant fracture orientations indicate ϕ of 30°. The value of σ_c is more scattered (Table 7) and the samples are also

denser than in the Drag Bh, resulting in somewhat higher vertical stress gradient. The results from the stress model (17) is included in the stress polygon for the Leknes samples (Figure 25). The first observation is that the stress model (green colour) predicts values outside of the frictional boundary for ϕ=30°, but that it is within ϕ40°. Further, combined SF-HF tests at 343 mbl result in T=-9.0 MPa, which is significant and thus have been incorporated in (14) and included in Figure 25 (dotted blue line). The stress polygon further suggest that the stress regime is near the transition from strike slip- to reverse fracturing regime, which is in accordance with the HSM stress model in (17).

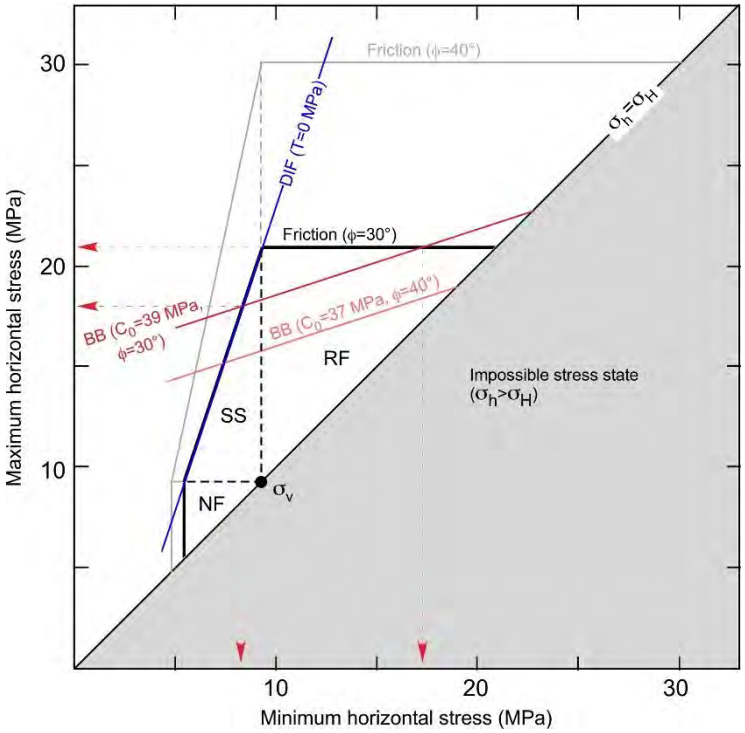

Figure 24. Stress polygon for borehole breakouts in the Drag Bh at 354 mbl.

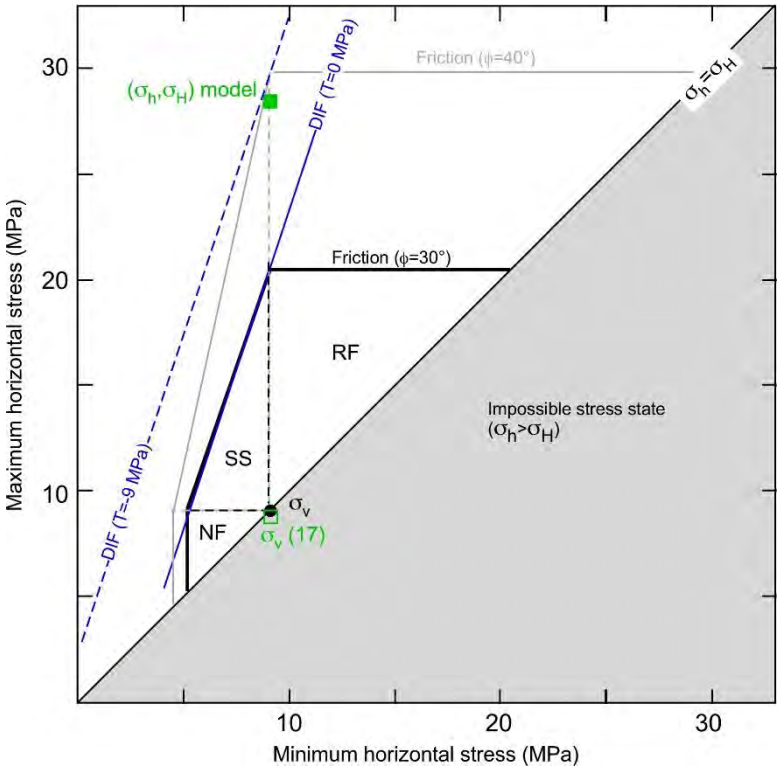

Figure 25. Stress polygon for borehole breakouts in the Leknes Bh at 337 mbl

7.2 Hydraulic stress measurements

The investigated borehole was not optimal for using HSM. Several intensely naturally-fractured sections were encountered, as well as sections of poor borehole quality due to drilling processes (e.g. spiral grooving and drill-bit sharpening grooves). In addition, the borehole had been drilled nearly vertical, which implies that televiewer orientation downhole is based on magnetometer sensors. The lack of input from accelerometer sensors implies somewhat reduced precision of the orientation of tested fractures.

Despite these limitations, the three-dimensional stress field could be determined with precision, although the resolution of the gradient of maximum horizontal stress is non-optimal. The successful fracturing tests at along the borehole clearly demonstrate that one principal stress is vertical (σ_v) and aligned with the borehole. Hence, the other two components are acting in the horizontal plane. Calculations of the weight of overburden from core density correspond well with the obtained trend of σ_v.

Figure 20 shows the magnitudes of normal stress (σ_n) that was measured. The analytical results suggest a linear trend of σ_h versus depth, whereas the trend for σ_H indicates large variability. However, the analytical methodology for determining σ_H is associated with large discrepancies and has in addition an uncertainty that is at least three times larger than that of σ_h. In total, of 15 tests yielded axial fractures and the average orientation of these fractures, and the average direction of σ_H is 150±12° MN. The declination for the Leknes Bh in September 2014 was 4.75°, implying that the average direction of σ_H to true North is 155±12° TN. This corresponds to the highest quality (A) for the stress indicator HF orientations within the World stress map quality ranking system (Table 4).

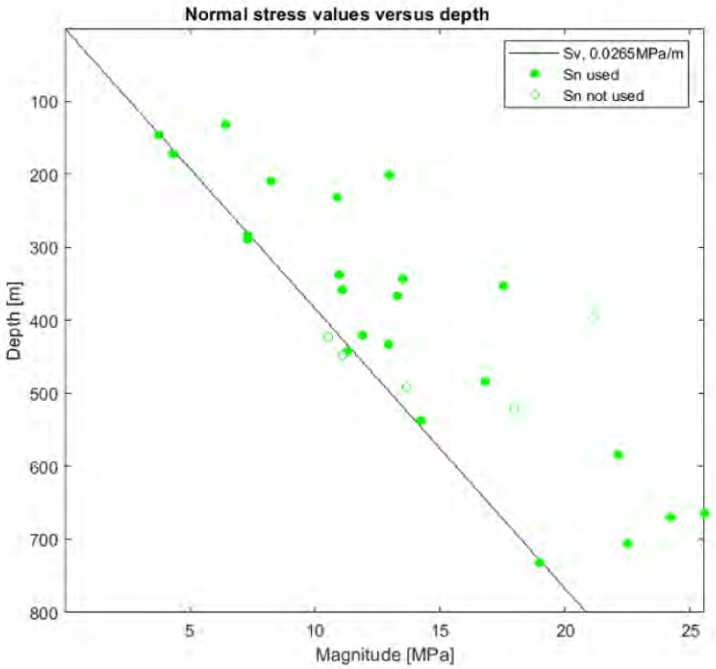

Figure 20. Results from testing, plotted as normal stresses of tests versus depth. The comparison with the theoretical a vertical stress gradient for a mean density of the overburden of 2.65 t/m3 reveals that the vertical stress likely is the lowest stress magnitude, signalling that the prevailing stress regime likely reflect reverse Andersonian faulting (i.e. where $\boldsymbol{\sigma_3 = \sigma_v}$). Note that filled circles denotes tests that are included in the solution of (17). The open are excluded from (17).

The data was included in an integrated stress determination model (e.g. *Ask et al. 2009*). A few tests could not be included in the solution, likely because of the problems encountered during data collection and effects of local stress anomalies. In addition, the variability of fracture orientations constraining all stress components was not optimal. As a result, the gradient of σ_H could not be resolved satisfactory. One may though conclude that the magnitude of σ_H is considerably larger than that of σ_h and σ_v. Hence, the

deviatoric stress is high along the entire length of the Leknes Bh. The numerical result yields the following (where z is vertical depths calculated from top of casing) at 400 m depth:

$$\sigma_h = 11.9 + 0.0237 \cdot (\mathrm{z} - 400) \text{ [MPa]}$$

$$\sigma_H = 29.7 + 0.0200 \cdot (\mathrm{z} - 400) \text{ [MPa]} \quad (17)$$

$$\sigma_v = 10.4 + 0.0261 \cdot (\mathrm{z} - 400) \text{ [MPa]}$$

$$\sigma_H\ (orientation) = 161.2 + 0.0051 \cdot (\mathrm{z} - 400) \text{ [° TN]}$$

Figure 21 shows the stress magnitudes and the orientation of σ_H (A-B) and the uncertainty of the model (C). It should be noted that σ_h and σ_v are rather similar in magnitude compared to σ_H. This is more clearly shown in Figure 22, where the maximum horizontal stress is plotted versus the vertical and minimum horizontal stress. The convergence of σ_h and σ_v with depth indicates that a strike slip stress regime acts at depth. Based on (17), this would occur just below 1 km depth (pending that the stress field is valid with depth).

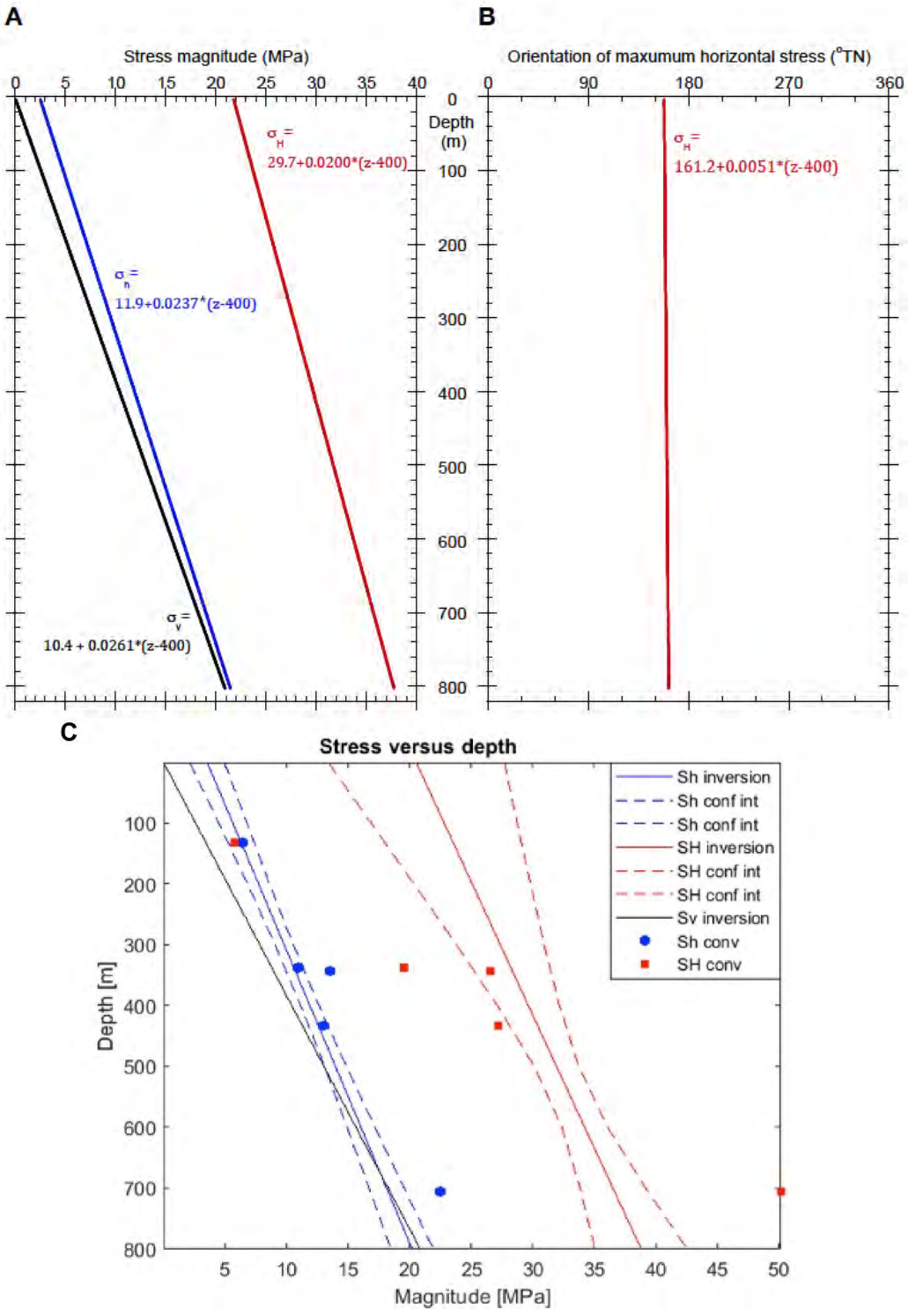

Figure 21. Results from hydraulic stress measurements testing in the Leknes Bh as shown in (17). A, Stress magnitudes versus depth; B, Orientation of maximum horizontal stress versus depth. C, Inversion result for σ_h, σ_H-, and σ_v-magnitudes are denoted with blue, red and black full lines, respectively. 90% confidence interval for σ_h - and σ_H-magnitudes are denoted with dashed blue and red lines, respectively. The analytical results for σ_h- and σ_H-magnitudes are denoted with blue circles respectively red squares.

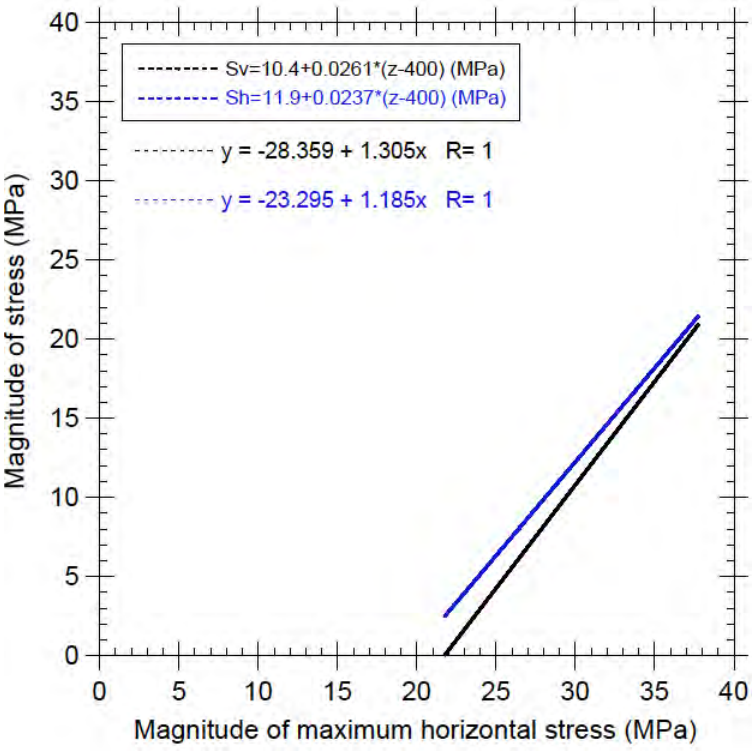

Figure 22. Maximum horizontal stress versus vertical and minimum horizontal stress.

8. Concluding remarks

The results of this study provide a good understanding on the state of stress in the Leknes Bh, and some information about the state of stress the Drag Bh.

The HSM comprised of SF, HF, and HTPF tests, which were conducted with a methodology and interpretation scheme in accordance with the recommendations of ISRM (*Haimson & Cornet 2003*). In total, 40 injection tests divided into 10 SF, 19 HF, and 11 HTPF tests were performed.

Several sections of intense natural fracturing were found in the Leknes Bh, together with sections with poor borehole quality as a result of drilling operations (e.g. spiral grooving and drill bit sharpening grooves). In addition, the borehole was drilled almost vertical (the borehole deviation is 0° according to *Olesen et al 2007*, and <5° according to logging results by *Elvebakk & Rønning 2011* and *Andersen 2018*), which implies that only magnetometers can be used to determine the televiewer orientation downhole. This results in less precise measurements of the orientation of the tested fractures.

Despite these limitations, the 3D stress field could be determined with precision, although the resolution of the gradient of maximum horizontal stress is sub-optimal (e.g. Figure 22). The successful HSM tests along the borehole clearly demonstrate that one principal stress is vertical and aligned with the borehole. Hence, the other two components are acting in the horizontal plane. As the result, we could compare $\sigma_{v\mathrm{v}}$ with the theoretical weight of the overburden rock mass using density measurements on cores; and we see that the measured- and theoretical σ_v are similar.

The analytical results suggest a linear trend of σ_h versus depths, whereas the trend for σ_H indicates large variability. However, the analytical methodology for determining σ_H is associated with large discrepancies and has, in addition, an uncertainty that is at least three times larger than that of σ_h. A few tests could not be included in the solution, likely as a result of the problems encountered during data collection and effects of local stress anomalies. In addition, the variability of fracture orientations constraining all stress components was sub-optimal. This meant that the gradient of σ_H could not be resolved satisfactory. One mayconclude that the magnitude of σ_H is considerably larger than that of σ_{h} and σ_{v}. Hence, the deviatoric stress is high along the entire length of the Leknes Bh. The result suggests that reverse faulting condition

prevails down to approximately 1 km depths, followed by strike-slip down to considerable depths provided that the stress field is continuous.

Equation (17) summarized the stress model, which has best fit at 400 m depth:

$$\sigma_h = 11.9 + 0.0237 \cdot (\mathrm{z} - 400) \text{ [MPa]}$$

$$\sigma_H = 29.7 + 0.0200 \cdot (\mathrm{z} - 400) \text{ [MPa]} \quad (17)$$

$$\sigma_v = 10.4 + 0.0261 \cdot (\mathrm{z} - 400) \text{ [MPa]}$$

$$\sigma_H\ (orientation) = 161.2 + 0.0051 \cdot (\mathrm{z} - 400)\ \text{[° TN]}$$

In total, 15 tests yielded axial fractures and the average orientation of these fractures, and the direction of σ_H with respect to true north is 155±12°TN. This allowed a WSM ranking quality A of the results. Figure 27 shows a subset of the WSM, with the new data included. It is the first quality A stress data in the region.

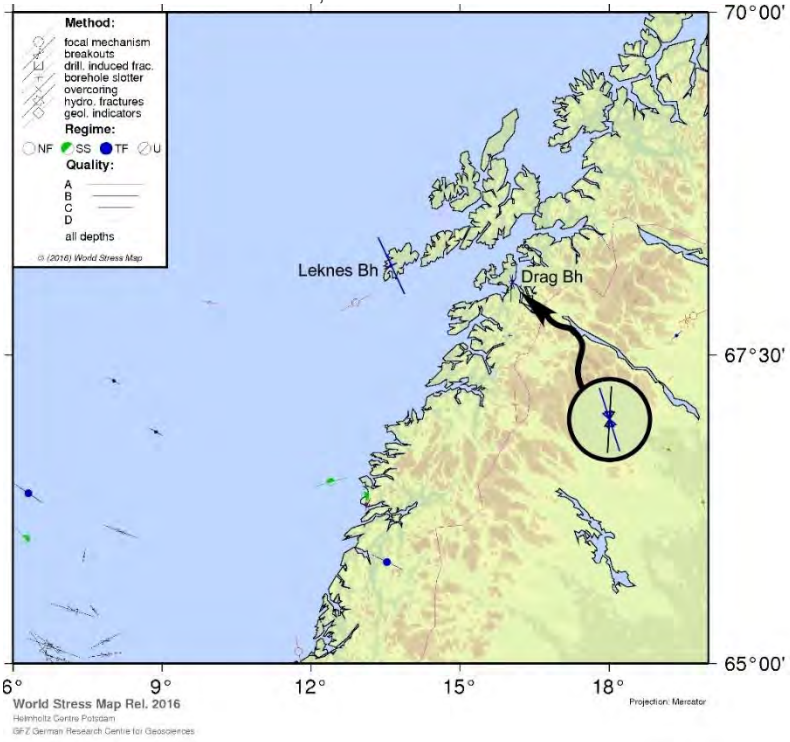

Figure 26. A Subset of the world stress map including the new data from this study (Heidbach et al. 2016). The black circle shows a blow-up of the D-quality data from Drag Bh. The blue line is based on Typea borehole breakouts. The black line is based on all data.

The knowledge is still limited on the state of in situ stress in the Drag Bh. A total of 11 stress indicators with a combined length of 15.4 m have been identified from 354-761 mbl in the Drag Bh (Tables 6-7). The stress indicators consisted of BB and DIFs, and were classified into Type a and b. The direction of σ_H with respect to true north is roughly N-S (3±15°TN) if all stress indicators are considered. If only Type a data are considered, five BB and DIF zones with a combined length of 5.6 m suggests a similar direction of σ_H (1±16°TN). Although standard deviation is low, and is consistent over a long depth interval, the short combined length only yield allowed a WSM ranking quality D for all results shown in Table 7. BBs and DIFs developed in less than 4% of the total length of the interval from 354-761 mbl. In Figure 26, the results from all data (σ_H=3±15°TN) are included in black (unknown stress state) and those for Type a BBs (σ_H 163±24°TN) are included in blue.

The stress regime has been estimated in the Drag Bh using methods (cf. (7-15)) and summarized in *Zoback et al. (2003*) and *Zoback (2007)*. Stress polygons were developed at two depths (Figures 24-25). The results suggest that tectonic regime for the BB at 354 m most likely is reverse faulting, but could also be strike slip faulting. It appears that the impermeable, low porosity rock in the Drag Bh and Leknes Bh are suitable for constraining stress polygons. The HSM data in the Leknes Bh at 337 m depth fits the model well, but also shows that the tensile strength is not negligible, as suggested by *Zoback et al.* (*2003*) and

Zoback (2007). Comparison of Figures 24 and 25 further shows that the differential stresses are significantly higher in Leknes Bh than in Drag Bh at the test depths (337-354 m).

9. References

Andersen, G., 2014: *Leknes and Drag, Norway: Geophysical borehole logging.* Rambøll data report. December 2014. Leknes and Drag logging_1100013662_1147310L_ GA20141218Av0.docx

Andersen, G., 2018: *Leknes and Drag, Norway: Geophysical borehole logging* (Review 1). Rambøll data report. June 2018. Leknes and Drag logging_1100013662_1147310L_GA20180603Av1.doc

Anderson, D.M., 1951: *The dynamics of faulting and dyke formation with applications to Britain*. Oliver and Boyd: Edinburgh, U.K., 206 pp.

Ask D., O. Stephansson, F.H. Cornet, M.V.S. Ask, 2009: Rock stress, rock stress measurements, and the Integrated Rock Stress Determination Method (ISDM). *Rock Mech. Rock Engr.*, 42: 559–584

Ask, D., M. Ask, P. Fredriksson, P., K.-J. Mattson, 2018: *Initial report of hydraulic stress measurements in the Leknes Bh, Lofoten, Norway*. Technical report, NGU*, to be submitted*

Ask, M.V.S., D. Ask, H. Elvebakk, O. Olesen, 2015: Stress Analysis in Boreholes Drag Bh and Leknes Bh, Nordland, North Norway. *Rock Mech. Rock Engr.*, 48: 1475–1484. doi 10.1007/s00603-014-0683-9.

ASTM, 2010: Standard test method for compressive strength and elastic moduli of intact rock core specimens under varying states of stress and temperatures. *American Society for Testing and Materials International*, ASTM Designation D 7012-10.

Barton, C.A., M.D. Zoback, K.L. Burns, 1988: In-situ stress orientation and magnitude at the Fenton geothermal site, New Mexico, determined from wellbore breakouts. *Geophys. Res. Lett.*, 15: 467-470.

Bell, J.S., D.I. Gough, 1979: Northwest-southeast compressive stress in Alberta: Evidence from oil wells. *Earth Planet. Sci. Lett.*, 45: 475-482.

Bredehoeft, J.D., R.D. Wolff, W.S. Keys, E. Schuter, 1976: Hydraulic fracturing to determine the regional stress field, Piceance Basin, Colorado. *Bull. Geol. Soc. Am.*, 87: 250-258.

Brudy, M., M.D. Zoback, 1993: Compressive and tensile failure of boreholes arbitrary inclined to principal stress axis: application to the KTB boreholes, Germany. *Int. J. Rock. Mech. Min. Sci.*, 30: 1035-1038.

Brudy, M., M.D. Zoback, 1999: Drilling-induced tensile wall-fractures: implications for determination of in-situ stress orientation and magnitude. *Int. J. Rock. Mech. Min. Sci.*, 36: 191-215.

Brudy, M., M.D. Zoback, et al., 1997: Estimation of the complete stress tensor to 8 km depth in the KTB scientific drill holes: Implications for crustal strength. *J. Geophys. Res.,*102: 18453-18475.

Chang, C., L.C. McNeill, J.C. Moore, W. Lin, M. Conin, Y. Yamada, 2010: In situ stress state in the Nankai accretionary wedge estimated from borehole wall failures, *Geochem. Geophys. Geosyst*., 11: Q0AD04, doi:10.1029/2010GC003261.

Cornet, F.H., B. Valette, 1984: In situ determination from hydraulic injection test data. *J. Geophys. Res.*, 89: 11527-11537.

Cornet, F.H., 1993: The HTPF and the integrated stress determination methods. *Comprehensive Rock Engineering*, (J. Hudson, Ed.). Pergamon Press, Oxford, U.K., 3: 413-432.

Deltombe, J.L., R. Schepers, 2000: Combined Processing of BHTV Traveltime and Amplitude Images. *In*: *Proc. Int. Symp. Borehole Geophysics for Minerals, Geotechnical, and Groundwater applications, Golden, CO, U.S.*. Accessed 14 May 2014 at http://www.alt.lu/pdf/Deltombe_Schepers_MGLS2000.pdf.

Elvebakk H., J. Rønning, 2011: Geofysisk logging av borehull ved Drag, Tysfjord og Leknes, Lofoten. NGU, Trondheim. Accessed June 20 2018 at www.ngu.no/upload/Publikasjoner/Rapporter/2011/2011_014.pdf.

Fossen, H., 2016: *Structural geology*, 2nd Ed., Cambridge University Press, Cambridge, U.K.: 524 pp.

Haimson, B.C., F.H. Cornet, 2003: ISRM Suggested Methods for rock stress estimation – Part 3: hydraulic fracturing (HF) and/or hydraulic testing of pre-existing fractures (HTPF). *Int. J. Rock Mech. Min. Sci.*, 40: 1011-1020.

Heidbach, O., M. Rajabi, K. Reiter, M. Ziegler, WSM Team, 2016: *World Stress Map Database Release 2016*. GFZ Data Services. doi.org/10.5880/WSM.2016.001

Hickman, S.H., J.F. Svitek, M.G. Langseth, 1984: Borehole televiewer log of Hole 395A. *Init. Repts. DSDP*, 78B: 709-715, doi:10.2973/dsdp.proc.78b.107.1984.

Hillis, R.R., S.D. Reynolds, 2000: The Australian Stress Map. *J. Geol. Soc., London*, 157: 915-921.

Hubbert, K.M., D.G. Willis, 1957: Mechanics of hydraulic fracturing. *Petroleum Transactions*, AIME T.P. 4597 201: 153-166.

Hudson, J.A., F.H. Cornet, R. Christiansson, 2003: ISRM Suggested Methods for rock stress estimation—Part 1: Strategy for rock stress estimation. *Int. J. Rock Mech. Min. Sci.,* 40: 991–998.

Ito T., K. Evans, K. Kawai, K. Hayashi, 1999: Hydraulic fracturing reopening pressure and the estimation of maximum horizontal stress. *Int. J. Rock Mech. Min. Sci. & Geomech. Abstr.*, 36: 811-826.

Jaeger, J.C., N.G.W. Cook, 1969: *Fundamentals of rock mechanics*. Methuen: London, U.K., 513 pp.

Janutyte, I., C. Lindholm, O. Olesen, 2017: Relation between seismicity and tectonic structures offshore and onshore Nordland, northern Norway. *Norwegian J. Geol.*, 97: 211–225, doi: 10.17850/njg97-3-02.

Kirsch, G., 1898: Die Theorie der Elastizität und die Bedürfnisse der Festigkeitslehre. Zeit Ver. Dt. Ingenieure, 42, p. 797-807.

Lund, B., M.D. Zoback, 1999: Orientation and magnitude of in situ stress to 6.5 km depth in the Baltic Shield, Int. J. Rock Mech. Min. Sci., 36, 169-190.

Mardia, K.V. 1972: *Statistics of directional data: probability and mathematical statistics*. Academic Press: London, U.K., 357 pp.

Mastin, L., 1988: Effect of borehole deviation on breakout orientations. *J. Geohys. Res.*, 93: 9187-9195.

Maystrenko, Y.P., O. Olesen, L. Gernigon, S. Gradmann, 2017: Deep structure of the Lofoten-Vesterålen segment of the Mid-Norwegian continental margin and adjacent areas derived from 3-D density modeling. *J. Geophys. Res., Solid Earth*, 122: 1402–1433.

Moos, D., M.D. Zoback, 1990: Utilization of observations of well bore failure to constrain the orientation and magnitude of crustal stresses: Application of continental, Deep Sea Project and Ocean Drilling Program boreholes. *J. Geohys. Res.*, 95: 9305-9325.

Olesen. O., N. Balling, et al. 2007: *KONTIKI Final Report, CONTInental Crust and Heat Generation In 3D.* The Geological Survey of Norway: Trondheim, Norway. NGU Report 2007.042, 438 pp.

Peska, P., M.D. Zoback, 1995: Compressive and tensile failure of inclined well bores and determination of in situ stress and rock strength. *J. Geohys. Res.*, 100: 12791-12811.

Plumb, R.A., 1989: Fracture patterns associated with incipient borehole breakouts. *In*: Rock at great depth (Eds. M. Maury, D. Fourmaintaux), A.A Balkema: Rotterdam, the Netherlands, 2: 761-768.

Ratigan, J.L., 1992: The use of the fracture reopening pressure in hydraulic fracturing stress measurements. *Rock Mech. Rock Eng.,* 25: 125-136.

Rutqvist, J., C.-F. Tsang, O. Stephansson, 2000: Uncertainty in the principal stress estimated from hydraulic fracturing measurements due to the presence of the induced fracture. *Int. J. Rock Mech. & Geomech. Abstr.,* 37: 107-20.

Saffer, D.M., P.B. Flemings, et al. 2013: In situ stress and pore pressure in the Kumano Forearc Basin, offshore SW Honshu from downhole measurements during riser drilling. *Geochem. Geophys. Geosyst*., 14 (5), doi:10.1002/ggge.20051.

Skår, Ø. 2002: U-Pb geochronology and geochemistry of early Proterozoic rocks of the tectonic basement windows in central Nordland, Caledonides of north-central Norway. *Precambrian Research*, 116: 265-283.

Stephansson, O., 1983: Sleeve fracturing for rock stress measurements in boreholes. *In*: *In situ testing*, *Proc. Int. Symp*. *Essais en Place, Paris*, 2: 571-578.

Tarantola, A., B. Valette, 1982: Generalized non-linear inverse problem solved using the least square criterion. *Rev. Geophys. Space Phys.*, 20: 219-232.

Thiercelin, M., J. Desroches, 1993: Improving the pertformance of open hole stress tools. *Int. J. Rock Mech. & Geomech. Abstr.*, 30: 1249-1252.

Thiercelin, M., J. Desroches, A. Kurkjian, 1994: Open hole stress tests in shale. Improving the performance of open hole stress tools. In. *Proc.. Int. Symp. on Rock Mech. in Petr. Eng, Eurock '94, Delft*, A.A. Balkema: Rotterdam, the Netherlands: 921-987.

Tingay M., J. Reinecker, B. Müller, 2016: Borehole breakout and drilling-induced fracture analysis from image logs. In: O. Heidbach (Ed.), *World Stress Map Scientific Technical Report 16-01: WSM quality ranking scheme, database description and analysis guidelines for stress indicator*: 33-41. Accessed 12 June 2018 at: http://www.world-stress-map.org/fileadmin/wsm/pdfs/WSM_STR_16_01.pdf.

Vernick, L., M.D. Zoback, 1992: Estimation of maximum horizontal principal stress magnitude from stress-induced well bore breakouts in the Cajon Pass Scientific Research Borehole. *J. Geophys. Res*, 97(B4): 5109-5119.

Wilson, M.R., 1980. Granite types in Sweden. *GFF.* 102: 167-176.

WSM, 2008: *WSM quality ranking scheme 2008*. Accessed 12 June 2018 at: http://www.world-stress-map.org/fileadmin/wsm/pdfs/WSM_quality_ranking_scheme_2008.pdf on 20 June 2018.

Zajac, B.J., J.J. Stock, 1997: Using borehole breakouts to constrain the complete stress tensor: Results from the Siljan Deep Drilling Project and offshore Santa Maria Basin, California. *J. Geophys. Res.*, 102: 10083-10100.

Zemanek, J., E.E. Glenn, et al. 1970: Formation, evaluation by inspection with the borehole televiewer. Computers and Geosciences, 20 (7/8): 7171-7182.

Zheng Z., N.G.W. Cook, L. Myer, 1988: Borehole breakout stress measurements. *Proc. U.S. Symp. Rock Mech.,* A.A Balkema: Rotterdam, the Netherlands, *29:* 471-478.

Zoback, M.D., 2007: *Reservoir Geomechanics*, Cambridge University Press: New York, U.S., 449 pp.

M.D. Zoback, D. Moos, L. Mastin, R.N. Andersson, 1985: Borehole breakouts and in-situ stress*. J. Geophys. Res.*, 90: 5523-5530.

Zoback, M.D., C.A. Barton, M. Brudy, D.A. Castillo, T. Finkbeiner, B.R. Grollimund, D.B Moos, P. Peska, C.D. Ward, D.J. Wiprut, 2003: Determination of stress orientation and magnitude in deep wells. *Int. J. Rock Mech. Min. Sci.* 40: 1049–1076.

Zoback, M.D., L. Mastin, C.A. Barton, 1987: In situ stress measurements in deep boreholes using hydraulic fracturing, wellbore breakouts, and Stonely wave polarization. *In Proc. Int. Symp Rock Stress and Rock Stress Measurements*, Centek: Luleå, Sweden: 289-299.

Åhäll, K.-I. & Larson, S.Å., 2000: Growth-related 1.85-1.55 Ga magmatism in the Baltic Shield; a review addressing the tectonic characteristics of Svecofennian, TIB 1-related and Gothian events. *GFF*, 122: 193-206.

CHAPTER 9: THE REGIONAL 3D STRESS FIELD OF NORDLAND, NORTHERN NORWAY - INSIGHTS FROM NUMERICAL MODELLING

Authors: S. Gradmann[1], O. Olesen[1], M. Keiding1 and Y. Maystrenko[1]

Affiliation: [1]Geological Survey of Norway

Abstract

The Nordland area in NW Norway is one of the seismically most active areas in Fennoscandia. It exhibits patterns of coastal extension, which are in contradiction to the first-order regional stress pattern that reflects compression from ridge-push. The regional stress field is considered to stem from the interaction of ridge push and GIA (glacial isostatic adjustment); the local stress field mainly results from gravitational stresses, as well as the flexural effects of erosion and sediment deposition.

We develop finite element numerical models of crustal scale to study the 3D stress field, using existing geometric constraints from previous geophysical studies. Internal body forces, induced by variations in density, topography or Moho depth, already yield significant deviatoric stresses, which have often been omitted in previous stress models. We show that these can strongly influence the near-surface stress regime. Similarly, existing weakness zones (such as faults) control the local stress pattern. In addition, redistribution of sediment and rock mass, which occurred mainly under Pleistocene glaciation in the Nordland area, can modify the stress field significantly on a semi-regional scale. We consider this process the main driver for the coastal extension, in particular in areas where erosion has been high.

1. Introduction

3D stress modelling can reveal factors that control the regional as well as semi-regional stress field. This has only been done for a few scenarios worldwide: glacial unloading in Fennoscandia (*Lund et al.*, 2009), foreland basins in Germany, Switzerland or Canada (*Buchmann and Connolly*, 2007; *Heidbach et al.*, 2014; *Reiter and Heidbach*, 2014; *Hergert et al.*, 2015) or the major bounding fault in the Marmara Sea (*Hergert and Heidbach*, 2011). Here we investigate the stress effects along a continental margin including both onshore and offshore areas, in particular the narrow, formerly glaciated margin of northern Norway.

The stress field of Norway has been investigated in a number of regional studies, yet large gaps exist, in particular around the study area in NW Norway (*Heidbach et al.*, 2008, Figure 1). *Fejerskov et al.* (2000) compiled existing rock stress measurements and showed that the main horizontal stress field along the North Sea and Atlantic margins is oriented NW-SE (with WNW-ESE and NNE-SSW trends in along the northern North Sea segment). This pattern is consistent with the direction of the Mid-Atlantic Ridge push, which is considered to control the primary orientation of the horizontal stress field (e.g., *Fejerskov and Lindholm*, 2000). In-situ stress measurements from two deep boreholes have recently been added to the data base (*Ask et al.*, 2018). Along the Barents Sea coast offshore northern Norway, the stress orientation is mainly N-S and thus parallel to the continental margin (*Fejerskov et al.*, 2000). Seismological studies (*Byrkjeland et al.*, 2000; *Fjeldskaar et al.*, 2000) confirm the overall stress pattern but also describe a number of local deviations from it. In particular, fault plane solutions from earthquakes along the Nordland coast indicate NW-SE extension while NW-SE compression is mapped further offshore.

The stress field from the Alpine compression is seen in a N-S oriented major horizontal stress axis all across southern and central Europe. This trend is not detected in Norway or Sweden, north of the TESZ (Trans-European Suture Zone), which de facto decouples northern Europe from the Alpine stress field.addition to the anomalous stress field, the Nordland margin exhibits considerable high seismicity for a passive continental margin. In this study we investigate the present-day stress regime through numerical modelling and try to determine which factors contribute to the neotectonic activity observed today.

1.1 The Study Area

The Lofoten-Vesterålen Margin is located at the passive NW rifted margin of the European plate (Figure 1 a). It is generally far away from any plate boundary where tectonically induced seismicity is primarily located. Rifting occurred c. 54 Ma ago (*Talwani and Eldholm*, 1977). The Lofoten-Vesterålen Margin is a narrow and steep margin with mountains up to 1000 m reaching the coast and a steep gradient in Moho depth (*Breivik et al.*, 2017; *Mansour et al.*, 2018). This is in stark contrast to the neighbouring margin

segment to the south, where the several hundred kilometers wide Vøring margin adjoins the more gentle topography of Mid Norway.

The geology of the Nordland region is controlled by Caledonian nappes overlying Pre-Cambrian basement. The latter is exposed in several tectonic windows on the mainland and on the Lofoten-Versterålen archipelago. The latter formed as a basement high between the Ribban and Vestfjorden basins during extensive rifting throughout the Mesozoic. The steep margin of the Nordland coast was exposed to many glaciations and Neogene erosion of up to two kilometers (e.g. *Riis*, 1996; *Dowdeswell et al.*, 2010; *Norwegian Petroleum Directorate*, 2010). During the Pleistocene in particular, rapid outboard growth of the shelf occurred, depositing up to 2000 m of glacial sediments, termed the Naust Formation (*Dallan et al.*, 1988; *Rise et al.*, 2005; *Montelli et al.*, 2017).

1.2 Neotectonics and Seismicity

Neotectonic activity along the Lofoten-Vesterålen margin has long been noticed and documented (*Olesen et al.*, 2013b, and references therein). Enhanced seismic activity along the coast and outboard the Lofoten Archipelago has been registered over the past century ((Figure 2b). The signal from the post-glacial uplift, which is largest over central Fennoscandia, diminishes toward the coast to approximately zero. However, the gradient in the uplift rate is highest here along the coast (*Keiding et al.*, 2015).

GPS data from a local network around Ranafjord (red rectangle in Figure 2b show an irregular pattern of local uplift and possible local extension and subsidence (*Kierulf*, 2017). In addition, a number of post-glacially active faults have been mapped in the Norwegian hinterland and northern Sweden. These were mainly reactivated by the removal of the ice load around the end of glaciation but current microseismicity is still high in the vicinity of the faults. Thus, surface deformation is ongoing in the Nordland area and coincides with a large uplift rate gradient; yet the local deformation pattern is different than the regional GIA pattern.

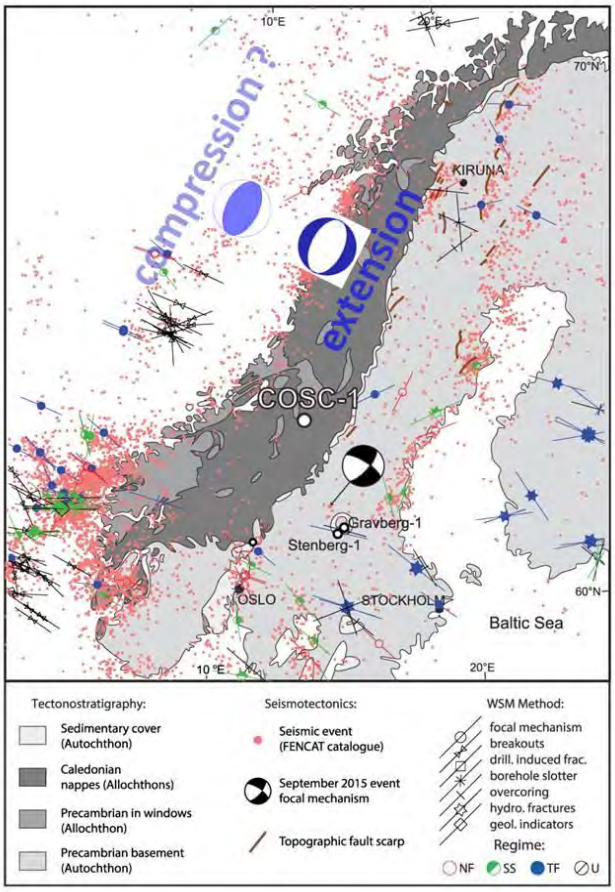

Figure 1: Orientation of maximum horizontal stress (world stress map database, Heidbach et al., 2008) and seismicity in western Scandinavia. Focal plane solutions mark the coastal extension and presumed offshore compression for the study area. Figure modified from Wenning et al. (2017).

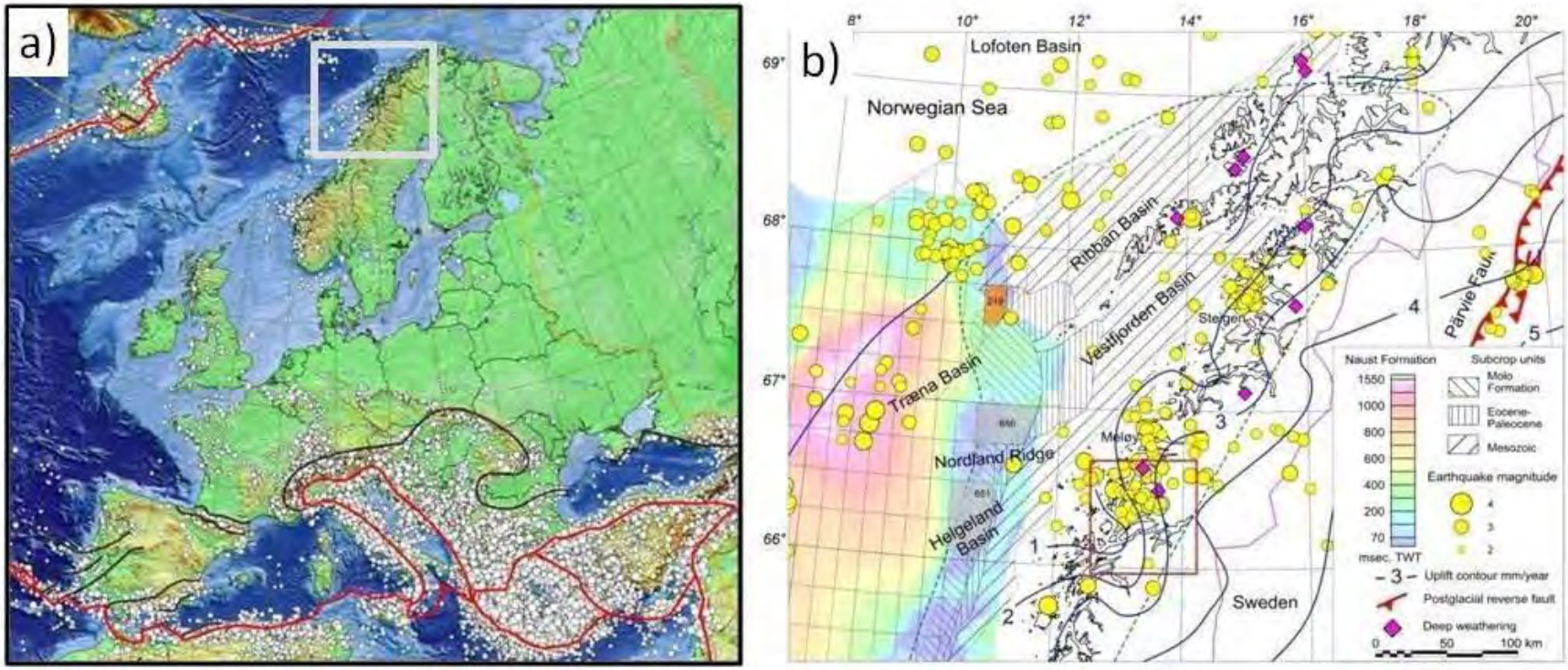

Figure 2: a) Overview of the European plate boundaries and the location of the study area. b) Neotectonics in the study area. From Olesen et al. (2013a).

The seismicity of the Lofoten-Vesterålen Margin (*Byrkjeland et al.*, 2000; *Janutyte et al.*, 2017) reveals a number of hitherto unexplained characteristics that have motivated the current study: The seismic events are distributed unevenly along the margin. High seismicity runs along a band along the coast and in an area offshore located outboard the Vestfjorden Basin (Figure 2 b). The Vestfjorden Basin itself is almost aseismic. To the south, where the Bivrost Lineament marks the transition to the wider Vøring margin, the number of earthquakes rapidly decreases. In addition to the special event distribution, analysis of fault plane solutions reveal that the coastal earthquakes are predominantly extensional (*Fjeldskaar et al.*, 2000; *Byrkjeland et al.*, 2000; *Michalek et al.*, 2018; *Janutyte et al.*, 2017). The large offshore earthquakes have been assigned a compressional character in previous studies (*Hicks and Lindholm*, 2000; *Fjeldskaar et al.*, 2000; *Byrkjeland et al.*, 2000). New data from smaller earthquakes do not confirm this compressive stress regime. *Janutyte et al.* (2017) observe a mixture of fault, strike-slip and thrust events, while *Michalek et al.* (2018) consider the recently collected offshore data too noisy to constrain fault plane solutions.

2. The Modelling Approach

Any stress field can be considered as the sum of different components, which in turn are often classified as long-wavelength (regional) and short-wavelength (local) components. An exhaustive list may not exist, but the commonly discussed components are the following (Figure 3):

Gravitational stresses result from the material properties of the subsurface itself. Density contrasts (e.g. topography, Moho) are considered the main contributor.

Tectonic stresses can dominate the stress field in tectonically active regions. For the Norwegian continental margin, only the ridge push force can be invoked.

The deformation of the lithosphere due to unloading of the Pleistocene ice sheet creates stresses here referred to as GIA-induced stresses.

The major unknown stress component in our study area is the influence of erosion and associated isostatic land uplift as well as fast and local sediment deposition during the Pleistocene and associated subsidence. The isostatic response is accompanied by lithospheric flexure, and thus by bending stresses. It is not known to which degree the stresses evoked during the Pleistocene sediment deposition are still present today. Over long timescales, stresses are usually considered transient, yet many unexplained stress configurations exist that may have their origin in the earlier formation of structure and stresses. Stress dissipation will thus not only play a role for unloading/loading, but also for the correct estimate of the background stresses (as discussed later). Additionally, faults or weakness zones may alter the stress field locally.

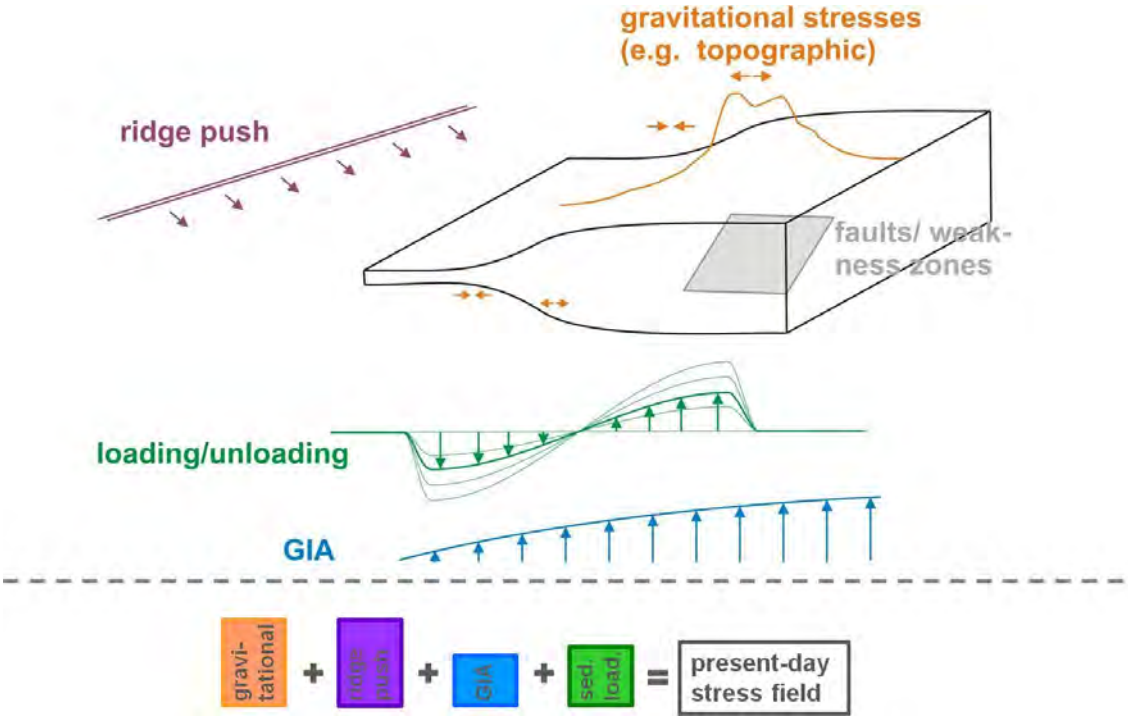

Figure 3: Schematic presentation of the stress field components contributing to the present-day stress regime on the Nordland margin.

We use COMSOL Multiphysics to forward model 3D regional stresses in a continental margin-type setting similar to the Nordland area. The model comprises the layers of sediments, crystalline crust and lithospheric mantle over an area of 470x560 km and down to 60 km depth (Figure 4). For certain tests, a larger model area of 830x970 km was chosen. The interface geometries are taken from available data sets published in recent years. The topography is taken from the ETOPO1 data set (*Amante and Eakins*, 2009). The top basement (base sediment) horizon is a combination from the compilation of *Olesen et al.* (2010) and the global sediment thickness map (*Divins*, 2003). The Moho depth is taken from the compilation of *Grad et al.* (2009). The layer materials are given linear elastic properties (Table 1). A linear elastic rheology is commonly used in stress and strain calculations to best determine the effects of stress changes and stress distribution. As discussed further below, linear elastic rheology has its limitation when looking at in-situ background stress (which developed over millions to billions of years) rather than the response to present-day stress changes or large tectonic stress. For short-term processes such as active tectonics, the lithospheric mantle is considered rigid. Over long time-scales, however (e.g. for stress dissipation), a ductile mantle may be more appropriate.

In addition to the material properties, gravity is defined as acting in the negative z-direction and boundary conditions are chosen as free slip (roller boundary conditions). The model bottom at 60 km represents an arbitrary level in the lithospheric mantle, well below the Moho but above the lithosphere-asthenosphere boundary, except for the distal oceanic regions where the LAB approximately coincides with our model depth. We chose free slip bottom constraints to allow lateral displacement of the lithospheric mantle. Such boundary conditions have been used in many other studies numerically investigating the 3D stress field (e.g., *Buchmann and Connolly*, 2007; *Hergert and Heidbach*, 2011).

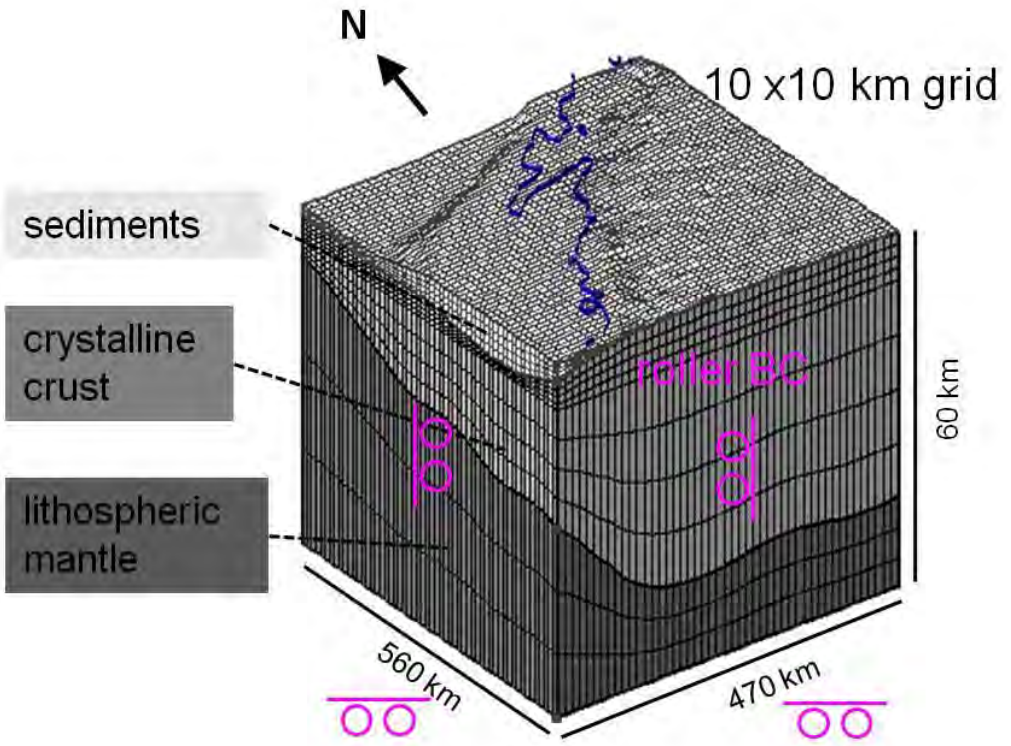

Figure 4: Design of initial model.

Table 1: Properties of the model materials.

Material	Density	Young's modulus	Poisson's Ratio
sediments	2700 kg/m^3	60 GPa	0.3
cryst. crust	2800 kg/m^3	70 GPa	0.3
mantle	3300 kg/m^3	90 GPa	0.3

With these preparations, the initial model is sufficiently constrained and solutions for the stress field can be found. Such a solution is, however, in several respects different than what observations suggest (Figure 5). In the absence of regional tectonic stresses, the Earth's in-situ stresses are near-lithostatic at depth greater than a couple of kilometres. This is reflected in the ratio k of maximum horizontal stress σ_H to vertical stress σ_V, which becomes close to one as measured in multiple deep boreholes worldwide (Figure 5**Error! Reference source not found.**, center). k-values larger than one (as mainly near the surface), indicate compression. Despite the large data scatter, a general trend from k-values larger than 1 near the surface to k-values around 1 at larger depth is dominant. An empiric formula for this trend has been developed by *Sheorey* (1994), which depends only on the Young's modulus E and depth z: $k=0.25+E * 10^{-9*} 1/z$.

In contrast, in a linear elastic system, where horizontal and vertical stresses and strain are related through the Poisson's ratio v, the stress ratio k is much smaller than one and constant with depth $k_{linear\text{-}elastic}= v/(1- v)$, and $k=0.33$ for $v=0.25$, a Poisson's ratio common in rocks. The reason for the different stress distribution in Earth and in a simple linear elastic uniaxially loaded system is considered to be the curvature of the Earth,

which leads to increased horizontal stresses with depth with respect to the simple uniaxial system, as well as the cooling history (*Sheorey*, 1994; *Buchmann and Connolly*, 2007; *Hergert and Heidbach*, 2011).

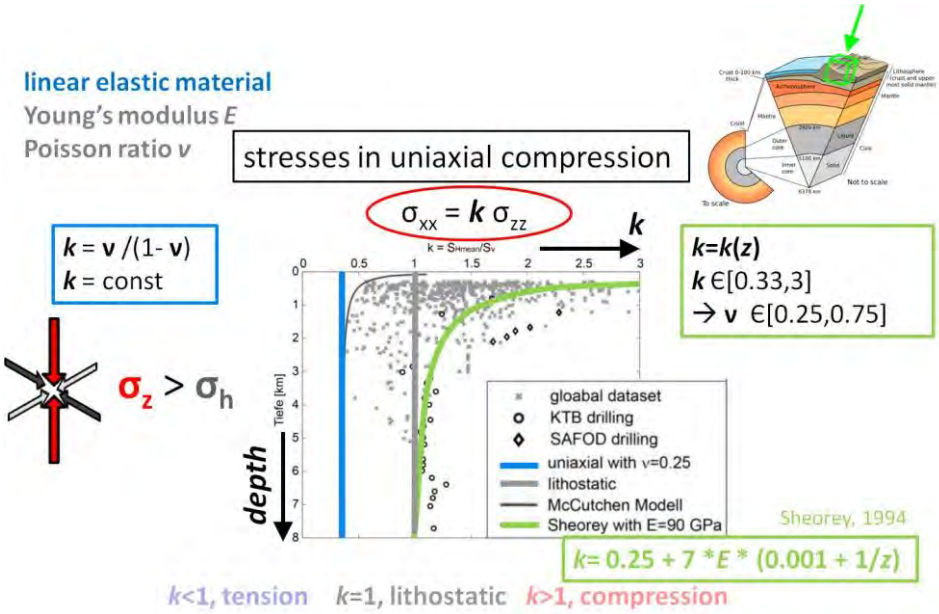

Figure 5: Graphic displaying the difference in the stress regime between a linear elastic model and global observations form deep borehole measurements (taken from Hergert and Heidbach, 2011).

A solution to the problem of obtaining adequate background stresses in a linear elastic model can be achieved by including tilted sides of the model. Such a strategy has been used in previous 3D stress modelling studies (*Lund et al.*, 2009; *Hergert and Heidbach*, 2011; *Gritto et al.*, 2014) and is also followed in the present study. We thus embed the model of our study area into a larger box with tilted sides (Figure 6) to obtain the desired background stresses (respective *k*-values), consistent with observations. The resulting stress tensor is extracted and subsequently applied as initial conditions onto the smaller model so that this remains manageable in size and geometry for subsequent modelling steps.

Calibration of the Sheorey box model requires knowledge of the deep stress field and/or good control over the (linear elastic) material properties. Neither is given for the study area. The closest deep boreholes are the Gravberg and Stenberg sites in south-central Sweden (Figure 1; *Lund and Zoback*, 1999) where a compressional to strike-slip system prevails (*k*=1.1) and in the Kola superdeep borehole on the Kola peninsula. Here, *k*-values of approximately 0.78 have been reported for several kilometer depth (*Savchenko*, 2004). We thus design models that yield *k*-values at great depth between 0.7 and 0.9.

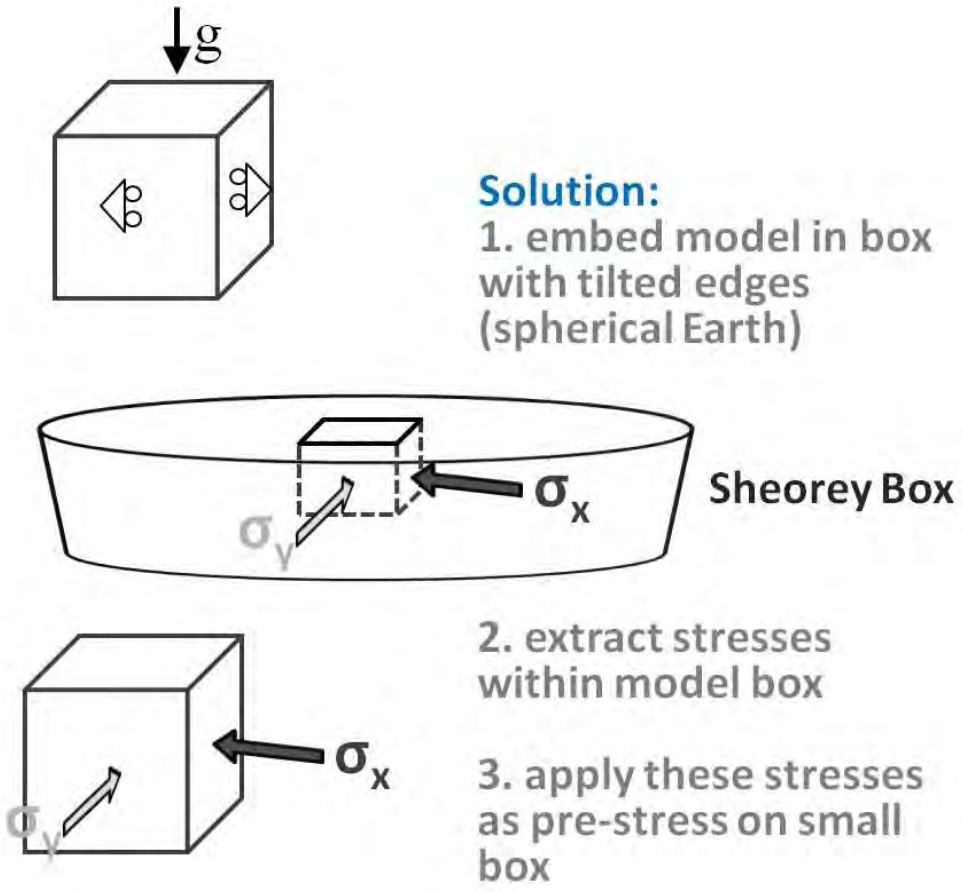

Figure 6: Modelling approach for obtaining Sheorey-type stresses in the model domain of the Study area.

Figure 7 shows a comparison of the *k*-values along selected vertical profiles for the case of a purely linear-elastic model under uniaxial compression with either vertical sides (Figure 7 b) or embedded in a larger box with tilted sides (Figure 7 **Error! Reference source not found.**c). It is clearly seen that only the latter shows the desired decrease of *k*-values with depth and a near-constant value at greater depths which is not far from one (lithostatic state).

3. Model Results

3.1 The Background Model

We are interested in the overall stress regime as well as the areas of potential failure. The *k*-value is a useful value for evaluating the stress regime, yet it is based on a 2D or plain-strain configuration and, i.e., strike-slip regimes cannot be represented by it. The so-called regime stress ratio (*RSR*) takes the three-dimensionality into account (*Simpson*, 1997): $RSR = (n_{fault} + 0.5) + (-1)^{n_{fault}*}(R - 0.5)$. $R=(\sigma_2 - \sigma_3) / (\sigma_1 - \sigma_3)$ and n_{fault} is 0 for normal faulting, 1 for strike-slip faulting and 2 for thrust faulting regimes.

Both *k*− and *RSR*−representations (Figure 8) indicate that the model is in a tensile regime near the shelf edge and a compressional (thrust faulting) regime onshore. This is opposite to the observed stress pattern and needs further investigations, as is discussed below. At larger depths, the stresses are near-lithostatic with *k*-values just below one. The very-near-surface values in the deep offshore basin show compression, but these values cannot be considered reliable, because they result from extrapolation of stresses calculated within each element onto the model surface. Thus, the very top element(s) of the model should be omitted from interpretation.

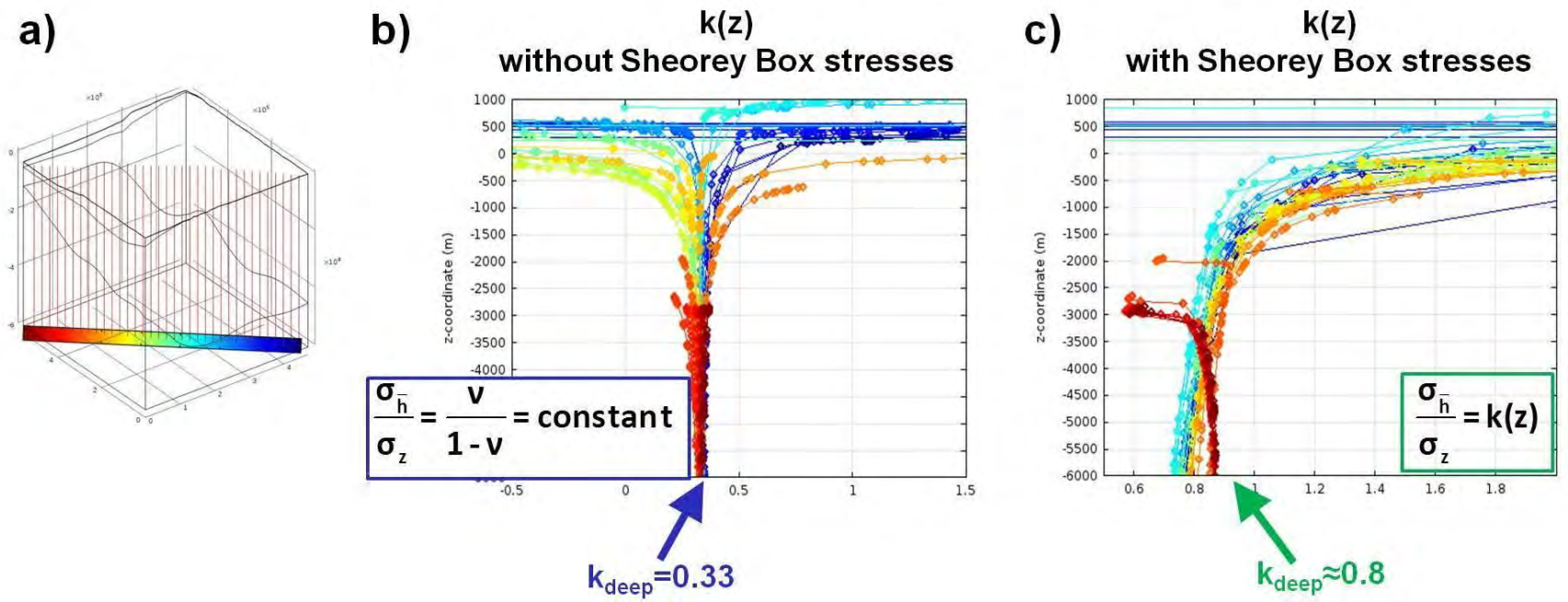

Figure 7: Comparison of k-values (simplified stress regime) of a model with linear elastic rheology and Sheorey-type treatment. a) Location of vertical lines, along which data is shown. Colour bar indicates the position-related colour coding used in Figures b and c. b) k-values of a linear-elastic model with vertical sides. c) k-values of a linear-elastic model embedded in large box with tilted sides.

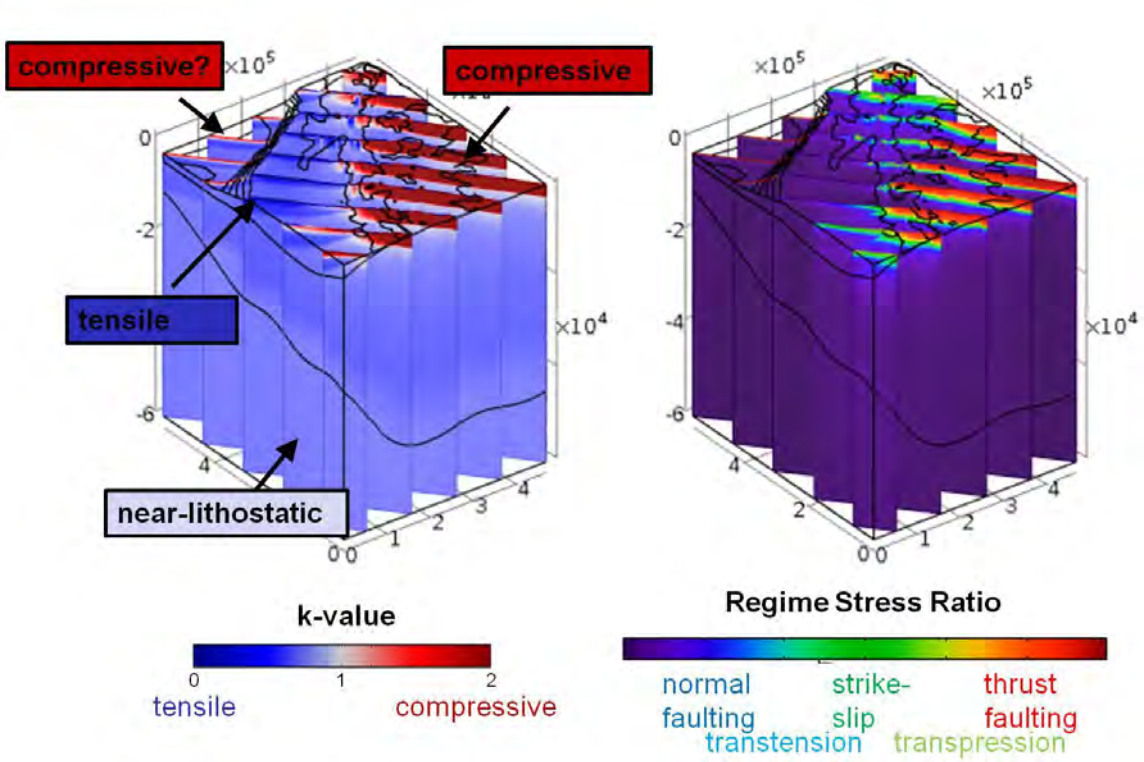

Figure 8: Analysing the background stress model.

The overall change in the crustal stress field (offshore tension, onshore compression) observed in the models stems from the geometry and property changes along the Moho. This is clearly seen in synthetic models that comprise only the Moho as a non-horizontal interface (Figure 9 a). While the model material is not moving per se, it still experiences elastic deformation (red arrows in Figure 9 b), which takes the direction of gravity-driven down-slope sliding. Here, all three layers are strongly coupled and elastic deformation affects the entire model domain. The effect of topography is similar but opposite and partially cancels the effect of the Moho (Figure 9 c-f). The magnitude of the effect depends on the geometry, density contrast but also other rheological parameters, mainly the Poisson's ratio

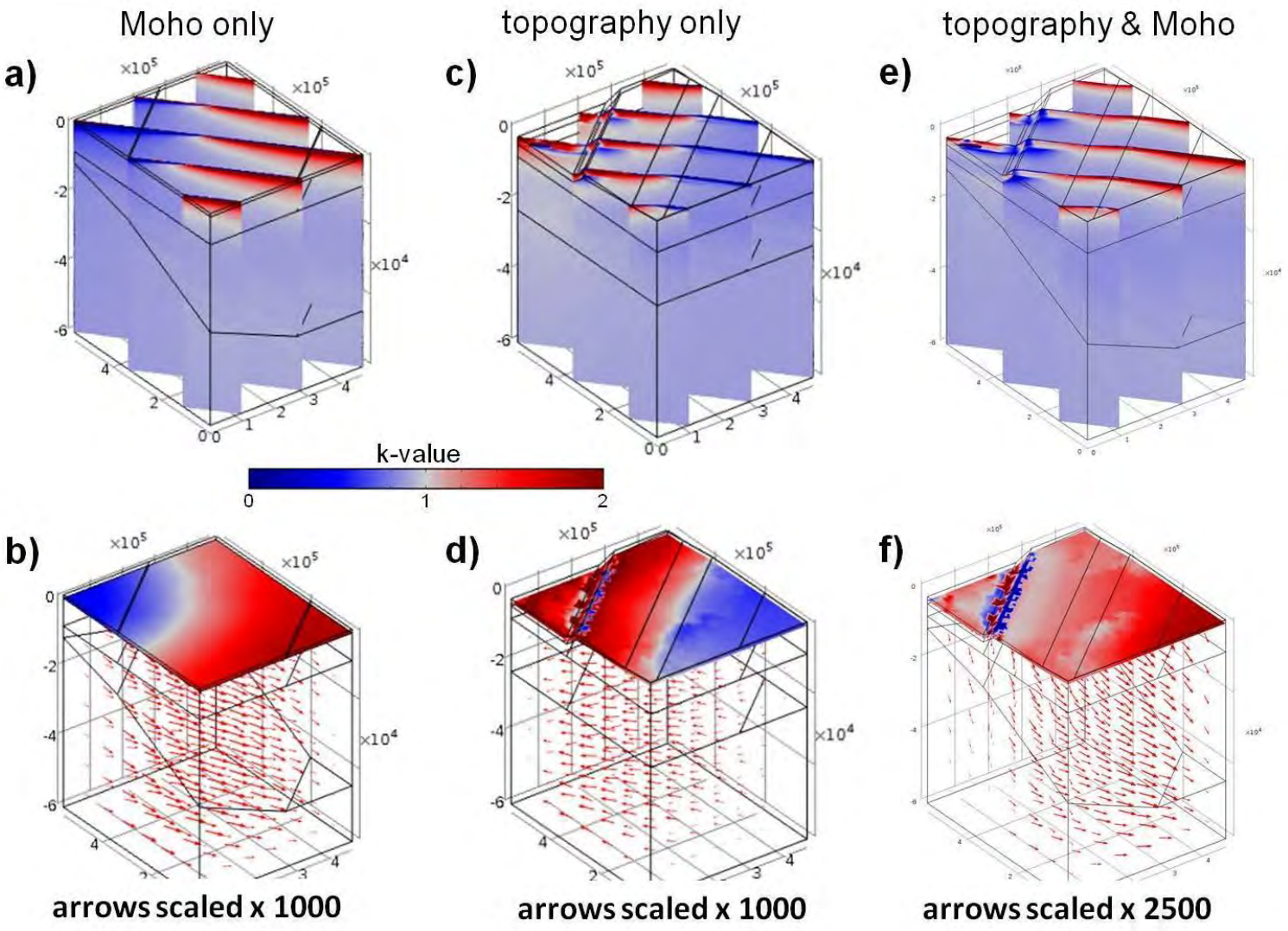

Figure 9: Synthetic models testing the influence of the topography and the Moho boundary. a,b) Model with horizontal surface and Moho as non-horizontal interface. c,d) Model with topography and horizontal Moho. e,f) Model with topography and non-horizontal Moho.

We do not think that the effect visualized in the models here is actually present in the Nordland area (or any other continental margin). The simple linear-elasticity under gravity does not give credit to all the processes that operated during the formation and alteration (thinning) of the crust. Furthermore, large stress inequalities may have dissipated over time. Yet, we have little control over how the actual background stress field looks like. While we cannot resolve this issue in the current study, we focus on the changes to the background stress field, not the absolute stresses. These are what determine the anomalous stress pattern in Nordland and are controlled by the different stress field components listed in section 3. We investigate these separately in the following sections and subsequently discuss their combination and interplay.

3.2 Ridge Push

The ridge push force (RPF) stems from the difference in density distribution between the elevated oceanic crust at the mid-Atlantic ridge and the cooler, lower-lying crust of the margin (*Watts*, 2001). The ridge-push force is thus strictly speaking not a tectonic force (which should stem from dynamic movement of the plates). For the purpose of studying its effect on the Nordland margin, however, it is suitable to consider it as an external force.

The RPF has been well studied and analytical calculations exist. It is commonly calculated as a depth-independent force (equivalent to the gravitational potential energy GPE) whereas a depth-dependence may play a large role (e.g., *Naliboff et al.*, 2012). The magnitude of the RPF offshore Norway has been estimated to be up to 30 MPa (*Fejerskov and Lindholm*, 2000).

Figure 10 shows a model with a simplified RPF (constant at 10 MPa) acting at 45 degrees to the model boundaries from a NW-direction. In comparison to the background model (Figure 8), the overall stress field is more compressional (less tensile) throughout the entire model area. This is simply the result of the increased horizontal stress exerted by the RPF. The vertical stress is only slightly increased, which is the effect of linear elastic deformation controlled by the model material's Poisson's ratio. The effect of increased horizontal stresses is also seen in Figure 11 where the *RSR*, failure potential (*FP*) and principle stress directions are shown. The failure potential is in 2D defined as the ratio of differential stress to average stress: $FP = 2*(\sigma_1 - \sigma_2)/(\sigma_1 + \sigma_2)$. The equivalent in 3D is the ratio of von-Mises stress to confining pressure. The increase in horizontal stress executed by the ridge push leads the rotation of the maximum horizontal stress σ_H into a NW-SE direction. This stress pattern is consistent with the observed pattern depicted in the World Stress Map (Figure 1) and confirms earlier conclusions that the RPF is primarily controlling the present-day stress regime in Nordland (*Fejerskov and Lindholm*, 2000).

The largest variations in *RSR* and failure potential occur in the uppermost five kilometers of the model although the boundary load that represents the RPF is constant with depth. In the upper kilometers, topographic influence is high and horizontal stresses are similar to or larger than the vertical stress. If the RPF is calculated as a depth-dependent entity, the already small changes introduced by RPF at depth larger than 10 km (Figure 8 and 10) would be even smaller. The effects in the uppermost kilometers would remain similar, but depend on the net value of the RPF.

It can be argued that the RPF is mainly supported by the crust and that the mantle behaves viscously over long timescales and cannot support stresses. This can be modelled by applying the RPF only to the crust and giving the mantle the properties of a weak material (e.g. E=5 GPa). In equivalent models (not shown here), the effect of the RPF decreases inland where the crust is thicker and where the increase in horizontal stress is distributed over a larger volume of crust than in the offshore and coastal parts.

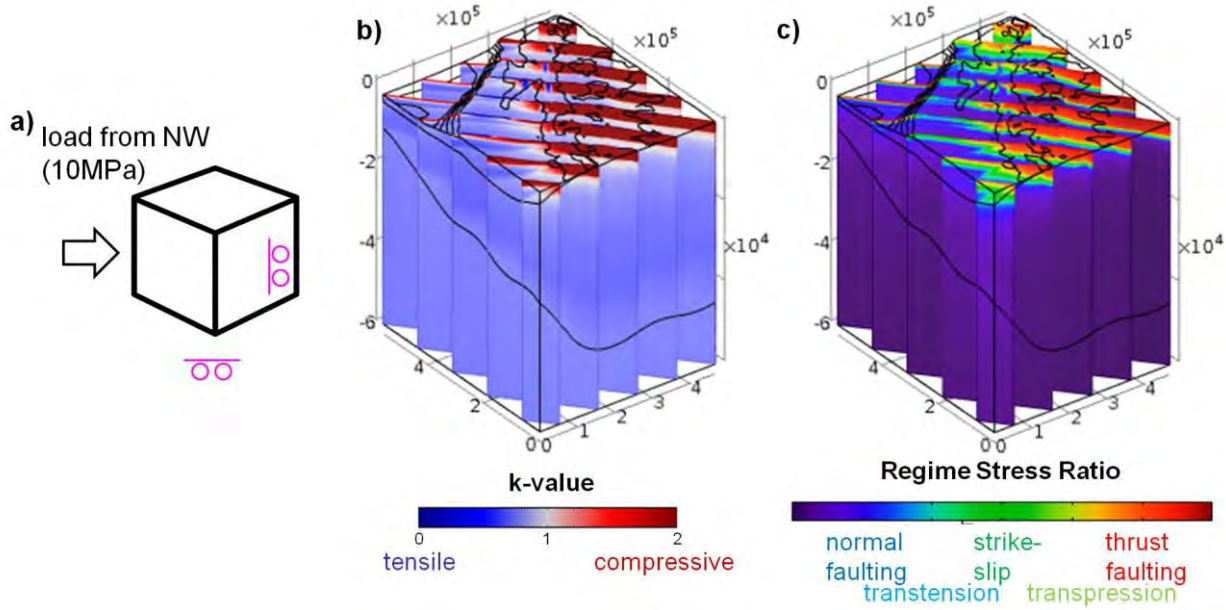

Figure 10: Analysing the effects of ridge push. a) Conceptual model design with ridge push force acting at NW side. b) k-values of model domain. c) Regime-stress-ratio of model domain.

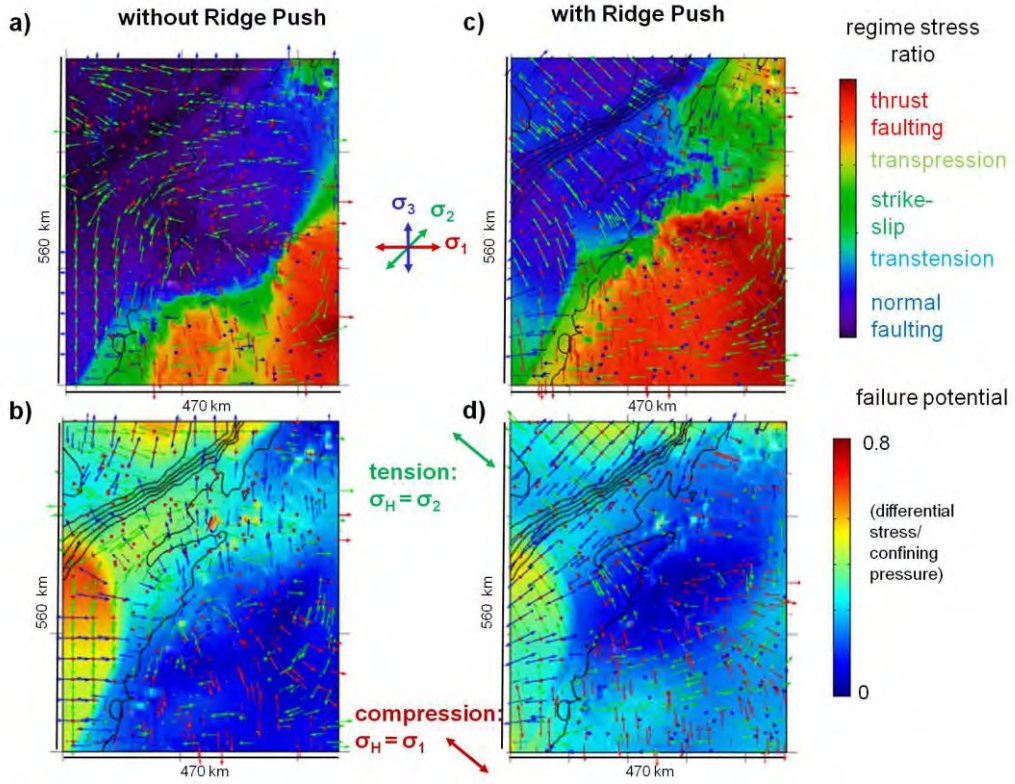

Figure 11: Analysing the effects of ridge push at 2000 m burial depth. a,b) RSR and failure potential of model without ridge-push force. c,d) RSR and failure potential of model with ridge-push force. Coloured arrows show the principal stress directions.

3.3 Glacial Isostatic Adjustment (GIA)

The unloading effect caused by the melting of the Scandinavian ice sheet is a still ongoing process. GPS velocities and various forms of sea level gauges show a maximum uplift and radial extension around the northern Gulf of Bothnia and a reduced signal in Norway, which diminishes to nearly neutral values near the coast (Figure 12 a). Modelling the lithospheric stress and strain related to GIA over time has been the subject of many previous and ongoing studies (*Lund et al.*, 2009; *Steffen et al.*, 2006; *van der Wal et al.*, 2013; *Steffen et al.*, 2014).

Here, the load changes of an existing ice-sheet model are applied to a mechanical model of the lithosphere-asthenosphere system. The resulting uplift history, which strongly varies with different mantle viscosities, is compared to observations from sea level gauges and a best-fit model is determined. We here use the best-fit model of *Steffen et al.* (2006) for which the resulting stress tensors were extracted at different depth levels on a 100x100 km grid. These stresses (Figure 12 b-d) show values of 1-5 MPa at 5 km depth and diminish quickly at larger depths. These values are then applied as additional initial stress conditions to our background model.

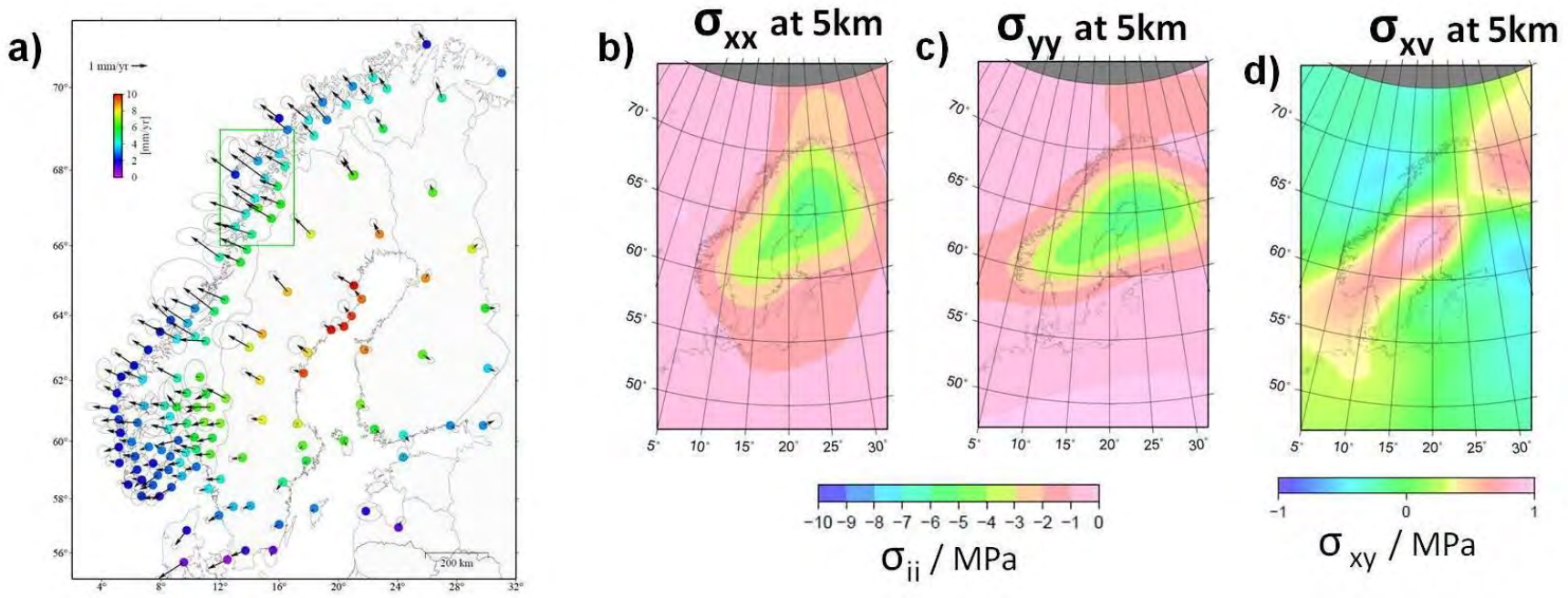

Figure 12: a) Observed GPS velocities (vertical and horizontal) in Scandinavia. From Kierulf et al. (2014). b-d) Horizontal stresses at 5km depth extracted from the GIA model of Steffen et al. (2006).

In order to better detect the large-scale stresses, we extend the model area to 960x820 km using the same interface data sets as before. The corresponding models without and with GIA-stresses are shown in Figure 13. The present-day GIA-effects do not change the stress field significantly. Only very small changes are locally observed (marked with arrows in Figure 13). Larger stresses likely existed right after the last glacial maximum and have not been fully dissipated. The effects shown in Figure 13 thus present a minimum scenario. While the present-day effects do not constrain the local stress field, it cannot be ruled out that they may assist in triggering earthquakes on pre-stressed faults.

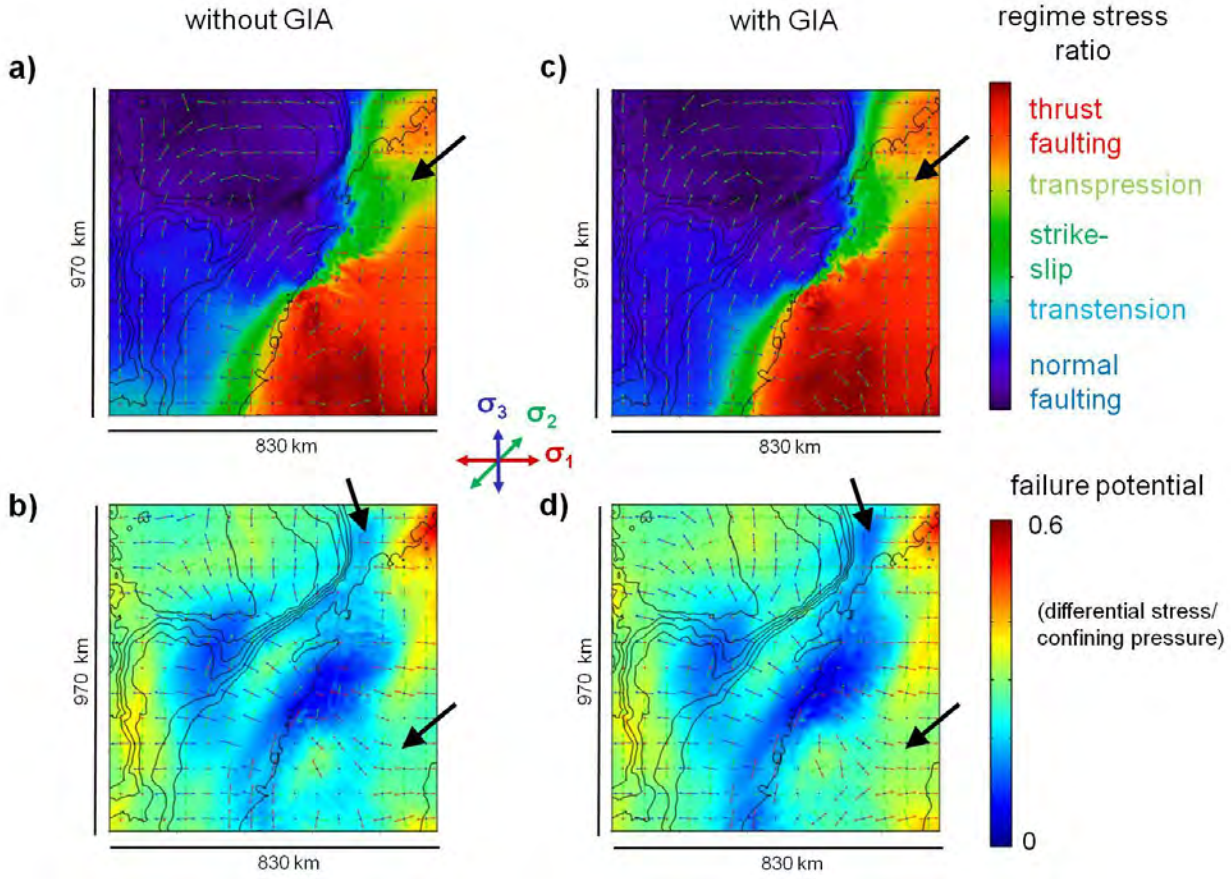

Figure 13: a,b) RSR and failure potential of model without GIA-stresses at 2000 m burial depth. c,d) RSR and failure potential of model results with GIA stresses at 2000 m burial depth.

3.4 Sediment Redistribution

The main part of the Pleistocene Naust Formation (Figure 14 a) was deposited over a relatively short time of 1.5 Ma. The load of the up to 1.5 km thick sediment package must have led to isostatic adjustment of the lithosphere, flexure, and thus to bending stresses. The local depression created by the sediment loading would result in upper crustal compression and lower lithospheric extension (Figure 14 b). In the domain of Pleistocene erosion (Vestfjorden Basin and onshore areas) the respective erosion (up to 520 m; *Dowdeswell et al.*, 2010) and corresponding uplift and flexure would have resulted in near-surface extension and deep lithospheric compression. We first tested the respective effects of loading and flexure in a set of synthetic models.

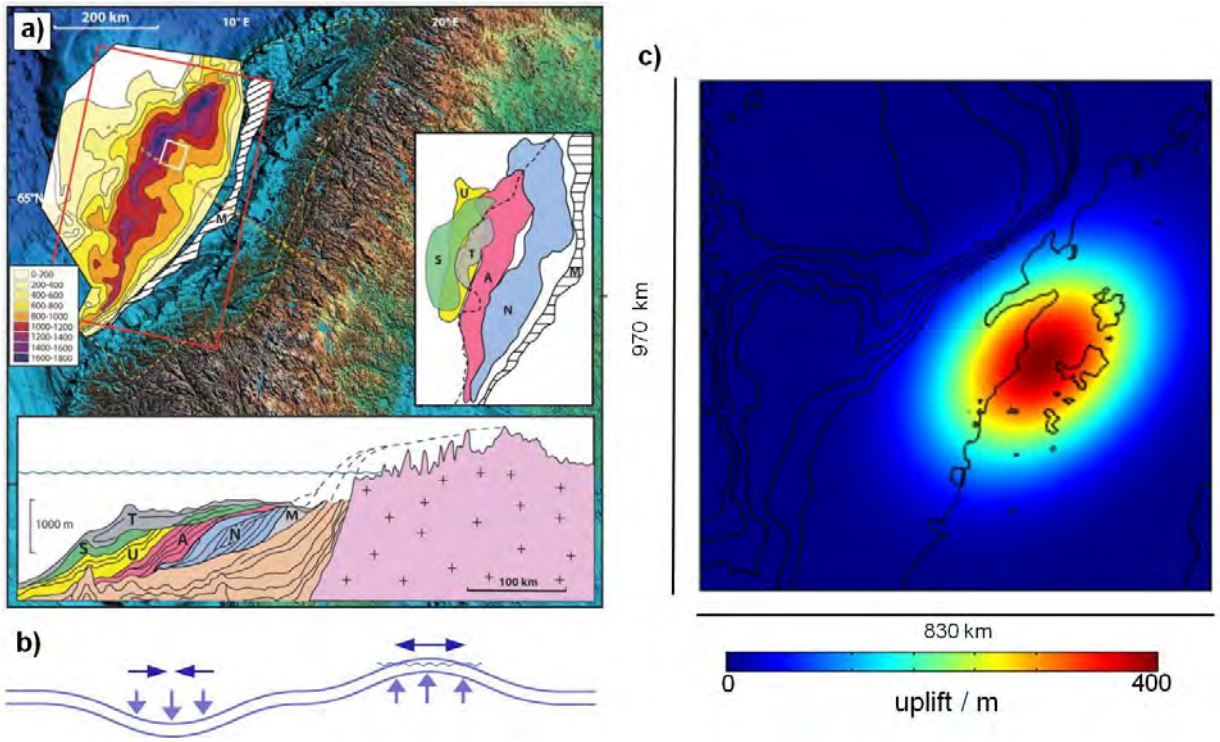

Figure 14: a) Thickness and location of the NAUST formation and estimated area of associated Pleistocene erosion (From Dowdeswell et al., 2010). b) Schematic for sediment-deposition-related subsidence and compression offshore and erosion-related uplift and extension onshore. c) Simplified test-function for regional uplift.

In the linear-elastic formulation used in the models presented here, bending as a result of a surface load can only occur if the underlying layer is weak. In the real world, the sub-lithospheric mantle behaves viscously and can therefore accommodate lithospheric bending. In the current models, a weak mantle can be modelled by assigning a very low Young's modulus (e.g. E=5 GPa), yet the resulting deformation and stress field are different to that of a viscous substratum. Using a fully elasto-viscous formulation would add more unknown parameters to the underlying equations (viscosity, Maxwell relaxation time) and complicate the modelling. Adjusting the free-slip bottom boundary condition to allow for vertical movement of the model material is not an option either. Gravity would cause all material to escape through the bottom of the model domain. As a work-around, we estimate the expected deformation separately based on local isostasy and apply this deformation as a boundary condition to the crust. The elastic stresses induced by this deformation are the bending stresses associated with the original loading.

Because the offshore compression is dominated by the ridge push signal (and the new seismological studies detect no separate, distinct compressional offshore regime), it will be nearly impossible to try to isolate a flexure-dependant signal from the overall RP-derived compression. We thus focus on the coastal extension and the effects of up to 500 m of Pleistocene erosion. 14 c shows a simple uplift function for the study area, which was designed to roughly mimic the estimated distribution of Pleistocene erosion (Figure 14 a). Neither the actual amount nor the timing of erosion is well constrained and the isostatic response generally yields a smoothed and broader signal, controlled by the lithosphere's rigidity. The removal of 500 m of crustal rocks will under local isostasy lead to an uplift of approximately 400 m. This calculation is based on average crustal and mantle values of ρ_c=2680 kg/m^3 and ρ_m=3350 kg/m^3, respectively. Higher crustal densities (i.e. lower density contrast to the mantle) would give even higher uplift values.

Without considering flexure, the unloading itself would show a compressional effect, opposite to the expected flexural tension. This can be explained by the paramount decrease in vertical stress σ_z, whereas the horizontal stresses decrease to a lesser degree, as controlled by the Poisson's ratio. The bending stresses associated with a 400 m high uplift, however, show a much larger effect (Figure 15) and are dominating the local stress field. A normally compressional stress regime is turned into an extensional one and the forebulge of the flexure brings the material at the NE and SW model edges closer to failure (failure potential FP>0.75). Such enormous effects of surface (un-)loading on the stress field have been calculated

and discussed previously. *Stein et al.* (1989) calculated the bending stresses induced by the glacial sedimentary load on a passive continental margin in 2D. Onshore erosion was not considered. The calculated effects on the stress field were much larger than what could be supported by stress measurements in offshore boreholes. *Stein et al.* (1989) then suggested that stress dissipation and visco-elastic effects can over time reduce the bending stresses.

Along the Lofoten-Vesterålen Margin, the main sediment deposition and erosion ceased several hundred thousand years ago and the ongoing or subsequent isostatic adjustment likely only lasted a couple of ten thousand years. There are a number of arguments for and against the idea of preservation of ancient stresses in the present-day stress field (*McGarr*, 1988). It is beyond the scope of this paper to give a conclusive answer on this issue. Yet we have to assume that stress dissipation is certainly an important factor, but that certain effects nevertheless continue until present day. Evidence for this is seen in the high seismicity in the Nordland area and the GNSS observations that additionally record aseismic deformation. We thus calculate the potential effects of erosion as a fraction of the initially defined uplift function. Figure 15 b,d shows the respective effects for ten percent of the full bending. Here, almost no difference can be seen to the background model.

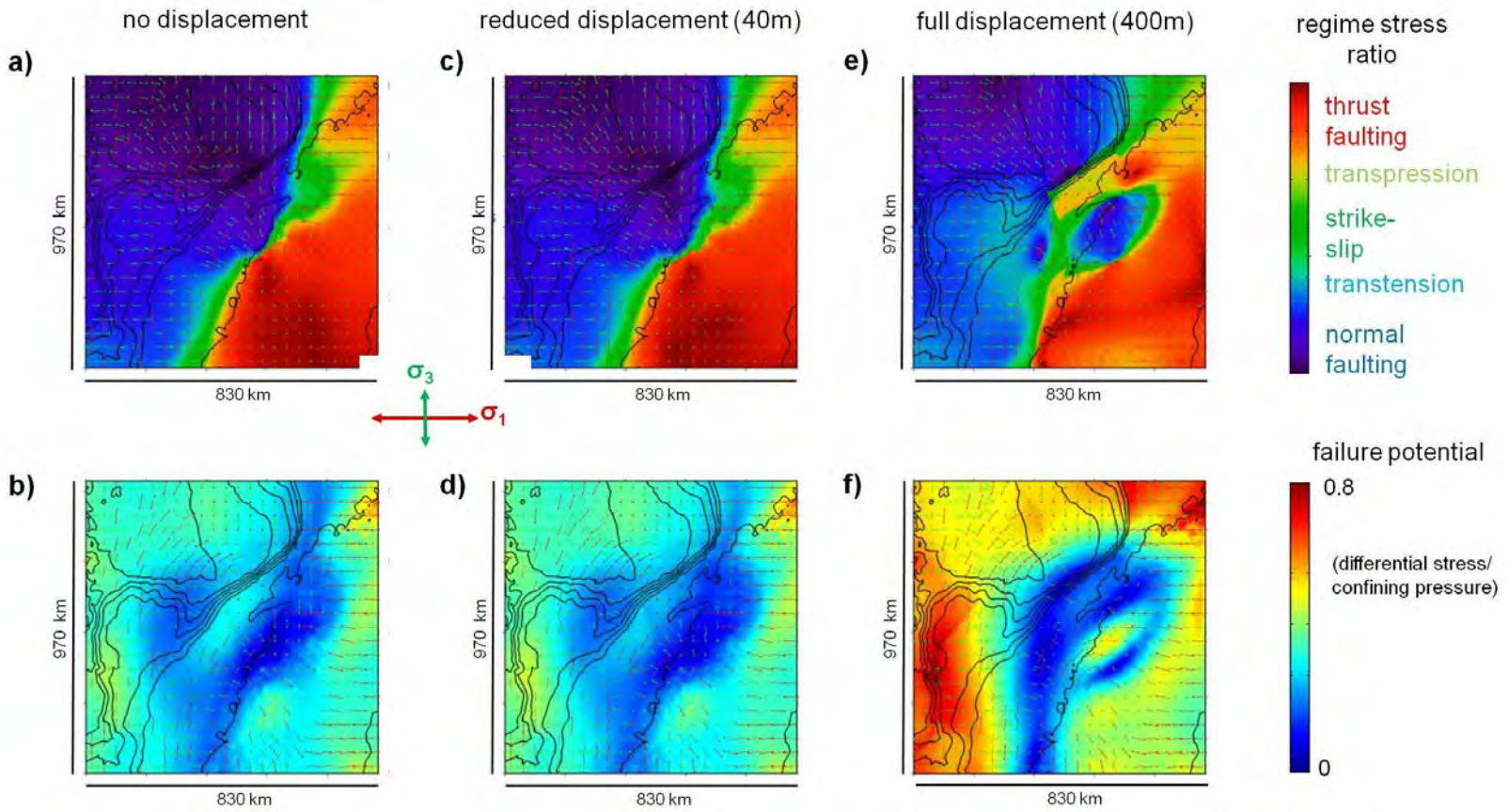

Figure15: Model results of numerical experiments investigating the effects of erosional uplift at 2000 m burial depth. a,b) RSR and failure potential of model without uplift. c,d) RSR and failure potential of model with maximum uplift of 40 m. e, f) RSR and failure potential of model with maximum uplift of 400 m. See Figure 14c for uplift function.

3.5 Faults and Weakness Zones

The Lofoten-Vesterålen Margin is dissected by a large number of faults (Figure 16 but their distribution changes relatively abruptly across the Bivrost Lineament to less densely spaced faults. This lineament separates the Lofoten-Vesterålen Margin from the wider Vøring margin to the south.

In a set of synthetic models, the effect of pre-existing weakness zones (e.g. active or dormant faults) on the local stress pattern was tested. Figure 17 shows an excerpt of the tests performed on these models.

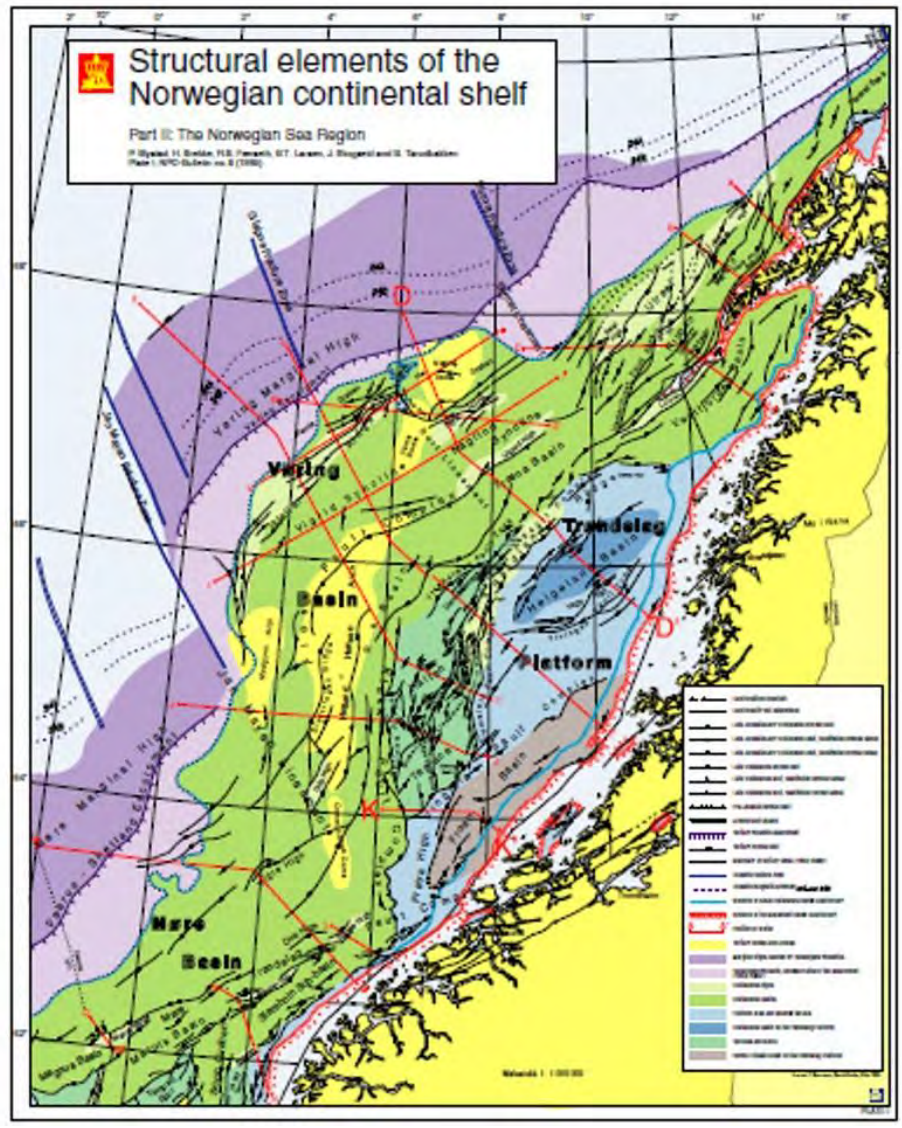

Figure 16: Structural Elements of the Norwegian Margin. The Lofoten-Vesterålen Margin is characterized by high fault density and is separated to the south from the Vøring margin by the Bivrost Lineament (Blystad et al., 1995).

A pre-existing weakness zone is modelled as a thin elastic plate and is characterized by the geometry of a plane and a spring constant *sc*, which here varies from $sc=10^5$-10^8 N/m^2. The spring constant defines the strength of a fault represented by a spring foundation at the fault interface. Furthermore, the length, angle and lateral position of the fault are varied. The results show that seaward dipping faults indeed create a local tensional stress field in an overall compressive setting (Figure 17 c). It is thus justified to assume that at least some faults or set of faults along the Nordland margin have a low strength. These faults then in turn

modify the stress field towards a more tensional state, facilitating normal faulting and strike-slip faulting in an otherwise compressional regime (as dominated by ridge push).first-order patterns of seismicity in Nordland do not correlate well with mapped faults, only one concurrence of seismicity with a mapped fault (Grønna fault) has been detected (*Janutyte et al.*, 2017). Relative relocation of the earthquakes (*Michalek et al.*, 2018), however, reveal some alignment of events, both in horizontal and vertical extent. There must thus be some seismically active faults in the subsurface. A large part of the seismicity occurs as clusters and swarms. These may go in hand with regional deformation together with an arising tensional stress field from flexural uplift.

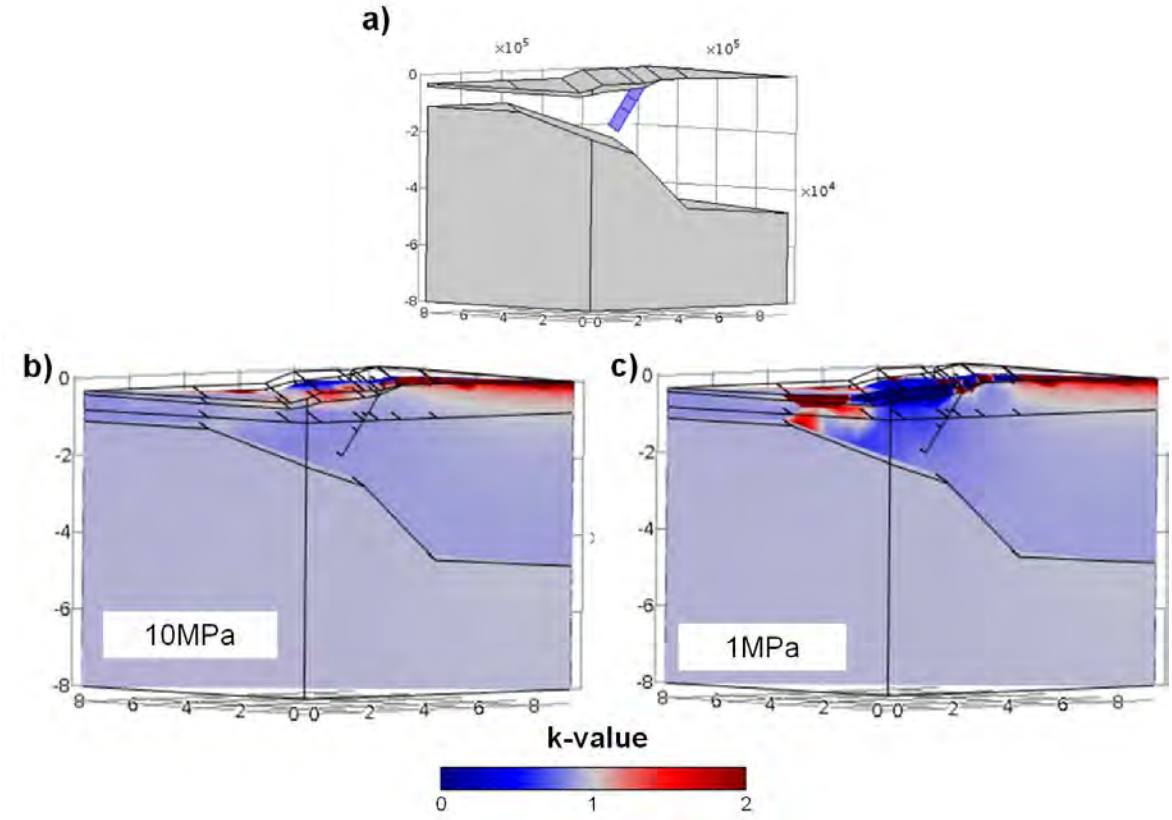

Figure 17: synthetic models showing the effects of weak faults on the local stress regime. a) Design of synthetic model showing a seaward dipping fault in the crust. b) k-value of model with relatively high fault spring constant. The stress field is compressional near the surface and almost neutral in the crust. c) k-value of model with low fault spring constant. The stress field is tensional in the hanging wall of the fault.

4. Discussion

The numerical models presented in this study show a wide range of effects of the stress field components on a continental margin. The smallest effect is calculated for the process of glacial isostatic uplift. It barely modifies the background stress field. However, this is the only stress-field component that represents a dynamic process, thus imposes stress changes on the study area, which may more likely serve as a trigger for earthquakes than the long-term, static stress modelled by the other processes.

The largest, and least expected effect is caused by the contrast in material properties (density and Poisson's ratio) across interfaces. Here, only topography, top basement and the Moho are included in the models, because they represent the largest density contrasts in the lithosphere. The narrow continental margin of the Nordland area shows relatively extreme values of topography (up to 1000 m high mountains along the coast) and Moho depth (Moho deepening more than 20 km over a distance of only 100-150 km). The Moho depth grid used in this study (*Grad et al.*, 2009) has a smoothed, long-wavelength representation of the Moho gradient. The underlying refraction seismic data was either recorded offshore and on the Lofoten-Vesterålen archipelago or inland (*Grad et al.*, 2009). Across the coastal areas and Vestfjorden Basin, the Moho depth values were largely interpolated.

The strong effect of topography and Moho on the stress field is a direct result of the linear elastic rheology of the model and their inability to consider other (previous) geodynamic and thermal processes. Previous authors come to the conclusion that the Moho interface does not play a significant role on the stress field (*Reiter and Heidbach*, 2014). However, their tests did not isolate the effects of Moho and topography, which are actually opposite, but considered them together. *Maury et al.* (2014) calculated the 3D stress field of the Paris Basin and extended their model to 200 km depth. They conclude that the lithosphere-asthenosphere boundary (LAB), which serves as a transition of elastic to visco-elastic behaviour, has a major influence on the regional crustal stress field. Our results thus more or less confirm the findings of *Maury et al.* (2014) that deep interfaces have a strong effect on the regional crustal stress field.

We do not observe stresses corresponding to the Moho effect in the present-day stress field of Nordland. In quite an opposite manner has extension been documented for the coastal areas. We thus conclude that the Moho effect, as seen in the models, is not present in the observed Nordland stress field. Why the Moho effect is actually so small or absent may be connected to the Earth's rheology (and thus the initial background stress) and stress release and dissipation over time. A respective investigation would require a more complex modelling approach (e.g. plasticity or thermal effects) and cannot be done in the current study. But we can conclude that the effects of topography and Moho do not cause the coastal extension and that we thus have to look for other stress-field components.

Ridge push increases the horizontal stress and thus leads to an overall more compressional (less tensional) stress field, both in the offshore and onshore areas. While this effect is well suited to explain the observed direction of the maximum horizontal stress σ_H, it again cannot explain the coastal extension.

Erosion and flexural uplift yield the desired tensional effect in areas of high erosion. But the magnitude of the effect is unclear. Just like for GIA, the main deformation will have occurred some ten thousand years after unloading. If strong tensional stresses existed, they may likely have been released and not been upheld until today. Nevertheless, the regime may have remained in tension and close to failure and the current seismic activity is a sign of small changes to this stress field, which can trigger failure. What a corresponding trigger could be, is not clear. Perhaps recent and ongoing (fluvial and glacial) erosion still contribute to the flexural uplift and thus continuously keeps the stress field near failure.

The presence of faults and pre-existing weakness zones facilitates deformation and would create tension on the thinning wedge of the passive marginâ€™s crust. In the calculations here, the faults do not have to be active (merely weak) in order to generate the tensional stress field. This in turn could then (re-)activate other faults in the vicinity. The Nordland margin is dissected by faults. Their density decreases to the south, where also fewer earthquakes are observed, and in the Vestfjorden Basin which appears as mainly aseismic. Faults may be deeply buried by several kilometres of sediments and be therefore not well mapped. Earthquakes, however, propagate well through the crust and movement below the Vestfjorden Basin would have been recorded by the array installed within the NEONOR2 project (*Janutyte et al.*, 2017). The overlying sediments, in turn, may modify the pressure regime (pore-fluid pressure) such that seismic activity remains low.

Seismicity in the Nordland region seems to occur within irregular volumes (clusters and swarms) as well as along lineaments (*Janutyte et al.*, 2017; *Michalek et al.*, 2018). This is, however, an observation over a relatively short timespan and the question whether this pattern can be considered representative for the general behaviour over the last few thousand (influenced by deglaciation) or ten thousand of years (influenced by glacial erosion) cannot be answered. A diffuse seismicity pattern can be in agreement with a local flexural component. Here, bending stresses are introduced that are independent of the pre-existing tectonic history and thus the fault patterns. Where existing faults are favourable oriented, they could be reactivated and thus localize the seismicity and deformation.

In summary, we conclude that flexural uplift can lead to the extensional regime observed on the Nordland coast, assisted by the fault distribution. When it comes to triggering of the earthquakes, an ongoing mechanism such as flexural uplift caused by local erosion seems most reasonable, especially where the uplift rate gradient is high.

5. References

Amante, C., and B. Eakins (2009), ETOPO1 - 1 arc-minute global relief model: procedures, data sources and analysis, *Tech. rep.*, National Geophysical Data Center, National Oceanographic and Atmospheric Administration, 10.7289/V5C8276M, NOAA Technical Memorandum NESDIS NGDC-24.

Ask, M., D. Ask, and Others (2018), Stress Measurements in the NEONOR2 project, *Tech. rep.*, Luleå Technical University.

Blystad, P., H. Brekke, R. Faerseth, B. Larsen, J. Skogseid, and B. Tørudbakken (1995), Structural elements of the Norwegian continental shelf. Part II: the Norwegian Sea Region, *Norwegian Petroleum Directorate Bulletin*, *8*, 1–45.

Breivik, A. J., J. I. Faleide, R. Mjelde, E. R. Flueh, and Y. Murai (2017), A new tectono-magmatic model for the Lofoten/Vesterålen Margin at the outer limit of the Iceland Plume influence, *Tectonophysics*, *718*, 25 – 44, 10.1016/j.tecto.2017.07.002.

Buchmann, T. J., and P. T. Connolly (2007), Contemporary kinematics of the Upper Rhine Graben: A 3D finite element approach, *Global and Planetary Change*, *58*(1), 287 – 309, 10.1016/j.gloplacha.2007.02.012.

Byrkjeland, U., H. Bungum, and O. Eldholm (2000), Seismotectonics of the Norwegian continental margin, *Journal of Geophysical Research: Solid Earth*, *105*(B3), 6221–6236, 10.1029/1999JB900275.

Dallan, A., D. Worsley, and K. Ofstad (1988), lithostratigraphic scheme for the Mesozoic and Cenozoic succession offshore mid- and northern Norway, *Norwegian Petroleum Directorate Bulletin*, *4*, 1–65.

Divins, D. (2003), Total sediment thickness of the World's oceans and marginal seas, NOAA-National Geophysical Data Center, Boulder, CO, USA.

Dowdeswell, J. A., D. Ottesen, and L. Rise (2010), Rates of sediment delivery from the Fennoscandian Ice Sheet through an ice age, *Geology*, *38*(1), 3, 10.1130/G25523.1.

Fejerskov, M., and C. Lindholm (2000), Crustal stress in and around Norway: an evaluation of stress-generating mechanisms, *Geological Society, London, Special Publications*, *167*(1), 451–467, 10.1144/GSL.SP.2000.167.01.19.

Fejerskov, M., C. Lindholm, A. Myrvang, and H. Bungum (2000), Crustal stress in and around Norway: a compliation of in situ stress observations, *Geological Society, London, Special Publications*, *167*(1), 441–449, 10.1144/GSL.SP.2000.167.01.18.

Fjeldskaar, W., C. Lindholm, J. F. Dehls, and I. Fjeldskaar (2000), Postglacial uplift, neotectonics and seismicity in Fennoscandia, *Quaternary Science Reviews*, *19*(14), 1413–1422.

Grad, M., T. Tiira, and E. W. Group (2009), The Moho depth map of the European Plate, *Geophysical Journal International*, *176*(1), 279–292.

Gritto, R., D. Dreger, O. Heidbach, and L. Hutchings (2014), Towards the understanding of induced seismicity in enhanced geothermal systems, *Tech. Rep. DE-EE0002756*, Array Information Technology, Greenbelt (MD), United States, 10.2172/1154937.

Heidbach, O., M. Tingay, A. Barth, J. Reinecker, D. Kurfess, and B. Müller (2008), The World Stress Map database release 2008, *Tech. rep.*, GFZ Potsdam, 10.1594/GFZ.WSM.Rel2008.

Heidbach, O., T. Hergert, K. Reiter, and S. Giger (2014), Local stress field sensitivity analysis - Case Study Nördlich Lägern, *Tech. Rep. NAB 13-88*, NAGRA - Nationale Genossenschaft für die Lagerung radioaktiver Abfälle.

Hergert, T., and O. Heidbach (2011), Geomechanical model of the Marmara Sea region - II. 3-D contemporary background stress field, *Geophysical Journal International*, *185*(3), 1090–1102, 10.1111/j.1365-246X.2011.04992.x.

Hergert, T., O. Heidbach, K. Reiter, S. B. Giger, and P. Marschall (2015), Stress field sensitivity analysis in a sedimentary sequence of the Alpine foreland, northern Switzerland, *Solid Earth*, *6*(2), 533–552, 10.5194/se-6-533-2015.

Hicks, H., E.C. Bungholm, and C. Lindholm (2000), Stress inversion of earthquake focal mechanism solutions from onshore and offshore Norway, *Norsk Geologisk Tidsskrift*, *80*, 235–250.

Janutyte, I., C. Lindholm, and O. Olesen (2017), Relation between seismicity and tectonic structures offshore and onshore Nordland, northern Norway, *Norwegian Journal of Geology*, *97*(3), 211–225.

Keiding, M., C. Kreemer, C. Lindholm, S. Gradmann, O. Olesen, and H. Kierulf (2015), A comparison of strain rates and seismicity for Fennoscandia: depth dependency of deformation from glacial isostatic adjustment, *Geophysical Journal International*, *202*(2), 1021–1028, 10.1093/gji/ggv207.

Kierulf, H. P. (2017), Analysis strategies for combining continuous and episodic GNSS for studies of neo-tectonics in Northern Norway, *Journal of Geodynamics*, *109*, 32–40, 10.1016/j.jog.2017.07.002.

Kierulf, H. P., H. Steffen, M. J. R. Simpson, M. Lidberg, P. Wu, and H. Wang (2014), A GPS velocity field for Fennoscandia and a consistent comparison to glacial isostatic adjustment models, *Journal of Geophysical Research: Solid Earth*, *119*(8), 6613–6629, 10.1002/2013JB010889.

Lund, B., and M. Zoback (1999), Orientation and magnitude of in situ stress to 6.5 km depth in the Baltic Shield, International Journal of Rock Mechanics and Mining Sciences, 36(2), 169 – 190, 10.1016/S0148-9062(98)00183-1.

Lund, B., P. Schmidt, and C. Hieronymus (2009), Stress evolution and fault stability during the Weichselian glacial cycle, Tech. Rep. TR-09-15, Uppsala University, Geophysics.

Mansour, W. B., R. W. England, S. Fishwick, and M. Moorkamp (2018), Crustal properties of the northern Scandinavian mountains and Fennoscandian shield from analysis of teleseismic Receiver Functions, Geophysical Journal International, 240(1), 386–401, 10.1093/gji/ggy140.

Maury, J., F. H. Cornet, and M. Cara (2014), Influence of the lithosphere-asthenosphere boundary on the stress field northwest of the Alps, Geophysical Journal International, 199(2), 1006–1017, 10.1093/gji/ggu289.

McGarr, A. (1988), On the state of lithospheric stress in the absence of applied tectonic forces, Journal of Geophysical Research: Solid Earth, 93(B11), 13,609–13,617, 10.1029/JB093iB11p13609.

Michalek, J., N. Tjåland, A. Drottning, M. Strømme, B. Storheim, S. Rondenay, and L. Ottemöller (2018), Report on seismic observations within the NEONOR2 project in the Nordland region, Norway, Tech. rep., Bergen University.

Montelli, A., J. Dowdeswell, D. Ottesen, and S. Johansen (2017), Ice-sheet dynamics through the Quaternary on the mid-Norwegian continental margin inferred from 3D seismic data, Marine and Petroleum Geology, 80, 228–242, 10.1016/j.marpetgeo.2016.12.002.

Naliboff, J., C. Lithgow-Bertelloni, L. Ruff, and N. de Koker (2012), The effects of lithospheric thickness and density structure on Earth's stress field, Geophysical Journal International, 188(1), 1–17, 10.1111/j.1365-246X.2011.05248.x.

Norwegian Petroleum Directorate (2010), Geofaglig vurdering av petroleumsressursene i havområdene utenfor Lofoten, Vesterålen og Senja, Report, Norwegian Petroleum Directorate.

Olesen, O., M. Brönner, J. Ebbing, J. Gellein, L. Gernigon, J. Koziel, T. Lauritsen, R. Myklebust, C. Pascal, M. Sand, D. Solheim, and S. Usov (2010), New aeromagnetic and gravity compilations from Norway and adjacent areas: methods and applications, Geological Society, London, Petroleum Geology Conference series, 7, 559–586, 10.1144/0070559.

Olesen, O., H. Kierulf, M. Brönner, E. Dalsegg, O. Fredin, and T. Solbakk (2013a), Deep weathering, neotectonics and strandflat formation in Nordland, northern Norway, *Norwegian Journal of Geology*, *93*(3), 189–213.

Olesen, O., H. Bungum, J. Dehls, C. Kindholm, C. Pascal, and D. Roberts (2013b), Neotectonics, seismicity and contemporary stress field in Norway - mechanisms and implications, in *Quaternary Geology of Norway*, vol. 13, edited by L. Olsen, O. Fredin, and O. Olesen, pp. 145–174, Geological Survey of Norway.

Reiter, K., and O. Heidbach (2014), 3-D geomechanical-numerical model of the contemporary crustal stress state in the Alberta Basin (Canada), *Solid Earth*, *5*(2), 1123–1149, 10.5194/se-5-1123-2014.

Riis, F. (1996), Quantification of Cenozoic vertical movements of Scandinavia by correlation of morphological surfaces with offshore data, *Global and Planetary Change*, *12*(1), 331 – 357, 10.1016/0921-8181(95)00027-5.

Rise, L., D. Ottesen, K. Berg, and E. Lundin (2005), Large-scale development of the mid-Norwegian margin during the last 3 million years, *Marine and Petroleum Geology*, *22*(1), 33 – 44, 10.1016/j.marpetgeo.2004.10.010.

Savchenko, S. (2004), Estimate of stress-strain state of rocks in the area of drilling Kola ultradeep well, *Journal of Mining Science*, *40*(1), 24 – 30, 10.1023/B:JOMI.0000041524.15187.83.

Sheorey, P. (1994), A theory for in situ stresses in isotropic and transverseley isotropic rock, *International Journal of Rock Mechanics and Mining Sciences and Geomechanics*, *31*(1), 23 – 34, 10.1016/0148-9062(94)92312-4.

Simpson, R. W. (1997), Quantifying Anderson's fault types, *Journal of Geophysical Research: Solid Earth*, *102*(B8), 17,909–17,919, 10.1029/97JB01274.

Steffen, H., G. Kaufmann, and P. Wu (2006), Three-dimensional finite-element modeling of the glacial isostatic adjustment in Fennoscandia, *Earth and Planetary Science Letters*, *250*(1), 358 – 375, 10.1016/j.epsl.2006.08.003.

Steffen, H., G. Kaufmann, and R. Lampe (2014), Lithosphere and upper-mantle structure of the southern Baltic Sea estimated from modelling relative sea-level data with glacial isostatic adjustment, *Solid Earth*, *5*(1), 447–459, 10.5194/se-5-447-2014.

Stein, S., S. Cloetingh, N. Sleep, and R. Wortel (1989), Passive margin earthquakes, stresses and rheology, in *Earthquakes at North-Atlantic Passive Margins: Neotectonics and Postglacial Rebound*, *NATO ASI Series*, vol. 266, edited by S. Gregersen and P. Basham, pp. 231–259, Springer, Dordrecht.

Talwani, M., and O. Eldholm (1977), Evolution of the Norwegian-Greenland Sea, *Geological Society of America Bulletin*, *88*(7), 969–999, 10.1130/0016-7606(1977)88<969:EOTNS>2.0.CO;2.

van der Wal, W., A. Barnhoorn, P. Stocchi, S. Gradmann, P. Wu, M. Drury, and B. Vermeersen (2013), Glacial isostatic adjustment model with composite 3-D Earth rheology for Fennoscandia, *Geophysical Journal International*, *194*(1), 61–77, 10.1093/gji/ggt099.

Watts, A. (2001), *Isostasy and flexure of the lithosphere*, Cambridge University Press, Cambridge, UK, p. 458.

Wenning, Q. C., T. Berthet, M. Ask, A. Zappone, J.-E. Rosberg, and B. S. Almqvist (2017), Image log analysis of in situ stress orientation, breakout growth, and natural geologic structures to 2.5Â km depth in central Scandinavian Caledonides: Results from the COSCâ€ 1 borehole, *Journal of Geophysical Research: Solid Earth*, *122*(5), 3999–4019, 10.1002/2016JB013776.

Chapter 10: Deep Structure of the Lofoten-Vesterålen Segment of the Mid-Norwegian Continental Margin and Adjacent Areas Derived From 3-D Density Modeling

Authors: Y. P. Maystrenko[1], O. Olesen[1], L. Gernigon[1], and S. Gradmann[1]

Affiliation: [1]Geological Survey of Norway, P.O. Box 6315 Torgården, N-7491 Trondheim

Journal: Journal of Geophysical Research

Publishing Date: 30 Dec 2016 (Online)

DOI: http://dx.doi.org/10.1002/2016JB013443

Pages: 60 (Proof version)

http://dx.doi.org/10.1002/2016JB013443

Deep structure of the Lofoten-Vesterålen segment of the Mid-Norwegian continental margin and adjacent areas derived from 3D density modeling

Y. P. Maystrenko, O. Olesen, L. Gernigon, and S. Gradmann

Geological Survey of Norway (NGU), Trondheim, Norway

Correspondence to: Yuriy Maystrenko (yuriy.maystrenko@ngu.no)

Key Points:

- 3D structural/density lithospheric-scale model
- Thick sedimentary succession within the Røst Basin
- Low-density mantle beneath the Lofoten-Vesterålen continental margin

Abstract

To understand the major structural features of the sedimentary cover and crystalline crust of the Lofoten-Vesterålen margin and the northern part of the Vøring segment of the Mid-Norwegian continental margin, a lithosphere-scale 3D structural model has been constructed. This model extends from the exposed crystalline rocks of the Fennoscandian Shield in the east to the Cenozoic oceanic domain of the Norwegian-Greenland Sea in the west, covering the Vestfjorden, Ribban and Røst basins and the northern parts of the Vøring Basin and Trøndelag Platform. All available published and/or released data have been used to set the initial 3D model which has been validated by means of 3D density forward modeling to obtain a gravity-consistent 3D structural/density model. Results from the 3D density modeling reveal that relatively thick sedimentary rocks are present in the distal Røst Basin below the lava flows. The presence of a low-density more than 20-km thick granitic body has been modeled within the middle-upper crystalline crust beneath the eastern part of the Vestfjorden Basin and the adjacent mainland. Moreover, the results of the 3D density modeling indicate the presence of an atypical low-density lithospheric mantle beneath a large part of the Lofoten-Vesterålen margin which is required to fit the regional component of the modeled gravity with the observed one. The pronounced crustal feature within the model area is the Bivrost Lineament that appears to be the deeply-seated lithosphere-scale boundary that delineates clearly the Lofoten-Vesterålen segment from the Vøring margin showing contrasting densities and crustal thicknesses.

1 Introduction

The Mid-Norwegian passive continental margin can be subdivided into three structural and crustal segments, comprising the Møre, the Vøring and the Lofoten-Vesterålen margin segments [*Blystad et al.*, 1995]. This study focuses on the northern part of the Vøring margin and the Lofoten-Vesterålen margin (Figure 1). The narrow Lofoten-Vesterålen margin represents the north-eastern and uplifted part of the Mid-Norwegian continental margin, comprising a pronounced, steep shelf edge. The Lofoten-Vesterålen archipelago is, together with the adjacent Norwegian mainland, characterized by a complex topography, which is the result of several phases of relief generation and erosion formed during the long geological development of this area (Figure 1a). On the shelf in the vicinity of the archipelago, the bathymetry is relatively shallow (100-400 m on average). To the west, a pronounced step in bathymetry is clearly recognizable between the Norwegian shelf and the deeper oceanic domain of the Norwegian-Greenland Sea (Figure 1a).

Since the second half of the last century, the sedimentary infill and deep structures of the Lofoten-Vesterålen continental margin have been systematically investigated, mainly for hydrocarbon exploration,. These investigations include (1) onshore geological mapping [e.g., *Sigmond*, 2002], (2) drilling of boreholes [*NPD*, 2016; *Olesen et al.*, 2007b; *SINTEF*, 2016], (3) interpretation of both shallow seismic reflection [*Bergh et al.*, 2007; *Eidvin et al.*, 2007; *Eig*, 2012; *Hansen et al.*, 2009, 2012; *Mokhtari and Pegrum*, 1992; *Olesen et al.*, 2004; *Dag Ottesen et al.*, 2009; *Rise et al.*, 2005; *Rise et al.*, 2013], and (4) deep refraction seismic data [*Avedik et al.*, 1984; *Breivik et al.*, 2009; *Breivik et al.*, 2014; *Drivenes et al.*, 1984; *Goldschmidt-Rokita et al.*, 1988; *Kodaira et al.*, 1995; *Mjelde et al.*, 1996; *Mjelde et al.*, 1992; 1993b; *Mjelde et al.*, 2003; *Mjelde et al.*, 2001; *Sellevoll*, 1983], as well as (5) potential field studies in 2D [*Fichler et al.*, 1999; *Olesen et al.*, 1997; *Tsikalas et al.*, 2005] and in 3D [*Brönner et al.*, 2013; *Gradmann and Ebbing*, 2015; *Olesen et al.*, 2002].

Two of the most prominent regional-scale gravity features of the observed gravity field over the North Atlantic region are located within our study area (Figure 1b). The first important feature represents the NE-SW trending parallel chains of positive gravity anomalies over the Lofoten-Vesterålen archipelago and adjacent basement highs (Figure 1b). The second important anomaly is the pronounced gravity low covering the onshore and offshore transition in the eastern part of the archipelago,. The origin and significance of these gravity anomalies remain particularly unclear.

The main goal of this potential field study is to understand the major structural and crustal configuration of the Lofoten-Vesterålen margin from the mainland to the oceanic domain. Since the last attempt to understand the deep structure of the Lofoten region at the regional scale in 2D and 3D by *Olesen et al.* [2002] and *Tsikalas et al.* [2005], our knowledge about the regional distribution of sedimentary rocks has been improved by several studies [*Bergh et al.*, 2007; *Eidvin et al.*, 2007; *Eig*, 2012; *Hansen et al.*, 2009, 2012; *Olesen et al.*, 2004; *Dag Ottesen et al.*, 2009; *Rise et al.*, 2005; *Rise et al.*, 2013]. Besides, new data about deep structure of the crystalline crust have been obtained within the study area [*Ben Mansour et al.*, 2014; *Breivik et al.*, 2014; *Olsson et al.*, 2008; *Ottemoller and Midzi*, 2003]. All together, these new data provide us with additional structural constraints, allowing further improvements of our understanding the deep structure of the Lofoten-Vesterålen margin. Moreover, significant improvements in 3D modeling software and further development of the hardware allowed us to obtain a new 3D structural/density model for the study area.

The new 3D structural/density model (for location, see blue frame in Figure 1a) has been constructed in the framework of the NEONOR2 project, 'Neotectonics in Nordland - implications for petroleum exploration'. The 3D model covers all major tectonic units of the Lofoten-Vesterålen continental margin (Figure 2), including major sedimentary depocentres in the Røst, Ribban and Vestfjorden basins. In addition, the model extends towards the northern Vøring Basin and Trøndelag Platform. Further 3D density modeling has been carried out using IGMAS+ software (the Interactive Gravity and Magnetic Application System [*Götze*, 2010; *Götze*, 1978; *Götze and Lahmeyer*, 1988; *Schmidt and Götze*, 1998] in order to obtain a data-based and gravity-consistent 3D density and structural model for the entire study area. 3D modelling offers the possibility to perform a density analysis by considering the gravity effects in all directions, allowing us to avoid possible mistakes and edge effects during the interpretation of some of the speculative gravity anomalies.

2 Geological settings

Due to uplift and erosion, the Lofoten-Vesterålen continental margin (LVCM) is the only rift segment of the Mid-Norwegian continental margin where the crystalline basement is locally exposed. Within a large part of the Lofoten-Vesterålen archipelago and the mainland, the preserved Palaeozoic and Mesozoic sedimentary rocks lying on top of the older crystalline basement are very thin and/or mostly absent, similar to other parts of the Mid-Norwegian continental margin. The exposed basement rocks are mostly represented by remnants of the

Caledonian allochthons which were overthrusted onto the Precambrian rocks of the Fennoscandian Shield during the Silurian-Early Devonian Scandian phase of the Caledonian Orogeny [e.g., *Gee et al.*, 2008; *Roberts and Gee*, 1985]. During this regional-scale overthrusting, several oceanic and continental terranes were amalgamated along the western continental margin of the Baltican palaeocontinent. The Precambrian crystalline rocks are locally exposed within so-called 'basement windows' in places where the Caledonian rocks are absent or very thin [*Sigmond*, 2002]. During post-Caledonian times, the Mid-Norwegian continental margin was affected by a major extensional event in the Devonian [e.g., *Fossen*, 2010]. Subsequently, several rifting episodes affected both the LVCM and adjacent Vøring margin [*Eig*, 2012; *Hansen et al.*, 2012; *Tsikalas et al.*, 2001]. In the Late Palaeocene-Early Eocene (~55 Ma) continental break-up led to the formation of oceanic lithosphere within the North Atlantic region [e.g., *Gaina et al.*, 2009; *Gernigon et al.*, 2012; *Olesen et al.*, 2007a; *Srivastava and Tapscott*, 1986; *Talwani and Eldholm*, 1977].

In the southwest, the LVCM is bounded by the Bivrost Lineament (Figure 2), which separates this marginal segment from the deeper and wider Cretaceous Vøring Basin and the Triassic-Jurassic Trøndelag Platform in the south [*Blystad et al.*, 1995]. The Bivrost Lineament is clearly recognizable at both shallow and deep crustal levels [e.g., *Olesen et al.*, 2002; *Tsikalas et al.*, 2005]. It represents a major structural change between the LCVM and the northern Vøring margin where much thicker Cretaceous and Cenozoic depocentres (up to 8-9 km) are observed [*Brekke*, 2000; *Hansen et al.*, 2012]. At deep crustal levels, the Bivrost Lineament is also characterized by a relatively steep gradient at depth of the Moho [*Olesen et al.*, 2002; *Tsikalas et al.*, 2005]. North of the Bivrost lineament, the Moho is generally deeper, the basement depth is shallower, and crustal densities are lower [*Ebbing et al.*, 2012].

Tectonically, the LVCM includes the Røst, Ribban and Vestfjorden basins, which are separated by the Utrøst and Lofoten ridges (Figure 2). The NE-SW-trending, narrow Ribban and Vestfjorden basins contain a relatively thick syn-rift Lower Cretaceous sequence of marine shales and turbiditic sedimentary rocks [*Eig*, 2012; *Hansen et al.*, 2012; *Tsikalas et al.*, 2005]. According to geological and seismic data, Triassic and Jurassic sedimentary rocks of different origin are also present within the Ribban and Vestfjorden basins [*Eig*, 2012; *Færseth*, 2012; *Hansen et al.*, 2012]. The presence of older sedimentary rocks is rather uncertain but the Paleozoic sedimentary rocks can be still preserved within the deepest parts of the study area [e.g., *Eig*, 2012; *Mokhtari and Pegrum*, 1992].

In contrast to the above-mentioned Vøring, Ribban and Vestfjorden basins, the pre-Cretaceous and Cretaceous structural levels of the Røst Basin, to the west, are not clear due to

a presence of breakup-related intrusive and extrusive rocks in this area (see limit of basalts in Figure 2). A large part of the Røst Basin is covered by relatively thin lavas flows, the so-called Lofoten Margin Flows [*Berndt et al.*, 2001]. To the west, the syn-breakup flood basalts have been identified by seaward-dipping reflector sequences along reflection seismic lines in the study area [*Tsikalas et al.*, 2002]. Moreover, deep seismic refraction data indicate the presence of a lower-crustal layer with a velocity of 6.7 km/s beneath the LVCM [e.g., *Breivik et al.,* 2014; *Mjelde et al.*, 1993; *Mjelde et al.*, 1997]. Where the velocity is more than 7.0 km/s [e.g., Mjelde et al., 2009], this lower-crustal layer may at least partially represent a combination of syn-breakup massive magmatic underplating close to the base of the crust or/and mafic intrusions into the pre-existing continental crust (e.g., White et al., 2008). The early Cenozoic continental breakup resulted in the formation of the oceanic lithosphere beneath the present-day Norwegian-Greenland Sea where the Cenozoic Lofoten Basin is situated (Figure 2). Finally, during the late Cenozoic, the entire LVCM, excluding the Røst Basin, was structurally inverted and exposed due to uplift and erosion [*Færseth*, 2012; *Løseth and Tveten*, 1996]. Additional erosional events occurred during the Quaternary glacial periods when ice sheets and glaciers finally removed the remnant sedimentary rocks and existing weathered crystalline crust from the mainland, creating the present-day landscape with the relatively deep fjords and the stripped mountains [*Dowdeswell et al.*, 2006; *Olesen et al.*, 2013; *Riis*, 1996].

3 Input structural data

During the construction of the 3D model, priority has been given to the most recent original data, such as the borehole data, deep refraction and reflection seismic lines and teleseismic receiver function data. The pre-existing compilations have only been used to fill the gaps between the original high-quality data. If the existing compilations do not cover the space between the original high-quality data, interpolation and/or extrapolation of the original data have been applied for the input 3D model that has been structurally adjusted during the 3D density modeling. Bathymetry and topography for the model area have been acquired from the Norwegian Mapping Authority.

3.1 Sedimentary cover

For the sedimentary successions (Figure 3), the main datasets represent the results of reflection seismic interpretation. The TWT isochron maps from *Rise et al.* [2005; 2010; 2006], *Dowdeswell et al.* [2006; 2010], *Eidvin et al.* [2007; 2014], *Ottesen et al.* [2012; 2009] and *Chand et al.* [2011], all together indicated as NGU data (Marine geology, 2014) in Figure 3, have been used for the Brygge-Naust interval (Cenozoic succession without Paleocene). The TWT structure maps from Gernigon (NGU unpublished data) have been considered for the Paleocene, Cretaceous and pre-Cretaceous sedimentary successions within the area which is covered by the 3D structural model from *Maystrenko and Gernigon* [2015]. For the Cretaceous successions within the rest of the LVCM area, the TWT structure and isochron maps have been taken from *Hansen* [2009], *Hansen et al.* [2012] and *Eig* [2012]. The thickness of the Bjørnøya Fan Slide Complex from *Hjelstuen et al.* [2007] is representative for the uppermost Cenozoic sedimentary rocks within the northwestern corner of the 3D model (Figure 3). In addition, a pre-existing 3D structural model of the Mid-Norwegian continental margin [*Maystrenko and Scheck-Wenderoth*, 2009; *Scheck-Wenderoth et al.*, 2007], the TWT structure maps from *Brekke* [2000] and configuration of sedimentary rocks and basalts along the transects in *Tsikalas et al.* [2005] have been partially used to fill the gaps between the more recent datasets described above. The marginal limits of the sedimentary successions have mainly been taken from the Geological Map of Land and Sea Areas of Northern Europe [*Sigmond*, 2002] and have been partially adjusted in the light of recent data from *Hansen* [2009] and *Hansen et al.* [2012].

The derived TWT thickness maps have then been depth-converted using interval velocities and the obtained thicknesses have been calibrated and cross-checked with the available borehole data [*NPD*, 2016; *SINTEF*, 2016]. The interval velocities for the uppermost sedimentary rocks, represented by Naust and Kai (S2; mainly Neogene-Quaternary), have been set to be constant and are equal to 2050 m/s (Table 1). The interval velocities for the Brygge (S3; mainly Eocene-Oligocene), Paleocene and Cretaceous (S4-5) have been calculated according to a simple equation (1) based on the best regional fit between the calculated true vertical thicknesses and the existing borehole data:

$$V_i = V_0 + k_z * z \quad (1)$$

where V_i is the interval velocity [m/s] (Table 1), V_0 is the velocity at z=0 [m/s], k_z is the vertical velocity gradient [m/s/m] and z is the depth to the base of the layer [m].

All datasets have been merged and gridded together in terms of thickness maps for the following sedimentary intervals: (S1) the Bjørnøya Fan Slide Complex (base of the Bjørnøya Fan Slide Complex-sea floor), (S2) the Naust-Kai (base of the Naust-sea floor), (S3) the Brygge Formation (top of the Paleocene/top of the oceanic layer 2AB (basalts)-base of the Kai Formation), (S4) the Upper Cretaceous-Paleocene (near top Cenomanian-top of the Paleocene, the Lower Cretaceous (base Cretaceous unconformity-near top Cenomanian), (S5) the pre-Cretaceous (Jurassic, Triassic and older sedimentary rocks). During the 3D density modeling, modifications have been mainly applied to the Lower Cretaceous and pre-Cretaceous sedimentary successions. The rest of the sedimentary layers have not been modified or only slightly modified during the modeling.

The uppermost sedimentary layers (S1 and S2) of the 3D model are both shown in Figure 4a, as they are not overlapping. The Bjørnøya Fan Slide Complex (S1) is only present within the Lofoten and Røst basins (cf. Figures 3 and 4a), whereas the present-day distribution of the Naust-Kai succession (S2) is mostly restricted to the Vøring Basin and the Trøndelag Platform with a partial occurrence to the northeast of the Bivrost Lineament (Figure 4a). The Bjørnøya Fan Slide Complex is 0.2-1.0 Ma old and includes three buried mega-slides, containing thick debris units [*Hjelstuen et al.*, 2007]. The Bjørnøya Fan Complex is characterized by a typical slide pattern, reaching more than 700 m of thickness in the centre of the slide complex with radially decreasing thickness towards the marginal parts of the slide. The Naust-Kai interval is prominently thickened (up to more than 1.8 km) within the narrow NW-SE-trending elongated zone at the northwestern and southwestern sides of the Utgard High (Figure 4a), delineating the continental slope.

The Brygge Formation (Figure 4b; S3) is generally thin within the greater part of the northern parts of the Vøring Basin and the Trøndelag Platform, ranging from 80-90 m to 400 m on average. Within the Lofoten and Røst basins, the Brygge Formation is characterized by several depocentres where the thickness of the sedimentary rocks is locally more than 2 km. However, the distribution and thickness pattern of the Cenozoic remains locally uncertain within the Lofoten and Røst basins. Therefore, in the framework of this study, the Brygge Formation in Figure 4b can locally include parts of the Kai Formation and even Paleocene deposits in the Lofoten and Røst basins. The southeastern distribution limit of the Brygge Formation in the Røst Basin coincides spatially with the steep continental slope of the LVCM, demonstrating a bathymetric control on the present-day distribution of these sedimentary rocks.

The Paleocene and the Upper Cretaceous sedimentary rocks (S4) have been merged into one layer because their seismic patterns are very similar in local sub-basins such as the Hel Graben where the Paleocene proves to be relatively thick [*Lundin et al.*, 2013; *Williams and Magnus*, 2013]. It was, thus, not always possible to distinguish confidently between the Paleocene and Upper Cretaceous successions where borehole data are absent. The Upper Cretaceous-Paleocene sequence is characterized by three depocentres in the Hel Graben, Någrind Syncline and Træna Basin, which are separated by the Nyk and Utgard highs (Figure 4c). One of these depocentres has a rounded shape and is located in the Hel Graben where the total Upper Cretaceous-Paleocene succession reaches more than 9 km. In the LVCM, NE-SW elongated depocentres with sediment thicknesses varying from 5 to 8 km in the Någrind Syncline and from 4 to 6 km in the Træna Basin can be observed (Figuure 4c). The increase in average thickness of the Upper Cretaceous-Paleocene sedimentary succession from the Træna Basin to the Hel Graben suggests a migration of the depocentres [e.g., *Lien*, 2005]. It is important to note that there is no information about the Upper Cretaceous and/or the Paleocene successions within the largest part of the Røst Basin, but a thin Upper Cretaceous succession is locally preserved in the Ribban Basin [*Sigmond*, 2002; *SINTEF*, 2016]. Therefore, the Upper Cretaceous-Paleocene sedimentary succession is most likely present in the Røst Basin and has been indifferently included into the undivided Paleocene, Cretaceous and pre-Cretaceous sedimentary rocks within the Røst Basin during the 3D density modeling.

3.2 Crystalline crust and lithospheric mantle

The depth to the top of the crystalline basement is mainly constrained by deep refraction seismic lines [*Breivik et al.*, 2009; *Breivik et al.*, 2014; *Kodaira et al.*, 1995; *Mjelde et al.*, 1992; 1993; *Mjelde et al.*, 2003; *Mjelde et al.*, 2001] and interpretation of the deep reflection seismic data [*Hansen et al.,* 2012] (Figure 5). The basement topography between the above-mentioned datasets has been obtained by an interpolation and/or extrapolation of the existing data with partial use of data derived from the previous regional-scale compilations of the top of the crystalline basement by *Olesen et al.* [2002] and *Ebbing and Olesen* [2010]. 3D structural models of the Mid-Norwegian margin by *Scheck-Wenderoth et al.* [2007], *Maystrenko and Scheck-Wenderoth* [2009], *Maystrenko and Gernigon* [2015] have been used in the areas, which have not been covered by the previous datasets. The obtained top-basement topography has been finally cross-checked by a few boreholes [*NPD,* 2016; *SINTEFF,* 2016] which were drilled through the crystalline basement (Figure 5).

The model area is partially or completely covered by several European-scale and smaller compilations of the Moho topography [*Artemieva and Thybo*, 2013; *Ebbing and Olesen*, 2010; *Grad et al.*, 2009; *Kelly et al.*, 2007; *Tesauro et al.*, 2008], showing only a rough regional pattern for the Moho. Therefore, depth to the Moho and configuration of the crystalline crust have been mainly constrained by the original OBS refraction data [*Breivik et al.*, 2014; *Kodaira et al.,* 1995; *Mjelde et al.,* 1992, 1993, 2001, 2003] and the COOP2 3D structural model of the Vøring Basin area [*Maystrenko and Gernigon,* 2015] with some local adjustments from the previously published compilations and 3D structural models [*Olesen et al.,* 2002; *Ebbing et al.,* 2006; *Scheck-Wenderoth et al.,* 2007; *Maystrenko and Scheck-Wenderoth,* 2009; *Ebbing and Olesen,* 2010]. Besides, the teleseismic receiver function data [*Ben Mansour et al.*, 2014; *Olsson et al.*, 2008; *Ottemoller and Midzi*, 2003] have been considered to constrain the Moho topography in the onshore parts of the 3D model.

Contrary to the sedimentary and crustal levels, the lithosphere-asthenosphere boundary is much less constrained by available data. The lithosphere-asthenosphere boundary which has been considered for the modeling, has been taken from *Calcagnile* [1982], *Artemieva* [2006] and *Ebbing et al.* [2012]. The depth to the lithosphere-asthenosphere boundary beneath the oceanic crustal domain has been derived according to empirical relations between lithospheric age and Love and Rayleigh wave-phase velocity [*Zhang and Lay*, 1999]. The age of oceanic lithosphere in the North Atlantic has been taken from *Müller et al.* [2008]. This basic age-dependent depth of the lithosphere-asthenosphere boundary approximates the gradual thermal cooling effects of the oceanic lithosphere after the Early Cenozoic continental breakup.

4 3D density modeling

The initial 3D structural model has been tested by gravity forward modeling and has been locally modified to match the observed gravity signal.

4.1 Method

The 3D density modeling has been performed by use of the IGMAS+ software package (the Interactive Gravity and Magnetic Application System [*Götze*, 2010; *Götze*, 1978; *Götze and Lahmeyer*, 1988; *Schmidt and Götze*, 1998]). The modeling considers a triangulation between the different structural depth maps of the initial 3D structural model and

2D vertical slices through this model. The triangulation is a 3D meshing algorithm which is characterized by multiple polyhedra with triangulated planes between the top and the base of each layer.

The procedure of our 3D density modeling includes interactive changes of the geometry and density of the layers along 27, E-W-oriented, vertical slices through the NEONOR2 study area (Figure 6). The distance between these 2D working planes is 16 km which is sufficiently short to model the major crustal features of the study area. The 2D working slices are parallel to each other and their positions have been chosen to cross the most important gravity anomalies and the main structural units of the model area in order to avoid some potential artifacts as a result of the 3D triangulation between the 2D vertical slices.

Constant and compaction-related densities have been assigned to the different polyhedra. In the case of constant densities, the integral gravity effect of all triangulated polyhedra gives the total gravity effect of the 3D structural/density model. In order to consider the increase of densities with depth according to exponential functions (2-5), the sedimentary cover has been additionally voxelised (the horizontal voxel size is 4 km and the vertical one is 100 m).

The continental lithospheric domain and, especially, the oceanic one are not fully covered by the NEONOR2 3D structural model (Figure 2). Therefore, the 3D model has been laterally extended in all directions, exceeding the original frame of the NEONOR2 model area. The major structural features of the North Atlantic region and Fennoscandia have been schematically included into the extended parts of the 3D structural model to avoid major boundary and regional-scale gravity effects. A schematic representation of the extended parts becomes more and more detailed when approaching to the NEONOR2 3D model. This increase of the model resolution has been applied in order to consider local-scale structural and compositional changes in the close vicinity of the model. The less constrained extended parts have been used in order to consider the long-wavelength gravity effects from the oceanic and continental domains. These extended parts of the model allow us to take into consideration the gravity effects from the relatively shallow lithosphere-asthenosphere boundary and Moho beneath the oceanic domain and the relatively deep locations of these interfaces beneath Fennoscandia. However, detailed 3D density modeling has been conducted only within the main NEONOR2 study area (Figures 1 and 2).

Due to inherent non-uniqueness of potential field modeling, densities and structural models can produce the same or similar modeled gravity response. Such uncertainties have

been greatly reduced by using available structural information and available geophysical constraints. More to the point, the 3D density modeling implies that the lateral influence of masses is considered in three dimensions, thus reducing the number of alternative solutions. The modeled gravity field is very sensitive to geometrical changes of interfaces where the strongest density contrast is present, such as the base of sedimentary rocks/the top of the crystalline crust at a shallow level and the Moho discontinuity at a deeper one. The Moho topography is relatively well constrained by deep-seismic data over large parts of the modeled offshore area (Figure 5). The stratigraphy and the top of the crystalline basement depth are also in good agreement with the geological outcrops and borehole data available at shallow levels. In contrast, the boundary between the pre-Cretaceous or Cretaceous sedimentary rocks and the crystalline crust is not always properly defined by seismic data within the deeper parts of the Vøring, Ribban and Vestfjorden basins and is still not clear within the Røst Basin as well. The deep sedimentary successions in these basins are most likely highly compacted. In this case, the density contrast between the sedimentary infill and the crystalline crust could be extremely low or even inverted [*Reynisson*, 2010]. Consequently, similarities in densities of the highly compacted sedimentary rocks and the crystalline crust enhance the uncertainties in determining the depth to the top of the crystalline basement by the 3D density modeling within the deeper areas of the model. In this situation, the correctness of the 3D density modeling is strongly dependent on the quality of the input structural data or alternative magnetic modeling (not considered in this study). The uncertainties in densities and geometries increase with depth as a result of the decreasing resolution of the input data and the sensitivity of the gravity signal. The estimated uncertainties in densities and geometries at the level of the upper crust are typically less than 10%, whereas the uncertainties increase with depth as a result of the decreasing resolution of the input data and the sensitivity of the gravity signal, reaching 10% or even more at the lower-crustal and uppermost mantle levels. This is especially true in the case of the depth to the base of the lithosphere which is the deepest boundary in the model. To reduce all these uncertainties, additional data would be required.

Moreover, the accuracy of the model is also dependent on the chosen grid resolution in addition to the quality of the input data. For this regional and lithosphere-scale study, the horizontal resolution of our regional-scale 3D model has been taken to be 4 km at the level of the sedimentary rocks and 16 km at the level of the crystalline crust and the lithospheric mantle. Therefore, some significant changes in depth at distances shorter than the horizontal resolution of the model cannot be properly reproduced in our model, leading to local large

misfits between the original input data and the resulted grids. This is especially true for the upper crustal level where significant changes in geometry of the sedimentary layers occur at relatively short distances. However, this resolution-related complexity is also relevant for the deep crustal levels because the resolution of the model is lower at the level of the crystalline crust, although the geometry does not vary so drastically as in the case of sedimentary rocks.

4.2 Densities

During the 3D density modeling, densities have been set with constant values for the crystalline rocks (Table 2). Densities of sedimentary rocks have been assigned to be depth-dependent in order to take into account the compaction of sedimentary rocks with depth. The density of the Bjørnøya Fan Slide Complex (S1) has been set to be constant with a relatively low value of 1600 kg/m^3. This low value of the density reflects the fact that the transported rocks of the Bjørnøya Fan Slide Complex are most likely less compacted compared with the surrounding sedimentary rocks.

Four equations have been derived to describe compaction-related increasing densities with depth for the rest of sedimentary rocks. Due to limited information about the densities of sedimentary rocks within the LVCM, the measured densities from the Vøring and Møre basins [*Reynisson*, 2010] have been considered to derive the exponential functions for the NEONOR2 model area. We assume that the major trend in density distribution with depth of the compacted sedimentary rocks does not change drastically within the areas where sedimentary rocks are relatively thick. However, because the LVCM was partially uplifted and eroded, some of the compacted sedimentary rocks have been shifted to shallower depths.

The empirical functions illustrate the exponential increase of densities with depth for sedimentary cover and have been subdivided into four groups based on the distribution of the measured densities with depth and stratigraphy. These groups are the following: (1) Naust-Kai formations (S2) and Paleocene (S4); (2) Brygge Formation (S3); (3) Cretaceous (S4-5) and (4) pre-Cretaceous (S6). The numbers in the empirical functions have been chosen to produce a curve for the depth-dependent densities, which predict the major trend in the measured densities.

The first group of sedimentary rocks is represented by the low-compacted Naust-Kai succession and the slightly more compacted Paleocene sedimentary rocks, the measured densities of which form one cluster with similar densities according to distribution of the

416 measured densities from *Reynisson* [2010]. Therefore, a single function (2) has been derived
417 for both the Naust-Kai and the Paleocene:
418
419 $\rho(z)=2700-1150*\exp(0{,}00042*-z)$ (2)
420 where ρ is density [kg/m^3] and z is depth [m].
421
422 The measured densities of the Brygge Formation vary from 1623 to 2270 kg/m^3. These
423 values are reflected by the equation (3):
424
425 $\rho(z)=2700-1450*\exp(0{,}00045*-z)$ (3)
426
427 The measured densities of the Cretaceous are characterized by a wide range of values,
428 varying from 1910 to 2790 kg/m^3 in the deepest parts of the basin. The derived function (4)
429 for the Cretaceous has been set to reproduce and approximate more or less average densities
430 of this wide range:
431
432 $\rho(z)=2700-700*\exp(0{,}00037*-z)$ (4)
433
434 The last group of sedimentary rocks is the pre-Cretaceous which consists of
435 undifferentiated Jurassic, Triassic and/or older sedimentary rocks. Measured densities are
436 available only for the Jurassic and Triassic. Therefore, the empirical function (5) is mainly
437 representative for the Jurassic-Triassic interval (and mainly for the upper parts of these
438 stratigraphic units):
439
440 $\rho(z)=2700-400*\exp(0{,}00027*-z)$ (5)
441
442 The densities of the crystalline crust (Table 2) have been chosen to represent the main
443 lithological composition of each basement layer. The upper-crustal densities have been
444 derived from the NGU petrophysical electronic database [*Olesen et al.*, 1993; *Olesen et al.*,
445 2010]. This database provides measured density values of the crystalline rocks, which are
446 exposed at the Earth's surface within the model area (Figure 5). If information about the
447 density was absent in the NGU database or if the specific basement layer is not exposed at the
448 surface, average literature values have been used to set supposed basement lithologies. The
449 uppermost crystalline layer is represented mainly by gabbro to anorthosite and metamorphic

rocks (UC1) with a high density of 2820-2856 kg/m^3. These rocks represent the equivalent of conventional lower-mid-crustal rocks [*Christensen and Mooney*, 1995], which were brought close to the surface mainly during the Caledonian Orogeny. On the contrary, adjacent upper-crustal rocks (UC2) with a low density of 2640 kg/m^3 are also observed. A typical upper-crustal density of 2675 kg/m^3 has been assigned to the regional upper-crustal layer (UC3) which has the broadest distribution beneath the greater part of the model area. The modeled middle crystalline crust (MC) has a density of 2760 kg/m^3 on average. The chosen density for the lower crystalline crust (LC) has been taken to be 2878 kg/m^3. The high-density lower crust (HDLC) is characterized by increasing velocities, which exceed 6.7 km/s. In places where the velocity of this lower-crustal layer is more than 7.0 km/s, it is partially represented by the magmatically underplated lower crust in the vicinity of the oceanic crustal domain [*Mjelde et al.*, 2002], as well as this layer can be represented by the high-grade metamorphic rocks to partially eclogitised inherited lower crust [*Gernigon et al.*, 2004; *Mjelde et al.*, 2013; *Mjelde et al.*, 2016; *Mjelde et al.*, 2009a]. The average density of this high-velocity, lower-crustal layer has been taken to be in the range of 2985-3070 kg/m^3. A density of 2920 kg/m^3 has been additionally assigned to high-density intracrustal layer (HDIC). The high-density intracrustal layer (HDIC) has been included into the 3D density model to explain the misfit between the observed and the calculated gravity where the presence of the denser high-density/high-velocity lower-crustal layer (HDLC) was not enough. In general, these assigned densities for the crystalline rocks (Table 2) are similar to those which were used during previous density modeling within the Mid-Norwegian continental margin [e.g., *Ebbing et al.*, 2006; *Maystrenko and Scheck-Wenderoth*, 2009; *Maystrenko and Gernigon*, 2015; *Olesen et al.*, 2002; *Reynisson*, 2010; *Tsikalas et al.*, 2005].

Furthermore, three additional crustal layers have been included into the model to represent the oceanic crustal domain. These three layers are equivalent to the oceanic layers 2AB, 3A and 3B. The uppermost layer (OL2AB) of these layers consists mainly of flood basalts and diabase dykes. The average density of this layer has been set to 2650 kg/m^3 within the model area, assuming the presence of tuffs in addition to the basalts. The mid-crustal oceanic layer 3A (OL3A) is considered to be a mixture of sheeted dykes and gabbroic intrusions and has therefore been assigned a density of 2850 kg/m^3. The lowest oceanic crustal layer 3B (OL3B) has properties of gabbros and ultramafic rocks. The lower-crustal oceanic layer 3B is partially continuous with the high-velocity lower-crustal layer in terms of seismic velocities and spatial position. Therefore, a density of 3010-3040 kg/m^3 has been set for this layer which is similar to the density of the high-density lower continental crust.

A significant change in velocity from 6.8-7.5 km/s within the lower crust to more than 8.0 km/s within the uppermost mantle is observed at the Moho interface [*Kodaira et al.,* 1995; *Mjelde et al.,* 1992, 1993, 1996, 2001, 2003]. This prominent jump in P-velocities indicates a discrete increase of densities within the uppermost mantle compared to the lower crust. Considering the thermal state of the whole lithospheric mantle, an average density of the lithospheric mantle has been set to be 3220 kg/m^3. Finally, an average density of 3160 kg/m^3 has been assigned to the uppermost asthenosphere in order to mimic differences in the thermal state between the oceanic and continental lithospheric domains.

4.3 Observed gravity field

The free-air gravity from the new global gravity DTU13 compilation [*Andersen et al.*, 2014] was used during the 3D density modeling (Figures 1b and 7a). One of the most remarkable anomalies of the observed gravity field (Figure 7a) is associated with the regional-scale gravity low over the eastern part of the Vestfjorden Basin and adjacent mainland. On the Bouguer gravity anomaly map the gravity low extends up to the Sarek area in Sweden and has therefore been called the Vestfjorden-Sarek gravity low by *Olesen et al.* [2002]. As *Gradmann and Ebbing* [2015] point out, the low in the Free-Air gravity is shifted by c. 100 km to the west and does not cover the high topography of the Sarek mountains. The Bouguer gravity low is locally less than -100 mGal, implying a significant mass deficit in that area. In contrast, the Lofoten-Vesterålen positive gravity anomaly is up to more than 100 mGal, indicating a mass excess immediately to the west from the described negative gravity anomaly. There is also a lower-amplitude chain of the positive gravity anomalies over the Utrøst Ridge and Utgard highs with the Utgard gravity high shifted laterally along the Bivrost Lineament (Figure 7a). This chain of gravity highs is bounded in the west by the distinguished gravity low over the Røst Basin. The complex topography of the relatively high mountains is reflected by several strong, positive, free-air gravity anomalies over the mainland.

5 Results of the 3D density modeling

The modeled gravity response of the final 3D model (Figure 7b) is characterized by a good fit with the observed gravity field (Figure 7a). All large-scale gravity anomalies have been successfully reproduced during the modeling, suggesting that our 3D model resolves the

main regional-scale structural and compositional features of the LVCM and adjacent areas. Offshore, the difference between the observed and the modeled gravity fields varies from -10 to +10 mGal on average, being in the range of -5 to +5 mGal in most of the continental margin (Figure 7c). In contrast, a number of short-wavelength misfits between the observed and the calculated gravity fields show more than ±20-30 mGal differences over the mountains in the mainland. These large misfits are related to the fact that both the gridded topography and the gridded free-air gravity anomalies have been used during the 3D density modeling. However, the free-air gravity anomalies are very sensitive to the gravity effect of the topography. Unfortunately, in the case of both gridded topography and gridded free-air gravity, the local lack of coincidence between the measured topography and gravity cannot be avoided. For this reason, the main effort has been restricted to fit the long-wavelength component of the observed gravity signal.

5.1 Modeled basalt and sedimentary rocks

The input geometry of the main sedimentary successions (S1, S2, S3 and S4, Table 2) (Figure 4) has not been changed during the 3D density modeling. In contrast, the thickness of the oceanic layer 2AB (OL2AB), the Lower Cretaceous (S5) and the pre-Cretaceous (S6) (Figure 8) sequences have locally been modified during the modeling to improve the fit between the modeled gravity and the observed one.

The obtained configuration of the oceanic layer 2AB (OL2AB) is characterized by the presence of the zone of the thickened basalts, which is trending NE-SW parallel to the continent-ocean boundary and widens and thickens towards the southwest (Figure 8a). The thickness of this layer is 1.6-2.8 km in the northeastern part of this zone and increases to more than 3.3-4.6 km in the southwest. The rest of this layer has a thickness of around 200-600 m on average.

The Lower Cretaceous succession (S5) is particularly thick within several relatively narrow elongated zones which correspond to different sub-basins of the Vøring Basin and the Lofoten-Vesterålen continental margin, such as the Någrind Syncline, and the Træna, Ribban and Vestfjorden basins (Figure 8b). In contrast, the basement highs, such as the Utgard High, and the Utrøst and Lofoten ridges, are characterized by the strong thinning of the sedimentary rocks or even the lack of the Lower Cretaceous successions. This kind of thickness pattern reflects the fact that the highest rate of subsidence was localized within the extensional graben and syn-tectonic sub-sag structures formed during the Early Cretaceous rifting. The thickest

552 Lower Cretaceous is observed within the Någrind Syncline where its thickness reaches more
553 than 12 km, whereas the Lower Cretaceous sedimentary rocks are only up to 6.5-7 km thick in
554 the Træna, Ribban and Vestfjorden basins with some local thickening to more than 8 km
555 within the northeastern part of the continental margin.
556 The pre-Cretaceous sedimentary rocks (Figure 8c; S6) represent another structural
557 level of the model area. The thickest pre-Cretaceous succession (more than 8.5 km) is
558 observed within the northeastern part of the Trøndelag Platform (Figure 8c). The Vestfjorden
559 Basin is characterized by the presence of the thickened pre-Cretaceous in the southwestern
560 part where its thickness reaches more than 6 km. The Någrind Syncline and the Træna Basin
561 also show thick pre-Cretaceous sedimentary rocks.
562 Once more, it is important to mention that the distribution of sedimentary rocks in the
563 Røst Basin is very uncertain and, therefore, only one sedimentary layer (S4-6) has been
564 modeled within the Røst Basin below the basalts (Figure 8d). This layer is representative for
565 the Paleocene, Cretaceous and pre-Cretaceous sedimentary rocks which are most likely
566 present in this basin below the basaltic lavas. The modeled sedimentary rocks are up to 8-10
567 km thick within the central and southeastern parts of the Røst Basin but they thin strongly
568 towards the oceanic crustal domain (Figure 8d).
569
570 5.2 Modeled major depth interfaces
571
572 The structural pattern at the top of the crystalline basement is complex (Figure 9a). On
573 the mainland, the top basement corresponds to the Earth's surface. Within the study area, three
574 prominent zones can be distinguished at the top of the crystalline basement level (Figure 9a):
575 (1) the northern Vøring Basin with deeply located basement and intermediate basement horst
576 (e.g., Utgard High), (2) the Trøndelag Platform with moderate top basement depths and (3)
577 the Lofoten-Vesterålen proximal domain with a shallow basement. Structurally, the Vøring
578 Basin and the Trøndelag Platform are separated by the Bivrost Lineament from the Lofoten-
579 Vesterålen segment. The deepest top of the crystalline basement underlies the Någrind
580 Syncline, reaching locally to a depth of more than 20 km. The other sub-basins of the Vøring
581 Basin, such as the Hel Graben and Træna Basin, are also characterized by the deep basement
582 with an average depth of 13-16 km. In contrast, the basement topography is relatively shallow
583 on the Trøndelag Platform where the depth to the base of sedimentary rocks is mainly in the
584 range of 7-10 km. Furthermore, the basement is shallower within a large part of the LVCM.
585 There, the crystalline crust is even exposed at the Earth's surface on the Lofoten-Vesterålen

586 archipelago and at the sea floor within the Utrøst Ridge. On the contrary, the Røst and
587 Vestfjorden basins are up to 10-11 km deep (Figure 9a).
588 The obtained Moho topography (Figure 9b) has been partially modified during the 3D
589 density modeling and, therefore, the resulting map includes post-compilation changes within
590 the areas where coverage by the deep seismic data is limited (Figure 5). The Moho depth
591 varies generally from less than 11 km beneath the oceanic crustal domain to more than 48 km
592 beneath the continent. The LVCM is characterized by a strong variation of the Moho depth. A
593 significant necking of the crust and a shallow base of the crust (shallower than 14-15 km) is
594 located beneath the Røst Basin. In the proximal part of the LVCM, the Ribban and
595 Vestfjorden basins show a deeper position for the Moho (25-28 km depth on average). There
596 is a narrow Moho uplift to around 21.5 km depth beneath the southwestern continuation of the
597 Lofoten Ridge (Figure 9b). The Vøring Basin is characterized by a shallow Moho at depths of
598 18.5-19.5 km beneath the Utgard High. In the Vøring Basin, the necking zone (where crust is
599 < 10 km) is rather expected to lie east of the Træna Basin where the crust is extremely thin.
600 This contrasts with a previous interpretation by Redfield and Osmundsen (2016) suggesting
601 the necking zone along the Utgard High, which is not so drastically thin in the light of our
602 new crustal thickness reevaluation. To the east, the Trøndelag Platform is characterized by a
603 25-28 km-deep Moho on average.
604 The modeled base of the lithosphere is more than 190 km deep beneath the mainland
605 (Figure 9c), whereas the oceanic crustal domain is underlain by a 50-60 km-deep lithosphere-
606 asthenosphere boundary. The continental margin represents a transition zone from the
607 continent towards the ocean and, therefore, the depth to the lithosphere-asthenosphere
608 boundary varies from less than 70 km along the continent-ocean boundary to more than 110
609 km in the vicinity of the coastline.
610 The white line in Figures 9b and 9c outlines the area where a significantly lower
611 density of the lithospheric mantle has been included into the 3D density model in order to fit
612 the observed and the calculated gravity anomalies over the LVCM. The density has been set
613 to be 3185-3202 kg/m^3, compared to the rest of the lithospheric mantle which has been
614 assigned a density of 3220 kg/m^3. The modeled lateral extent of this atypical lithospheric
615 mantle with the reduced density coincides with the Bivrost Lineament in the southwest. The
616 vertical extent of the anomalous lithospheric mantle, however, is uncertain because an
617 increased density contrast to higher values, compared to the used one (18-35 kg/m^3), will
618 automatically lead to a decrease of the thickness of the low-density mantle. Therefore, the

619 modeled low-density mantle is a first-order approximation of the expected lower density
620 mantle material beneath the LVCM.
621
622 5.3 Modeled crystalline crust
623
624 The crystalline crust of the investigated area consists of several layers with different
625 densities (Figures 10 and 11). The upper crystalline rocks have been subdivided into three
626 layers (UC1, UC2 and UC3) during the modeling. The uppermost layer of the crystalline
627 rocks is represented by the high-density upper crust (Figure 10a; UC1) and is associated with
628 the gabbroic to anorthositic and metamorphic rocks, exposed at the Earth's surface [*Sigmond*
629 2002]. The distribution of these high-density rocks is not so clear within offshore areas
630 covered by sedimentary rocks and the structure and nature of the bedrock here was mainly
631 obtained with the help of the 3D density modeling. The thickness of the high-density upper-
632 crustal layer varies markedly within the model area, reaching more than 4-5 km locally
633 (Figure 10a). The second upper-crustal layer is the low-density layer (Figure 10b; UC2) that
634 has a density of 2640 kg/m^3 and is more than 20 km thick locally in the area where the
635 Vestfjorden-Sarek gravity low is observed (cf. Figures 7a and 10b). Lithologically, this layer
636 can be represented by metasediments and/or granite. The last upper-crustal layer (Figure 10c;
637 UC3) has been assigned a typical average upper-crustal density of 2675 kg/m^3. This regional
638 upper-crustal layer is thickest (more than 12-15 km) within the areas where sedimentary rocks
639 are thin or absent, whereas outlines of all sedimentary depocentres are clearly distinguished
640 by either strong thinning or even the absence of this layer (cf. Figures 4, 8 and 10c). The latter
641 indicates that a large part of the crystalline crust is relatively dense beneath the sedimentary
642 depocentres where thick sedimentary successions are present and has thus not been assigned
643 to the upper-crustal layer.
644 The modeled middle crust (Figure 10d; MC) can be interpreted as granitoids and/or
645 gneisses within the continental crustal domain, having a density of 2745-2775 kg/m^3 (less
646 dense in the southwestern part of the model). The thickness pattern of the continental middle-
647 crustal layer (Figures 10d) shows strong thinning and/or pinching out beneath the sedimentary
648 depocentres and thickening in the areas where sedimentary rocks are thin or absent. This
649 continental middle-crustal layer is thickest (more than 17-22 km thick) beneath the Lofoten-
650 Vesterålen archipelago (Figure 10d). Oceanic layer 3A (Figure 10e) corresponds to the
651 oceanic gabbroic middle crust and has a thickness in the range of 3-5 km on average.

Four layers have been included in the lower crust of the study area. The uppermost lower-crustal layer represents the lower crust of Baltica (Figure 10f; LC). This layer has been only modeled beneath the mainland and the Lofoten-Vesterålen archipelago and its limit of distribution is almost parallel to the coast of Norway. This layer is the thickest in the southwestern part of the studied mainland where it is more than 17-18 km thick (Figure 10f). The next lower-crustal layer is related to the high-density zones within the crystalline crust of the model area (Figure 11a). The geometry of the high-density lower-crustal layer has been kept to be closer to the initial shape of high-velocity lower-crustal layer. The less dense high-density intracrustal layer has been used to overcome this restriction in a proper way. This layer consists of several thick bodies beneath the continental margin, reaching up to more than 10 km beneath the Lofoten islands (Figure 11a). The lowermost crustal layer in the model is a high-density lower-crustal layer which consists of the two separated units: (1) the continental high-density lower crust (Figure 11b) and (2) the high-density lower oceanic crust (Figure 11c). The high-density lower-crustal layer corresponds to the lower-crustal and high-velocity lower-crustal layers according to Ocean Bottom Seismometers experiments [*Breivik et al.*, 2014; *Kodaira et al.,* 1995; *Mjelde et al.,* 1992, 1993, 1996, 2001, 2003]. The continental part of this high-density lower-crustal layer is characterized by the presence of the very thick narrow bodies, of more than 12 km, observed beneath the Nyk and Utgard highs and along the western coast of the Lofoten-Vesterålen archipelago (Figure 11b). There are also wide zones of the relatively thick high-density lower crust (up to 9.5 km thick) immediately to the south of the Vestfjorden Basin and beneath the Utrøst Ridge.

The significantly thickened high-density lower crust beneath the Nyk High is a part of the high-velocity lower-crustal body with P-wave velocities from 7.1 km/s to 7.6 km/s [e.g., *Mjelde et al.,* 2009]. According to *Mjelde et al.* [2009, 2016] this lower-crustal body (see red frame in Figure 11b) continues with almost identical physical properties into oceanic layer 3B (OL3B) across the continent-ocean boundary. Actually, the density of 3040 kg/m^3 has been taken to be the same for the oceanic layer 3B (Figure 11c) and the part of the continental high-density lower crust which corresponds to the Vøring high-velocity lower-crustal body from *Mjelde et al.* [2009].

The oceanic layer 3B consists of ultramafic rocks and is characterized by NE-SW-trending areas of thickening near the continent-ocean boundary (Figure 11c). The oceanic lower-crustal layer is more than 5 km thick in the northeast and reaches more than 7 km within the southwestern part where it encounters the Vøring high-velocity lower-crustal body deduced from the OBS data [Mjelde et al., 2009].

686
687 5.4 Final 3D model
688
689 The finally obtained 3D structural/density model is shown in Figure 12. The horizontal
690 grid spacing of the model is 4 km at the level of the sedimentary cover and 16 km at the level
691 of the crystalline crust. The coordinate system used is the Universal Transverse Mercator
692 (UTM) zone 32 (Northern Hemisphere), based on the World Geodetic System 1984
693 (WGS84). The final 3D model consists of 18 layers from the base of the lithosphere to the
694 present-day Earth´s surface, summarized in Table 2.
695 To illustrate the overall crustal architecture of the LVCM, selected cross-sectional
696 snap-shots through the 3D structural/density model are shown along three selected W-E-
697 running 2D vertical slices (Figure 13) and two NE-SW-trending slices (Figure 14). The
698 locations of these five vertical slices (Figure 6) have been chosen to illustrate the major
699 tectonic and structural features across the study area (Figures 13 and 14).
700 The first vertical slice (Line 1) is located within the southern part of the model area
701 (Figure 6), crossing the Vøring Basin, the Trøndelag Platform and the mainland. Along this
702 slice (Figure 13a), a significant thickening of the high-density lower-crustal layer is visible
703 within the Utgard High, demonstrating that sedimentary rocks lie directly on the more than 10
704 km-thick high-density crystalline rocks. The internal structure of the Cretaceous Træna Basin
705 is clearly distinguished by the thick Cretaceous depocentre, whereas the Trøndelag Platform is
706 highlighted by an increased thickness of the pre-Cretaceous strata (Figure 13a).
707 Along the second vertical slice (Line 2), the Early Cretaceous Ribban and Vestfjorden
708 basins are shown (Figure 13b). The main reason for selecting this vertical slice is related to
709 two prominent gravity anomalies, such as the Lofoten gravity high over the Lofoten Ridge
710 and the Vestfjorden-Sarek gravity low over the eastern part of the Vestfjorden and the
711 adjacent mainland. The modelled Lofoten gravity high mainly originated from the
712 superimposed effects of the density contrasts related to the presence of the high-density
713 upper-crustal rocks (UC1), the uplifted and thickened lower-middle crust (MC). Immediately
714 to the east, the modeled remarkably thickened low-density upper-crustal layer (UC2) is
715 mainly responsible for the Vestfjorden-Sarek gravity low. A similar interpretation has been
716 proposed by *Olesen et al.* [2002] and *Gradmann and Ebbing* [2015] who have also introduced
717 a low-density granitic body to explain the Vestfjorden-Sarek gravity low. Besides, *Gradmann*
718 *and Ebbing* [2015] have shown that an additional contribution from a deeper source in the
719 lithospheric mantle (LM) is also possible. In our model this additional deep source is

720 represented by the atypical low-density mantle, which is outlined by the white lines along this
721 slice (Figure 13b).
722 Towards the north, the next slice (Line 3) shows the northern continuation of the low-
723 density upper-crustal layer (UC2) described above. In addition, the internal structure of the
724 Røst and the Cenozoic Lofoten basins is demonstrated (Figure 13c). Along this section, the
725 gravity low over the Røst Basin is partially associated with the thick sedimentary rocks (S4-6)
726 modeled and expected beneath the syn-breakup basalts.
727 Vertical slices 1, 2 and 3 are also interesting in terms of the regional-scale gravity
728 response associated with the positions of the Moho and lithosphere-asthenosphere boundary.
729 It is obvious that both the Moho and the base of the lithosphere appear to become shallower
730 towards the west (Figure 9). The Moho uplift is associated with an uplift of the high-density
731 mantle material which is only partially compensated by the presence of the relatively thick
732 low-density sedimentary rocks within the different depocentres. A constant density in the
733 upper mantle (LM) below the continental and the oceanic lithospheric domains would cause a
734 long-wavelength misfit between the observed and modeled gravity of more than 80-100 mGal
735 in the western part of the slices in Figure 13. Consequently, the oceanic mantle has to be less
736 dense than the continental one. Similar issues and discrepancies have already been modelled
737 to be related to the large thermal effect of the oceanic lithosphere of the North Atlantic region
738 [*Breivik et al.*, 1999; *Maystrenko and Scheck-Wenderoth*, 2009; *Maystrenko and Gernigon*,
739 2015; *Olesen et al.*, 2002; *Ritzmann et al.*, 2002; *Schmidt-Aursch and Jokat*, 2005]. In our
740 study, the regional thermal effect of the oceanic lithosphere has been included into the 3D
741 structural/density model by a density jump from 3160 to 3220 kg/m^3 at the lithosphere-
742 asthenosphere boundary (Figure 9c). Therefore, the varying depth to the lithosphere-
743 asthenosphere boundary 'mimics' different thermal gradients within the crust: where
744 lithosphere is thick, the thermal gradient is low, and where the lithosphere is thin, the thermal
745 gradient is high.
746 Vertical slices 4 and 5 (Lines 4 and 5) demonstrate the necessity to include a low-
747 density lithospheric mantle (LM) beneath the LVCM (Figure 14). The homogeneous
748 lithospheric mantle throughout the whole continental margin imposes a 40-60 mGal misfit
749 between the observed and modeled gravity which is especially pronounced over the Lofoten
750 Ridge (Figure 14b).
751
752 **6 Discussion**
753

754 6.1 Sedimentary infill of the Røst Basin
755
756 A remarkable gravity low is observed over the Røst Basin (Figure 7a) where deep
757 Paleocene, Cretaceous and pre-Cretaceous structural levels are masked by the syn-breakup
758 basaltic lavas. Unfortunately, the gravity pattern over the Røst Basin is complicated by the
759 bathymetry effect which has a relatively steep gradient at the continental slope with a jump
760 from 200-400 m on the continental shelf to more than 3 km on the abyssal plain of the
761 Lofoten Basin (cf. Figures 2 and 7). This increase in water depth creates a mass deficit which
762 is partially responsible for the Røst gravity low. In addition, there are two mapped Quaternary
763 submarine slides, the Nyk and Trænadjupet slides [*Hjelstuen et al.*, 2007; *Laberg and Vorren*,
764 2000; *Lindberg et al.*, 2004], and additional smaller and, presumably, older ones are present
765 along the continental slope, implying that the uppermost sedimentary rocks are most likely
766 affected by a lesser degree of compaction. Therefore, the increased bathymetry and lower
767 dense Cenozoic sedimentary rocks are partially responsible for the Røst Basin gravity low.
768 Furthermore, the above-described mass deficit is overcompensated by relatively dense
769 basaltic lavas (Figure 8a) and by the uplifted mantle material expected due to the sharp
770 necking of the crust observed towards the Røst Basin (Figure 9b). Additional mass deficit
771 could be explained by the presence of Paleocene-Cretaceous and pre-Cretaceous sedimentary
772 rocks. Limited reflection seismic data [*Mokhtari and Pegrum*, 1992], deep refraction seismic
773 lines [*Mjelde et al.,* 1992] and previous 2D/3D gravity models [*Sellevoll et al.,* 1988; *Olesen*
774 *et al.,* 2002; *Tsikalas et al.,* 2005] indicate that the basaltic lava is definitely underlain by a
775 relatively thick sedimentary succession. The problem remains as to how to define the
776 thickness and age of this sub-basaltic sediments. According to structural relationships
777 between the adjacent areas of the Vøring Basin (e.g., Hel Graben) and the Lofoten-Vesterålen
778 margin, these presumed sedimentary rocks should be mainly Cretaceous-Paleocene in age.
779 This is especially likely in the context of the drilled thick Paleocene in the Hel Graben [e.g.,
780 *Lundin et al.,* 2013], implying an option to also have similar thick Paleocene successions
781 within the Røst Basin as well. Furthermore, structural and gravity correlation with the Trømsø
782 and Bjørnøya basins 300-600 km farther north also suggests that the low gravity trend
783 observed along the necking zone of the shelf coincides with thick, syn-rift, Cretaceous
784 depocentres lying either directly on top of very thin crust or directly on top of exhumed and
785 boudined lower crust or possibly exhumed and partly serpentinized mantle [e.g., *Gernigon et*
786 *al.*, 2015]. The possible presence of older Mesozoic (Triassic-Jurassic) or Paleozoic
787 sedimentary rocks is not clear because none of them have been drilled in the vicinity of the

788 Røst Basin. On the other hand, Upper Permian limestone has been drilled at the western
789 margin of the Nordland Ridge and can be correlated with the Permian in East Greenland
790 [*Halland et al.*, 2014], supporting a possibility for the presence of the Permian in the Røst
791 Basin. Triassic-Jurassic rocks which have been drilled at the eastern slope of the Utrøst Ridge
792 [*Hansen,* 2009; *SINTEF,* 2016] could be present underneath the basalts as well. In this case,
793 the modeled thick sedimentary rocks within the Røst Basin (Figure 8d) can also include
794 Jurassic sedimentary rocks, the upper sequence of which is regarded as the main source rocks
795 for hydrocarbons found so far on the Norwegian Continental Shelf. The latter implies that the
796 Røst Basin can be considered as a potential area for exploration and prospecting of deep-
797 water oil and gas resources beneath the basalts.
798
799 6.2 The Lofoten gravity high
800
801 The Lofoten gravity high (Figures 1b and 7) has a complex origin from the several
802 depth levels. First of all, there is a clear spatial correlation between the position of the Lofoten
803 positive gravity anomaly and the Lofoten archipelago (c.f. Figures 1a and 1b) which is
804 characterized by a relatively high topography (more than 500-700 m locally) compared to the
805 adjacent onshore areas where depth to the sea floor is around 100 m on average, reaching
806 more than 400 m in the Vestfjorden. Therefore, the free-air gravity anomaly over the Lofoten
807 archipelago is partially associated with the density contrast related to the difference in
808 elevation. The second level is also obvious and is related to a density contrast between the
809 uplifted crystalline rocks of the Lofoten Ridge and relatively low-density sedimentary rocks
810 within the adjoining Ribban and Vestfjorden basins (Figure 9a). However, the above-
811 described observable jumps in densities at the level of the upper crust are not sufficient to
812 produce more than a 120 mGal gravity high over the Lofoten Ridge. Therefore, other density
813 contrasts are required in order to produce this gravity anomaly. These additional density
814 contrasts are related to the uplifted Moho within the southeastern part of the Lofoten Ridge
815 (Figure 9b) and are associated mainly with the increased density of the crystalline rocks
816 within the Lofoten Ridge (Figures 10a and d) in contrast to the modelled low-density
817 crystalline rocks in the vicinity of the Ribban and Vestfjorden basins (Figures 10b and c). The
818 crystalline rocks of the Lofoten Ridge are represented by mangerite and different gabbroic to
819 anorthositic rocks which are well mapped at the surface of the Lofoten archipelago [e.g.,
820 *Sigmond*, 2002]. According to the measured densities of rock samples in Norway [*Olesen et*
821 *al.*, 2010], the crystalline rocks from the Lofoten area are characterized by increased densities,

822 ranging from 2750 kg/m3 within a large part of the Lofoten Ridge to more than 2850 kg/m3
823 within the southeastern part of the ridge. In the case of our 3D model, this spatial distribution
824 of the measured densities is reflected by a presence of the high-density (2820-2856 kg/m3)
825 upper-crustal rocks within the southeastern part of the Lofoten Ridge (UC1; Figure 10a) and
826 by a strong thickening of the middle crust in the NE (MC; Figure 10d). Moreover, the
827 southeastern part of the Lofoten gravity high is partially associated with an increased
828 thickness of the high-density intracrustal rocks (HDIC; Figure 11a) that, alternatively, can be
829 replaced by increasing thickness of the modeled high-density upper-crustal rocks (UC1;
830 Figure 10a) and, therefore, remains uncertain. As a concluding statement, the results of 3D
831 density modeling indicate that more than 70% of the Lofoten gravity high is mainly
832 associated with the density contrast between the uplifted crystalline rocks with typical middle-
833 crustal densities of 2775 kg/m^3 within the Lofoten Ridge and relatively thick sediments in the
834 Ribban and Vestfjorden basins, as well as a thickening of the low-density upper crust from
835 both sides significantly increases the magnitude of this anomaly. The rest of the above-
836 described density contrasts play a comparatively secondary role in the origin of this positive
837 anomaly.
838
839 6.3 The Vestfjorden-Sarek gravity low
840
841 In the present study, the Vestfjorden-Sarek gravity low is considered to be associated
842 mainly with the extremely thick low-density upper-crustal rocks (UC2) which extend to more
843 than 20 km depth (Figure 10b). In addition, a low-density lithospheric mantle has been
844 included into the 3D density model to compensate the long-wavelength component of the
845 Vestfjorden-Sarek gravity low. In a previous contribution, *Olesen et al.* [2002] managed to
846 reproduce this prominent gravity low during the 3D density modeling without any additional
847 mass deficit in the mantle. *Olesen et al.* [2002] proposed that this low-density body could
848 have been a granitic body of the Transscandinavian Igneous Belt [*Hogdahl et al.*, 2004].
849 Furthermore, *Gradmann and Ebbing* [2015] have tested alternative scenarios to explain the
850 Vestfjorden-Sarek gravity anomaly by modelling gravity and isostasy in a thermally-
851 petrophysically self-consistent model. Their three end-member models comprise (1) a low-
852 density upper crust as a part of the Transscandinavian Igneous Belt; (2) a deeper Moho; and
853 (3) a low-density uppermost mantle. Whereas the gravity fit is acceptable for all scenarios, the
854 isostatic criterion becomes harder to fulfill when deeper low-density sources are involved.
855 The granites of the Transscandinavian Igneous Belt as a likely source for the upper-crustal

856 low-density rocks are favored, yet it should be pointed out that no similar gravity anomaly
857 exists where the Transscandinavian Igneous Belt is present elsewhere (southern and central
858 Sweden as well as through the tectonic windows of Trøndelag, Nordland and Troms into the
859 Precambrian terranes of Lofoten-Vesterålen and the coastal areas of Troms as evidenced by
860 surface outcrops and aeromagnetic data) [*Olesen et al.*, 1997; *Olesen et al.*, 2002].
861 Furthermore, there are no similar granites present where a possible continuation of the gravity
862 low exists in NE Greenland [*Gradmann and Ebbing,* 2015].

863 The present study, which includes low-density material in both the upper crust and the
864 uppermost mantle, generally agrees with the suggestion that the modeled, thick, low-density
865 upper-crustal rocks can represent one of the batholiths of the Transscandinavian Igneous Belt
866 which have been well studied in Sweden [*Hogdahl et al.*, 2004]. The dominant lithology of
867 rocks of the Transscandinavian Igneous Belt is monzodiorite to granite [*Hogdahl et al.*, 2004].
868 The assigned densities for the low-density rocks are very low in both cases, 2640 kg/m^3 in our
869 study and 2660 kg/m^3 in *Olesen et al.* [2002]. These densities seem to be very low for
870 basement rocks. However, the densities of rocks collected in the basement windows within
871 the Vestfjorden-Sarek gravity low can be even lower according to NGU laboratory
872 measurements [*Olesen et al.,* 1993, 2010]. Nevertheless, the density of this granitic body
873 should increase with depth due to lithostatic compression and assuming a typical geothermal
874 gradient [e.g., *Korchin*, 2015]. If a stronger geothermal gradient is assumed, the overall
875 pressure-related density increase with depth can, at least partially, be compensated or
876 smoothed. High heat production of the Transscandinavian Igneous Belt granites, as measured
877 in many parts of central and southern Fennoscandia (average 2.6 μW/m^3, locally up to 4
878 μW/m^3 according to *Slagstad* [2008]), seems to support this idea. However, the granites
879 sampled in the study area show much lower heat production values of less than 1.5 μW/m^3
880 [*Olesen et al.*, 2007b].

881 The recently collected receiver function data [*Ben Mansour et al.,* 2014] indicate that
882 the Vestfjorden-Sarek negative anomaly is not particularly characterized by an extreme
883 thickening of the crust. Alternatively, a deep mantle origin for this gravity anomaly is strongly
884 suggested in our 3D model. A combination between low-density block of the lithospheric
885 mantle and a low-density upper-crustal granitic body is a reasonable explanation for the
886 Vestfjorden-Sarek gravity anomaly. Our conclusion about the origin of this anomaly is thus
887 consistent with the one proposed by *Gradmann and Ebbing* [2015]. They concluded that an
888 upper-crustal source for this anomaly is the most probable one but an additional contribution
889 from a deeper source is required to compensate for an otherwise too high buoyancy. This

deeper source can be represented by the low-density lithospheric mantle (Figure 13b) which is discussed in the next sub-chapter.

Therefore, our preferred interpretation is that the Vestfjorden-Sarek gravity low is mostly associated with a strong thickening of the low-density granitic layer in that area (Figures 10b and 13b). In addition to the crustal origin of this negative gravity anomaly, responsible for a steep gradient of this anomaly, the regional-scale component, related to the atypically low-density mantle, provides up to approximately 30% of the required mass deficit on average as indicated by a difference between the modeled gravity responses for the models with uniform and non-uniform lithospheric mantle in Figure 13b.

For completeness, we would like to mention another possible explanation for the origin of the Vestfjorden-Sarek negative gravity anomaly. Sedimentary or metasedimentary rocks of the pre-Caledonian continental margin of Baltica may still be preserved at great depths beneath the Caledonian allochthon in the area of the Vestfjorden-Sarek anomaly. These hypothetical old sedimentary rocks could be associated with the Vestfjorden-Sarek gravity low. In this case, the question arises: how to explain the presence of the Baltican Precambrian basement rocks which are exposed within the basement windows? Actually, there is no direct evidence that these basement windows necessarily represent the autochtonous crystalline rocks of Baltica. Thus, it is possible to suggest that some of these Precambrian crystalline rocks could be displaced as a part of the Caledonian nappes during the Caledonian Orogeny, assuming that the Caledonian allochthonous rocks were overthrust onto the sedimentary basins of the pre-Caledonian Baltican continental margin. The density of the buried and, thus, highly compacted or even metamorphosed sedimentary rocks should not drastically differ from the low-density crystalline rocks as modeled in this study. The densities of these inferred sedimentary rocks can be even lower than those used for the low-density upper-crustal rocks, allowing us to reduce the thickness of the low-density body. However, this hypothetical suggestion is not yet supported by independent data and is only mentioned to complete the list of possible scenarios for the origin of the Vestfjorden-Sarek negative gravity anomaly.

Additional explanation for the gravity low is that the area is currently undergoing uplift, which is supported by recent studies of neotectonic activity in this region (Olesen et al., 2013). However, the region is relatively small (<100 km in E-W extension) and, depending on the lithosphere's strength, may or may not compensate vertical loads within this region only.

6.4 The high-density lower-crustal layer

924

925 The high-density lower-crustal layer is supposed to be represented by intermediate- to
926 high-grade metarmorphic rocks for the greater part of the study area where densities of 2985-
927 2995 kg/m^3 have been assigned. The nature of the high-density lower crust is most likely
928 different in places with strong thickening of this layer beneath the Nyk and Utgard highs
929 (Figure 11b). Within the Utgard High, almost the entire crystalline crust is represented by the
930 high-density lower-crustal layer which reaches a shallow depth. The very high density (3070
931 kg/m^3) of the entire crystalline crust of the Utgard High can be partially associated with
932 magmatic sills which have been reported from close to the Utgard High and have P-wave
933 velocities of more than 7 km/s [*Berndt et al.*, 2000]. However, the high-density core of the
934 Utgard High is too massive and is located relatively far away from the early Cenozoic
935 breakup to be purely associated with the Cenozoic sill intrusions. Moreover, the Utgard High
936 already affected the deformation pattern and therefore formation occurred much earlier than
937 the Eocene breakup. Therefore, the presence of this central horst is most likely related to
938 inherited high-density Caledonian basement which could have been partly intruded by
939 breakup-induced intrusions [e.g., *Neumann et al.*, 2013].
940 Thickening of high-density lower crust beneath the Nyk High is a part of the high-
941 velocity lower-crustal body [e.g., *Mjelde et al.,* 2009b] which can consist of mafic rocks
942 emplaced during the last rift phase and break-up, representing a mafic underplating close to
943 the base of the continental crust [*Mjelde et al.*, 2016; *Mjelde et al.*, 2009b] or mafic intrusions
944 into the lower continental crust [*White et al.*, 2008]. *Gernigon et al.* [2004] showed, however,
945 that the high-velocity lower-crustal bodies in the outer Vøring Basin influenced the basin
946 geometry and structures before the onset of drastic magmatism. Moreover, *Wangen et al.*
947 [2011] have shown that the scenario with the high-velocity lower-crustal body as only syn-
948 breakup underplating requires an unrealistic amount of extension and, therefore, the origin of
949 this body could be associated with the pre-existing high-density lower crust in addition to syn-
950 breakup underplating. In this case, the high-density lower-crustal layer can also be locally
951 represented by the pre-breakup high-pressure granulite and/or eclogitized rocks related to the
952 Caledonian Orogeny or to serpentinised mantle rocks [*Ebbing et al.*, 2006; *Faleide et al.*,
953 2008; *Gernigon et al.*, 2004; *Gernigon et al.*, 2006; *Mjelde et al.*, 2016; *Raum et al.*, 2006].
954

955 6.5 Low-density mantle
956

In order to be consistent with the observed gravity, our 3D structural/density model requires low-density mantle material beneath the LVCM compared to the Vøring margin (Figures 9b, c). The necessity of having low-density mantle beneath the LVCM is clearly illustrated by Figure 14, which demonstrates that the relatively dense upper and middle crystalline rocks beneath the Lofoten Ridge and the less dense sedimentary cover of the Træna Basin are located at the same depth levels from the Earth's surface to more than 10 km depth (Figure 14a). Moreover, the high-density uppermost mantle rocks are present within the interval of 4-5 km at the same depths as the middle-upper-crustal rocks below the Hel Graben along vertical slice 5 (Figure 14b). In addition, the basaltic oceanic layer 2AB of the Lofoten-Vesterålen segment with the density of 2650 kg/m^3 and the shallow sedimentary rocks of the Hel Graben with the density of less than 2450 kg/m^3 are also at the same depths (Figure 14b). These examples indicate that there is an obvious mass excess within the LVCM compared to the Vøring margin, if the lithospheric mantle has a uniform density. In the case of the homogeneous lithospheric mantle throughout the whole model, a misfit between the modeled gravity and observations reaches more than 40-50 mGal (Figure 14). Reasonable changes in the topography of the lithosphere-asthenosphere boundary cannot compensate this mass excess within the LVCM. We do not have enough data to clearly define the precise geometry of the atypical mantle, nor its density distribution at depth. However, there is a clear mass deficit in the lithospheric mantle beneath the greater part of the LVCM. The whole depth interval of the lithospheric mantle beneath part of the Lofoten-Vesterålen margin has been roughly assigned density of 3185-3202 kg/m^3 which is 18-35 kg/m^3 less compared to the density of 3220 kg/m^3 within the rest of the lithospheric mantle. Theoretically, this mass deficit can also be associated with either a smaller mantle body in the uppermost mantle or a larger one at deeper intervals.

Based on the tomographic estimates, Bannister et al. [1991] obtained a regional-scale low P- and S-wave velocity anomaly in the mantle beneath the Lofoten region and also suggested the presence of atypical low-density sub-Moho material in this area. The tomographic results of Bannister et al. [1991] are supported by a Rayleigh wave tomography by Pilidou et al. [2005] who have shown that the isolated S-wave low-velocity anomalous zone in the mantle at depths of 75-100 km beneath our study area can be traced to depths of 200-250 km where it joins the large low-velocity anomaly beneath the North Atlantic region. However, this low-velocity anomaly is not so obvious but still recognizable in the case of the model of the upper-mantle S-wave velocity beneath northwestern Europe by Weilde and Maupin [2008], a full waveform inversion for upper-mantle structure beneath Europe by

Fichtner and Trampert [2011] and a S-velocity model of the North Atlantic region by Rickers et al. [2013]. Thus, our results are supported by the seismic tomography data, indicating that our low-density upper-mantle zone can be associated with the low-velocity anomaly observed beneath the study area. The origin of the low-density mantle can be related to both thermal and compositional variations. Possibly, it could represent an influence of a remnant of an old subduction slab, as recently imaged and modeled underneath the East Greenland Margin [Schiffer et al., 2016]. Testing this hypothesis will require additional and more detailed investigations, one of which can be density inversion using simultaneously both gravity and seismic tomography data.

6.6 The Bivrost Lineament

According to *Blystad et al.* [1995], the Bivrost Lineament has been originally defined as a dextral shift which could have been active during several tectonic reactivations in the area. Furthermore, there is also pronounced recent seismic activity within the study area [e.g., *Keiding et al.*, 2015], indicating that this area is not tectonically quiet and, consequently, some previously active faults, including the Bivrost Lineament, could have been reactivated. Previously, the Bivrost Lineament has also been traced within the oceanic lithospheric domain as the Bivrost Fracture Zone [*Tsikalas et al,.* 2002], but *Olesen et al.* [2007a] have shown that this interpreted Bivrost Fracture Zone was simply a data artifact due to poor navigation and low resolution of the vintage aeromagnetic datasets. According to their interpretation of new aeromagnetric data, this oceanic fracture zone does not exist.

The NW-SE-trending Bivrost Lineament separates the wide and very deep Vøring Cretaceous sag-basin from the narrow and tectonically uplifted LVCM [*Brekke*, 2000]. Consequently, the Bivrost Lineament is already recognizable at the level of sedimentary cover that is reflected at the top of the crystalline basement geometry (Figure 9a). The distribution of the Cenozoic and the Upper Cretaceous sedimentary rocks (S2-S4) demonstrates that important structural changes in the thickness pattern occur along this boundary, which separates the area with thickened sedimentation in the Vøring Basin from the Lofoten-Vesterålen margin where sedimentary rocks are thin or even absent (Figure 4). Furthermore, the Bivrost Lineament is also pronounced at the level of the Lower Cretaceous and pre-Cretaceous sedimentary successions (Figures 8b-c). The lineament marks the limits between the thick Lower Cretaceous (S5) in the Någrind Syncline and Træna Basin from the northeast, as well as the strongly thickened pre-Cretaceous succession (S6) on the Trøndelag Platform.

Within the middle-upper crust (Figures 10a-d), the Bivrost Lineament is not so prominent and only some minor changes in structural trends can be attributed to this crustal feature. In contrast, the Bivrost Lineament shows thickness pattern variations of the high-density lower-crustal layer (Figure 11b; HDLC). The thickened high-density lower crust of the Nyk and Utgard highs is possibly shifted in relation to thickened high-density lower-crustal layer (HDLC) located beneath the Røst High and immediately to the south of the Vestfjorden Basin. The latter suggests the presence of a major transfer zone that affects both sedimentary and deeper crustal levels. Besides, the high-density lower-crustal layer is featured by the wide and moderately thickened zones on the northeastern side of the Bivrost Lineament, whereas the strongly thickened zones of this layer are narrow on the southwestern side of the lineament (Figure 11b). Furthermore, the Moho uplifts beneath the Røst Basin and the southwestern Lofoten Ridge are directly located in front of the Moho depressions on the opposite side of the Bivrost Lineament (Figure 9b). This contrast is particularly obvious between the uplifted Moho beneath the Røst Basin and the deeper Moho beneath the northwestern part of the Vøring Basin with a depth difference is more than 8 km across the lineament. Finally, the southwestern limit of the inferred low-density lithospheric mantle is also bounded by the Bivrost Lineament (Figures 9b-c), indicating that this lineament also reflects a mantle boundary. It seems that the presence of the Bivrost Lineament and the related first-order segmentation of the Mid-Norwegian margin, can be tracked down to the mantle level. Thus, the Bivrost Lineament is the major crustal contact and a long-life transfer system that has influenced the crust and sedimentary basin segmentation since the beginning of the rifting on the Mid-Norwegian continental margin. The Bivrost Lineament may also coincide with the Nesna Shear Zone onshore [*Eide et al.*, 2002; *Olesen et al.,* 2002]. However, this reactivated detachment zone is probably restricted to upper-crustal levels (a pre-existing nappe contact) and has not necessarily affected the whole continental crust. However, a deeper Precambrian contact and/or shear zone controlling the location of the Nesna Shear Zone before, during and after the Caledonian collapse cannot be excluded.

Despite significant influence at both crustal and mantle levels, the contrasting physical properties along the Bivrost transfer system did not influence the segmentation of the adjacent oceanic lithosphere in terms of a fracture zone. This contrasts with the Jan Mayen tectonic corridor which represents a regional-scale transfer zone between the Møre and Vøring basins and is reflected by the structural style of the pre-Cretaceous and Early Cretaceous rift system [*Gernigon et al.,* 2015]. The Jan Mayen corridor seems to have influenced the late segmentation of the adjacent oceanic domain [*Gernigon et al.,* 2015]. Surprisingly, this is not

the case for the Bivrost Lineament. The Jan Mayen corridor appears to be a wider crustal transfer system compared with the Bivrost Lineament. The Jan Mayen corridor also separated the intra-sag crustal regions which have been affected by serious crustal thinning, whereas the Brivrost lineament separates thin from thicker crustal domains (sag/platform). Despite these differences it remains unclear why the 'almost' similar lithosphere-scale Bivrost fault zone did not guide or influence the strain localization and the formation of the oceanic fracture zone during the continental breakup in the early Cenozoic.

7 Conclusions

The main achievements of this study may be summarized as the following:

The lithosphere-scale 3D structural/density model of the LVCM and the northern Vøring margin, including adjacent continental and oceanic domains, has been successfully constructed. The obtained 3D model summarizes our current knowledge about both the sedimentary cover and the crystalline crust of the study area, showing that the top of the crystalline basement is deeply located within the Vøring Basin. The Trøndelag Platform is characterized by moderate depths to the basement and the Lofoten-Vesterålen margin has a generally uplifted basement. According to the 3D density modeling, the sub-basaltic Røst Basin is characterized by the presence of relatively thick Cretaceous-Paleocene and possibly older sedimentary successions.

The Vestfjorden-Sarek gravity low is most likely related to the presence of a low-density thick granitic body within the middle-upper crystalline crust. Alternatively or in addition to the low-density granite, this gravity low can be also partially associated with old pre-Caledonian metasedimentary rocks.

The obtained Moho topography varies generally from shallower than 11 km beneath the oceanic crustal domain to more than 48 km beneath the mainland. The investigated continental margin is characterized by a significantly varying depth to the Moho which is uplifted beneath the Røst Basin, the Utgard High and the Lofoten Ridge.

The results of the 3D density modeling indicate two types of large-scale density heterogeneities in the lithospheric mantle. The first density heterogeneity is related to an increase of mantle temperatures towards the Mid-Atlantic Ridge. The second one is an (inherited?) low-density zone within the lithospheric mantle modeled beneath a large part of the LVCM. The precise shape of the low-density mantle zone is not defined in detail and its origin can be associated with both thermal disturbances and compositional variations.

Finally, the Bivrost Lineament appears to be a deep-seated crustal and lithospheric transfer zone, along which both sedimentary, crustal and mantle blocks with contrasting densities and diverse thicknesses are juxtaposed. Our study highlights the presence of lateral rheological heterogeneities which may explain the first-order segmentation of the Mid-Norwegian margin. In this case, the Bivrost Lineament can be interpreted as a long-lived, inherited, rheologically weak zone which controlled the rift segmentation and the first-order structural style of the Mid-Norwegian continental margin. Compared to similar large-scale transfer systems along the Mid-Norwegian continental margin (e.g., the Jan Mayen tectonic corridor), its influence on subsequent oceanic segmentation is limited.

Acknowledgements

This study has been performed in the framework of the NEONOR2 project, 'Neotectonics in Nordland - implications for petroleum exploration'. The project is supported by the Norwegian Research Council, Aker BP, DEA, DONG Energy, the Geological Survey of Norway (NGU), Lundin, Maersk Oil, Noreco, Norske Shell, Norwegian Petroleum Directorate, Repsol, Statoil and VNG. We are grateful to the Marine Geology group at the Geological Survey of Norway (NGU) and especially to Leif Rise for providing us the key data on post-Paleocene sedimentary infill within the study area. We are also grateful to Sabine Schmidt and Christian Plonka for providing help with the IGMAS+ software. The constructed 3D structural model is available by contacting the corresponding author at yuriy.maystrenko@ngu.no. Special thanks go to two anonymous reviewers for valuable and constructive comments which helped to improve the manuscript, and our gratitude to David Roberts for the improved English.

References

Andersen, O. B., P. Knudsen, S. Kenyon, and S. Holmes (2014), Global and arctic marine gravity field from Recent satellite altimetry (dtu13), *Conference and Technical Exhibition - European Association of Geoscientists and Engineers*, *76*.

Artemieva, I. M., and H. Thybo (2013), EUNAseis: A seismic model for Moho and crustal structure in Europe, Greenland, and the North Atlantic region, *Tectonophysics*, *609*, 97-153.

Artemieva, I. M., H. Thybo, and M. K. Kaban (2006), Deep Europe today; geophysical synthesis of the upper mantle structure and lithospheric processes over 3.5 Ga, *Memoirs of the Geological Society of London*, *32*, 11-41.

Avedik, F., D. Berendsen, H. Fucke, S. Goldflam, H. Hirschleber, R. Meissner, M. A. Sellevoll, and W. Weinrebe (1984), Seismic investigations along the Scandinavian 'Blue Norma' profile, *Annales Geophysicae [1983]*, *2*(5), 571-577.

Bannister, S. C., B. O. Ruud, and E. S. Husebye (1991), Tomographic estimates of sub-Moho seismic velocities in Fennoscandia and structural implications, *Tectonophysics*, *189*(1-4), 37-53.

Ben Mansour, W., M. Moorkamp, R. W. England (2014), Joint inversion of seismological data and magnetotelluric data for the northern Scandinavian mountains. AGU Fall Meeting, Abstract T23B-4668, San Francisco, USA

Bergh, S. G., K. Eig, O. S. Kløvjan, T. Henningsen, O. Olesen, and J. A. Hansen (2007), The Lofoten-Vesteralen continental margin: a multiphase Mesozoic-Palaeogene rifted shelf as shown by offshore-on shore brittle fault-fracture analysis, *Norw J Geol*, *87*(1-2), 29-58.

Berndt, C., O. P. Skogly, S. Planke, O. Eldholm, and R. Mjelde (2000), High-velocity break-up related sills in the Vøring Basin off Norway, *Journal of Geophysical Research*, *105*(B12), 28443-28455.

Berndt, C., S. Planke, E. Alvestad, F. Tsikalas, and T. Rasmussen (2001), Seismic volcanostratigraphy of the Norwegian Margin: constraints on tectonomagmatic break-up processes, *J Geol Soc London*, *158*, 413-426.

Blystad, P., H. Brekke, R. B. Færseth, B. T. Larsen, J. Skogseid, and B. Tørudbakken (1995), Structural elements of the Norwegian continental shelf, Part II. The Norwegian Sea Region, *Norwegian Petroleum Directorate Bulletin*, *8*, 0-45.

Breivik, A.J., J.I. Faleide, R. Mjelde, R. Flueh (2009), Magma productivity and early seafloor spreading rate correlation on the northern Vøring Margin, Norway - Constraints on mantle melting, *Tectonophysics*, 468, 206-223.

Breivik, A.J., J.I. Faleide, R. Mjelde, Y. Murai, E.R. Flueh (2014), Breakup Style and Magmatic Underplating West of the Lofoten Islands, Norway, Based on OBS Data, AGU Fall meeting, Abstract T53B-4673, San Francisco, USA.

Breivik, A. J., J. Verhoef, and J. I. Faleide (1999), Effect of thermal contrasts on gravity modeling at passive margins: Results from the western Barents Sea, *J Geophys Res-Sol Ea*, *104*(B7), 15293-15311.

Brekke, H. (2000), The tectonic evolution of the Norwegian Sea continental margin with emphasis on the Vøring and Møre basins. In Nøttvedt, A. et al. (eds.) Dynamics of the Norwegian Margin, *Geological Society, London, Special Publications*, *136*, 327-378.

Broenner, M., L. Gernigon, and A. Nasuti (2013), Lofoten-Vesterålen Aeromagnetic Survey 2011 – LOVAS-11 – Acquisition, processing and interpretation report *Rep.NGU*

Calcagnile, G. (1982), The lithosphere-asthenosphere system in Fennoscandia, *Tectonophysics*, *90*(1-2), 19-35.

Chand, S., L. Rise, J. Knies, H. Haflidason, B. O. Hjelstuen, and R. Boe (2011), Stratigraphic development of the south Voring margin (Mid-Norway) since early Cenozoic time and its influence on subsurface fluid flow, *Mar Petrol Geol*, *28*(7), 1350-1363.

Christensen, N. I., and W. D. Mooney (1995), Seismic velocity structure and composition of the continental crust; a global view, *Journal of Geophysical Research*, *100*(B6), 9761-9788.

Dowdeswell, J. A., D. Ottesen, and L. Rise (2006), Flow switching and large-scale deposition by ice streams draining former ice sheets, *Geology [Boulder]*, *34*(4), 313-316.

Dowdeswell, J. A., D. Ottesen, and L. Rise (2010), Rates of sediment delivery from the Fennoscandian ice sheet through an ice age, *Geology [Boulder]*, *38*(1), 3-6.

Drivenes, G., M. A. Sellevoll, V. Renard, F. Avedik, and J. Pajchel (1984), The continental margin/crustal structure off the Lofoten Islands, Northern Norway. In: Spencer, A.M. petroleum Geology of the North European Margin, *London, Graham & Trotman*, 211-216.

Ebbing, J., and O. Olesen (2010), New compilation of top basement and basement thickness for the Norwegian continental shelf reveals the segmentation of the passive margin system, *Petroleum Geology Conference Proceedings*, *7*, 885-897.

Ebbing, J., E. Lundin, O. Olesen, and E. K. Hansen (2006), The mid-Norwegian margin: a discussion of crustal lineaments, mafic intrusions, and remnants of the Caledonian root by 3D density modelling and structural interpretation, *J Geol Soc London*, *163*, 47-59.

Ebbing, J., R. W. England, T. Korja, T. Lauritsen, O. Olesen, W. Stratford, and C. Weidle (2012), Structure of the Scandes lithosphere from surface to depth, *Tectonophysics*, *536*, 1-24.

Eide, E.A., P.T. Osmundsen, G.B. Meyer, M.A. Kendrick, F. Corfu (2002), The Nesna Shear Zone, north-central Norway: an 40Ar/39Ar record of Early Devonian - Early Carboniferous ductile extension and unroofing, *Norw J Geol*, 82(4), 317-339.

Eidvin, T., and Y. Rundberg (2007), Post-Eocene strata of the southern Viking Graben, northern North Sea; integrated biostratigraphic, strontium isotopic and lithostratigraphic study, *Norw J Geol*, *87*(4), 391-450.

Eidvin, T., T. Bugge, and M. Smelror (2007), The Molo Formation, deposited by coastal progradation on the inner Mid-Norwegian continental shelf, coeval with the Kai Formation to the west and the Utsira Formation in the North Sea, *Norw J Geol*, *87*(1-2), 75-142.

Eidvin, T., F. Riis, and E. S. Rasmussen (2014), Oligocene to lower Pliocene deposits of the Norwegian continental shelf, Norwegian Sea, Svalbard, Denmark and their relation to the uplift of Fennoscandia; a synthesis, *Mar Petrol Geol*, *56*, 184-221.

Eig, K. (2012), Lofoten and Vesteralen; promised land or Fata Morgana?, *GEO ExPro*, *9*(5), 54-58.

Faleide, J. I., F. Tsikalas, A. J. Breivik, R. Mjelde, O. Ritzmann, O. Engen, J. Wilson, and O. Eldholm (2008), Structure and evolution of the continental margin off Norway and Barents Sea, *Episodes*, *31*(1), 82-91.

Fichler, C., E. Rundhovde, O. Olesen, B. M. Saether, H. Rueslatten, E. Lundin, and A. G. Dore (1999), Regional tectonic interpretation of image enhanced gravity and magnetic data covering the mid-Norwegian shelf and adjacent mainland, *Tectonophysics*, *306*(2), 183-197.

Fichtner, A., and J. Trampert (2011), Resolution analysis in full waveform inversion, *Geophys J Int*, *187*(3), 1604-1624.

Fossen, H. (2010), Extensional tectonics in the North Atlantic Caledonides: a regional view, in *Continental Tectonics and Mountain Building: The Legacy of Peach and Horne*, edited by R. D. Law, R. W. H. Butler, R. E. Holdsworth, M. Krabbendam and R. A. Strachan, pp. 767-793, The Geological Society of London, London.

Færseth, R. B. (2012), Structural development of the continental shelf offshore Lofoten–Vesterålen, northern Norway, *Norw J Geol*, *92*, 19-40.
Gee, D. G., H. Fossen, N. Henriksen, and A. K. Higgins (2008), From the early Paleozoic platforms of Baltica and Laurentia to the Caledonide orogen of Scandinavia and Greenland, *Episodes*, *31*(1), 44-51.
Gernigon, L., J. Koziel, and A. Nasuti (2012), Jan Mayen Aeromagnetic Survey JAS-12 – Part A: acquisition and processing., *report Rep. 2012.069*, 117 pp, Geological Survey of Norway (NGU), Trondheim.
Gernigon, L., J. C. Ringenbach, S. Planke, and B. Le Gall (2004), Deep structures and breakup along volcanic rifted margins: insights from integrated studies along the outer Voring Basin (Norway), *Mar Petrol Geol*, *21*(3), 363-372.
Gernigon, L., A. Blischke, A. Nasuti, and M. Sand (2015), Conjugate volcanic rifted margins, sea-floor spreading, and microcontinent; insights from new high-resolution aeromagnetic surveys in the Norway Basin, *Tectonics*, *34*(5), 907-933.
Gernigon, L., F. Lucazeau, F. Brigaud, J. C. Ringenbach, S. Planke, and B. Le Gall (2006), A moderate melting model for the Voring margin (Norway) based on structural observations and a thermo-kinematical modelling: Implication for the meaning of the lower-crustal bodies, *Tectonophysics*, *412*(3-4), 255-278.
Goldschmidt-Rokita, A., M. A. Sellevoll, H. B. Hirschleber, and F. Avedik (1988), Results of two seismic refraction profiles off Lofoten, Northern Norway, *Special Publication - Norges Geologiske Undersokelse*, *3*, 49-57.
Grad, M., T. Tiira, and ESC-Working-Group (2009), The Moho depth map of the European Plate, *Geophys J Int*, *176*(1), 279-292.
Gradmann, S., and J. Ebbing (2015), Large-scale gravity anomaly in Northern Norway; tectonic implications of shallow or deep source depth and a possible conjugate in northeast Greenland, *Geophys J Int*, *203*(3), 2070-2088.
Götze, H. J. (1978), Ein numerisches Verfahren zur Berechnung der gravimetrischen Feldgrößen drei-dimensionaler Modellkörper, *Arch. Met. Geoph. Biokl. Ser.*, *A(25)*, 195-215.
Götze, H. J., and B. Lahmeyer (1988), Application of three-dimensional interactive modeling in gravity and magnetics, *Geophysics*, *53*(8), 1096-1108.
Götze, H.-J. (2010), IGMAS+; a new 3D gravity, FTG and magnetic modelling software tool, *Rep.*, 91-96 pp, Geoscience Australia : Canberra, A.C.T., Australia.
Halland, E. e. a. (2014), CO2 storage Atlas, Norwegian Continental Shelf, edited, http://www.npd.no/en/Publications/Reports/Compiled-CO2-atlas/.
Hansen, J., D. A. Jerram, K. McCaffrey, and S. R. Passey (2009), The onset of the North Atlantic Igneous Province in a rifting perspective, *Geological Magazine*, *146*(3), 309-325.
Hansen, J. A. (2009), Onshore-offshore tectonic relations on the Lofoten and Vesterålen Margin, *A dissertation for the degree of Philosophiae Doctor*, 229.
Hansen, J. A., S. G. Bergh, and T. Henningsen (2012), Mesozoic rifting and basin evolution on the Lofoten and Vesterålen Margin, North-Norway; time constraints and regional implications, *Norw J Geol*, *91*, 203-228.
Hjelstuen, B. O., O. Eldholm, and J. I. Faleide (2007), Recurrent Pleistocene mega-failures on the SW Barents Sea margin, *Earth and Planetary Science Letters*, *258*(3-4), 605-618.
Hogdahl, K., U. B. Andersson, and O. Eklund (2004), The Transscandinavian igneous belt (TIB) in Sweden; a review of its character and evolution*Rep.*, Geological Survey of Finland : Espoo, Finland, Finland.
Keiding, M., C. Kreemer, C. D. Lindholm, S. Gradmann, O. Olesen, and H. P. Kierulf (2015), A comparison of strain rates and seismicity for Fennoscandia; depth dependency of deformation from glacial isostatic adjustment, *Geophys J Int*, *202*(2), 1021-1028.

Kelly, A., R. W. England, and P. K. H. Maguire (2007), A crustal seismic velocity model for the UK, Ireland and surrounding seas, *Geophys J Int*, *171*(3), 1172-1184.
Kodaira, S., A. Goldschmidt-Rokita, J. M. Hartmann, H. B. Hirschleber, T. Iwasaki, T. Kanazawa, H. Krahn, S. Tomita, and H. Shimamura (1995), Crustal structure of the Lofoten continental margin, off northern Norway, from ocean-bottom seismographic studies, *Geophys J Int*, *121*(3), 907-924.
Korchin, V. A. (2015), Low-velocity zones of thermobaric origin in the crystalline crust, *Geophys J Int*, *37*(5), 46-65.
Laberg, J. S., and T. O. Vorren (2000), The Traenadjupet Slide, offshore Norway; morphology, evacuation and triggering mechanisms, *Marine Geology*, *171*(1-4), 95-114.
Lien, T. (2005), From rifting to drifting: effects on the development of deep-water hydrocarbon reservoirs in a passive margin setting, Norwegian Sea, *Norw J Geol*, *85*(4), 319-332.
Lindberg, B., J. S. Laberg, and T. O. Vorren (2004), The Nyk Slide; morphology, progression, and age of a partly buried submarine slide offshore northern Norway, *Marine Geology*, *213*(1-4), 277-289.
Lundin, E. R., A. G. Dore, K. Ronning, and R. Kyrkjebo (2013), Repeated inversion and collapse in the Late Cretaceous-Cenozoic northern Voring Basin, offshore Norway, *Petroleum Geoscience*, *19*(4), 329-341.
Løseth, H., and E. Tveten (1996), Post-Caledonian structural evolution of the Lofoten and Vesterålen offshore and onshore areas, *Norsk Geol Tidsskr*, *76*, 215-230.
Maystrenko, Y., and M. Scheck-Wenderoth (2009), Density contrasts in the upper mantle and lower crust across the continent-ocean transition: constraints from 3-D gravity modelling at the Norwegian margin, *Geophys J Int*, *179*(1), 536-548.
Maystrenko, Y., and L. Gernigon (2015), 3D crustal and thermal modelling, in *COOP Phase 2 - Crustal Onshore-Ofshore Project*, edited by O. Olesen, et al., pp. 215-375.
Mjelde, R., S. Kodaira, and M. A. Sellevoll (1996), Crustal structure of the Lofoten Margin, N Norway, from normal incidence and wide-angle seismic data: A review, *Norsk Geol Tidsskr*, *76*(3), 187-198.
Mjelde, R., A. Goncharov, and R. D. Muller (2013), The Moho; boundary above upper mantle peridotites or lower-crustal eclogites; a global review and new interpretations for passive margins, *Tectonophysics*, *609*, 636-650.
Mjelde, R., T. Kvarven, J. I. Faleide, and H. Thybo (2016), Lower-crustal high-velocity bodies along North Atlantic passive margins, and their link to Caledonian suture zone eclogites and early Cenozoic magmatism, *Tectonophysics*, *670*, 16-29.
Mjelde, R., M. A. Sellevoll, H. Shimamura, T. Iwasaki, and T. Kanazawa (1992), A Crustal Study Off Lofoten, N Norway, by Use of 3-Component Ocean Bottom Seismographs, *Tectonophysics*, *212*(3-4), 269-288.
Mjelde, R., M. A. Sellevoll, H. Shimamura, T. Iwasaki, and T. Kanazawa (1993a), Crustal Structure beneath Lofoten, N Norway, from Vertical Incidence and Wide-Angle Seismic Data, *Geophys J Int*, *114*(1), 116-126.
Mjelde, R., M. A. Sellevoll, H. Shimamura, T. Iwasaki, and T. Kanazawa (1993b), Ocean Bottom Seismographs Used in a Crustal Study of an Area Covered with Flood-Basalt Off Lofoten, N Norway, *Terra Nova*, *5*(1), 76-84.
Mjelde, R., T. Raum, A. Kandilarov, Y. Murai, and T. Takanami (2009), Crustal structure and evolution of the outer More margin, NE Atlantic, *Tectonophysics*, *468*(1-4), 224-243.
Mjelde, R., H. Shimamura, T. Kanazawa, S. Kodaira, T. Raum, and H. Shiobara (2003), Crustal lineaments, distribution of lower-crustal intrusives and structural evolution of the Voring Margin, NE Atlantic; new insight from wide-angle seismic models, *Tectonophysics*, *369*(3-4), 199-218.

Mjelde, R., S. odaira, H. Shimamura, T. Kanazawa, H. Shiobara, E. W. Berg, and O. Riise (1997), Crustal structure of the central part of the Vøring basin, mid-Norway margin, from ocean bottom seismographs, *Tectonophysics*, *227*, 235-257.

Mjelde, R., J. Kasahara, H. Shimamura, A. Kamimura, T. Kanazawa, S. Kodaira, T. Raum, and H. Shiobara (2002), Lower-crustal seismic velocity-anomalies; magmatic underplating or serpentinized peridotite? Evidence from the Voring Margin, NE Atlantic, *Marine Geophysical Researches*, *23*(2), 169-183.

Mjelde, R., P. Digranes, M. Van Schaack, H. Shimamura, H. Shiobara, S. Kodaira, O. Naess, N. Sorenes, and E. Vagnes (2001), Crustal structure of the outer Voring Plateau, offshore Norway, from ocean bottom seismic and gravity data, *J Geophys Res-Sol Ea*, *106*(B4), 6769-6791.

Mokhtari, M., and R. M. Pegrum (1992), Structure and evolution of the Lofoten continental margin, offshore Norway, *Norsk Geol Tidsskr*, *72*, 339-355.

Muller, R. D., M. Sdrolias, C. Gaina, and W. R. Roest (2008), Age, spreading rates, and spreading asymmetry of the world's ocean crust, *Geochem Geophy Geosy*, *9*.

Neumann, E. R., H. Svensen, C. Tegner, S. Planke, M. Thirlwall, and K. E. Jarvis (2013), Sill and lava geochemistry of the mid-Norway and NE Greenland conjugate margins, *Geochem Geophy Geosy*, *14*(9), 3666-3690.

NPD (2016), The NPD's fact pages; well data summary sheets, edited, Norwegian Petroleum Directorate.

Olesen, O., M. Reitan, and P. O. Sæther (1993), Petrofysisk Database PETBASE 3.0, Brukerbeskrivelse, edited, NGU, Trondheim, Norway.

Olesen, O., T. H. Torsvik, E. Tveten, K. B. Zwaan, H. Loseth, and T. Henningsen (1997), Basement structure of the continental margin in the Lofoten-Lopphavet area, northern Norway: Constraints from potential field data, on-land structural mapping and palaeomagnetic data, *Norsk Geol Tidsskr*, *77*(1), 15-30.

Olesen, O., H. Bungum, C. Lindholm, L. Olsen, C. Pascal, and D. Roberts (2013), Neotectonics, seismicity and contemporary stress field in Norway – mechanisms and implications, in *Geological Survey of Norway Special Publication*, edited, pp. 145-174.

Olesen, O., E. Lundin, O. Nordgulen, P. T. Osmundsen, J. R. Skilbrei, M. A. Smethurst, A. Solli, T. Bugge, and C. Fichler (2002), Bridging the gap between the onshore and offshore geology in Nordland, northern Norway, *Norw J Geol*, *82*(4), 243-262.

Olesen, O., L. H. Blikra, A. Braathen, J. F. Dehls, L. Olsen, L. Rise, D. Roberts, F. Riis, J. I. Faleide, and E. Anda (2004), Neotectonic deformation in Norway and its implications: a review, *Norw J Geol*, *84*(1), 3-34.

Olesen, O., J. Ebbing, E. Lundin, E. Mauring, J. R. Skilbrei, T. H. Torsvik, E. K. Hansen, T. Henningsen, P. Midbøe, and M. Sand (2007a), An improved tectonic model for the Eocene opening of the Norwegian-Greenland Sea: Use of modern magnetic data, *Mar Petrol Geol*, *24*(1), 53-66.

Olesen, O., et al. (2010), New aeromagnetic and gravity compilations from Norway and adjacent areas: methods and applications, *Geological Society, London, Petroleum Geology Conference series*, *7*, 559-586.

Olesen, O., et al. (2007b), KONTIKI Final Report, CONTInental Crust and Heat Generation In 3D, edited.

Olsson, S., R. G. Roberts, and R. Bodvarsson (2008), Moho depth variation in the Baltic Shield from analysis of converted waves, *Gff*, *130*(3), 113-122.

Ottemoller, L., and V. Midzi (2003), The crustal structure of Norway from inversion of teleseismic receiver functions, *Journal of Seismology*, *7*(1), 35-48.

Ottesen, D., J. A. Dowdeswell, L. Rise, and T. Bugge (2012), Large-scale development of the mid-Norwegian shelf over the last three million years and potential for hydrocarbon reservoirs in glacial sediments, *Geological Society Special Publications*, *368*.
Ottesen, D., L. Rise, E. S. Andersen, T. Bugge, and T. Eldvin (2009), Geological evolution of the Norwegian continental shelf between 61 degrees N and 68 degrees N during the last 3 million years, *Norsk Geol Tidsskr*, *89*(4).
Ottesen, D., L. Rise, E. S. Andersen, T. Bugge, and T. Eidvin (2009), Geological evolution of the Norwegian continental shelf between 61 degrees N and 68 degrees N during the last 3 million years, *Norw J Geol*, *89*(4), 251-265.
Pilidou, S., K. Priestley, E. Debayle, and O. Gudmundsson (2005), Rayleigh wave tomography in the North Atlantic; high resolution images of the Iceland, Azores and Eifel mantle plumes, *Lithos*, *79*(3-4), 453-474.
Raum, T., R. Mjelde, H. Shimamura, Y. Mural, E. Brastein, R. M. Karpuz, K. Kravlk, and H. J. Kolsto (2006), Crustal structure and evolution of the southern Voring basin and voring transform margin, NE Atlantic, *Tectonophysics*, *415*(1-4), 167-202.
Redfield, T.F., P.T. Osmundsen (2015), Some remarks on the earthquakes of Fennoscandia: A conceptual seismological model drawn from the perspectives of hyperextension, *Norwegian Journal of Geology*, 94, 233–262.
Reynisson, F. (2010), Deep structure and sub-basalt exploration of the mid-Norwegian margin with emphasis on the Møre margin, PhD thesis, 142 pp, Norwegian University of Science and Technology, Trondheim.
Rickers, F., A. Fichtner, and J. Trampert (2013), The Iceland-Jan Mayen plume system and its impact on mantle dynamics in the North Atlantic region; evidence from full-waveform inversion, *Earth and Planetary Science Letters*, *367*, 39-51.
Riis, F. (1996), Quantification of Cenozoic vertical movements of Scandinavia by correlation of morphological surfaces with offshore data.; Impact of glaciations on basin evolution; data and models from the Norwegian margin and adjacent areas, *Global Planet Change*, *12*, 331-357.
Rise, L., D. Ottesen, K. Berg, and E. Lundin (2005), Large-scale development of the mid-Norwegian margin during the last 3 million years, *Mar Petrol Geol*, *22*(1-2), 33-44.
Rise, L., S. Chand, B. O. Hjelstuen, H. Haflidason, and R. Boe (2010), Late Cenozoic geological development of the south Voring margin, mid-Norway, *Mar Petrol Geol*, *27*(9), 1789-1803.
Rise, L., D. Ottesen, O. Longva, A. Solheim, E. S. Andersen, and S. Ayers (2006), The Sklinnadjupet Slide and its relation to the Elsterian glaciation on the mid-Norwegian margin, *Mar Petrol Geol*, *23*(5), 569-583.
Rise, L., R. Boe, F. Riis, V. K. Bellec, J. S. Laberg, T. Eidvin, S. Elvenes, and T. Thorsnes (2013), The Lofoten-Vesteralen continental margin, north Norway; canyons and mass-movement activity, *Mar Petrol Geol*, *45*, 134-149.
Ritzmann, O., W. Jokat, R. Mjelde, and H. Shimamura (2002), Crustal structure between the Knipovich Ridge and the Van Mijenfjorden (Svalbard), *Marine Geophysical Researches*, *23*(5-6), 379-401.
Roberts, D., and D. G. Gee (1985), An introduction to the structure of the Scandinavian Caleonides, paper presented at The Caledonide Orogen-Scandinavia and related areas, Wiley, Chisterster.
Scheck-Wenderoth, M., T. Raum, J. I. Faleide, R. Wjelde, and B. Horsfield (2007), The transition from the continent to the ocean: a deeper view on the Norwegian margin, *J Geol Soc London*, *164*, 855-868.
Schiffer, C., N. Balling, J. Ebbing, B. H. Jacobsen, and S. B. Nielsen (2016), Geophysical-petrological modelling of the East Greenland Caledonides – Isostatic support from crust and upper mantle, *Tectonophysics*.

Schmidt-Aursch, M. C., and W. Jokat (2005), The crustal structure of central East Greenland - II: From the Precambrian shield to the recent mid-oceanic ridges, *Geophys J Int*, *160*(2), 753-760.

Schmidt, S., and H. J. Götze (1998), Interactive visualization and modification of 3D-models using GIS-functions, *Physics and Chemistry of the Earth*, *23*(3), 289-295.

Sellevoll, M. A. (1983), A study of the Earth´s crust in the Island area of Lofoten-Vesterålen, Northern Norway, *Norges geologiske undersøkelse Bulletin*, *70*, 235-243.

Sigmond, E. M. O. (2002), Geological map, land and sea areas of northern Europe, 1:4 million, Geological Survey of Norway, Trondheim.

Sigmond, E. M. O. (2002), Geological Map, Land and Sea Areas of Northern Europe, Geological Survey of Norway.

SINTEF (2016), Stratigraphic drilling / Corehole Map / Technical data, edited, https://www.sintef.no/projectweb/ik-stratigraphic-drilling/corehole-map/technical-data/

Slagstad, T. (2008), Radiogenic heat production of Archaean to Permian geological provinces in Norway, *Norsk Geologisk Tidsskrift = Norwegian Journal of Geology*, *88*(3), 149-166.

Srivastava, S. P., and C. R. Tapscott (1986), Plate kinematics of the North Atlantic The geology of North America, edited, pp. 379-404, Geol. Soc. Am. : Boulder, CO, United States, United States.

Talwani, M., and O. Eldholm (1977), Evolution of the Norwegian-Greenland Sea, *Geol Soc Am Bull*, *88*, 969-999.

Tesauro, M., M. K. Kaban, and S. A. P. L. Cloetingh (2008), EuCRUST-07; a new reference model for the European crust, *Geophysical Research Letters*, *35*(5), @CitationL05313-@CitationL05313.

Tsikalas, F., J. I. Faleide, and A. Eldholm (2001), Lateral variations in tectono-magmatic style along the Lofoten-Vesterahen volcanic margin off Norway, *Mar Petrol Geol*, *18*(7), 807-832.

Tsikalas, F., O. Eldholm, and J. I. Faleide (2002), Early Eocene sea floor spreading and continent-ocean boundary between Jan Mayen and Senja fracture zones in the Norwegian-Greenland Sea, *Marine Geophysical Researches*, *23*(3), 247-270.

Tsikalas, F., O. Eldholm, and J. I. Faleide (2005), Crustal structure of the Lofoten-Vesteralen continental margin, off Norway, *Tectonophysics*, *404*(3-4), 151-174.

Wangen, M., R. Mjelde, and J. I. Faleide (2011), The extension of the Voring margin (NE Atlantic) in case of different degrees of magmatic underplating, *Basin Research*, *23*(1), 83-100.

Weidle, C., and V. Maupin (2008), An upper-mantle S-wave velocity model for northern Europe from Love and Rayleigh group velocities, *Geophys J Int*, *175*(3), 1154-1168.

White, R. S., L. K. Smith, A. W. Roberts, P. A. F. Christie, N. J. Kuznir, and iSIMM_team (2008), Lower-crustal intrusion on the North Atlantic continental margin, *Nature*, *452*(27), 460-464.

Williams, R., and C. Magnus (Eds.) (2013), *East Greenland - Hel Graben conjugate margin connection. Norway - East Greenland Conjugate Margins*.

Zhang, Y.-S., and T. Lay (1999), Evolution of oceanic upper mantle structure, *Physics of the Earth and Planetary Interiors*, *114*(1-2), 71-80.

Table 1. Velocity parameters for depth conversion

Layer index	Layer	Velocity at z=0 V_0 [m/s]	Vertical velocity gradient k_z [1/s]
W	Water	1480	0
S2	Naust-Kai	2050	0
S3	Brygge	2000	0.05
S4	Paleocene	2050	0.09
S5	Upper Cretaceous	2400	0.12
S6	Lower Cretaceous	2700	0.17

Table 2. Densities of the layers of the 3D structural model used during the 3D density modelling (lithology of sedimentary rocks is derived from *NPD* [2016]).

Layer index	Layer of the 3D structural model	Dominant lithology	Density ρ [kg/m^3]
W	Sea water	--------	1030
S1	Bjørnøya Fan Slide Complex	clastics	1600
S2	Naust and Kai	mainly shale with minor sandstone	*Eq. (2)
S3	mainly Brygge	mainly shale with very minor sandstone	*Eq. (3)
OL2AB	Oceanic layer 2AB	basalts and tuffs	2650
S4	Upper Cretaceous-Paleocene	mainly shale with some sandstone	*Eqs. (2) and (4)
S5	Lower Cretaceous	mainly shale with minor sandstone and limestone	*Eq. (4)
S6	Pre-Cretaceous	mainly shale with some sandstone	*Eq. (5)
S4-6	Pre-breakup sedimentary rocks of	mainly shale with sandstone	*Eqs. (2), (4) and (5)
UC1	Upper-crustal high-density crystalline rocks	gabbro to anorthositic rocks, metamorphic rocks	2820-2856
UC2	Low-density upper-crustal layer	metasedimentary rocks or granite	2640
UC3	Upper-crustal regional layer	granite and gneiss	2675
MC	Middle crust	granitoids and/or gneiss	2745-2775
LC	Lower crust	metamorphic rocks	2878
HDIC	High-density intracrustal layer	mafic granulites, gabbros	2920
OL3A	Oceanic layer 3A	sheeted dykes/gabbroic intrusions	2850
HDLC	Continental high-density lower-crustal layer	gabbro	2985-3070
OL3B	Oceanic layer 3B	gabbro, high-grade metamorphic rocks	3010-3040
LM	Lithospheric mantle	peridotite	3185-3220

Figures' captions

Figure 1. (a) Location of the study area within the North Atlantic region (bathymetry and topography from the Norwegian Mapping Authority). (b) Free-air gravity anomalies over the North Atlantic area [*Andersen et al.,* 2014].

Figure 2. Tectonic settings within the Lofoten-Vesterålen and the northern Vøring segments of the Mid-Norwegian continental margin, superimposed on the bathymetry, with location of the 3D structural/density model [after *Blystad et al.* 1995; *Sigmond,* 2002; *Hansen,* 2009; *Hansen et al.,* 2012; bathymetry from the Norwegian Mapping Authority]. COB is the continent-ocean boundary.

Figure 3. Datasets used for the sedimentary cover.

Figure 4. Thicknesses of the upper sedimentary rocks: (a) the Bjørnøya Fan Slide Complex and the Naust-Kai interval (S1-2); (b) the Brygge Formation, possibly with Kai Formation and Paleocene in the Lofoten and Røst basins (S3); (c) the Upper Cretaceous-Paleocene without the Røst Basin (S4 COB - continent-ocean boundary, HG - Hel Graben, NH - Nyk High, NR - Nordland Ridge, TB - Træna Basin, TP - Trøndelag Platform, UH - Utgard High, VB - Vøring Basin.

Figure 5. Datasets used for the internal configuration of the crystalline crust and for the Moho topography.

Figure 6. Location of the 2D vertical slices used to build the 3D structural/density model of the study area. The selected slices (Figures 13 and 14) are highlighted by thick magenta lines and numbers. COB is the continent-ocean boundary.

Figure 7. (a) Observed free-air gravity anomaly over the model area (Andersen et al. 2013). (b) Modeled gravity anomaly (this study). (c) Residual gravity anomaly showing the difference between the observed gravity field (Figure 7a) and the modeled one (Figure 7b). COB - continent-ocean boundary, HG - Hel Graben, NH - Nyk High, NR - Nordland Ridge, TB - Træna Basin, TP - Trøndelag Platform, UH - Utgard High, VB - Vøring Basin.

Figure 8. Thicknesses of basalts and the lower sedimentary rocks: (a) oceanic layer 2AB (basalts; OL2AB); (b) the Lower Cretaceous without the Røst Basin (S5); (c) the pre-Cretaceous without the Røst Basin (S6). (d) Cumulative thickness of the undivided Paleocene, Cretaceous and pre-Cretaceous within the Røst Basin (S4-6). COB - continent-ocean boundary, HG - Hel Graben, NH - Nyk High, NR - Nordland Ridge, TB - Træna Basin, TP - Trøndelag Platform, UH - Utgard High, VB - Vøring Basin.

Figure 9. The major modeled surfaces: (a) top of the crystalline basement; (b) Moho topography; (c) depth to lithosphere-asthenosphere boundary. COB - continent-ocean boundary, HG - Hel Graben, NH - Nyk High, NR - Nordland Ridge, TB - Træna Basin, TP - Trøndelag Platform, UH - Utgard High, VB - Vøring Basin.

Figure 10. Thicknesses of the upper, middle and lower-crustal rocks: (a) the upper-crustal high-density crystalline rocks (UC1); (b) the low-density upper-crustal body (UC2); (c) the regional upper-crustal layer (UC3); (d) the middle crust (MC); (e) the oceanic layer 3A (OL3A); (f) the lower crust (LC). COB - continent-ocean boundary, HG - Hel Graben, NH - Nyk High, NR - Nordland Ridge, TB - Træna Basin, TP - Trøndelag Platform, UH - Utgard High, VB - Vøring Basin.

Figure 11. Thicknesses of the high-density intracrustal and lower-crustal rocks: (a) the high-density intracrustal layer (HDIC); (b) the high-density lower-crustal layer below the continental crustal domain (red line outlines the lower-crustal high-velocity (V_p>7 km/s) body according to *Mjelde et al.* [2009]; HDLC); (c) the oceanic layer 3B (OL3B). COB - continent-ocean boundary, HG - Hel Graben, NH - Nyk High, NR - Nordland Ridge, TB - Træna Basin, TP - Trøndelag Platform, UH - Utgard High, VB - Vøring Basin.

Figure 12. The 3D structural/density model of the study area. Bathymetry and topography from the Norwegian Mapping Authority. Indexation of the layers is the same as in Table 2. COB is the continent-ocean boundary.

Figure 13. Selected vertical slices 1, 2 and 3 across the 3D structural/density model of the Lofoten-Vesterålen and the northern Vøring segments of the Mid-Norwegian continental margin. The locations of the slices are shown in Figure 6. Indexation of the layers is the same as in Table 2. COB is the continent-ocean boundary.

Figure 14. Selected NE-SW-trending vertical slices 5 and 4 through the 3D structural/density model of the Lofoten-Vesterålen and the northern Vøring segments of the Mid-Norwegian continental margin. The locations of the slices are shown in Figure 6. The legend for the coloring of the layers is shown in Figure 13.

Figures 1a and 1b

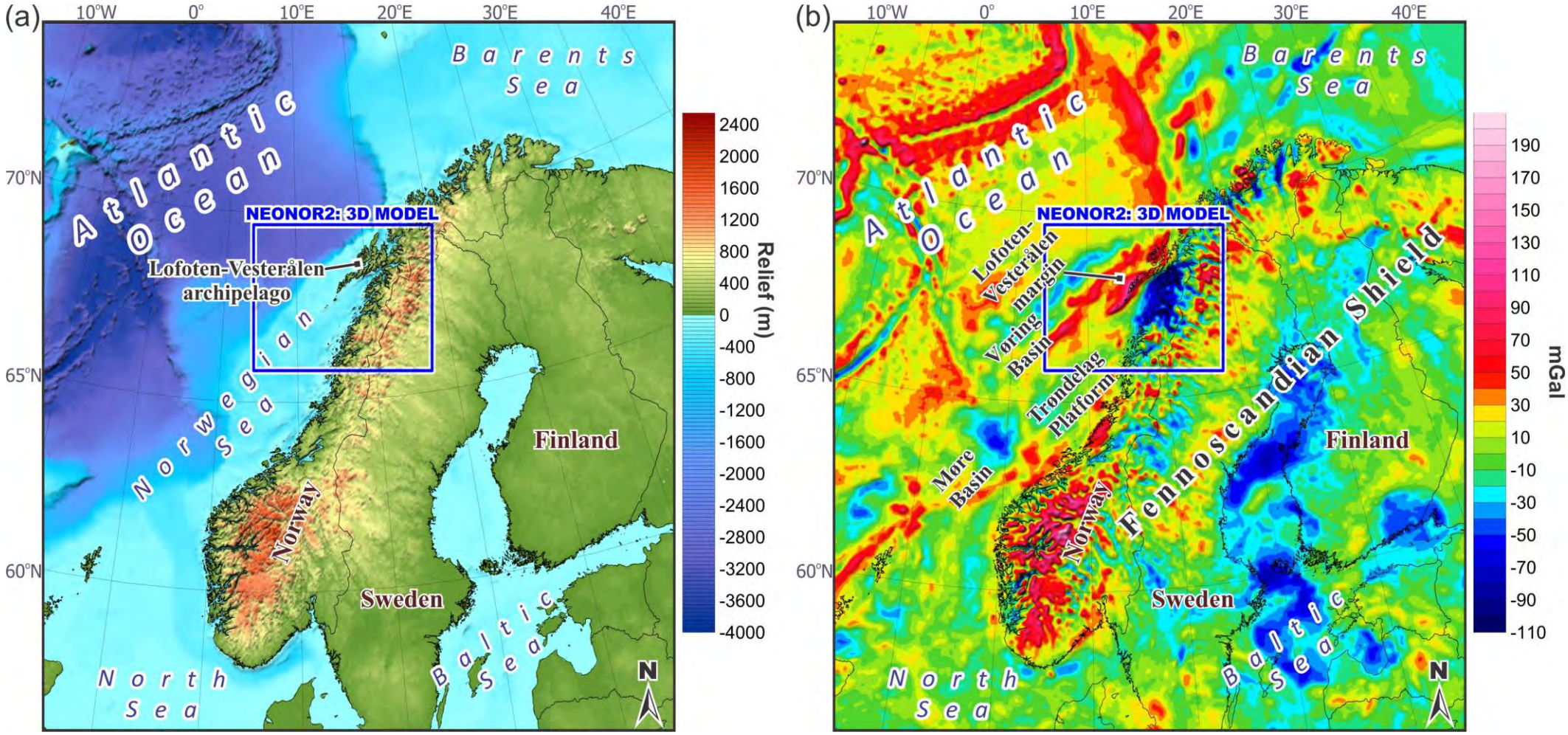

Figure 2

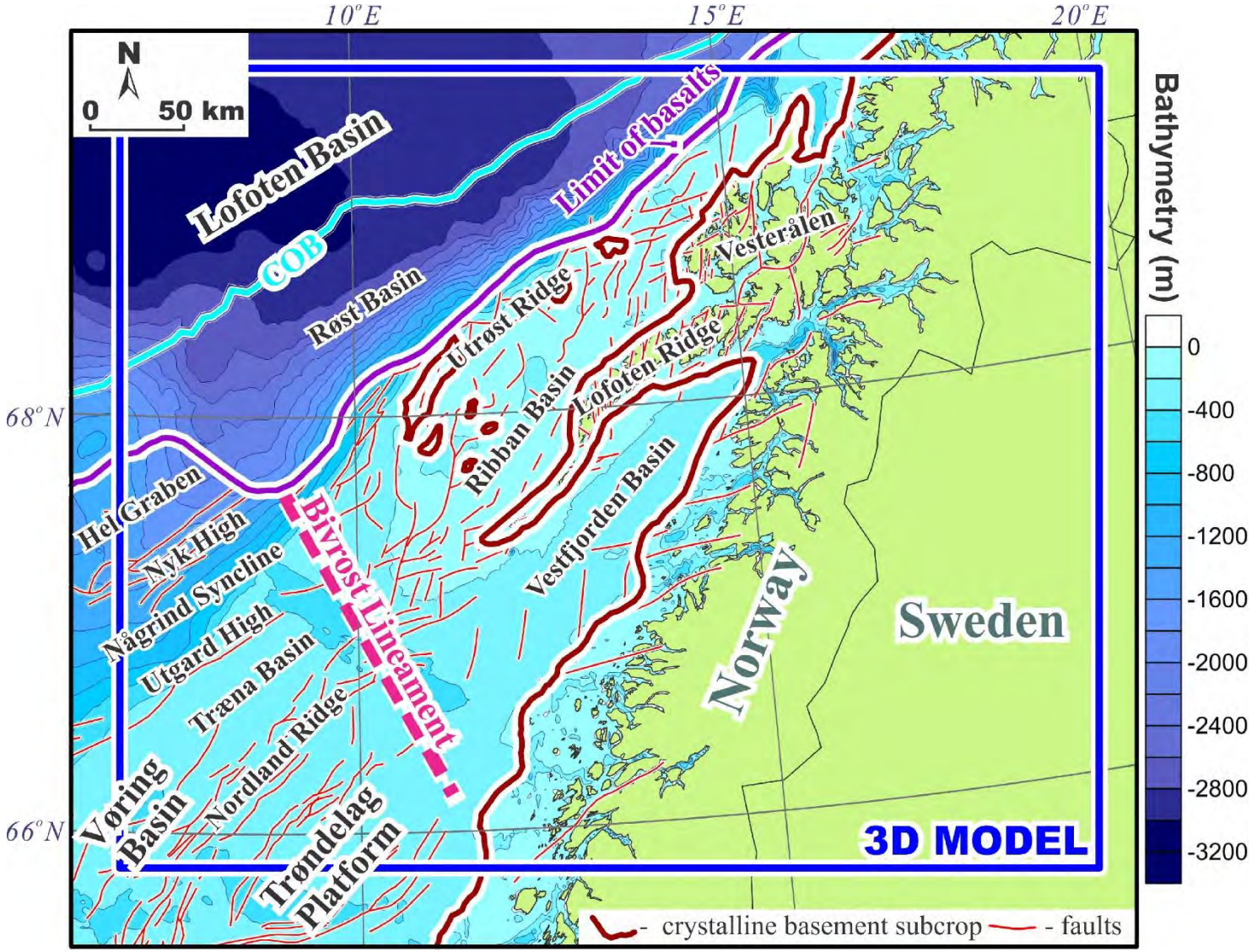
10°E
15°E
20°E
68°N
66°N
N
0
50 km
Lofoten Basin
COB
Limit of basalts
Røst Basin
Utrøst Ridge
Vesterålen
Lofoten Ridge
Ribban Basin
Hel Graben
Nyk High
Nagrind Syncline
Bivrost Lineament
Vestfjorden Basin
Utgard High
Træna Basin
Nordland Ridge
Vøring Basin
Trøndelag Platform
Norway
Sweden
3D MODEL
Bathymetry (m)
0
-400
-800
-1200
-1600
-2000
-2400
-2800
-3200
- crystalline basement subcrop
- faults

Figure 3: A and B

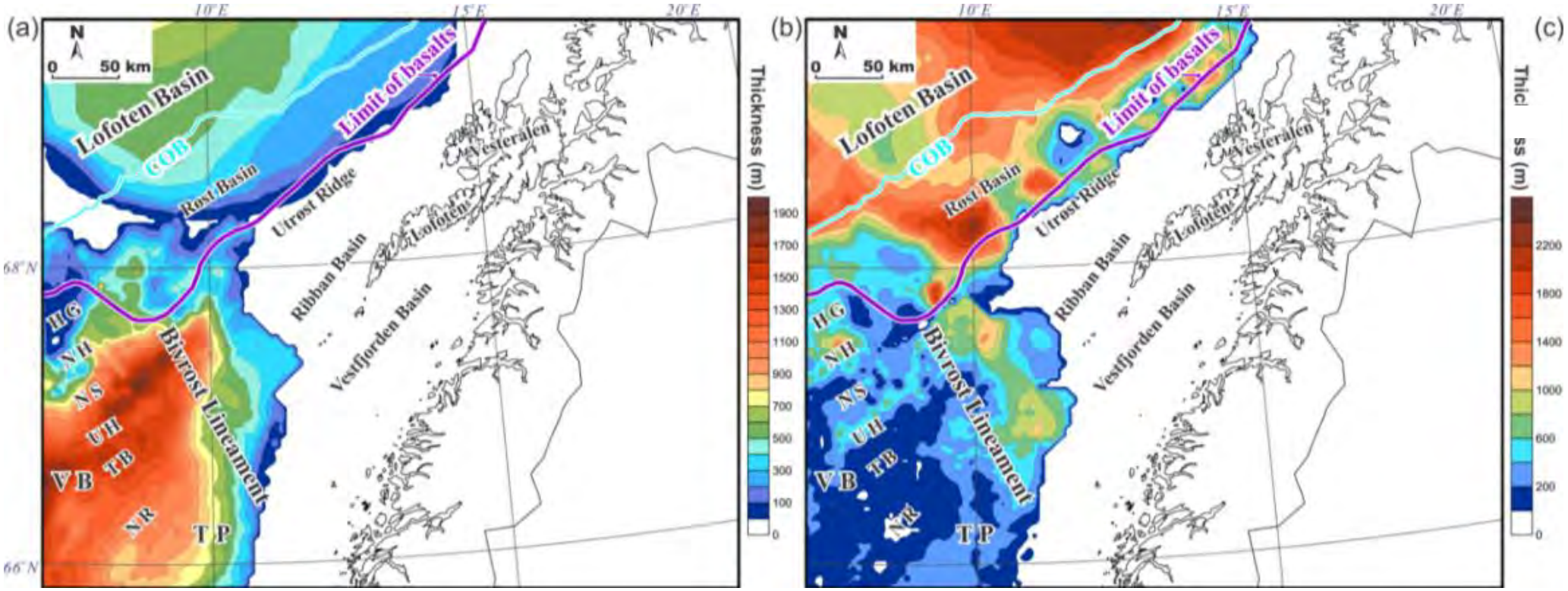

Figure 4 c

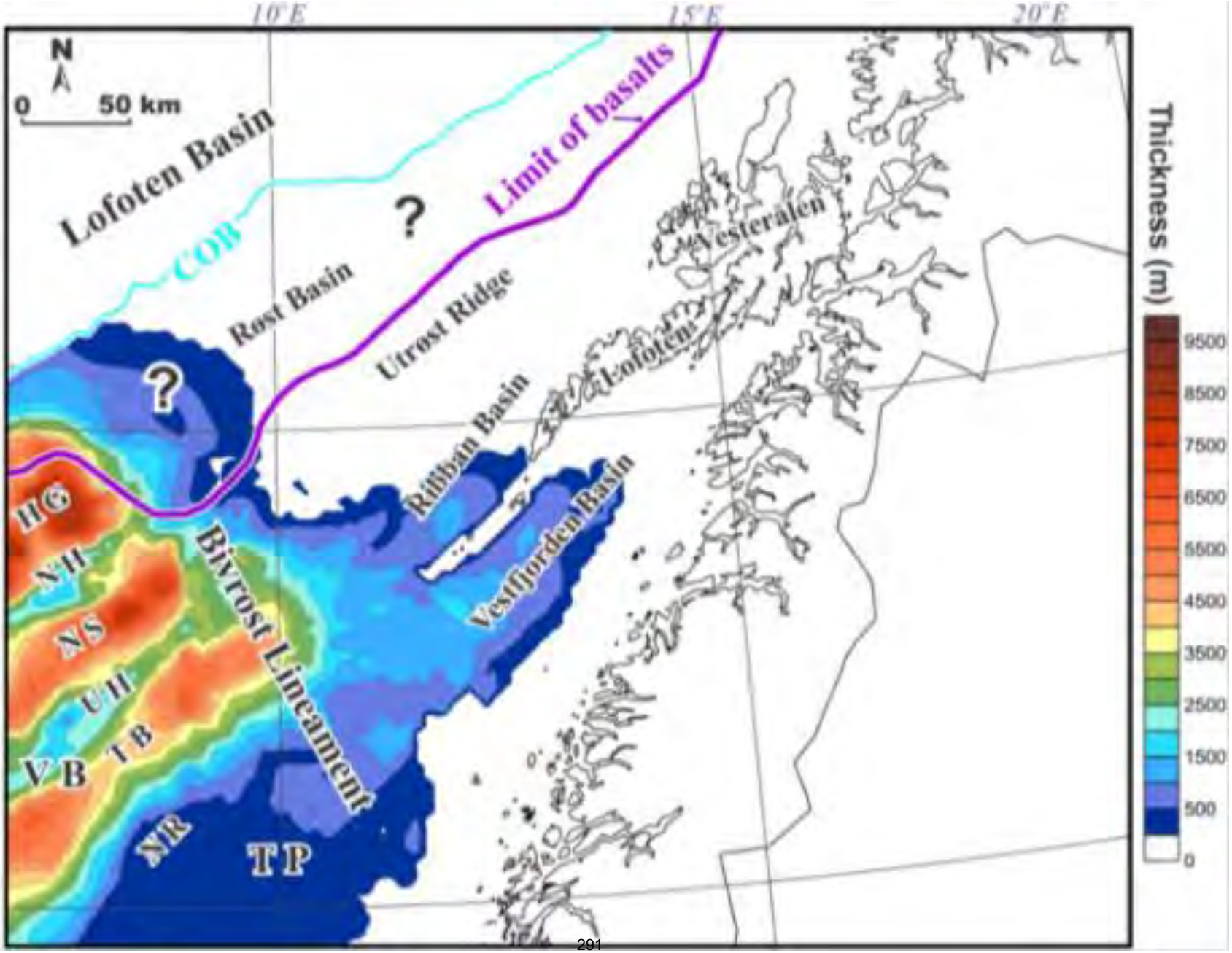
10°E
15°E
20°E
N
0
50 km
Lofoten Basin
COB
?
Limit of basalts
Røst Basin
Utrøst Ridge
Vesterålen
Lofoten
?
Ribban Basin
Vestfjorden Basin
HG
NH
NS
UH
VB
TB
Bivrost Lineament
NR
TP
Thickness (m)
9500
8500
7500
6500
5500
4500
3500
2500
1500
500
0

Figure 5

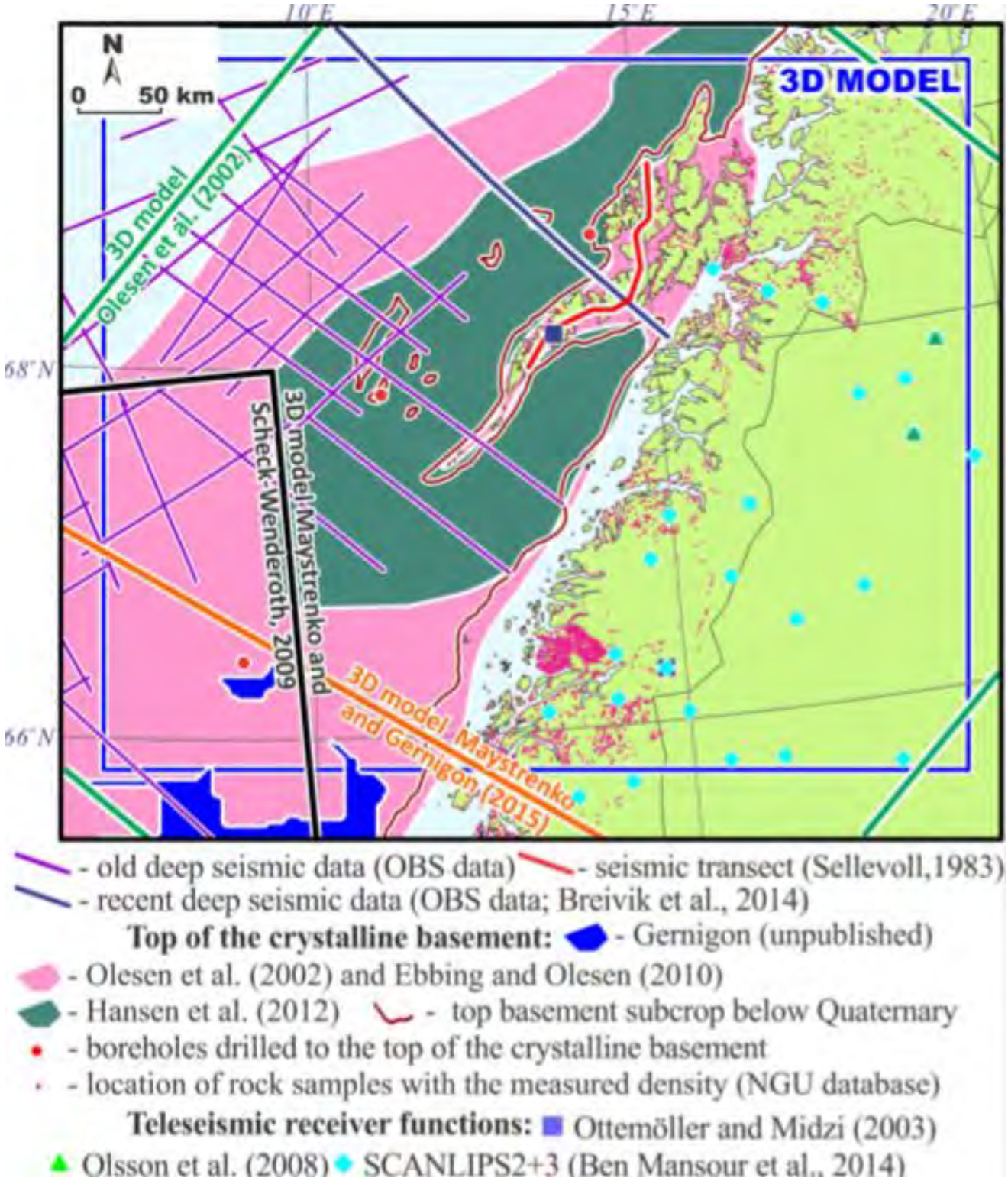
10°E
15°E
20°E
N
0
50 km
3D MODEL
3D model Olesen et al. (2002)
68°N
66°N
3D model Maystrenko and Scheck-Wenderoth, 2009
3D model Maystrenko and Gernigon (2015)
- old deep seismic data (OBS data)
- seismic transect (Sellevoll,1983)
- recent deep seismic data (OBS data; Breivik et al., 2014)
Top of the crystalline basement:
- Gernigon (unpublished)
- Olesen et al. (2002) and Ebbing and Olesen (2010)
- Hansen et al. (2012)
- top basement subcrop below Quaternary
- boreholes drilled to the top of the crystalline basement
- location of rock samples with the measured density (NGU database)
Teleseismic receiver functions:
Ottemöller and Midzi (2003)
Olsson et al. (2008)
SCANLIPS2+3 (Ben Mansour et al., 2014)

Figure 6

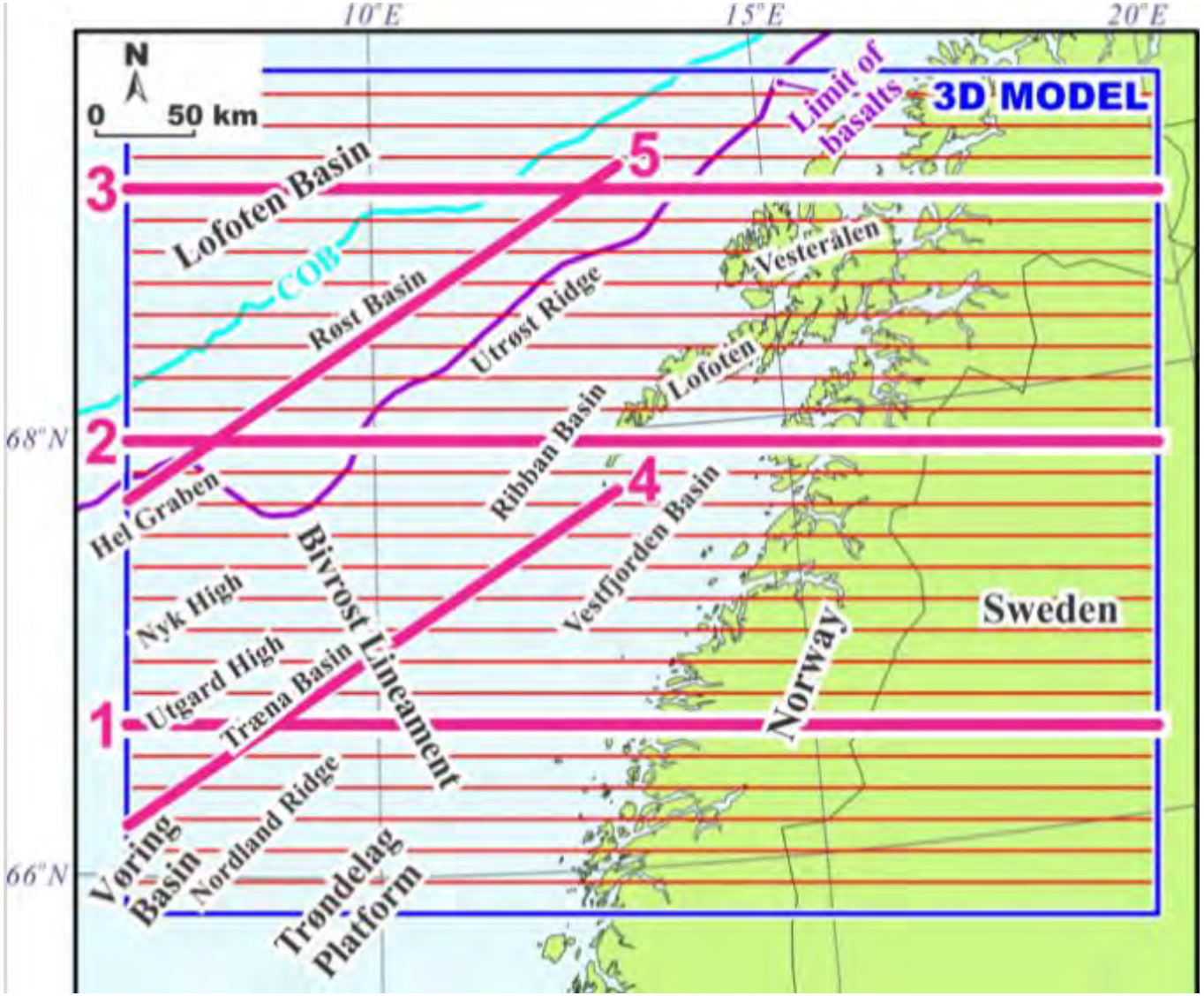
10°E
15°E
20°E
68°N
66°N
N
0
50 km
3D MODEL
Limit of basalts
COB
Lofoten Basin
Røst Basin
Utrøst Ridge
Vesterålen
Lofoten
Ribban Basin
Hel Graben
Bivrost Lineament
Nyk High
Utgard High
Træna Basin
Vestfjorden Basin
Sweden
Norway
Vøring Basin
Nordland Ridge
Trøndelag Platform
1
2
3
4
5

Figure 7

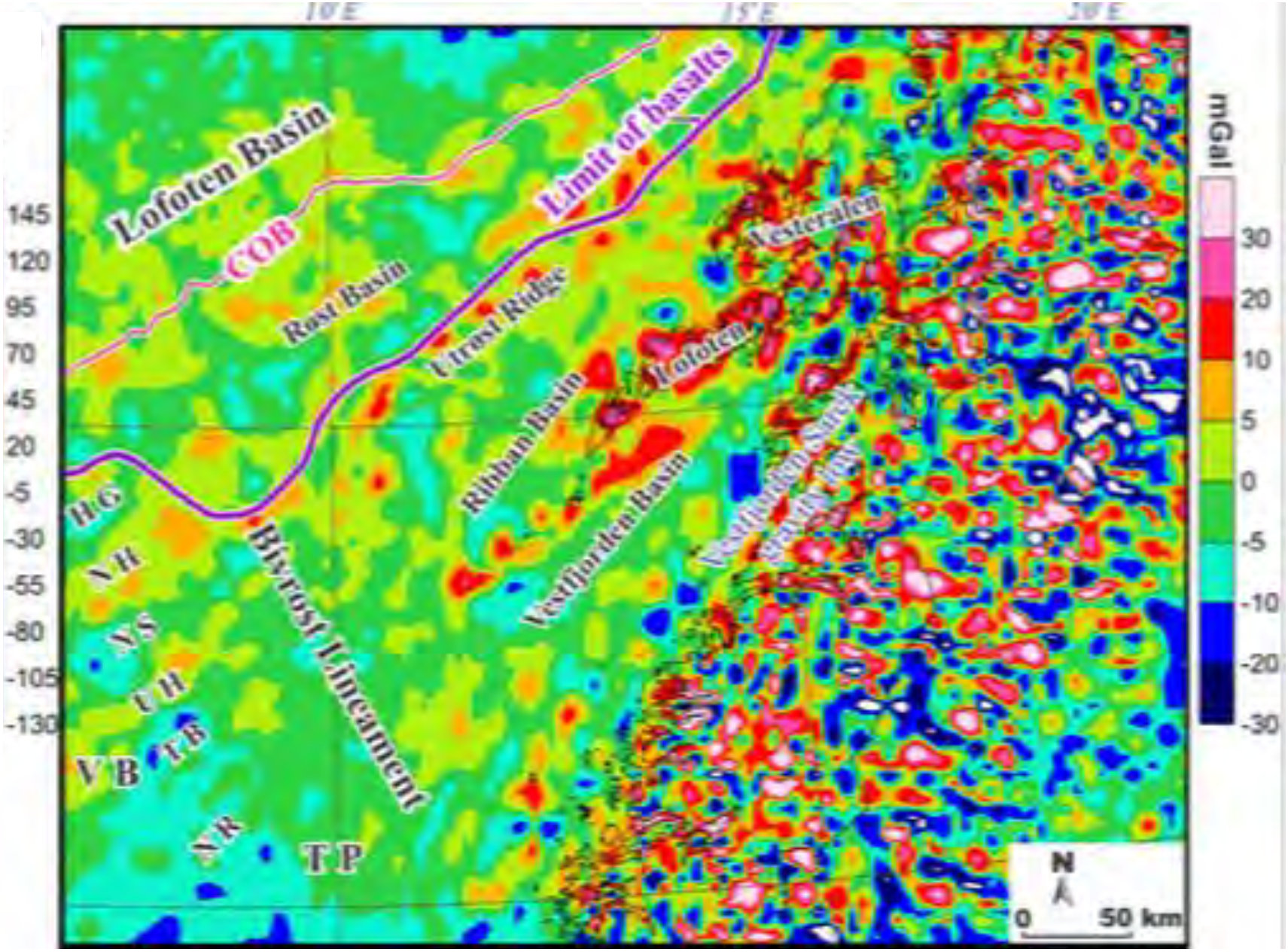
10E
15E
30E
Lofoten Basin
COB
Rost Basin
Utrost Ridge
Limit of basalts
Ribban Basin
Lofoten
Vesteralen
Vestfjorden Basin
Vestfjorden-Vanna Fault Complex
Bivrost Lineament
H.G
V H
N S
U H
T B
V B
V R
T P
145
120
95
70
45
20
-5
-30
-55
-80
-105
-130
mGal
30
20
10
5
0
-5
-10
-20
-30
N
0
50 km

Figure 8

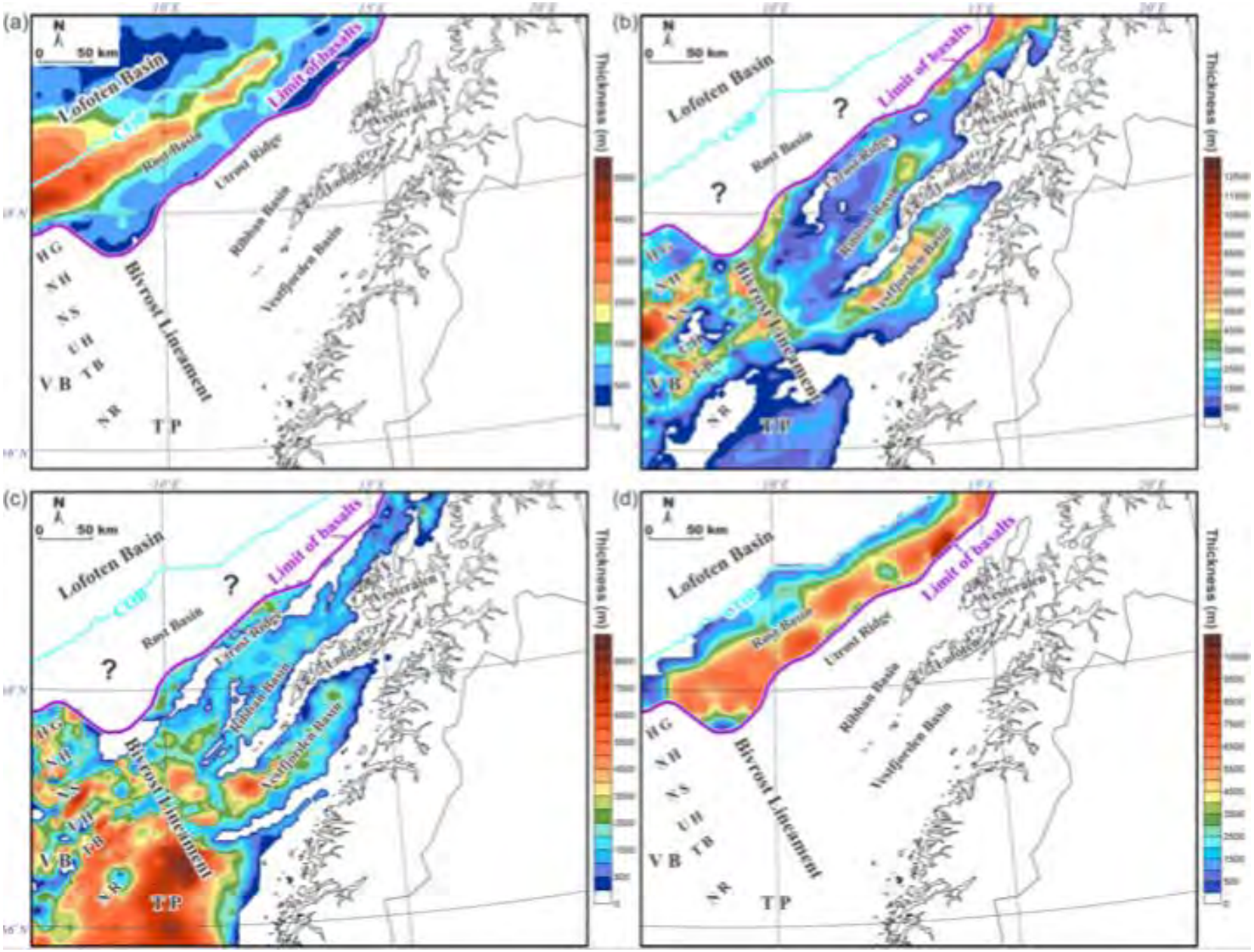
(a)
(b)
(c)
(d)
N
0 50 km
Lofoten Basin
Limit of basalts
Røst Basin
Utrøst Ridge
Ribban Basin
Vestfjorden Basin
Bivrost Lineament
HG
NH
NS
UH
VB
TB
NR
TP
Thickness (m)

Figures 9 a. b. c

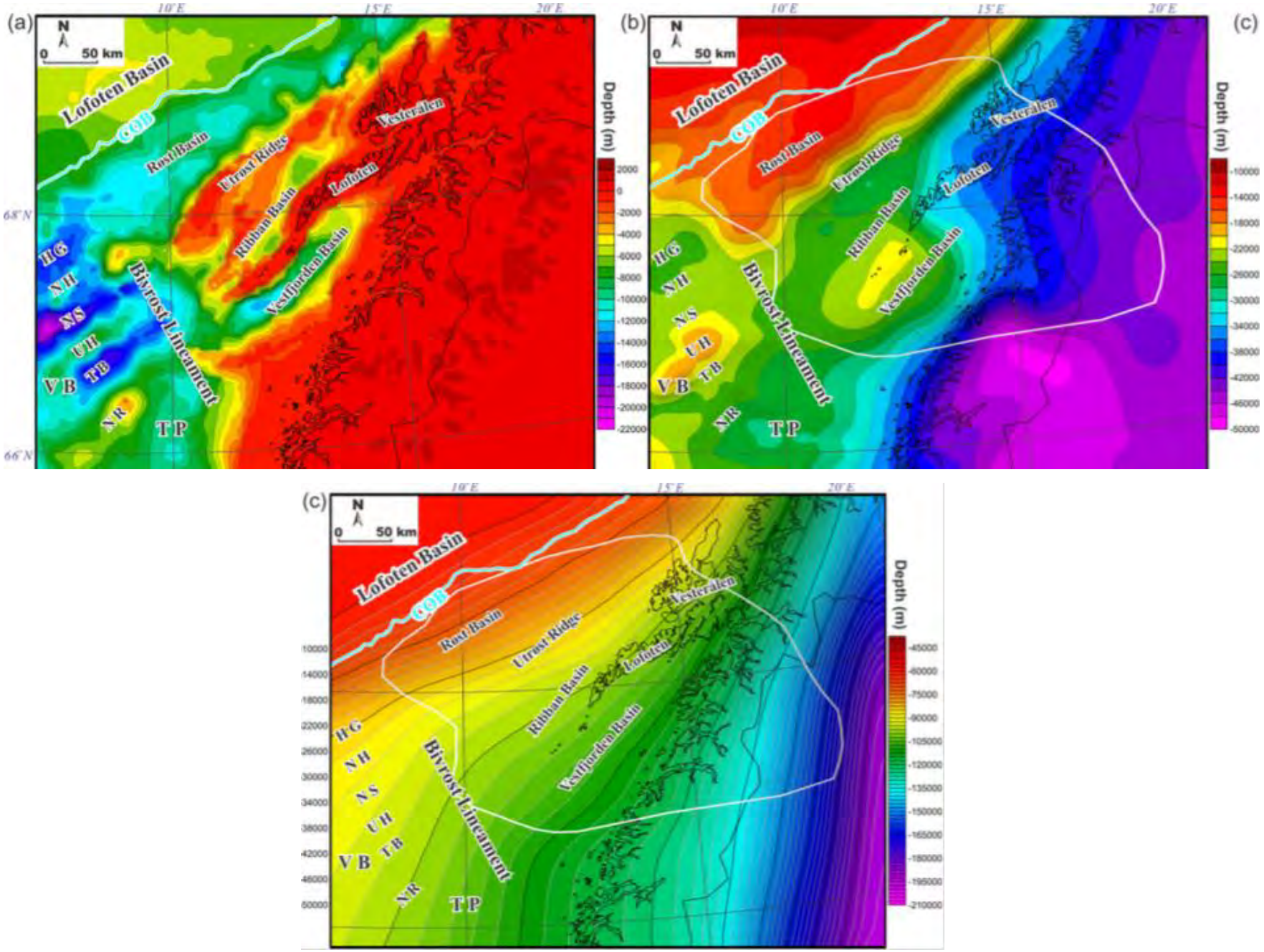

Figure 10

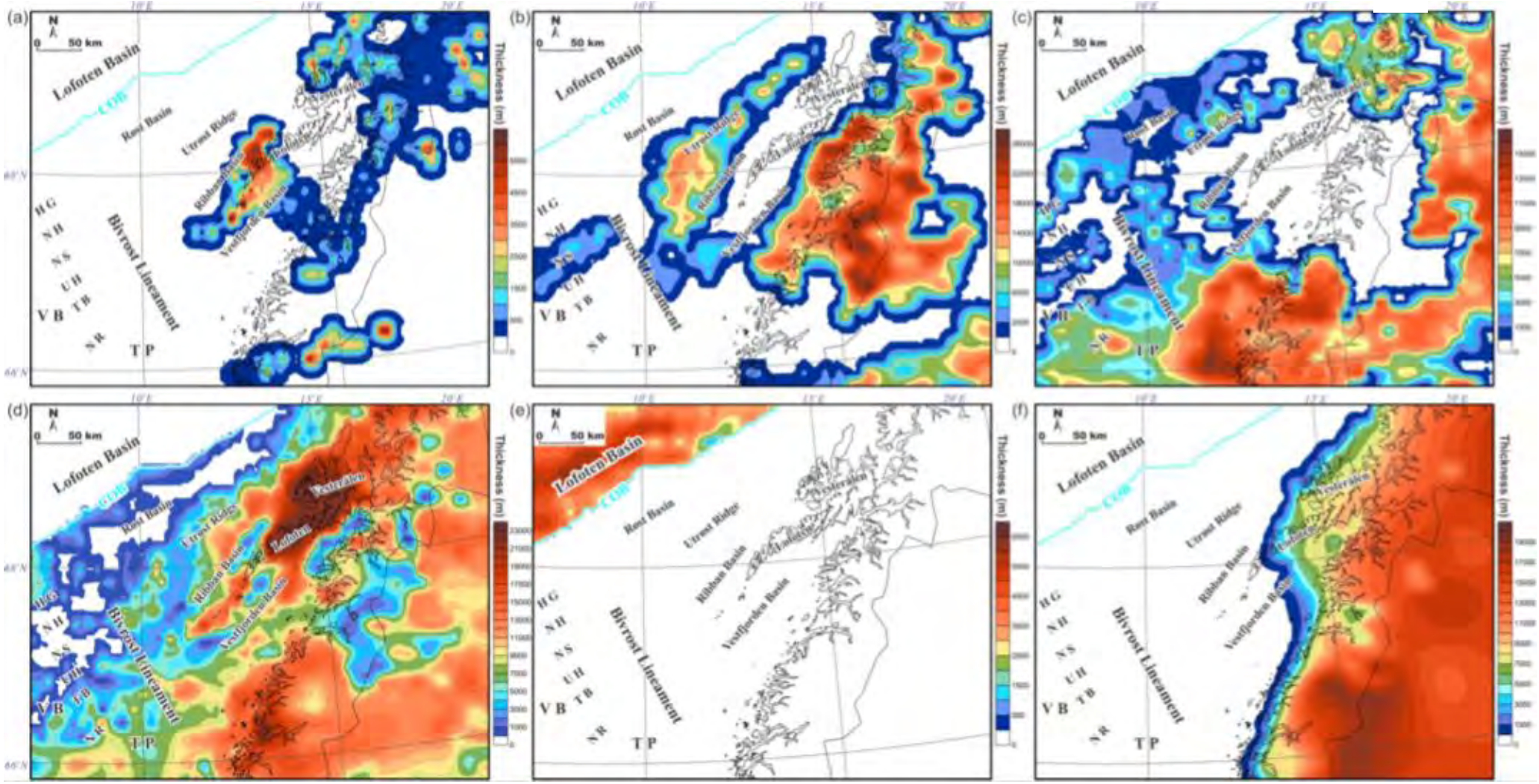
(a)
(b)
(c)
(d)
(e)
(f)
N
0 50 km
Lofoten Basin
COB
Røst Basin
Utrost Ridge
Ribban Basin
Vestfjorden Basin
Bivrost Lineament
HG
NH
NS
UH
VB
TB
NR
TP
Thickness (m)

Figure 11 a b c

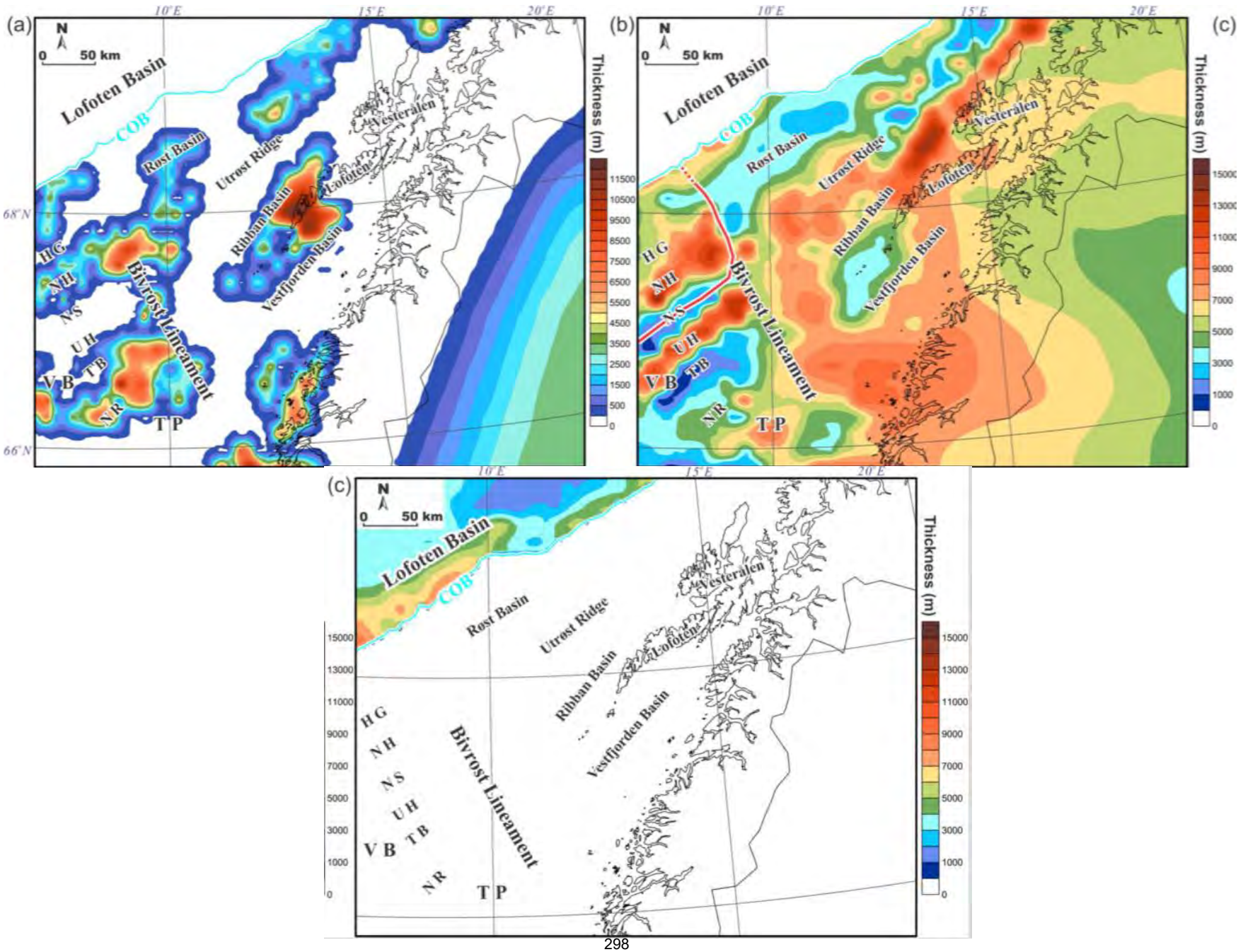

Figure 12

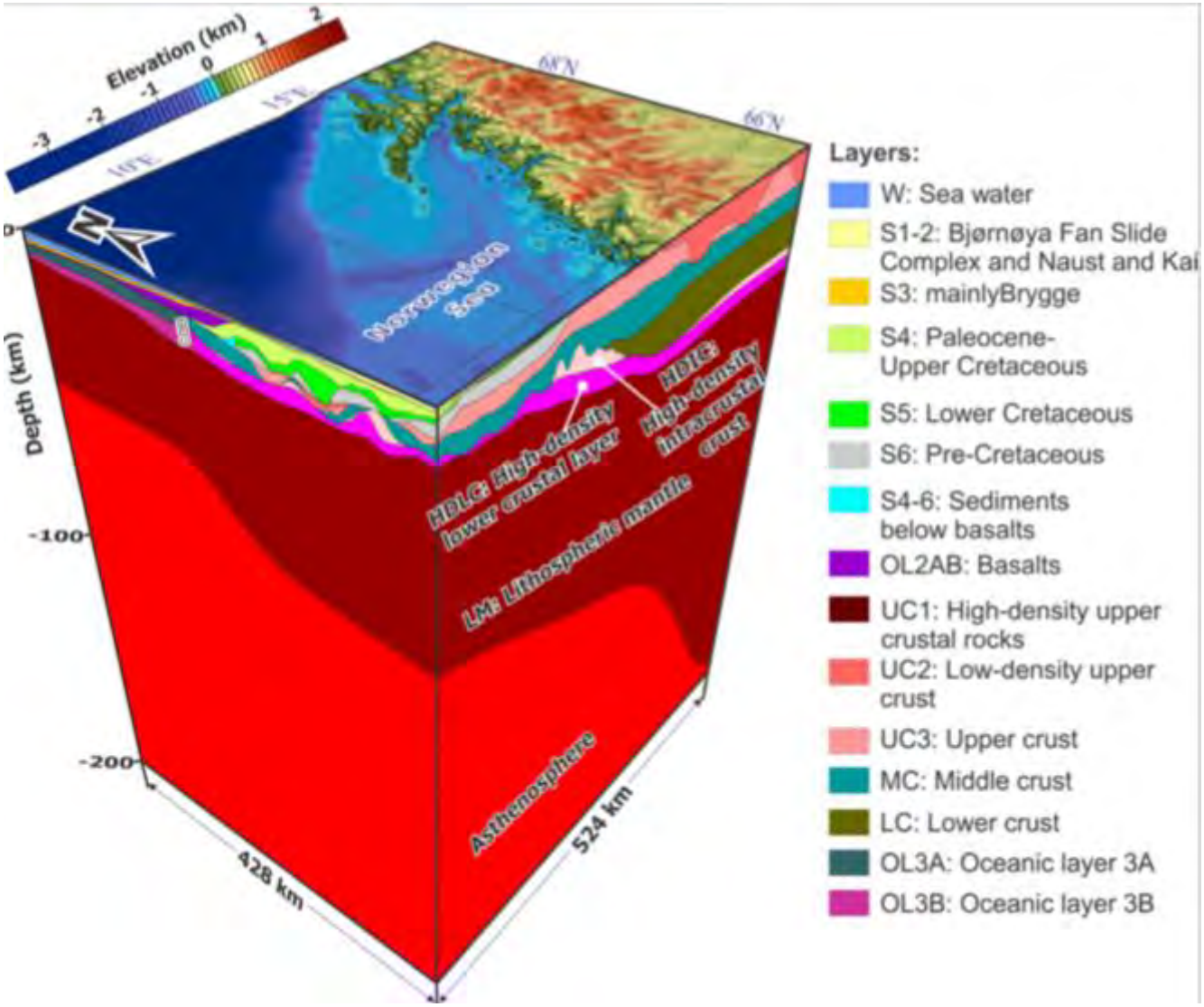
Elevation (km)
-3
-2
-1
0
1
2
10°E
15°E
66°N
68°N
Depth (km)
0
-100
-200
Norwegian Sea
HDLC: High-density lower crustal layer
HDLC: High-density intracrustal crust
LM: Lithospheric mantle
Asthenosphere
428 km
524 km
Layers:
W: Sea water
S1-2: Bjørnøya Fan Slide Complex and Naust and Kai
S3: mainlyBrygge
S4: Paleocene-Upper Cretaceous
S5: Lower Cretaceous
S6: Pre-Cretaceous
S4-6: Sediments below basalts
OL2AB: Basalts
UC1: High-density upper crustal rocks
UC2: Low-density upper crust
UC3: Upper crust
MC: Middle crust
LC: Lower crust
OL3A: Oceanic layer 3A
OL3B: Oceanic layer 3B

Figure 13

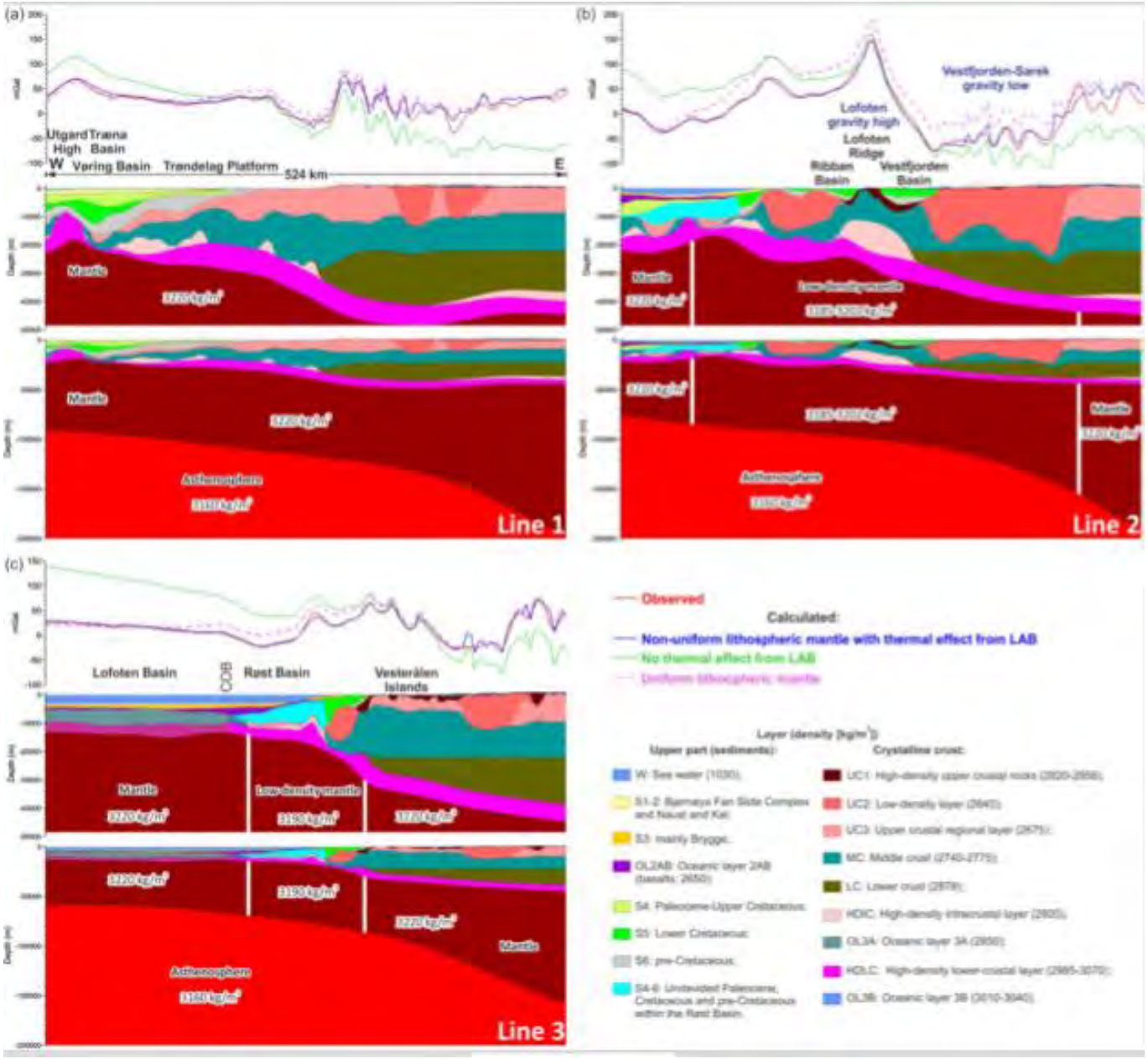
(a)
Utgard High
Trænа Basin
W
Vøring Basin
Trøndelag Platform
524 km
E
Mantle
Asthenosphere
Line 1
(b)
Vestfjorden-Sørsk gravity low
Lofoten gravity high
Lofoten Ridge
Ribban Basin
Vestfjorden Basin
Mantle
Low-density mantle
Asthenosphere
Line 2
(c)
Lofoten Basin
COB
Rest Basin
Vesterålen Islands
Mantle
Low-density mantle
Asthenosphere
Line 3
Observed
Calculated:
Non-uniform lithospheric mantle with thermal effect from LAB
No thermal effect from LAB
Uniform lithospheric mantle
Layer (density [kg/m³])
Upper part (sediments):
W: Sea water (1030);
S1-2: Bjarmøya Fan Slide Complex and Naust and Kai;
S3: mainly Brygge;
OL2AB: Oceanic layer 2AB (basalts: 2650);
S4: Paleocene-Upper Cretaceous;
S5: Lower Cretaceous;
S6: pre-Cretaceous;
S4-6: Undivided Paleocene, Cretaceous and pre-Cretaceous within the Rest Basin.
Crystalline crust:
UC1: High-density upper crustal rocks (2920-2956);
UC2: Low-density layer (2640);
UC3: Upper crustal regional layer (2675);
MC: Middle crust (2740-2775);
LC: Lower crust (2879);
HDIC: High-density intracrustal layer (2800);
OL3A: Oceanic layer 3A (2850);
HDLC: High-density lower-crustal layer (2985-3070);
OL3B: Oceanic layer 3B (3010-3040).

Figure 14

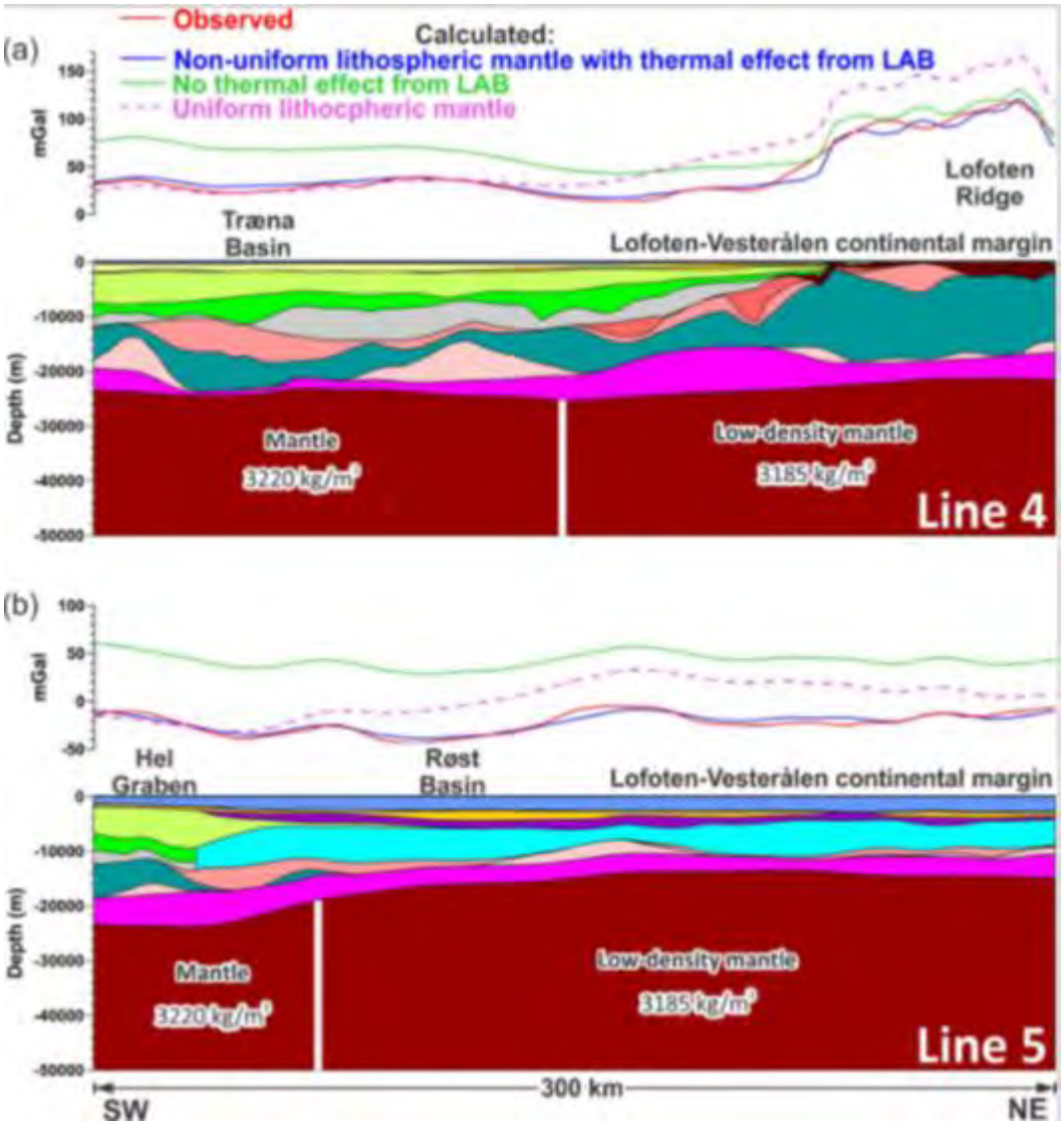
(a)
Observed
Calculated:
Non-uniform lithospheric mantle with thermal effect from LAB
No thermal effect from LAB
Uniform lithocpheric mantle
mGal
Træna Basin
Lofoten Ridge
Lofoten-Vesterålen continental margin
Depth (m)
Mantle
3220 kg/m³
Low-density mantle
3185 kg/m³
Line 4
(b)
mGal
Hel Graben
Røst Basin
Lofoten-Vesterålen continental margin
Depth (m)
Mantle
3220 kg/m³
Low-density mantle
3185 kg/m³
Line 5
300 km
SW
NE

CHAPTER 11: 3-D THERMAL EFFECT OF LATE CENOZOIC EROSION AND DEPOSITION WITHIN THE LOFOTEN–VESTERÅLEN SEGMENT OF THE MID-NORWEGIAN CONTINENTAL MARGIN

Authors: Y. P. Maystrenko[1], L. Gernigon[1], O. Olesen[1], O. Ottesen[1] and L. Rise[1]

Affiliation: [1]Geological Survey of Norway, P.O. Box 6315 Torgården, N-7491 Trondheim

Journal: Geophysical Journal International

Publishing Date: May 2018 (Online)

DOI: http://dx.doi.org/10.1093/gji/ggy013

Pages: 66 (proof)

3D thermal effect of late Cenozoic erosion and deposition within the Lofoten-Vesterålen segment of the Mid-Norwegian continental margin

Yuriy Petrovich Maystrenko, Laurent Gernigon, Odleiv Olesen, Dag Ottesen and Leif Rise

Geological Survey of Norway, Leiv Eirikssons vei 39, 7040 Trondheim, Norway
E-mail corresponding author (Yuriy Petrovich Maystrenko): yuriy.maystrenko@ngu.no

for Geophysical Journal International

SUMMARY

A 3D subsurface temperature distribution within the Lofoten-Vesterålen segment of the Mid-Norwegian continental margin and adjacent areas has been studied to understand the thermal effect of late Cenozoic erosion of old sedimentary and crystalline rocks and subsequent deposition of glacial sediments during the Pleistocene. A lithosphere-scale 3D structural model of the Lofoten-Vesterålen area has been used as a realistic approximation of the geometries of the sedimentary infill, underlying crystalline crust and lithospheric mantle during the 3D thermal modelling. The influence of late Cenozoic erosion and sedimentation has been included during the 3D thermal calculations. In addition, the 3D thermal modelling has been carried out by taking also into account the influence of early Cenozoic continental breakup. The results of the 3D thermal modelling demonstrate that the mainland is generally colder than the basin areas within the upper part of the 3D model. The thermal influence of the early Cenozoic breakup is still clearly recognizable within the western and deep parts of the Lofoten-Vesterålen margin segment in terms of the increased temperatures. The thermal effects of the erosion and deposition within the study area also indicate that a positive thermal anomaly exists within the specific sub-areas where sedimentary and crystalline rocks were eroded. A negative thermal effect occurs in the sub-areas affected by subsidence and subsequent sedimentation. The erosion-related positive thermal anomaly reaches its maximum of more than +27 ^{o}C at depths of 17-22 km beneath the eastern part of the Vestfjorden Basin. The most pronounced deposition-related negative anomaly shows a minimum of around -70 ^{o}C at 17-20 km depth beneath the Lofoten Basin. The second negative anomaly is located within the north-eastern part of the Vøring Basin and has minimal values of around -48 ^{o}C at 12-14 km depth. These prominent thermal anomalies are associated with the sub-areas where relatively high erosional and depositional rates were observed for late Cenozoic time.

Key words: Heat flow, Europe, Numerical modelling, Neotectonics, Sedimentary basin processes, Continental margins: divergent, Atlantic Ocean.

1 INTRODUCTION

The Lofoten-Vesterålen margin represents an uplifted segment in the north-eastern area of the Mid-Norwegian continental margin, covering the area around the Lofoten-Vesterålen archipelago (Fig. 1). The Mid-Norwegian continental margin is a rifted passive margin where a continental breakup took place in the early Cenozoic about 55 Ma ago (e.g. Talwani and Eldholm, 1977, Brekke, 2000, Srivastava & Tapscott, 1986, Faleide *et al.* 2008, Gernigon *et al.* 2015, Olesen *et al.* 2007).

During the last decades, the tectonic evolution and structure of the Lofoten-Vesterålen segment and adjacent areas have been thoroughly studied by both geological and geophysical methods, including geological mapping (e.g. Sigmond, 2002), drilling of wells (Olesen *et al.* 2007b, NPD, 2017), interpretation of reflection seismic data (Mokhtari and Pegrum, 1992, Bergh *et al.* 2007, Eidvin *et al.* 2007, Ottesen *et al.* 2009, Hansen *et al.* 2012, Rise *et al.* 2013, Montelli *et al.* 2017) and refraction seismic data analysis (Avedik *et al.* 1984, Drivenes *et al.* 1984, Goldschmidt-Rokita *et al.* 1988, Mjelde *et al.* 1992, Kodaira *et al.* 1995, Mjelde *et al.* 1996, Mjelde *et al.* 2001, Mjelde *et al.* 2003, Mjelde *et al.* 1995, Breivik *et al.* 2009, Breivik *et al.* 2017). In addition, 2D and 3D potential field modelling helped further to understand the deep structure of this region (e.g. Fichler *et al.* 1999, Olesen *et al.* 2002, Tsikalas *et al.* 2005, Brönner *et al.* 2013, Gradmann and Ebbing, 2015, Maystrenko *et al.* 2017).

The study area is characterized by a prominent contrasting relief, changing at a relatively short distance from elevations higher than 1.5 km within the Scandes Mountains onshore to bathymetries deeper than -3 km within the oceanic Lofoten Basin offshore (Fig. 2). In addition to this contrasting relief, the crystalline rocks are exposed on the Earth's surface over most of the mainland (e.g. Sigmond, 2002). The preserved sedimentary rocks are mainly represented by the relatively thin Jurassic and Cretaceous sequences in the north-eastern part of the Andøya Island (Dalland, 1975, Smelror *et al.* 2001). The crystalline rocks also crop out at the sea floor within the structural highs and near the coastline (Sigmond, 2002). Moreover, the Nordland area is characterised by increased seismicity and neotectonic activities (Keiding *et al.* 2015, Janutyte *et al.* 2017). The above-mentioned direct indications of neotectonics together with the additional neotectonic features have been summarised by Olesen *et al.* (2013, 2004) for this tectono-structurally complex area.

In this study, the main goal is to model and reveal the 3D conductive thermal pattern beneath the Lofoten-Vesterålen margin, the adjacent parts of the mainland and the adjacent Atlantic Ocean. In particular, our study has been performed to recognize the temporal changes of the subsurface 3D thermal pattern during the late Cenozoic uplift and erosion of the mainland and the north-eastern part of the Lofoten-Vesterålen margin segment and the rapid deposition of the eroded material within the south-western part of the Lofoten-Vesterålen margin and the adjacent north-eastern part of the Vøring Basin. The lithosphere-scale 3D structural model of the Lofoten-Vesterålen segment of the Mid-Norwegian margin from Maystrenko *et al.* (2017) has been taken as the main structural background for the 3D thermal modelling. This 3D structural model represents the most recent structural approximation of the deep subsurface, covering the major tectonic units of the Lofoten-Vesterålen area and the north-eastern part of the Vøring Basin (Fig. 2).

2 TECTONIC OVERVIEW AND PREVIOUS WORK

The Lofoten-Vesterålen continental margin and the adjacent mainland had already undergone significant uplift and erosion during the Scandian phase of the Caledonian Orogeny in the Silurian-Early Devonian (Roberts and Gee, 1985) when large-scale overthrusting and following uplift were caused by amalgamation of several terranes to the Baltican protomargin. During the Devonian, the Caledonian Orogen collapsed as a result of a regional extension (Steltenpohl *et al.* 2004, Fossen, 2010). During the Late Paleozoic-Mesozoic, several extensional events led to the formation of the Permian, Triassic and Jurassic sub-basins within the Trøndelag Platform (e.g. Blystad *et al.* 1995, Brekke, 2000), the Jurassic-Cretaceous depocenters within the Ribban and Vestfjorden basins, possibly including the lava-flow-covered Røst Basin (Tsikalas *et al.* 2001, Hansen *et al.* 2012, Færseth, 2012, Eig, 2012). During Late Jurassic-Creataceous, large tectonic and thermal Cretaceous subsidence affected the adjacent Vøring Basin (e.g. Gernigon *et al.* 2004, Lien, 2005, Mjelde *et al.* 2016). The continental break-up finally split the Laurasia paleocontinent in the late Paleocene-early Eocene and the present-day Mid-Norwegian continental margin and the oceanic Lofoten Basin started to form (Talwani and Eldholm, 1977).

During the Cenozoic, the Lofoten-Vesterålen segment of the Mid-Norwegian continental margin has undergone a continuous or episodic uplift which was followed by erosion and/or non deposition over a large part of the Lofoten-Vesterålen margin (e.g. Løseth and Tveten, 1996, Riis, 1996, Færseth, 2012). The most recent erosion occurred during the Quaternary glacial periods when preserved sedimentary and existing weathered crystalline rocks were removed by glacial erosion, forming the typical present-day Norwegian landscape, the so-called strandflat (Olesen *et al.* 2013, Holtedahl, 1998). The strandflat is particularly well developed south of the Lofoten margin, along the coast of Helgeland (Olesen *et al.* 2013, Holtedahl, 1998). The eroded material were deposited farther offshore, creating significant depocenters of the glacier-derived Naust Formation during Pleistocene times (e.g. Rise *et al.* 2005b, Dowdeswell *et al.* 2010a, Dowdeswell *et al.* 2006, Ottesen *et al.* 2009, Montelli *et al.* 2017). Moreover, elevated passive continental margins have also been well documented in other places of the world (e.g. Greenland, NE Brazil, South Africa) but, like in the case of the Mid-Norwegian margin, there is still no common geodynamic model that can fully explain their origin (e.g. Green *et al.* 2017).

The origin and nature of the late Cenozoic uplift are still a matter of debate and obviously resulted from the superposition of several factors (Løseth and Tveten, 1996, Riis, 1996, Færseth, 2012, Fjeldskaar *et al.* 2000). Four major phases of the Cenozoic uplift in the Paleogene, middle Miocene, late Pliocene and Pleistocene have been identified by Riis (1996). The Paleogene uplift was interpreted as a marginal uplift related to the opening of the North Atlantic Ocean and the late Pliocene event was considered to be due to unloading (Riis, 1996). On the other hand, the reasons of the middle Miocene and Pleistocene phases remain globally unknown. Riis & Fjeldskaar (1992) have shown that the postglacial uplift is not totally isostatically compensated and Fjeldskaar *et al.* (2000) have proposed that this uplift has also a tectonic origin. Furthermore, the ridge push forces associated with Cenozoic sea-floor spreading in the North Atlantic Ocean has also been proposed as a primary explanation for the Fennoscandian uplift (e.g. Fejerskov & Lindholm, 2000).

In spite of many uncertainties about the causes of these Cenozoic uplift events, the magnitude of the uplift at different time intervals and the amount of the eroded material have

been approximately quantified by use of different methods. Based on apatite fission track and (U–Th)/He analyses, the post-Caledonian denudation history of western Fennoscandia is characterised by clearly defined and relatively high cooling rates throughout the whole Cenozoic (Hendriks & Andriessen, 2002, Hendriks *et al.* 2010, Davids *et al.* 2013, Ksienzyk *et al.* 2014). Particularly, the present-day exposed Earth's surface in Lofoten and Vesterålen could be characterized by relatively high paleotemperatures at the beginning of the Cenozoic, ranging from 30 to 90 ^{o}C recorded at different locations (Hendriks *et al.* 2010). Hendriks *et al.* (2010) indicate a differential uplift of the Lofoten-Vesterålen area with magnitude variations from 1 to more than 3 km locally during the Cenozoic. Furthermore based on the study of the weathered crystalline crust, Olesen *et al.* (2013) have suggested that the Pleistocene erosion was about 500 m along the coastline in the Nordland area. In SW Norway, Steer *et al.* (2012) have proposed that significant erosion must have also taken place in the close vicinity to present-day high elevation during the late Pliocene and Quaternary glaciations. However, they did not consider the erosion within the inner shelf. Based on the volume of the Pleistocene Naust Formation off mid Norway, Dowdeswell *et al*. (2010) suggested a similar amount of average glacial erosion over the mainland and inner shelf. The estimated thickness of the restored matrix of the Cenozoic deposits at the close vicinity of the highly elevated Scandes Mountains within the study area could possibly reach more than 3 km as modelled by Goledowski *et al.* (2013). In contrast, the amount of erosion, predicted by the erosional model of Medvedev & Hartz (2015), suggests that it should not be more than 1.5 km over the area located near the high-altitude Scandes Mountains in the study area and should only reach ca. 1.75 km locally within some fjords. Based on maximum estimated burial depth in offshore wells and wells on the Andøya Island, a total erosion in the Lofoten and Vesterålen region could have reached up to 2 km between the Andøya Island and the mainland (Eig 2012, NPD 2010).

3 INPUT STRUCTURAL DATASETS

Bathymetry and topography have been taken from the Norwegian Mapping Authority and the sedimentary infill of the 3D structural model has been already described in Masytrenko et al. (2017). In this paper, the uppermost sedimentary layers of the Bjørnøya Fan Slide Complex and the Kai-Naust formations (middle Miocene-Pleistocene interval) have been subdivided into four layers in order to investigate the thermal effect of erosion and deposition during the Pleistocene time interval. Therefore, the detailed sedimentary units for the input 3D model is represented by the following layers (Figs. 3 and 4; numbering is according to Maystrenko *et al.* (2017)):

(1) the Naust Formation (sequences U, S and T) and analogues in the Lofoten Basin (layer 2.1; Pleistocene with age of ca. 0.6-0 Ma);

(2) the Naust Formation (sequence A) and analogues in the Lofoten Basin (layer 2.2; Pleistocene with age of ca. 1.5-0.6 Ma);

(3) the Naust Formation (sequence N) and analogues in the Lofoten Basin (layer 2.3; lower Pleistocene with age of ca. 2.7-1.5 Ma);

(4) the Kai Formation and the Molo Formation (layer 2.4; middle Miocene-Pliocene with age of ca. 18-2.7 Ma);

(5) the Brygge Formation and the undefined Cenozoic (layer 3; mainly Eocene-lower Miocene with age of ca. 56-18 Ma);

(6) the Upper Cretaceous-Paleocene (near top Cenomanian-top Paleocene) without sedimentary succession in the Røst Basin (layers 5-6);
(7) the Lower Cretaceous (base Cretaceous unconformity-near top Cenomanian) without sedimentary succession in the Røst Basin (layer 7);
(8) the pre-Cretaceous (Jurassic, Triassic, Permian and older sedimentary rocks) without sedimentary succession in the Røst Basin (layer 8);
(9) the undivided pre-Cretaceous, Cretaceous and Paleocene within the Røst Basin (layers 5-8).

It is important to note that the Kai-Naust and Brygge formations correspond to the Nordland and Hordaland groups, respectively, and the Paleocene corresponds to the Rogaland group. The Upper Cretaceous and the Lower Cretaceous do not exactly correlate with the Shetland and Cromer Knoll groups within some local areas (e.g. Dalland *et al.* 1988).

The maps for the Brygge-Naust (Eocene-Pleistocene) interval within the Lofoten-Vesterålen and Vøring segments of the Mid-Norwegian continental margin (Fig. 3) have been compiled by using data from Rise *et al.* (2005a), Eidvin *et al*. (2007), Dowdeswell *et al.* (2010), Rise *et al. (2010)* and Ottesen *et al.(2012)*, whereas maps for the post-break-up interval in the Lofoten Basin (Fig. 3) have been derived from Fiedler & Faleide (1996), Hjelstuen *et al.* (2007) and Laberg *et al.(2012)*. In particular, the mega-slide 2 of the Bjørnøya Fan Slide Complex with age of ca. 0.78-0.5 Ma from Hjelstuen *et al.* (2007) has been merged with the Naust Formation (U, S and T sequences; ca. 0.6-0 Ma) and the mega-slide 1 of the Bjørnøya Fan Slide Complex with age of ca. 1.5-0.78 Ma has been added to the Naust Formation (A sequence; ca. 1.5-0.6 Ma). In addition, thicknesses of the fluvio-glacial erosional material with ages of ca. 0.7-0, 1.5-07 and 2.7-1.5 Ma from Fiedler & Faleide (1996) and Laberg *et al.* (2012) have been merged with the Naust Formation (U, S and T sequences; ca. 0.6-0 Ma), Naust Formation (A sequence; ca. 1.5-0.6 Ma) and Naust Formation (N sequence; ca. 2.7-1.5 Ma), respectively. There are small differences in age between the merged successions but the most important area of our study corresponds to the Mid-Norwegian margin rather than the Lofoten Basin. Therefore, the Naust ages from Dowdeswell *et al.* (2010) have been assigned to the merged sedimentary layers in Fig. 3. The thickness pattern of the Naust sequences and analogues (Figs. 3a, b and c) is characterized by two distinct zones dominated by mega-slides within the Lofoten Basin and a more complex pattern within the SW Lofoten-Vesterålen margin and NE Vøring Basin. The sedimentary sequences in the Lofoten Basin are mostly represented by eroded sedimentary rocks from the Barents Sea area (Fiedler & Faleide 1996, Hjelstuen *et al.* 2007, Laberg *et al.* 2012). In contrast, the Naust sequences show more local origin from the adjacent mainland or the north-eastern part of the Lofoten-Vesterålen margin (e.g. Dowdeswell *et al.* 2010b, Rise *et al.* 2010, Ottesen *et al.* 2012). The thickest part of the Naust Formation corresponds to the sequence N, reaching more than 1600 m (Fig. 3c), and the thickest sedimentary rocks of the Lofoten Basin are analogues to sequence A of the Naust Formation, reaching more than 1300 m (Fig. 3b). Unfortunately, there is no direct information about the analogues of the Kai and Brygge Formations within the Lofoten Basin where the age of the sedimentary sequences still remains uncertain (Figs. 3d and e). We have included the undefined Cenozoic sedimentary layers, excluding the Paleocene, together with the Brygge Formation within the Lofoten Basin and the entire oceanic crustal domain of the study area (Fig. 3e).

The Paleocene, Cretaceous and pre-Cretaceous (Fig. 4) have been taken from Brekke (2000), Hansen (2009), Maystrenko & Scheck-Wenderoth (2009), Hansen *et al.(2012)*, Eig (2012), NGU data (Gernigon 2014) and Maystrenko *et al.* (revised). Sedimentary rocks within

the Røst Basin and the pre-Cretaceous have been described in details by Maystrenko *et al.* (2017). The pre-break-up sedimentary rocks in Fig. 4 are thick and are characterised by a broad zone of distribution south of the Bivrost Lineament (Figs. 4a, b and c). On the other hand, the Paleocene, Cretaceous and pre-Cretaceous are generally thinner with relatively thick sequences restricted to the Ribban and Vestfjorden basins.

The thickness pattern for different levels of the crystalline crust (Fig. 5) is based on the recent 3D density modelling by Maystrenko *et al. (2017)* constrained by different geophysical data including (1) deep seismic refraction and reflection lines (Mjelde *et al.* 1992, Mjelde *et al.* 1993, Mjelde *et al.* 2003, Kodaira *et al.* 1995, Mjelde *et al.* 2001, Breivik *et al.* 2009, Hansen *et al.* 2012, Breivik *et al.* 2017), (2) teleseismic receiver function data (Ottemoller and Midzi, 2003, Olsson *et al.* 2008, Ben Mansour *et al.* 2014) and (3) additional structural base and isopach maps (Maystrenko & Scheck-Wenderoth 2009, Ebbing & Olesen 2010, Maystrenko *et al.* revised).

The top of the crystalline basement (Fig. 6a) (Maystrenko *et al.* 2017) is divided into two zones by the Bivrost Lineament. The Vøring Basin and the Trøndelag Platform south-west of the lineament show a very deeply located basement (more than 15-17 km deep), whereas the Lofoten-Vesterålen margin has shallower basement depths (8-11 km). To the east, the near-coast shelf has very shallow basement (less than 1 km deep) which crops out at the Earth's surface within the Lofoten-Vesterålen archipelago and the mainland. The Moho topography (Fig. 6b) (Maystrenko *et al.* 2017) is deeply located (at around 40 km on average) beneath the mainland, has moderate depths (20-28 km) beneath the continental margin and is shallow (11-14 km depths) within the ocean domain.

The lithosphere-asthenosphere boundary (Fig. 6c) beneath the mainland has been derived from Calcagnile (1982), Artemieva *et al.* (2006), and Ebbing *et al.* (2012). The depth to the lithosphere-asthenosphere boundary beneath the oceanic domain has been obtained according to empirical relations between lithospheric age (Muller *et al.* 2008) and Love and Rayleigh wave-phase velocity provided by Zhang & Lay (1999).

The upper mantle of the Lofoten-Vesterålen margin and the adjacent areas is characterized by the presence of a low-velocity/low-density zone (see thick magenta line in Figs. 6b and c) based on seismic tomography (Bannister *et al.* 1991, Pilidou *et al.* 2005, Yakovlev *et al.* 2012, Hejrani *et al.* 2017) and 3D density modelling (Maystrenko *et al.* 2017). The origin of the low-velocity/low-density mantle can be related to both thermal and compositional variations but is still not known in detail.

4 RECONSTRUCTION OF EROSION

In order to reconstruct the Cenozoic erosion history of the Lofoten-Vesterålen margin, the estimated thickness of the eroded material from NPD (2010) and Eig (2012) has been mainly used. This reconstruction is based on maximal burial depth from wells located offshore and on the Andøya Island. It can, therefore, be considered as a reasonable estimate of the magnitude of the erosion within the Lofoten-Vesterålen region. The total thickness of the eroded material (Eig 2012, NPD 2010) has been only reconstructed for the offshore part of the study area. The estimates for onshore areas have been calculated by interpolation and/or extrapolation of the existing offshore values. In addition, results of the apatite fission track analyses (Hendriks & Andriessen 2002, Hendriks *et al.* 2010, Davids *et al.* 2013) have been considered to control the reconstructed thickness of the eroded rocks onshore. Finally, the reconstructed thickness onshore

has been corrected by the topography, assuming that the present-day relief of the Earth's surface was similar to the paleo-topography of the top basement prior to the erosion. The eroded material could be mainly represented by the Cretaceous, Jurassic and older sedimentary rocks, the weathered crystalline rocks, as well as by the Cenozoic sedimentary sequences locally. Comparison of the derived thickness of the reconstructed eroded rocks at the end of the Cretaceous (Fig. 7a) with the previous results of the combined study of the vertical motions caused by glacial erosion with Apatite Fission Track (AFT) analysis by Medvedev & Hartz (2015) demonstrates, in general, some qualitative and quantitative similarities over the large part of the mainland. However, our values are slightly higher locally.

The reconstructed total thickness of the eroded rocks in Fig. 7a can represent the distribution of the eroded material prior to latest Cretaceous-earliest Cenozoic tectonic events (Gernigon *et al.* 2003, Lundin *et al.* 2013, Ren *et al.* 2003, Ren *et al.* 1998). Therefore, this total thickness could still exist at the end of the Cretaceous. This is supported by the reflection seismic data offshore by the regionally traced near base Cenozoic unconformity in the Vøring and Møre basins (e.g. Brekke, 2000) which indicate a regional uplift and locally erosion.

The next step of reconstruction of the erosional history within the study area aims to estimate the amount of erosion during the different Cenozoic time intervals and main depositional stages. The amount of erosion has been calculated for the Paleocene, Brygge, Kai, Naust (N), Naust (A) and Naust (U, S and T) intervals for which we have the present-day thicknesses (Figs. 3 and 4a). The reconstruction of the erosion during each stage has been done proportionally to the volume of the deposited. In other words, the percentage of the deposited volume from the total volume of the deposited Cenozoic for each interval has been used to calculate the volume of eroded material in relation to the total volume of erosion (Table 6), represented by the thickness in Fig. 7a. It is important to note that the volume of the post-breakup Cenozoic from the Lofoten Basin has been excluded from our calculations since these sedimentary rocks are mostly the result of large erosion in the Western Barents Sea region (Fiedler & Faleide, 1996, Hjelstuen *et al.* 2007, Laberg *et al.* 2012). Therefore, the sedimentary sequences within the Lofoten Basin do not really have a strong and direct relationship with regards to the reconstructed and specific erosion of the Lofoten-Vesterålen margin and adjacent mainland. Furthermore, the thick Paleocene within the Hel Graben (Lundin *et al.* 2013), Zastrozhnov et al. submitted) and a possibly similar Paleocene sequence in the Røst Basin have also been excluded from the total volume of the deposited Cenozoic since these deposits represent the eroded material sourced from Lower and Upper Cretaceous sedimentary rocks (NPD, 2017) at the conjugate Greenland side of the proto-Atlantic region (Petersen *et al.* 2015, Meinhold *et al.* 2013).

According to Table 4, the volume of the eroded material is slightly more than two times higher than the volume of the deposited sedimentary rocks. The volume of the undefined Cenozoic in the case of layer 3 is around 27782 km^3. Some of the eroded material on the eastern slope of the Scandes Mountains was not transported to the Lofoten-Vesterålen margin and the estimated volume of this material is approximately 14430 km^3. The volume of the total deposited material is estimated to be 62718+27782=90500 km^3 and the total eroded material is approximately 136122-14430=121692 km^3. In this case, the total volume of the eroded material is only by 34% larger than the deposited one. This mismatch can be explained by several processes including: differential erosion and transportion of the fine-grained eroded material to the Atlantic ocean, dissolution of carbonates, lose due to wind transport and other processes

related to transport and deposition of the eroded products. Based on Table 6, the thickness of the eroded rocks has been calculated for each stage and, finally, has been step-by-step subtracted from the total thickness of the eroded material at the end of the Cretaceous (Fig. 7a). The derived thicknesses of the eroded rocks (Fig. 14) show gradual decrease of the reconstructed thicknesses throughout the Cenozoic as a result of continuous erosion.

5 METHODOLOGY

The 3D temperature distribution within the Lofoten-Vesterålen margin and the adjacent areas has been obtained with help of COMSOL Multiphysics, which is a finite-element analysis software package. During the 3D thermal simulations, the Heat Transfer Module has been used to model the stationary and time-dependent heat transfer in solid materials by heat conduction. The detailed description of the methodology has been already given by Maystrenko & Gernigon (accepted) and, here, the most important points of the used approach will be only repeated and the particular features of the 3D thermal modelling applied in this study will be described.

The 3D conductive thermal field has been calculated between two thermal boundary conditions at the Earth's surface/sea floor and the lithosphere-asthenosphere boundary. In particular, the upper thermal boundary condition has been set as time-dependent average temperatures at the Earth's surface and the sea-floor. The annual average air temperatures from Raab & Vedin (1995) and Tveito *et al.* (2000) represent the present-day temperature at the Earth´s surface onshore, whereas the temperature at the sea floor offshore has been taken to be dependent on the bathymetry (Table 1) based on Ottersen (2009) and Korablev *et al. (2014)*.

In addition, the detailed palaeoclimatic changes of the surface temperature during the last two glaciations (the Saalian and Weichselian glacial periods) have been considered during the 3D thermal modelling. A model of the spatio-temporal variations of the ice cover within Scandinavia during the Weichselian glacial period (Fig. 9) by Olsen *et al.* (2013) has been used for reconstruction of the palaeoclimatic conditions during the Weichselian glaciation. When the study area was covered by the ice sheet, a temperature of -0.5 °C has been chosen at the Earth´s surface beneath the ice cover as previously used and discussed by Slagstad *et al.* (2009). Sea-floor palaeotemperatures during the glacial periods has been set to be 0 °C that is in agreement with reconstructed temperature anomalies for the Norwegian Sea by Eldevik *et al.* (2014). Palaeotemperatures at the ice-free Earth's surface have been taken from Schmittner *et al.* (2011), indicating that the near-surface air temperature difference could be about -20 °C lower compared to the pre-industrial period and is only valid for the Last Glacial Maximum when the air temperatures were at its lowest level during the last glaciation. In order to take into account this fact, temperatures lower than -11 °C from Schmittner *et al.* (2011) have been decreased by 1-4 °C. Palaeotemperatures along the marginal parts of the ice cover have been obtained by an interpolation between -0.5 °C beneath the ice cover and the palaeotemperatures over the ice-free land areas. The same palaeoclimatic scenario was also applied for the Saalian glacial/Eemian interglacial period (220,000-118,000 years BP), considering that palaeoclimatic conditions were relatively similar during the Weichselian and Saalian glacial periods (e.g. Andersen and Borns,

1994). The palaeotemperatures during the last 8000 years (Table 2; Fig. 10) have been obtained according to Davis *et al.* (2003), Nesje *et al.* (2008), Mann *et al.* (2009) and Seppä *et al.* (2009).

During the Weichselian glaciation, the global palaeo sea level was 80-120 m lower than the present-day one (e.g. Hasenclever *et al.* 2017). However, the glacial erosion of the sedimentary cover could have been locally significant (Fig. 7). We expect that the present-day bathymetry was different from the one that existed during the Wechselian time. Therefore, a zone showing a gradual transition of temperatures from the mainland conditions towards the sea has been included into the paleotemperature scenario for the whole Weichselian glaciation (Fig. 10), including the present-day offshore areas covered by the reconstructed eroded sediments in Fig. 7. The reconstructed average palaeotemperatures (Fig. 10) show that the study area was mostly characterised by much lower temperatures during the Weichselian glaciation compared to the present-day conditions (Fig. 8).

The Cenozoic palaeoclimatic scenario reflects a continuous decrease of the palaeotemperature from 18 °C 66 Ma ago to present-day air temperature over the mainland (Zachos *et al.* 2001, Pekar *et al.* 2006, Rise *et al.* 2006, Eldrett *et al.* 2009, Ehlers *et al.* 2011, Hansen *et al.* 2013, Inglis *et al.* 2017). A temperature variation from 8 °C 45 Ma ago to 0 °C at the present-day sea floor within the deep sea was also considered (Zachos *et al.* 2001, Ravelo *et al.* 2004, Pekar *et al.* 2006, Filippelli and Flores, 2009, Hansen *et al.* 2013).

The lithosphere-asthenosphere boundary (Fig. 6c) has been chosen as a lower thermal boundary condition with a 1300 °C isotherm (e.g. Turcotte & Schubert, 2002). Besides, temperature at the lower thermal boundary has been enhanced within the low-velocity/low-density zone of the upper mantle (Figs. 6b and c). This has been done in accordance with the results of seismic tomography which indicate a decrease of a S-velocity by ca. 3% at 100 km depth in relation to the reference velocity model or even by more than 3% in relation to the surrounding mantle (e.g. Pilidou *et al.* 2005, Hejrani *et al.* 2017). Taking into account that the S-velocity changes by 1–2% per 100 ◦C (Cammarano *et al.* 2003) or even by 1% per 100 ◦C (Lee, 2003), we can infer that about +250 ^{o}C thermal anomaly at 100 km depth can be at least partially responsible for the origin of the low-velocity zone within the upper mantle.

Moreover, the density contrast between the low-density lithospheric mantle and the surrounding mantle of 18–35 kg/m^3 within the entire column of the lithospheric mantle (Maystrenko *et al.* 2017) can be translated to even higher temperature contrast than 250 ^{o}C at 100 km depth. A +250 ^{o}C mantle low-velocity/low-density zone at 100 km depth has been chosen as a compromise value because the origin of the low-velocity/low-density mantle can be also the result of compositional variations in addition to changes of pressure and temperature. Therefore, the thermal anomaly of +250 ^{o}C has been set for the 100 km deep or slightly deeper base of the anomalous lithospheric mantle. This thermal anomaly at 100 km depth has been further projected, proportionally to the thickness of the lithosphere, to the base of the shallower lithosphere within the zone with the low-velocity/low-density lithospheric mantle.

The influence of the early Cenozoic continental breakup has been coarsely included into the 3D thermal modelling workflow in terms of two additional lithosphere-asthenosphere

boundaries: the first one represents the lithospheric configuration immediately after the continental breakup, c. 55 Ma ago (Fig. 11a) and the second one represents a colder and thickened lithosphere expected at the end of the deposition of the Brygge Formation (18 Ma ago; Fig. 11b). These two time-steps (55 Ma and 18 Ma) allow us to roughly simulate the increased thermal effect during the continental breakup in the early Cenozoic and the subsequent cooling of the oceanic lithosphere during the rest of the Cenozoic. As a major limitation of the model, the precise position of the lithosphere-asthenosphere boundary during the Early Eocene breakup is still poorly known, but numerical models (e.g. Chen & Lin 2004, Kawakatsu *et al.* 2009) along modern spreading axis predict a shallow position of the 1300°C isotherm. In our study, the depth to the base of the lithosphere 55 Ma ago has been tentatively taken to be 13-17 km deep beneath the present-day oceanic domain, representing the newly formed Cenozoic lithosphere. According to estimations for 0 Ma oceanic lithosphere by Zhang & Lay (1999), the taken depth position of the lithosphere-asthenosphere boundary 55 Ma ago could theoretically vary in the range of ±5 km. The present-day depths of the lithosphere-asthenosphere boundary deeper than 95 km have not been changed, whereas the depth to the base of the lithosphere between the Cenozoic oceanic domain and the more than 95-km-deep lithosphere has been obtained by linear interpolation, assuming that the continental lithosphere has been at least partially affected by thinning in the vicinity of the oceanic domain (Fig. 11a). The lithosphere-asthenosphere boundary at 18 Ma ago (Fig. 11b) has been calculated in the same way as the present-day one according to empirical relations between the age of the lithosphere and seismic velocities in Zhang & Lay (1999). We cannot exclude the large inherent uncertainties in our palaeo-depths estimations of lithosphere-asthenosphere boundaries (Fig. 11). They could be related to potential small-scale changes in the intensity of the syn-breakup magmatism which could locally enhance the geothermal gradient and modify the thermal properties of the deep continental crust. However, breakup and associated magmatic processes are still unclear and require a more detailed study which is outside the scope of our investigation. Consequently, the influence of the local syn-breakup magmatism has been mainly neglected in the present study whereas the large-scale one is considered in terms of the uplifted lithosphere-asthenosphere boundary 55 Ma ago (Fig. 11a).

The thermal effects of the post-breakup uplift and erosion within the study area with further deposition of the Naust (Pleistocene), Kai (middle Miocene-Pliocene) and Brygge (Eocene-lower Miocene) formations (layers 2.1-2.3, 2.4 and 3, respectively; Fig. 3) have been included into the 3D thermal modelling workflow, allowing us to focus more specifically on the time-dependent perturbations in the subsurface thermal regime due to the post-Paleocene erosion and sedimentation.

The 3D thermal modelling workflow includes the following steps:

(1) Calculation of a steady-state 3D conductive thermal field after the continental breakup 55 Ma ago. The Brygge, Kai and Naust formations (Eocene-Pleistocene interval; Fig. 3) have been excluded from these calculations, whereas a new layer, represented by the reconstructed eroded rocks at the end of the Paleocene (Fig. 7b), has been added to the top of the model. The lower thermal boundary is represented by the 1300 ^{o}C isotherm at the inferred lithosphere-

asthenosphere boundary 55 Ma ago (Fig. 11a) and the top of the eroded rocks is set as a new upper thermal boundary. The top of the Upper Cretaceous-Paleocene deposits (layers 5-6) or deeper/older rocks have been used as the upper thermal boundary in places where the eroded rocks were not restored. Porosity of the pre-breakup sedimentary succession has been readjusted to shallower depth conditions by subtraction of the thickness of the post-breakup sedimentary package (Brygge, Kai and Naust formations; Eocene-Pleistocene interval) from the present-day depths and correction of the present-day deep sea floor position. Accordingly, the porosity-dependent thermal conductivities and densities of the sedimentary cover have been adjusted to shallower depths.

(2) Calculation of the time-dependent (transient) 3D conductive thermal field from 55 Ma ago to the end of Brygge interval in the early Miocene 18 Ma ago. The calculated 3D temperature distribution from step (1) has been used as the initial temperature condition at the beginning of the time-dependent calculations (55 Ma ago). The Kai and Naust formations (middle Miocene-Pleistocene interval; Figs. 3a-d) have been excluded from these calculations, whereas a new layer, represented by the reconstructed eroded rocks for the end of the Brygge interval (Fig. 7c), has been added to the top of the model. The lower thermal boundary has been represented by the 1300 ^{o}C isotherm at the inferred lithosphere-asthenosphere boundary at 18 Ma ago (Fig. 11b) and the top of the eroded rocks has been set as a new upper thermal boundary. Top of the Brygge Formation (layers 3) or deeper/older rocks have been used as the upper thermal boundary in places where the eroded rocks were not restored. Accordingly, the porosity of the pre-breakup sedimentary succession has been adjusted to shallower depth conditions compared to the present-day ones by subtracting the total thickness of the Kai and Naust formations (Eocene-Pleistocene interval) from the present-day depths and correction of the present-day deep sea floor position.

(3) Calculation of the time-dependent (transient) 3D conductive thermal field during the Kai interval from 18 Ma ago to 2.7 Ma ago. The final calculated 3D temperature distribution from the previous step (2) has been used as initial temperature condition at the beginning of the time-dependent calculations (18 Ma ago). The whole Naust Formation (Pleistocene interval; Figs. 3a-c) have been excluded from these calculations, whereas a new layer, represented by the reconstructed eroded rocks at the end of the Kai interval (Fig. 7d), has been added to the top of the model. The lower thermal boundary has been represented by the 1300 ^{o}C isotherm at the present-day as a new upper thermal boundary. Top of the Kai Formation (layer 2.4) or deeper/older rocks have been used as the upper thermal boundary in places where the eroded rocks were not restored. Accordingly, porosity of the pre-breakup sedimentary succession has been adjusted to shallower depth conditions compared to the present-day ones by subtracting the total thickness of the Naust Formation (Pleistocene interval) from the present-day depths and correction of the present-day deep sea floor position.

(4) Calculation of the time-dependent (transient) 3D conductive thermal field during the Naust (N) interval from 2.7 Ma ago to 1.5 Ma ago. The final calculated 3D temperature distribution from step (3) has been used as initial temperature condition at the beginning of the time-dependent calculations (2.7 Ma ago). The sequences A, U, S and T of the Naust Formation

(Pleistocene interval; Figs. 3a and b) have been excluded from these calculations, whereas a new layer, represented by the reconstructed eroded rocks for the end of the Naust (N) interval (Fig. 7e), has been added to the top of the model. The lower thermal boundary has been represented by the 1300 ^{o}C isotherm at the present-day lithosphere-asthenosphere boundary (Fig. 6c) and the top of the eroded rocks has been taken to be an upper thermal boundary. Top of the sequence N of the Naust Formation (layer 2.3) or deeper/older rocks have been used as the upper thermal boundary in places where the eroded rocks were not restored. Porosity of the pre-breakup sedimentary succession has been adjusted to shallower depth conditions compared to the present-day ones by subtracting the total thickness of the sequences A, U, S and T of the Naust Formation (Pleistocene interval; Figs. 3a and b) from the present-day depths and correction of the present-day deep sea floor position.

(5) Calculation of the time-dependent (transient) 3D conductive thermal field during the Naust (A) interval from 1.5 Ma ago to 0.6 Ma ago. The final calculated 3D temperature distribution from step (4) has been used as initial temperature condition at the beginning of the time-dependent calculations (1.5 Ma ago). The sequences U, S and T of the Naust Formation (Pleistocene interval; Fig. 3a) have been excluded from these calculations, whereas a new layer, represented by the reconstructed eroded rocks at the end of the Naust (A) interval (Fig. 7d), has been added to the top of the model. The lower thermal boundary has been represented by the 1300 ^{o}C isotherm at the present-day lithosphere-asthenosphere boundary (Fig. 6c) and the top of the eroded rocks has been taken to be an upper thermal boundary. Top of sequence A of the Naust Formation (layer 2.2) or deeper/older rocks have been used as the upper thermal boundary in places where the eroded rocks were not restored. Porosity of the pre-breakup sedimentary succession has been adjusted to shallower depth conditions compared to the present-day ones by subtracting the total thickness of the sequences U, S and T of the Naust Formation (Pleistocene interval; Fig. 3a) from the present-day depths and correction of the present-day deep sea floor position.

(6) This is a final step which includes a time-dependent (transient) calculation of the 3D conductive thermal field from 0.6 Ma ago to the present-day. The final calculated 3D temperature distribution from step (5) has been used as initial temperature condition at the beginning of the time-dependent calculations (0.6 Ma ago). The lower thermal boundary has been represented by the 1300 ^{o}C isotherm at the present-day lithosphere-asthenosphere boundary (Fig. 6c) and the top of the 3D structural model (present-day sea floor and Earth's surface onshore) has been considered as the upper thermal boundary. Porosity has been estimated according to the present-day depths.

During all steps of the 3D thermal modelling, the eroded rocks have been assumed to be mainly represented by sedimentary rocks and weathered crystalline crust which is characterized by density and porosity similar to sedimentary rocks rather than crystalline ones. The porosity of the eroded rocks has been kept the same for all steps as it is in the case of complete reconstructed eroded sequence (Fig. 7a) with zero-level at the top of this sequence, assuming that a possible decompaction of these rocks due to erosion was very minor or even absent at each time step.

During all steps, paleotemperature at the upper thermal boundary has been taken to be time-dependent in accordance with Tables 1-3 and Fig. 10.

6 THERMAL PROPERTIES

Thermal properties represented by specific heat capacity, thermal conductivity and radiogenic heat production (Table 5) have been assigned for each layer of the 3D structural model.

The thermal conductivity for the sedimentary cover has been taken from the previous estimations of the matrix thermal conductivity from wells within the northern part of the Viking Graben (Brigaud *et al.* 1992), the Mid-Norwegian continental margin and adjacent areas (Eldholm *et al.* 2005, Pascal & Midttømme 2006, Pascal 2015), and based on unconsolidated sampled sedimentary rocks from the Vøring Basin according to Midttømme *et al.* (1995). The obtained thermal conductivities of sedimentary rocks have been cross-validated with results of measurements of rock samples with similar lithology (Čermak & Rybach 1982, Clauser 2011) and the wide-ranging thermal conductivities of different sedimentary rocks, summarized by Midttømme & Roaldset (1999). The thermal conductivity of basalts (layer 4) has been set to be 1.8 W/mK on average according to Balling *et al.* (2006). Thermal conductivities of the upper crystalline crustal rocks have been set to be in the range of the rock-sample measurements within the Norwegian mainland (e.g. Olesen *et al.* 1993, Slagstad *et al.* 2009, Maystrenko *et al.* 2015b). The mentioned thermal conductivities of the sedimentary infill, basalts and upper-crustal rocks have been supplemented with published values for the deeper crystalline crust and the lithospheric mantle (Čermak and Rybach, 1982, Wollenberg and Smith, 1987, Hofmeister, 1999, Artemieva *et al.* 2006, Scheck-Wenderoth & Maystrenko 2008, Scheck-Wenderoth & Maystrenko 2013, Maystrenko *et al.* 2014).

The thermal conductivity of sedimentary rocks has been set to be temperature- and porosity-dependent to take into account changes of the thermal conductivity as a result of increasing temperature and decreasing porosity with depth. The thermal conductivity of the fluid in the pores of sedimentary rocks has been set to be the temperature-dependent thermal conductivity of water according to Wagner & Kretzschmar (2008). The thermal conductivities of the crystalline rocks have set to be only dependent on temperature because the average porosities of the crystalline rocks are usually extremely low at the regional scale and can, therefore, be neglected. The empirical equations from Sass *et al.* (1992) and Vosteen & Schellschmidt (2003) have been used to describe a dependence of thermal conductivities of sedimentary and crystalline rocks on temperature. The thermal conductivity of the lithospheric mantle has been set to be both pressure and temperature dependent according to Hofmeister (1999) and van den Berg *et al.* (2001). Porosity and density of the sedimentary rocks have been obtained based on exponential functions of increasing densities with depth in Maystrenko *et al.* (2017) and densities of the crystalline rocks have been also taken from Maystrenko *et al.* (2017). The detailed description on how the temperature-, pressure- and porosity-dependent thermal conductivities have been calculated is given in Maystrenko & Gernigon (accepted).

The chosen specific heat capacity (Table 4) has been set to be constant for each layer of the 3D model during the 3D thermal modelling, representing the temperature-dependent average values of the specific heat capacity based on laboratory measurements at different temperature conditions according to Čermak & Rybach (1982), Afonso *et al.* (2005) and Clauser (2011).

The radiogenic heat production of sedimentary layers of the 3D model has been derived from the results of gamma-ray logging in selected wells according to the empirical relationship between total natural gamma and radiogenic heat production in Bücker & Rybach (1996). An example of the used natural gamma ray logs and the derived radiogenic heat production is shown in Fig. 12. The chosen wells are located within the south-western part of the model area (Fig. 13) where the sedimentary cover has been drilled for the purposes of the petroleum industry. There are only a few shallow wells, drilled through the sedimentary cover within the rest of the Lofoten-Vesterålen margin and, unfortunately, well logs of these shallow wells are not easily accessible.

Based on the results of calculations, the average radiogenic heat production of the sedimentary rocks shows a wide range of values from 0.47 $\mu W/m^3$ to 2.02 $\mu W/m^3$ (Table 6). The stratigraphic subdivison of the used wells do not include sequences N, A, U, S and T of the Naust Formation (NPD 2017) and, therefore, the average values for the total Naust Formation have been used for the Naust (N), Naust (A) and Naust (U, S and T) intervals (layers 2.1-2.3). Moreover, the Nordland Group (Naust plus Kai formations) has been only indicated in some wells. In this case, the same value of the radiogenic heat production has been used for both the Naust and Kai formations. This is actually supported by well 6510/2-1 R where the Naust and Kai formations are characterised by the same values of the radiogenic heat production (Table 6). The derived average values of the radiogenic heat production for each sedimentary layer have been further used to construct maps by interpolation between these values in the used wells with extrapolation to the areas without the well data (Fig. 13).

The uppermost layers, represented by Naust (layers 2.1-2.3) and Kai (layer 2.4), are characterised by a very similar pattern of the derived radiogenic heat production (cf. Figs. 13a and b) in spite of a fact that some values are different (Table 6). A similar distribution of the radiogenic heat production is also found for the Brygge (Fig. 13c) and the Upper Cretaceous-Paleocene layers (Fig. 13d). Moreover, the relatively high radiogenic heat production in wells 6607/5-1 and the relatively low one in wells 6507/5-1, 6510/2-1 R and 6608/8-1, representative for the south-western corner of the model area, are clearly or partially recognisable in maps for the Naust, Kai and Brygge formations, the Upper Cretaceous-Paleocene and the Lower Cretaceous (cf. Figs. 13a-e). The latter means that the similar pattern of the radiogenic heat production is characteristic of the more than 100-million-year-long stratigraphic interval. This long-term inheritance for the Cretaceous-Cenozoic interval has already been identified in the Vøring and Møre basins by Maystrenko & Gernigon (accepted), indicating a possible inheritance in clastic material transportation from original localities with the increased or decreased content of the radiogenic elements. Alternatively, it may indicate a differential sorting of the eroded products during transportation from source-to-sink. The deposition of sedimentary rocks with a more argillaceous composition in particular areas of the Mid-Norwegian continental margin may

explain the local increase of the heat production within specific areas because argillaceous rocks are usually characterised by a higher radiogenic heat production compared to more sandy sedimentary rocks (e.g. Čermak & Rybach, 1982, McKenna & Sharp 1998, Villa *et al.* 2010).

The assigned radiogenic heat productions of the upper and middle-crustal layers (layers 9, 10-11 and 12; Figs. 5b-d) onshore are mainly based on the measured radiogenic heat production for different geological/lithological units of Norway (Slagstad 2008, Slagstad *et al.* 2009, Slagstad & Lauritsen 2013). The radiogenic heat production of the oceanic crust, lower continental crust and the lithospheric mantle (layers 13-18; Figs. 5e-h) have been set to be constant (Table 5) according to published values for the assumed lithological composition of each layer (Čermak & Rybach, 1982, Scheck-Wenderoth & Maystrenko 2008, Villa *et al.* 2010). To remove a misfit between measured and modelled temperatures in the available wells offshore, lateral changes in the radiogenic heat production of the upper and middle continental crust have been applied. Other possible explanations for some local changes of the observed temperature could be associated with atypical fluid flow, strong variations in thermal conductivities, structural uncertainties and/or limited resolution of our 3D model. The above-mentioned alternative hypothesises would, however, require additional structural data and sampling material to be tested, as well as simulation of other physical processes, such as fluid flow etc.. Absence of the detailed structural data and supplementary measurements together with technical difficulties in modelling of the detailed fluid flow at the scale of our 3D model do not allow us to test the variety of other possible reasons in addition to the variable radiogenic heat production. On the other hand, the radiogenic heat production of the crystalline rocks varies within the mainland (e.g. Slagstad 2008, Pascal & Rudlang 2016), implying that possible variability exists offshore as well. During the 3D thermal modelling, several models with different values of the radiogenic heat production have been tested to fit the measured and modelled temperatures in the available wells.

The upper crystalline crust is characterised by the increased radiogenic heat production up to 2.2 $\mu W/m^3$ within the NS-striking zone onshore in the middle of the southern part of the model area (Fig. 14a). Towards the north, a wide zone with the increased heat production (2 $\mu W/m^3$) corresponds to the thickened low-density upper crustal layer inferred by Maystrenko *et al.* (2017). Both areas with the increased radiogenic heat can be represented by granite, granitic gneiss and/or granitoids with the increased content of the radiogenic elements similar to the Precambiran Transscandinavian Igneous Belt granites which are characterised by the average radiogenic heat production of 2.6 $\mu W/m^3$ (locally up to 4 $\mu W/m^3$) according to Slagstad (2008). Within the south-western part of the model area, the radiogenic heat production varies from 0.2 to 2.5 $\mu W/m^3$ (Fig. 14a), indicating a possible lithological differentiation of the upper crust there.

The middle crust is characterised by an average radiogenic heat production of ca. 0.86 $\mu W/m^3$ within the most part of the study area (Fig. 14b) and slightly increased to 0.92 $\mu W/m^3$ within the areas where the upper-crustal layer is absent (cf. Figs. 5c and 14b). The same pattern of the radiogenic heat production as in the case of the upper crust has been applied within the south-western part of the model area (cf. Figs. 14a and 14b). The thicknesses of the upper and middle crust within the south-western part of the model area is mostly in the range of 0.5-4 km

and 1-5 km on average, respectively, with some local thickening and thinning. These relatively small thicknesses of the upper-middle crustal layers implies that the assigned radiogenic heat production does not drastically affect the modelled temperatures in that area compared to the mainland where the thickness of these layers is 12 km on average with local thickening up to more than 20 km. Therefore, if our assumption with varying radiogenic heat production offshore appears to be partially erroneous, the regional-scale pattern of the modelled temperature should not strongly change.

7 RESULTS OF THE 3D THERMAL MODELLING

The 3D conductive thermal pattern beneath the study area (Fig. 15) have been modelled by assigning thermal properties (Tables 5 and 6) to the layers of the 3D structural model from Maystrenko *et al.* (2017), assigning thermal boundary conditions at the top and bottom of the 3D model (e.g. Figs. 6c, 8, 10 and 11; Tables 1, 2 and 3) and including thermal influence of the Cenozoic erosion and deposition (Fig. 7; Table 4).

7.1 Temperature within the upper part of the 3D model

The results of the 3D thermal modelling for the upper part of the 3D structural model are shown in Fig. 16 and are represented by the temperature maps of six horizontal model slices at depth below sea level of 2, 5, 7, 10, 15 and 18 km. It can be seen that the mainland is generally colder compared to the continental margin (Fig. 16). At depth of 2 km below sea level, the Scandes Mountains are clearly reflected by the increased temperatures beneath the mainland (cf. Figs. 2 and 16a). This is a result of the topographic effect due to a presence of the 1-1.5 km elevated Scandes Mountains compared to the rest of the mainland where the relief is smoother and deeper. The upper thermal boundary has been set at the Earth's surface and, therefore, the elevated relief of the Scandes Mountains adds an additional 1-1.5 km to the distance from the upper thermal boundary to the depths below sea level in Fig. 16. This topographic thermal effect of the Scandes Mountains is still well visible at depth of 5 km and even deeper where it is smoothed by other thermal effects. In contrast, the thermal influence of the deep bathymetry offshore is reflected by the decreased temperature beneath the Lofoten Basin (Fig. 16) where the sea floor is located at depths of more than 2-3 km (Fig. 2). Actually, the white (blanked) area in Fig. 16a outlines the bathymetry deeper than 2 km. The shape of this blanked area is still clearly recognisable in terms of the lower temperatures at depths of 5 and 7 km (Figs. 16b and c), reflecting the steeply deepening sea bottom which corresponds to the upper thermal boundary and, therefore, pulls the influence of the low (ca. 0 ^{o}C) deep sea temperatures down to greater depths.

The eastern part of the mainland is noticeably colder than the continental margin (Fig. 16). This difference in temperature between the mainland and the continental margin increases with depth (Fig. 16), mainly reflecting both a chimney effect of the relatively high-thermally conductive, crystalline rocks, exposed at the Earth's surface within the mainland, and a very deep location of the lower thermal boundary, represented by the base of the lithosphere, beneath the mainland (Figs. 6c and 11).

The next interesting aspect of the thermal pattern within the upper part of the 3D model is related to the straight spatial relationship between areas with thick sedimentary infill and areas with increased temperatures within the Lofoten-Vesterålen margin and the Vøring Basin (cf. Figs. 3, 4 and 16). This feature of temperature distribution is associated with the low thermal conductivity of the sedimentary cover which enhanced the heat storage within the areas with thickened sedimentary rocks. This thermal insulation effect is more intensive to the northeast from the Bivrost Lineament compared to the smoother effect observed to the southeast and particularly pronounced at depths of 2-7 km (Fig. 16a-c). This kind of differentiation of the modelled temperatures is a result of the thermal effects of the Cenozoic erosion and deposition which are described in detail further in the text. Moreover, superposition of (1) different temperature-increasing effects (thermal insulation by the thick sedimentary rocks within the Røst Basin and the Hel Graben (Fig. 4) and significant shallowing of the lower thermal boundary towards the oceanic domain (Figs. 6c and 11)) and (2) opposite temperature-decreasing effects (deep bathymetry (Fig. 2) and thick, less than 2.7 Ma old, sedimentary rocks within the Lofoten Basin (Fig. 3a-c)) are responsible for a NE-SW-trending zone with increased temperature within the Røst Basin and the Hel Graben which is especially pronounced at depths of 10, 15 and 18 km (Figs. 16d-f). This zone of increased temperature should have extended towards the oceanic Lofoten Basin, if the bathymetry would not be so deep and if the thickness of the young and, therefore, thermally not equilibrated Pleistocene sedimentary rocks would not be so thick there.

The major controlling factor of the modelled temperatures at the top of the crystalline basement (Fig. 17) is related to the geometry of the top-basement (Fig. 6a), clearly showing that the deeper top basement corresponds to the highest modelled temperatures and vice versa. Thus, the highest temperatures have been modelled within the deepest parts of the Vøring Basin where the modelled temperatures are 400-450 °C on average (Fig. 17), whereas the Ribban and Vestfjorden basins are characterised by lower temperature less than 300 °C on average with some local increase to more than 350 °C within the Vestfjorden Basin. The modelled temperatures on the mainland and the Lofoten-Vesterålen archipelago purely reproduce the present-day Earth´s surface temperature (cf. Figs. 8 and 17) because the crystalline basement crops out at the Earth's surface there.

7.1.1 Modelled temperature vs. measured temperature

The obtained temperatures within the uppermost part of the 3D model have been compared with measured temperatures in available wells which are shown in Fig. 18. Positions of the wells with only drill-stem test (DST) temperatures offshore and temperatures from well loggings onshore (Fig. 18a) are plotted separately from the locations of all available wells, including the wells with less reliable bottom-hole temperatures (BHT), in Fig. 18b. Due to a fact that only a few wells with DST temperatures are available offshore and their restricted location close to each other (Fig. 18a), the BHT have been particularly used to check the calculated temperatures with the measured ones. However, it is important to notice that BHT can be disturbed by circulation of the drilling fluid and, therefore, are less reliable compared to DST temperatures (temperature of

fluids, thermally equilibrated with the containing sedimentary rocks) and temperature logs (measured under thermal equilibrium conditions in the wells). In this case, a comparison between the observations and the results of the 3D thermal modelling is separately provided for the wells with DST temperatures and temperature logs (Figs. 18a and 19a; Table 7) and for the wells with BHT (Figs. 18b and 19b; Table 8).

Comparison between the modelled and measured temperatures demonstrates that the large part of the obtained temperatures are in reasonable agreement with the main tendency in distribution of the measured temperatures (Fig. 19). The latter is especially true when only DST and temperature logs are considered (Fig. 19a). Larger misfits are present when compared with the BHT estimation (Fig. 19b). To investigate the magnitude of these misfits in detail, an additional study has been carried out by plotting the difference between the measured and modelled temperatures in tables (Tables 7 and 8) and the related maps (Fig. 18). According to the Table 7 and Fig. 18a, it is clear that most of the misfits (92.3%) between the modelled and measured DST and well-logs temperatures are in the range of ±5 °C with only one well showing a misfit of slightly higher than 5 °C (Table 7). In contrast, if the wells with BHT are also considered in addition to the previous wells, only around 51% of the misfits are in the range of ±5 °C and the misfits with a range of ±10 °C form almost 85% of total amount of the used wells (Table 8). Consequently, the large portion of the reasonable differences for this kind of regional-scale study stays in the range of ±10 °C, indicating that the major trend of the measured temperatures have been reasonably well reproduced during our 3D thermal modelling.

Misfits larger than ±10 °C are also present in Table 8. The spatial distribution of these larger misfits (Fig. 18b) demonstrates that the wells with large differences of ±20 °C are closely located to the wells with the smaller differences of ±10 °C or even ±5 °C. However, there is almost no way to reduce such a large differences because the distance between the wells with different misfits is locally less than the 4 km horizontal resolution provided by our 3D structural model. Any attempt to reduce the misfit in a particular well with large misfit will automatically increase the misfit in the closely-located well(s) and vice versa. Moreover, the local-scale thermal pattern for each particular well cannot be reproduced during our simulations without including a more detailed lithological section of these wells and surrounding areas. This is technically very difficult in the case of the regional-scale 3D thermal modelling. Most of the large misfits are possibly caused by relatively local processes, such as fluid flow. In the case of intensive fluid flow, circulation of the heated or cooled fluids through the sedimentary rocks can play an important role in terms of convective or advective heat transfers in addition to the modelled regional-scale heat conduction.

7.2 Temperature within the lower part of the 3D model

The modelled temperatures within the lower part of the 3D model are shown in Fig. 20 by using the temperature maps for four horizontal slices through the 3D thermal model at depth below sea level of 25, 40, 80 and 100 km. From these maps Fig. (20), it is even more obvious that the areas beneath the mainland are characterised by lower temperatures compared to the continental margin and the oceanic domain. This is due to the fact that the thermal influence of the lower

thermal boundary configuration (Figs. 6c and 11) becomes more evident at great depths where the distance to the base of the lithosphere becomes shorter. The deepening of the lower thermal boundary beneath the mainland causes a decrease in temperatures there, whereas the shallowing of the lithosphere-asthenosphere boundary beneath the oceanic domain results in increased modelled temperatures (cf. Figs. 6c, 11 and 20). Moreover, the shape of the low-velocity/low-density mantle is reflected by the increased modelled temperatures as a result of the predefined 250 ^{o}C thermal anomaly at the depth of 100 km projected to the lower thermal boundary, assuming that the low-velocities and -densities within this atypical mantle is at least partially related to its enhanced temperature in addition to possible compositional variations.

In addition to the above-described deep-seated temperature-controlling factors, the near-surface thermal influence is still recognisable at depth of 25 km. Decreased temperatures within the Lofoten Basin compared to the Røst Basin and the Utrøst Ridge (Fig. 20a) is due to the deep bathymetry and the deposition of the Pleistocene sedimentary rocks, which are thermally not equilibrated. In contrast, the modelled thermal trend is already strongly controlled by the shape of the lower thermal boundary at a depth of 40 km (cf. Fig. 6c and 20b). At depths of 80 and 100 km, the white (blanked) area corresponds to sub-lithospheric mantle, i.e. located beneath the lower thermal boundary. Therefore, the configuration of the lower thermal boundary, represented by the lithosphere-asthenosphere boundary, has a major impact on the modelled temperature distribution within the deep part of the 3D model.

The calculated temperatures at the Moho discontinuity level (Fig. 21) partially reflects its geometry (Fig. 6b). The key factor controlling the modelled temperature at the Moho is not only its depth position but also the distance between the Moho and the lower thermal boundary, i.e. thickness of the lithospheric mantle. Therefore, both Moho depth and the thickness of the lithospheric mantle mainly control the distribution of the modelled temperature at the Moho. In addition, one of the secondary factors are related to a higher radiogenic heat production of the crystalline crust compared to the lithospheric mantle rocks (more than 10 times lower on average) (Table 5). Therefore, the thickness of the crust plays an important role as well. The interaction between these factors can be recognised at the temperature map in Fig. 21 where two maxima of the modelled temperature have different origin. The first temperature maximum (up to more than 800 ^{o}C) is located beneath the mainland in the south of the model area where the Moho topography is the deepest (46-48 km depth on average; Fig. 6b). Therefore, this maximum of the modelled temperature is mainly caused by the depth position of the Moho and partially by the thickening of the internally more heat productive crystalline crust. The second temperature maximum (up to 800 ^{o}C) is located beneath the Lofoten-Vesterålen archipelago (Fig. 21) where the Moho is about 10 km shallower compared to the previous temperature maximum. However, the lithosphere-asthenosphere boundary is about 25 km deeper beneath the first temperature maximum, indicating that the distance between the Moho and the lower thermal boundary is 25 km more in that place compared to the thinner lithospheric mantle beneath the Lofoten-Vesterålen archipelago. Therefore, the reduced distance from the Moho to the deep heat from the Earth's interior beneath the Lofoten-Vesterålen archipelago plays an important role in addition to

a relatively deep position of the Moho there. The rest of the modelled temperatures at the Moho level reflects the dominance of the Moho topography as the controlling factor.

7.3 Vertical slices through the 3D model

Three 2D vertical slices (Fig. 22) through the 3D thermal model (Fig. 15) have been selected to illustrate cross-sectional view at the modelled temperatures. The locations of these cross-sections have been chosen to be at the same location as the crustal sections described in Maystrenko *et al.* (2017). These slices allow us to see the vertical distribution of the modelled temperature (Fig. 22) in addition to the horisontal ones, shown in Figs. 16 and 20. The increased temperature within the low-velocity/low-density mantle has been displayed along all three vertical slices in Fig. 22. A zone with the increased temperature within the anomalous mantle is especially pronounced near the lithosphere-asthenosphere boundary along the vertical slice 2 (Fig. 22b) which crosses this low-velocity/low-density zone almost in the middle (Fig. 2). In contrast, the vertical slices 1 and 3 crosses the marginal parts of the anomalous mantle (Fig. 2) and, therefore, the related increase of temperature is smoother compared to that one in slice 2 (cf. Figs. 22a and c and Fig. 22b). The thermal anomaly within the low-velocity/low-density mantle becomes very smoothed at shallow depths where it is almost not recognisable. The remarkable feature along the vertical slices is absence of the straightforward correlation between an uplift of the modelled isotherms and the shallow Moho (Fig. 19). This is mostly due to the fact that the lower thermal boundary at the base of the lithosphere is shallow within the western part of the model area. In addition, the thermal influence of the positive thermal anomaly within the anomalous mantle is superimposed on the thermal trend controlled by the configuration of the lower thermal boundary. The thermal influence of the shallowing lithosphere-asthenosphere boundary is more pronounced along slice 3 which crosses the oceanic domain to the west (Fig. 22c). It confirms the thermal influence of the early Cenozoic continental breakup, reflected by the shallowing base of the lithosphere, is still clearly recognizable within the western part of the Lofoten-Vesterålen margin segment in terms of the increased temperatures. The modelled regional-scale thermal pattern is also affected by the insulation effect of the thick low-thermally conductive sedimentary rocks which is particularly obvious along slice 1 where the modelled isotherm are slightly uplifted beneath the Vøring Basin.

7.4 Thermal effect caused by the erosional and depositional processes

The transient 3D thermal modelling shows that the modelled temperatures beneath the reconstructed eroded rocks (Fig. 7) gradually decreased through the Cenozoic (Fig. 23), reaching the highest values at the end of the Cretaceous (Fig. 23a) when the thickness of the eroded material was the largest one and consequently the base of the reconstructed rocks was at its maximal burial depth (Fig. 7a). At the end of the Cretaceous, the modelled temperatures beneath the reconstructed rocks could have reached up to 90 ^{o}C within the north-eastern part of the Vestfjorden Basin and more than 80 ^{o}C near the Andøya Island and further west in the southern

part of the Lofoten Ridge (Fig. 23a). The modelled temperatures at the base of the eroded rocks decreased as a result of the Cenozoic uplift and erosion, indicating a progressive cooling of the Lofoten-Vesterålen margin and the adjacent areas. Decrease in the modelled temperatures is directly proportional to the estimated amount of the material eroded during each time interval (cf. Figs. 7 and 23).

The thermal effects of the simultaneous erosion and deposition has been estimated by calculating the temperature difference between the results of the 3D thermal modelling when taking into account or not the erosion and subsequent deposition. In other words, the calculated temperatures of the model without consideration of the erosion and deposition during the modelling workflow have been subtracted from the modelled temperatures in the case of the model with erosion and deposition. The resulted differences are shown in terms of temperature maps in Fig. 24, showing that a positive thermal anomaly should exist within the areas where the sedimentary and/or crystalline rocks were eroded, whereas the negative values appear to be present in the Vøring and Lofoten basins showing the most important Cenozoic depocentres. Thermal anomalies in Fig. 24 are shown at different depths, indicating that these anomalies are very smoothed towards the thermal equilibrium at the shallow depths (e.g. 2 km in Fig. 24a), whereas the erosion/deposition-related anomalies are characterised by high amplitudes at greater depths (Figs. 24c and d). At a depth of 2 km, the positive anomaly near the Lofoten Ridge is only around 7 ^{o}C and the negative one within the Vøring Basin is about -14 ^{o}C. In contrast, the erosion-caused positive thermal anomaly within the Vestfjorden Basin is up to 17, 24 and 27 ^{o}C and the negative thermal anomaly within the Vøring Basin is almost -33, -47 and -40 ^{o}C at 5, 10 and 25 km depth, respectively. The same is true for the negative temperature anomaly modelled beneath the Lofoten Basin where the amplitudes varies with depth from -33 ^{o}C at 5 km depth to almost -64 ^{o}C at 25 km depth. Our results support the previous 2D modelling by Pascal & Midttømme (2006) who concluded that the thermal state of the SW part of our study area was likely affected by strong modifications due to glacial erosion and deposition during the Quaternary.

According to the calculated 3D temperature cube, the differences between the modelled temperature with and without thermal effect by the erosion and deposition, the obtained erosion-related positive thermal anomaly reaches its maximum of more than +27 ^{o}C at depths of 17-22 km beneath the eastern part of the Vestfjorden Basin. The deposition-related negative anomaly is situated within the north-eastern part of the Vøring Basin, showing a minimal values of ca. -48 ^{o}C at 12-14 km depth. The most prominent negative anomaly is characterized by a minimum of ca. -70 ^{o}C at 17-20 km depth beneath the oceanic Lofoten Basin. These zones of maximum and minima of the obtained thermal anomalies are mainly associated with the areas where relatively rapid erosion and deposition took place during the late Cenozoic time in the Pleistocene. Moreover, the described-above erosion/deposition-related thermal disturbances beneath the Vestfjorden and Vøring basins are still characterised by relatively high amplitudes at more than 60 km depth within the continental margin. On the other hand, the negative thermal anomaly is already very smoothed at 55 km depth beneath the Lofoten Basin. The amplitudes of the positive and negative thermal anomalies are mainly controlled by the distances to the upper and lower

thermal boundaries because the system reaches a thermal equilibrium faster at shorter distance to the boundary condition. In addition, thermal properties (mainly thermal diffusivity) of rocks play an important role in distribution of thermally non-equilibrated zones within the 3D thermal model both vertically and laterally.

8 DISCUSSION

The regional configuration of the modelled erosion/deposition-induced zones with non-equilibrated temperatures within the study area are dependent on several factors. The most important parameter are the reconstructed thickness of the eroded rocks, the local influence of fluid flow and paleoclimatic scenario.

One of the most critical factors is the reliability of the reconstructed thickness of the eroded rocks (Fig. 7a), the offshore part of which is based on the published map of NPD (2010) and Eig (2012) and, therefore, is strongly dependent on these input data. In order to validate the reconstructed erosion locally on Andøya, the vitrinite reflectance data from the Andøya Island (Bjorøy *et al.* 1980) have been independently used. The comparison shows that if a new kinetic vitrinite reflectance model 'basin%R_o' by Nielsen *et al.* (2017) is used, the estimated maximum burial temperature is around 80 ^oC for the rocks containing the vitrinite reflectance of 0.45 %R_o on average. In the case of our study, the modelled temperature at the base of the total reconstructed thickness of the eroded rocks within the eastern Andøya Island is also around 80 ^oC (Fig. 23a). Therefore, this fits between the vitrinite reflectance-based and the modelled temperatures definitely. Such similar independnat results supports our final total thickness estimation of the eroded material within at least the eastern part of Andøya where the rock samples of Cretaceous and Jurassic age were collected and studied by Bjorøy *et al.* (1980). In addition, our own results demonstrate a gradual decrease of temperature at the present-day surface beneath the eroded succession during the Cenozoic (Fig. 7). This variation coincides with the general trend of decreasing temperatures trough the Cenozoic, predicted by independent results of the apatite fission track analyses onshore (Hendriks & Andriessen 2002, Hendriks *et al.* 2010, Davids *et al.* 2013). However, precise comparison of our modelled temperatures at different time intervals of the Cenozoic with the Cenozoic temperatures according to the apatite fission track analyses is difficult due to different resolution of the methods.

Based on our total reconstructed thickness of the eroded material at the end of the Cretaceous (Fig. 7a), the main depocentre was localized over the adjacent offshore areas to the Lofoten-Vesterålen archipelago and shows a thickness maxima within the Vestfjorden and near the Andøya Island. This is partially supported by the recent studies on the vertical motions caused by glacial erosion with an Apatite Fission Track (AFT) analysis by Medvedev & Hartz (2015) who have also obtained the thickest eroded succession within the NW Vestfjorden and adjacent smaller fjords. However, our own estimation of the erosion within the western part of the Lofoten-Vesterålen archipelago and the adjacent offshore areas is larger compared to that reconstructed by Medvedev & Hartz (2015). It is, however, important to note that Medvedev & Hartz (2015) have already indicated that the exhumation of the outermost (western) Lofoten islands was significantly underestimated in their study and, therefore, indirectly supports our higher values of the reconstructed thickness there.

For completeness, we would like to mention that the restored thickness maximum of the Cenozoic deposits as it is modelled by Goledowski *et al.* (2013) in the close vicinity to the present-day high elevation of the Scandes Mountains in the study area. Goledowski *et al.* (2013) have also calculated paleotemperatures of more than 60-70 ^{o}C at the present-day surface beneath this thick reconstructed Cenozoic matrix. However, neither our estimates nor results from Medvedev & Hartz (2015) fit the trend of the reconstructed erosion proposed in Goledowski *et al.* (2013). Moreover, results of inverse modelling of fission-track data by Hendriks & Andriessen (2002) does not really support stronger uplift of the high-elevated area on the mainland in relation to the adjacent Lofoten-Vesterålen archipelago (e.g. Hendriks *et al.* 2010, Davids *et al.* 2013) at least within the northern part of the study area. Nevertheless, the limited amount of the studied samples does not completely exclude the possibility proposed by Goledowski *et al.* (2013).

The next important disturbing factor is related to possible fluid flows through both the sedimentary and crystalline rocks within the study area. It has already been mentioned above that some of the large misfits between the modelled and observed temperatures in the wells offshore may indicate a local disturbance of the regional conductive thermal field by additional convective and/or advective heat transfer caused by the circulation of fluids (mainly groundwater) through the Mesozoic-Cenozoic sedimentary rocks. Theoretically, the conditions are especially favourable for the fluid flow through the less consolidated uppermost part of the sedimentary cover represented by the young sedimentary rocks of the Naust Formation within the Lofoten-Vesterålen margin and the Vøring Basin and its analogues within the Lofoten Basin. The possibility of significant fluid flows is supported by the ocean drilling program (ODP Site 642) which is located further south on the Vøring Plateau. This well shows evidences of a relatively strong fluid inflow (Channell *et al.* 2005). Therefore, the modelled temperatures can be theoretically disturbed by the fluid circulation trough very porous sedimentary rocks expected within the uppermost Cenozoic sedimentary successions. Moreover, the theoretical differentiation between upper and middle crystalline crust into blocks with different radiogenic heat production (Fig. 14) can alternatively be indicative for the temperatures enforced by the fluid flow within the sedimentary cover in places with the assigned increased radiogenic heat production and vice versa. Furthermore, the results of 2D modelling of coupled groundwater flow and heat transfer (Maystrenko *et al.* 2015a) point to a possibility of groundwater flow through the crystalline rocks onshore, implying that the modelled erosion-induced positive thermal anomaly can, in reality, be significantly reduced and/or even locally enhanced by a differently cooled and/or heated groundwater, respectively. The influence of the groundwater flow could be especially strong during the melting of the ice sheets. The resulting cold water could advectively cool the subsurface by flowing through the faults and cracks, reactivated due during tectonic and related-isostatic uplift.

Possible undulations of the inferred paleotemperatures at the Earth surface and the sea floor (Figs. 8 and 10; Tables 1-3) can also affect the calculated thermal anomalies at the shallow depths (mainly within 2 km from the upper thermal boundary). It is obvious that the used paleoclimatic scenario is rather simplified for the large part of the Cenozoic prior to the Weichselian glacial period ca. 110,000 years ago (Table 3). In addition, the relatively detailed paleotemperature distribution during the Weichselian glaciation (Fig. 10) is partially uncertain

and can vary significantly. The main uncertainties are also related to some parts of the study area which were periodically free of ice and sea water. Therefore, the modelled temperature, especially near the coastline within the areas with shallow bathymetry, can be possibly affected by the uncertainties in the Weichselian paleoclimatic conditions within those areas.

In addition, the configuration of the lower thermal boundary (Figs. 6c and 11) is also partially uncertain, especially for the time steps 55 and 18 Ma ago and within the low-velocity/low-density zone within the upper mantle. It is obvious that the thermal influence of the younger oceanic lithosphere was stronger compared to the present-day one but the magnitude of this difference related to breakup is still difficult to estimate precisely. The same is true for the predefined +250 ^{o}C thermal anomaly at 100 km depth projected to the lower thermal boundary which must be theoretically present within the low-density/velocity mantle, but again the precise amplitude of this anomaly is uncertain. Moreover, the geometry of the lithosphere-asthenosphere boundary itself is somewhat speculative within the anomalous mantle area of the continental margin which also contribute to the uncertainties in the modelled temperatures with depth towards the lower thermal boundary.

9 CONCLUSIONS

The obtained results of the time-dependent 3D conductive thermal modelling for the Lofoten-Vesterålen margin, the north-east Vøring Basin and the adjacent areas demonstrate that the present-day subsurface temperature is characterized by the presence of thermally nonequilibrated zones clearly influenced by the Cenozoic erosion and deposition within the study area.

The erosion-induced positive thermal anomaly has its maximum of more than +27 ^{o}C at depths of 17-22 km beneath the eastern part of the Vestfjorden Basin where an erosion was paricularly strong during the last 2.7 million years. The accompanying negative anomaly within the north-eastern part of the Vøring Basin has minimal values of around -48 ^{o}C at 12-14 km depth and is mainly the result of the relatively rapid deposition of the Naust Formation during the Pleistocene. Moreover, the most intensive deposition-related negative anomaly is almost -70 ^{o}C at 17-20 km depth beneath the oceanic Lofoten Basin where the rapid Pleistocene deposition was accompanied by submarine mega-sliding of the sedimentary rocks sourced from the Barents Sea.

Besides, the thermal influence of the early Cenozoic continental breakup is still recognizable within the western part of the Lofoten-Vesterålen region in terms of the increasing temperatures towards the oceanic domain at the same depth levels.

In addition to heat conduction, convective and/or advective heat transfers are indicated by large misfits between the modelled and measured temperatures within some local wells which are located relatively close to the majority of the wells with much better fits, implying that the modelled erosion/deposition-related thermal anomalies could be theoretically also affected by the groundwater flow.

Acknowledgements

This study has been supported in the framework of the NEONOR2 project by the Norwegian Research Council, the Geological Survey of Norway, the Norwegian Petroleum Directorate, the Norwegian Mapping Authority, Aker BP, DONG E & P Norge, E.ON E & P Norge, Lundin

Norway, Maersk Oil Norway, Norske Shell, Norwegian Energy Company (Noreco), Repsol Exploration Norge, DEA Norge, Statoil and VNG Norge.

References

Afonso, J.C., Ranalli, G. & Fernandez, M., 2005. Thermal expansivity and elastic properties of the lithospheric mantle; results from mineral physics of composites, *Physics of the Earth and Planetary Interiors,* 149**,** 279-306.

Andersen, B.G. & Borns Jr., H.W. 1994. The Ice Age World, *Scandinavian University Press (Universitetsforlaget AS)*, Oslo. 208 pp.

Artemieva, I.M., Thybo, H. & Kaban, M.K., 2006. Deep Europe today; geophysical synthesis of the upper mantle structure and lithospheric processes over 3.5 Ga, *Memoirs of the Geological Society of London,* 32**,** 11-41.

Avedik, F., Berendsen, D., Fucke, H., Goldflam, S., Hirschleber, H., Meissner, R., Sellevoll, M.A. & Weinrebe, W., 1984. Seismic investigations along the Scandinavian 'Blue Norma' profile, *Annales Geophysicae [1983],* 2**,** 571-577.

Bannister, S.C., Ruud, B.O. & Husebye, E.S., 1991. Tomographic estimates of sub-Moho seismic velocities in Fennoscandia and structural implications, *Tectonophysics,* 189**,** 37-53.

Bell, R.E., Jackson, C.A.L., Elliott, G.M., Gawthorpe, R.L., Sharp, I.R. & Michelsen, L., 2014. Insights into the development of major rift-related unconformities from geologically constrained subsidence modelling; Halten Terrace, offshore mid Norway, *Basin Research,* 26**,** 203-224.

Ben Mansour, W., Moorkamp, M. & England, R.W., 2014. Joint inversion of seismological data and magnetotelluric data for the northern scandinavian mountains, *American Geophysical Union Fall Meeting,* 2014**,** @AbstractT23B-4668.

Bergh, S.G., Eig, K., Kløvjan, O.S., Henningsen, T., Olesen, O. & Hansen, J.A., 2007. The Lofoten-Vesterålen continental margin: a multiphase Mesozoic-Palaeogene rifted shelf as shown by offshore-onshore brittle fault-fracture analysis, *Norw. J. Geol.,* 87**,** 29-58.

Bjorøy, M., Hall, K. & Vigran, J.O., 1980. An organic geochemical study of Mesozoic shales from Andøya, North Norway, *Physics and Chemistry of the Earth,* 12**,** 77-91.

Blystad, P., Brekke, H., Færseth, R.B., Larsen, B.T., Skogseid, J. & Tørudbakken, B., 1995. Structural elements of the Norwegian continental shelf, Part II. The Norwegian Sea Region, *Norwegian Petroleum Directorate Bulletin,* 8**,** 0-45.

Breivik, A.J., Faleide, J.I., Mjelde, R. & Flueh, E.R., 2009. Magma productivity and early seafloor spreading rate correlation on the northern Vøring Margin, Norway - Constraints on mantle melting, *Tectonophysics,* 468**,** 206-223.

Breivik, A.J., Faleide, J.I., Mjelde, R., Flueh, E.R. & Murai, Y., 2017. A new tectono-magmatic model for the Lofoten/Vesterålen Margin at the outer limit of the Iceland Plume influence, *Tectonophysics*.

Brekke, H., 2000. The tectonic evolution of the Norwegian Sea continental margin with emphasis on the Vøring and Møre basins. In Nøttvedt, A. et al. (eds.) Dynamics of the Norwegian Margin, *Geological Society, London, Special Publications,* 136**,** 327-378.

Brigaud, F., Vasseur, G. & Caillet, G., 1992. Thermal state in the North Viking Graben (North Sea) determined from oil exploration well data, *Geophysics,* 57**,** 69-88.

Brönner, M., Gernigon, L. & Nasuti, A., 2013. Lofoten-Vestfjorden Aeromagnetic Survey 2011 (LOVAS): Acquisition, processing and interpretation report, pp. 136, Geological Survey of Norway, Trondheim.

Buecker, C. & Rybach, L., 1996. A simple method to determine heat production from gamma-ray logs, *Mar. Petrol. Geol.,* 13**,** 373-375.

Calcagnile, G., 1982. The lithosphere-asthenosphere system in Fennoscandia, *Tectonophysics,* 90**,** 19-35.

Cammarano, F., Goes, S., Vacher, P. & Giardini, D., 2003. Inferring upper-mantle temperatures from seismic velocities, *Physics of the Earth and Planetary Interiors,* 138**,** 197-222.

Čermak, V. & Rybach, L., 1982. Thermal properties: Thermal conductivity and specific heat of minerals and rocks. *in Physical Properties of Rocks*, pp. 305-343, ed. Angenheister, G. Springer, Berlin.

Channell, J.E.T., Sato, T., Kanamatsu, T., Stein, R., Zarikian, C.A.A., Malone, M.J., Higgins, S.M., Aboud, E., Acton, G.D., Akimoto, K., Bailey, I., Bjørklund, K.R., Evans, H., Fang, N., Ferretti, P., Gruetzner, J., Guyodo, Y.J.B., Hatakeda, K., Harris, R., Hagino, K., Hefter, J.N., Judge, S.A., Kulhanek, D.K., Nanayama, F., Nielsen, S.H.H., Ohno, M., Rashid, H., Sanchez, F.J.S., Voelker, A. & Zhai, Q., 2005. Site U1315, *Proceedings of the Integrated Ocean Drilling Program,* 303/306.

Chen, Y.J. & Lin, J., 2004. High sensitivity of ocean ridge thermal structure to changes in magma supply; the Galapagos spreading center, *Earth and Planetary Science Letters,* 221**,** 263-273.

Clauser, C., 2011. Thermal storage and transport properties of rocks. *in Heat capacity and latent heat, Encyclopedia of Solid Earth´s Geophysics*, pp. 1423-1431, ed. Gupta, H. Springer, Dordrecht.

Dalland, A., 1975. The Mesozoic Rocks of Andøya, Northern Norway, *Norges geologiske undersøkelse,* 316**,** 271-287.

Dalland, A., Worsley, D. & Ofstad, K., 1988. A lithostratigraphic scheme for the Mesozoic and Cenozoic succession offshore mid- and northern Norway, *Norwegian Petroleum Directory Bulletin,* 4**,** 0-65.

Davids, C., Wemmer, K., Zwingmann, H., Kohlmann, F., Jacobs, J. & Bergh, S.G., 2013. K/Ar illite and apatite fission track constraints on brittle faulting and the evolution of the Northern Norwegian passive margin, *Tectonophysics,* 608**,** 196-211.

Davis, B.A.S., Brewer, S., Stevenson, A.C. & Guiot, J., 2003. The temperature of Europe during the Holocene reconstructed from pollen data, *Quaternary Sci Rev,* 22**,** 1701-1716.

Dowdeswell, J.A., Ottesen, D. & Rise, L., 2006. Flow switching and large-scale deposition by ice streams draining former ice sheets, *Geology,* 34**,** 313-316.

Dowdeswell, J.A., Ottesen, D. & Rise, L., 2010. Rates of sediment delivery from the Fennoscandian Ice Sheet through an ice age, *Geology,* 38**,** 3-6.

Drivenes, G., Sellevoll, M.A., Renard, V., Avedik, F. & Pajchel, J., 1984. The continental margin/crustal structure off the Lofoten Islands, Northern Norway. In: Spencer, A.M. petroleum Geology of the North European Margin, *London, Graham & Trotman***,** 211-216.

Ebbing, J., England, R.W., Korja, T., Lauritsen, T., Olesen, O., Stratford, W. & Weidle, C., 2012. Structure of the Scandes lithosphere from surface to depth, *Tectonophysics,* 536**,** 1-24.

Ebbing, J. & Olesen, O., 2010. New compilation of top basement and basement thickness for the Norwegian continental shelf reveals the segmentation of the passive margin system, *Petroleum Geology Conference Proceedings,* 7**,** 885-897.

Ehlers, J., Gibbard, P.L. & Hughes, P.D., 2011. Quaternary glaciations, extent and chronology; a closer look, Elsevier: Amsterdam, Netherlands, Netherlands.

Eidvin, T., Bugge, T. & Smelror, M., 2007. The Molo Formation, deposited by coastal progradation on the inner Mid-Norwegian continental shelf, coeval with the Kai

Formation to the west and the Utsira Formation in the North Sea, *Norw. J. Geol.,* 87**,** 75-142.

Eig, K., 2012. Lofoten and Vesterålen; promised land or Fata Morgana?, *GEO ExPro,* 9**,** 54-58.

Eldevik, T., Risebrobakken, B., Bjune, A.E., Andersson, C., Birks, H.J.B., Dokken, T.M., Drange, H., Glessmer, M.S., Li, C., Nilsen, J.E.O., Otterå, O.H., Richter, K. & Skagseth, O., 2014. A brief history of climate; the northern seas from the last glacial maximum to global warming, *Quaternary Sci. Rev.,* 106**,** 225-246.

Eldholm, O., Thiede, J. & Party, S.S., 2005. Thermal conductivity of ODP Hole 104-642C, *PANGAEA*.

Eldrett, J.S., Greenwood, D.R., Harding, I.C. & Huber, M., 2009. Increased seasonality through the Eocene to Oligocene transition in northern high latitudes, *Nature [London],* 459**,** 969-973.

Faleide, J.I., Tsikalas, F., Breivik, A.J., Mjelde, R., Ritzmann, O., Engen, O., Wilson, J. & Eldholm, O., 2008. Structure and evolution of the continental margin off Norway and Barents Sea, *Episodes,* 31**,** 82-91.

Fejerskov, M. & Lindholm, C.D., 2000. Crustal stress in and around Norway; an evaluation of stress-generating mechanisms.; Dynamics of the Norwegian margin, *Geological Society Special Publications,* 167**,** 451-467.

Fichler, C., Rundhovde, E., Olesen, O., Sæther, B.M., Rueslåtten, H., Lundin, E. & Doré, A.G., 1999. Regional tectonic interpretation of image enhanced gravity and magnetic data covering the Mid-Norwegian shelf and adjacent mainland, *Tectonophysics,* 306**,** 183-197.

Fiedler, A. & Faleide, J.I., 1996. Cenozoic sedimentation along the southwestern Barents Sea margin in relation to uplift and erosion of the shelf, *Global & Planetary Change,* 12**,** 75-93.

Filippelli, G.M. & Flores, J.-A., 2009. From the warm Pliocene to the cold Pleistocene; a tale of two oceans, *Geology,* 37**,** 959-960.

Fjeldskaar, W., Lindholm, C.D., Dehls, J.F. & Fjeldskaar, I., 2000. Postglacial uplift, neotectonics and seismicity in Fennoscandia, *Quaternary Sci. Rev.,* 19**,** 1413-1422.

Fossen, H., 2010. Extensional tectonics in the North Atlantic Caledonides:a regional view. *in Continental tectonics and mountain building: the legacy of Peach and Horne*, pp. 767-793, eds. Law, R. D., Butler, R. W. H., Holdsworth, R. E., Krabbendam, M. & Strachan, R. A. The Geological Society of London.

Færseth, R.B., 2012. Structural development of the continental shelf offshore Lofoten–Vesterålen, northern Norway, *Norw J Geol,* 92**,** 19-40.

Gernigon, L., Blischke, A., Nasuti, A. & Sand, M., 2015. Conjugate volcanic rifted margins, sea-floor spreading, and microcontinent; insights from new high-resolution aeromagnetic surveys in the Norway Basin, *Tectonics,* 34**,** 907-933.

Gernigon, L., Ringenbach, J.C., Planke, S. & Le Gall, B., 2004. Deep structures and breakup along volcanic rifted margins: insights from integrated studies along the outer Vøring Basin (Norway), *Mar Petrol Geol,* 21**,** 363-372.

Gernigon, L., Ringenbach, J.C., Planke, S., Le Gall, B. & Jonquet-Kolstø, H., 2003. Extension, crustal structure and magmatism at the outer Vøring Basin, Norwegian margin, *J Geol Soc London,* 160**,** 197-208(112).

Goldschmidt-Rokita, A., Sellevoll, M.A., Hirschleber, H.B. & Avedik, F., 1988. Results of two seismic refraction profiles off Lofoten, Northern Norway, *Special Publication - Norges Geologiske Undersøkelse,* 3**,** 49-57.

Goledowski, B., Egholm, D.L., Nielsen, S.B., Clausen, O.R. & McGregor, E.D., 2013. Cenozoic erosion and flexural isostasy of Scandinavia, *Journal of Geodynamics,* 70**,** 49-57.

Gradmann, S. & Ebbing, J., 2015. Large-scale gravity anomaly in Northern Norway; tectonic implications of shallow or deep source depth and a possible conjugate in northeast Greenland, *Geophys J Int,* 203**,** 2070-2088.

Green, P.F., Japsen, P., Chalmers, J.A., Bonow, J.M. & Duddy, I.R., 2017. Post-breakup burial and exhumation of passive continental margins: Seven propositions to inform geodynamic models, *Gondwana Research*.

Hansen, J., Sato, M., Russell, G. & Kharecha, P., 2013. Climate sensitivity, sea level, and atmospheric carbon dioxide, *Phil. Trans. Roy. Soc.,* A371**,** 20120284.

Hansen, J.A., 2009. Onshore-offshore tectonic relations on the Lofoten and Vesterålen Margin, A dissertation for the degree of Philosophiae Doctor**,** 229.

Hansen, J.A., Bergh, S.G. & Henningsen, T., 2012. Mesozoic rifting and basin evolution on the Lofoten and Vesterålen Margin, North-Norway; time constraints and regional implications, *Norw J Geol,* 91**,** 203-228.

Hasenclever, J., Knorr, G., Ruepke, L.H., Koehler, P., Morgan, J., Garofalo, K., Barker, S., Lohmann., G. & Hall, I.R., 2017. Sea level fall during glaciation stabilized atmospheric CO2 by enhanced volcanic degassing, *Nature Communications,* 8:15867.

Hejrani, B., Balling, N., Jacobsen, B.H. & England, R., 2017. Upper-mantle velocities below the Scandinavian Mountains from P- and S-wave traveltime tomography, *Geophys J Int,* 208**,** 177-192.

Hendriks, B.W.H. & Andriessen, P.A.M., 2002. Pattern and timing of the post-Caledonian denudation of northern Scandinavia constrained by apatite fission-track thermochronology, *Geological Society Special Publications,* 196**,** 117-137.

Hendriks, B.W.H., Osmundsen, P.T. & Redfield, T.F., 2010. Normal faulting and block tilting in Lofoten and Vesteralen constrained by apatite fission track data, *Tectonophysics,* 485**,** 154-163.

Hjelstuen, B.O., Eldholm, O. & Faleide, J.I., 2007. Recurrent Pleistocene mega-failures on the SW Barents Sea margin, *Earth and Planetary Science Letters,* 258**,** 605-618.

Hofmeister, A.M., 1999. Mantle values of thermal conductivity and the geotherm from photon lifetimes, *Science,* 283**,** 1699-1706.

Holtedahl, H., 1998. The Norwegian strandflat – a geomorphological puzzle, *Norsk Geologisk Tidsskrift = Norwegian Journal of Geology,* 78**,** 47-66.

Inglis, G.N., Collinson, M.E., Riegel, W., Wilde, V., Farnsworth, A., Lunt, D.J., Valdes, P., Robson, B.E., Scott, A.C., Lenz, O.K., Naafs, B.D.A. & Pancost, R.D., 2017. Mid-latitude continental temperatures through the early Eocene in Western Europe, *Earth and Planetary Science Letters,* 460**,** 86-96.

Janutyte, I., Lindholm, C. & Olesen, O., 2017. Relation between seismicity and tectonic structures offshore and onshore Nordland, northern Norway, *Norw J Geol*.

Kawakatsu, H., Kumar, P., Takei, Y., Shinohara, M., Kanazawa, T., Araki, E. & Suyehiro, K., 2009. Seismic evidence for sharp lithosphere-asthenosphere boundaries of oceanic plates, *Science,* 324**,** 499-502.

Keiding, M., Kreemer, C., Lindholm, C.D., Gradmann, S., Olesen, O. & Kierulf, H.P., 2015. A comparison of strain rates and seismicity for Fennoscandia; depth dependency of deformation from glacial isostatic adjustment, *Geophys J Int,* 202**,** 1021-1028.

Kodaira, S., Mjelde, R., Sellevoll, M.A., Hirschleber, H.B., Iwasaki, T., Kanazawa, T. & Shimamura, H., 1995. Crustal transect across the Lofoten volcanic passive continental

margin, N Norway, obtained by use of ocean bottom seismographs, and implications for its evolution, *Journal of Physics of the Earth,* 43**,** 729-745.

Korablev, A., Smirnov, A. & Baranova, O.K., 2014. Climatological Atlas of the Nordic Seas and Northern North Atlantic. *in NOAA Atlas NESDIS*, pp. 122, eds. Seidov, D. & Parsons, A. R.

Ksienzyk, A.K., Dunkl, I., Jacobs, J., Fossen, H. & Kohlmann, F., 2014. From orogen to passive margin; constraints from fission track and (U-Th)/He analyses on Mesozoic uplift and fault reactivation in SW Norway, *Special Publication - Geological Society of London,* 390**,** 679-702.

Laberg, J.S., Andreassen, K. & Vorren, T.O., 2012. Late Cenozoic erosion of the high-latitude southwestern Barents Sea shelf revisited, *Geol Soc Am Bull,* 124**,** 77-88.

Lee, C.-T.A., 2003. Compositional variation of density and seismic velocities in natural peridotites at STP conditions; implications for seismic imaging of compositional heterogeneities in the upper mantle, *Journal of Geophysical Research,* 108.

Lien, T., 2005. From rifting to drifting: effects on the development of deep-water hydrocarbon reservoirs in a passive margin setting, Norwegian Sea, *Norw J Geol,* 85**,** 319-332.

Lundin, E.R., Dore, A.G., Rønning, K. & Kyrkjebo, R., 2013. Repeated inversion and collapse in the Late Cretaceous-Cenozoic northern Vøring Basin, offshore Norway, *Petroleum Geoscience,* 19**,** 329-341.

Løseth, H. & Tveten, E., 1996. Post-Caledonian structural evolution of the Lofoten and Vesterålen offshore and onshore areas, *Norsk Geol Tidsskr,* 76**,** 215-230.

Mann, M.E., Zhang, Z., Rutherford, S., Bradley, R.S., Hughes, M.K., Shindell, D., Ammann, C., Faluvegi, G. & Ni, F., 2009. Global signatures and dynamical origins of the Little Ice Age and Medieval climate anomaly, *Science,* 326**,** 1256-1260.

Maystrenko, Y. & Scheck-Wenderoth, M., 2009. Density contrasts in the upper mantle and lower crust across the continent-ocean transition: constraints from 3-D gravity modelling at the Norwegian margin, *Geophys. J. Int.,* 179**,** 536-548.

Maystrenko, Y.P., Gernigon, L., Nasuti, A., Olesen, O., revised. Deep structure of the Mid-Norwegian continental margin (the Vøring and Møre basins) according to 3D density and magnetic modelling. *Geophysical Journal International*.

Maystrenko, Y.P., Gernigon, L., accepted. 3D temperature distribution beneath the Mid-Norwegian continental margin (the Vøring and Møre basins). *Geophysical Journal International*.

Maystrenko, Y.P., Elvebakk, H.K., Ganerød, G.V., Lutro, O., Olesen, O. & Rønning, J.S., 2014. 2D structural and thermal models in southeastern Norway based on the recently drilled Årvollskogen well and 2D density, magnetic and thermal modelling, *Geothermal Energy,* 2.

Maystrenko, Y.P., Olesen, O. & Elvebakk, H.K., 2015a. Indication of deep groundwater flow through the crystalline rocks of Southern Norway, *Geology,* 43**,** 327-330.

Maystrenko, Y.P., Olesen, O., Gernigon, L. & Gradmann, S., 2017. Deep structure of the Lofoten-Vesterålen segment of the Mid-Norwegian continental margin and adjacent areas derived from 3-D density modeling, *Journal of Geophysical Research: Solid Earth,* 122**,** 1402-1433.

Maystrenko, Y.P., Slagstad, T., Elvebakk, H.K., Olesen, O., Ganerød, G.V. & Rønning, J.S., 2015b. New heat flow data from three boreholes near Bergen, Stavanger and Moss, southern Norway, *Geothermics,* 56**,** 79-92.

McKenna, T.E. & Sharp, J.M., Jr., 1998. Radiogenic heat production in sedimentary rocks of the Gulf of Mexico basin, South Texas, *AAPG Bulletin,* 82**,** 484-496.

Medvedev, S. & Hartz, E.H., 2015. Evolution of topography of post-Devonian Scandinavia; effects and rates of erosion, *Geomorphology,* 231**,** 229-245.
Meinhold, G., Morton, A.C. & Avigad, D., 2013. New insights into peri-Gondwana paleogeography and the Gondwana super-fan system from detrital zircon U-Pb ages, *Gondwana Research,* 23**,** 661-665.
Midttømme, K. & Roaldset, E., 1999. Thermal conductivity of sedimentary rocks; uncertainties in measurement and modeling, *Geological Society Special Publications,* 158**,** 45-60.
Midttømme, K., Sættem, J., Roaldset, E. & Zielinski, G.W., 1995. Thermal conductivity of unconsolidated marine sediments from Vøring Basin, Norwegian Sea, *Conference and Technical Exhibition - European Association of Geoscientists and Engineers,* 57**,** @abstr.F004-@abstr.F004.
Mjelde, R., Digranes, P., Van Schaack, M., Shimamura, H., Shiobara, H., Kodaira, S., Naess, O., Sorenes, N. & Vagnes, E., 2001. Crustal structure of the outer Voring Plateau, offshore Norway, from ocean bottom seismic and gravity data, *J. Geophys. Res.-Sol. Earth,* 106**,** 6769-6791.
Mjelde, R., Kodaira, S. & Sellevoll, M.A., 1996. Crustal structure of the Lofoten Margin, N Norway, from normal incidence and wide-angle seismic data: A review, *Norsk Geol Tidsskr,* 76**,** 187-198.
Mjelde, R., Kvarven, T., Faleide, J.I. & Thybo, H., 2016. Lower crustal high-velocity bodies along North Atlantic passive margins, and their link to Caledonian suture zone eclogites and early Cenozoic magmatism, *Tectonophysics,* 670**,** 16-29.
Mjelde, R., Sellevoll, M.A., Shimamura, H., Iwasaki, T. & Kanazawa, T., 1992. A Crustal Study Off Lofoten, N Norway, by Use of 3-Component Ocean Bottom Seismographs, *Tectonophysics,* 212**,** 269-288.
Mjelde, R., Sellevoll, M.A., Shimamura, H., Iwasaki, T. & Kanazawa, T., 1993. Crustal structure beneath Lofoten, N. Norway, from vertical incidence and wide-angle seismic data, *Geophys J Int,* 114**,** 116-126.
Mjelde, R., Sellevoll, M.A., Shimamura, H., Iwwasaki, T. & Kanazawa, T., 1995. S-Wave Anisotropy Off Lofoten, Norway, Indicative of Fluids in the Lower Continental-Crust, *Geophys J Int,* 120**,** 87-96.
Mjelde, R., Shimamura, H., Kanazawa, T., Kodaira, S., Raum, T. & Shiobara, H., 2003. Crustal lineaments, distribution of lower crustal intrusives and structural evolution of the Voring Margin, NE Atlantic; new insight from wide-angle seismic models, *Tectonophysics,* 369**,** 199-218.
Mokhtari, M. & Pegrum, R.M., 1992. Structure and evolution of the Lofoten continental margin, offshore Norway, *Norsk Geol Tidsskr,* 72**,** 339-355.
Montelli, A., Dowdeswell, J.A., Ottesen, D. & Johansen, S.E., 2017. Ice-sheet dynamics through the Quaternary on the mid-Norwegian continental margin inferred from 3D seismic data, *Mar. & Petrol. Geol.,* 80**,** 228-242.
Muller, R.D., Sdrolias, M., Gaina, C. & Roest, W.R., 2008. Age, spreading rates, and spreading asymmetry of the world's ocean crust, *Geochem Geophy Geosy,* 9.
Nesje, A., Dahl, S.O., Thun, T. & Nordli, O., 2008. The 'Little Ice Age' glacial expansion in western Scandinavia; summer temperature or winter precipitation?, *Climate Dynamics,* 30**,** 789-801.
Nielsen, S.B., Clausen, O.R. & McGregor, E., 2017. Basin%Ro: A vitrinite reflectance model derived from basin and laboratory data, *Basin Research,* 29**,** 515-536.
NPD, 2010. *Geofaglig vurdering av petroleumsressursene i havområdene utenfor Lofoten, Vesterålen og Senja,* Norwegian Petroleum Directorate.

NPD, 2017. The NPD's fact pages; well data summary sheets. Norwegian Petroleum Directorate. http://factpages.npd.no/FactPages/Default.aspx?nav1=wellbore&nav2=PageView|Exploration|All&nav3=6753 (January 2017).

Olesen, O., Balling, N., Barrère, C., Breiner, N., Davidsen, B., Ebbing, J., Elvebakk, H., Gernigon, L., Koziel, J., Lutro, O., Midttømme, K., Nordgulen, Ø., Olsen, L., Osmundsen, P.T., Pascal, C., Ramstad, R.K., Rønning, J.S., Skilbrei, J.R., Slagstad, T. & Wissing, B., 2007b. KONTIKI Final Report, CONTInental Crust and Heat Generation In 3D, NGU Report 2007.042.

Olesen, O., Blikra, L.H., Braathen, A., Dehls, J.F., Olsen, L., Rise, L., Roberts, D., Riis, F., Faleide, J.I. & Anda, E., 2004. Neotectonic deformation in Norway and its implications: a review, *Norw J Geol,* 84**,** 3-34.

Olesen, O., Bungum, H., Lindholm, C., Olsen, L., Pascal, C. & Roberts, D., 2013. Neotectonics, seismicity and contemporary stress field in Norway – mechanisms and implications. *in Geological Survey of Norway Special Publication*, pp. 145-174.

Olesen, O., Ebbing, J., Lundin, E., Mauring, E., Skilbrei, J.R., Torsvik, T.H., Hansen, E.K., Henningsen, T., Midbøe, P. & Sand, M., 2007. An improved tectonic model for the Eocene opening of the Norwegian-Greenland Sea: Use of modern magnetic data, *Mar Petrol Geol,* 24**,** 53-66.

Olesen, O., Lundin, E., Nordgulen, Ø., Osmundsen, P.T., Skilbrei, J.R., Smethurst, M.A., Solli, A., Bugge, T. & Fichler, C., 2002. Bridging the gap between the onshore and offshore geology in Nordland, northern Norway, *Norw J Geol,* 82**,** 243-262.

Olesen, O., Reitan, M. & Sæther, P.O., 1993. Petrofysisk database PETBASE 3.0, Brukerbeskrivelse, NGU, Trondheim, Norway, *NGU Internrapport 93.023.*

Olsen, L., Sveian, H., Bergstrøm, B., Ottesen, D. & Rise, L., 2013. Quaternary glaciations and their variations in Norway and on the Norwegian continental shelf. *in Quaternary Geology of Norway*, pp. 27-78, eds. Olsen, L., Fredin, O. & Olesen, O. Geological Survey of Norway Special Publication, Trondheim.

Olsson, S., Roberts, R.G. & Bodvarsson, R., 2008. Moho depth variation in the Baltic Shield from analysis of converted waves, *GFF,* 130**,** 113-122.

Ottemoller, L. & Midzi, V., 2003. The crustal structure of Norway from inversion of teleseismic receiver functions, *Journal of Seismology,* 7**,** 35-48.

Ottersen, G., 2009. *A digital temperature archive for the Norwegian Sea,* edn, Vol. 6, pp. Pages, Institute of Marine Research, Bergen.

Ottesen, D., Dowdeswell, J.A., Rise, L. & Bugge, T., 2012. Large-scale development of the mid-Norwegian shelf over the last three million years and potential for hydrocarbon reservoirs in glacial sediments, *Geological Society Special Publication,* 368.

Ottesen, D., Rise, L., Andersen, E.S., Bugge, T. & Eidvin, T., 2009. Geological evolution of the Norwegian continental shelf between 61 degrees N and 68 degrees N during the last 3 million years, *Norw J Geol,* 89**,** 251-265.

Pascal, C., 2015. Heat flow of Norway and its continental shelf, *Mar Petrol Geol,* 66**,** 956-969.

Pascal, C. & Midttømme, K., 2006. *Impact of recent glacial erosion on subsurface temperatures: the Mid-Norwegian Margin,* edn, Vol. 2006.088, pp. Pages.

Pascal, C. & Rudlang, T., 2016. Discovery of highly radioactive granite in the Bergen Region, *Norw J Geol,* 96**,** 319-328.

Pekar, S.F., DeConto, R.M. & Harwood, D.M., 2006. Resolving a late Oligocene conundrum; deep-sea warming and Antarctic glaciation, *Palaeogeography, Palaeoclimatology, Palaeoecology,* 231**,** 29-40.

Petersen, T.G., Hamann, N.E. & Stemmerik, L., 2015. Tectono-sedimentary evolution of the Paleogene succession offshore northeast Greenland, *Mar Petrol Geol,* 67**,** 481-497.

Pilidou, S., Priestley, K., Debayle, E. & Gudmundsson, O., 2005. Rayleigh wave tomography in the North Atlantic: high resolution images of the Iceland, Azores and Eifel mantle plumes, *Lithos,* 79**,** 453-474.

Raab, B. & Vedin, H., 1995. *The National Atlas of Sweden: Climate, Lakes, and Rivers*, Bokförlaget Bra Böcker, Höganäs, Sweden.

Ravelo, A.C., Andreasen, D.H., Lyle, M., Lyle, A.O. & Wara, M.W., 2004. Regional climate shifts caused by gradual global cooling in the Pliocene Epoch, *Nature,* 429**,** 263-267.

Ren, S.C., Faleide, J.I., Eldholm, O., Skogseid, J. & Gradstein, F., 2003. Late Cretaceous-Paleocene tectonic development of the NW Voring Basin, *Mar Petrol Geol,* 20**,** 177-206.

Ren, S.C., Skogseid, J. & Eldholm, O., 1998. Late Cretaceous-Paleocene extension on the Vøring Volcanic Margin, *Marine Geophysical Researches,* 20**,** 343-369.

Riis, F., 1996. Quantification of Cenozoic vertical movements of Scandinavia by correlation of morphological surfaces with offshore data, *Global & Planetary Change,* 12**,** 331-357.

Riis, F. & Fjeldskaar, W., 1992. On the magnitude of the late Tertiary and Quaternary erosion and its significance for the uplift of Scandinavia and the Barents Sea, *Special Publication - Norwegian Petroleum Society, NPF,* 1**,** 163-185.

Rise, L., Bøe, R., Riis, F., Bellec, V.K., Laberg, J.S., Eidvin, T., Elvenes, S. & Thorsnes, T., 2013. The Lofoten-Vesterålen continental margin, north Norway; canyons and mass-movement activity, *Mar Petrol Geol,* 45**,** 134-149.

Rise, L., Chand, S., Hjelstuen, B.O., Haflidason, H. & Bøe, R., 2010. Late Cenozoic geological development of the south Vøring margin, mid-Norway, *Mar Petrol Geol,* 27**,** 1789-1803.

Rise, L., Ottesen, D., Berg, K. & Lundin, E., 2005a. Large-scale development of the mid-Norwegian margin during the last 3 million years, *Mar Petrol Geol,* 22**,** 33-44.

Rise, L., Ottesen, D., Berg, K. & Lundin, E., 2005b. Large-scale development of the mid-Norwegian margin during the last 3 million years.; Ormen Lange; an integrated study for the safe development of a deep-water gas field within the Storegga Slide Complex, NE Atlantic continental margin, *Mar Petrol Geol,* 22**,** 33-44.

Rise, L., Ottesen, D., Longva, O., Solheim, A., Andersen, E.S. & Ayers, S., 2006. The Sklinnadjupet Slide and its relation to the Elsterian glaciation on the mid-Norwegian margin, *Mar Petrol Geol,* 23**,** 569-583.

Roberts, D. & Gee, D.G., 1985. An introduction to the structure of the Scandinavian Caledonides. *in The Caledonide orogen - Scandinavia and related areas*, pp. 55-68, eds Gee, D. & Sturt, B. A. John Wiley & Sons, Chichester.

Sass, J.H., Lachenbruch, A.H., Moses, T.H., Jr. & Morgan, P., 1992. Heat flow from a scientific research well at Cajon Pass, California, *Journal of Geophysical Research,* 97**,** 5017-5030.

Scheck-Wenderoth, M. & Maystrenko, Y., 2008. How warm are passive continental margins? A 3-D lithosphere-scale study from the Norwegian margin, *Geology,* 36**,** 419-422.

Scheck-Wenderoth, M. & Maystrenko, Y.P., 2013. Deep control on shallow heat in sedimentary basins, *Energy Procedia,* 40**,** 266-275.

Schmittner, A., Urban, N.M., Shakun, J.D., Mahowald, N.M., Clark, P.U., Bartlein, P.J., Mix, A.C. & Rosell-Mele, A., 2011. Climate sensitivity estimated from temperature reconstructions of the last glacial maximum, *Science,* 334**,** 1385-1388.

Seppa, H., Bjune, A.E., Telford, R.J., Birks, H.J.B. & Veski, S., 2009. Last nine-thousand years of temperature variability in northern Europe, *Climate of the Past,* 5**,** 523-535.

Sigmond, E.M.O., 2002. Geological map, land and sea areas of northern Europe, 1:4 million. *in Commision for the Geological Map of the World,* Geological Survey of Norway, Trondheim.

Slagstad, T., 2008. Radiogenic heat production of Archaean to Permian geological provinces in Norway, *Norsk Geologisk Tidsskrift - Norwegian Journal of Geology,* 88**,** 149-166.

Slagstad, T., Balling, N., Elvebakk, H., Midttømme, K., Olesen, O., Olsen, L. & Pascal, C., 2009. Heat-flow measurements in Late Palaeoproterozoic to Permian geological provinces in south and central Norway and a new heat-flow map of Fennoscandia and the Norwegian-Greenland Sea, *Tectonophysics,* 473**,** 341-361.

Slagstad, T. & Lauritsen, T. 2013. Heat production calculations, in COOP Phase I - Crustal Onshore-Offshore Project, *NGU Report* 2013.002, 74-111, eds. Olesen, O., Brönner, M., Ebbing, J., Elvebakk, H., Gellein, J., Koziel, J., Lauritsen, T., Lutro, O., Maystrenko, Y., Müller, C., Nasuti, A., Osmundsen, P.T., Slagstad, T. & Storrø G..

Smelror, M., Mørk, A., Mørk, M.B.E., Weiss, H.M. & Løseth, H., 2001. Middle Jurassic-Lower Cretaceous transgressive-regressive sequences and facies distribution off northern Nordland and Troms, Norway. *in Sedimentary Environments Offshore Norway - Palaeozoic to Recent*, pp. 211-232, eds. Martinsen, O. J. & Dreyer, T. NPF Special Publications.

Srivastava, S.P. & Tapscott, C.R., 1986. Plate Kinematics of the North Atlantic. In : Vogt, P .R. & Tucholke, B.E . (eds) The western North Atlantic Region, *Geological Society of America, Special Publications***,** 379-404.

Steer, P., Huismans, R.S., Valla, P.G., Gac, S. & Herman, F., 2012. Bimodal Plio-Quaternary glacial erosion of fjords and low-relief surfaces in Scandinavia, *Nature Geoscience,* 5**,** 635-639.

Steltenpohl, M.G., Hames, W.E. & Andresen, A., 2004. The Silurian to Permian history of a metamorphic core complex in Lofoten, northern Scandinavian Caledonides, *Tectonics,* 23**,** 1-23.

Talwani, M. & Eldholm, O., 1977. Evolution of the Norwegian-Greenland Sea, *Geol Soc Am Bull,* 88**,** 969-999.

Tsikalas, F., Eldholm, O. & Faleide, J.I., 2005. Crustal structure of the Lofoten-Vesterålen continental margin, off Norway, *Tectonophysics,* 404**,** 151-174.

Tsikalas, F., Faleide, J.I. & Eldholm, A., 2001. Lateral variations in tectono-magmatic style along the Lofoten-Vesterålen volcanic margin off Norway, *Mar Petrol Geol,* 18**,** 807-832.

Turcotte, D.L. & Schubert, G., 2002. *Geodynamics,* Cambridge University Press : Cambridge, United Kingdom, United Kingdom.

Tveito, O.E., Førland, E., Heino, R., Hanssen-Bauer, I., Alexandersson, H., Dahlström, B., Drebs, A., Kern-Hansen, C., Jónsson, T., Vaarby Laursen, E. & Westman, Y., 2000. *Nordic temperature maps,* edn, Vol. DNMI-Report 09/00 KLIMA, pp. Pages.

van den Berg, A.P., Yuen, D.A. & Steinbach, V., 2001. The effects of variable thermal conductivity on mantle heat-transfer, *Geophysical Research Letters,* 28**,** 875-878.

Villa, M., Fernandez, M. & Jimenez Munt, I., 2010. Radiogenic heat production variability of some common lithological groups and its significance to lithospheric thermal modeling, *Tectonophysics,* 490**,** 152-164.

Vosteen, H.-D. & Schellschmidt, R., 2003. Influence of temperature on thermal conductivity, thermal capacity and thermal diffusivity for different types of rock, *Physics and Chemistry of the Earth,* 28**,** 499-509.

Wagner, W. & Kretzschmar, H.-J., 2008. International Steam Tables – Properties of Water and Steam Based on the Industrial Formulation IAPWS-IF97. Springer-Verlag, Berlin.

Wollenberg, H.A. & Smith, A.R., 1987. Radiogenic heat production of crustal rocks; an assessment based on geochemical data, *Geophysical Research Letters,* 14**,** 295-298.

Yakovlev, A.V., Bushenkova, N.A., Koulakov, I.Y. & Dobretsov, N.L., 2012. Structure of upper mantle in Arctic region based on data of regional seismotomography, *Geology and Geophysics,* 53**,** 1261-1272.

Zachos, J., Pagani, M., Sloan, L., Thomas, E. & Billups, K., 2001. Trends, rhythms, and aberrations in global climate 65 Ma to present, *Science,* 292**,** 686-693.

Zhang, Y.-S. & Lay, T., 1999. Evolution of oceanic upper mantle structure, *Physics of the Earth and Planetary Interiors,* 114**,** 71-80.

Table 1. Average annual present-day temperature at the sea floor of the Norwegian Sea.

Bathymetry, m	100	300	500	600	700	750	800	850 and deeper
Temperature, °C	7	6	5	4	3	2	1	0

Table 2. Relative changes of the palaeotemperatures in comparison to the present-day temperature for the last 8000 years.

Time, years before present BP	0	400	7500	8000
	Present day	Little Ice Age	Holocene Climate Optimum	
Temperature difference in relation to present day, °C	0	-0.4	+1	-1

Table 3. Paletemperatures during the Cenozoic (based on Zachos *et al.* 2001, Pekar *et al.* 2006, Rise *et al.* 2006, Eldrett *et al.* 2009, Filippelli and Flores, 2009, Ehlers *et al.* 2011, Hansen *et al.* 2013, Inglis *et al.* 2017).

№	Time, Ma ago	Mainland temperature, °C	Deep sea temperature, °C
1	66	18	-
2	55	17.5	-
3	45	14	8
4	34	10	3
5	25	11.5	5
6	18	10.5	4
7	16	12	6
8	12	9	3
9	5	6	1
10	3.6	+3 °C to present-day temperature	0
11	0.45	present-day temperature	present-day temperature
12	0.35	the same as glacial maximum 27000 years ago in Fig. 9	the same as glacial maximum 27000 years ago in Fig. 9
13	0.228	present-day temperature	present-day temperature
14	0.220-0.118	the same as 0.110-0.0105 Ma ago	the same as 0.110-0.0105 Ma ago
15	0.110-0.0105	Fig. 9	Fig. 9

Table 4. Volume of the rocks deposited and eroded during the Cenozoic within the Lofoten-Vesterålen margin and the adjacent continent. The Naust analogues in the Lofoten Basin, the undefined Cenozoic of layer 3 and the Paleocene in the Hel Graben and Røst Basin are excluded from the calculations.

№	Layer	Age [Ma]	Volume of the deposited material, $V_{deposited}$ [km^3]	Percent-age of total Cz, %	Volume of eroded material, V_{eroded} [km^3]
2.1	Naust U, S, T	0.6-0	6956	11.1	15134
2.2	Naust A	1.5-0.6	6722	10.7	14541
2.3	Naust N	2.7-1.5	18645	29.7	40428
2.4	Kai	18-2.7	3882	6.2	8440
3	Brygge	56-18	13612	21.7	29538
5	Paleocene	66-56	12901	20.6	28041
	Total Cenozoic		62718	100	136122

Table 5. Thermal properties of the layers of the 3D structural model used during the 3D thermal modelling (lithology of sediments is derived from Bell *et al.* (2014) and from NPD (2017)).

№	Layer of the 3D structural model	Dominant lithology	Specific heat capacity C_p [J/kgK]	Thermal conductivity scale value k_r [W/mK]	Radiogenic heat production S [μW/m^3]
2.1-2.3	Naust	mainly shale and sandstone	1180	2.3	0.59-2.0
2.4	Kai	mainly shale and sandstone	1180	2.3	0.57-1.9
3	Brygge and undefined Cenozoic	mainly shale and sandstone	1180	2.2	0.48-1.6
4	Oceanic layer 2AB	basalts and tuffs	880	1.8	0.4
5-6	Upper Cretaceous-Paleocene	88% shale, 12% sandstone	1180	2.5	0.68-1.87
7	Lower Cretaceous	92% shale, 3% sandstone, 5% limestone	1180	2.4	0.83-1.99
8	Pre-Cretaceous	80% shale, 20% sandstone	1180	3.3	1.12-2.2
5-8	Undivided Paleocene and Cretaceous of the Røst Basin	87% shale, 11% sandstone, 2% limestone	1180	2.5	1.4
xx	Eroded material	mainly sedimentary deposits with crystalline rocks	1180	3.0	1.4
9	Upper crustal high-density crystalline rocks	gabbro to anorthositic rocks, metamorphic rocks	880	2.9	0.4
10-11	Upper crust	metasediments and/or granite and gneiss	880	3.2	1.5-2 (0.2-2.5)
12	Middle crust	granitoids and/or gneiss	950	3.1	0.86 (0.1-2.5)
13	Lower crust	metamorphic rocks	1050	3.0	0.32
14	High-density intra-crustal layer	mafic granulites, gabbros	1050	3.0	0.32
15	Oceanic layer 3A	sheeted dykes/gabbroic intrusions	1050	2.7	0.4
16-17	High-density lower-crustal layer and oceanic layer 3B	gabbro and high-grade metamorphic rocks	1100	2.8-3.1	0.2
18	Lithospheric upper mantle	peridotite	1200	4.79	0.03

Table 6. Average radiogenic heat production of sedimentary rocks, derived from gamma ray logs, in the selected wells. Units of radiogenic heat production are $\mu W/m^3$ (Fm. is formation and Gr. is group).

Well	Naust Fm. (layers 2.1-2.3)	Kai Fm. (layer 2.4)	Hordaland Group (layer 3)	Rogaland-Shetland Group (layer 5-6)	Cromer Knoll Gr. (layer 7)	pre-Cretaceous (layer 8)
6507/5-1	1.2	0.9	0.7	0.75	0.93	1.13
6510/2-1 R	0.68	0.68	0.72	0.69	0.94	1.65
6610/7-2	0.86	0.86?	0.47	0.67	0.82	1.1
6707/10-1	0.54	0.54?	-	1.02	-	-
6607/5-1	2.02	1.92	-	1.88	2	-
6608/8-1	1.18	1.35	1.41	1.49	-	1.69
6610/2-1 S	0.88	0.88?	1.46	1.68	1.16	2.56
6706/6-1	1	0.57	1	1.2	-	-
6710/10-1	1.24	1.24?	1.6	1.5	-	-

Table 7. Difference between modelled temperatures and measured ones (measured values minus the modelled ones) from different wells located inside the detailed 3D model area. Only the DST (drill-stem test) temperatures are used.

№	Temperature range of differences between modelled and measured temperatures	Percentage of values, %	Number of values
4	from -5 to 5	92.3	12
5	from 5 to 10	7.7	1

Table 8. Difference between modelled temperatures and measured ones (measured values minus the modelled ones) in available deep wells located inside the detailed 3D model area. In addition to the DST (drill-stem test) temperatures, the less reliable bottom-hole temperatures (BHT) are also included.

№	Temperature range of differences between modelled and measured temperatures	Percentage of values, %	Number of values
3	from -20 to -10	1.9	1
4	from -10 to -5	17.0	9
5	from -5 to 5	50.9	27
6	from 5 to 10	17.0	9
7	from 10 to 20	13.2	7

Figures

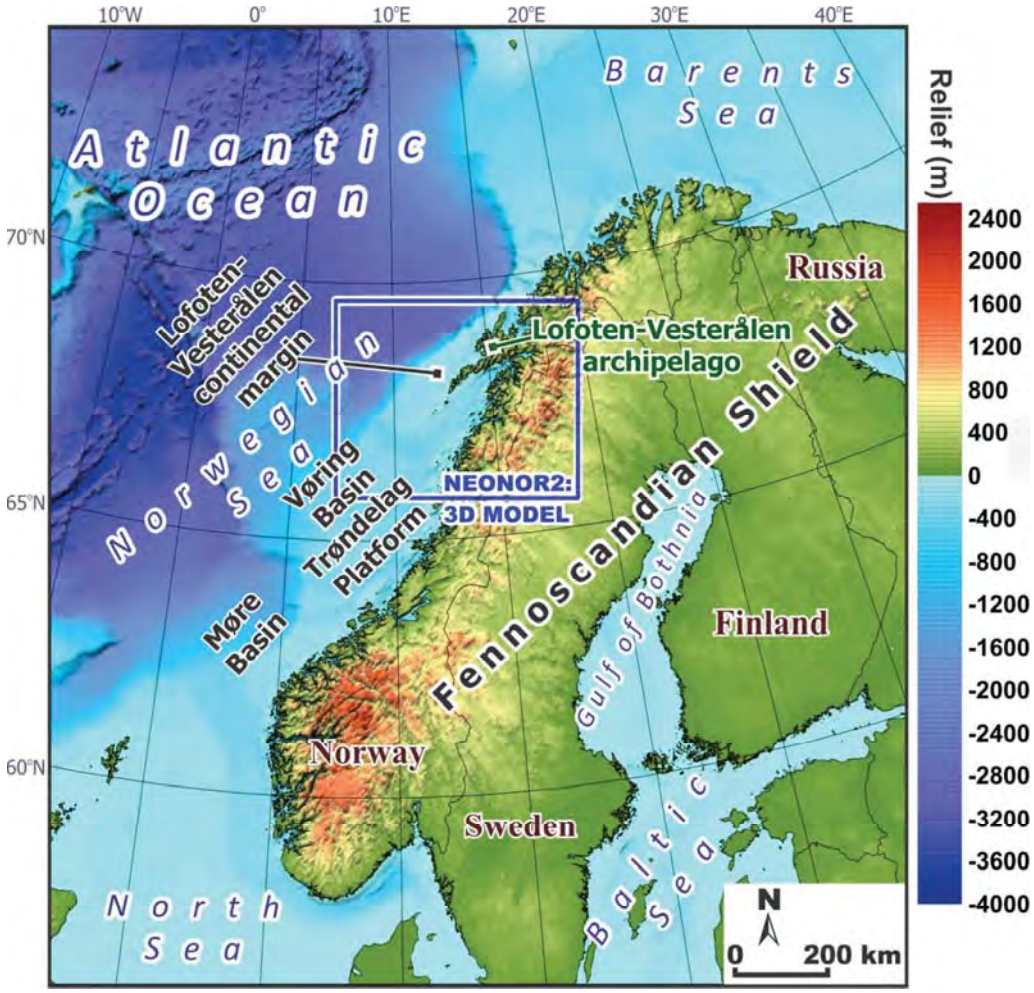

Figure 1. Overview map of north-western Europe (bathymetry and topography from the Norwegian Mapping Authority) with location of the lithosphere-scale 3D structural/thermal model of the Lofoten-Vesterålen margin segment and adjacent areas (blue frame).

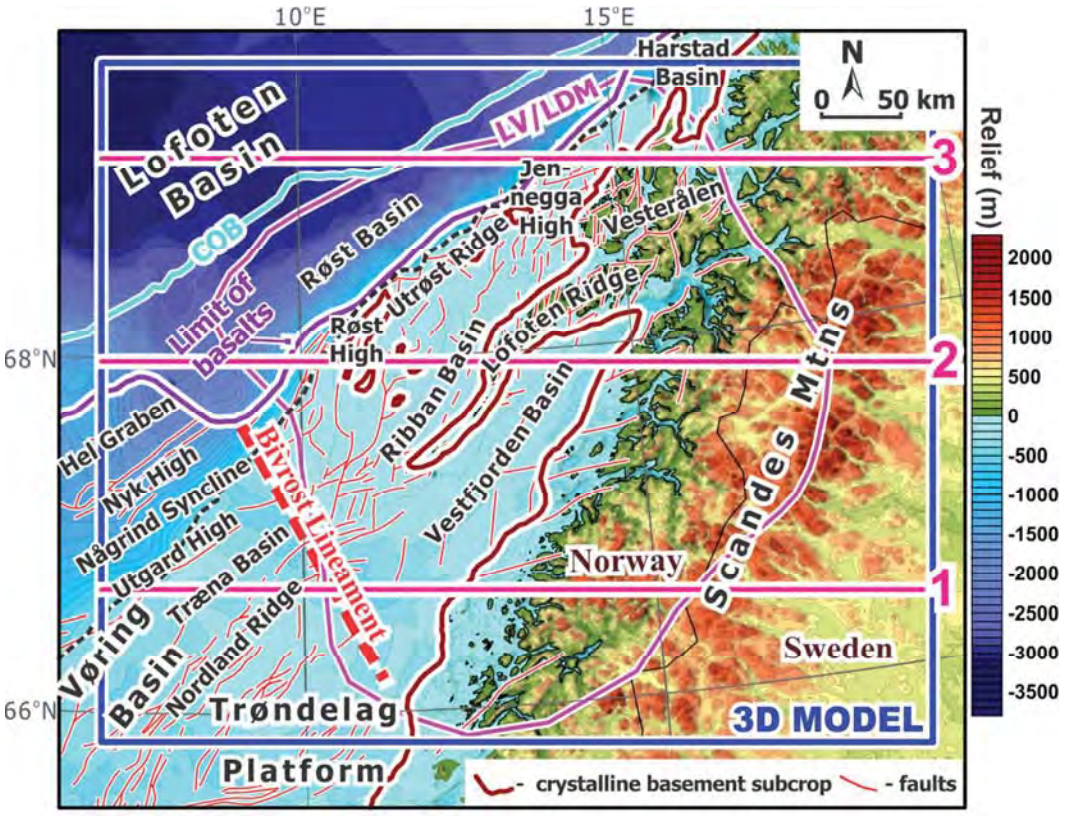

Figure 2. Tectonic configuration within the Lofoten-Vesterålen and the northern Vøring segments of the Mid-Norwegian continental margin, superimposed on the bathymetry and topography, with location of the 3D structural/thermal model (based on Blystad *et al.* 1995, Sigmond, 2002, Hansen, 2009, Hansen *et al.* 2012) (bathymetry and topography from the Norwegian Mapping Authority). Thick magenta lines correspond to the selected vertical slices, shown in Figure 20. Black dashed line corresponds to the present-day shelf edge. Abbreviations: COB - the continent-ocean boundary and LV/LDM - low-velocity/low-density mantle.

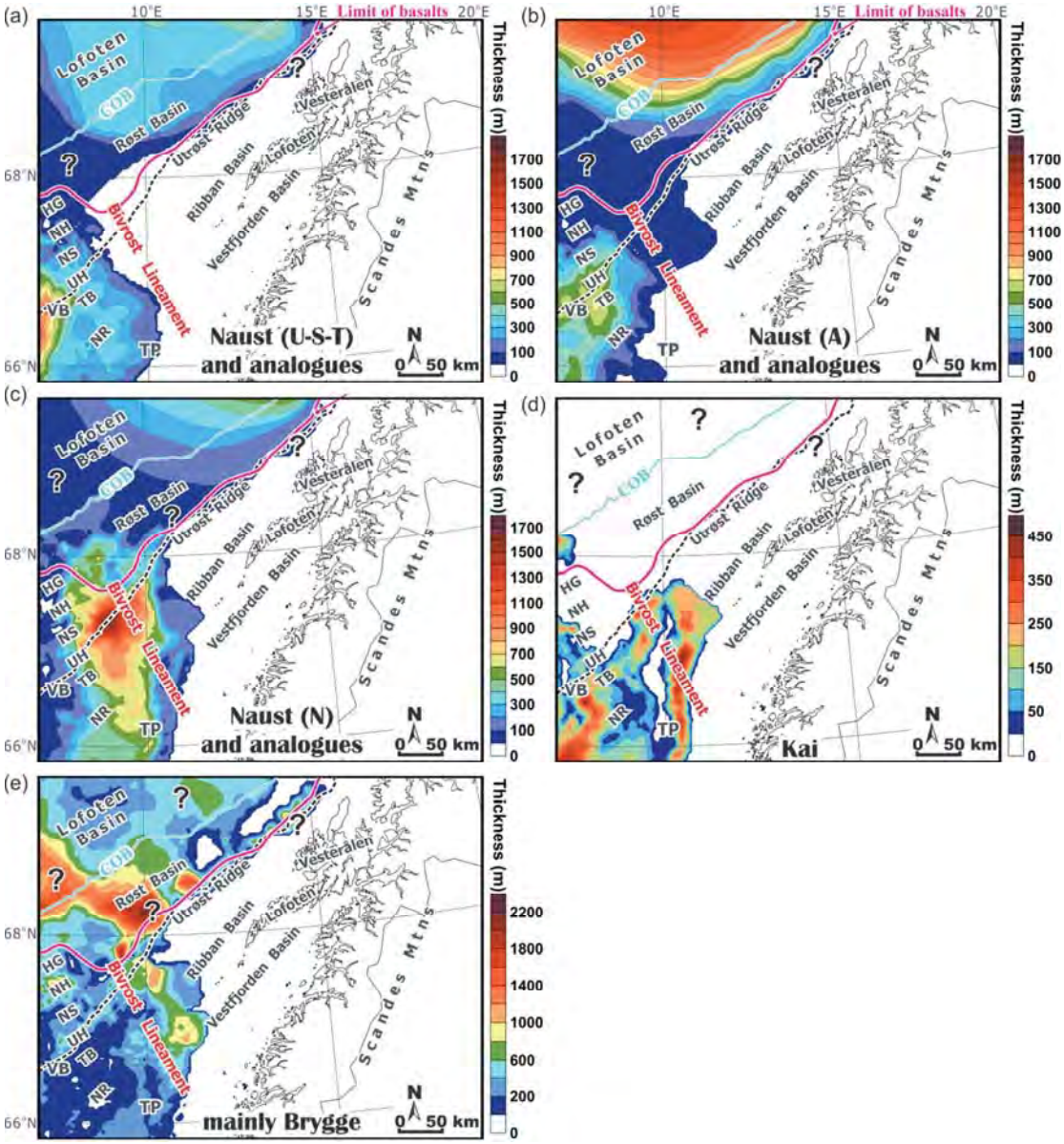

Figure 3. Thicknesses of the Cenozoic post-break-up sedimentary rocks: (a) the Naust Formation (sequences U, S and T) and analogues (layer 2.1), (b) the Naust Formation (sequence A) and analogues (layer 2.2), (c) the Naust Formation (sequence N) and analogues (layer 2.3), (d) the Kai Formation (layer 2.4) and (e) the Brygge Formation (Eocene-lower Miocene) and the undefined Cenozoic (layer 3) (based on Fiedler and Faleide, 1996b, Rise *et al.* 2005a, Eidvin *et al.* 2007, Hjelstuen *et al.* 2007, Dowdeswell *et al.* 2010a, Rise *et al.* 2010, Laberg *et al.* 2012, Ottesen *et al.* 2012). Black dashed line corresponds to the present-day shelf edge. Abbreviations: COB - continent-ocean boundary, HG - Hel Graben, NH - Nyk High, NR - Nordland Ridge, NS - Någrind Syncline, TB - Træna Basin, TP - Trøndelag Platform, UH - Utgard High and VB - Vøring Basin.

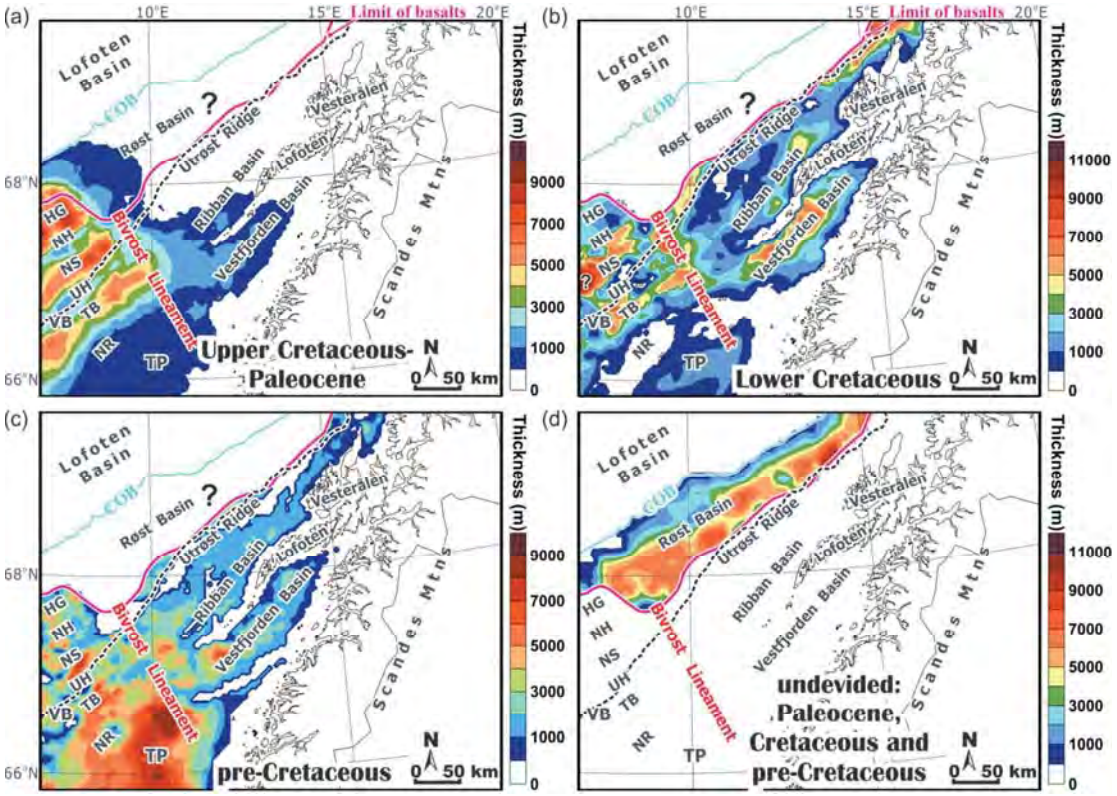

Figure 4. Thicknesses of the pre-break-up sedimentary rocks: (a) the Upper Cretaceous-Paleocene without the Røst Basin (near top Cenomanian-top Paleocene; layers 5-6), (b) the Lower Cretaceous without the Røst Basin (base Cretaceous unconformity-near top Cenomanian; layer 7), (c) the pre-Cretaceous without the Røst Basin (layer 8) and (d) the undivided Paleocene, Cretaceous and pre-Cretaceous within the Røst Basin (layers 5-8) (based on Brekke, 2000, Hansen, 2009, Maystrenko and Scheck-Wenderoth, 2009, Hansen *et al.* 2012, Eig, 2012, Maystrenko *et al.* 2017) NGU data (Gernigon 2014) and Maystrenko *et al.* revised). Black dashed line corresponds to the present-day shelf edge. Abbreviations: COB - continent-ocean boundary, HG - Hel Graben, NH - Nyk High, NR - Nordland Ridge, NS - Någrind Syncline, TB - Træna Basin, TP - Trøndelag Platform, UH - Utgard High and VB - Vøring Basin.

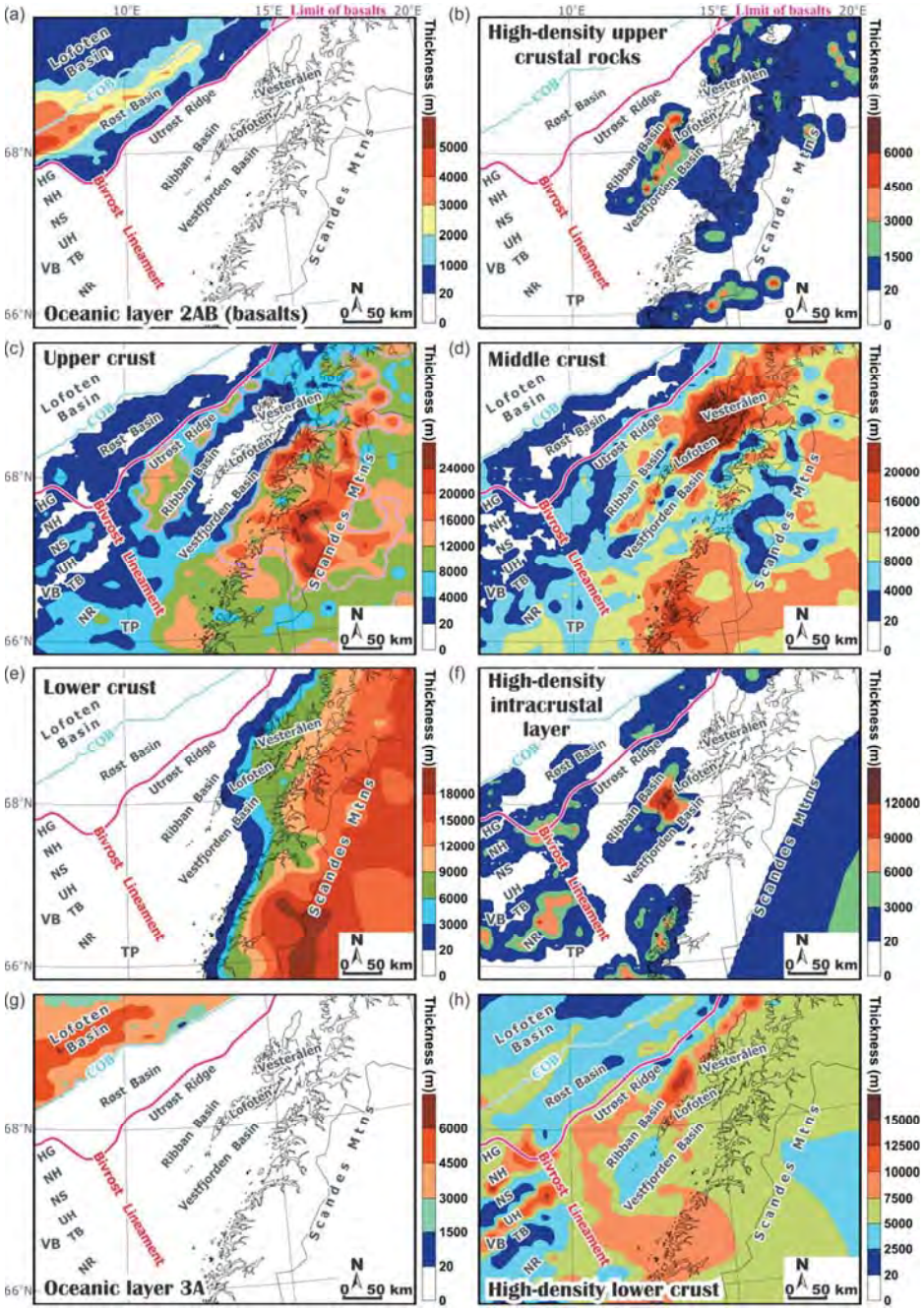

Figure 5. Thicknesses according to Maystrenko *et al.* ((2017)): (a) the oceanic layer 2AB (layer 4), (b) the upper crustal high-density rocks (layer 9), (c) the upper crust (layers 10-11), (d) the middle crust (layer 12), (e) the lower crust (layer 13), (f) the high-density intra-crustal layer (layer 14), (g) the oceanic layer 3A (layer 15) and (h) the deep high-density lower-crustal layer including the oceanic layer 3B (layers 16-17). Abbreviations: COB - continent-ocean boundary, HG - Hel Graben, NH - Nyk High, NR - Nordland Ridge, NS - Någrind Syncline, TB - Træna Basin, TP - Trøndelag Platform, UH - Utgard High and VB - Vøring Basin.

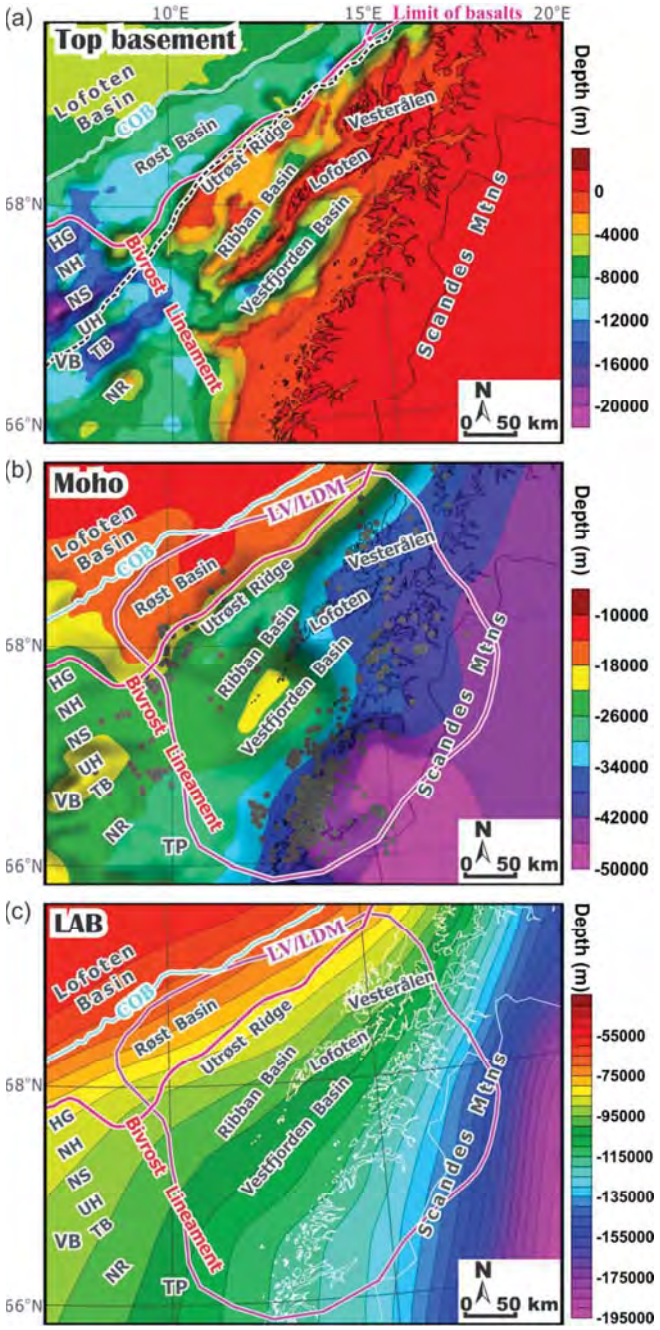

Figure 6. (a) Depth to the top of the crystalline basement, (b) Moho topography and (c) depth to the lithosphere-asthenosphere boundary. Black dashed line corresponds to the present-day shelf edge. Abbreviations: COB - continent-ocean boundary, HG - Hel Graben, LAB - lithosphere-asthenosphere boundary, LV/LDM - low-velocity/low-density mantle, NH - Nyk High, NR - Nordland Ridge, NS - Någrind Syncline, TB - Træna Basin, TP - Trøndelag Platform, UH - Utgard High and VB - Vøring Basin.

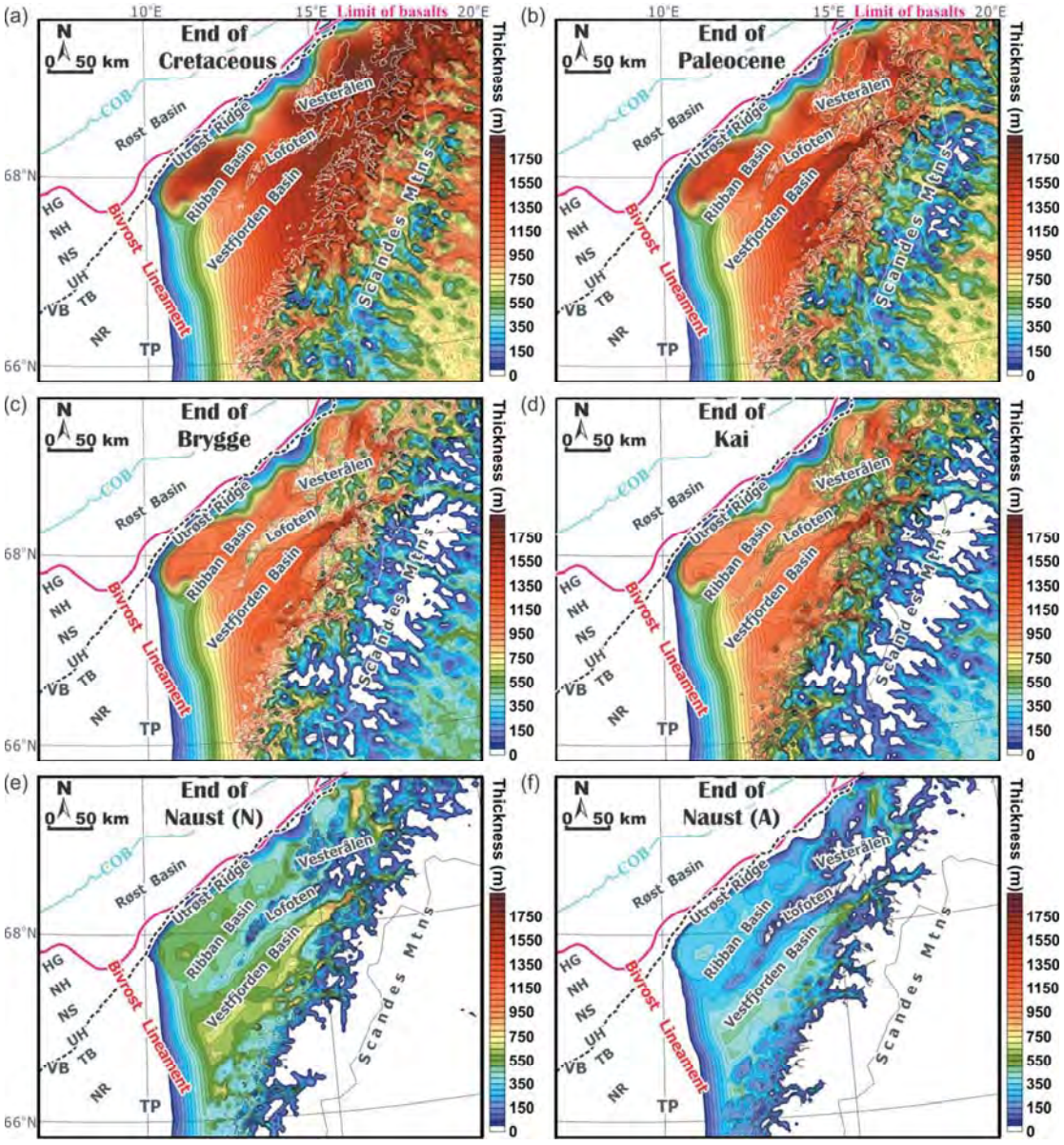

Figure 7. Reconstructed thicknesses of the eroded material during the Cenozoic: at the end of the Cretaceous (a), at the end of the Paleocene (b), at the end of the Brygge (c), at the end of the Kai (d), at the end of the Naust N (e) and at the end of the Naust A (f). Black dashed line corresponds to the present-day shelf edge. Abbreviations: COB - continent-ocean boundary, HG - Hel Graben, NH - Nyk High, NR - Nordland Ridge, NS - Någrind Syncline, TB - Træna Basin, TP - Trøndelag Platform, UH - Utgard High and VB - Vøring Basin.

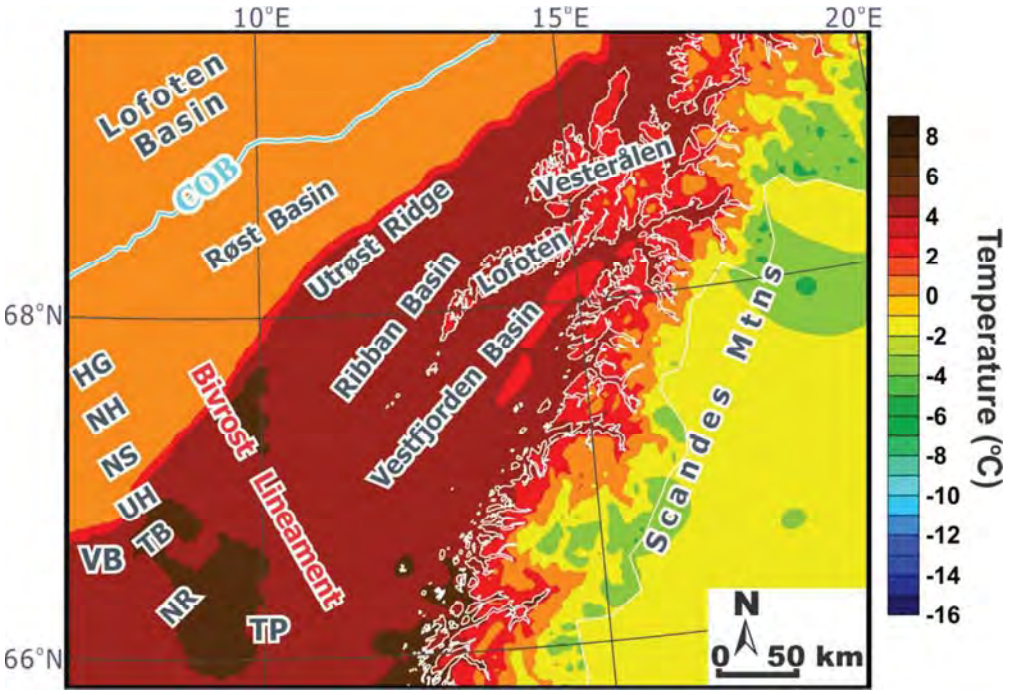

Figure 8. Present-day upper thermal boundary: annual average air temperatures at the Earth's surface and average sea-floor temperatures (based on Raab and Vedin, 1995, Tveito *et al.* 2000, Ottersen, 2009, Korablev *et al.* 2014). Abbreviations: COB - continent-ocean boundary, HG - Hel Graben, LV/LDM - low-velocity/low-density mantle, NH - Nyk High, NR - Nordland Ridge, NS - Någrind Syncline, TB - Træna Basin, TP - Trøndelag Platform, UH - Utgard High and VB - Vøring Basin.

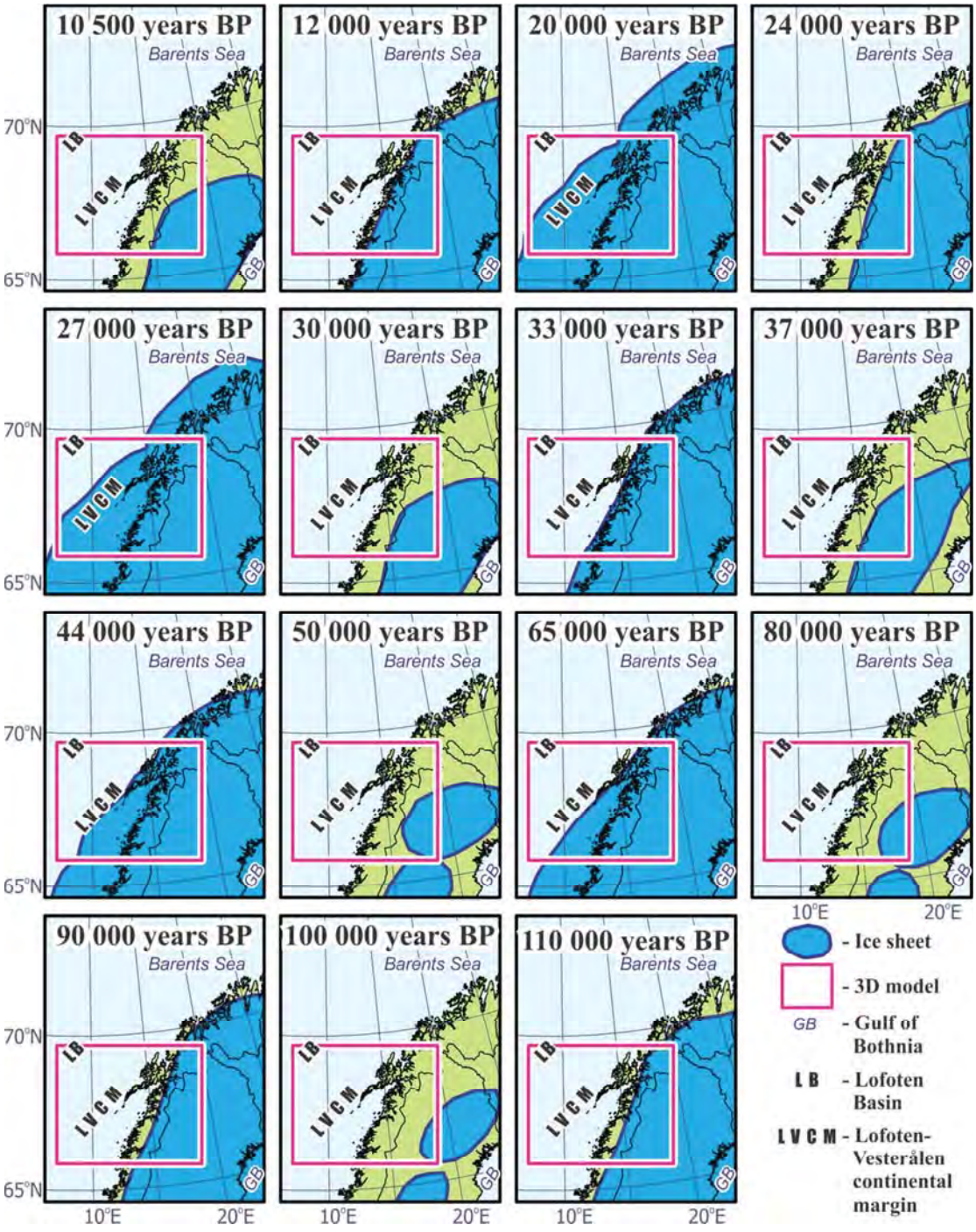

Figure 9. Ice cover variations during the Weichselian glacial period according to Olsen *et al.* 2013. The magenta frame correspond to the 3D structural/thermal model.

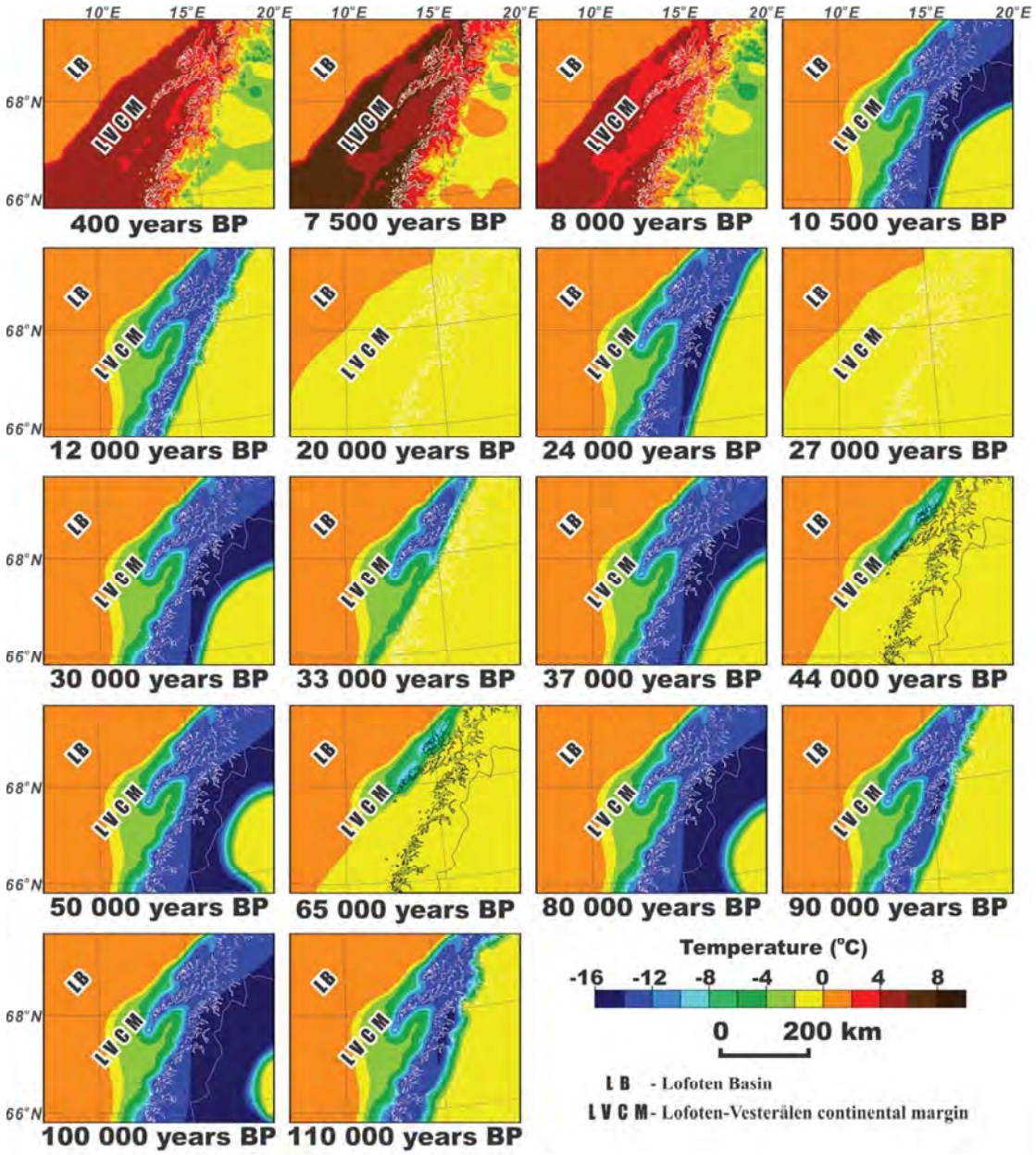

Figure 10. Average palaeotemperatures at the Earth´s surface and the sea floor during the Weichselian glacial period within the area covered by the 3D structural/thermal model.

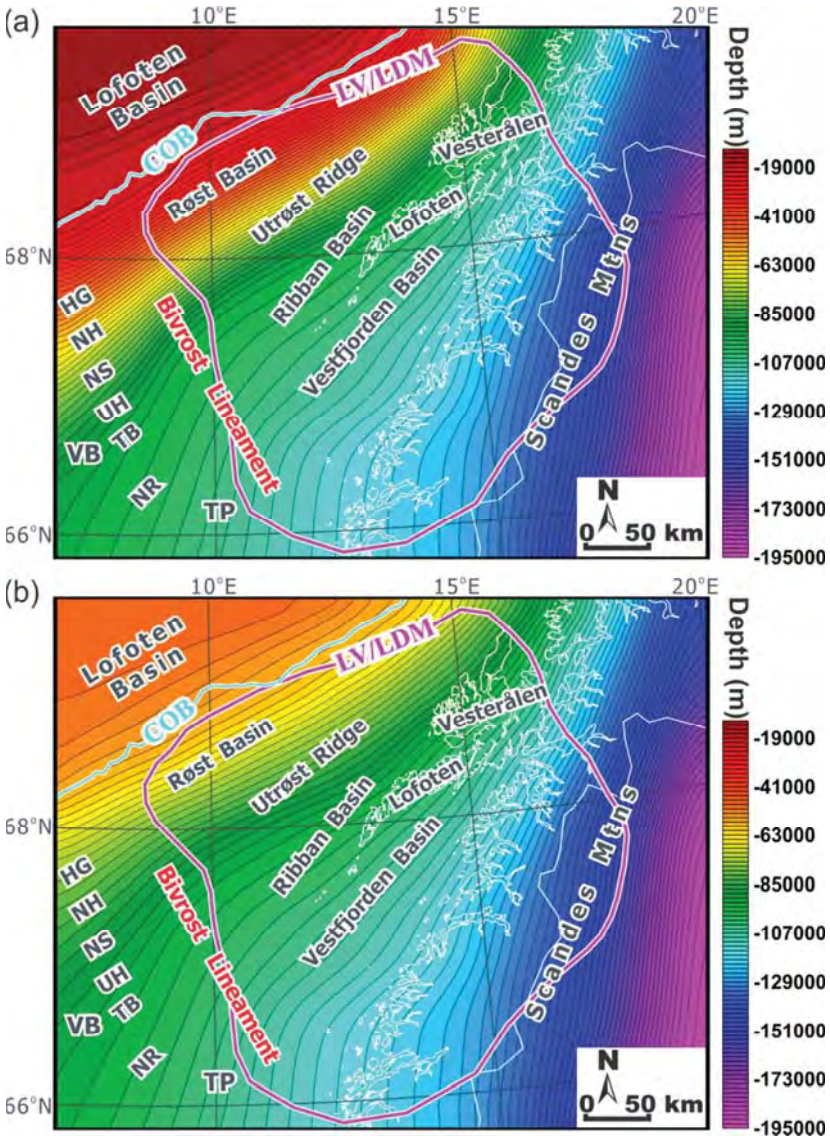

Figure 11. Inferred depths to the lithosphere-asthenosphere boundary corresponding to the 1300 ºC isotherm after the continental breakup 55 Ma ago (a) and at the end of the Brygge interval 18 Ma ago (b). Abbreviations: COB - continent-ocean boundary, HG - Hel Graben, LV/LDM - low-velocity/low-density mantle, NH - Nyk High, NR - Nordland Ridge, NS - Någrind Syncline, TB - Træna Basin, TP - Trøndelag Platform, UH - Utgard High and VB - Vøring Basin.

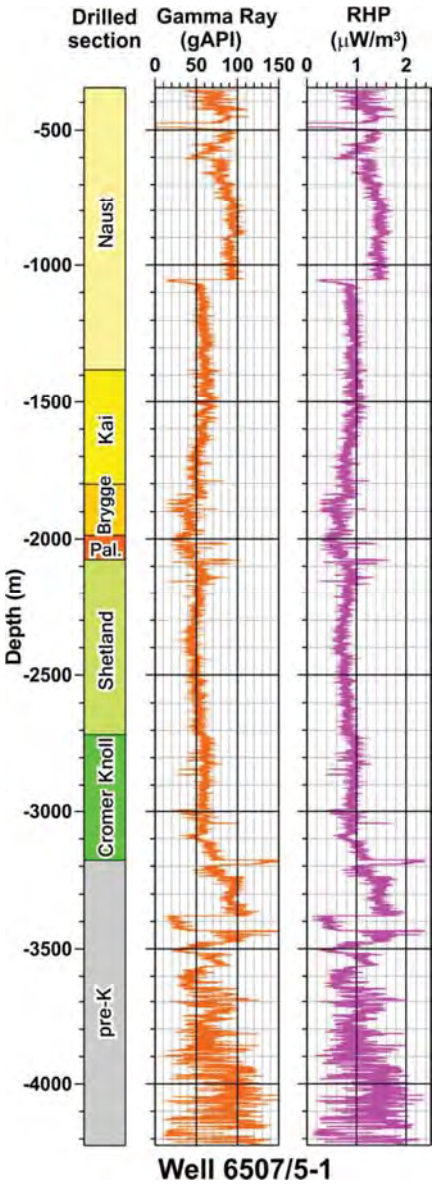

Figure 12. Example of the plot with stratigraphy, total natural gamma and calculated radiogenic heat production for one of the wells (well 6507/5-1) used to calculate the radiogenic heat production of sedimentary infill (stratigraphy and gamma ray log are from NPD (2017)).

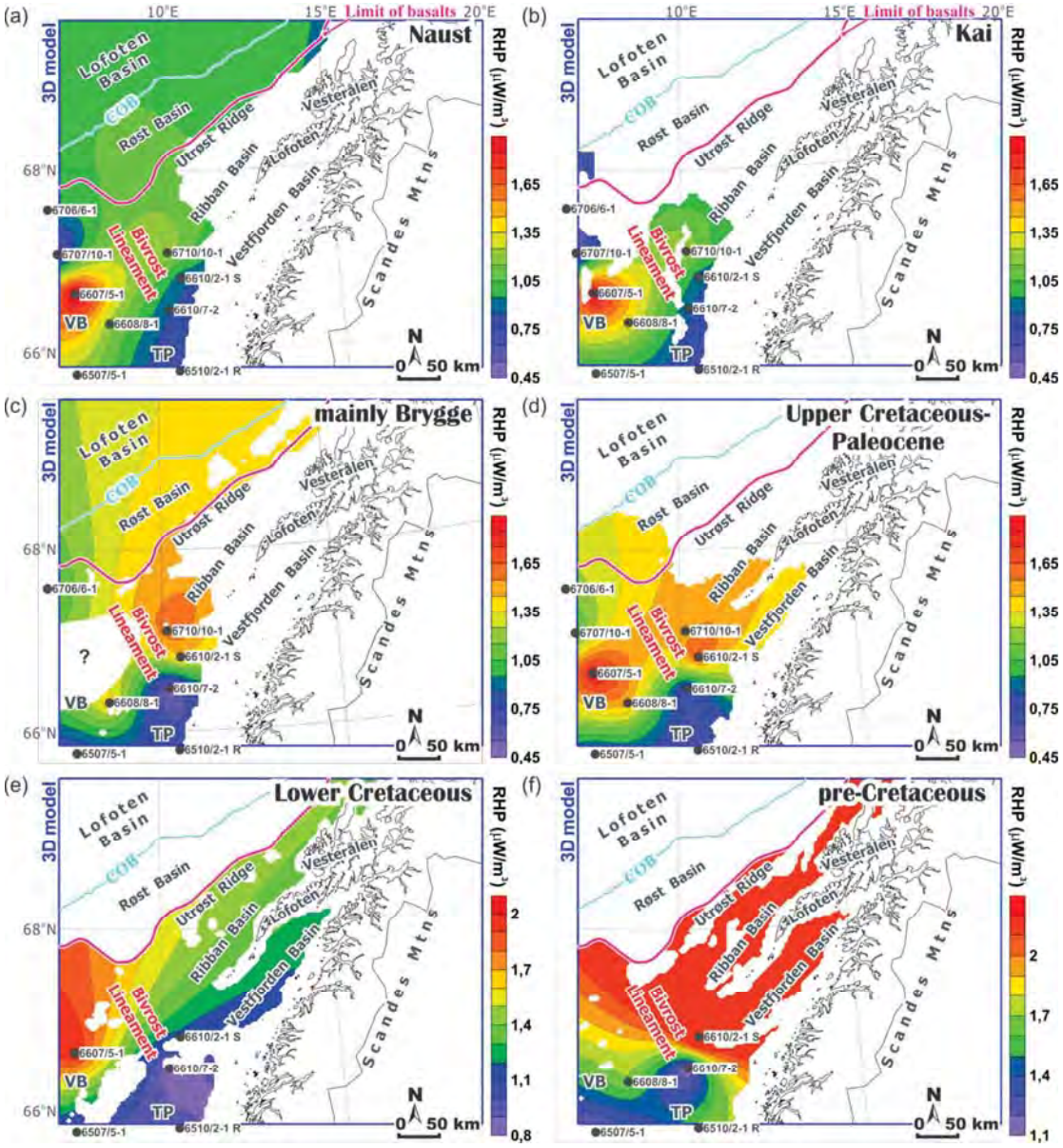

Figure 13. Radiogenic heat production of the sedimentary layers, obtained based on the well data: the Naust (middle Miocene-Pleistocene) formation (a), the Kai Formation (b), Brygge (Eocene-lower Miocene) Formation (c), the Upper Cretaceous-Paleocene (d), the Lower Cretaceous (e) and the pre-Cretaceous (f). Black circles indicate location of the wells used to derive the radiogenic heat production. Abbreviations: COB - continent-ocean boundary, TP - Trøndelag Platform and VB - Vøring Basin.

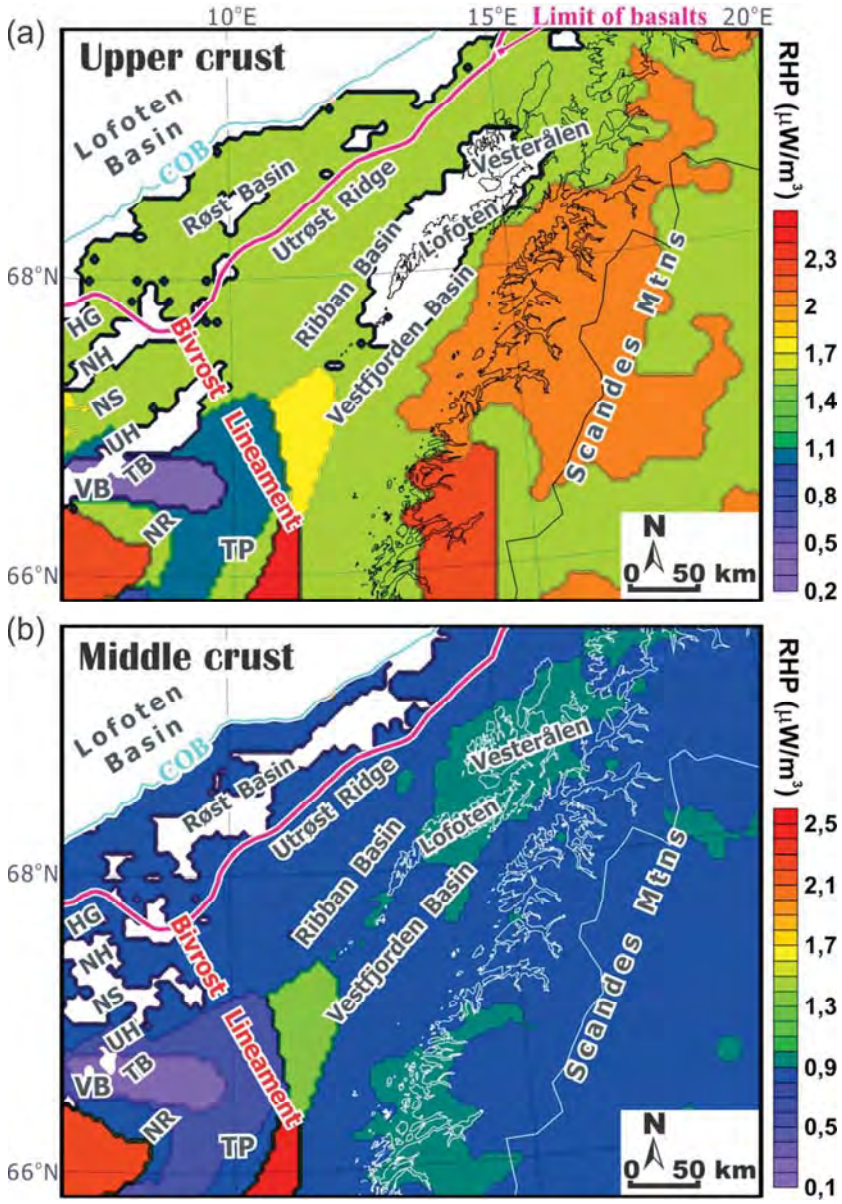

Figure 14. Radiogenic heat production of the upper crystalline crust (a; layers 10-11) and the middle crystalline crust (b; layer 12). Abbreviations: COB - continent-ocean boundary, HG - Hel Graben, NH - Nyk High, NR - Nordland Ridge, NS - Någrind Syncline, TB - Træna Basin, TP - Trøndelag Platform, UH - Utgard High and VB - Vøring Basin.

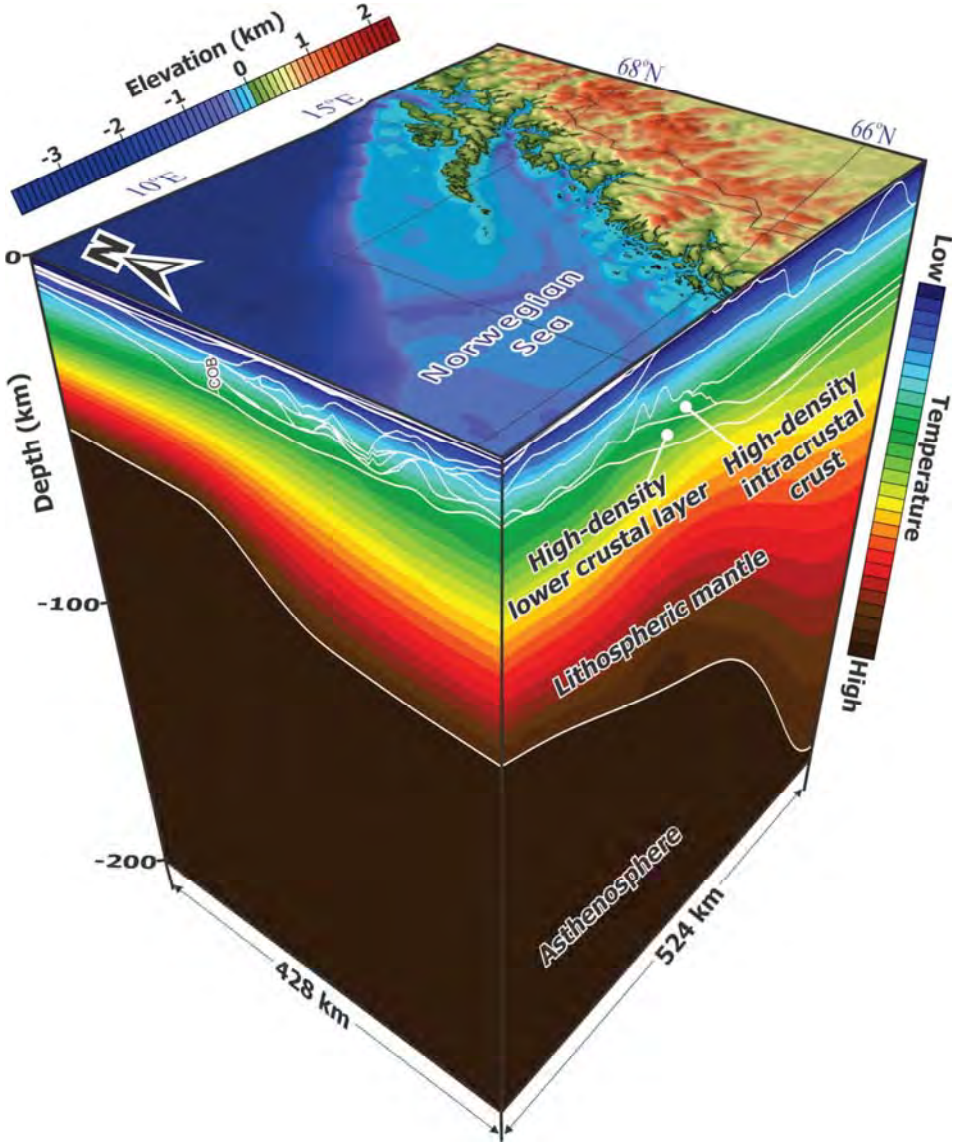

Figure 15. The lithosphere-scale 3D thermal model of the Lofoten-Vesterålen segment of the Mid-Norwegian continental margin and adjacent areas. Slightly more than three times vertically exaggerated.

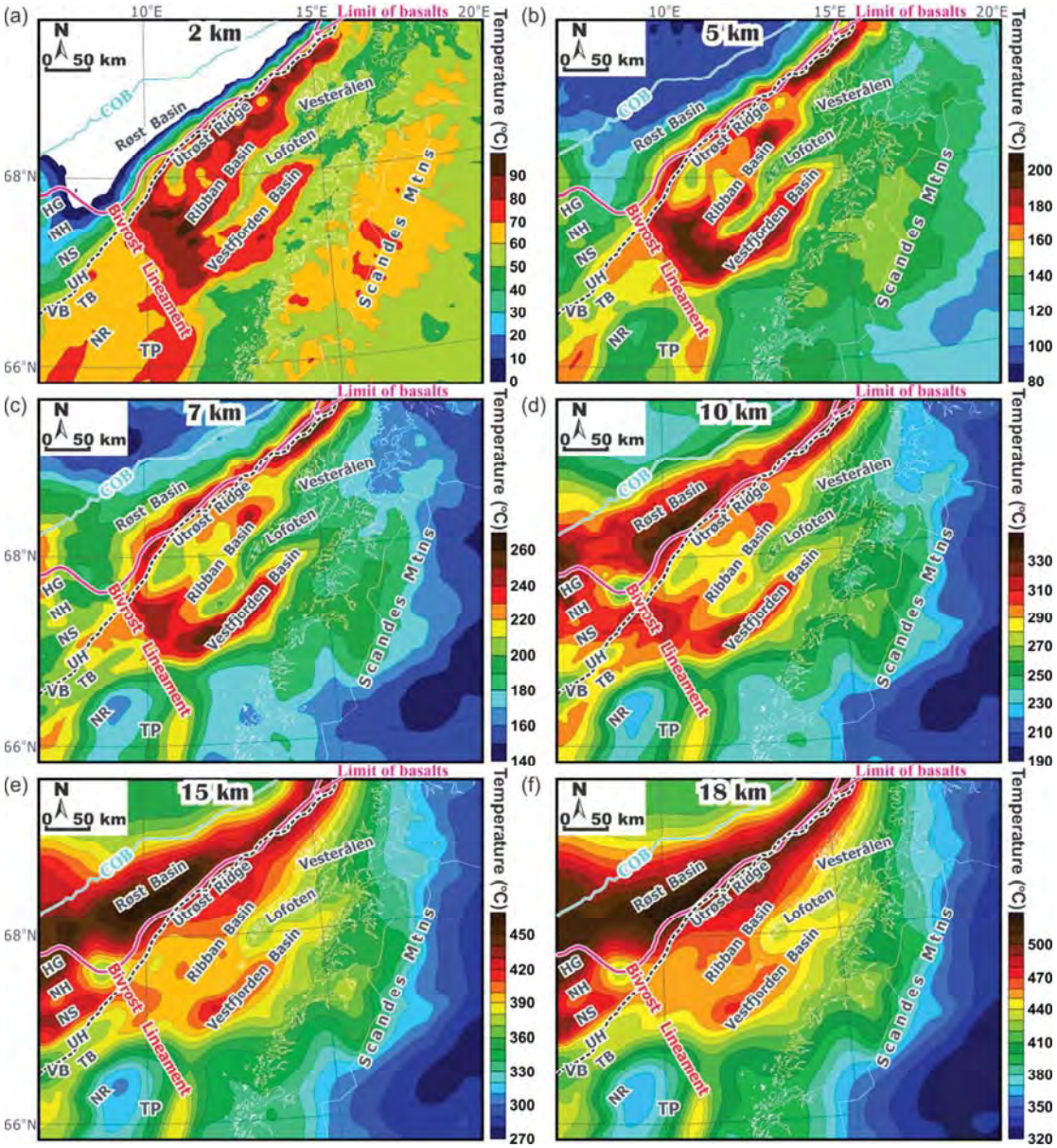

Figure 16. Maps with modelled temperatures at the present day within the upper part of the 3D thermal model (Fig. 15), represented by the temperature horisontal slices for the depths (below sea level) of 2 km (a), 5 km (b), 7 km (c), 10 km (d), 15 km (e) and 18 km (f). Black dashed line corresponds to the present-day shelf edge. Abbreviations: COB - continent-ocean boundary, HG - Hel Graben, NH - Nyk High, NR - Nordland Ridge, NS - Någrind Syncline, TB - Træna Basin, TP - Trøndelag Platform, UH - Utgard High and VB - Vøring Basin.

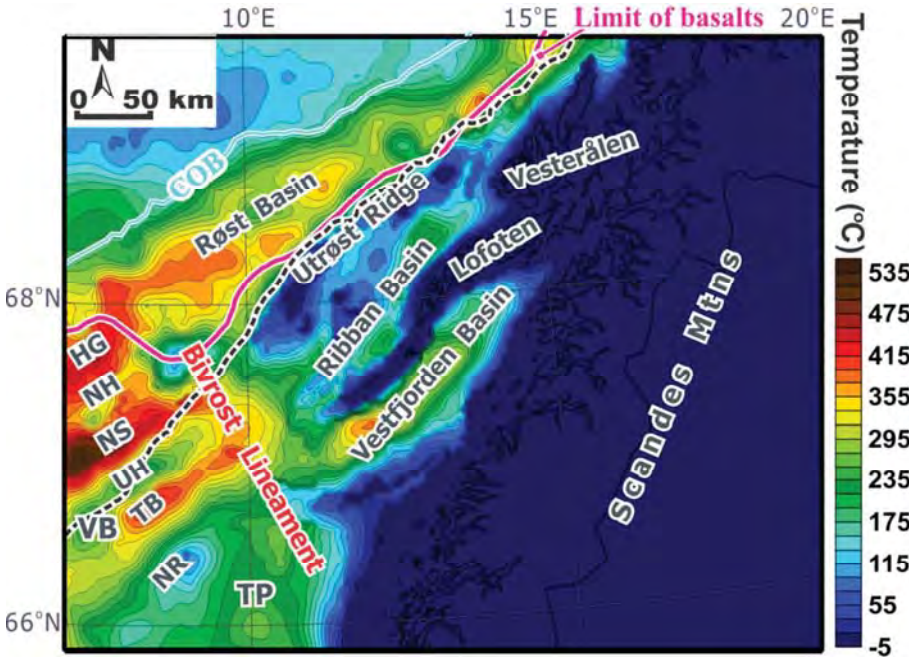

Figure 17. Modelled present-day temperatures at the top of the crystalline basement. Black dashed line corresponds to the present-day shelf edge. Abbreviations: COB - continent-ocean boundary, HG - Hel Graben, NH - Nyk High, NR - Nordland Ridge, NS - Någrind Syncline, TB - Træna Basin, TP - Trøndelag Platform, UH - Utgard High and VB - Vøring Basin.

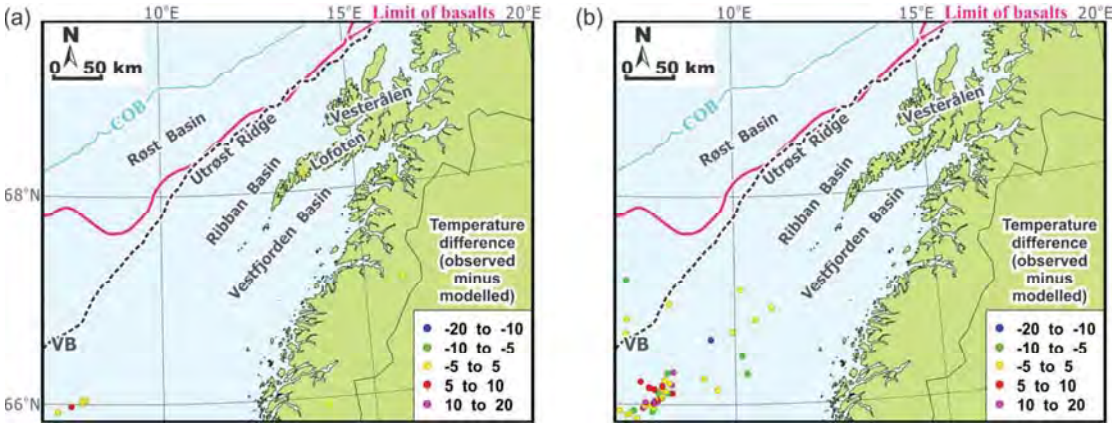

Figure 18. Location of the available wells with the measured temperatures and spatial distribution of the temperature variations (measured temperatures minus the modelled ones) within the 3D model area. (a) Wells with drill-stem test (DST) temperatures offshore and temperature logs onshore and (b) wells with less reliable bottom-hole temperatures (BHT) together with temperatures in the wells in Figure 17a. Black dashed line corresponds to the present-day shelf edge.

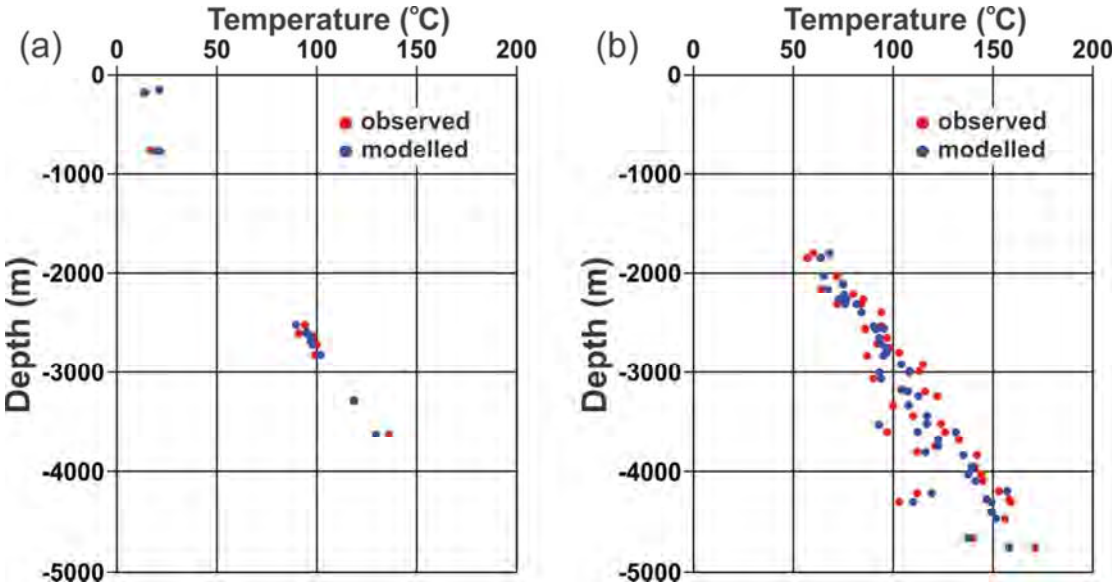

Figure 19. Comparison of the modelled (blue dots) and the observed (red dots) temperatures for the available wells with only drill-stem test (DST) temperatures and temperature logs (a) and bottom-hole temperatures (BHT) together with temperatures in Figure 18a.

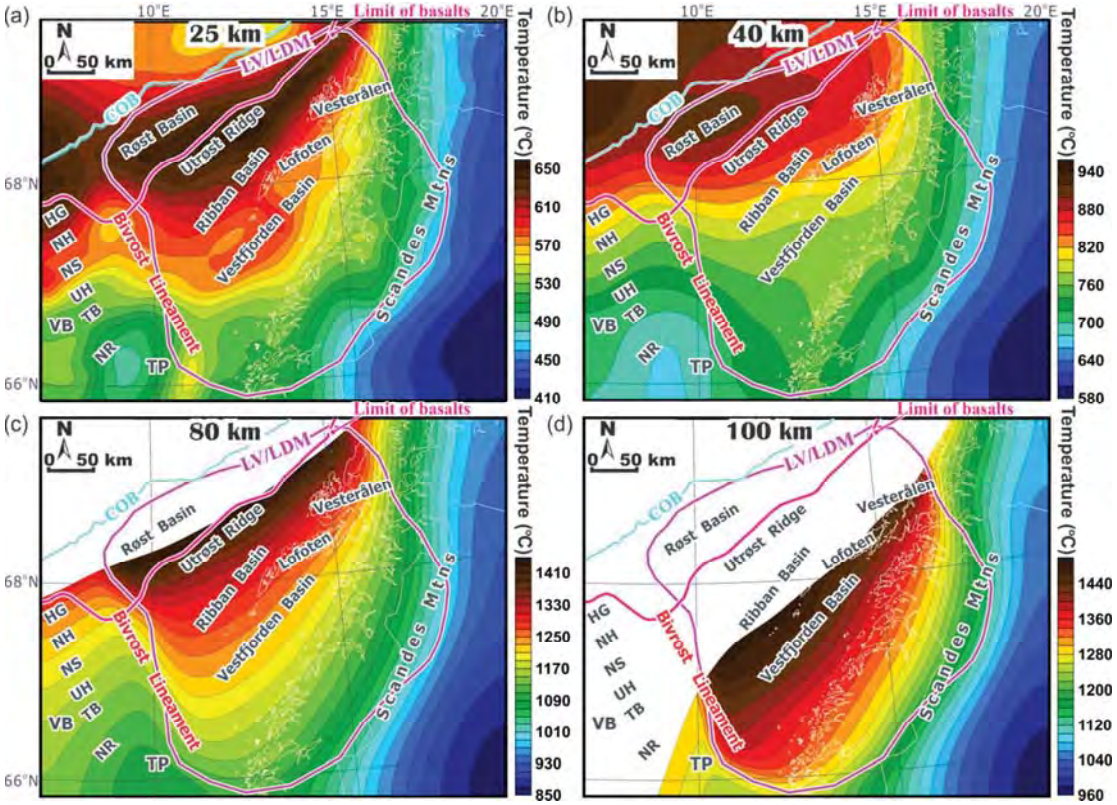

Figure 20. Maps with modelled temperatures at the present day within the lower part of the 3D thermal model (Fig. 15), represented by the temperature horisontal slices below sea level for the depths of 25 km (a), 40 km (b), 80 km (c) and 100 km (d). Abbreviations: COB - continent-ocean boundary, HG - Hel Graben, LV/LDM - low-velocity/low-density mantle, NH - Nyk High, NR - Nordland Ridge, NS - Någrind Syncline, TB - Træna Basin, TP - Trøndelag Platform, UH - Utgard High and VB - Vøring Basin.

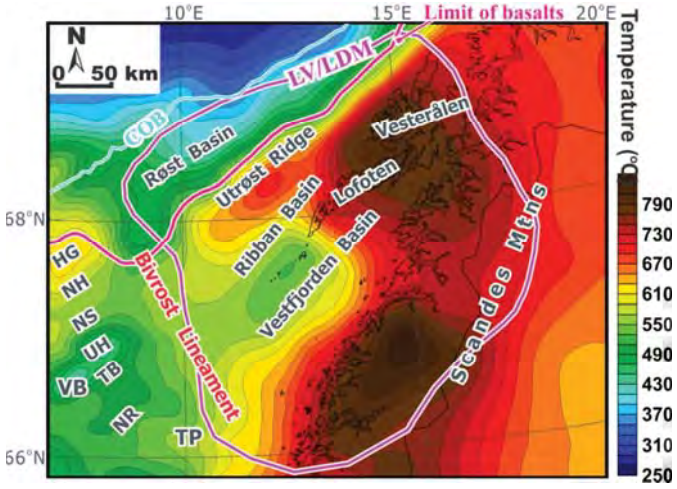

Figure 21. Modelled present-day temperatures at the Moho. Abbreviations: COB - continent-ocean boundary, HG - Hel Graben, LV/LDM - low-velocity/low-density mantle, NH - Nyk High, NR - Nordland Ridge, NS - Någrind Syncline, TB - Træna Basin, TP - Trøndelag Platform, UH - Utgard High and VB - Vøring Basin.

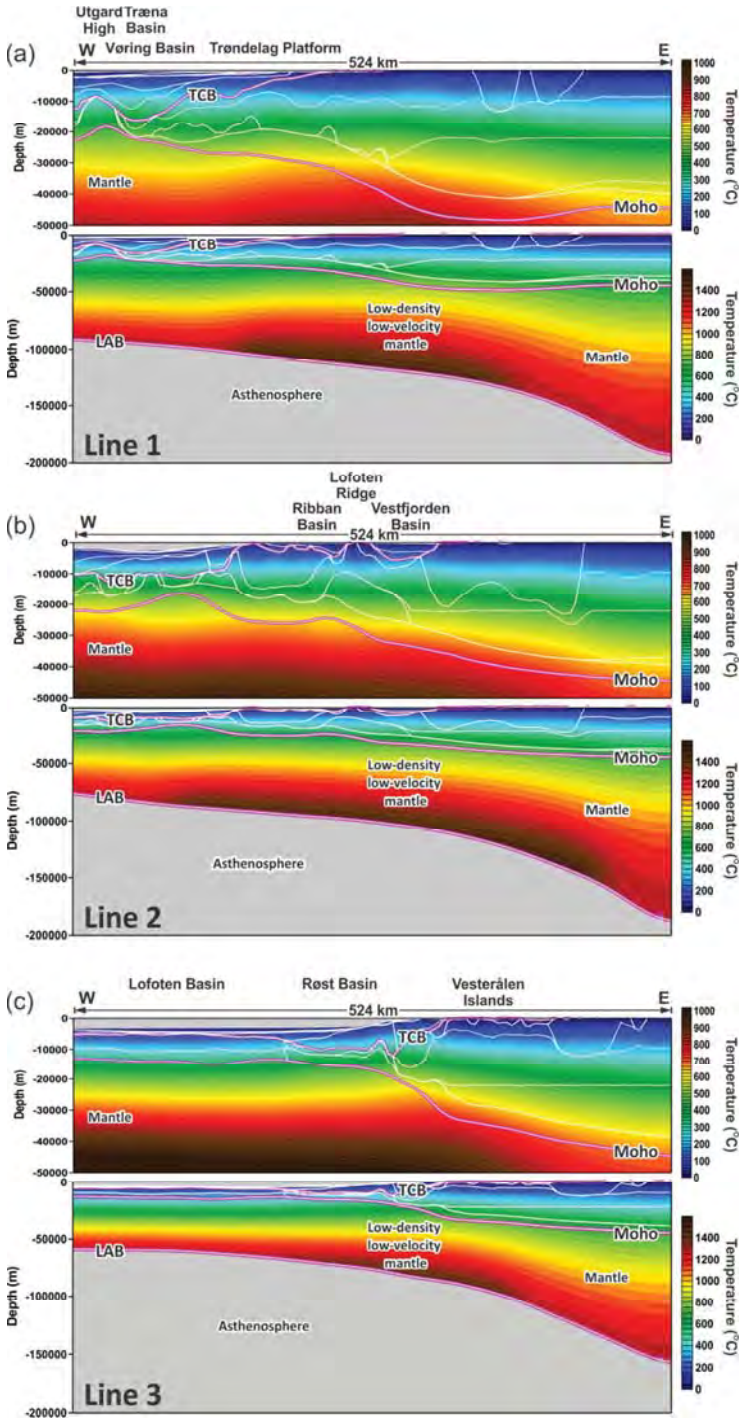

Figure 22. Present-day distribution of the modelled temperatures along three selected 2D vertical slices through the 3D thermal model (for the location see Fig. 2). Abbreviations: LAB - lithosphere-asthenosphere boundary and TCB - top of the crystalline basement.

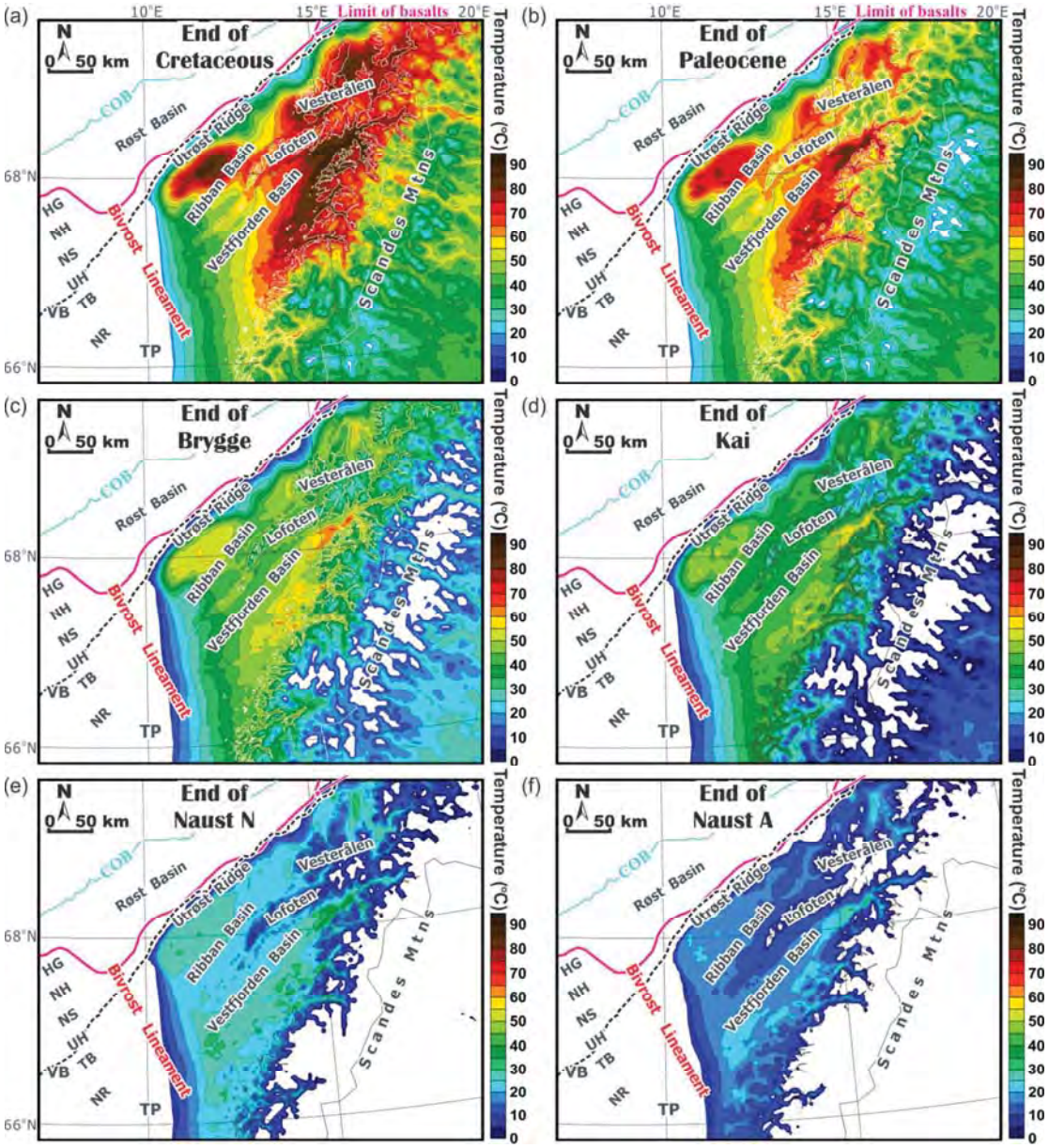

Figure 23. Temperatures at the base of the eroded sediments: at the end of the Cretaceous (a), at the end of the Paleocene (b), at the end of the Brygge (c), at the end of the Kai (d), at the end of the Naust N (e) and at the end of the Naust A (f). Black dashed line corresponds to the present-day shelf edge. Abbreviations: COB - continent-ocean boundary, HG - Hel Graben, NH - Nyk High, NR - Nordland Ridge, NS - Någrind Syncline, TB - Træna Basin, TP - Trøndelag Platform, UH - Utgard High and VB - Vøring Basin**.**

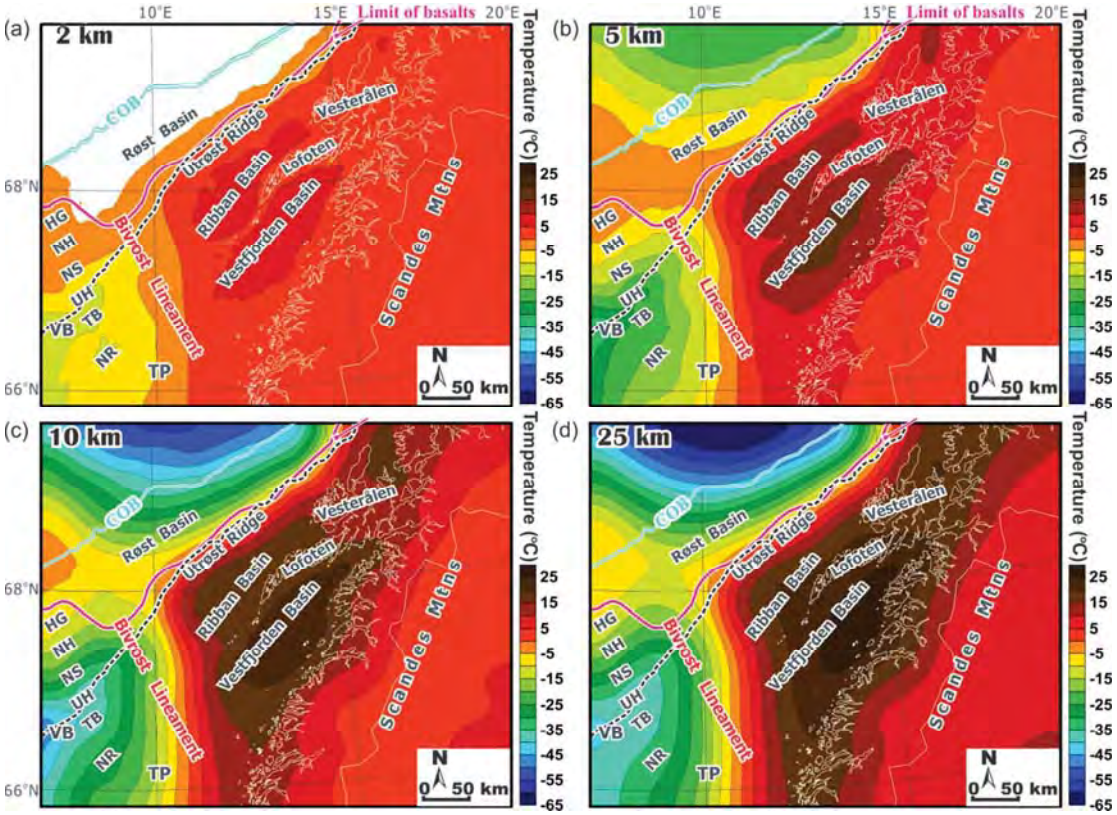

Figure 24. Thermal anomalies due to erosion and deposition during the Cenozoic, calculated as a difference between the modelled temperatures with the thermal effect of erosion/deposition and the modelled temperatures without this effect. Black dashed line corresponds to the present-day shelf edge. Abbreviations: COB - continent-ocean boundary, HG - Hel Graben, NH - Nyk High, NR - Nordland Ridge, NS - Någrind Syncline, TB - Træna Basin, TP - Trøndelag Platform, UH - Utgard High and VB - Vøring Basin.

CHAPTER 12: A COMPARISON OF STRAIN RATES AND SEISMICITY FOR FENNOSCANDIA: DEPTH DEPENDENCY OF DEFORMATION FROM GLACIAL ISOSTATIC ADJUSTMENT

Authors: M. Keiding,[1] C. Kreemer,[2] C.D. Lindholm,[3] S. Gradmann, [1] O. Olesen[1] and H.P. Kierulf[4]

Affiliation: [1]Geological Survey of Norway, P.O. Box 6315 Torgården, N-7491 Trondheim; [2]Nevada Bureau of Mines and Geology, and Seismological Laboratory, University of Nevada, Reno, NV 89557, USA; [3]NORSAR, Kjeller, Norway; [4]Geodetic Institute, Norwegian Mapping Authority, Hønefoss, Norway

Journal: Geophysical Journal International 202

Publishing Date: June 2018 (Online)

DOI: http://dx.doi.org/10.1093/gji/ggv207

Pages: 8

Geophys. J. Int. (2015)
GJI Geodynamics and tectonics
doi: 10.1093/gji/ggv207

A comparison of strain rates and seismicity for Fennoscandia: depth dependency of deformation from glacial isostatic adjustment

M. Keiding,[1] C. Kreemer,[2] C. D. Lindholm,[3] S. Gradmann,[1] O. Olesen[1] and H. P. Kierulf[4]

[1]*Geological Survey of Norway, Trondheim, Norway. E-mail: marie.keiding@ngu.no*
[2]*Nevada Bureau of Mines and Geology, and Seismological Laboratory, University of Nevada, Reno, NV 89557, USA*
[3]*NORSAR, Kjeller, Norway*
[4]*Geodetic Institute, Norwegian Mapping Authority, Hønefoss, Norway*

Accepted 2015 May 14. Received 2015 May 13; in original form 2015 February 24

SUMMARY

We investigate the influence of the glacial isostatic adjustment (GIA) on the deformation at the surface and at seismogenic depths in Fennoscandia. The surface strain rate field, derived from geodetic data, is controlled by GIA which causes NW–SE extension of up to 4×10^{-9} yr^{-1} in most of mainland Fennoscandia, surrounded by regions of radial shortening towards the centre of uplift. The seismic deformation field, derived from a new compilation of focal mechanisms, shows consistent NW–SE compression on the Norwegian continental margin and a tendency towards tension in mainland Fennoscandia. The seismic moment rate is at least two orders of magnitude smaller than the geodetic moment rate. We propose that the low level of seismicity and the tendency toward tensional focal mechanisms in mainland Fennoscandia may be explained by the destructive interference of the regional stress from ridge push with the flexural stress due to GIA.

Key words: Seismicity and tectonics; Intra-plate processes; Lithospheric flexure; Neotectonics.

1 INTRODUCTION

It is generally accepted that the interseismic surface strain rates in plate boundary zones reflect crustal strain rates (e.g. Kreemer *et al.* 2014), which are related to seismicity through the seismic coupling (Bird & Kagan 2004). However, the relationship between strain rates at the surface and deformation at seismogenic depths is not well known in intraplate regions undergoing glacial isostatic adjustment (GIA), and the influence of GIA on present-day seismicity is still debated.

At the peak of the last glaciation around 20 000 yr ago, most of Canada and northern United States (the Laurentide region), Scotland and Fennoscandia were covered under up to 2–3 km thick ice sheets. Within the latest phase of the deglaciation, around 9000 yr ago, an extraordinary pulse of seismicity occurred in northern Fennoscandia, likely due to a combination of crustal deweighting, high pore pressures and long-term tectonic compression (Muir Wood 1989b; Lund *et al.* 2009). The seismicity probably included a number of $M > 7$ earthquakes and resulted in prominent, up to 155 km long fault scarps as well as coincident land slides and liquefaction phenomena (e.g. Lagerbäck 1992; Dehls *et al.* 2000; Olesen *et al.* 2013a).

Today, seismicity remains relatively high in both Fennoscandia and the Laurentide region. Several authors have argued that the GIA is at least partially responsible for the elevated seismicity in parts of the Laurentide region (e.g. Stein *et al.* 1979; Wu & Johnston 2000; Mazzotti *et al.* 2005) and Fennoscandia (Arvidsson 1996; Muir-Wood 2000; Hicks *et al.* 2000b). For example, Hasegawa & Basham (1989) noted the correlation of high levels of seismicity, steep gradients in free-air gravity and steep gradient in postglacial uplift along the northeastern periphery of the Canadian shield and concluded that there may be a causal relationship.

With this work, we investigate the deformation at the surface and at seismogenic depths in Fennoscandia, and discuss the implications for the question how GIA affects the seismicity.

2 PRESENT-DAY DEFORMATION IN FENNOSCANDIA

Here, we present an overview of the present-day deformation in Fennoscandia and the data that are included in the following analyses.

2.1 Surface deformation

The first-order pattern of surface deformation in Fennoscandia is dominated by GIA, which has been constrained by a number of

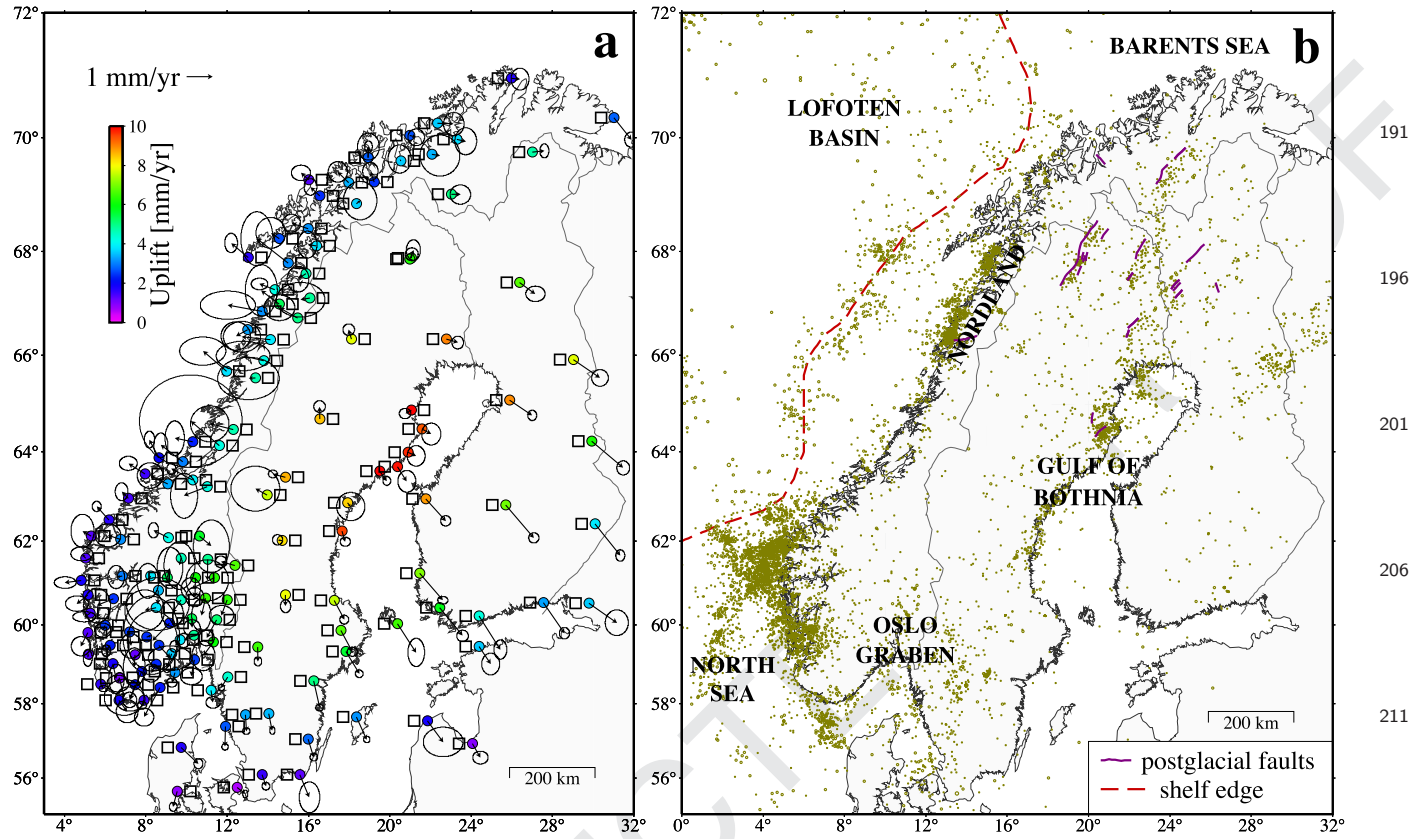

Figure 1. (a) GPS velocities from Kierulf *et al.* (2014) with 95 per cent confidence ellipses. The ITRF2008 velocities are referenced to the stable Eurasian frame. (b) Earthquakes during 1980–2011 from the FENCAT catalogue.

independent data sets, notably tide gauges, gravity change, levelling and GPS data (for a review, see Steffen & Wu 2011). A joint effort to study the GIA by means of GPS data was launched in the early 1990s with the BIFROST project (e.g. Lidberg *et al.* 2010) through which a GPS network with a typical spacing of 100–200 km between neighbouring stations was established in Fennoscandia. GPS data from the BIFROST network have been combined with results from levelling and tide-gauge measurements to get detailed constraints on the uplift in Fennoscandia (Vestøl 2006). The GPS velocity field of Norway was analysed by Kierulf *et al.* (2013), who included stations mainly established for navigational purposes in addition to the stations built for crustal deformation studies. Finally, Kierulf *et al.* (2014) combined data from the spatially dense Norwegian network with data from the BIFROST network and other high-quality GPS stations in north-central Europe to produce a new GPS velocity field for Fennoscandia (see Fig. 1a). The GIA causes uplift of up to 10 mm yr^{-1} in the northern part of the Gulf of Bothnia, decreasing to 1–2 mm yr^{-1} along the southern coast of Norway. The horizontal velocity field is also to a first order controlled by the uplift, which causes outward spreading of 1–2 mm yr^{-1} relative to the uplift centre (Kierulf *et al.* 2014).

2.2 Seismicity

A catalogue of the seismicity in Fennoscandia dating back to year 1375 is available from the joint Nordic earthquake bulletin, FENCAT, maintained by University of Helsinki (e.g. Mäntyniemi *et al.* 2004). Fig. 1(b) shows all earthquakes from FENCAT during 1980–2011. The seismicity in Fennoscandia is low to intermediate in intensity and mainly located in the upper 20 km of the crust. The highest seismicity occurs in the rifted continental margin, particularly along the shelf-edge and in the strongly faulted regions near the failed rifts in the North Sea and near the coast of southwestern Norway (e.g. Lindholm *et al.* 2005). The oceanic crust is mostly aseismic, however, unusually high seismic activity occurs in the eastern Lofoten Basin, possibly due to local flexure of the lithosphere related to rapid deposition of glacial sediments (Byrkjeland *et al.* 2000).

In mainland Fennoscandia, the seismicity is mostly low, both in terms of frequency and magnitude, but there are a few exceptions to this. A major occurrence of seismicity is southwestern Norway, a region strongly faulted by post-Caledonian faults and shear zones (Bøe *et al.* 2010). Another important occurrence of seismicity is Nordland (see Fig. 1b), where two shallow earthquake swarms occurred in recent years (Atakan *et al.* 1994; Bungum *et al.* 1982). The largest known historical earthquake in Fennoscandia occurred in Nordland in 1819 and has been estimated to have a M_S=5.8 (Muir Wood 1989a; Bungum & Olesen 2005). At present-day, the seismicity in Nordland is characterized by swarm activity with magnitudes rarely reaching 4. Microseismicity is associated with the post-glacial faults in northern Fennoscandia (Arvidsson 1996; Lindblom *et al.* 2015). Some seismicity also occurs along the Swedish coast in the Gulf of Bothnia and in southern Sweden and the Oslo Graben.

2.3 Focal mechanisms

The most recent compilation of earthquake focal mechanisms in Norway included 112 mechanisms and was presented by Hicks *et al.* (2000a). Here, we present a new compilation of focal mechanisms in Norway including an additional three published

Table 1. Previously unpublished earthquake focal mechanisms in Norway.

Date	Latitude	Longitude	Depth	ML	T-tr	T-pl	P-tr	P-pl	Strike	Dip	Rake	Quality
2000.11.26	60.038	5.474	11	2.6	307	52	66	21	116	36	31	B
2000.11.29	59.851	6.980	15	2.6	205	3	115	8	250	82	−176	B
2000.12.08	60.131	4.786	4	3.8	174	8	73	53	230	48	−141	A
2001.06.22	60.105	7.352	15	2.6	175	4	265	9	310	81	−4	B
2003.12.15	61.674	2.653	10	3.3	200	6	292	24	334	69	−13	B
2010.12.20	59.900	5.366	17	3.3	14	10	279	28	60	63	−167	B
2012.03.24	60.634	6.401	15.3	3.0	16	17	281	14	58	68	178	A

T, tensional axis; P, compressional axis; tr, trend; pl, plunge.

mechanisms (Hicks & Ottemöller 2001; Ottemöller *et al.* 2005; Sørensen *et al.* 2007), seven previously unpublished mechanisms from the Norwegian National Seismic Network (Table 1) and seven mechanisms from the Global CMT Project (Ekström *et al.* 2012). This new compilation of Norwegian focal mechanisms is, to the best of our knowledge, complete. In the following analysis, we also include 109 published mechanisms for Sweden, Finland and Baltica (Slunga 1979; Slunga & Ahjos 1986; Henderson 1991; Arvidsson & Kulhanek 1994; Uski *et al.* 2003, 2006; Juhlin & Lund 2011; Smedberg *et al.* 2012). The compilation of Fennoscandian focal mechanisms is presented in a table and figure in the supplementary material.

The focal mechanisms on the continental margin are relatively deep, with depths below 9 km, and are typically reverse to strike-slip with WNW–ESE to NW–SE trending axes of compression, aligning approximately with the spreading direction from the mid-Atlantic ridge (Hicks *et al.* 2000a). The mechanisms in mainland Fennoscandia are often shallower than on the continental margin and show larger variation in style and direction. Mechanisms around the post-glacial faults in northern Fennoscandia are mostly reverse, but normal faulting and strike-slip are common elsewhere. A small number of Swedish mechanisms seem to be located in the deeper parts of the lower crust, with focal depths as deep as 40 km (Arvidsson & Kulhanek 1994).

3 SURFACE STRAIN RATE FIELD

We estimate strain rates from the horizontal velocities of Kierulf *et al.* (2014), using the method of Haines and Holt (for a detailed review of the methodology, see Holt *et al.* 2000; Beavan & Haines 2001). The method assumes that the lithosphere behaves as a continuum. The observed velocity field is parameterized using a rotation vector function at the surface of a sphere, and the rotation vector function is then expanded on a curvilinear grid using bi-cubic Bessel interpolation. The distribution of GPS stations in the velocity field of Kierulf *et al.* (2014) is irregular, as the GPS network in Norway includes a large number of stations that were installed for navigational purposes. Thus, it is difficult to define a grid that fits the station distribution perfectly everywhere. As the GPS network in Norway includes many stations with larger uncertainties, we choose to use a rather coarse grid, with cell size of approximately 2° longitude by 1° latitude, which allows for some smoothing in Norway and fits well the station distribution in rest of Fennoscandia. The strain rate method requires as input an *a priori* strain rate variance for each grid cell, and this *a priori* variance controls the balance between the fit to the data and the smoothness of the interpolated velocity field. The surface deformation in Fennoscandia is characterized by diffuse, intraplate deformation everywhere, thus we apply a uniform *a priori* strain rate variance for all grid cells, and we choose a value which results in a fit to the observed velocities with a reduced chi-squared of 2.0. Finally, the strain rates are calculated as the spatial derivatives of the interpolated velocity field:

$$\dot{\epsilon}_{xx} = \frac{\partial v_x}{\partial x}, \quad \dot{\epsilon}_{yy} = \frac{\partial v_y}{\partial y}, \quad \dot{\epsilon}_{xy} = \frac{1}{2}\left(\frac{\partial v_x}{\partial y} + \frac{\partial v_y}{\partial x}\right), \tag{1}$$

where v is velocity, x is longitude and y is latitude.

The results are presented in Fig. 2(a) as the principal strain rates as well as the areal strain rate, defined as $\frac{1}{2}(\dot{\epsilon}_{xx} + \dot{\epsilon}_{yy})$. An NE–SW elongated signal of expansion covers most of Fennoscandia, closely resembling the pattern of the glacial isostatic uplift bulge. The highest areal strain rates are seen in the Gulf of Bothnia and south-central Sweden. The region of expansion is surrounded by regions of contraction. The transition from expansion to contraction follows the Finnish border to Russia, crosses southern Sweden and southern Norway and runs along the western coast of Norway up to the Barents Sea. Along the western coast of Norway, several of the outermost GPS stations lie in the region of contraction, indicating that the areal expansion does not extend into the offshore regions. This is, however, not the case along the northern coast of Norway, where the signal of expansion extends to the outermost GPS stations, indicating that the change from expansion to contraction occurs offshore. The notion that parts of the Barents Sea are currently undergoing expansion is consistent with flexural uplift, as observed by 800–1000 m erosion in the southern Barents Sea during the Plio-Pleistocene (Riis & Fjeldskaar 1992).

The principal strain rates are plotted on top of the areal strain rates in Fig. 2(a). Within the region of expansion, they show a consistent pattern of up to 4×10^{-9} yr^{-1} extension in the NW–SE direction. The dominant NW–SE direction of extension is caused by the NE–SW elongation of the uplift bulge in Fennoscandia. The only marked deviation from this pattern is seen in southwestern Norway, where the extension is rotated towards N–S, consistent with the continuation of the uplift bulge towards Scotland. In the regions of contraction that surround the broad signal of areal expansion, the principal shortening axis always trends radially away from the centre of uplift. An earlier study of the strain rates in northern Europe showed a similar radial pattern of shortening in north-central Europe (Nocquet *et al.* 2005).

We obtain a minimum estimate of the geodetic moment rate, using the formula (Holt *et al.* 1995)

$$\dot{M}_0^G = 2\mu V\left(\left|\frac{1}{2}(\dot{\epsilon}_{xx} + \dot{\epsilon}_{yy})\right| + \sqrt{\frac{1}{4}(\dot{\epsilon}_{xx} - \dot{\epsilon}_{yy})^2 + \dot{\epsilon}_{xy}{}^2}\right), \tag{2}$$

where μ is the shear modulus (here we use $\mu = 32$ GPa) and V is the cell volume calculated as the grid cell area multiplied by the seismogenic thickness (here we use 20 km based on the typical depth of seismicity in the region). The geodetic moment rate gives an estimate of how much moment is accumulating, assuming that the strain rates at the surface are representative of the strain rate in the seismogenic part of the crust. The formula assumes that the

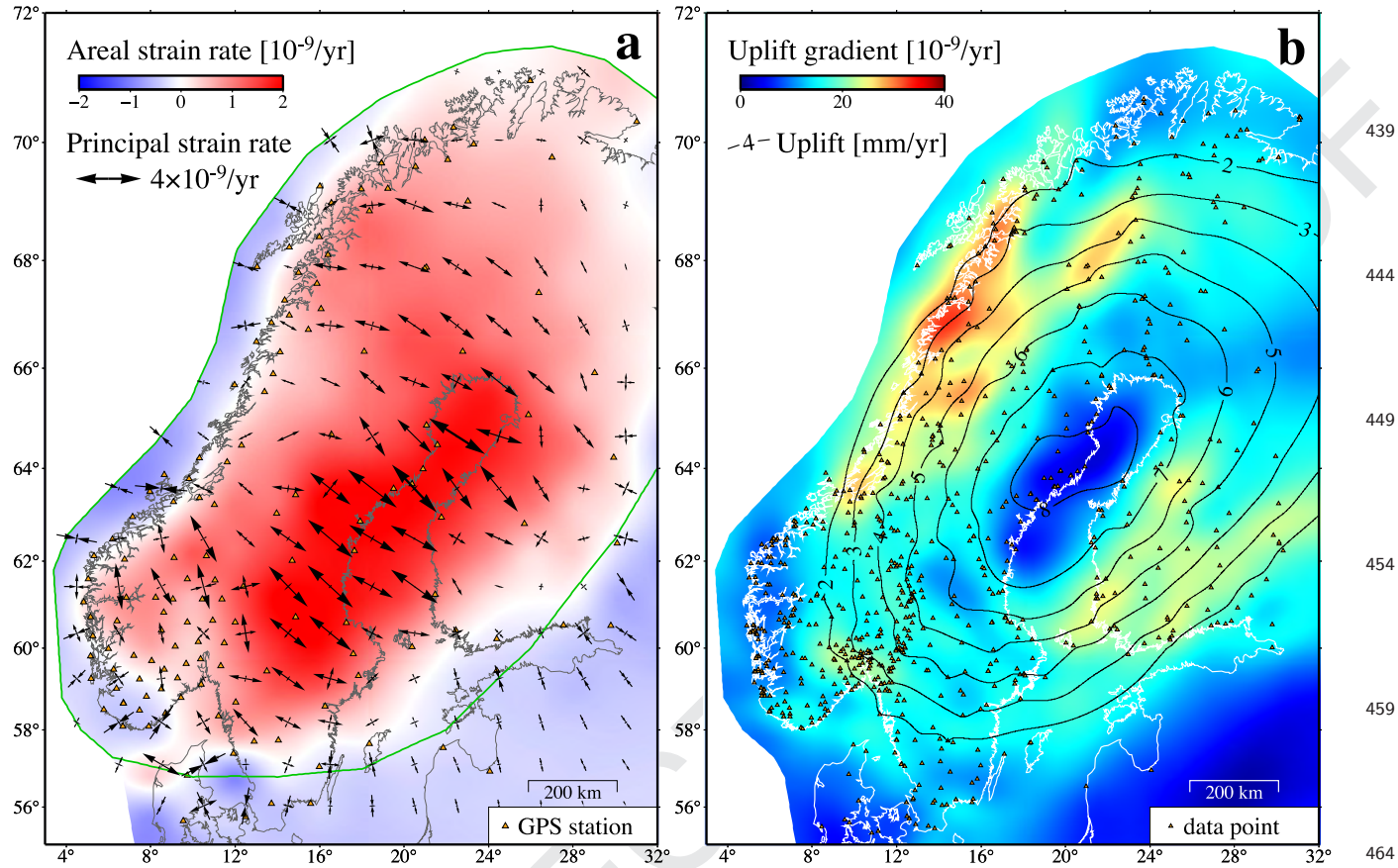

Figure 2. Surface deformation. (a) Horizontal areal strain rates (contour colours) and principal strain rates (arrows), based on GPS velocities from Kierulf *et al.* (2014). Positive values of areal strain rates indicate expansion and negative values indicate contraction in the horizontal plane. The green line shows the region used for the estimate of the total geodetic moment rate. (b) Uplift gradient based on GPS, levelling and tide-gauge data (Vestøl 2006). The gradient field has been smoothed with a spatial low pass filter before contouring.

areal strain occurs with equal shear strain on 45° dip-slip faults oriented at 90° to the principal horizontal strain directions, and that the remaining shear strain (the $\sqrt{\frac{1}{4}(\dot{\epsilon}_{xx} - \dot{\epsilon}_{yy})^2 + \dot{\epsilon}_{xy}{}^2}$ component of the formula) occurs on vertical strike-slip faults oriented at 45° to the principal strain directions. Any other dip angle requires a greater moment release, thus the moment rate formula yields a minimum estimate (Holt *et al.* 1995). Furthermore, the estimated moment rate only accounts for strain in the horizontal plane, thus the actual geodetic moment rate is probably higher. For the region encircled by the green line in Fig. 2(a), we estimate a total moment rate of 3.5×10^{18} Nm yr^{-1}, which we will later compare to estimates of the seismic moment rate from earthquakes.

An inspection of the velocity field in Fig. 1(a) indicates that the vertical strain rate may be several times larger than the horizontal strain rate. We are not able to calculate the strain rate in the vertical direction because we have no constraints on how the velocities change with depth. A measure of the vertical strain can, however, be obtained by considering the horizontal gradient of the uplift, defined as $\frac{\partial v_z}{\partial x} + \frac{\partial v_z}{\partial y}$, where v is velocity, z is vertical, x is longitude and y is latitude, as before. We calculate the uplift gradient from the data of Vestøl (2006), which includes levelling and tide-gauge measurements in addition to the vertical GPS velocities. The estimated uplift gradient field (Fig. 2b) shows a clear maximum in Nordland, where the two shallow earthquake swarms and Fennoscandia's largest earthquake were recorded, and where present-day activity of small events is high (see Fig. 1b).

4 DEFORMATION AT SEISMOGENIC DEPTHS

We use the compilation of focal mechanisms from the Norwegian continental margin and mainland Fennoscandia to examine the style of seismic strain release. To avoid introducing artefacts due to poorly constrained focal mechanisms, we only include mechanisms with quality A/B (for the Norwegian mechanisms which have a quality rating) and magnitudes of at least 2, which leaves 126 of 224 mechanisms within the region shown in Fig. 3(a). The focal mechanisms are first transformed to moment tensors (e.g. Lay & Wallace 1995), assuming that all magnitudes are equal to moment magnitudes (M_W), related to moments by the empirical relationship $\log M_0 = \frac{3}{2} M_W + 9.0$ (Hanks & Kanamori 1979). For clusters of events we calculate one average moment tensor, weighted by the earthquake moments. We then rotate each moment tensor into the principal-axis system to determine the maximum compressional and tensional deformation in the horizontal plane. The results are shown in Fig. 3(a). On the continental margin, the focal mechanisms show consistent WNW–ESE compression. In mainland Fennoscandia, the mechanisms show more variation between tension, compression and strike-slip and the directions are also seen to vary. The axes of compression often trend approximately NW–SE, consistent with the direction on the continental margin, but deviations from this pattern are seen in Nordland and near the Swedish coast to the Gulf of Bothnia. The variation in mainland Fennoscandia is partly due to the fact that the earthquakes are often small and therefore

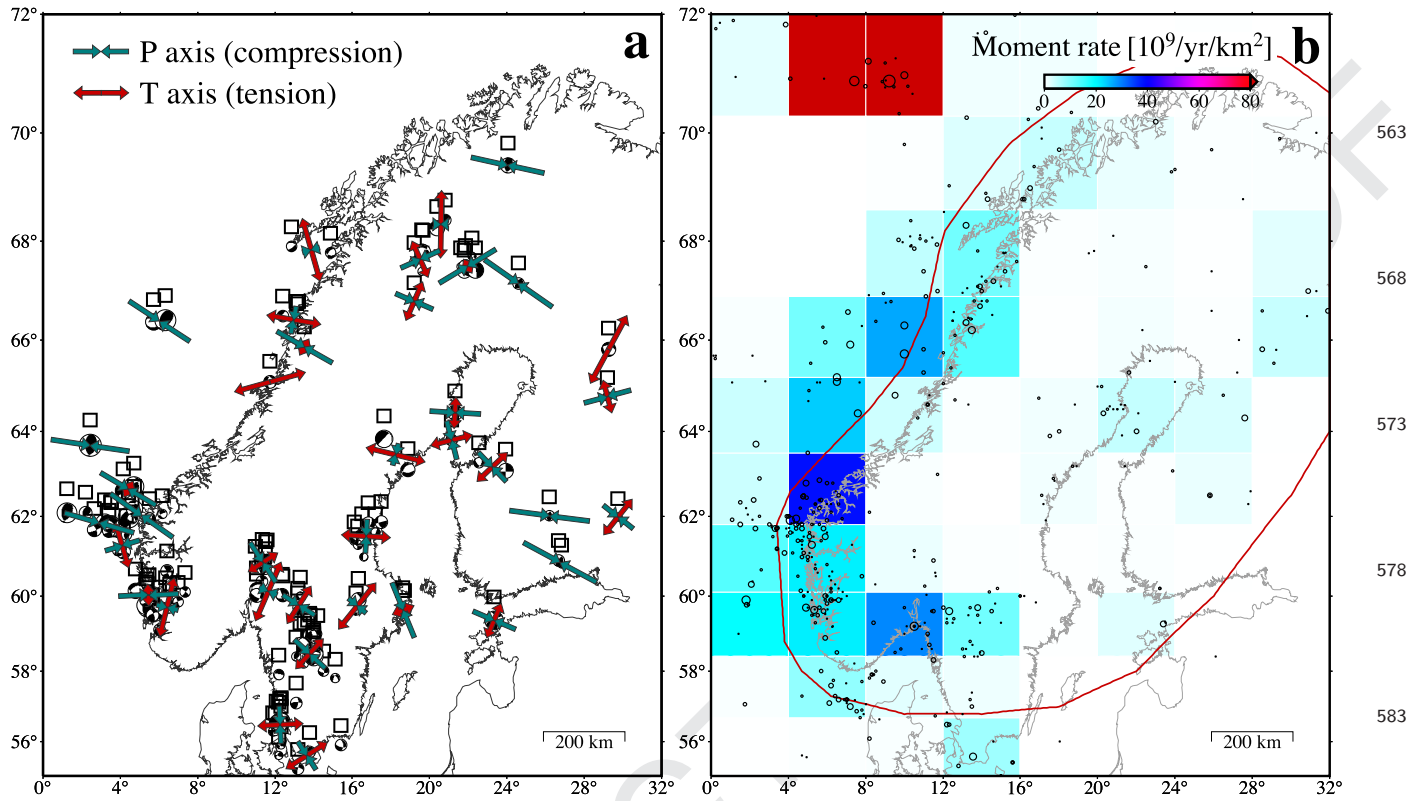

Figure 3. Deformation at seismogenic depth. (a) Focal mechanisms with horizontal P (compression) and T (tension) axes. Note that each pair of P and T axes only reflects the relative magnitudes of the two axes, not their absolute magnitudes relative to other events or event clusters. (b) Moment rates from summation of earthquake moments during 1900–2011 from the FENCAT catalogue. The red line shows the region used for the estimate of the total seismic moment rate.

more prone to reflect local conditions related to weakness zones or stress perturbations. However, a larger variation and a tendency toward tensional deformation in mainland Fennoscandia, compared to the continental margin, seem to be robust features, also when we consider only the larger events.

In order to quantify the seismic strain release, we calculate seismic moment rates from historical earthquakes. Here, we use all earthquakes from FENCAT during 1900–2011 to take advantage of the improvement of the completeness of the earthquakes records obtained after the onset of instrumental earthquake recordings around the beginning of the 20th century. We assume that the earthquake magnitudes are moment magnitudes, sum the moments on a grid and normalize the results to the area of each grid cell. The estimated moment rates in Fig. 3(b) show a coherent zone of high rates along the continental margin and along the western coast of Norway, and considerably lower rates further inland. As a side note, we see very high moment rates in the oceanic Lofoten Basin, where a seismic sequence occurred in 1959. The total seismic moment rate within the area encircled by the red line in Fig. 3(b) is 0.8×10^{16} Nm yr^{-1}, which is more than two orders of magnitude smaller than the geodetic moment rate within the same area.

Although the moment rates from the summation of historical earthquake moments show a relatively coherent pattern, the time period of a little more than hundred years only covers a fraction of the estimated return time of the largest events in Fennoscandia (Bungum *et al.* 2005), causing uncertainty on the derived moment rate estimate from historical earthquakes. We obtain a second, independent, estimate by calculating the expected seismic moment rate within the area encircled by the red line in Fig. 3(b), using the magnitude–frequency distribution of earthquakes during 1980–2011 and the formula of Molnar (1979):

$$\dot{M}_0^S = \frac{\alpha}{1-\beta} M_{0,\max}{}^{1-\beta}, \quad \alpha = 10^{(a+6b)}, \quad \beta = \frac{2}{3}b. \tag{3}$$

Here $M_{0,\max}$ is the moment of the expected largest possible earthquake in the region, and a and b are constants related to the magnitude–frequency relationship $\log_{10}N = a - bM$, where N is the annual number of events with magnitudes greater or equal to M. We obtain a maximum likelihood estimate of b (Utsu 1966; Marzocchi & Sandri 2003), and we estimate the a value from the intersection of the maximum likelihood line with the y-axis. The estimate of the expected moment rate is very dependent on the maximum moment, $M_{0,\max}$, which we do not know in detail. The largest historical earthquake in Fennoscandia had a magnitude of 5.8, as mentioned above. For the Norwegian continental margin, a maximum earthquake magnitude of 6–7 has been estimated (Bungum *et al.* 2005), and the maximum magnitude in mainland Fennoscandia is probably at the lower end of this range. If we assume that a maximum moment equivalent of an M_w=6.0 event is representative for the region within the red line in Fig. 3(b), we get a total moment rate of 1.3×10^{16} Nm yr^{-1}, which is in reasonable agreement with the estimate of 0.8×10^{16} Nm yr^{-1} from summation of historical earthquakes, suggesting that the inferred seismic moment rate is stable. In any case, the seismic moment rate is at least two orders of magnitude smaller than the geodetic moment rate from the horizontal strain rates.

5 DISCUSSION

Our analysis of the deformation at the surface (from geodetic data) and at seismogenic depth (from earthquake data) shows that there are large differences in the moment rates and to some extent also the style of deformation. The seismic moment rate in mainland Fennoscandia is at least two orders of magnitude smaller than the geodetic moment rate estimated from surface strain rates. A comparison of the style and direction of the strain rates shows slightly better agreement. In mainland Fennoscandia, where the surface deformation is dominated by a broad signal of extensional strain (see Fig. 2a), the focal mechanisms do show a tendency towards tensional deformation, but the pattern is more varied and the directions are often opposite to the NW–SE extension at the surface (see Fig. 3a). On the continental margin, there may be a better agreement, with NW–SE shortening in both the surface and seismic strain rate fields, but at the current stage, the comparison is much limited as we do not have surface observations offshore.

This raises the question why there is such discrepancy between the deformation at the surface and at seismogenic depth. While the GIA clearly dominates the surface strain rate field, its influence on the seismic deformation is not obvious. In order to explain this, we have to consider how GIA influences the deformation at the surface and at depth.

There is a depth dependency of the flexural stress and strain induced by GIA. The flexural stress decreases from the surface to zero at mid-lithospheric depth and then increase again with opposite sign towards the bottom of the lithosphere. Considering that most earthquakes in Fennoscandia occur in the upper 20 km of the crust, this depth dependency of the flexure could explain a moment difference of up to 40 per cent between the surface and seismogenic depth in a 100 km thick lithosphere, but this is much less than the observed difference. We do not consider it likely that the actual deformation at seismogenic depth is completely different from the surface strain rate, thus the deformation at seismogenic depth likely occurs mostly aseismically. But why is the strain induced by GIA not released in earthquakes?

The seismicity occurs in response to the state of stress, which in Fennoscandia is a result of the interaction of the regional stress field, flexural stress due to GIA as well as other stress generating mechanisms (e.g. Bungum *et al.* 2010). The regional, or tectonic, stress field seems to be controlled by plate boundary forces, which, in Fennoscandia, is primarily the ridge push from the Mid-Atlantic spreading ridge. This ridge push causes deviatoric NW–SE compression, which is consistent with the general trend of focal mechanisms, as also pointed out by, for example, Lindholm *et al.* (2000).

The stress induced by GIA depends on the ice history and mantle relaxation time, in addition to lithospheric thickness. During glaciation, the ice load causes downward flexure of the lithosphere, which results in contractional strain at the surface and compressive stress in the upper part of the down-bending lithosphere. After the onset of deglaciation, the upward flexure causes extensional strain at the surface and a change of the stress in the upper lithosphere towards less compressional or even tensional, depending on how much of the stress induced by the ice load had relaxed before the onset of deglaciation. Fig. 4(a) shows the case where no stress relaxation has occurred. In this case, the flexural stress in the upper part of the uplifting lithosphere will gradually become less compressive until it reaches zero as the uplift ends. Fig. 4(b) shows the other end-member case, where the lithosphere has reached equilibrium with the ice load before the onset of deglaciation. In this case, the flexural stress in the upper part of the uplifting lithosphere will be

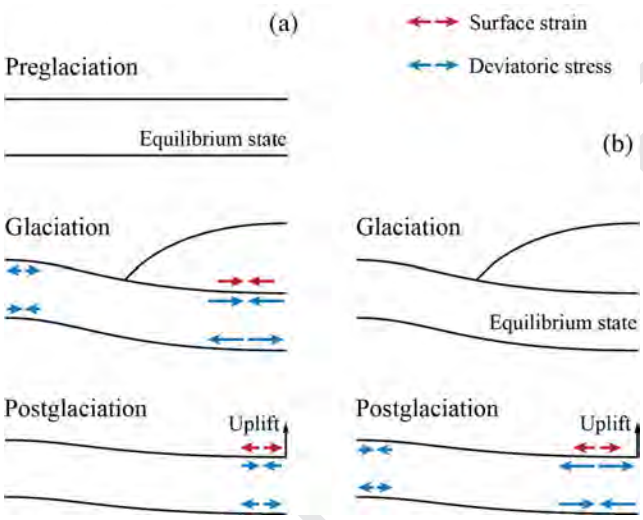

Figure 4. Two end-member cases for describing flexural stress induced by glacial isostatic adjustment. (a) No relaxation of the stress due to the ice load has occurred before the onset of deglaciation. (b) The stress due to the ice load has completely equilibrated before the onset of deglaciation. The figure is adapted from Fejerskov & Lindholm (2000,fig. 5).

tensional from the onset of deglaciation. Numerical evaluation of stress generating mechanisms in Fennoscandia shows that such tensional stress may reach a magnitude comparable to the stress from ridge push, if the lithosphere was in equilibrium with the ice load (Stein *et al.* 1989; Fejerskov & Lindholm 2000). Considering common relaxation times, the Fennoscandian glaciation history with frequent loading and unloading during the last 110 000 yr makes it unlikely that the lithosphere had reached equilibrium before the onset of deglaciation (Holger Steffen, private communication, 2014), but some stress relaxation probably had occurred.

The considerable tensional component of many focal mechanisms in mainland Fennoscandia suggests that the present-day stress is in fact influenced by tensional flexural stress due to GIA. This was previously suggested by Arvidsson & Kulhanek (1994) for Fennoscandia and similarly by Stein *et al.* (1979) for the Laurentide region. On the Norwegian continental margin, the variation between compressional and strike-slip focal mechanisms indicates that the minimum compressive horizontal stress and the vertical stress at seismogenic depth are of similar magnitudes. If the flexural stress in mainland Fennoscandia is characterized by NW–SE tension, similar to the pattern of the surface strain rates, then the interaction of the regional stress and the GIA stress will cause the NW–SE stress to become less compressional, such that the three principal stresses become more similar in magnitude (Fig. 5). The GIA induced accumulation of strain in the NW–SE direction, therefore, leads to decreased differential stress and thus a decrease in seismicity. On the continental margin, the flexural stress will be small in magnitude, but it will interfere constructively with the stress from ridge push to slightly increase the NW–SE compressional stress.

Our analysis follows along the lines of the study by Muir-Wood (2000), who ascribed the present-day seismicity in Fennoscandia to the interaction of ridge push and GIA stress. While we note that the occurrence of seismicity also reflects other conditions than the stress field, such as crustal heterogeneity and pre-existing weakness zones, we agree that the very low level of seismicity and more mixed style of seismic deformation in mainland Fennoscandia may be explained by the destructive interference of the regional stress with the GIA stress. Interestingly, the

COLOUR ONLINE, B&W IN PRINT

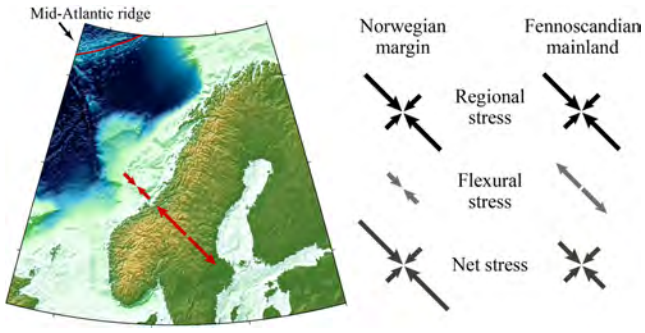

Figure 5. Schematic illustration of the hypothesized stress at seismogenic depth, illustrating the interaction of the regional stress due to the mid-Atlantic ridge push and the flexural stress due to glacial isostatic adjustment. The red arrows indicate surface strain.

relatively high seismicity in southwestern Norway occurs within the region of areal expansion, but the extension here deviates from the general NW–SE trend, which could lead to a less destructive interference.

The occurrence of seismicity in Nordland, where the uplift gradient is also high, may indicate that GIA plays a role in generating seismicity in this region. However, it has also been suggested that the high uplift gradient in the region is partly due to flexure induced by recent sediment redistribution (Olesen *et al.* 2013b). Furthermore, the Nordland region is characterized by deep fjords and steep mountains, making it likely that gravitational stresses due to the high topography contrasts increase seismicity levels.

6 CONCLUSIONS

We investigate how GIA influences the state of stress and deformation in Fennoscandia, through analysis of surface strain rates and seismicity.

(1) The surface strain rate field, derived from horizontal GPS data, shows a signal of expansion that covers most of mainland Fennoscandia with extensional strain rates of up to 4×10^{-9} yr^{-1} in the NW–SE direction.

(2) The uplift gradient, derived from a combination of GPS, levelling and tide-gauge measurements, shows the highest deformation rates in Nordland, Norway, where seismicity is also high.

(3) The seismic deformation field, derived from a new compilation of Fennoscandian focal mechanisms, shows consistent NW–SE shortening on the Norwegian continental margin and a more mixed deformation pattern in mainland Fennoscandia.

(4) The seismic moment rate, derived from historical earthquakes as well as the moment–frequency relationship of recent earthquakes, is at least two orders of magnitude smaller than the geodetic moment rate derived from the GPS strain rates.

Our analyses indicate that the GIA influences the present-day state of stress in Fennoscandia by diminishing the NW–SE compressional stress due to the ridge push from the Mid-Atlantic ridge. This leads to low differential stress and thus low seismicity rates with highly variable focal mechanisms in mainland Fennoscandia. Other sources of stress such as high topography and flexuring due to sediment redistribution may also influence the state of stress in Fennoscandia, particularly in southwestern Norway and Nordland. Future numerical modelling may help distinguishing between the potential sources of seismicity in Fennoscandia.

ACKNOWLEDGEMENTS

We wish to thank Hilmar Bungum for fruitful discussions and comments on the paper. Lars Ottemöller from University of Bergen did a careful evaluation the new focal mechanisms from the Norwegian National Seismic Network, and Marja Uski and Björn Lund kindly assisted with the focal mechanisms from Finland and Sweden. Constructive reviews from two anonymous reviewers helped improve the manuscript. The FENCAT earthquake catalogue of the University of Helsinki, Finland, is available at http://www.helsinki.fi/geo/seismo/. The figures were prepared with GMT (Wessel *et al.* 2013). This work was supported by the Geological Survey of Norway, the Norwegian Research Council, Norwegian Petroleum Directorate, Det norske oljeselskap, DONG E&P Norge, E.ON E&P Norge, Lundin Norway, Maersk Oil Norway, Norske Shell, Norwegian Energy Company (Noreco), Repsol Exploration Norge, DEA Norge, Statoil and VNG Norge.

REFERENCES

Arvidsson, R., 1996. Fennoscandian earthquakes: whole crustal rupturing related to postglacial rebound, *Science*, **274**(5288), 744–746.

Arvidsson, R. & Kulhanek, O., 1994. Seismodynamics of Sweden deduced from earthquake focal mechanisms, *Geophys. J. Int.*, **116**(2), 377–392.

Atakan, K., Lindholm, C.D. & Havskov, J., 1994. Earthquake swarm in Steigen, northern Norway: an unusual example of intraplate seismicity, *Terra Nova*, **6**(2), 180–194.

Beavan, J. & Haines, J., 2001. Contemporary horizontal velocity and strain rate fields of the Pacific-Australian plate boundary zone through New Zealand, *J. geophys. Res.*, **106**(B1), 741–770.

Bird, P. & Kagan, Y.Y., 2004. Plate-tectonic analysis of shallow seismicity: apparent boundary width, beta, corner magnitude, coupled lithosphere thickness, and coupling in seven tectonic settings, *Bull. seism. Soc. Am.*, **94**(6), 2380–2399.

Bøe, R., Fossen, H. & Smelror, M., 2010. Mesozoic sediments and structures onshore Norway and in the coastal zone, *NGU Bulletin*, **450**, 15–32.

Bungum, H. & Olesen, O., 2005. The 31st of August 1819 Lurøy earthquake revisited, *Norw. J. Geol.*, **85**, 245–252.

Bungum, H., Vaage, S. & Husebye, E.S., 1982. The Meløy earthquake sequence, northern Norway: Source parameters and their scaling relations, *Bull. seism. Soc. Am.*, **72**(1), 197–206.

Bungum, H., Lindholm, C. & Faleide, J.I., 2005. Postglacial seismicity offshore mid-Norway with emphasis on spatio-temporal-magnitudal variations, *Mar. Pet. Geol.*, **22**(1–2), 137–148.

Bungum, H., Olesen, O., Pascal, C., Gibbons, S., Lindholm, C. & Vestøl, O., 2010. To what extent is the present seismicity of Norway driven by post-glacial rebound?, *J. Geol. Soc.*, **167**, 373–384.

Byrkjeland, U., Bungum, H. & Eldholm, O., 2000. Seismotectonics of the Norwegian continental margin, *J. geophys. Res.*, **105**(B3), 6221–6236.

Dehls, J.F., Olesen, O., Olsen, L. & Blikra, L.H., 2000. Neotectonic faulting in northern Norway; the Stuoragurra and Nordmannvikdalen postglacial faults, *Quat. Sci. Rev.*, **19**(14–15), 1447–1460.

Ekström, G., Nettles, M. & Dziewoóski, A.M., 2012. The global CMT project 2004–2010: Centroid-moment tensors for 13,017 earthquakes, *Phys. Earth planet. Inter.*, **200–201**, 1–9.

Fejerskov, M. & Lindholm, C., 2000. Crustal stress in and around Norway: an evaluation of stress-generating mechanisms, *Geol. Soc. Lond.*, **167**, 451–467.

Hanks, T.C. & Kanamori, H., 1979. A moment magnitude scale, *J. geophys. Res.*, **84**(B5), 2348–2350.

Hasegawa, H.S. & Basham, P.W., 1989. Spatial correlation between seismicity and postglacial rebound in eastern Canada, in *Earthquakes at North-Atlantic Passive Margins: Neotectonics and Postglacial Rebound*, pp. 483–500, eds Gregersen, S. & Basham, P.W., NATO ASI Series.

Henderson, J., 1991. An estimate of the stress tensor in Sweden using earthquake focal mechanisms, *Tectonophysics*, **192**(3–4), 231–244.

Hicks, E.C. & Ottemöller, L., 2001. The ML 4.5 Stord/Bømlo, southwestern Norway, earthquake of 12 August 2000, *Norsk Geologisk Tidsskrift*, **81**, 293–304.

Hicks, E.C., Bungum, H. & Lindholm, C.D., 2000a. Stress inversion of earthquake focal mechanism solutions from onshore and offshore Norway, *Norsk Geologisk Tidsskrift*, **80**, 235–250.

Hicks, E.C., Bungum, H. & Lindholm, C.D., 2000b. Seismic activity, inferred crustal stresses and seismotectonics in the Rana region, Northern Norway, *Quat. Sci. Rev.*, **19**(14–15), 1423–1436.

Holt, W.E., Li, M. & Haines, A.J., 1995. Earthquake strain rates and instantaneous relative motions within central and eastern Asia, *Geophys. J. Int.*, **122**, 569–593.

Holt, W.E., Chamot-Rooke, N., Le Pichon, X., Haines, A.J., Shen-Tu, B. & Ren, J., 2000. Velocity field in Asia inferred from Quaternary fault slip rates and Global Positioning System observations, *J. geophys. Res.*, **105**(B8), 19185–19209.

Juhlin, C. & Lund, B., 2011. Reflection seismic studies over the end-glacial Burträsk fault, Skellefteå, Sweden, *Solid Earth*, **2**, 9–16.

Kierulf, H.P., Ouassou, M., Simpson, M. J.R. & Vestøl, O., 2013. A continuous velocity field for Norway, *J. Geod.*, **87**(4), 337–349.

Kierulf, H.P., Steffen, H., Simpson, M. J.R., Lidberg, M., Wu, P. & Wang, H., 2014. A GPS velocity field for Fennoscandia and a consistent comparison to glacial isostatic adjustment models, *J. geophys. Res.*, **119**(8), 6613–6629.

Kreemer, C., Blewitt, G. & Klein, E.C., 2014. A geodetic plate motion and Global Strain Rate Model, *Geochem. Geophys. Geosyst.*, **15**(10), 3849–3889.

Lagerbäck, R., 1992. Dating of Late Quaternary faulting in northern Sweden, *J. geol. Soc. Lond.*, **149**, 285–291.

Lay, T. & Wallace, T.C., 1995. *Modern Global Seismology*, Academic Press.

Lidberg, M., Johansson, J.M., Scherneck, H.-G. & Milne, G.A., 2010. Recent results based on continuous GPS observations of the GIA process in Fennoscandia from BIFROST, *J. Geodyn.*, **50**(1), 8–18.

Lindblom, E., Lund, B., Tryggvason, A., Uski, M., Bödvarsson, R., Juhlin, C. & Roberts, R., 2015. Microearthquakes illuminate the deep structure of the endglacial Pärvie fault, northern Sweden, *Geophys. J. Int.*, **201**, 1704–1716.

Lindholm, C., Roth, M., Bungum, H. & Faleide, J.I., 2005. Probabilistic and deterministic seismic hazard results and influence of the sedimentary Møre Basin, NE Atlantic, *Mar. Pet. Geol.*, **22**(1–2), 149–160.

Lindholm, C.D., Bungum, H., Hicks, E. & Villagran, M., 2000. Crustal stress and tectonics in Norwegian regions determined from earthquake focal mechanisms, *Geol. Soc. London Spec. Publ.*, **167**, 429–439.

Lund, B., Schmidt, P. & Hieronymus, C., 2009. *Stress evolution and fault stability during the Weichselian glacial cycle, Tech. Rep. TR-09-15*, Swedish Nuclear Fuel and Waste Management Co, Stockholm, Sweden.

Mäntyniemi, P., Husebye, E.S., Kebeasy, T. R.M., Nikonov, A.A., Nikulin, V. & Pacesa, A., 2004. State-of-the-art of historical earthquake research in Fennoscandia and the Baltic Republics, *Ann. Geophys.*, **47**(2/3), 611–619.

Marzocchi, W. & Sandri, L., 2003. A review and new insights on the estimation of the b-value and its uncertainty, *Ann. Geophys.*, **46**(6), 1271–1282.

Mazzotti, S., James, T.S., Henton, J. & Adams, J., 2005. GPS crustal strain, postglacial rebound, and seismic hazard in eastern North America: The Saint Lawrence valley example, *J. geophys. Res.*, **110**(B11), 1–16.

Molnar, P., 1979. Earthquake recurrence intervals and plate tectonics, *Bull. seism. Soc. Am.*, **69**(1), 115–133.

Muir Wood, R., 1989a. The Scandinavian earthquakes of 22 December 1759 and 31 August 1819, *Disasters*, **12**(3), 223–236.

Muir Wood, R., 1989b. Extraordinary deglaciation reverse faulting in northern Fennoscandia, in *Earthquakes at North-Atlantic Passive Margins: Neotectonics and Postglacial Rebound*, pp. 141–173, eds Gregersen, S. & Basham, P.W., NATO ASI Series.

Muir-Wood, R., 2000. Deglaciation Seismotectonics: a principal influence on intraplate seismogenesis at high latitudes, *Quat. Sci. Rev.*, **19**(14–15), 1399–1411.

Nocquet, J.-M., Calais, E. & Parsons, B., 2005. Geodetic constraints on glacial isostatic adjustment in Europe, *Geophys. Res. Lett.*, **32**(6), 1–5.

Olesen, O., Bungum, H., Dehls, J., Lindholm, C., Pascal, C. & Roberts, D., 2013a. Neotectonics, seismicity and contemporary stress field in Norway – mechanisms and implications, *NGU Spec. Publ.*, **13**, 145–174.

Olesen, O., Kierulf, H.P., Brönner, M., Dalsegg, E., Fredin, O. & Solbakk, T., 2013b. Deep weathering, neotectonics and strandflat formation in Nordland, northern Norway, *Norw. J. Geol.*, **93**, 189–213.

Ottemöller, L., Nielsen, H.H., Atakan, K., Braunmiller, J. & Havskov, J., 2005. The 7 May 2001 induced seismic event in the Ekofisk oil field, North Sea, *J. geophys. Res.*, **110**(B10), 1–15.

Riis, F. & Fjeldskaar, W., 1992. On the magnitude of the late Tertiary and Quaternary erosion and its significance for the uplift of Scandinavia and the Barents Sea, in *Structural and Tectonic Modelling and its Applications to Petroleum Geology*, Vol.1 of NPF Special Publication, pp. 163–185, eds Larsen, R.M., Brekke, H., Larsen, B.T. & Talleraas, E., Elsevier.

Slunga, R., 1979. Source mechanisms of a Baltic earthquake inferred from surface-wave recordings, *Bull. seism. Soc. Am.*, **69**(6), 1931–1964.

Slunga, R. & Ahjos, T., 1986. Fault mechanisms of Finnish earthquakes, crustal stresses and faults, *Geophysica*, **22**(1–2), 1–13.

Smedberg, I., Uski, M., Tiira, T., Komminaho, K. & Korja, A., 2012. Intraplate earthquake swarm in Kouvola, south-eastern Finland, in *EGU General Assembly 2012*, Vienna, Austria.

Sørensen, M.B., Ottemöller, L., Havskov, J., Atakan, K., Hellevang, B. & Pedersen, R.B., 2007. Tectonic processes in the Jan Mayen Fracture Zone based on earthquake occurrence and bathymetry, *Bull. seism. Soc. Am.*, **97**(3), 772–779.

Steffen, H. & Wu, P., 2011. Glacial isostatic adjustment in Fennoscandia – A review of data and modeling, *J. Geodyn.*, **52**(3–4), 169–204.

Stein, S., Sleep, N.H., Geller, R.J., Wang, S.-C. & Kroeger, G.C., 1979. Earthquakes along the passive margin of eastern Canada, *Geophys. Res. Lett.*, **6**(7), 537–540.

Stein, S., Cloething, S., Sleep, N.H. & Wortel, R., 1989. Passive margin earthquakes, stresses and rheology, in *Earthquakes at North-Atlantic Passive Margins: Neotectonics and Postglacial Rebound*, pp. 231–259, eds Gregersen, S. & Basham, P.W., NATO ASI Series.

Uski, M., Hyvönen, T., Korja, A. & Airo, M.-L., 2003. Focal mechanisms of three earthquakes in Finland and their relation to surface faults, *Tectonophysics*, **363**(1–2), 141–157.

Uski, M., Tiira, T., Korja, A. & Elo, S., 2006. The 2003 earthquake swarm in Anjalankoski, south-eastern Finland, *Tectonophysics*, **422**, 55–69.

Utsu, T., 1966. A statistical significance test of the difference in the b-value between two earthquake groups, *J. Phys. Earth*, **14**(2), 37–40.

Vestøl, O., 2006. Determination of postglacial land uplift in Fennoscandia from leveling, tide-gauges and continuous GPS stations using least squares collocation, *J. Geod.*, **80**(5), 248–258.

Wessel, P., Smith, W. H.F., Scharroo, R., Luis, J. & Wobbe, F., 2013. Generic Mapping Tools: improved version released, *EOS, Trans. Am. geophys. Un.*, **94**(45), 409–410.

Wu, P. & Johnston, P., 2000. Can deglaciation trigger earthquakes in N. America?, *Geophys. Res. Lett.*, **27**(9), 1323–1326.

SUPPORTING INFORMATION

Additional Supporting Information may be found in the online version of this article:

Figure S1. Location and depth distribution of focal mechanisms in Table S1. Note that the spikes at depths 10, 15, 20 and 33 km are due to fixed depths (http://mnras.oxfordjournals.org/lookup/suppl/doi:10.1093/gjiras/ggv207/-/DC1).

Please note: Oxford University Press is not responsible for the content or functionality of any supporting materials supplied by the authors. Any queries (other than missing material) should be directed to the corresponding author for the paper.

CHAPTER 13: DO ELEVATED PRECIPITATION RATES AND ANOMALOUS UPPER MANTLE CAUSE INTRAPLATE SEISMICITY IN NORWAY?

Authors: YP Maystrenko[1], Marco Brönner[1], [2], Odleiv Olesen[1], Tuomo Mikael Saloranta[3] and Trond Slagstad[1]

[1] Geological Survey of Norway (NGU), Trondheim, Norway; [2]Norwegian University of Science and Technology, IGP, Trondheim, Norway; [3]Norwegian Water Resources and Energy Directorate (NVE), Oslo, Norway

Abstract:

Two enigmatic regions of high intraplate seismicity in Norway (Western Norway and the Nordland area) show a temporal correlation between the number of earthquakes within the upper crystalline crust and intensity of rain and snow melt at the Earth's surface. Moreover, these discrete zones of high seismic activity coincide spatially with prominent, low-velocity and, most likely, thermally anomalous zones in the upper mantle. We conclude that the high seismicity is mainly controlled by the anomalous upper mantle, along with topography-induced gravitational potential energy and crustal density variations. Precipitation-induced, seasonal increases in pore-fluid pressure within the fractured crystalline bedrock, enhance the mantle- and gravity-controlled seismicity.

Globally, the concentration of high and continuous seismicity along the boundaries of tectonic plates can be well explained by stress localization related to plate movements 1,2. In contrast, the mainly rare and sporadic seismicity within the interior of tectonic plates, so called intraplate seismicity, is poorly understood 3. Coastal Norway is a prominent region of intraplate seismicity, with two clearly defined clusters in SW Norway and the Nordland county (Fig. 1a). Earthquake magnitudes are generally low to intermediate, but larger earthquakes, with magnitudes greater than 4.0 are also recorded regularly 4,5. The origin of this seismicity has been the subject of several investigations since the beginning of the 1980's, when the Norwegian earthquakes were recorded in larger quantities on the digital seismic networks, and several interpretations have been proposed 6-9.

In this study, we discuss the spatial correlation between high intraplate seismicity and upper-mantle, low-velocity anomalies, and statistically analyze the temporal relationship between seismicity and atmospheric precipitation rate, and suggest a new mechanism to explain regional, intraplate seismicity. Details concerning the data and workflow are described in Methods.

1. Overview

Postglacial isostatic adjustment, Quaternary glacial erosion and Mid-Atlantic ridge push have been considered to explain the intraplate seismicity along the Norwegian coast. Postglacial uplift is highest within the central Scandinavian peninsula, where the thickness of the last ice sheet was the greatest 10. In contrast, coastal Norway was mainly located at the margin of the last ice sheet 11 and uplift rates due to missing ice masses should be consequently significantly less for these areas. Erosion during the Quaternary glacial periods is well documented by thick, glacially derived sediments deposited on the Norwegian shelf 12. However, the intensity of glacial erosion started to decline around 10,000 years ago, when the Weichselian ice sheet started to retreat. The tectonic forces related to opening of the Atlantic Ocean along the Mid-Atlantic ridge have also been considered as a possible trigger for seismicity in Norway 8. However, forces related to these three possible scenarios were relatively uniformly distributed and cannot readily explain the localized seismicity in Western Norway and the Nordland area. Although earthquakes can be generated by the above-mentioned processes, it is unlikely that these forces can explain the two well-defined zones of localized, present-day seismicity in Western Norway and the Nordland area (Fig. 1a). Therefore, the two clearly distinguished zones of elevated seismic activity (Fig. 1a) must be explained by a different or at least an additional process(es).

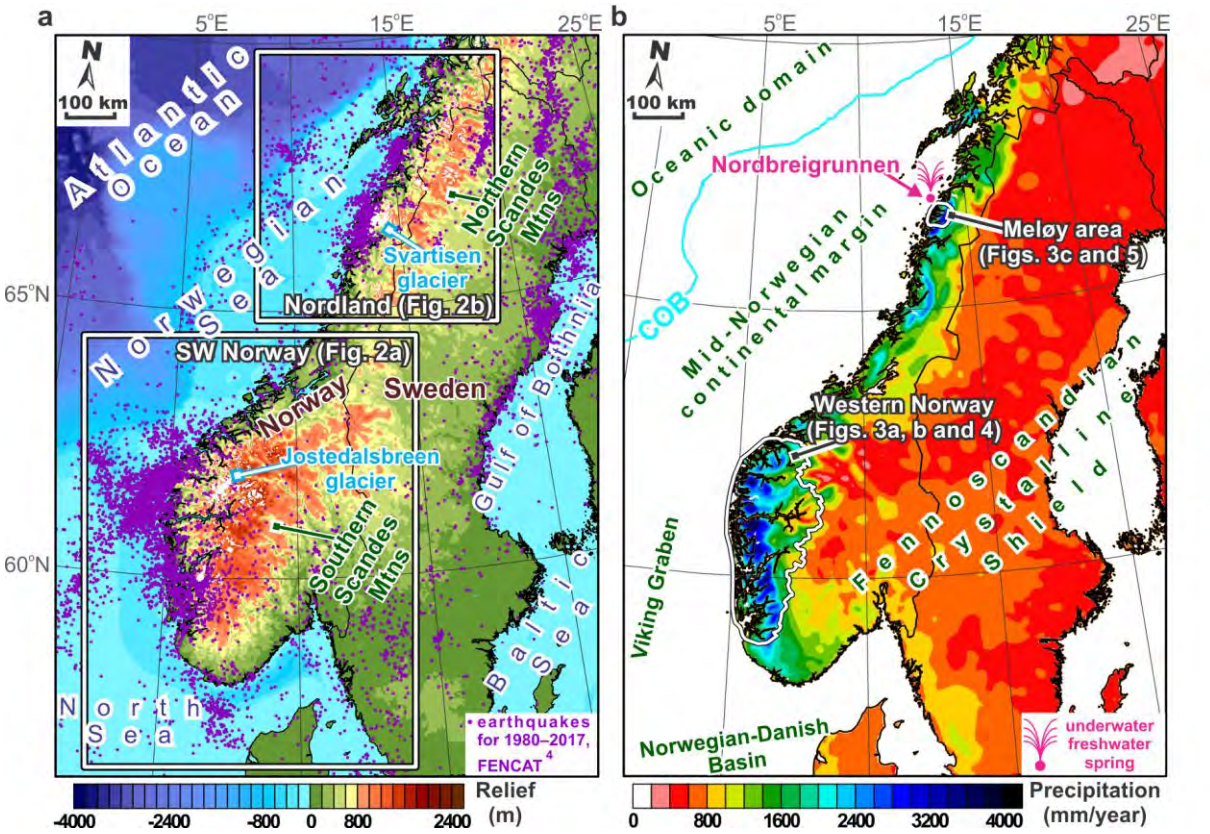

Figure 1 a) Seismicity pattern over western Scandinavia 4 (relief from the Norwegian mapping authority). b) Normal annual precipitation 19,46,47. Study areas are indicated by white outlines. COB is the continent-ocean boundary after Gernigon (unpublished data). Location of the Nordbreigrunnen seafloor freshwater spring according to Storrø 42. Glaciers (white areas in Fig. 1a) are based on NSIDC 54.

The areas under consideration are characterized by highly contrasting relief (Fig. 1a). Tectonically, the mainland is mainly represented by the Fennoscandian Shield and Caledonian nappes with crystalline rocks exposed at the surface 13, whereas the adjacent northern North Sea and the Mid-Norwegian continental margin are covered by up to 15-18 km-thick sequences of sedimentary rock. Therefore, the gravitational forces due to variations in topography and existing heterogeneities and density variations within the crust must be considered to explain the cumulated seismicity in Norway.

In addition, variations in deep structure can contribute to localize the seismicity in coastal Norway. We observe that the zones of elevated seismicity coincide spatially with anomalous upper mantle (Fig. 2), characterized by low seismic P- and S-wave velocities 14-18, indicating that there is a direct or indirect relationship between anomalous mantle and high seismicity. In contrast, the less seismically active Mid-Norway region (Fig. 1a) is not underlain by anomalous upper mantle.

The precipitation map for Norway (Fig. 1b) shows that the areas with the most seismic activity also have the highest precipitation rates. The high mountains act as barriers to eastward flow of moist Atlantic air, causing increased precipitation along their western, windward side. According to the Norwegian Meteorological Institute 19, the average annual precipitation reaches more than 3000 mm on the western slopes of the Southern and Northern Scandes mountains, where elevated seismicity is observed (Fig. 1b), implying a spatial correlation with precipitation.

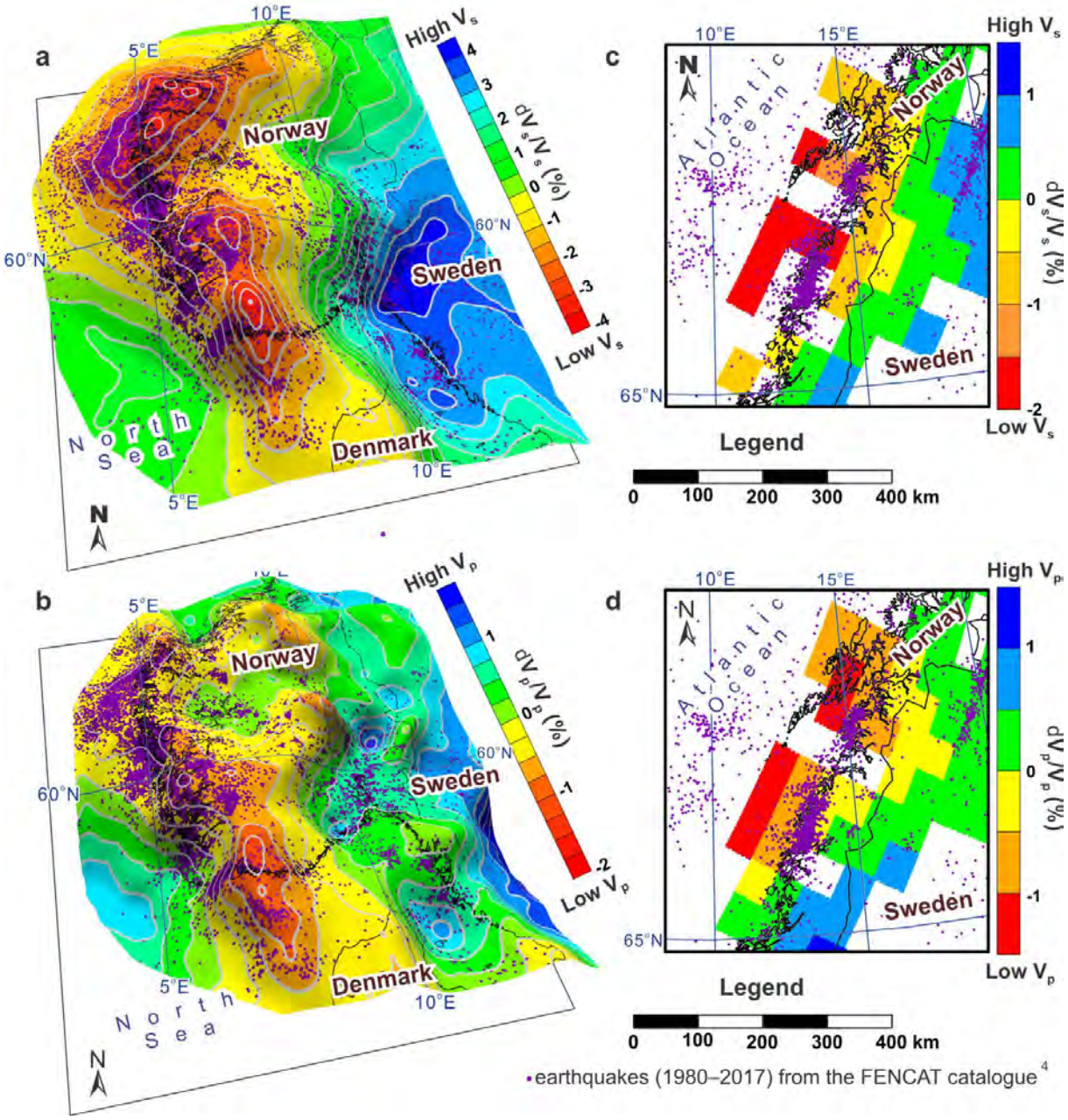

Figure 2 Upper-mantle velocity pattern with superimposed earthquakes [4]: a, S-wave and b, P-wave velocity patterns at a depth of 50 km within Western Norway [17] and b, S-wave and d, P-wave velocity patterns at depths of 100-200 km within the Nordland area [15].

2. Tectonic reasons for the seismicity

Using one of the most detailed seismic tomographic models for SW Scandinavia 17, we observe a good spatial correlation between the crests of pronounced P- and S-wave low-velocity anomalies in the upper mantle and earthquake activity in the crust of Western Norway (e.g. Fig. 2a, b). Kolstrup et al. 17 noticed this correlation and proposed that the upper-mantle, low-velocity anomaly beneath Western Norway may be responsible for localization of intraplate stress within the crust. Similarly, Assumpcao et al. 20 suggested that thermally induced weakening of the low-velocity, upper mantle below the Brazilian Platform can cause a localization of intraplate seismicity in the brittle crust above. Despite lower resolution, seismic tomography in the Nordland area 15 also show some correlation between a P- and S-wave low-velocity anomaly and the location of densely concentrated crustal earthquakes (Fig. 2c, d).

The low-velocity, upper-mantle anomalies are most likely related to elevated temperatures 21, possibly augmented by compositional variations within the upper mantle, similarly to other upper-mantle anomalies

observed beneath areas with increased seismicity in North and South America 20,22-24. Examples from western and eastern USA 22-25 are especially significant since the data from the USArray 26 have enhanced our knowledge on both location of earthquakes and the deep structure of the region. The thick continental lithosphere of the eastern United States, subjected to relatively uniform, large-scale tectonic stresses, is characterized by the presence of a low-velocity, upper-mantle anomaly beneath the seismically active, intraplate New Madrid zone 22,24. Geodynamic modeling has shown that a zone of reduced P-wave velocity and high attenuation in the upper mantle beneath the New Madrid seismic zone is most likely caused by increased temperature and could be responsible for increased seismicity in this area 22. Moreover, based on large-scale tomographic images for southeastern USA, Biryol et al. 24 have shown that regions of relatively hot mantle lithosphere are weak and could result in the observed broad zone of elevated seismicity. Furthermore, Becker et al. 23 have shown that the high intraplate seismicity in the western USA can be related to changes in flow within the low-velocity upper mantle. According to Becker et al. 23, the important conclusion is that active mantle flow could be one of the major contributors to seismogenic intraplate deformation, whereas gravitational potential energy variations play a rather minor role within the area, which is characterized by very similar relief pattern and deep structure to that of Western Norway and the Nordland area.

Levandovski et al. 27 have shown that gravitational body forces focus North American intraplate earthquakes. Similarly, Western Norway and the Nordland area are characterized by the presence of pronounced density inhomogeneities in the crust 28,29, and bounded by 900-1500 m-high mountains to the east. The high elevation of the proximal mountains is reflected in the presence of several glaciers, two of which, the Jostedalsbreen and Svartisen glaciers (Fig. 1a), are the largest ice masses in Scandinavia. Therefore, gravitational forces due to density variations in the crust and variations in surface topography are an alternative or additional stress source for of localized seismicity in Norway.

In summary, we suggest that the location of two prominent regions of high seismicity in Western Norway and the Nordland area is possibly to a large extent controlled by the presence of low-velocity, hot and weak upper mantle. Moreover, the gravitational stresses due to variations in topography and density variations within the crust can be considered a possible additional source for the observed localized seismicity.

3. Precipitation vs. Seismicity

A relationship between earthquake frequency 5,30 and volume of water from rain and snow melt 31-34 has been quantified for two onshore areas (Fig. 1b) by calculating the linear correlation coefficient for different time delays (Fig. 3). The calculations show that the correlation coefficients are relatively high in all cases (Fig. 3a).

According to the cross-correlation, if the frequency of earthquakes is shifted 49-108 days back in time, the occurrence rate of earthquakes correlates well with temporal changes of water volume (Figs. 4-5). Thus, in addition to a spatial correlation (cf. Figs. 1a and 1b), there is also a temporal correlation between seismicity and variations in surface water flux in Western Norway and the Nordland area. These relationships may indicate that the seismically active zones are at least partially related to atmospheric precipitation-derived groundwater flow through fractured crystalline rocks. The presence of fractures and/or microfractures within the study areas is supported by studies of the surface geology 35 and some of the 500-800 m-deep boreholes drilled through fractured crystalline rocks, and anomalously low subsurface temperatures in Western Norway are consistent with deep, regional-scale groundwater flow through these fracture systems (Maystrenko et al., 2015).

Artificial, fluid-induced seismicity is relatively well known from long-term monitoring of hydraulic fracturing within oil and gas fields and fracking for enhanced geothermal systems 36. Precipitation-derived groundwater recharge has also been proposed to trigger seismicity 37-40. Although a direct relationship between precipitation and seismicity has been demonstrated locally 37, it has remained hypothetical for larger regions, especially for crystalline rocks, with suggestions that prominent intraplate seismicity is induced by increases in pore-fluid pressure from groundwater recharge 40. Here, we demonstrate that variations in rain and snow melt are reflected in earthquake frequency at a regional scale, thus our statistical analysis supports the hypothesis of Costain 40. This is particularly obvious for the ~57000 km2 area in Western Norway (Fig. 1b) where, despite the large size of the region, a correlation coefficient between precipitation and the occurrence rate of earthquakes is up to 0.48 over a one-year (2011) interval (Fig. 3a) and is even 0.64 for 2014 (Fig. 3b). In the case of Western Norway, the employed NNSN catalogue 5 is characterized by the partial presence of human-induced seismicity, which is difficult to exclude from our analysis. To minimize an influence of artificial seismological events, all earthquakes from 5

a.m. to 10 p.m. GMT within and near large quarries, factories and two large urban areas of Bergen and Stavanger have been excluded from the correlation analysis for Western Norway. The comprehensive correlation analysis has shown that a delay between earthquake occurrence and variations in water volume at the surface is 118 and 100 days as observed for the one-year time intervals (2011 and 2014, respectively) in Western Norway (Fig. 3a and b). In Western Norway, the obtained delay varies from slightly less than 50 to more than 150 days for the period 2005-2014, indicating that earthquakes utilize continuously changing fracture patterns in the crystalline rocks.

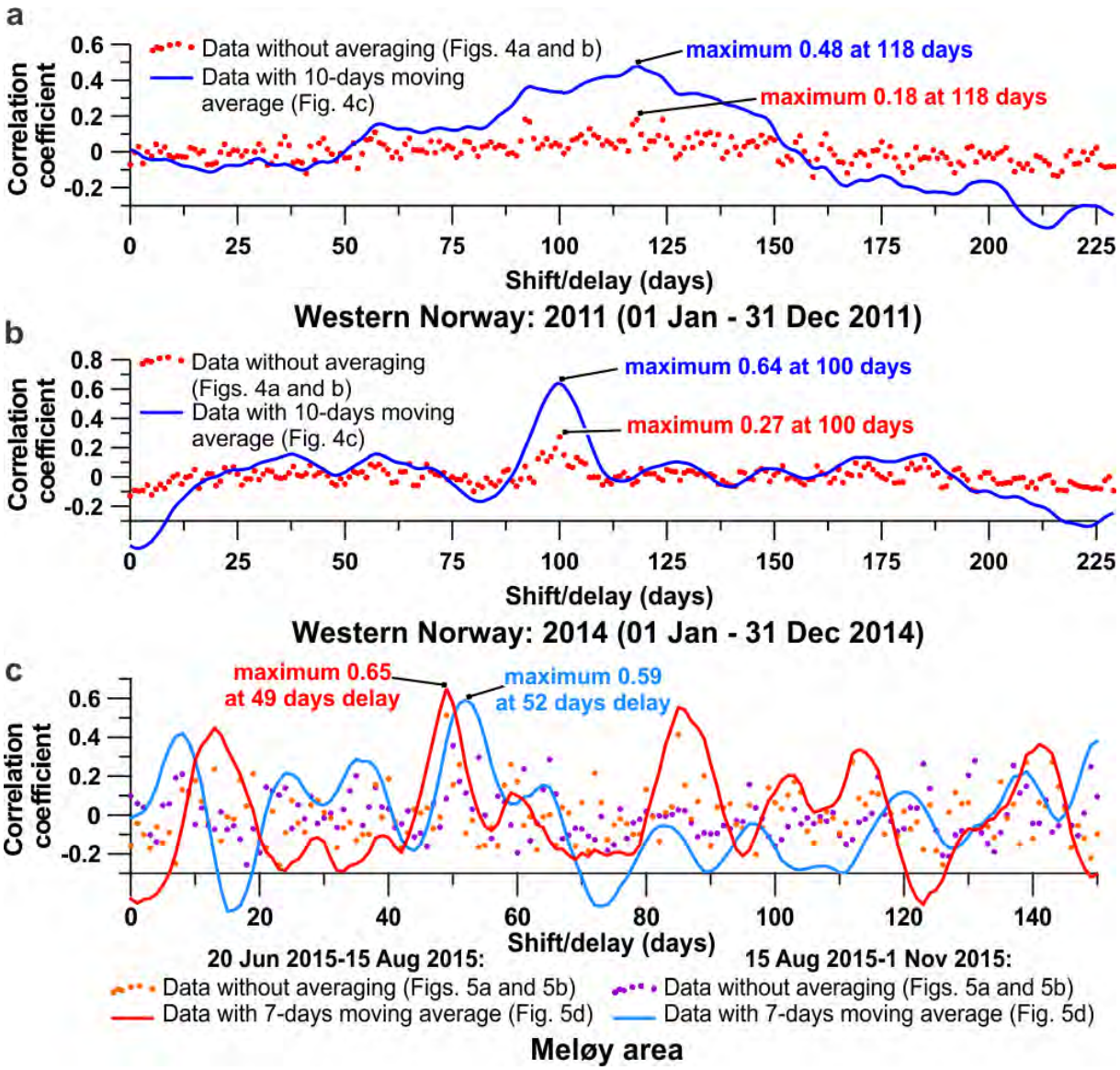

*Figure 3 Linear correlation coefficients as a function of time delay between earthquakes [5,30] and volume of water at the Earth's surface due to rain and snow melt [31,32,34] for the selected time intervals in Western Norway (**a** and **b**) and the Meløy area (**c**).*

In the smaller Meløy area (1968 km2; Fig. 1b), a good correlation between precipitation and occurrence rate of earthquakes was observed for an 11-month time interval, with a correlation coefficient of around 0.59-0.65 (Fig. 3c), showing that the lag time between precipitation and induced seismicity is around 49-52 days (Fig. 5d). According to the relationship between the delay of groundwater-recharge diffusion peak, hydraulic diffusivity and diffusion distance 40, the estimated hydraulic diffusivity for the fractured crystalline rocks is in the range of 0.04-1.1 m2/s for a depth interval of 1-5 km (Fig. 5c), which would roughly represent the diffusion distance if most fractures in the crystalline rocks are subvertical. The obtained values for hydraulic diffusivity are within the range of measured values for fractured crystalline rocks 41, suggesting that they are realistic. In addition, the presence of zones of decreased salinity and increased temperature of seawater, including a fresh-water spring 7 km off the Meløy area 42 (Fig. 1b), strongly supports our hypothesis that precipitation-induced groundwater flow is present in the region. Unfortunately, there is yet

no direct data on underwater fresh-water springs in the open sea off Western Norway. However, there might be quite a few underwater springs at the sea floor near Western Norway according to NGU marine geologists (personal communication), originally supposed to be isolated Quaternary water reservoirs. Moreover, the almost parallel-coast occurrence of numerous pockmarks in the North Sea at some distance from Western Norway 43 can be, at least partially, considered as possible indication of regional-scale groundwater flow there.

Despite the observed strong spatial and temporal correlation between earthquake frequency and precipitation, this relationship does not hold everywhere, supporting the argument that groundwater flow is not the primary cause of seismicity, but rather a trigger for unloading existing critical stresses. The implication is that the upper crust is locally overstressed and that even a small amount of groundwater can induce an earthquake. Without such stress, even relatively high precipitation rates, e.g., in the southernmost part of Nordland, do appear to cause elevated seismicity (Fig. 1). High seismicity in Nordland county is restricted to areas underlain by low-velocity upper mantle (Fig. 2c, d) Thus, precipitation-induced pore-fluid pressure diffusion appears to trigger release of localized crustal stress related to an underlying weak upper mantle, causing frequent, mainly low-intensity earthquakes, conversely, preventing stress release through less frequent but larger earthquakes that could potentially cause significant damage at the surface. Our observations are in agreement with the results from one-year fluid extraction and one-year fluid injection experiments in the more than 8 km-deep KTB-HB borehole in Germany, which have shown that pore pressure increases of not more than 0.01-1 bar can trigger earthquakes 44. Climate-change, with its anticipated change in regional precipitation pattern, may influence the seismic activity in areas of intraplate seismic activity, increasing the risk of large earthquakes in regions that become dryer and decreasing the risk by triggering more frequent but smaller earthquakes in regions that become wetter.

At the global scale, precipitation-derived groundwater recharge can also be considered a trigger of intraplate seismicity where seismicity coincides with a high precipitation rate. Besides, similar regional-scale, precipitation-related seismicity may also occur along the boundaries of tectonic plates, where most of earthquakes are generally supposed to be purely tectonically triggered. Thus, our findings can help identify earthquakes occurring in response to precipitation in other seismically active parts of our planet, highlighting tectonic causes. In other words, exclusion of more easily predictable precipitation-related seismicity from the whole seismicity pattern can potentially help resolve the frequency and predictability of more damaging, tectonically triggered earthquakes.

4. Conclusions

Two prominent zones of intraplate seismicity in Western Norway and the Nordland county are most likely controlled by the presence of low-velocity, high-temperature zones in the upper mantle. The effects of gravitational forces cannot be excluded within these areas with high topography and inhomogeneous crystalline crust. A strong temporal correlation between seismicity and precipitation suggests that precipitation-related, groundwater flow through fractured crystalline bedrock acts as a trigger on seismicity. The mechanism behind earthquake initiation is associated with a periodic pore-fluid pressure increase within the cracks and fractures of the upper-crustal crystalline bedrock resulting from groundwater recharge with gradual pore-fluid pressure diffusion to depth. Conversely, the effects of glacial isostatic adjustment, Mid-Atlantic ridge push and Quaternary erosion or sedimentation are most likely relatively minor but can be superimposed on the seismicity above the anomalous mantle zones in Western Norway and the Nordland area, where conditions are especially favorable for strain and stress localization above weak mantle.

5. Methods

To analyse the seismicity in western Scandinavia, we have used three available catalogues. One of the catalogues of the seismicity in Fennoscandia (FENCAT) is available from the joint Nordic earthquake bulletin, maintained by the Institute of Seismology, University of Helsinki 4. The FENCAT catalogue has been used to analyse the spatial distribution of the earthquakes and to visualize the major features of seismic pattern of the whole Scandinavia in Fig. 1a. The next seismological catalogue has been provided by the University of Bergen together with NORSAR and contains more detailed information about the earthquakes in Norway based on the seismological stations from the Norwegian National Seismic Network 5. Both catalogues may also include anthropogenic seismic events as from mining or other explosions. The NNSN catalogue was the main dataset for analysing the spatial association of increased seismicity with the upper-mantle, low-velocity, low-density anomalies and for investigating spatial and temporal relationship between the seismicity and atmospheric precipitation. The NNSN catalogue has been cleaned by removing all earthquakes from 5 a.m. to 10 p.m. GMT within and near large quarries, factories and two large urban

areas of Bergen and Stavanger, allowing us to exclude the largest part of the human induced seismicity from the correlation analysis of the earthquake occurrence and atmospheric precipitation. The last, local catalogue has been maintained in the framework of the NEONOR2 project 'Neotectonics in Nordland - Implications for petroleum exploration' 30. The NEONOR2 catalogue is also included into the NNSN catalogue 5 and is based on 27 seismological stations which have been in operation during the period of 2013-2016 along the coast of the Nordland county, northern Norway 30. This detailed and time-restricted catalogue has been carefully cleaned from the artificial seismological events and has been additionally used, as one of the most reliable datasets, to understand the recent seismicity pattern in the Nordland area (e.g. the Meløy area).

The atypically low-velocity upper mantle beneath Western Norway and the Nordland area is already recognizable on the seismological images at the scale of the North Atlantic region 16 or at Europe-scale 45. However, the resolution of the mentioned-above large-scale tomographies, which show a rather general trend of the regional velocity pattern beneath western Scandinavia, is not sufficiently detailed for our purposes. Therefore, more detailed seismological studies 15,17 have been considered to compare the areas with the intensive seismicity and anomalous upper mantle. The main source of the deep structure beneath south-western Norway is the upper-mantle P- and S-wave velocities in a digital form based on multiscale, finite-frequency P and S 3D seismic tomography 17. For upper-mantle structure below the Nordland area, the recently published results of P- and S-wave traveltime tomography 15 were applied.

For the regional overview of the normal annual precipitation over Scandinavia (Fig. 1b), three datasets have been used: 19 has been used for Norway, 46 has been taken as the representative one for Sweden and 47 has been used to cover the adjacent Danish and Finnish territories.

Digital gridded data of the daily amount of water due to rain and snow melt for the period of 1959-2016 34 have been used in order to estimate the variations of water volume at the Earth's surface due to raining and melting of snow within the study area. These maps have been provided by the Norwegian Water Resources and Energy Directorate (NVE) and are derived from the atmospheric precipitation and snow melt model of Norway 31-33.

The first part of the present study concerned the spatial relationship between the deep P- and S-wave velocity anomalies and localized seismicity. This has been done by a comparison of all available upper-mantle velocity models 14-18,45,48-52 and modelled low-density upper mantle 28,29 with the observed seismicity 4,5,30 in general at the large scale. The detailed comparative analysis has been performed by plotting together the upper mantle anomalies from most recent seismic tomographies 15,17 and earthquakes within two areas with increased seismicity in Western Norway and in the Nordland area (Fig. 2).

The second part of our study was an attempt to find a possible influence of changes in atmospheric precipitation on the intensity of the shallow seismicity (down to 5 km depth) within four regions, such as Western Norway and the Meløy area, including the offshore areas of Western Norway (Figs. 1b). The Western Norway and Meløy areas have been chosen as representative for the regional and local areas with both increased seismicity and atmospheric precipitation. In addition, the offshore areas adjacent to Western Norway (Fig. 1b) have been considered to see if there is also a relationship between seismicity and precipitation within the closely located offshore region. The statistical comparison has been done for each particular area by using the number of shallow earthquakes 5,30 and variations in total water volume per day, originated from rain and snow melt 31-34, for the period of 2005-2016. It was assumed that the volume of groundwater correlates with the total water volume at the Earth's surface and that the groundwater mainly flows in the same direction as the surface water flux. Therefore, the calculated total water volume at the surface within the investigated areas over the mainland has been restricted to the drainage basins of the particular rivers based on a spatial distribution of discharge areas in Norway 53. The watersheds between the drainage basins has been taken as limits for the large region (Western Norway), whereas limits of the Meløy area have been chosen to cover the densely distributed earthquakes within the smaller region.

In general, cross correlation between the original data on changes of water volume at the surface and number of earthquakes is problematic due to a reason that changes of surface water volume represent a continuous process, whereas earthquakes are rather discrete events. On the other hand, a high number of earthquakes have been registered for a long-time interval in Western Norway and the Nordland area. In this case, the recorded seismicity can be considered as a continuous process which represents occurrence rates of earthquakes. To avoid an influence of short-time delays, a moving average has been applied to all data sets prior to the correlation analysis, helping us to enhance the existing correlation. A 30-days moving average has been applied for ten-year time interval in Western Norway (Fig. 4c), whereas the 7- and 10-

days moving averages have been used in the case of shorter time intervals (1 year, 5 months and less) in Western Norway and the Meløy area (Figs. 3, 4d and 5d). However, it is obvious that fractional number of earthquakes per day is not physically possible, but fractional number of occurrence rate of earthquakes per day is physically correct. Therefore, term of occurrence rate of earthquakes is used for the averaged data of number of earthquakes per day. Correlation analysis has been performed by calculation of the correlation coefficients.

These linear correlation coefficients (Fig. 3) have been calculated with help of function 'CORREL' in Microsoft Excel 2016. Based on the calculated correlation coefficients, graphical comparison has been also done by plotting together graphs with the averaged water volume at the surface and occurrence rate of earthquakes (Figs. 4c, d and 5d).

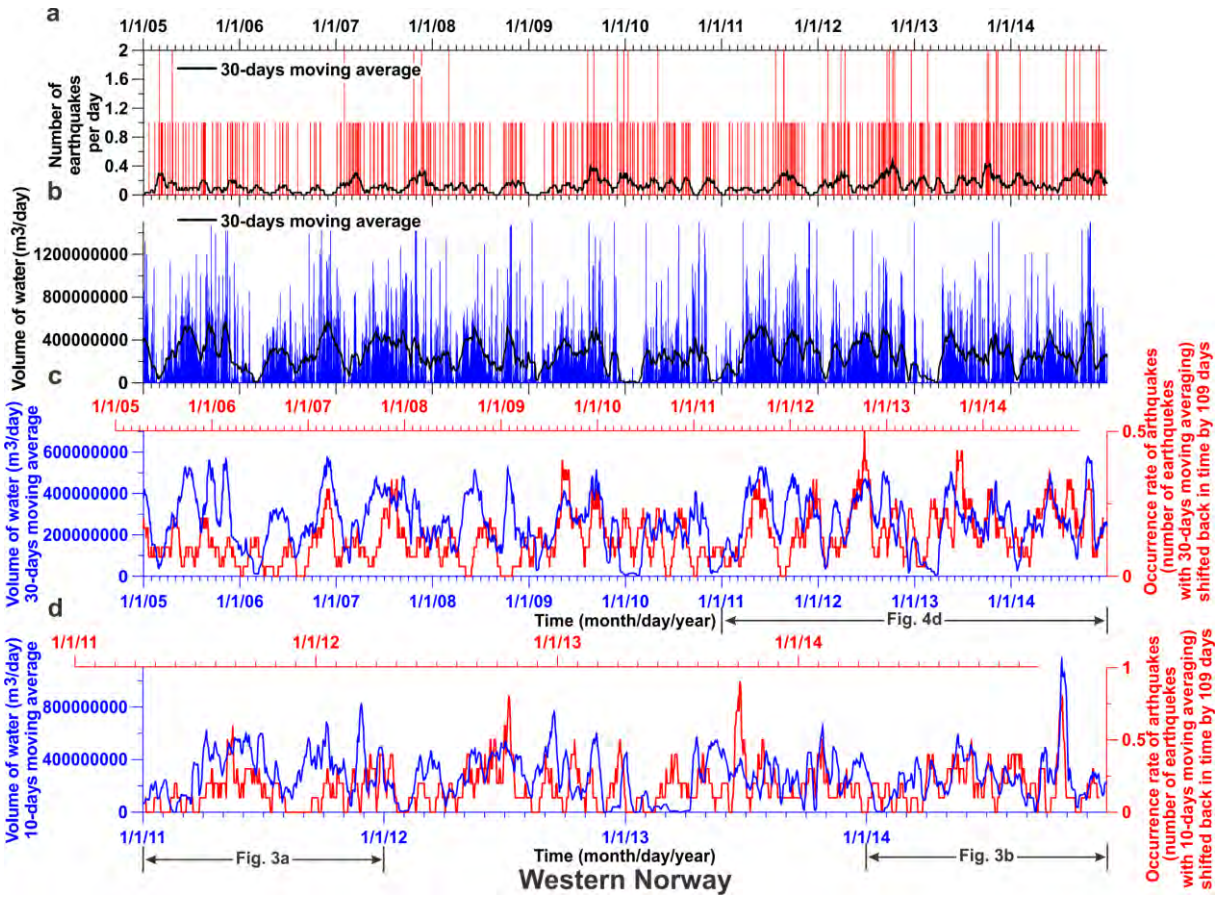

Figure 4 a), Number of shallow (not deeper than 5 km) earthquakes per day 5 in Western Norway in the period 2005-2014. Earthquakes with undefined depth are also included. b) Total volume of precipitation-derived water at the Earth's surface in Western Norway 31,32,34. 30-day moving average is shown by the black line in a and b. c and d) Correlation between the occurrence rate of earthquakes, represented by the 30- and 10-day moving averages, shifted by 109 days compared to a, and the 30- and 10-day averaged volume of water from b, respectively.

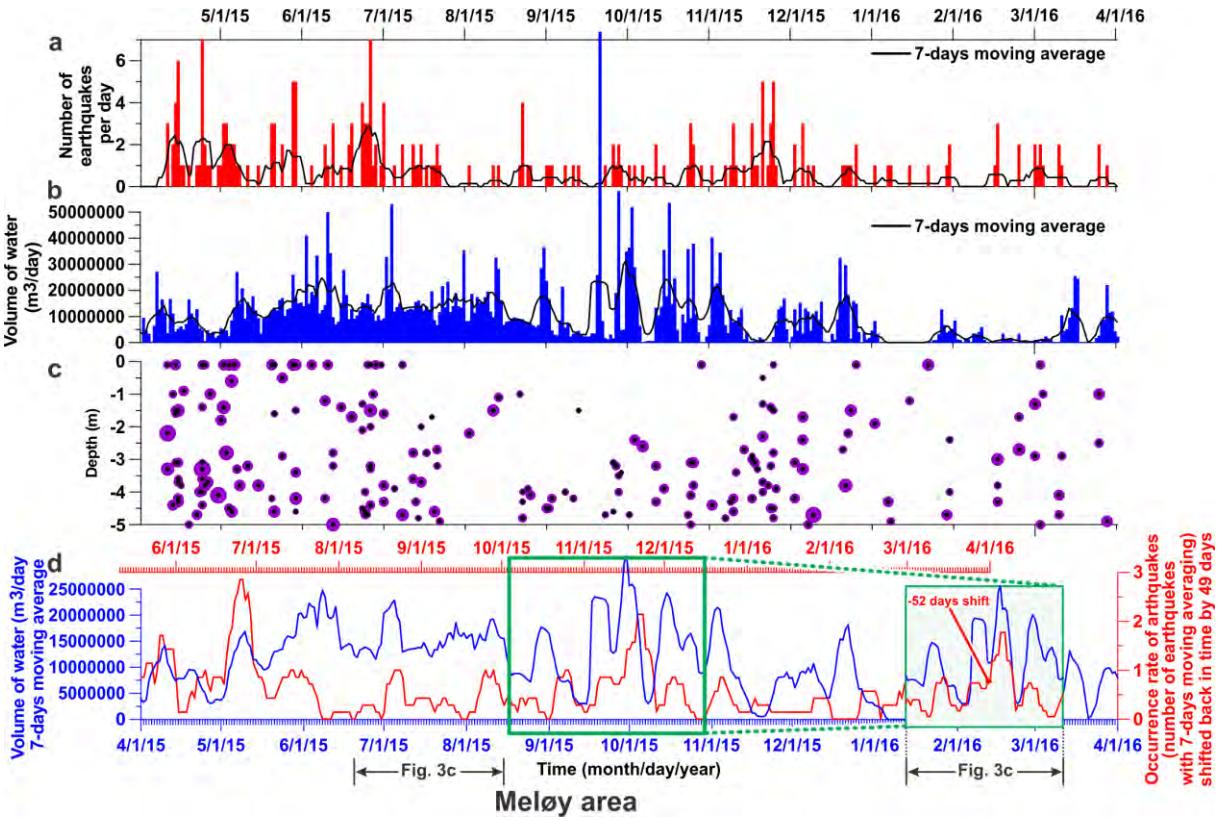

Figure 5 a) Number of shallow (not deeper than 5 km) earthquakes per day in the Meløy area (01.04.2015-01.04.2016) [30]. Earthquakes with undefined depth are also included. b) Total volume of precipitation-derived water at the Earth's surface in the Meløy area [31,32,34]. 7-day moving average is shown by the black line in a and b. c) Location of earthquakes with depth (size of circles reflects magnitude of earthquakes). d) Correlation between the occurrence rate of earthquakes, represented by the 7-day moving averages, shifted by -49 (-52) days compared to a, and the averaged volume of water from b.

6. References

1 Isacks, B. L. in Geophysics 1061-1071 (Springer US, 1989).

2 Stein, S. & Klosko, E. Earthquake mechanisms and plate tectonics. International Geophysics 81, 69-78, doi:10.1016/S0074-6142(02)80210-8 (2002).

3 Talwani, P. E. Intraplate Earthquakes. (Cambridge University Press, 2014).

4 FENCAT. Catalog of earthquakes in Northern Europe, <http://www.seismo.helsinki.fi/english/bulletins/index.html> (2017).

5 NNSN. Norwegian National Seismic Network, <http://seismo.geo.uib.no/> (2016).

6 Olesen, O. et al. Neotectonics, seismicity and contemporary stress field in Norway – mechanisms and implications, 2013).

7 Bungum, H., Lindholm, C. & Faleide, J. I. Postglacial seismicity offshore mid-Norway with emphasis on spatio-temporal-magnitudal variations. Mar Petrol Geol 22, 137-148 (2005).

8 Fejerskov, M., Lindholm, C. D., Myrvang, A. & Bungum, H. Crust stress in and around Norway; a compilation of in situ stress observations.; Dynamics of the Norwegian margin. Geological Society Special Publications 167, 441-449 (2000).

9 Byrkjeland, U., Bungum, H. & Eldholm, O. Seismotectonics of the Norwegian continental margin. Journal of Geophysical Research: Solid Earth 105, 6221-6236, doi:doi:10.1029/1999JB900275 (2000).

10 Fjeldskaar, W., Lindholm, C., Dehls, J. F. & Fjeldskaar, I. Postglacial uplift, neotectonics and seismicity in Fennoscandia. Quaternary Sci Rev 19, 1413-1422, doi:https://doi.org/10.1016/S0277-3791(00)00070-6 (2000).

11 Olsen, L., Sveian, H., Bergstrøm, B., Ottesen, D. & Rise, L. in Quaternary Geology of Norway Vol. 13 (eds L. Olsen, O. Fredin, & O. Olesen) 27-78 (Geological Survey of Norway Special Publication, 2013).

12 Dowdeswell, J. A., Ottesen, D. & Rise, L. Rates of sediment delivery from the Fennoscandian ice sheet through an ice age. Geology [Boulder] 38, 3-6, doi:10.1130/g25523.1 (2010).

13 Sigmond, E. M. O. (Geological Survey of Norway, 2002).

14 Bannister, S. C., Ruud, B. O. & Husebye, E. S. Tomographic estimates of sub-Moho seismic velocities in Fennoscandia and structural implications. Tectonophysics 189, 37-53 (1991).

15 Hejrani, B., Balling, N., Jacobsen, B. H. & England, R. Upper-mantle velocities below the Scandinavian Mountains from P- and S-wave traveltime tomography. Geophys J Int 208, 177-192, doi:10.1093/gji/ggw370 (2017).

16 Pilidou, S., Priestley, K., Debayle, E. & Gudmundsson, O. Rayleigh wave tomography in the North Atlantic; high resolution images of the Iceland, Azores and Eifel mantle plumes. Lithos 79, 453-474, doi:10.1016/j.lithos.2004.09.012 (2005).

17 Kolstrup, M. L., Hung, S.-H. & Maupin, V. Multiscale, finite-frequency P and S tomography of the upper mantle in the southwestern Fennoscandian Shield. Geophys J Int 202, 190-218, doi:10.1093/gji/ggv130 (2015).

18 Maupin, V. et al. The deep structure of the Scandes and its relation to tectonic history and present day topography. Tectonophysics 602, 15-37, doi:10.1016/j.tecto.2013.03.010 (2013).

19 NMI. Kart med nedbørnormal for Norge: Gjelder for normalperioden 1961–1990, <http://met.no/Klima/Klimastatistikk/Klimanormaler/Nedbor/> (2013).

20 Assumpcao, M. et al. Intraplate seismicity in SE Brazil: stress concentration in lithospheric thin spots. Geophys J Int 159, 390-399(310) (2004).

21 Slagstad, T., Maystrenko, Y., Maupin, V. & Gradmann, S. An extinct, Late Mesoproterozoic, Sveconorwegian mantle wedge beneath SW Fennoscandia, reflected in seismic tomography and assessed by thermal modelling. Terra Nova, n/a-n/a, doi:10.1111/ter.12310 (2018).

22 Chu, R., Wei, L., Helmberger, D. V. & Gurnis, M. Hidden hotspot track beneath the Eastern United States. Nature Geoscience 6, 963-966, doi:10.1038/ngeo1949 (2013).

23 Becker, T. W. et al. Western US intermountain seismicity caused by changes in upper mantle flow. Nature 524, 458-461, doi:10.1038/nature14867 (2015).

24 Biryol, C. B., Wagner, L. S., Fischer, K. M. & Hawman, R. B. Relationship between observed upper mantle structures and recent tectonic activity across the Southeastern United States. Journal of Geophysical Research: Solid Earth 121, 3393-3414, doi:10.1002/2015jb012698 (2016).

25 Liu, L. & Zoback, M. D. Lithospheric strength and intraplate seismicity in the New Madrid seismic zone. Tectonics 16, 585-595, doi:10.1029/97tc01467 (1997).

26 USArray. USArray - A continental-scale seismic observatory, <http://www.usarray.org/> (2017).

27 Levandowski, W., Zellman, M. & Briggs, R. Gravitational body forces focus North American intraplate earthquakes. Nature Communications 8, 14314, doi:10.1038/ncomms14314 (2017).

28 Maystrenko, Y. P., Olesen, O., Gernigon, L. & Gradmann, S. Deep structure of the Lofoten-Vesteralen segment of the Mid-Norwegian continental margin and adjacent areas derived from 3-D density modeling. Journal of Geophysical Research: Solid Earth 122, 1402-1433, doi:10.1002/2016jb013443 (2017).

29 Maystrenko, Y. P., Olesen, O., Ebbing, J. & Nasuti, A. Deep structure of the northern North Sea and south-western Norway based on 3D density and magnetic modelling. Norw J Geol 97, 169-210, doi:10.17850/njg97-3-01 (2017).

30 Janutyte, I., Lindholm, C. & Olesen, O. Relation between seismicity and tectonic structures offshore and onshore Nordland, northern Norway. Norw J Geol 97, 161-175, doi:10.17850/njg97-03-02 (2017).

31 Saloranta, T. M. Operational snow mapping with simplified data assimilation using the seNorge snow model. Journal of Hydrology 538, 314-325, doi:10.1016/j.jhydrol.2016.03.061 (2016).

32 Saloranta, T. M. New version (v.1.1.1) of the seNorge snow Model and Snow Maps for Norway. Vol. Rapport 6-2014 30 (Norwegian Water Resources and Energy Directorate, 2014).

33 Saloranta, T. M. Simulating more accurate snow maps for Norway with MCMC parameter estimation method. The Cryosphere Discuss. 2014, 1973-2003, doi:10.5194/tcd-8-1973-2014 (2014).

34 Senorge. Rain and snow melt maps, <http://www.senorge.no/index.html?p=senorgeny&st=water&m=bmNVEGrey%3BMapLayer_qtt%3B&l=en&d=1501668000000&e=-1578728%7C6122545%7C2582816%7C8249375&fh=0%3B2468> (2017).

35 Gudmundsson, O., Fjeldskaar, I. & Gjesdal, O. Fracture-generated permeability and groundwater yield in Norway. Norges qeoloqiske undersøkelse Bulletin 439, 61-69 (2002).

36 Shapiro, S. A. Fluid-induced seismicity. (Cambridge University Press, 2015).

37 Hainzl, S., Kraft, T., Wassermann, J., Igel, H. & Schmedes, E. Evidence for rainfall-triggered earthquake activity. Geophysical Research Letters 33, L19303-L19303, doi:10.1029/2006gl027642 (2006).

38 Muco, B. Statistical investigation on possible seasonality of seismic activity and rainfall-induced earthquakes in Balkan area. Physics of the Earth and Planetary Interiors 114, 119-127 (1999).

39 Martini, F., Bean, C. J., Saccorotti, G., Viveiros, F. & Wallenstein, N. Seasonal cycles of seismic velocity variations detected using coda wave interferometry at Fogo volcano, São Miguel, Azores, during 2003–2004. Journal of Volcanology and Geothermal Research 181, 231-246, doi:https://doi.org/10.1016/j.jvolgeores.2009.01.015 (2009).

40 Costain, J. K. Ground water recharge as the trigger of naturally occurring intraplate earthquakes. Special Publication - Geological Society of London 432, 91-118, doi:10.1144/sp432.9 (2016).

41 Talwani, P., Cobb, J. S. & Schaeffer, M. F. In situ measurements of hydraulic properties of a shear zone in northwestern South Carolina. Journal of Geophysical Research 104, 14, doi:10.1029/1999jb900059 (1999).

42 Storrø, G. Hydrogeologiske og maringeologiske undersøkelser av Nordbreigrunnen i Meløy kommune. Nordland fylke., 13 (Geological Survey of Norway (NGU), Trondheim, 2013).

43 Hovland, M. & Judd, A. G. Seabed pockmarks and seepages; impact on geology, biology and the marine environment. (Graham & Trotman, London, United Kingdom, 1988).

44 Shapiro, S. A. et al. Fluid induced seismicity guided by a continental fault; injection experiment of 2004/2005 at the German Deep Drilling Site (KTB). Geophysical Research Letters 33, doi:10.1029/2005gl024659 (2006).

45 Weidle, C. & Maupin, V. An upper-mantle S-wave velocity model for northern Europe from Love and Rayleigh group velocities. Geophys J Int 175, 1154-1168, doi:10.1111/j.1365-246X.2008.03957.x (2008).

46 SMHI. Dataserier med normalvärden för perioden 1961-1990, <https://www.smhi.se/klimatdata/meteorologi/dataserier-med-normalvarden-1.7354> (2017).

47 Tveito, O. E. et al. Nordic precipitation maps. Vol. DNMI-Report 22/97 Klima (Norwegian Meteorological Institute, 1997).

48 Rickers, F., Fichtner, A. & Trampert, J. The Iceland-Jan Mayen plume system and its impact on mantle dynamics in the North Atlantic region; evidence from full-waveform inversion. Earth and Planetary Science Letters 367, 39-51, doi:10.1016/j.epsl.2013.02.022 (2013).

49 Wawerzinek, B., Ritter, J. R. R. & Roy, C. New constraints on the 3D shear wave velocity structure of the upper mantle underneath Southern Scandinavia revealed from non-linear tomography. Tectonophysics 602, 38-54, doi:DOI 10.1016/j.tecto.2012.12.033 (2013).

50 Hejrani, B., Balling, N., Jacobsen, B. H. & Tilmann, F. Upper-mantle P- and S-wave velocities across the northern Tornquist Zone from traveltime tomography. Geophys J Int 203, 437-458, doi:10.1093/gji/ggv291 (2015).

51 Medhus, A. B. et al. Upper-mantle structure beneath the Southern Scandes Mountains and the Northern Tornquist Zone revealed by P-wave traveltime tomography. Geophys J Int 189, 1315-1334, doi:DOI 10.1111/j.1365-246X.2012.05449.x (2012).

52 Bijwaard, H., Spakman, W. & Engdahl, E. R. Closing the gap between regional and global travel time tomography. Journal of Geophysical Research 103, 30, doi:10.1029/98jb02467 (1998).

53 Borgvang, S. A. et al. Riverine inputs and direct discharges to Norwegian coastal waters - 2005. Vol. Report TA-2245/2007 (Norwegian Institute for Water Research, 2005).

54 NSIDC, W. a. (ed NSIDC: National Snow and Ice Data Center) (Boulder, Colorado USA., 2012).

Acknowledgments

This study has been partially supported in the framework of the NEONOR2 project. We extend our gratitude to Sofie Gradmann, Conrad Lindholm, Valerie Maupin, Jan Michalek and Lars Ottelmöller for support with data and fruitful discussions.

Author contributions

Y.P.M. proposed the main idea of this study, performed the scientific analysis and interpretation of the obtained results. M.B. helped to find evidences of the groundwater flow through the crystalline basement, participated in calculation of the correlation between the seismicity and precipitation. O.O. supervised monitoring of seismicity and neotectonics in Norway in framework of the NEONOR2 project, participated in calculation of the correlation between the seismicity and precipitation. T.M.S. was responsible for the precipitation-related part of the study and prepared the digital gridded data of the daily amount of water due to rain and snow melt for the period of 1959-2016 in Norway. T.S. was responsible for the geology and tectonic development of the study areas. All authors deeply participated in discussing the results, in writing the text and in approval of the manuscript.

Chapter 14: Neotectonic map, Norway and adjacent areas

Scale: 1:3 000 000

Keiding, M., Olesen, O. & Dehls, J.

MAP DESCRIPTION

The mapped area includes Norway, Denmark, Sweden, Finland, Svalbard and part of the North Sea, the Norwegian Sea, the Greenland Sea and the western Barents Sea.

Neotectonics is the study of motion and deformation of Earth's crust that are current or recent in geologic time, here considered to be the Neogene and the Quaternary. Figure 1 shows Neogene deformation, while the main map and Figures 2 and 3 show Quaternary deformation.

There are nine major components of neotectonic deformation in the map area:

1. Oceanic spreading in the Norwegian-Greenland Sea

2. Neogene uplift and erosion of the mainland, Svalbard and the Barents Sea

3. Pliocene-Pleistocene deposition on the Norwegian margin

4. Submarine slides on the Norwegian margin

5. Quaternary volcanism on Svalbard and Jan Mayen

6. Quaternary glacial isostatic adjustment

7. The postglacial Lapland Fault Province

8. The state of stress

9. Seismicity

1. Oceanic spreading

Spreading in the Norwegian-Greenland Sea initiated in early Eocene (Talwani and Eldholm, 1977). The ridge push force from the oceanic spreading ridges probably causes NW-SE compressive stresses in Fennoscandia.

2. Neogene uplift and erosion

South Norway and Lofoten were uplifted approximately 1 km during the Neogene, mainly during Pliocene-Pleistocene (Fig. 1 on attached poster). The corresponding erosion of the coastal areas is estimated to have reached a maximum of 800-1000 m in South Norway and slightly more in Lofoten (Riis, 1996). The Barents Sea and Svalbard have been subject to considerable uplift and erosion, with a maximum of about 3 km on Svalbard (Henriksen et al., 2011).

3. Pliocene-Pleistocene deposition

Thick sediment packages were deposited on the Norwegian margin due to the uplift and erosion during the Pliocene-Pleistocene (Fig. 1 on attached poster). The thickest sediment packages of approximately 3 km were deposited in the northern Norwegian Sea (Faleide et al., 1996). Most of the deposition probably occurred due to glacial processes during the Quaternary.

4. Submarine slides

Large submarine slides are abundant along the Norwegian margin, and a number of these occurred during the Quaternary (Evans et al., 2005), as shown in the map. Two huge slides occurred in recent time: the Trænadjupet slide dated to 4 000 yrs B.P (Laberg et al., 2000) and the Storegga slide at 8 200 yrs B.P. (Solheim et al., 2005).

5. Volcanism

In northern Spitsbergen, Svalbard, there are several Quaternary volcanic extrusives and dykes. The best known of these is the Sverrefjellet volcano, which erupted around 1 My B.P. (Treimann, 2012). The volcanic island Jan Mayen hosts an active volcano, the Beerenberg volcano, which had its last eruption in 1970.

6. Glacial isostatic adjustment

The Quaternary glaciations caused repeated loading and unloading of the lithosphere beneath Fennoscandia. Today, the region is still uplifting due to the glacial isostatic adjustment following the last deglaciation which ended around 11 500 yrs B.P. The map shows contours from a land uplift model based on GPS observations and levelling and a geophysical model of the glacial isostatic adjustment (Vestøl et al., 2016). The present-day uplift has a maximum of around 10 mm/yr in the Gulf of Bothnia and causes extensional horizontal strain rates in most of Fennoscandia (Fig. 2, Keiding et al., 2015).

7. The postglacial Lapland Fault Province

A number of pronounced postglacial fault scarps are present in northern Fennoscandia (e.g. Lagerbäck and Sundh, 2008; Olesen et al., 2013; Sutinen et al., 2014). Several of the scarps have confirmed reverse displacement, and many are located in older weakness zones. The reverse Stuoragurra fault in Norway can be followed for more than 80 km (Fig. 3 on attached map).

The fault scarps probably formed due to an extraordinary pulse of seismicity, including a number of M>7 earthquakes, which occurred around the end of the last deglaciation. The seismicity is thought to have been triggered by the glacial unloading of the crust, which allowed the long-term compressive stress from plate tectonic forces to be released, perhaps aided by high pore pressures due to melt water percolating into the crust (Muir Wood, 1989). During recent years, Swedish and Finnish fault scarps and associated landslides have been mapped in detail using LiDAR (e.g. Mikko et al., 2015; Palmu et al., 2015).

8. The state of stress

Stress observations from measurements in deep boreholes are shown as azimuth of the maximum compressive stress from the World Stress Map database (Heidbach et al., 2016) as well as new data in Nordland (Olesen et al., 2018). A trend of NW-SE compressive stress is apparent on the Norwegian margin and in large parts of Fennoscandia, whereas other regions such as the Barents Sea and the North Sea show considerable variation in stress azimuth.

Indirect stress observations are obtained from earthquake focal mechanisms. The map shows a compilation of Norwegian, Swedish and Finnish earthquake focal mechanisms (Keiding et al., 2015) as well as new focal mechanisms in Nordland (Olesen et al., 2018). On the continental margin, the focal mechanisms typically indicate reverse faulting with NW-SE compressive axes. On land, the focal mechanisms indicate a larger variation between strike-slip, reverse and normal faulting.

9. Seismicity

The map shows earthquake locations and magnitudes during 1980–2012 (FENCAT, 2018). The present-day seismicity in Fennoscandia is low to intermediate, with the highest moment release along the continental margin and in western Norway. Earthquakes occur at relatively large depths of 10-30 km on the continental margin and at shallower depth on land. The largest historical earthquake in mainland Norway was the 31 August 1819 Lurøy earthquake in Nordland with MS=5.8.

10. References

Evans, D., Z. Harrison, P. M. Shannon, J. S. Laberg, T. Nielsen, S. Ayers, R. Holmes, R. J. Hoult, B. Lindberg, H. Haflidason, D. Long, A. Kuijpers, E. S. Andersen and P. Bryn, 2005. Palaeoslides and other mass failures of Pliocene to Pleistocene age along the Atlantic continental margin of NW Europe. Marine and Petroleum Geology 22, 1131–1148.

Faleide, J. I., A. Solheim, A. Fiedler, B. O. Hjelstuen, E. S. Andersen and K. Vanneste, 1996. Late Cenozoic evolution of the western Barents Sea-Svalbard continental margin. Global and Planetary Change 12, 53–74.

FENCAT, 2018. A joint Fennoscandian earthquake catalogue courtesy of University of Helsinki. Retrieved January 2018 from http://www.helsinki.fi/geo/seismo/english/bulletins/.

Heidbach, O., M. Rajabi, K. Reiter, M. Ziegler and WSM Team 2016. World Stress Map 2016. GFZ Data Services. http://doi.org/10.5880/WSM.2016.001.

Henriksen, E., H. M. Bjørnseth, T. K. Hals, T. Heide, T. Kiryukhina, O. S. Kløvjan, G. B. Larssen, A. E. Ryseth, K. Rønning, K. Sollid and A. Stoupakova, 2011. Uplift and erosion of the greater Barents Sea: impact on prospectivity and petroleum systems. Geological Society, London, Memoirs 35, 271–281.

Keiding, M., C. Kreemer, C. D. Lindholm, S. Gradmann, O. Olesen and H. P. Kierulf, 2015. A comparison of strain rates and seismicity for Fennoscandia: depth dependency of deformation from glacial isostatic adjustment. Geophysical Journal International 202, 1021–1028.

Kierulf, H. P., H. Steffen, M. J. R. Simpson, M. Lidberg, P. Wu and H. Wang, 2014. A GPS velocity field for Fennoscandia and a consistent comparison to glacial isostatic adjustment models. Journal of Geophysical Research 119, 1–17.

Laberg, J., S., and T. O. Vorren, 2000. The Trænadjupet Slide, offshore Norway - morphology, evacuation and triggering mechanisms. Marine Geology 171, 95–114.

Lagerbäck, R. and M. Sundh, 2008. Early Holocene faulting and paleoseismicity in northern Sweden. Geological Survey of Sweden, Research Paper C 836.

Mikko, H., C. A. Smith, B. Lund, M. V. S. Ask and R. Munier, 2015. LiDAR-derived inventory of post-glacial fault scarps in Sweden. GFF 137, 334–338.

Muir Wood, R., 1989. Extraordinary deglaciation reverse faulting in northern Fennoscandia. In: Gregersen, S., and P. W. Basham (eds.) Earthquakes at North-Atlantic Passive Margins: Neotectonics and Postglacial Rebound, NATO ASI Series, 141–173.

Olesen, O., H. Bungum, J. Dehls, C. Lindholm, C. Pascal and D. Roberts, 2013. Neotectonics, seismicity and contemporary stress field in Norway - mechanisms and implications. In: Olsen, L., O. Fredin and O. Olesen (eds.) Quaternary Geology of Norway, Geological Survey of Norway Special Publication 13, 145–174.

Olesen, O., M. Ask, D. Ask, J. F. Dehls, S. Gradmann, I. Janutyte, M. Keiding, H. P. Kierulf, T. R. Lauknes, C. Lindholm, Y. Maystrenko, J. Michalek, L. Olsen, L. Ottemöller, D. Ottesen, F. Riis, L. Rise, 2018. NEONOR2 final report – Neotectonics in Nordland – implications for petroleum exploration. NGU Report 2018.010.

Ottesen, D., L. Rise, E. S. Andersen, T. Bugge and T. Eidvin, 2010. Geological evolution of the Norwegian continental shelf between 61ºN and 68ºN during the last 3 million years. Norwegian Journal of Geology 89, 251–265.

Ottesen, D., J. A. Dowdeswell and T. Bugge, 2014. Morphology, sedimentary infill and depositional environments of the Early Quaternary North Sea Basin (56°–62°N). Marine and Petroleum Geology 56, 123–146.

Palmu, J.-P., A. E. K. Ojala, T. Ruskeeniemi, R. Sutinen and J. Mattila, 2015. LiDAR DEM detection and classification of postglacial faults and seismically-induced landforms in Finland: a paleoseismic database. GFF 137, 344–352.

Riis, 1996. Quantification of Cenozoic vertical movements of Scandinavia by correlation of morphological surfaces with offshore data. Global and Planetary Change 12, 331–357.

Solheim, A., K. Berg, C. F Forsberg and P. Bryn, 2005. The Storegga Slide complex: repetitive large scale sliding with similar cause and development. Marine and Petroleum Geology 22, 97–107.

Sutinen, R., E. Hyvönen, M. Middleton and T. Ruskeeniemi, 2014. Airborne LiDAR detection of postglacial faults and Pulju moraine in Palojärvi, Finnish Lapland. Global and Planetary Change 115, 24–32.

Talwani, M. and O. Eldholm, 1977. Evolution of the Norwegian-Greenland Sea. Geological Society of America Bulletin 88, 969–999.

Treimann, A. H., 2012. Eruption age of the Sverrefjellet volcano, Spitsbergen Island, Norway. Polar Research 31, 1–7.

Vestøl, O. et al., 2016. NKG2016LU – A new land uplift model for Fennoscandia and the Baltic region, courtesy of NKG Working Group of Geoide and Height Systems.

Reference to the map:

Keiding, M., O. Olesen, J. Dehls, 2018. Neotectonic map of Norway and adjacent areas. Geological Survey of Norway.

Acknowledgements: The map was produced as part of the NEONOR2 project. Dag Ottesen, Leif Rise, Fridtjof Riis, Henrik Mikko, Antti Ojala, Peter Japsen and Olav Vestøl contributed data or other information to the map.

NEOTECTONIC MAP
NORWAY AND ADJACENT AREAS

Scale: 1:3 000 000

MAP DESCRIPTION

The mapped area includes Norway, Denmark, Sweden, Finland, Svalbard and part of the North Sea, the Norwegian Sea, the Greenland Sea and the western Barents Sea.

Neotectonics is the study of motion and deformation of Earth's crust that are current or recent in geologic time, here considered to be the Neogene and the Quaternary. Figure 1 shows Neogene deformation, while the main map and Figures 2 and 3 show Quaternary deformation.

There are nine major components of neotectonic deformation in the map area:
1. Oceanic spreading in the Norwegian-Greenland Sea
2. Neogene uplift and erosion of the mainland, Svalbard and the Barents Sea
3. Pliocene-Pleistocene deposition on the Norwegian margin
4. Submarine slides on the Norwegian margin
5. Quaternary volcanism on Svalbard and Jan Mayen
6. Quaternary glacial isostatic adjustment
7. The postglacial Lapland Fault Province
8. The state of stress
9. Seismicity

1. Oceanic spreading
Spreading in the Norwegian-Greenland Sea initiated in early Eocene (Talwani and Eldholm, 1977). The ridge push force from the oceanic spreading ridges probably causes NW-SE compressive stresses in Fennoscandia.

2. Neogene uplift and erosion
South Norway and Lofoten were uplifted approximately 1 km during the Neogene, mainly during Pliocene-Pleistocene (Fig. 1). The corresponding erosion of the coastal areas is estimated to have reached a maximum of 800-1000 m in South Norway and slightly more in Lofoten (Riis, 1996). The Barents Sea and Svalbard have been subject to considerable uplift and erosion, with a maximum of about 3 km on Svalbard (Henriksen et al., 2011).

3. Pliocene-Pleistocene deposition
Thick sediment packages were deposited on the Norwegian margin due to the uplift and erosion during the Pliocene-Pleistocene (Fig. 1). The thickest sediment packages of approximately 3 km were deposited in the northern Norwegian Sea (Faleide et al., 1996). Most of the deposition probably occurred due to glacial processes during the Quaternary.

4. Submarine slides
Large submarine slides are abundant along the Norwegian margin, and a number of these occurred during the Quaternary (Evans et al., 2005), as shown in the map. Two huge slides occured in recent time: the Trænadjupet slide dated to 4 000 yrs B.P (Laberg et al., 2000) and the Storegga slide at 8 200 yrs B.P. (Solheim et al., 2005).

5. Volcanism
In northern Spitsbergen, Svalbard, there are several Quaternary volcanic extrusives and dykes. The best known of these is the Sverrefjellet volcano, which erupted around 1 My B.P. (Treimann, 2012). The volcanic island Jan Mayen hosts an active volcano, the Beerenberg volcano, which had its last eruption in 1970.

6. Glacial isostatic adjustment
The Quaternary glaciations caused repeated loading and unloading of the lithosphere beneath Fennoscandia. Today, the region is still uplifting due to the glacial isostatic adjustment following the last deglaciation which ended around 11 500 yrs B.P. The map shows contours from a land uplift model based on GPS observations and levelling and a geophysical model of the glacial isostatic adjustment (Vestøl et al., 2016). The present-day uplift has a maximum of around 10 mm/yr in the Gulf of Bothnia and causes extensional horizontal strain rates in most of Fennoscandia (Fig. 2, Keiding et al., 2015).

7. The postglacial Lapland Fault Province
A number of pronounced postglacial fault scarps are present in northern Fennoscandia (e.g. Lagerbäck and Sundh, 2008; Olesen et al., 2013; Sutinen et al., 2014). Several of the scarps have confirmed reverse displacement, and many are located in older weakness zones. The reverse Stuoragurra fault in Norway can be followed for more than 80 km (Fig. 3).

The fault scarps probably formed due to an extraordinary pulse of seismicity, including a number of M>7 earthquakes, which occurred around the end of the last deglaciation. The seismicity is thought to have been triggered by the glacial unloading of the crust, which allowed the long-term compressive stress from plate tectonic forces to be released, perhaps aided by high pore pressures due to melt water percolating into the crust (Muir Wood, 1989). During recent years, Swedish and Finnish fault scarps and associated landslides have been mapped in detail using LiDAR (e.g. Mikko et al., 2015; Palmu et al., 2015).

8. The state of stress
Stress observations from measurements in deep boreholes are shown as azimuth of the maximum compressive stress from the World Stress Map database (Heidbach et al., 2016) as well as new data in Nordland (Olesen et al., 2018). A trend of NW-SE compressive stress is apparent on the Norwegian margin and in large parts of Fennoscandia, whereas other regions such as the Barents Sea and the North Sea show considerable variation in stress azimuth.

Indirect stress observations are obtained from earthquake focal mechanisms. The map shows a compilation of Norwegian, Swedish and Finnish earthquake focal mechanisms (Keiding et al., 2015) as well as new focal mehanisms in Nordland (Olesen et al., 2018). On the continental margin, the focal mechanisms typically indicate reverse faulting with NW-SE compressive axes. On land, the focal mechanisms indicate a larger variation between strike-slip, reverse and normal faulting.

9. Seismicity
The map shows earthquake locations and magnitudes during 1980–2012 (FENCAT, 2018). The present-day seismicity in Fennoscandia is low to intermediate, with the highest moment release along the continental margin and in western Norway. Earthquakes occur at relatively large depths of 10-30 km on the continental margin and at shallower depth on land. The largest historical earthquake in mainland Norway was the 31 August 1819 Lurøy earthquake in Nordland with MS=5.8.

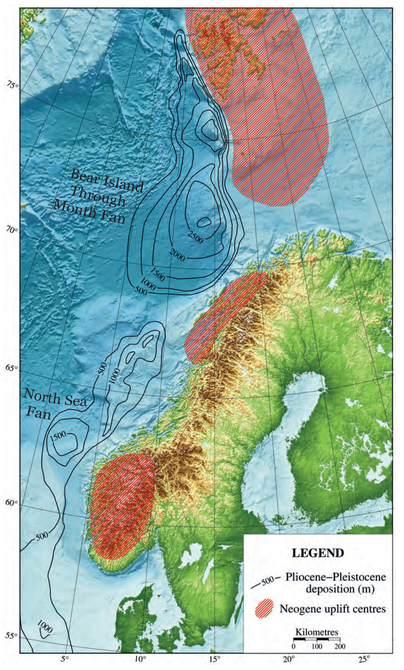

Figure 1: Neogene uplift centres and regions of Pliocene-Pleistocene deposition. The data are modified from Riis (1996), Faleide et al. (1996), Ottesen et al. (2010, 2014) and Henriksen et al. (2011).

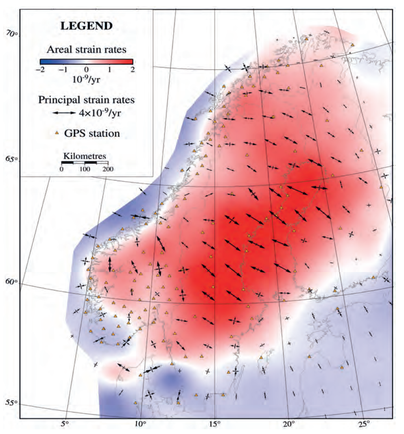

Figure 2: Horizontal strain rates estimated from continuous GPS velocities from Kierulf et al. (2014). The contour colours show areal strain rates defined as $\frac{1}{2}(\varepsilon_{xx}+\varepsilon_{yy})$, where x is longitude and y is latitude. Positive values of areal strain rates indicate expansion and negative values indicate contraction. The arrows show the principal strain rates, i.e. the largest and smallest strain rates in the horizontal plane. Figure modified from Keiding et al. (2015).

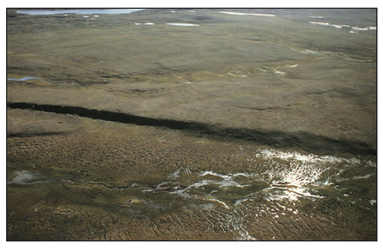

Figure 3: Aerial photo of the Stuoragurra fault in the Lapland Fault province, looking east, approximately 12 km NNE of Masi. The scarp has a maximum of 7 m height. Photo: Odleiv Olesen, 1989.

References

Evans, D., Z. Harrison, P. M. Shannon, J. S. Laberg, T. Nielsen, S. Ayers, R. Holmes, R. J. Hoult, B. Lindberg, H. Haflidason, D. Long, A. Kuijpers, E. S. Andersen and P. Bryn, 2005. Palaeoslides and other mass failures of Pliocene to Pleistocene age along the Atlantic continental margin of NW Europe. Marine and Petroleum Geology 22, 1131–1148.

Faleide, J. I., A. Solheim, A. Fiedler, B. O. Hjelstuen, E. S. Andersen and K. Vanneste, 1996. Late Cenozoic evolution of the western Barents Sea-Svalbard continental margin. Global and Planetary Change 12, 53–74.

FENCAT, 2018. A joint Fennoscandian earthquake catalogue courtesy of University of Helsinki. Retrieved January 2018 from http://www.helsinki.fi/geo/seismo/english/bulletins/.

Heidbach, O., M. Rajabi, K. Reiter, M. Ziegler and WSM Team 2016. World Stress Map 2016. GFZ Data Services. http://doi.org/10.5880/WSM.2016.001.

Henriksen, E., H. M. Bjørnseth, T. K. Hals, T. Heide, T. Kiryukhina, O. S. Kløvjan, G. B. Larssen, A. E. Ryseth, K. Rønning, K. Sollid and A. Stoupakova, 2011. Uplift and erosion of the greater Barents Sea: impact on prospectivity and petroleum systems. Geological Society, London, Memoirs 35, 271–281.

Keiding, M., C. Kreemer, C. D. Lindholm, S. Gradmann, O. Olesen and H. P. Kierulf, 2015. A comparison of strain rates and seismicity for Fennoscandia: depth dependency of deformation from glacial isostatic adjustment. Geophysical Journal International 202, 1021–1028.

Kierulf, H. P., H. Steffen, M. J. R. Simpson, M. Lidberg, P. Wu and H. Wang, 2014. A GPS velocity field for Fennoscandia and a consistent comparison to glacial isostatic adjustment models. Journal of Geophysical Research 119, 1–17.

Laberg, J., S., and T. O. Vorren, 2000. The Trænadjupet Slide, offshore Norway - morphology, evacuation and triggering mechanisms. Marine Geology 171, 95–114.

Lagerbäck, R. and M. Sundh, 2008. Early Holocene faulting and paleoseismicity in northern Sweden. Geological Survey of Sweden, Research Paper C 836.

Mikko, H., C. A. Smith, B. Lund, M. V. S. Ask and R. Munier, 2015. LiDAR-derived inventory of post-glacial fault scarps in Sweden. GFF 137, 334–338.

Muir Wood, R., 1989. Extraordinary deglaciation reverse faulting in northern Fennoscandia. In: Gregersen, S., and P. W. Basham (eds.) Earthquakes at North-Atlantic Passive Margins: Neotectonics and Postglacial Rebound, NATO ASI Series, 141–173.

Olesen, O., H. Bungum, J. Dehls, C. Lindholm, C. Pascal and D. Roberts, 2013. Neotectonics, seismicity and contemporary stress field in Norway - mechanisms and implications. In: Olsen, L., O. Fredin and O. Olesen (eds.) Quaternary Geology of Norway, Geological Survey of Norway Special Publication 13, 145–174.

Olesen, O., M. Ask, D. Ask, J. F. Dehls, S. Gradmann, I. Janutyte, M. Keiding, H. P. Kierulf, T. R. Lauknes, C. Lindholm, Y. Maystrenko, J. Michalek, L. Olsen, L. Ottemöller, D. Ottesen, F. Riis, L. Rise, 2018. NEONOR2 final report – Neotectonics in Nordland – implications for petroleum exploration. NGU Report 2018.010.

Ottesen, D., L. Rise, E. S. Andersen, T. Bugge and T. Eidvin, 2010. Geological evolution of the Norwegian continental shelf between 61°N and 68°N during the last 3 million years. Norwegian Journal of Geology 89, 251–265.

Ottesen, D., J. A. Dowdeswell and T. Bugge, 2014. Morphology, sedimentary infill and depositional environments of the Early Quaternary North Sea Basin (56°–62°N). Marine and Petroleum Geology 56, 123–146.

Palmu, J.-P., A. E. K. Ojala, T. Ruskeeniemi, R. Sutinen and J. Mattila, 2015. LiDAR DEM detection and classification of postglacial faults and seismically-induced landforms in Finland: a paleoseismic database. GFF 137, 344–352.

Riis, 1996. Quantification of Cenozoic vertical movements of Scandinavia by correlation of morphological surfaces with offshore data. Global and Planetary Change 12, 331–357.

Solheim, A., K. Berg, C. F Forsberg and P. Bryn, 2005. The Storegga Slide complex: repetitive large scale sliding with similar cause and development. Marine and Petroleum Geology 22, 97–107.

Sutinen, R., E. Hyvönen, M. Middleton and T. Ruskeeniemi, 2014. Airborne LiDAR detection of postglacial faults and Pulju moraine in Palojärvi, Finnish Lapland. Global and Planetary Change 115, 24–32.

Talwani, M. and O. Eldholm, 1977. Evolution of the Norwegian-Greenland Sea. Geological Society of America Bulletin 88, 969–999.

Treimann, A. H., 2012. Eruption age of the Sverrefjellet volcano, Spitsbergen Island, Norway. Polar Research 31, 1–7.

Vestøl, O. et al., 2016. NKG2016LU – A new land uplift model for Fennoscandia and the Baltic region, courtesy of NKG Working Group of Geoide and Height Systems.

Reference to the map:
Keiding, M., O. Olesen, J. Dehls, 2018.
Neotectonic map of Norway and adjacent areas.
Geological Survey of Norway.

Projection: Transverse Mercator
Longitude of central meridian: 15° 0′ 00″
Latitude of central meridian: 0° 0′ 00″
Datum: WGS84

Acknowledgements: The map was produced as part of the NEONOR2 project. Dag Ottesen, Leif Rise, Fridtjof Riis, Henrik Mikko, Antti Ojala, Peter Japsen and Olav Vestøl contributed data or other information to the map.

GEOLOGICAL
SURVEY OF
NORWAY

· NGU ·

Geological Survey of Norway
PO Box 6315, Sluppen
N-7491 Trondheim, Norway

Visitor address
Leiv Eirikssons vei 39
7040 Trondheim

Tel (+ 47) 73 90 40 00
E-mail ngu@ngu.no
Web www.ngu.no/en-gb/